
School of Chemical Sciences and Engineering
The University of New South Wales
Australia

# The computational fluid dynamics analysis and optimisation of process vessels used in the manufacture of military propellants and high explosives

A thesis submitted in partial fulfilment of the requirements for the degree of Doctor of Philosophy

By

**JIMMY LEA**
B.Eng (UNSW) and M.Eng (UNSW)

2nd July 2007

*The work in this thesis is dedicated to*

*GOD*

*whom I believe to be the creator of heaven and earth*

# ABSTRACT

This research focuses on the computational fluid dynamics modelling and simulation of the existing reactors and mixing tanks employed by the Australian Defence Industries to manufacture military propellants for gun projectiles and small rockets; high explosives for naval gun projectiles and aerial bombs. The main objective of this research is to gain a thorough understanding of these process vessels via research and to provide recommendations to improve their performance. Reactors and mixing tanks were chosen as the test unit operations because although they contribute significantly to the manufacturing process, reactors have frequently been poorly understood or in the case of mixing tanks, taken for granted. Consequently, there is a lack of comprehensive knowledge to support successful operations of these process vessels. In addition, this research also recommends using photocatalysis technology to destroy liquid wastes produced from such manufacturing activities.

For each product, a full characterisation was provided that included detailed theoretical analyses that presents a unique insight into the hydrodynamics occurring in these process vessels. The credibility of theoretical predictions was demonstrated via qualitative and quantitative validation using particle image velocimetry. Results from characterisation showed that the reactors and mixing tanks employed in the manufacture of military propellants, high explosives or aerial bombs were operating at sub-optimum conditions. To tackle this shortcoming, four ideal geometrical configurations that promised optimum performance were proposed for each of the test studies. These included a designer reactor for the manufacture of military propellants and effective mixing tanks for suspending high explosive particles, blending different high explosives and for manufacturing aerial bombs. The correct implementation of these recommendations will provide an optimum operation that achieves high product throughput and concurrently reduces reject rate.

Research was also conducted to formulate a set of multipurpose design guidelines for a suspension mixing tank. The design template created from the results will provide valuable information to researchers across industries in their quest to optimise any unit suspension mixing tank operated on the principle of mechanical agitation. Finally, modelling of reactive species was conducted on a laboratory-scale photoreactor, involving physical experiments to destroy toxic effluent aqueous phase.



# PUBLICATIONS & PRESENTATIONS

Lea J. and Adesina A.A. [2007], *Characterisation and optimisation of military propellant nitrocellulose*, In press, Chemical Engineering Science

Lea J. and Adesina A.A. [2007], *CFD enhanced multipurpose design guideline for a suspension mixing tank*, In press, International Journal of Chemical Reactor Engineering

Lea J. and Adesina A.A. [2007], *CFD-assisted optimisation of the nitrator design for military propellant production*, ICAEM July 2-4 2007, London, England

Lea J. and Adesina A.A. [2007], *Development of the design guidelines using CFD technology for a particles suspension mixing tank*, ICAEM July 2-4 2007, London, England

Lea J. and Adesina A.A. [2007], *CFD diagnosis of the cyclotol manufacturing plant: product quality and process operation*, Vol 2, Issue 1, Article 2, Page 1-43, Journal of Chemical Product and Process Modelling

Lea J., Reid J. and Adesina A.A. [2007], *CFD simulations of a suspension mixing tank for the pharmaceutical industries*, FLUIDS January 17-19 2007, Gold Coast, Australia

Lea J. and Adesina A.A. [2006], *Avoiding explosive outcomes*, Fluent News, fall issue, 26-27, Fluent USA

Lea J. and Adesina A.A. [2006], *Improving explosives production with fluid modelling,* Engineers Australia, November, 56-57, IEAust

Lea J. and Adesina A.A [2006], *Simulation of the mixing tank for the production of military high explosive RDX/TNT – A computational fluid dynamics approach*, CHEMECA September 17-20 2006, Auckland, New Zealand

Lea J. and Adesina A.A [2006], *Analysis of the mixing tank for cyclotol production*, APCCHE August 27-30 2006, Kuala Lumpur, Malaysia

Lea J., Gehrig A., Flavel P. and Adesina A.A [2005], *Optimisation of the nitrator for the production of nitrocellulose using computational fluid dynamics modelling*, PARARI Nov 8-10, Melbourne, Australia

Lea J., Gehrig A., Flavel P. and Adesina A.A [2005], *Application of numerical method for the characterisation of the nitrator employed for the manufacture of rocket propellant*, SciCADE May 23-27 2005, Nagoya, Japan

Lea J., Gehrig A., Flavel P. and Adesina A.A [2005], *The computational fluid dynamics modelling and simulation of nitrator employed for the manufacture of military propellant*, ICCHMT May 17-20 2005, Paris, France

# ACKNOWLEDGEMENT

I would like to sincerely express my heartfelt appreciation to my academic supervisor, Professor Adesoji A. Adesina for his mentorship and for transferring his technical knowledge to me. I am grateful to my manager, Mr. Paul Flavel of the Australian Defence Industries, for his sponsorship of my study and most importantly for believing in my vision. It would have been impossible to achieve this success without their involvement.

Special thanks go to the lobbying effort made by my friend and colleague, Dr. Patrick O'Flaherty, who also persistently ensured my research progressed without a hitch.

I am grateful to Mr. Andrew Gehrig and Mr. Howard Brettig for their strong support in the first year of my study.

I would like to thank Mr. Chirag Dave for spending a considerable amount of time to proof-read my thesis and Ms. Pamela Mort for providing feedback on the style of writing.

I would like to thank Mr. Daniel Van Orsouw and Mr. Vince Germano for providing excellent IT support in a timely fashion.

I would like to thank Ms. Dianne Ware, Ms. Kathryn Brooks, Ms. Sandra Church and Ms. Cindy Guild for their valuable support in many ways.

I would also like to thank Mr. Robert Hamson for providing assistance with the fabrication of several crucial mechanical components and for his friendship.

Finally but not least, I would like to sincerely thank the many employees of the Australian Defence Industries for their support and friendship which helped ensure the success of this study.

# ORIGINALITY STATEMENT

I hereby declare that this submission is my own work and to the best of my knowledge it contains no materials previously published or written by another person, or substantial proportions of the material which have been accepted for the award of any other degree or diploma at UNSW or any other educational institution, except where due acknowledgement is made in the thesis. Any contribution made to the research by others, with whom I have worked at UNSW or elsewhere, is explicitly acknowledged in the thesis. I also declare that the intellectual content of this thesis is the product of my own work, except to the extent that assistance from others in the project's design and conception or in style, presentation and linguistic expression is acknowledged.

# COPYRIGHT STATEMENT



# AUTHENTICITY STATEMENT

I certify that the Library deposit digital copy is a direct equivalent of the final officially approved version of my thesis. No emendation of content has occurred and if there are any minor variations in formatting, they are the result of the conversion to digital format.

Jimmy Lea, 2nd July 2007

# PAGE OF CONTENTS

# CHAPTER 1: INTRODUCTION

The following brief introduction provides an overview of the contents in each chapter:

*Chapter 1* – This chapter presents the objectives and the scope of this research work. This is followed by an overview of the computational fluid dynamics theory and applications.

*Chapter 2* – The literature review conducted on computational fluid dynamics used for modelling chemical reactors and mixing tanks, the rheology of fluids, the solidification process, statistical methods and photocatalysis is discussed.

*Chapter 3* – This chapter contains the modelling and simulation of the nitrator employed to manufacture nitrocellulose. Nitrocellulose is the main ingredient used to make military propellants and small rockets. The chapter begins with the characterisation of the existing nitrator followed by a recommendation to improve the nitrator performance. A section is dedicated to validation using particle image velocimetry (PIV). This chapter also provides an overview of the volume of fluid (VOF) multiphase model through the application of this model on the drawdown of air in the nitrator.

*Chapter 4* – This chapter details the use of CFD to generate a design template for a suspension mixing tank, which promised optimum performance. Ten important variables were investigated and the behaviour of each of these variables was characterised. The results from this chapter are applicable across the process industry particular in cases where mechanical agitation is used to suspend particles.

*Chapter 5* – The chapter addresses the modelling and simulation of "Research Department eXplosives" (RDX) particles suspended in water. RDX is one of the most powerful conventional explosives commonly used in military applications. The mixture model was used to characterise the suspension of RDX particles in the baffled holding tank. Existing unit operation failed to suspend the RDX particles homogeneously and the RDX particles failed to exit the tank at certain speed. Through this research work, several recommendations were made which ranged from the type impellers, impeller's spacing, size of motor to be installed and relocation of the bottom outlet.

*Chapter 6* – The RDX particles described in Chapter 5 were mixed with molten TNT in a mixing tank to produce RDX/TNT (composition B, cyclotol) military explosive. In this chapter, although the mixture model was used, the full Eulerian multiphase model for fluid-fluid system was described in anticipation of the work in Chapter 7. The results from this chapter provide information to plant engineers not previously possible. This enhanced understanding of the process and hence shed some light on an ongoing problem of excessive variation in final product composition.

*Chapter 7* – A few of the products covered in Chapter 6 were transported to another plant to be used as the main ingredient to produce aerial bombs such as the MK82 and MK84. These bombs are generally dropped onto a target from a fighter jet. A CFD modelling and simulation of the bomb incorporator, being the mixing tank used to blend the main ingredients RDX/TNT and aluminium powder, was used to diagnose existing performance. A recommendation was made with a view to increasing the bomb manufacturing rate. The chapter also describes the full Eulerian multiphase model for solid-fluid system. Although the system warranted the use of the mixture model, a simulation was conducted using the Eulerian model to compare the results from those produced through the mixture model.

*Chapter 8* – Treatment of the aqueous organic waste produced during the manufacture of explosive was discussed in this chapter. Emphasis was placed on the use of photocatalysis technology to destroy sulphonated organic species and inorganic salts, also known as red-water. An experiment using laboratory scale photoreactor was carried out to demonstrate the ability of this technology to destroy the waste. Modelling and simulation of this photoreactor was carried out to characterise the photocatalyst suspension and reaction rate.

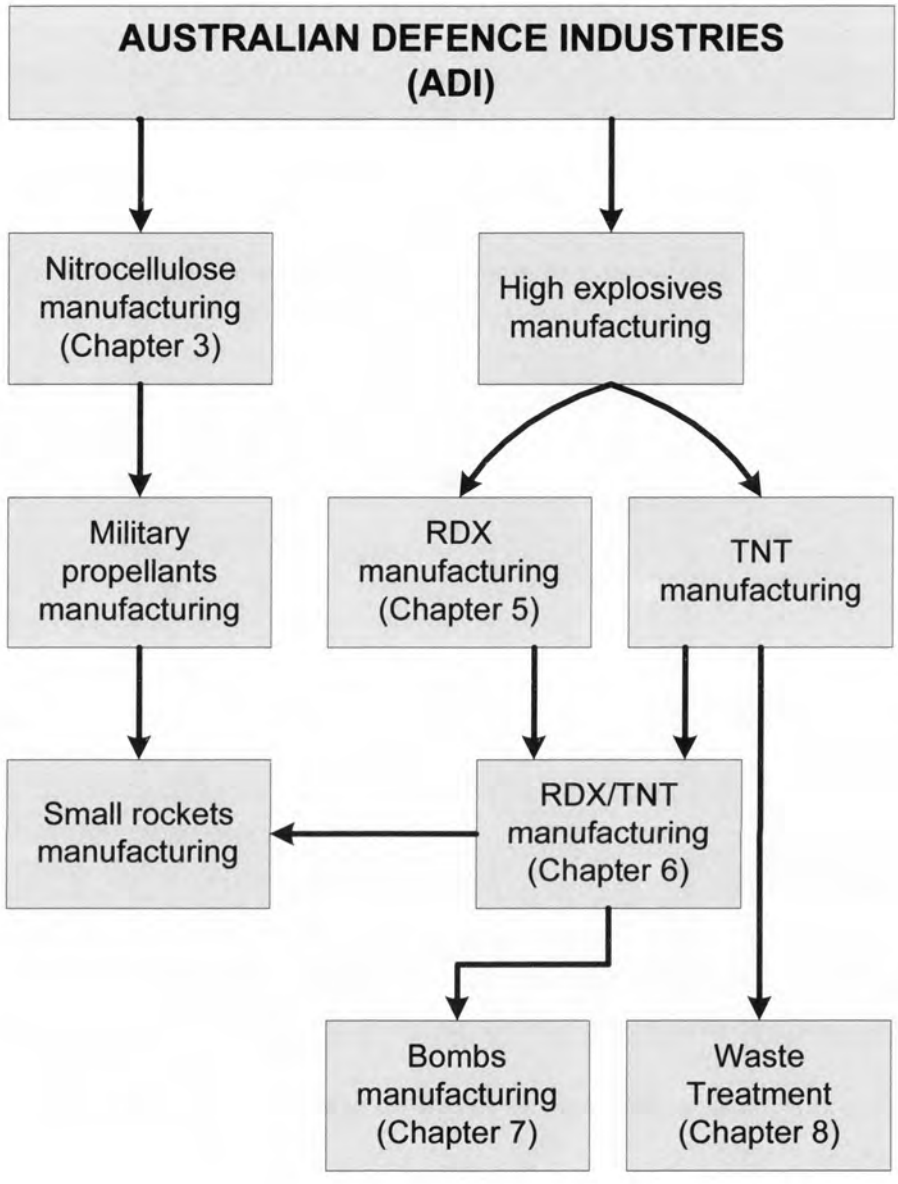


Figure 1.1: Activities covered in this research

Figure 1.1 shows the inter-relations among the activities covered from Chapters 1 to 8 to provide a sense of perspective on the scope of the modelling and simulation conducted in this research work.

## 1.1 Objectives of research

Modelling objective: The category of modelling carried out in this research work includes both the 'design' and 'learning' models.

*Design models* – are developed to provide information or results, which can be used directly for reactor design and engineering. To enhance the performance of the nitrator, design model "wish-list" includes:

- Higher throughput per unit volume
- More consistent nitrogen content
- Safer operation
- Reduced energy consumption
- Meets the specification the first time, every time

*Learning models* – are developed to assist in the understanding of basic concepts and to obtain specific information about unknown processes. Although the results obtained from such models may not lead directly to design information, they are generally useful for the stakeholders to make informed decisions. To understand the nitrator, learning model wish-list includes:

- Start-up and shut-down dynamics
- Multiplicity and stability of thermo-chemical processes occurring in the reactor
- Sensitivity of reactor performance with respect to mixing and residence time distributions
- Selectivity and by-product formation

The development of computational models to gather required information about the behaviour of industrial-scale chemical reactors is a complex task and requires specialised knowledge and approach. As a general guideline, to be commercially viable, the new reactor geometry and operating conditions must be practical, safe to operate and environmentally friendly.

Items in the wish-list will be translated into a quantitative form and a relationship will be established between the quantified performance indices and reactor geometry and operating conditions.

The modelling objective is therefore to realise the two wish-lists. The words 'modelling and simulation' in this research work refers to the use of computational fluid dynamics technology as the computation platform and the scope of research work is:

- The reactors used in the manufacture of military propellants
- A general purpose suspension mixing tank
- The holding tank used in the manufacture of high explosive RDX
- The mixing tank used in the manufacture of high explosive mixture RDX/TNT
- The bomb incorporators used in the manufacture of aerial bombs
- The laboratory scale photoreactor used to treat aqueous waste from the munition plant

Each application above has different process objectives and therefore requires different modelling and simulation approaches. Although they have different process objectives, inter-relationship exists thus ensuring operational continuity in the plant.

## 1.2 Computational fluid dynamics

The chemical process industries rely heavily on empiricism and correlations of overall parameters for non-ideal or non-equilibrium process conditions in the design, scale-up and running of unit operations such as the time-tested stirred tank, batch reactor or CSTR. Many of the stirred tank, batch reactor or CSTR (stirred reactors) unit operations used were designed by experts using rules of thumb. In many instances, these design heuristics amount to nothing more than the empirical approximations surrounded by uncertainties which frequently resulted in mixing-related economic losses estimated in the range of a few billion dollars in 1989 in the USA chemical industry alone [Paul et al. 2004]. There is a high possibility that these losses could be due to the fact that most of the existing knowledge on mixing phenomena is based on simplified models and empirical correlations, that usually attempt to establish quantitative relationships among spatially averaged parameters even when these are known to exhibit strong gradients in the stirred tank [Montante et al. 2001]. Such an approach is satisfactory in most applications but to achieve manufacturing process superiority, an in-depth study of the stirred reactors or mixing tank is a crucial strategy that aims to create the ultimate designer unit operation.

In two of the ADI munition plants, batch reactors and mixing tanks are responsible for converting raw materials to products such as propellants for small rockets, plastic explosives and bombs. Despite the importance of these unit operations, personnel do not have a good understanding of the hydrodynamics that occur inside these unit operations. This lack of knowledge has led to sub-optimum operation and operation-related issues such as final product quality. It was expected that through this PhD study, an in-depth understanding of these unit operations can be gained and the knowledge transferred to the plants.

*Computational fluid dynamics (CFD) is the science of predicting fluid flow, heat transfer, mass transfer, chemical reactions and related phenomena by solving the mathematical equations which govern these processes using a numerical process.*

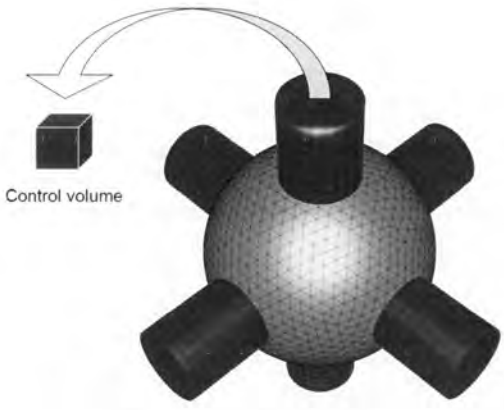


Figure 1.2: A domain discretised into finite set of control volumes or cells

Fluent® solvers are based on the finite volume method where a domain is discretised into a finite set of control volumes or cells [Anderson 1995], as shown in Figure 1.2.

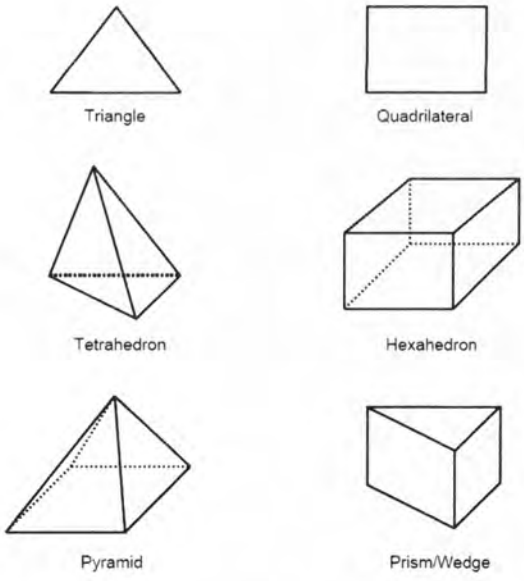


Figure 1.3: Various cell shapes

The shape of each individual cell is dependent upon the domain geometry. For 2-D modelling, the available shapes are triangle or quadrilateral. For 3-D modelling, the shapes available are tetrahedron, hexahedron, pyramid and prism/wedge. These shapes are shown in Figure 1.3.

General continuity equation for mass, momentum, energy [Blazek 2001] is then applied to each cell and discretised.

$$\frac{\partial \rho}{\partial t} = -(\nabla \cdot \rho \upsilon) \qquad \text{- 1.1}$$

where for this conversation of mass

$\frac{\partial \rho}{\partial t}$ : rate of increase of mass per unit volume
$-(\nabla \cdot \rho \upsilon)$ : net rate of mass addition per unit volume by convection

The conservation of momentum is given by:

$$\frac{\partial \rho \upsilon}{\partial t} = -(\nabla \cdot \rho \upsilon \upsilon) - \nabla p - (\nabla \cdot \tau) + \rho g \qquad \text{- 1.2}$$

where

$\frac{\partial \rho \upsilon}{\partial t}$ : rate of increase of momentum per unit volume
$-(\nabla \cdot \rho \upsilon \upsilon)$ : rate of momentum addition by convection per unit volume
$-\nabla p - (\nabla \cdot \tau)$ : rate of momentum addition by molecular transport per unit volume
$\rho g$ : external force on fluid per unit volume

Also, for the conservation of energy:

$$\frac{\partial}{\partial t}(\frac{1}{2}\rho \upsilon^2) = -(\nabla \cdot \frac{1}{2}\rho \upsilon^2 \upsilon) - (\nabla \cdot p\upsilon) - p(-\nabla \cdot \upsilon) - (\nabla \cdot (\tau \cdot \upsilon)) - (-\tau : \nabla \upsilon) + \rho(\upsilon \cdot g) \qquad \text{- 1.3}$$

with:

$\frac{\partial}{\partial t}(\frac{1}{2}\rho \upsilon^2)$ : rate of increase of kinetic energy per unit volume
$-(\nabla \cdot \frac{1}{2}\rho \upsilon^2 \upsilon)$ : rate of addition of kinetic energy by convection per unit volume
$-(\nabla \cdot p\upsilon)$ : rate of work done by pressure of surroundings on the fluid
$-p(-\nabla \cdot \upsilon)$ : rate of reversible conversion of kinetic energy into internal energy
$-(\nabla \cdot (\tau \cdot \upsilon))$ : rate of work done by viscous forces on the fluid
$-(-\tau : \nabla \upsilon)$ : rate of irreversible conversion from kinetic to internal energy
$+\rho(\upsilon \cdot g)$ : rate of work by external force on the fluid

The generalised Newton's law of viscosity may be expressed as [Bird et al. 2002]:

$$\tau_{ij} = -\mu\left(\frac{\partial \upsilon_j}{\partial x_i} + \frac{\partial \upsilon_i}{\partial x_j}\right) + \left(\frac{2}{3}\mu - \mathrm{K}\right)\left(\frac{\partial \upsilon_x}{\partial x} + \frac{\partial \upsilon_y}{\partial y} + \frac{\partial \upsilon_z}{\partial z}\right)\delta_{ij} \qquad \text{- 1.4}$$

$$\tau = -\mu\left(\nabla\upsilon + (\nabla\upsilon)^{+}\right) + \left(\frac{2}{3}\mu - \mathrm{K}\right)(\nabla\cdot\upsilon)\delta \qquad \text{- 1.5}$$

where

$\tau$ : viscous stress tensor

$\delta$ : unit tensor with components $\delta_{ij}$

$(\nabla\upsilon)$ : velocity gradient tensor with components $\left(\frac{\partial}{\partial x_i}\right)\upsilon_j$

$(\nabla\upsilon)^{+}$ : is the transpose of the velocity gradient tensor with components $\left(\frac{\partial}{\partial x_j}\right)\upsilon_i$

$(\nabla\cdot\upsilon)$ : divergence of the velocity vector

For constant $\rho$ and $\mu$, insertion of the Newtonian expression for $\tau$ from Equation (1.5) into the equation of motion (1.2) leads to the Navier-Stokes equation and is given by:

$$\rho\frac{D\upsilon}{Dt} = -\nabla p + \mu\nabla^2\upsilon + \rho g \qquad \text{- 1.6}$$

or in the Cartesian coordinates is given by:

$$\begin{aligned}
\rho\left(\frac{\partial \upsilon_x}{\partial t} + \upsilon_x\frac{\partial \upsilon_x}{\partial x} + \upsilon_y\frac{\partial \upsilon_x}{\partial y} + \upsilon_z\frac{\partial \upsilon_x}{\partial z}\right) &= -\frac{\partial p}{\partial x} + \mu\left[\frac{\partial^2\upsilon_x}{\partial x^2} + \frac{\partial^2\upsilon_x}{\partial y^2} + \frac{\partial^2\upsilon_x}{\partial z^2}\right] + \rho g_x \\
\rho\left(\frac{\partial \upsilon_y}{\partial t} + \upsilon_x\frac{\partial \upsilon_y}{\partial x} + \upsilon_y\frac{\partial \upsilon_y}{\partial y} + \upsilon_z\frac{\partial \upsilon_y}{\partial z}\right) &= -\frac{\partial p}{\partial y} + \mu\left[\frac{\partial^2\upsilon_y}{\partial x^2} + \frac{\partial^2\upsilon_y}{\partial y^2} + \frac{\partial^2\upsilon_y}{\partial z^2}\right] + \rho g_y \qquad \text{- 1.7} \\
\rho\left(\frac{\partial \upsilon_z}{\partial t} + \upsilon_x\frac{\partial \upsilon_z}{\partial x} + \upsilon_y\frac{\partial \upsilon_z}{\partial y} + \upsilon_z\frac{\partial \upsilon_z}{\partial z}\right) &= -\frac{\partial p}{\partial z} + \mu\left[\frac{\partial^2\upsilon_z}{\partial x^2} + \frac{\partial^2\upsilon_z}{\partial y^2} + \frac{\partial^2\upsilon_z}{\partial z^2}\right] + \rho g_z
\end{aligned}$$

The Navier-Stokes equation provides the usual starting point for the analysis of flow processes [Chung 2003]. The finite volume (FV) method uses the integral form of the conservation of equations as its starting point to ensure global conservation. The differential equation is integrated over the volume of each cell to obtain algebraic equations. Variable values are stored at the cell centres and interpolation is used to express variable values at cell faces in terms of the cell centre values. Surface and volume integrals are estimated using appropriate quadrature formulae. As a consequence, all algebraic equations per cell is obtained in which a number of neighbouring cell centre values appear as unknowns. FV methods can accommodate any type of grid and is therefore suitable for handling complex geometry.

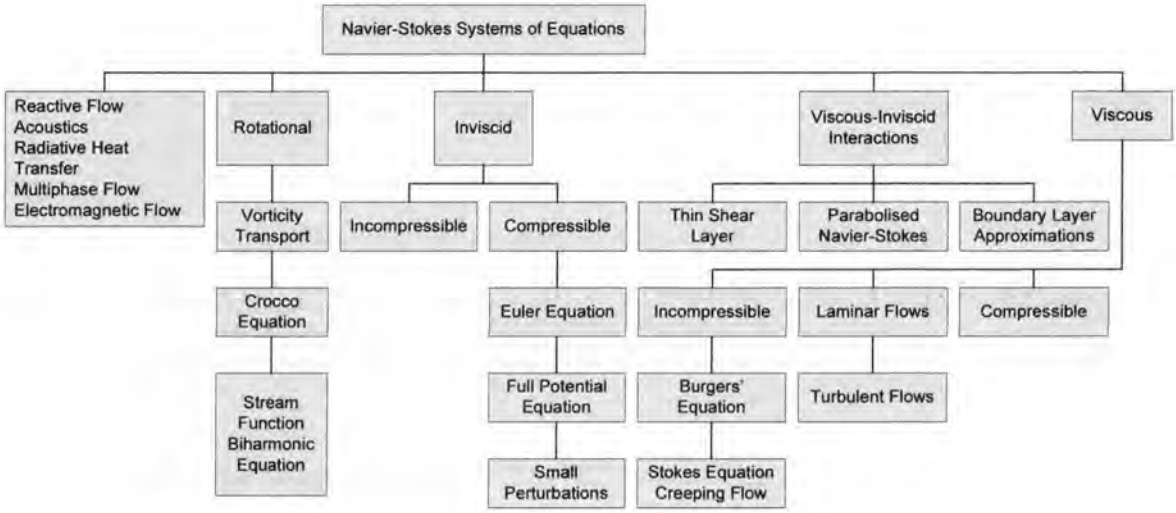


Figure 1.4: The Navier-Stokes systems of equations

Figure 1.4 shows the Navier-Stokes systems of equations that provide an overview of the different types of flows and cast in the Eulerian coordinates in which the current flow field is fixed at the reference coordinates [Date 2005]. For multiphase flows, however, it is convenient to work with the Lagrangian coordinates in which displacements of fluid or solid particles are tracked relative to the initial reference coordinates. Both Eulerian and Lagrangian coordinates may be coupled in dealing with certain physical phenomena.

Typically, the investigation of one variable will encompass 3 main stages in CFD, namely:

*STAGE 1: Pre-Processing*

Define modelling goals - set the objective of the modelling and simulation exercise

Identify the domain for modelling - define the scope

Create model geometry - import or draw the geometry of interest

Discretise model geometry - assign meshes into the geometry of interest

Examine mesh - examine the quality of meshes and remesh, if necessary

Assigning boundary zone - assign the boundary conditions

Exporting mesh - Export the mesh for computation in the solver

*STAGE 2: Computation done by solver*

Read the mesh file - read the file containing previously meshed geometry

Check file - check to see there are no inverted volumes

Display grid - display the mesh again to confirm the validity of geometry

Set solver settings - define steady or transient simulations

Define materials - define the physical properties of the materials

Set region - set special regions, example patching solid particles

Set operating conditions - set the direction of gravity force and operating pressure

Set boundary conditions - define the value of the boundary conditions,

Define viscous model - define whether flow is under laminar or turbulence

Define controls - define the under-relaxation factors and discretisation scheme

Iterate - Set the number of iteration and iterate

*STAGE 3: Post-processing*

Check solution - check to ensure that the solution has converged

Display contours and vectors - variables of interest

Report compute - variables of interest

These stages are shown graphically in Figure 1.5 [Fluent 2006].

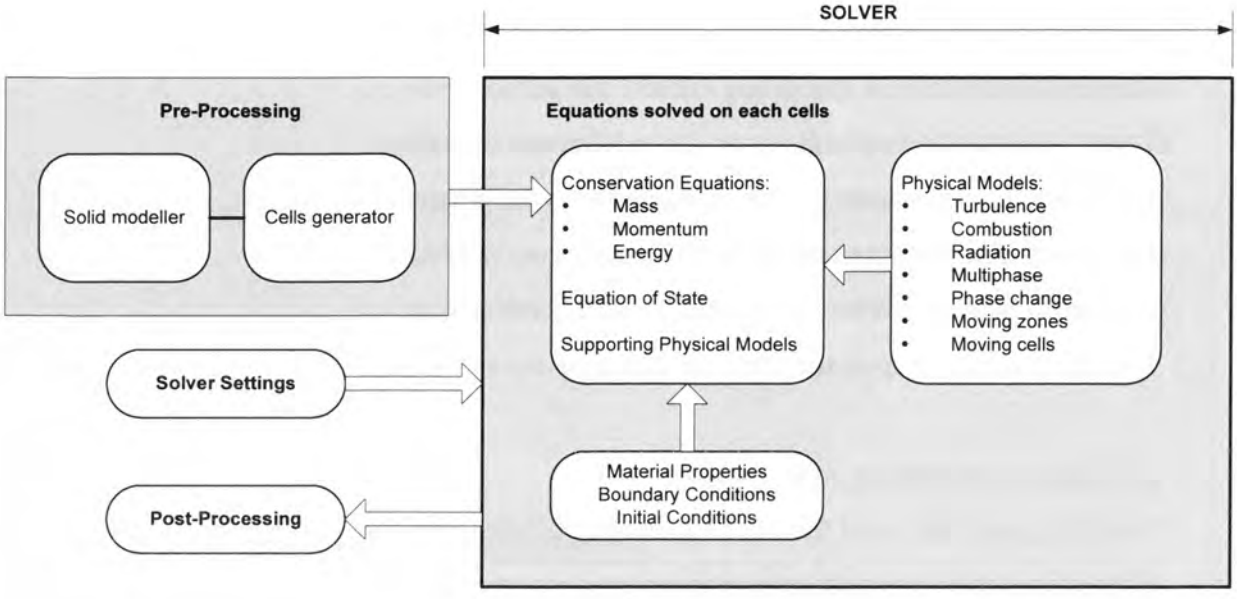


Figure 1.5: Overview of CFD stages

In general, the result of CFD analyses can be used for:

- Conceptual studies of new design
- Detailed product development
- Troubleshooting or characterisation
- Redesign or optimisation
- Risk threat analysis

CFD analysis complements testing and experimentation thereby reduces the total effort and associated costs required in the laboratory or pilot plant.

Existing technology suggests that processes, which are sensitive to local phenomena and reactant concentrations are often difficult to design or scale up, since these design correlations do not take local phenomena into account. Non-idealities introduced by scaling up of laboratory or pilot-scale equipment are difficult, if not impossible, to predict empirically. Significant improvements in the design capability and reliability of stirred reactors may be expected from advances in CFD modelling and simulations techniques.

CFD, developed by NASA engineers back in mid-1980s for transatmospheric space shuttle modelling, can overcome current stirred reactors design weaknesses [Anderson 1995]. CFD simulations present the only cost-effective means to acquire detailed information on flow and turbulence fields needed for realistic distributed-parameter process simulation. In addition to the economic benefit of CFD, with the CFD-based simulations, the actual size of the unit operation can be effectively modelled and simulated such that scale-up uncertainties and issues are avoided [Montante et al. 2001]. Driven by the increased competition in the market place and the need to decrease manufacturing cycle-time and overheads, recently chemical engineers, researchers and equipment designers are increasingly using CFD to analyse the flow and performance of process equipment, such as chemical reactors, stirred tanks, fluidised beds, cyclones, combustion systems, spray dryers, heat exchangers and pipeline arrays [Bakker et al. 2001].

Using CFD to model unit operation is important because even advanced experimental techniques such as the laser Doppler anemometry (LDA), laser Doppler velocimetry (LDV) and particle image velocimetry (PIV), which require the fluid concerned and its containment tank to be transparent to light transmission, may not have much practical application in an industrial setting since most of the tanks were constructed from non-transparent materials and the fluid concerned could be opaque [Aubin et al. 2004].

Most importantly, CFD applications are very important in situations where the potential legal and liability costs of hardware failures can be staggering to a government administration, organisation, the environment or the public. Examples of such situations where the high-consequence systems can never be tested include the modelling of the catastrophic failure of a full-scale containment building for a nuclear power plant, damage done to a skyscraper from explosion, nuclear weapon involved in a ground-transportation

accident and the risk assessment of underground nuclear-waste repositories [Oberkampf and Trucano 2002].

CFD is used to model and simulate a wide range of situations. These include:

- Modelling nuclear reactor [Becker and Laurien 2003],
- Deflagration-detonation processes [Popat et al. 1996; Rehm et al. 1998; www.hpcmo.hpc.mil],
- Nuclear and weapons of mass destruction (WMD) risk threat analysis [www.itsc.com],
- Heat and mass transfer processes during core melt discharge from a nuclear reactor pressure vessel [Dinh et al. 1996],
- The transport, diffusion, and evaporation of chemical and biological agents in and around 3D structures such as ships, tanks, aircraft and buildings [www.msiac.dmso.mil],
- The risk of discharge of a toxic material into a commercial aircraft cabin during flight [Garner et al. 2004],
- Emergency preparedness and response [Lee et al. 1997] and
- Smoke movement in a ventilated tunnel fire [Gao et al. 2004]

# CHAPTER 2: LITERATURE REVIEW

A literature review must be conducted on related topics prior to conducting any modelling and simulation work. This literature review is categorised into five major sections, namely:

- Chemical reactors and mixing tanks
- Rheology of fluids
- Solidification process
- Statistical methods
- Photocatalysis

The literature review on chemical reactors and mixing tanks include various investigations done on the CFD modelling and simulation on chemical reactors and mixing tanks. It includes the latest findings in the field of CFD modelling of chemical reactors and mixing tanks. The next part, the rheology of fluids, includes a study on the different kinds of fluids and their characteristics. This study is necessary because throughout this research work, different kinds of fluids will be encountered. Thus, a good understanding of the rheology of fluids will enhance knowledge in this field of specialisation and help in the provision of recommendations. An understanding of the solidification process is required to help understand what happen during the filling of bombs. It was felt that understanding the downstream process would aid in the provision of recommendation for the upstream process. However, it was more difficult to control and maintain consistency of the input variables in an actual plant than in a highly controlled environment such as a research laboratory. Consequently, technique such as statistical process control (SPC) must be employed to assess and determine whether the plant data were reliable. Finally, a literature review on the treatment of waste emanating from the manufacturing of explosives via photocatalysis technology was conducted.

## 2.1 Chemical reactors and mixing tanks

In this research work, a homogeneous reaction is one that involves only one phase. In contrast, a heterogeneous reaction involves more than one phase, and the reaction usually occurs at or very near the interface between the phases. An irreversible reaction is one that proceeds in only one direction and continues in that direction until the reactants are exhausted. A reversible reaction can proceed in either direction, depending on the concentrations of reactants and products relative to the corresponding equilibrium concentrations.

### 2.1.1 Reaction parameters

The dependence of the reaction rate $-r_A$ on the concentrations of the species present, is normally determined by experimental observation. One of the most common general forms of this dependence is the product of concentrations of the individual reaction species, each is raised to a power, for example:

$$-r_A = kC_A^{\alpha}C_B^{\beta} \qquad \text{- 2.1}$$

The exponents $\alpha$ and $\beta$ in the kinetic rate law are referred to as the reaction order. In this case, the reaction is $\alpha$ order with respect to reactant A and $\beta$ order with respect to reactant B. The overall order of the reaction order is $\alpha + \beta$ order reaction. In general, first- and second-order reactions are more commonly observed than zero- and third order reactions [Fogler 1992]. In addition, the order of reaction does not have to be an integer, nor does the order have to be an integer with respect to any individual component. If the reaction order of each species is identical with the stoichiometric coefficient of that species for the reactions as written, such reaction is called an elementary reaction. The reaction rate constant, $k$ typically follows the Arrhenius behaviour and is written as:

$$k(T) = Ae^{-\frac{E}{RT}} \qquad \text{- 2.2}$$

where

$A$ : pre-exponential factor

$E$ : activation energy, J $mol^{-1}$

$R$ : gas constant = 8.314 J $mol^{-1}$ $K^{-1}$

$T$ : absolute temperature, K

### 2.1.2 Mixing perspective

This section main focus is the application of CFD to the study of the hydrodynamics of mechanically agitated batch reactors. The section begins with an outline of the need to conduct such studies followed by more specific review that can be divided into single phase-, multiphase-, bubble column reactor, reaction runaway prevention and finally the conclusion which outlines the research gap in this area of study.

A reaction study is one in which emphasis is given to reaction-related issues by making simplifications in the underlying fluid dynamics in order to establish a relationship between the chemical reactor design and the performance of the reactor. Reactor engineering on the other hand, merges reaction engineering with the scrupulous modelling of underlying fluid dynamics to establish a relationship between actual chemical reactor design configuration and its performance [Ranade 2002]. The main emphasis of this research work is on chemical reactor engineering.

The process objective of a chemical reactor is to produce the desired product via bringing together the reactant molecules for molecular mixing to allow chemical reactions to occur, providing an appropriate process condition for a sufficient amount of time and allowing for the removal of products.

Thus, chemical reactor design depends to a great extent on mixing, which is the very first step in any chemical reaction. Participating reactants must be brought together for a chemical reaction to occur. In the absence of mixing, the reaction cannot even be initiated. Even when there is mixing, chemical reactions are influenced by the overall mixing time and, very important by the homogeneity of concentration both at the feed point and at the bulk solution in the tank. A good understanding of the theory on mixing is the first step towards optimising a chemical reactor. Therefore, the primary design objective for chemical reactors from a mixing perspective is to obtain a kinetically controlled or equilibrium-controlled reactor and to eliminate all limitations due to transport, predominantly heat and mass transfers.

In a situation where the chemical reactor is already operating and producing desired product, research work can be carried out to optimise the reactor delivering benefits emanating from:

- An overt improvement in reaction conversion and yield
- A reduced residence time distribution (RTD)
- A safer reactor operation
- A lower amount of waste produced

In a nutshell, to optimise the performance of a chemical reactor, a good knowledge of the chemical reactor design configuration from mixing perspective, an understanding of the reaction kinetic from the input process variables perspective and finally an understanding of the intrinsic relationship between the two is imperative.

The objective of this section is to address critical factors that affect mixing results, which has the propensity to determine the fate of chemical reactor performance. Because of this, this section is devoted to an in-depth understanding of the batch mixer.

Mixing is a contacting phenomena where materials are brought together to accomplish a process objective such as to obtain a homogeneous mixture, to keep solids in suspension, cause heat and mass transfer, effect a chemical reaction, obtain an emulsion, or transfer oxygen to micro-organisms.

In general, if mixing is to be carried out so as to produce a homogeneous mixture, it is necessary that two requirements are fulfilled: Firstly, there must be bulk or convective flow so that there are no dead or stagnant zones and secondly, there must be a zone of intensive mixing where the inhomogeneity is broken down. Both of these processes consume energy and ultimately the mechanical energy is dissipated as heat and the proportion of energy attributable to each varies from one process to another [Chhabra and Richardson 1999].

Many factors, including multi-variable interactions that affect the performance of a mixer. The known factors includes flow regime, mixing tank geometry, impeller geometry, feed flowrate, baffle dimensions and fluid properties. Due to the complex nature of the mixing process, until now, the empirical approach employing dimensionless groups was most frequently used for correlation of the process performance variables in mixing equipment. The issues that arise in the design and use of mixing equipment are the proper selection of the type, size, and operating conditions, which will perform a desired service. While technical feasibility is of ultimate importance, economic consideration, particularly keeping the combination of capital and operating costs low is nonetheless equally important. Moreover, sub-optimum reactor performance will not be able to produce excellent economic results and quite frequently, these are hidden because the problems have not been identified at the onset.

Flow regime and mixing mechanism is usually dependent on the impeller Reynolds number, defined as [Chopey 2004]:

$$N_{\mathrm{Re}} = \frac{\rho N D^2}{\mu} \qquad \text{- 2.3}$$

or in the case of a fluid passing through a duct, it is defined as [Perry and Green 1999]:

$$N_{\mathrm{Re}} = \frac{\rho U D}{\mu} \qquad \text{- 2.4}$$

$\rho$ : density of fluid, kg $m^{-3}$

$N$ : impeller rotational speed, rev $s^{-1}$

$U$ : velocity of fluid, m $s^{-1}$

$D$ : impeller diameter, m

$\mu$ : absolute viscosity, kg $m^{-1}s^{-1}$ or Pa.s

For Reynolds number ranging from 10 to 100, the mixing regime is laminar. For turbulent mixing regime, the Reynolds number is greater than 10,000. Transition mixing regime falls between the laminar and turbulent mixing regime, that is, 100 < transition < 10,000. Besides correlating the type of flow regime to the impeller Reynolds number, the mixing

time, impeller pumping rate, impeller power consumption, heat and mass transfer coefficients can also be correlated to this dimensionless group.

Laminar mixing is caused by fluid layers traversing over each other. The elongation and thinning of these fluid layers achieve large surface areas for contacting. In laminar regime, transport is not enhanced because inertial forces tend to die out quickly. Since the velocity gradients close to a moving impeller are high, the fluid elements in that region deform and stretch. They repeatedly elongate and become thinner each time they pass through the high shear rate zone. The elongation and thinning of the fluid elements give rise to stresses in the liquid which then effect a reduction in droplet size and increases in interfacial area by which means the desired degree of homogeneity is obtained. Although molecular diffusion can reduce inhomogeneity, its effect is not momentous until the fluid elements have been sufficiently reduced in size for their specific areas to become large. Ironically, the ultimate homogenisation of miscible liquids can only be brought about by molecular diffusion [Chhabra and Richardson 1999].

Turbulent mixing is the tumbling and retumbling of eddies. Eddies have different sizes and have different life spans. It is inherently complex and the calculation of flow fields prevailing in a mixing tank is not amenable to scrupulous theoretical approach. The inertia imparted by the impeller to the mixture is sufficient to cause the mixture to circulate throughout the tank and return to the impeller. Although turbulence occurs throughout the tank, the greatest existence would be near the impeller. Mixing by eddy diffusion is much faster than mixing by molecular diffusion and, consequently, turbulent mixing occurs much more rapidly than laminar mixing [Chhabra and Richardson 1999].

The transition mixing mechanism is thought to be a combination of the laminar and turbulent mixing mechanisms, although this may not always be the case. Unfortunately, transition mixing and the transition regime are poorly understood and have not been thoroughly studied. In addition, properties of the transition mixing regime do not necessarily represent an average of the laminar and turbulent properties. A common mistake in the industry is to assume this averaging. Processing in the turbulent regime is often sought due to the existence of enhanced transport occurring under this condition. As the Reynolds number increases from laminar to turbulent regime, transport improves, but only as a consequence of the behaviour in the laminar regime. Unfortunately, a natural

extension of this logic is to assume that, as the process progresses into the transition regime toward the turbulent regime, transport is further enhanced. However, this is a wrong and groundless assumption because the transition regime is a mixing regime which resembles neither laminar nor turbulent regime. In a nutshell, transport in the transition regime may be worse than in either the turbulent or laminar regime and thus, it is recommended that processing in the transition regime be avoided [Tatterson 1994].

There are two main types of mixing equipment employed in the industry, mechanical mixing and jet mixing. Since the scope of this research work is on stirred reactors, mixing design geometry is only confined to mechanical mixing.

Mechanical mixing encompasses the utilisation of an impeller driven by a prime mover of some sort. The impeller geometry and the tank geometry determine the final geometry of this mixing unit operation. This final geometry is the key to good mixing, and the determination of effective design geometry for mixing is very important. There are many variations in design of mixing equipment due to the enormous variations in mixing and contacting problems encountered. It is imperative that the process and its objectives are matched to the mixing design geometry.

A standard geometrical configuration for a mixing tank is shown in Figure 2.1. This universal design has been very useful in many applications and performs well the first time, to such extent that these standard geometries are multipurpose designs. Such designs are also typically the designs offered initially by the equipment vendors. However, as pointed out by a number of researchers mentioned in the literature review, changes in the design geometries led to improved mixing performance. Therefore, to achieve improved or optimum mixing performance in the mixing unit operation, it is imperative that the application of process-specific designs be employed. Thus, the quest to put together the crucial factors, that is, different design geometries that lead to an optimum mixing performance is a major part of this research work.

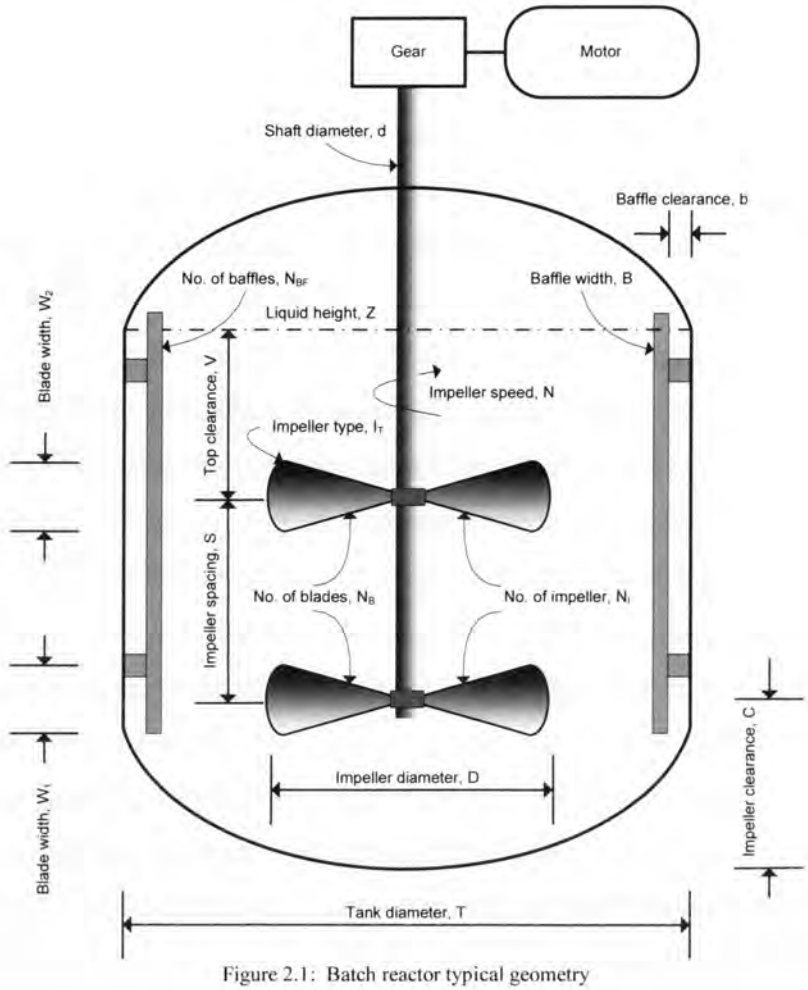


Figure 2.1: Batch reactor typical geometry

It is a common misconception that the only crucial factor in relation to impeller selection is the nature of process mixing. It is possible to use any impeller type, be it propeller, turbine or any other impeller type to satisfy a wide variety of services. However, the incorrect selection of impeller will result in a hefty price, normally in the form of higher than necessary power consumption and getting sub-optimised mixing performance including failure to achieve homogeneity of the mixture in the tank. Axial fluid flows in a vortexing low-viscosity liquid are low relative to its radial flows in the stirred tank. Increased vertical circulation rates may be obtained by mounting the impeller off-centre. Such position may be employed with either turbines or propeller impeller type. The secret to successfully employing such manoeuvre is the exact location of the impeller, since too far or too little off-centre in one direction or the other will cause greater swirling, erratic vortexing, and dangerously high shaft stresses. Changes in viscosity and tank size also affect the flow pattern in such vessels. In practice, off-centre mountings have been particularly effective in the suspension of paper pulp [Perry and Green 1999]

### 2.1.3 Baffles

Baffles are obstructions strategically situated in the mixing tank to redirect the mixture flow with the ultimate aim of enhancing mixing performance via increasing the contact surface area. Wall baffles serve to hinder or reduce the mixture flow in the mixing tank from rotating with the impeller. This increases the relative velocity between the impeller and the mixture and equally important, power input into the mixture. Both of these factors would then enhance the mixing performance in the turbulent regime. In most cases, employing baffles is not necessary when the mixing regime is laminar [Tatterson 1994].

Baffles also function to mitigate or inhibit the formation of the central vortex, produced from centrifugal force acting on the rotating liquid which is known to reduce mixing performance. Vortex flow moves in a circular fashion with little radial or axial motion. In multiphase mixing, existence of central vortex can cause component segregation and limit the rotational speed that may be used because once the central vortex reaches the impeller, severe air entrainment may occur. In addition, the swirling mass of liquid often generates an oscillating surge in the tank which coupled with the deep vortex may create large fluctuating force acting on the shaft. For Reynolds number greater than 2000 baffles are commonly used with turbine impellers and with on-centreline axial-flow impellers. The use of baffles results in a large top-to-bottom circulation without central vortexing or severely unbalanced fluid forces on the impeller shaft [Perry and Green 1999]. During agitation of a low-viscosity fluid, the rotating impellers tangential motion to the liquid and in the absence of baffles, this swirling motion approximates solid-body rotation in which little mixing actually occurs [Myers et al. 2002]. From this brief overview, the purpose of baffling is to convert radial flow into axial flow.

Conventional mixer designs emphasise the use of wall baffles giving the impression that mixing cannot be accomplished without wall baffles. Turbulent mixing can be accomplished without the use of baffle albeit mixing time can be much longer.

Baffles are very difficult to clean and cause the cleaning operation to be much longer than that for unbaffled tanks. Because of this, in some turbulent applications, wall baffles are not employed where cleaning between batches is necessary or in solid-liquid processes where the solids build up on baffles causing quality-control problems and safety related issues. To overcome deposition of solids on standard wall baffles, baffles are often located

1/72 tank diameter away from the tank wall to minimise accumulation of solids on or behind them. The size of baffles depends on the mixing process. For wall baffles, design heuristic states that a standard fully wall baffled tank is one which has four long vertical plates placed symmetrically around the tank's perimeter. Each baffle width is anything between 1/12 to 1/10 the tank diameter, and the baffle height must be higher than the mixture height. Such baffles normally provide near optimal performance due to the symmetric location of the baffles around the tank circumference. In the absence of literature data, the size of baffle can only be determined via empirical route or computer simulation.

In some applications however, the use of standard baffles may not produce the desired result. Such application includes floating solids draw-down or incorporation. It would be ineffective to use standard baffles because of their tendency to suppress the surface vortex. Such application requires the use of narrow or partial baffles. Narrow baffles are those where the width is 1/50 tank diameter and extend vertically parallel to the tank wall, from the top to the bottom. Again they are located at least 1/72 tank diameter away from the tank wall. On the other hand, a partial baffle having width similar to a standard baffle only extend from the bottom to half of the tank height. The principle behind such application is that both of these baffles allow surface vortex to form aiding the draw-down of solid particles and dispersion of the particles, unlike in the case of unbaffled tank where the particles concentrate around the region of the shaft.

Baffle systems for some chemical reactors can be intricate in which the effect of the baffling is controlled during the course of the reaction via changing the length and angle of the baffle in the flow.

### 2.1.4 Applications of computational fluid dynamics

Process modelling is a necessity in chemical process plants and improvements in the process simulation technology nowadays makes the simulation of entire plants a common scenario. Unfortunately, the majority of the models used by process simulation tools either ignore all spatial variations of properties within each unit operation by adopting a well-mixed assumption or are limited to simple idealised geometries. In addition, even in models that represented heat and mass phenomena to a high degree of detail, the treatment of fluid mechanics was generally somewhat basic and superficial. As a consequence, process simulation may offer only an incomplete and unsatisfactory description of processes in which local interactions between mixing and other phenomena [Bezzo et al. 2000]. In contrast, current CFD simulations typically model a single unit operation and thus provide much more accurate and detailed information than the simpler, lumped models used in process simulation software [Bakker et al. 2001]. Although the mixing of chemical reactants is a widespread activity in the chemical process plants, the mixing time predictions are usually based on empirical correlations. When a competitive side reaction is present, the final product distribution is often unknown until such time the reactor is built and operated. The effects of the position of the feed stream on the reaction by-products are usually complex. In addition, as mentioned earlier, the scale up of stirred tank reactors is not straightforward. Nienow and Inoue [1993] conducted experiment to demonstrate the importance of feed position, using a small tank and the semibatch barium sulphate method of Villermaux, as shown in Figure 2.2.

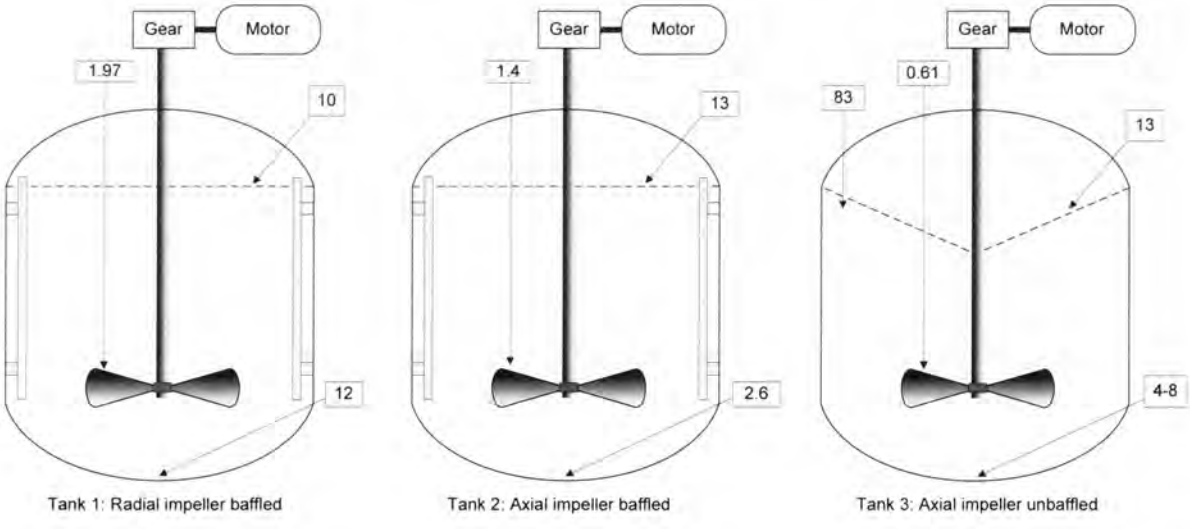


Figure 2.2: By-product selectivity as a function of feed position and reactor geometrical configuration

In these cases, the impeller rotational speed and feed rate were kept constant and only the position of feed, as represented by the arrows, was varied from one location to another. In all three cases, the power per unit tank volume was similar. The selectivity given was that of unwanted by-product where higher numbers mean that more by-products were generated. Tank 1 was agitated by a radial turbine. Since the turbulence intensity in the tank differs with position, the local mixing rate which leads to different by-product selectivity for different feed locations, changed too. At the high intensity region just entering the flow through the impeller or around the impeller tips, the turbulence intensity was high and the by-product formation was low. In contrast, at the liquid free surface where low turbulence intensity exists, the by-product selectivity was high. Similarly, at the tank bottom where radial impeller delivered little turbulence, the by-product selectivity was high as well. In tank 2, an axial-flow impeller was employed. Again, feed at the surface had the most by-product formation while feed in the vicinity of impeller gave the best result. Finally, tank 3 was unbaffled where high turbulence existed near the impeller region, which led to low by-product selectivity. The liquid surface and throat of the central vortex with its higher rotational fluid body motion and poor incorporation have very high by-product formation. In general, the fastest most immediate mixing of feeds with resident fluid occurs when the feed is introduced in the region with the shortest local mixing time constant. Placing feed away from region of high turbulence intensity will yield higher by-product selectivity.

CFD can provide a comprehensive, physical model that can be used to predict important information such as mixing time and reaction product distribution, especially as they relate to scale and feed position [Bakker and Fasano 2000]. Brucato et al. [2000] conducted a study to simulate a mixing-dependent process that consisted of two parallel reactions competing for a common reagent. From experimental work, it was discovered that in this system, the final selectivity of the process depended on agitation speed and therefore on the mixing history during the batch process. They discovered that their CFD 3D simulation results compared very well with experimental results leading to the conclusion that CFD modelling could be used for modelling mixing-dependent processes.

For single phase modelling, CFD predictions of stirred tank flows using momentum source boundary conditions were carried out where the predictions of the velocity field using the model were compared to detailed measurements of mean velocity components by LDA and

CFD simulations using LDA data as boundary conditions [Xu and McGrath 1996]. They concluded that using the momentum source model, the predicted velocity profiles and power as well as the flow numbers agreed well with experimental data and thus this momentum source model has demonstrated its ability to simulate the flow in stirred tanks and to produce realistic predictions. Between the performance of using the momentum source model and using LDA data as boundary conditions, they discovered that the momentum source model predicted the stirred tank flow at least as good as the prediction with full LDA boundary conditions for the pitched blade turbine. The weakness of this momentum source model was that the prediction accuracy was somewhat limited to radial flow and it did not represent well the time-dependent characteristics in stirred tanks [Xu and McGrath 1996].

Sheng et al. [1998] carried out CFD 2D simulations of stirred tank and validated its results using particle image velocimetry (PIV). In the validation studies, the spatial fields processed from PIV data were compared with CFD. Besides visual comparison, several tools were introduced to quantify the similarity and discrepancy between two spatial fields. These tools, including spatial spectrum, correlation and local correlation, proved to be effective. They were applied to the validation of CFD simulations of an axial-impeller stirred tank. This study concluded that boundary condition setting has the highest repercussion impact in the prediction of mean flow field. Hence, accurate boundary conditions obtained from experimental data containing both geometric and dynamic similarity with the simulated flow were required. Because of this, they felt that simple scale-up rules such as scaling by tip velocity widely used for stirred vessel CFD may be insufficient for predicting the correct mean velocity fields.

In relation to turbulent fields, the $k$-$\varepsilon$ RNG model qualitatively predicted the distribution of kinetic energy, $k$, turbulence dissipation rate, $\varepsilon$, and normal Reynolds stresses. In the impeller region, prediction were relatively satisfactory, while in the flow discharge region, CFD simulations underpredicted $k$ and $\varepsilon$ including normal Reynolds stresses. They attributed this underprediction to the existence of a large number of time-varying eddies with various sizes which they found by examining the instantaneous PIV measurements.

Revstedt et al. [1998] conducted simulations of a baffled reactor fitted with a single Rushton turbine using the LES approach. Through this study, they discovered that the qualitative dynamics of the flow was well captured, indicating that LES was a suitable approach for simulating such complex flow situations. They also reported that LES provided data that could not be computed by Reynolds averaged based turbulence modelling. In addition, they reported that radial acceleration was observed near the tip of the impeller. Such acceleration was attributed to the high levels of fluid entrainment in this area, due to the trailing vortex pair. From the quantitative perspective, velocity fluctuations differ from experimental results obtained using LDA especially near the impeller. They felt that this discrepancy could be due to the difference in geometry between measurements and simulations. They concluded their report by stating that the boundary conditions on the blade surface should be more accurately satisfied, confirming the findings of Sheng et al. [1998]. In contrast, Lamberto et al. [1999, 2001] successfully modelled the laminar flow behaviour inside an unbaffled stirred tank that employed a 6-blade radial flow impeller. The results were validated with experimental results obtained using PIV.

Sahu et al. [1999] used CFD modelling to develop rational design procedures for stirred tanks where they addressed the impeller-tank geometry to the flow field produced, established the energy balance in stirred tanks and developed an understanding of the linkage between the flow field and process objectives. In this study, five different designs of axial flow impellers were investigated. Zonal modelling where the vessel was divided into several zones, was used to predict the flow characteristics in regions far away from the impeller, where previously several researchers found that comparison between the experimental finding and numerical predictions were unsatisfactory. They concluded that the predicted values of the dimensionless radial and axial velocity were in good agreement with the experimental measurements, even though the tangential velocity showed a mixed trend. The prediction of the turbulent kinetic energy, $k$, were significantly improved using zonal modelling. CFD prediction of the turbulent energy dissipation rate, $\varepsilon$, with that estimated from impeller velocity and length scale calculated from auto-correlation, performed poorly.

Revstedt and Fuchs [2000] conducted similar modelling on a stirred reactor with a liquid volume of 0.64 $m^3$, where the effects of impeller type, namely dual Rushton impeller and dual Scaba 6SRGT impellers were studied using large eddy simulations (LES). Their

study led to the conclusion that, under equal power input, the tip velocity provided a proper scaling parameter when comparing geometrically similar turbines. This was in disagreement with the conclusion by Sheng et al. [1998]. The analysis of industrial multi-staged stirred coiled tanks using CFD was carried out by Alliet-Gaubert et al. [2006]. In this study, they mentioned that although CFD could not possibly simulate industrial cases in their whole complexity, nevertheless, CFD simulations may convey interesting information provided the analysis is well performed. Alliet-Gaubert et al. [2006] provided the power and power numbers that outlined the functioning cost, the axial flow numbers as a function of liquid medium viscosity and the impact of the liquid medium viscosity on the blending time.

Zalc et al. [2001] conducted extensive validation of computed laminar flow of Newtonian fluid in a stirred tank fitted with three Rushton turbines equally spaced apart vertically using ORCA software suite. Ten *Re* from 20 to 200 were investigated and an unstructured mesh, containing approximately 2 million tetrahedra cells, was employed. They found that using the ORCA software suite, the three fundamentals step of CFD, namely geometry modelling and its subsequent mesh generation, flow-field solution and analysis was performed within duration of 24 hours. According to Zalc et al. [2001], the ease of CFD application indicated that CFD has become a mature tool for the analysis of geometrically complex, industrially relevant mixing devices. In this study, their predicted values agreed very well with PIV data for bulk-flow patterns at several different agitation rates. Predicted sizes and locations of poor mixing regions agreed well with results of planar laser-induced fluorescence (PLIF). Therefore, they felt confident that CFD can rapidly and accurately obtain large amounts of quantitative data concerning flow fields in complex industrial devices.

For multiphase modelling, Kee and Tan [2002], used CFD MixSim 2D simulation to determine the minimum impeller speed required in a stirred tank to achieve a completely mixed suspension of spherical solid particles. Using visual observations, the results were compared to Zwietering's [1958] correlation where solid suspension was deemed to have been achieved when all the solid particles were in motion and that no particle remained on the bottom of the tank for more than 1 to 2 seconds. They concluded that the minimum impeller speed obtained from their simulation work agreed well with Zwietering's [1958] correlation. The difference between the two results was small with the result from

simulation registering 3.4% lower in revolution per minute than that obtained from the correlation.

Similarly, Bakker et al. [2000] also studied the effects of flow pattern on the solids spatial distribution in a stirred tank using LDA to conduct its physical experiment and CFD for its mathematical modelling of the system of interest. Single impeller and multiple impeller systems were studied in tanks with $H$=1.75$T$. The impellers employed were axial flow impellers pitched blade turbines (PBT) and high efficiency impellers (Chemineer HE-3). Their studies concluded that solids spatial distribution was greatly influenced by certain flow transitions. When the $D/T$ ($D$: impeller diameter; $T$: tank diameter) ratio and/or $C/T$ ($C$: impeller clearance) ratios were too large, the outflow of the impeller became more radial and the jet from the impeller was directed towards the tank wall. At the same time, the flow direction at the bottom reverses, directed inward, rather than outward as was the case with smaller $D/T$ and $C/T$ ratios axial flow pattern. However, this phenomenon seriously hampered solids suspension. From this deduction, they recommended that for most solids suspension applications, the impellers should therefore be operated in the axial flow regime. They also noticed that the just-suspended power draw increased dramatically at the two sides of $D/T$ ratio, which is at the very small and very large end of the $D/T$ ratios. They attribute this behaviour to the small velocities at the base of the tank to suspend the solids at very small $D/T$ ratio and the outflow becoming more radial causing solids to settle at the centre of the vessel base at very large $D/T$ ratio. Because of this, they felt that models that were only based on overall power draw of the impeller system will not be able to accurately predict the just-suspended speed and power draw.

It was also discovered that adding a second impeller did not decrease the just-suspended speed, $N_{js}$ but increased the homogeneity of the suspension, provided that the spacing between the impellers was not too large. This study showed that with one impeller system, one flow loop extending about half the liquid level was formed. Two impellers spaced at $S/D$=3 ($S$: impellers spacing) generated one large flow loop and the solids reached the level of the second impeller. But when the impellers were placed too far apart such that the spacing became $S/D$=3.7, zoning occurred and the flow between the impellers separated forming two flow loops were formed. Consequently, the solids did not reach the second impeller. Their main conclusion was that designing based on only $N_{js}$ or on power draw would not lead to an optimum design, rather, the impeller system has to be designed such

that it provides the optimum flow pattern for the suspension duty to be performed. According to Paul et al. [2004], cloud height improves with the addition of a second impeller even though such addition will not decrease the $N_{js}$ [Bakker et al. 2000].

A related study to determine the effect of multiple impeller was carried out by Harvey et al. [1997] where variables such as impeller size, spacing and baffles were investigated using CFD. They concluded that even though some discrepancies occurred, in general, predicted results agreed well with experimental results which led them to further conclude that computational techniques were an extremely valuable tool in determining the flow patterns and mixing in complex multiple impeller systems. In relation to the variables investigated, they discovered that changes in impeller spacing and sizing significantly affected compartmentalisation of the flow within the reactor.

Sha et al. [2001] also conducted a similar study but the focus was more on the difference in particle sizes and impeller location on the shaft. They began by modelling and simulating the suspension of single-size particles inside a stirred tank using commercial software CFX-4.2 and compared these CFD results with those physical experiment results carried out by Shamlou and Koutsakos [1989]. This comparison revealed that the results agreed with each other. After this validation, the authors simulated the effect of different particle sizes on particle distribution in both the axial and radial direction. At constant impeller rotational speed of 1,400 rpm, where the impeller was located in the middle of the shaft, particle size of 100 μm appeared to be well suspended even though its distribution is not uniform where low particle distribution was found to be at the top of the tank and below the propeller. From the simulation on 300 μm particle size, they concluded that the particle distribution uniformity decreases with increase in particle size. At 1,400 rpm, particle with size 700 μm or beyond were not suspended. At this operating condition, the particles concentrated in the centre and the corners of the tank's bottom, which showed clearly the dead zone of this stirred tank. The results from simulating 300 and 700 μm particle size also showed that particle distribution was higher near the wall of the stirred tank than anywhere else. This study also showed that particle distribution was at its maximum at position above the impeller and that the distribution decreases with increasing particle size. In contrast, with the exception of the 100 μm particle, the particle distribution for different sizes was at its minimum under the impeller. As for the 100 μm particle, the uniformity of

particle distribution increases with increasing mixing intensity. They also conducted simulation to determine the effect of particle size as a function of the impeller speed on the particle distribution at the bottom of the stirred tank. In this sub-objective, they concluded that higher impeller speed led to better particle suspension, echoing the results discovered by Kee and Tan [2002] where a minimum impeller speed was required to suspend solid particles. Overall, Sha et al. [2001] concluded that the multiphase model was able to illustrate suspension particle distribution.

The study of CFD multiphase modelling of liquid-solid system has also been extended to ultraviolet reactor for its disinfection application [Downey et al. 1998] and high-temperature solar chemical reactor [Meier et al. 1996]. A more complicated CFD modelling of gas-liquid-solid flow has also been applied successfully to photocatalytic system, incorporating ultraviolet radiation, where the experimental and predicted values had a correlation value of 0.974 [Pareek et al. 2003]. Other researchers whose work involved CFD modelling of a solid phase include Mathiesen et al. [2000] whose study was confined to the prediction of gas-solid system using the Eulerian model. Similarly, they concluded that predicted results agreed very well with experimental results.

Ochieng and Lewis [2006] conducted the CFD simulation of solids off-bottom suspension and the particles cloud height using CFX5.6/5.7, validated by LDA technology. Both authors concluded that CFD predictions of the off-bottom suspension and cloud height were better for small particles where the particles are smaller than 150 μm and for low solids loadings lower than 6% mass loading. They also mentioned that CFD simulations data can be used to develop empirical models that predict mixing features, which can enable improvements in the performance of the solid-liquid systems to be made, since the quality of mixing depends on these features.

While researchers such as Kee and Tan [2002], Bakker et al. [2000] and Sha et al. [2001] focused on improving solids suspension process, Ozcan-Taskin and Wei [2003] conducted a study to determine the effect of $D/T$ ratio on the draw-down of solids that float, due to their lighter density than the continuous medium. Although such a process was important in food processing, polymerisation reactions and fermentation processes, there has been little published work in this field of specialisation. From this experiment, they concluded that even though a higher speed was required, a smaller diameter impeller ($D/T$=1/3) was

more energy efficient in drawing down floating solids than impellers having a larger *D/T* ratio which tended to produce radial flow that directed the fluid to the tank wall, thus echoing results discovered by Bakker et al. [2000]. However, this result holds true so long as solids were not drawn down along with air through vortices. When air was drawn down together with the solids, the power demand could be lower with a larger diameter impeller. Other researchers who conducted work on the draw-down of floating solid particles include Kuzmanic and Ljubicic [2001] who used up-pumping pitch blade turbine and Bao et al. [2005] who studied the suspension of buoyant particles in a three phase stirred tank.

Montante et al. [2001] used the sliding mesh (SM) and multiple reference frame (MRF) approaches to model and simulate a stirred tank equipped with a Rushton turbine. Their main objective was to determine the capability of CFX 4.1 code to correctly predict the transition from the double- to single-loop flow pattern obtained when impeller clearance was reduced. They compared their results to those obtained previously via physical experimentation that employed LDA. This comparison revealed that the CFD code correctly predicted the flow pattern transition as well as the *C/T* ratios at which the transition occurred and the sharp drop in the power number accompanying the transition to the single-loop pattern. It also correctly predicted the slight increase in the discharge stream inclination above the horizontal discharge with decreasing clearance observed just before the abrupt drop in inclination below the horizontal discharge with the lowest clearance ratio. A detailed comparison was made at $C/T$=0.15 that included turbulence modelling using the standard $k$-$\varepsilon$ approach and flow pattern around impeller region. They reported under-estimation of the turbulence energy, echoing discoveries by Sheng et al. [1998] and over-estimated the impeller stream discharge angle. Several simulations were conducted to investigate the reasons for this discrepancy between simulation and experimental results. The effects of blade and baffle thickness, grid size, bottom wall friction and the turbulence approach adopted were studied. However, none of these improved the agreement with experimental results. Because of this, they felt that the single-loop flow pattern exhibited by low *C/T* ratio was a particularly severe benchmark for CFD techniques. Since both the Sliding Mesh and MRF approaches yielded similar results, they felt that the MRF approach would be more computationally economical.

The difference, be it under or over prediction, between the turbulence quantities predicted by CFD and results experimentally obtained is an issue at this point and must be resolved first because until such time where one can accurately predict such quantities in a single phase flow, it will be difficult, if not impossible to model and simulate complex multiphase flows, such as gas-liquid, solid-liquid, gas-liquid-solid where turbulence plays an important role to ensure heat and mass transfer effectiveness.

While Morud and Hjertager [1995] modelled the gas-liquid flow in a stirred vessel, Ranade and Deshpande [1999], Krishna et al. [2000], Rigopoulos and Jones [2003] successfully modelled the gas-liquid flow in a bubble column reactor. A similar study carried out by Khopkar [2003] included modelling the gas-liquid flow generated by a pitched-blade turbine in a stirred tank where such a process normally employs radial-flow impellers that offer a higher shear-to-flow ratio which in turn helped to disperse the sparged gas into smaller gas bubbles, rather than using axial-flow impellers. Dhotre et al. [2004] conducted a 2D CFD modelling to predict the flow pattern in bubble column reactors. The model was validated using available experimental data and extended to simulate the effect of the sparger design and *H/T* ratio on radial gas hold-up profiles. The researchers concluded that CFD was able to predict the variation of gas hold-up profiles as the function of the *H/T* ratio and the sparger design.

Matonis et al. [2002] developed a predictive, experimentally validated CFD model for gas-liquid-solid flow by developing a 3-D transient computer code for the coupled Navier-Stokes equation for each phase. This hydrodynamic model used the principle of mass conservation and momentum balance for each phase. The principal input was the viscosity of particulate, measured using a Brookfield viscometer and a PIV technique. The predicted time-average particle velocities and its concentrations agreed with the measurements done in the slurry bubble column with the continuous flow of liquid in the churn-turbulent regime. Particle velocities were measured using the PIV technique while its concentrations were determined using a combination of $\gamma$-ray and x-ray densitometers. Both the empirical and simulated results showed a down-flow of particles in the centre of the column and the up-flow near the tank wall. Finally, they concluded that computed horizontal distributions of granular temperature and the turbulent kinetic energy of particles, agreed with measurements done using a PIV technique, showing a marked improvement to the research carried out by Sheng et al. [1998] and Sahu et al. [1999].

Li et al. [2001] studied the bubble formation dynamics in gas-liquid-solid fluidisation at high pressures using CFD. Through this study, they discovered that at constant gas flowrate through the orifices, pressure has little effect on bubble formation, rather, it was affected significantly by the presence of particles. To be precise, the bubble formation time and bubble size were greater in liquid-solid suspensions than those in pure liquids at given gas and liquid velocities. Their CFD simulations also revealed the dynamic characteristics of the multi-bubble formation process. From the simulations, they confirmed that the leading bubble, through its wake, affected the formation process of the trailing bubble and multi-bubble formation process was strongly influenced by the complicated bubble wake flows induced by the adjacent bubbles. In addition, the behaviour of bubble formation from multi-orifices was different from that from a single orifice and the critical distance between two orifices for negligible interaction was found to be three times the bubble diameter. Most importantly, simulated bubble formation behaviour agreed well when validated against experimental results.

Up to this point, most CFD applications on stirred tank mentioned were confined to the optimisation of process performance. Dakshinamoorthy et al. [2004] used CFD simulations to study shortstopping runaway reactions in a stirred tank. Using the MRF approach they used Fluent® 6.2 solver and Gambit 2.0 to generate the cells and model 3D, laminar flows generated by a standard Rushton turbine. The stirred tank was divided into two regions: an inner region attached to the rotating impeller and shaft; and an outer region attached to the stationary baffles and the tank, as shown in Figure 2.3.

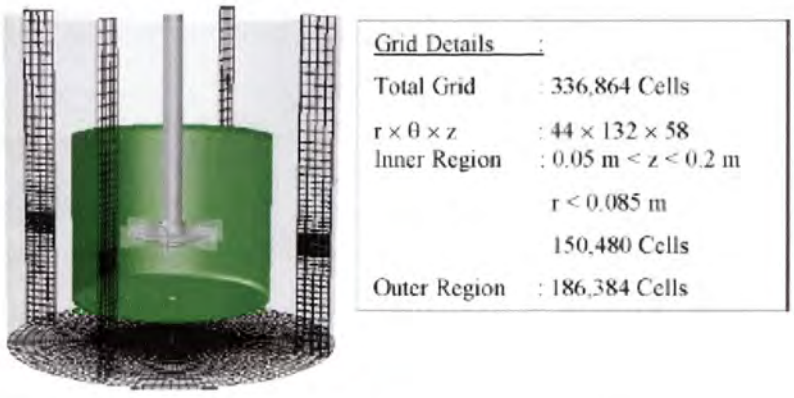


Figure 2.3: Solution domain and computational cells

The model equations for the inner or impeller region were solved using a rotating framework, while the equations for the outer or bulk region were solved using a stationary framework. Total cells used were 336,864 cells of which 150,480 belonged to the inner region and 186,384 belonged to the outer region. In this study, the effect of different inhibitor feed locations on the temperature distribution in the reactor with incomplete mixing was simulated. They discovered that the predicted results showed a significant effect of the feed locations on the predicted temperature distributions. The addition of the inhibitor at two locations in the reactor, 75% in the impeller discharge stream and 25% at the top of reactor, significantly improved the inhibition process. This combination was obtained by analysing the results of the first two feed locations, as shown in Figure 2.4.

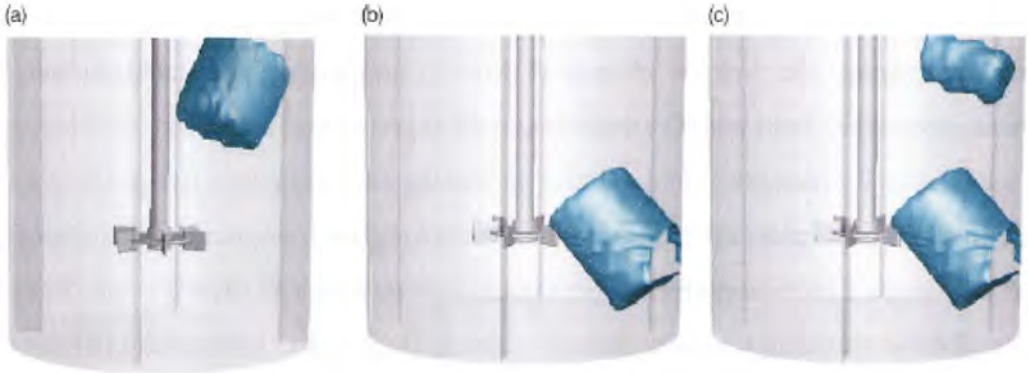


Figure 2.4: Inhibitor feed locations: (a) 1st location (b) 2nd location (c) 3rd locations

They also discovered that feeding excess inhibition material by 2.5 times the initial feed into the third feed locations significantly improved the performance of inhibition. They concluded that their computational model showed promising results and successfully represented the effect of the mixing behaviour on the inhibition process performance.

Similar application of CFD to develop a practical method to prevent runaway situation in chemical reactors was presented by Rudniak et al. [2004]. In this study, MixSim 2.0 was used to build and mesh the geometry while Fluent® 6.1 solver was used to solve the appropriate governing equations. The simulations conducted exhibited the local and instantaneous values of the flow velocity, reactant concentrations and reactor temperature. Rudniak et al. [2004] felt that such simulations are fundamental to indicate in advance the local non-uniformities of temperature appearing in the reactor and to estimate the possibility of the global thermal runaway propagation in the reactor, originating from the

hot-spots. In addition, such application will indicate the appropriate locations of where the temperature detectors should be positioned. They concluded that CFD can help to indicate dead-zones or temperature non-uniformities inside industrial reactors, which improve the safety criteria and efficiency of early warning detection systems.

Apart from these discoveries, other researchers who conducted virtual experiments using CFD included Endo et al. [2004] who utilised CFD capability to interpret nanotube growth rates, feedstock decomposition, by-product compositions, transport rates and reaction mechanisms in a chemical vapour deposition (CVD) reactor. Xuereb and Bertrand [1996] used CFD to model the 3-D hydrodynamics of a stirred tank agitated by a dual-propeller system that was filled with liquid having evolving rheological properties. From this study they concluded that for modelling of pseudo-plastic behaviour of many fluids, CFD provided them with good results but it remained impossible to take into account thixotropy or elasticity rheological properties which were often encountered in polymerisation.

Similar study carried out by Pedrosa and Nunhez [2000] found that the CFD model employed represented the flow, temperature and non-Newtonian viscosity fields rather well for a mixer system that employed the anchor impeller in laminar flow. Other researches who conducted studies in non-Newtonian media were Missirlis et al. [1998] on the simulation of viscoelastic expansion flows, where they concluded that the finite volume method was able to model such fluid rather competently.

On the simulation of shear-thinning liquids, Yildirim and Basaran [2001] concluded that their 1-D models were remarkably accurate at low stretching speeds but failed at high stretching speed. Kelly and Gigas [2003] conducted study on the behaviour of shear-thinning fluids, 0.1% pH 7 Carbopol, near axial-flow impellers, namely pitch-blade turbine (A200) and A315 the using MRF approach. Their model consisted of 158,000 grid cells, covering one-quarter of the tank and the impeller surface being the densest. The objectives of their study were to see how accurately a CFD model would predict power numbers and discharge angles of the impellers; to use the results of CFD modelling to determine whether the near-impeller "average shear rate" was truly just a linear function of impeller rotational speed in the transition flow regime and finally to use CFD modelling results obtained to determine an improved method for estimating the dependence of $N_P$ on $Re$ in the transitional-flow regime for shear-thinning fluids. Their investigations led to the part

conclusion that the A315 $N_P$ calculated by CFD agreed well (±4%) with the results obtained experimentally within *Re* range of 50-400. With A200 impeller, the power numbers simulated by CFD were 10-15% larger than those obtained experimentally. They attributed this significant difference to the possibility that a laminar-flow model was employed in a transitional-flow regime and/or the CFD model did not factor in all of the small local recirculation zones and swirls near the blade tip, which they felt could be significantly improved with additional grid refinement. As to the reason why A315 did not produce such great difference, they felt that it was due to the A315 hydrofoil design, which promoted less of such local swirling. Using LDV to measure the direction of velocity vectors, they compared the impeller discharge angles obtained via CFD to those from experiment where the angle convention used was 90° for completely radial discharge and 0° for completely axial (downward) discharge. While they did not specify the angle, the discharge angle for 0.1% pH 7 Carbopol was significantly less than that of Newtonian (glycerin) at the same *Re*, where the CFD model slightly overpredicted, that is, more radial discharge than it actually happened. Finally, from their CFD study, they found that the "effective shear rate" near the impeller was not simply a linear function of the impeller speed, rather, it depended on the flow behaviour index and the discharge angle in the transitional-flow regime.

As elaborated above, CFD has been used to predict the outcomes of many scenarios. Such predictions are beneficial in the development of public policy in the case of modelling terrorist attack scenario and the return of investment (ROI) assessment in the case of optimisation of unit operations. Thus, due to the impact that modelling and simulation prediction can have, the credibility of CFD results is of great concern to an organisation decision makers, public officials and other stakeholders who are affected by the decision that are based on these predictions. To increase the confidence of such stakeholders, CFD modelling and simulation results should be subjected to verification and validation (V&V) testing, where verification is the assessment of the accuracy of the solution to a CFD model by comparison with known solutions, while validation is the assessment of the accuracy of a CFD simulation by comparison with experimental data [Oberkampf and Trucano 2002]. Figure 2.5 depicts the role of V&V within the phased approach for modelling and simulation.

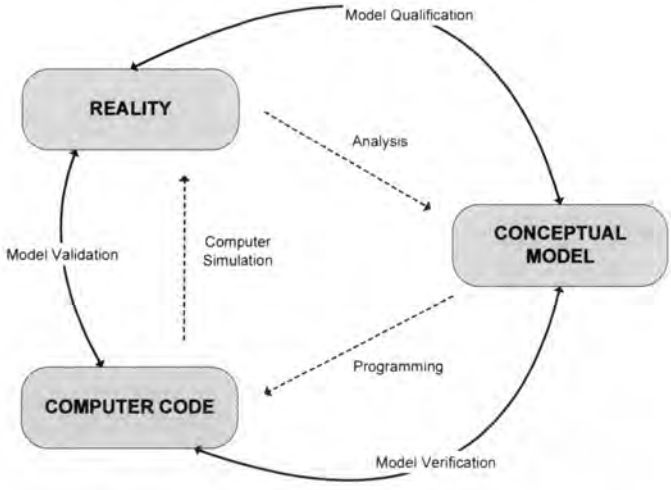


Figure 2.5: Phases of modelling and simulation and the role of V&V

In conclusion, in this literature review covered, majority of the published works on CFD used Fluent® or CFX software in stirred tanks were successfully validated by LDA [Xu and McGrath 1996; Revstedt et al. 1998; Bakker et al. 2000; Montante et al. 2001], LDV [Kelly and Gigas 2003] or PIV [Sheng et al. 1998 and Matonis et al. 2002] while the others used previously reported experimental results to validate their CFD predictions [Sha et al. 2001].

In general, many researchers reported great success with laminar flow modelling [Lamberto et al. 1999, 2001; Pedrosa and Nunhez 2000; Zalc et al. 2001; Kelly and Gigas 2003]. However, other researchers claimed that although CFD accurately predicted, both qualitatively and quantitatively, the axial-radial mean flow patterns, they under- or over-predicted the tangential velocity component and turbulent quantities such as the turbulent kinetic energy, $k$ and the turbulent energy dissipation rate, $\varepsilon$ [Sheng et al. 1998 and Montante et al. 2001].

The modelling mentioned were mostly confined to Newtonian fluid in non-reactive bench- or pilot-scale reactors, since it was difficult for CFD to capture thixotropy or elasticity rheological properties Xuereb and Bertrand [1996]. However, with the advancement of CFD technology, more researchers are beginning to successfully represent the behaviour of non-Newtonian fluids [Missirlis et al. 1998; Pedrosa and Nunhez 2000]. While there were many researchers who used CFD on stirred tanks, only a handful studied stirred reactors [Bakker and Fasano 2000; Brucato et al. 2000; Revstedt and Fuchs 2000].

Multiphase liquid-solid system modelling was confined to spherical particles, low solid-volume ratio and non-reactive system [Bakker et al. 2000; Sha et al. 2001; Kee and Tan 2004], except [Meier et al. 1996], where solar chemical reactor and [Downey et al. 1998], ultra-violet reactor were modelled. Multiphase liquid-solid-gas reactive system was successfully modelled by Pareek et al. [2003]. Research work carried out by Dakshinamoorthy et al. [2004] would be useful for extending the application of CFD based models for developing operating protocols for better control and the prevention of runaway reactions in a stirred tank reactor where physical experiments are too dangerous to carry out.

Apart from modelling unit operations, researchers also used CFD to model deflagration-detonation processes [Popat et al. 1996; Rehm et al. 1998; www.hpcmo.hpc.mil] and/or the impact of weapons, be it conventional or WMD, on civilisation [www.itsc.com] and high-consequence systems that can never be tested, such as nuclear core meltdown [Dinh et al. 1996].

Hitherto, CFD does not have the ability yet to replace the necessity for experiments, therefore, verification and validation must be carried out to gain the confidence of stakeholders affected by the CFD results [Oberkampf and Trucano 2002]. On the other hand, although CFD cannot eliminate the necessity for experiments, CFD can synergistically guide the experiments and accelerate the progress, while keeping the costs at a minimum and safety at a maximum.

## 2.2 Rheology of fluids

This section deals with the rheology of fluids and includes a study on the different kinds of fluids and their characteristics. It covers literature review and physical experimentation. This section is deemed as necessary because throughout this research work, different kinds of fluids will be encountered. Thus, a thorough understanding of the rheology of fluids will enhance fundamental knowledge in this field of specialisation that ultimately helps to solve and prescribe solutions for complex fluid-related problems.

### 2.2.1 Types of fluid

A fluid is bounded by two parallel plates of area A, separated by a small distance *dy*, as shown in Figure 2.6. The bottom plate is held fixed but the upper plate moved at velocity *u* when a force *F* is applied to it [Larson 1999]. The fluid trapped between the two plates continues to move as long as the force is applied. Under this situation, the shear stress is $\tau = F/A$ and the velocity gradient, known as the shear rate, having unit 1/s, is given as $\gamma = du/dy$. Since viscosity can be defined as the ratio of the shear stress to the shear rate ($\mu = \tau/\gamma$), a Newtonian fluid is any material whose plot of shear stress versus shear rate, also known as flow curve, is linear.

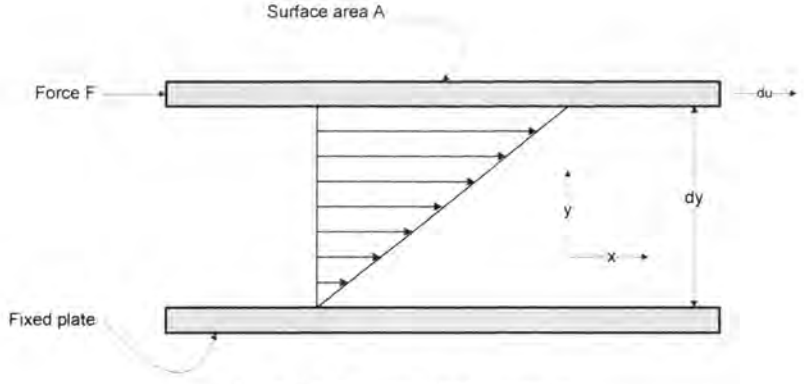


Figure 2.6: Newtonian fluid illustration

A non-Newtonian fluid is one whose flow curve is non-linear and does not pass through the origin. In other words, the apparent viscosity, defined as the ratio of the shear stress to the shear rate, is not constant at a given temperature and pressure but is dependent on flow conditions such as flow geometry, intensity of shear stress and duration of shearing.

Such fluids may be conveniently categorised into three major classes [Chhabra and Richardson 1999]:

- time-independent
- time-dependent
- visco-elastic

Fluids for which shear rate at any point is determined only by the value of the shear stress irrespective of the duration of the shearing. Within this class, there are three types of fluid, namely: pseudoplastic (shear-thinning), dilatant (shear-thickening) and viscoplastic as shown in Figure 2.7. The most common type of time-independent non-Newtonian fluid behaviour is pseudoplastic. Such fluid is characterised by a decrease in the apparent viscosity with increasing shear-rate. Hitherto, there are three well known mathematical modes for this fluid: the power-law or Ostwald de Waele model, the Carreau viscosity equation and the Ellis fluid model.

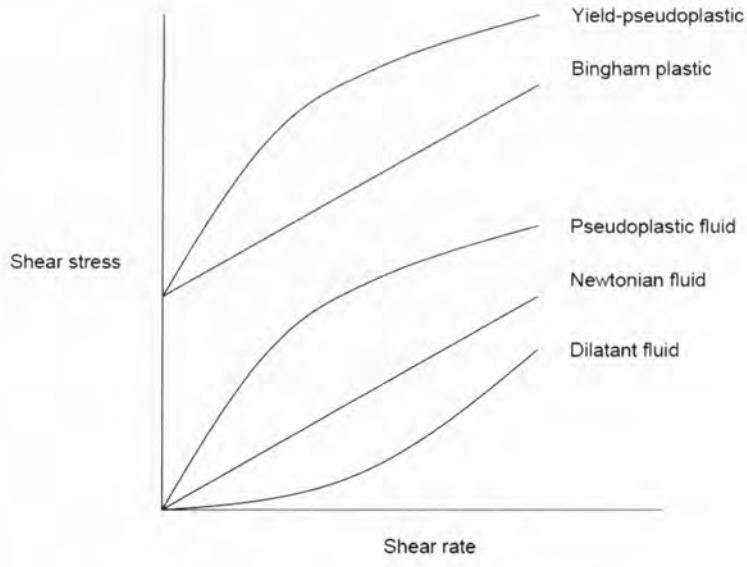


Figure 2.7: Types of time-independent flow behaviour

On the other hand, the apparent viscosity of dilatant fluids increases with increasing shear-rate, therefore this fluid is also known as shear-thickening. There is a great difference between turbulent flow conditions and dilatant flow behaviour. Both phenomena will increase the fluid viscosity however dilatant materials will show a steadily increasing

viscosity with increasing shear rate while the turbulent flow is characterised by a relatively sudden and substantial increase in viscosity above a certain shear rate. Moreover, the material may behave as a Newtonian or non-Newtonian below this point. Apart from this major characteristic, dilatants are similar to pseudoplastic in that they show no yield stress.

Viscoplastic fluid behaviour is characterised by the existence of a yield stress that must be exceeded before the fluid deforms or flows. However, when the externally applied stress is smaller than the yield stress, such material will deform elastically. Once the magnitude of the external stress has exceeded the value of the yield stress, the flow curve may be linear or non-linear but will not pass through the origin. An example of such fluid is called Bingham plastic which exhibit linear flow curve and is characterised by a constant plastic viscosity and a yield stress. On the other hand, a fluid possessing a yield stress and non-linear flow curve on linear coordinates is called a yield-pseudoplastic material. It is known that viscoplastic material also displays an apparent viscosity which decreases with increasing shear-rate. Mathematical models for viscoplastic behaviour include the Bingham plastic model, the Herschel-Bulkley fluid model and the Casson fluid model.

Despite the comprehensive classification within the time-independent class, the flow behaviour of many industrially important materials do not belong to this class, rather, they belong to a class called time-dependent materials. This class is reserved for more complex fluids for which there exists not only the relationship between shear stress and shear rate but the shear rate also depend on the duration of the shearing and their kinematic history. In reality, apparent viscosities may depend not only on the rate of shear but also on the duration for which the fluid has been subjected to shearing. For example, when materials such as bentonite-water suspensions, red mud suspensions (waste stream from aluminium industry), crude oils and certain foodstuffs are sheared at a constant rate following a long period of rest, their apparent viscosities decreases gradually as the 'internal' structure of the material is progressively broken down. As time proceeds, the number of structure available for break down also decreases, bringing the rate of change of apparent viscosity to zero. On the other hand, as the structure breaks down, the rate at which linkages can reform increases, so that eventually a state of dynamic equilibrium is reached where the rate of reform and breakdown are in harmony. Fluids belonging to this class can be subdivided into two classes: thixotropy and rheopexy as shown in Figure 2.8.

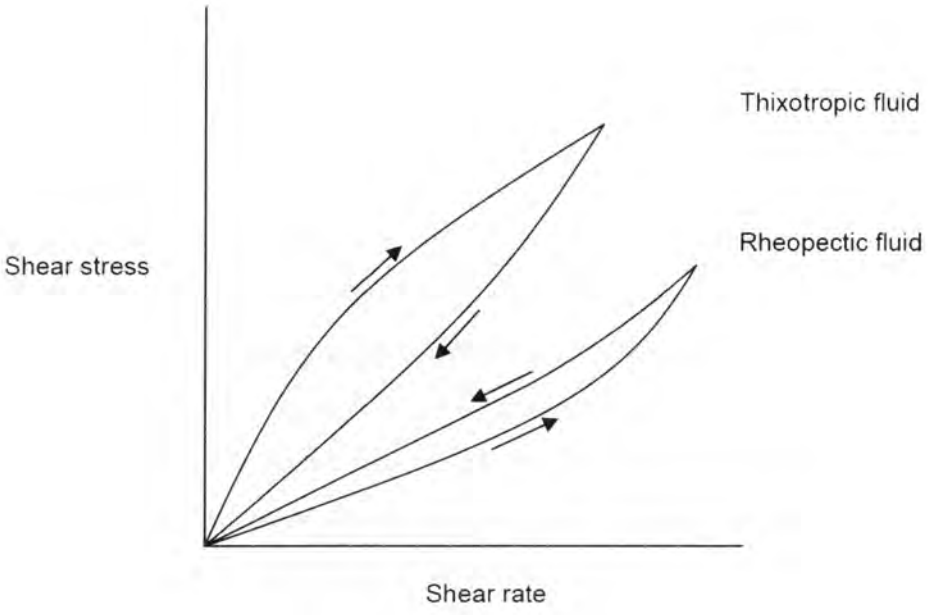


Figure 2.8: Types of time-dependent flow behaviour

A material is classified as thixotropy if the apparent viscosity decreases with the time of shearing even when it is sheared at a constant rate. If the flow curve is measured in a single experiment in which the shear rate is steadily increased at a constant rate from zero to some maximum value and then decreased at the same rate to zero again, a hysteresis loop is obtained. The height, shape and enclosed area of the hysteresis loop depend on the duration of shearing, the rate of increase or decrease of shear rate and the past kinematic history of the sample. Conversely, no hysteresis loop is observed for time-independent fluids. 'false body' is a term given to describe the thixotropic behaviour of viscoplastic materials. Although thixotropy is associated with the build-up of structure at rest and breakdown of structure under shearing, viscoplastic materials do not lose their solid-like properties completely and can still exhibit a yield stress that is regained only after a long recovery period, even though this is usually less than the original value of the untouched sample. Examples of materials exhibiting thixotropic behaviour include concentrated suspensions, emulsions, protein solutions and food stuffs.

Any material for which the apparent viscosity increases with time of shearing is classified as a rheopexy material. Hysteresis effects exist and reflected in the flow curve but in this case it is inverted, relative to that exhibited by a thixotropic material. In such fluid, the structure builds up by shear but breaks down when the material is at rest, behaving oppositely from the thixotropic material. For example, a study that uses a 42% aqueous gypsum paste found that after shaking, this material resolidified in 40 mins if at rest but only 20 s if the container was gently rolled in the palms of hands [Chhabra and Richardson 1999]. This shows that gentle shearing motion, via rolling, facilitates structure buildup but more intense motion destroys it. This means there is a critical amount of shear beyond which reformation of structure is not induced but breakdown occurs. In a practical sense, it is not uncommon for the same dispersion to display both thixotropy as well as rheopexy depending upon the shear rate and/or the concentration of solids.

It is impossible to postulate simple mathematical equations of general validity to describe time-dependent fluid behaviour, and it is normally necessary to perform measurements over the range of conditions of interest. A very important note is that the conventional flow curves are of limited uses unless they relate to the particular history of interest in the application. For instance, under industrial setting during the transfer of material from the holding tank to the pipe, the material enters the pipe slowly with minimum shearing. The flow curve should be based on tests performed on samples which have been stored under identical conditions and have not been subjected to shearing by transference to another tank. On the other hand, when the material undergoes vigorous agitation and shearing, such as in passage through a pump, the flow curve should be obtained using highly sheared pre-mixed material. If reliable flow property data are available, the zero shear and infinite shear flow curves can be used to form the bounds for the design of a flow system. Under constant pressure drop, the zero shear limit, representing maximum apparent viscosity, will provide a lower bound and the infinite shear conditions representing minimum apparent viscosity, will provide the upper bound on the flowrate. Similarly, under constant flowrate, the zero and infinite shear data can be used to establish the maximum and minimum pressure drops or pumping power.

Finally, a fluid that exhibits elastic and viscous effects almost immediately and in the absence of the time-dependent behaviour is called visco-elastic material. Materials such as polymer melt, polymer and soap solutions exhibit visco-elastic behaviour.

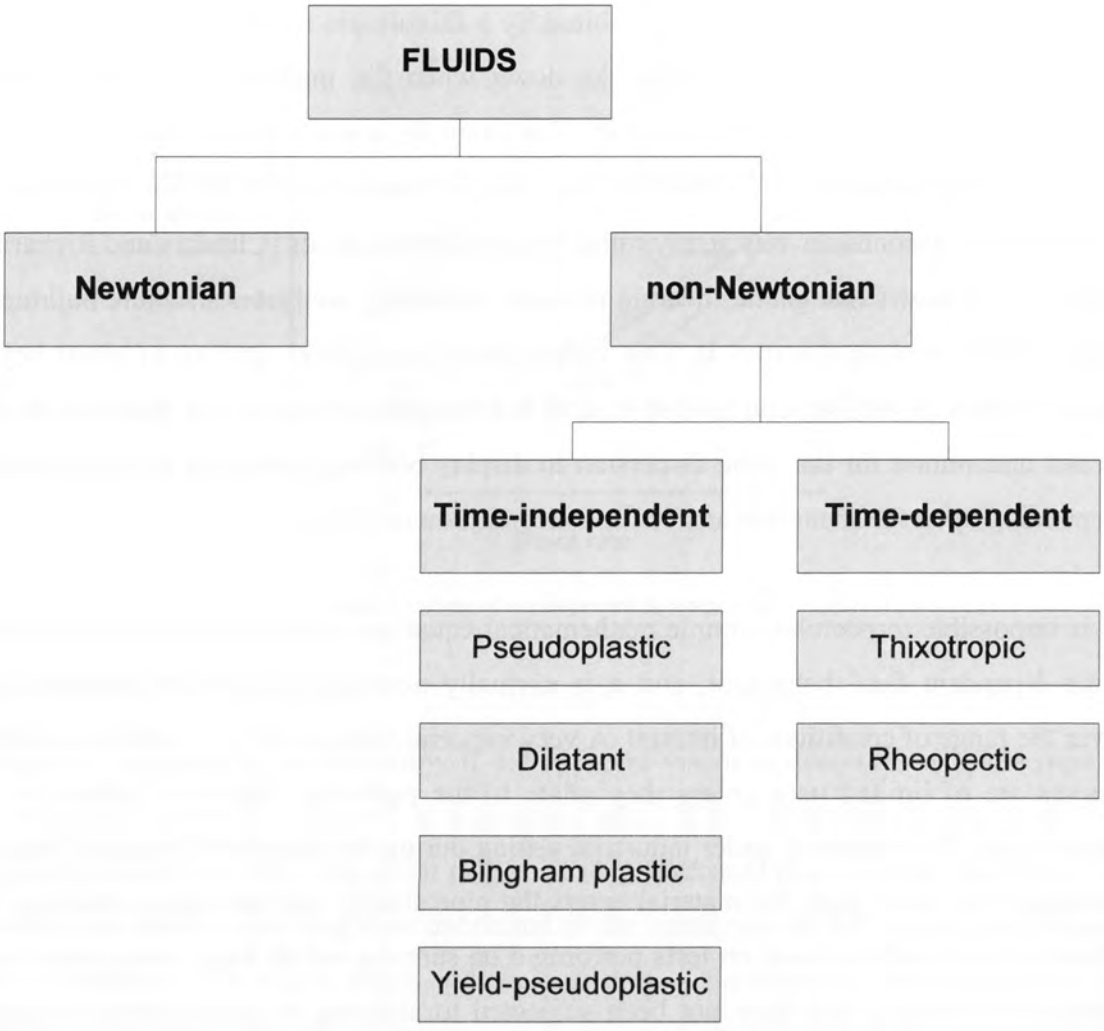


Figure 2.9: Map of various fluid types

Figure 2.9 shows the map that summarises various fluid types which were categorised as either Newtonian or non-Newtonian and further sub-categorised according to their behaviours.

### 2.2.2 Behaviour of TNT

Parry and Billon [1987] studied the rheology of molten TNT using two grades, commercial and ultra pure TNT. Their equipment consisted of a Haake RV 2 viscometer where the test sample was placed between a cylindrical cup and cylindrical rotor situated coaxially with the cup [Coussot 2005]. Shear was applied to the fluid by means of rotating the cylindrical motor. To control the temperature of the cylindrical cup, cylindrical rotor and the test sample, the three components were surrounded by a temperature vessel. Their study can be classified into one that aims to determine whether TNT was shear-dependent and the other, whether TNT was time-dependent material. To achieve their first objective, they subjected a sample over a range of continuously variable shear rates from rest to the maximum desired shear rate and back to rest, and plotting the resulting shear stress as a function of shear rate. The flow curve showed that when the commercial grade TNT was sheared at 95.4°C ranging from 0 to 5,300 $s^{-1}$, a linear relationship existed between the shear stress to the shear rate, providing a strong indication that TNT was a Newtonian fluid. Their second objective was achieved by shearing a test sample over a specified period of time at constant shear rate. A plot of the shear stress versus time was presented. Their results showed that when the same commercial grade TNT was sheared at 490 $s^{-1}$ for 6 hours, the viscosity remained unchanged. This result further reinforced the finding that TNT is a Newtonian fluid where its viscosity is independent of the shear rate and the duration of shearing. The discovery of TNT being a Newtonian fluid contradicted the conclusions of other published works which claimed that molten TNT exhibited dilatant behaviour with increasing shear rate. Despite this contradiction, it was felt that Parry and Billon [1987] works were credible, thus, TNT is accepted as a Newtonian fluid.

Using another piece of equipment that has a larger gap between the cylindrical cup and cylindrical rotor, the researchers discovered that at a lower viscosity, all flow curves exhibited a discontinuity at lower shear rates for experiments conducted at higher temperatures. They attributed this discontinuity phenomenon that came in the form of a relatively sudden and substantial increase in viscosity above a certain shear rate, to the transition from laminar to turbulent flow rather than the result of shear rate. In a nutshell, they disagreed that molten TNT should be classified as a dilatant material. In a practical sense, this implies that if the molten TNT is pumped at a high rate from one unit operation to another, thereby inducing turbulence, the viscosity will increase.

Finally, Parry and Billon [1990] also postulated that the temperature dependence of the viscosity of pure molten TNT was found to follow an Arrhenius-type relationship having the expression:

$$\mu = 0.000541 \exp^{\left(\frac{3570}{T}\right)} \quad \text{- 2.5}$$

where $T$ is temperature in Kelvin and $\mu$ is the viscosity in mPas. This expression is valid for temperature range between 82.0°C - 95.4°C.

However, for commercial grade TNT,

$$\mu = 0.000346 \exp^{\left(\frac{3720}{T}\right)} \quad \text{- 2.6}$$

A short experiment was carried out just to:

1. Observe the behaviour of TNT when it is being melted
2. To measure the viscosity of TNT as a function of temperature
3. Observe the behaviour of RDX when it is introduced into molten TNT

The equipment employed was: Brookfield synchro-lectric viscometer, model: RVT, serial number: 27868, Frequency: 50Hz running at 230V. It was supplied by Brookfield engineering laboratories, Stoughton, Massachusetts, USA. Spindle number used: 1 and spindle rotational speed: 100 rpm.

Figure 2.10: Initial melting of TNT flakes


Figure 2.11: Partial dissolution of RDX particles

Figure 2.10 shows TNT flakes starting to melt at 80.2°C. It took some time for it to be melted because care was taken not to use overly intense heat due to safety reasons. Figure 2.11 shows RDX particles suspended in molten TNT solution.

Figure 2.12: Various spindles

Figure 2.12 shows various spindles that can be used to measure the viscosity of a fluid. In this experiment, spindle number 1, the largest shown in the picture was used owing to the low viscosity of TNT to other non-Newtonian fluids. Readings were taken at different temperature. These readings were then multiplied by a factor of 1 to obtain the viscosity in centipoise. These results were then converted to Pa.s. Figure 2.13 shows that the viscosity of TNT is inversely proportional to the temperature and the data fitted a polynomial expression. This relationship, with an excellent regression of 1, can be described by:

$$\mu = -0.0001T^2 + 0.0166T - 0.6459 \qquad \text{- 2.7}$$

The results were higher than those obtained by Barry and Pillon [1990]. Assuming no wall slip condition, this discrepancy was attributed to the proximity of the spindle to the beaker bottom and side wall, resulting in wall effect. Naturally, this wall effect gave rise to a higher drag force which created more resistance to the spindle rotation. This higher resistance would lead to a higher viscometer reading and thus a higher viscosity. Due to this, the viscosity values of TNT in this experiment will not be used for modelling and simulation purposes. Repeating the experiment using a larger beaker was not feasible because to do so would require a far greater amount of high explosive. It was felt doing so would increase the risk, therefore for modelling and simulation purposes, the viscosity of TNT will be obtained from Parry and Billon [1990].

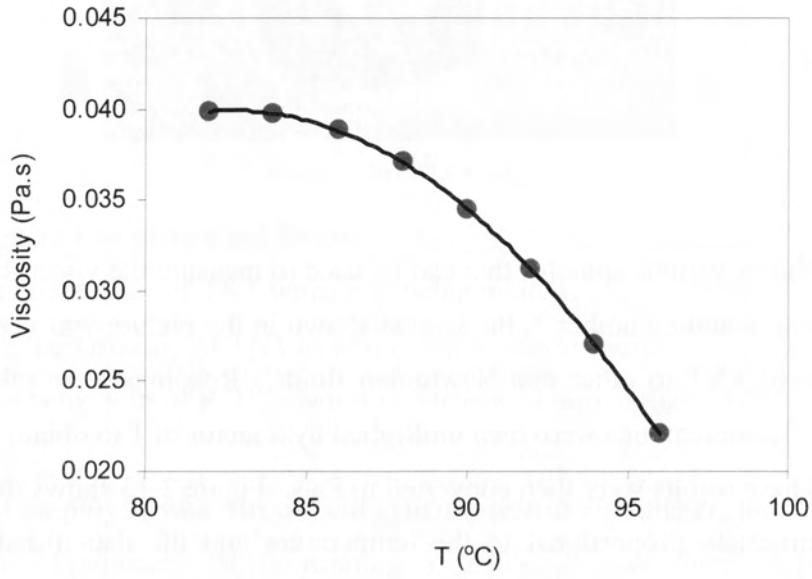


Figure 2.13: Viscosity of TNT as a function of temperature

### 2.2.3 Behaviour of RDX particles

Harzallah and Dupuis [2003] studied the rheological behaviour of $TiO_2$ particles suspension in polymer solutions. According to them, the flow properties of suspension fluids depend on several parameters, namely: the shape and size of particles, volume fraction, nature of the interactions between the particles and between the particles and the suspending medium. Consequently, several phenomena may appear such as a yield stress, thixotropy and pseudoplasticity. Such phenomena are a consequence of the evolution of the structure of the fluid under shear and the competition between Brownian and shear forces. The particles are subjected to competitive, attractive and repulsive interactions, and depending on the balance of these forces, the particles may form aggregates or flocs where shearing results decrease the radius of the enclosing spheres. Toorman [1997] studied the dense cohesive sediment suspensions that contain primarily clay particles. In this study, he discovered that the rheological behaviour of dense cohesive sediment suspensions is time-dependent, thixotropic due to changes in the flocculated structure as a results o f shear rate variations. Not every suspension mixture is thixotropic, Lee and Wagner [2003] studied colloid suspensions and claimed that the increase in such suspension mixture could induce dramatic changes in suspension microstructure, such as particles aggregation.

Although it is well established that the viscosity of suspensions increases with increasing solids volume concentration, Marti et al. [2005] studied the rheological properties of suspension mixture as a function of various physical and chemical properties of the suspended particles and the fluid as well. It is also well established that particles in suspension subjected to non-uniform shear fields can demix to assume very non-uniform concentration distribution and non-Newtonian velocity profiles. This migration takes place under conditions where inertial and colloidal forces can be considered negligible. In many one-dimensional flows, particles have been observed to migrate to low shear rate regions of the flow field [Graham et al. 1998].

High explosives containing RDX/TNT in 60:40 ratios is also known as cyclotol, hexolite, hexotol or more commonly known as composition B. Beeswax is added to reduce the sensitivity of this mixture. A few researchers studied the rheological property of cyclotol to properly understand the nature of this fluid. It has been well established that the viscosity of slurries is a function of the shape of the suspended solid particles and a lower

viscosity for a given solid volume fraction is obtainable with spherical particles because such particles provide minimum resistance to the slip-planes during laminar flow of the fluid. It has been shown that cyclotol mixture viscosity is dependent on the particle size distribution of RDX and that spherical RDX particles are preferred for low viscosity materials. Such particles can be obtained by carefully controlling the recrystallisation process [Eadie 1968]. Although it has been assumed that the increase in the viscosity of cyclotol mixture is due to the emergence of non-spherical particles after recrystallisation, the reduction of viscosity experienced on fast stirring was attributed to the particle size reduction and/or rounding of particles caused by interparticle collision or by shearing in the turbulent liquid [Eadie 1969].

Eadie [1971] also conducted experiment to explain the underlying reason on the thickening and shear-thinning behaviour exhibited by this mixture, using rotational viscometer. According to him, the viscosity of cyclotol increases with time at low shear rate and shows that there was an irreversible permanent increase in viscosity and reversible increase in viscosity, via high shearing rate. The permanent increase in viscosity was due to the partial dissolution of RDX in molten TNT (4% at 80°C and 9% at 120°C). When some of these dissolved RDX recrystallised, the particles shape and size changed, which eventually affected the mixture viscosity. In addition, the solubility RDX in molten TNT is a function of mixture temperature, which means if the temperature fluctuates as frequently occurred in an industrial mixing tank, the particle size distribution of the cyclotol mixture will be inconsistent from batch to batch leading to variation in the viscosity of this mixture. On the reversible increase in viscosity stage, he attributed this phenomenon to diffusion controlled, particle flocculation or agglomeration, which was known to increase the viscosity of emulsions and suspensions. The rate of increase in the reversible stage of the viscosity is dependent on the rate of shear and the maximum rate of thickening occurs at $N_{js}$. While the viscosity remained unchanged for cyclotol at rest, low shear rate promoted rate of particles interaction, thereby increasing viscosity, while excessively high shear rate broke up the agglomeration, thereby decreasing the viscosity.

While Eadie [1968] claimed that the increase in the cyclotol mixture viscosity due to recrystallisation of dissolved RDX particles is reversible by the action of fast stirring which resulted in more spherical RDX particles, Eadie [1971] claimed that the increase in cyclotol mixture viscosity due to recrystallisation of RDX particles is irreversible. To maintain low viscosity mixture, the particle size distribution of RDX must be controlled. According to Eadie [1971], the reversible component of the mixture viscosity is due to breaking up of agglomerated RDX particles at higher impeller speed, leading to a lower mixture viscosity. They also discovered that a higher impeller speed has little effect on the particle size distribution and particle shape of RDX.

Other researchers who conducted experiment to study the rheology of cyclotol had similar but non-identical results were Parry and Billon [1987]. These researchers, using rotational viscometer and kettle, discovered that unlike results claimed by Eadie [1971], the viscosity of cyclotol mixture increased even at rest. They also discovered that the cyclotol mixture developed from RDX particles coated with wax had thickened initially but maintained a constant viscosity for a further 20 hours. They felt that this was because of the wax coating provided resistance on the dissolution of RDX in molten TNT. After this period of time, TNT managed to diffuse through the wax layer or the wax layer degrades so that thickening occurred as a consequence of dissolution and recrystallisation of RDX particles, although at a slower rate than the uncoated batch.

An important discovery made was they could not find any evidence of recrystallisation in their polished specimens which contradicted the findings of Eadie [1971]. They attributed the initial thickening of cyclotol mixture to mechanical interference but did not rule out particle-particle interaction and electroviscous effects between RDX and TNT. They postulated that the increase in viscosity of cyclotol mixture occurred in two stages, an initial rapid increase in viscosity and a second stage consisting of slower thickening. They attributed the first stage to the agglomeration of RDX particles.

Despite the lack of evidence they agreed with other researchers who postulated that finer RDX particles allow a greater rate of recrystallisation to occur. Therefore, Parry and Billon [1987] attributed the second stage to the dynamic dissolution-recrystallisation of RDX in molten TNT, where recrystallised RDX particles assumed irregular shape that promoted greater interlocking of particles. Both stages could be reversed by employing rapid shear rate in the viscometer. However, they could not reverse the high viscosity using the kettle. The implication of this means that in most practical applications, the viscosity of cyclotol would probably increase irreversibly. In summary, both group of researchers agreed that the agglomeration of RDX particles and the dissolution-recrystallisation of a small fraction of RDX particles in molten TNT played a major role in the changes of cyclotol mixture.

While Eadie [1971] claimed that agglomeration can be reversed but recrystallisation cannot whereas, Parry and Billon [1987] claimed that using viscometer, both agglomeration and recrystallisation can be reversed but reversing the viscosity was not achievable using the kettle. The latter finding agrees with that of Eadie [1971] which discovered that stirring has little effect on the particle size and shape of RDX that eventually determines the viscosity of cyclotol mixture. In addition, even though Parry and Billon [1987] could not totally discount the increase in cyclotol mixture viscosity due to dissolution-recrystallisation of RDX particles, they could not find any significant evidence of recrystallisation of dissolved RDX particles in their polished specimens, which contradicted the findings of Eadie [1971].

Bouyer et al. [2004] studied the relationship between characteristic floc size and hydrodynamics in a mixing tank. Through this study, they answered their first question addressed at the relation between an average floc size and the viscous dissipation rate of kinetic energy. To achieve this, a first series of flocculation experiments were conducted in a mixing tank fitted with two impellers, a Rushton turbine and a Lightnin A310 impeller, for equivalent dissipated power conditions. They discovered that the average floc size is shown to depend on the global dissipation rate and does not depend on the impeller type. However, the floc size distributions were found to be significantly different for each impeller. They also answered the question addressed at the dependency of the floc size on the history of mixing. To achieve this, they conducted a second series of experiments consisted of flocculation, break-up, and reflocculation stages. These experiments showed

that the average floc sizes are similar after flocculation or reflocculation steps, but once again, the floc size distribution can be very different with different impellers.

This literature review means that if the mixing tank under industrial condition is not effective, the shear rate will not be homogeneous throughout the tank therefore the viscosity differs from one part of the tank to another. Non-homogeneous viscosity throughout the tank has several implications. Firstly, it will affect the particle distribution inside the tank because some regions will provide more fluid resistant to particles than the other regions. Meaning, some regions will have a higher density than others. In addition, the use of different impeller types will induce different kinetic energy dissipation rate which will then affect the particle size distribution and eventually affect the viscosity. Consequently, when the molten mixture emanating from such mixing tanks is poured to be solidified, the density variation will eventually lead to different contraction rate on solidification.

When the RDX was added to molten TNT, it was observed that the white coloured RDX particles became less visible and this was attributed to the partial dissolution of RDX in the molten TNT. And as the temperature was reduced to 85°C, recrystallisation of RDX occurred, as evidenced by the appearance of white component. The dissolution of RDX resulted in a higher RDX/TNT mixture while its recrystallisation resulted in a lower viscosity. These findings agree with those of Eadie [1971].

## 2.3 Solidification process

This section is mainly concerned with the application of CFD technology to the study of the solidification process. Although the CFD modelling and simulation of the solidification processes is outside the scope of this study, it is important to conduct literature review to understand its process because the products emanating from the mixing tank will be solidified. The section begins with an outline of CFD being used to understand the theory underlying the solidification process followed by more specific studies on filling and instantaneous filling.

The growth, shape and composition of equiaxed dendrites can be significantly influenced by their movement. Movement of free equiaxed grains is generally a result of gravitational forces which includes movement due to sedimentation or floating of the solid and movement due to convection patterns in the melt. Sedimentation or floating of grains is a result of density differences between the grains and the bulk liquid that arises from the rejection or incorporation of solute during the solidification process and solidification shrinkage. Convection in the melt is due to a combination of density differences resulting from temperature and composition variations in the liquid. This phenomenon is normally referred to as thermosolutal convection. Convection pattern is a function of how cooling is applied to the system, the concentration and density of the components [Rerko et al. 2003]. Such macroscopic redistribution of solutes leads to serious defect issue because this variation in solute distribution, especially if it forms a high composition gradient or a poor distribution of secondary phases, can lead to an inhomogeneous distribution of mechanical properties within the solidified structure. This phenomenon, which can lead to internal or surface crack, is called macrosegregation and manufacturers in the casting industry must deal with this on a day-by-day basis [Heinrich and Poirier 2004]. These composition variations have a detrimental impact on the subsequent processing behaviour and properties of cast materials. Due to the low diffusivity of the solutes in the solid state and the large distances involved, macrosegregation cannot be mitigated through processing of the casting once the solidification is completed. Cracks or air cavity formed during the solidification of RDX/TNT molten mixture inside military bombs may increase the bomb sensitivity that in turn can lead to handling hazard.

According to Beckermann [2001], the cause of macrosegregation is the relative movement or flow of segregated liquid or solid during solidification. Most molten mixture elements have a lower solubility in the solid than in the liquid phase. During undercooling, the solutes are therefore rejected in the liquid phase, leading to a continuous enrichment of the liquid phase and lower solute concentrations in the primary phase. The flow of solute-rich liquid or the movement of solute-poor solid in or out of the volume element will change the average composition of the volume element away from the nominal composition. Since solute can be advected over large distances, macrosegregation occurs. There are numerous causes of liquid or solid movement during the solidification process. According to Beckermann [2002] these are: flow that feeds the solidification shrinkage and the contractions of the liquid and solid during cooling; buoyancy induced flows due to thermal and solute gradients in the liquid: the thermal and solute buoyancy forces can either aid or oppose each other, depending on the direction of the thermal gradient and whether the rejected solutes cause an increase or decrease in the density of the liquid; forced flows due to pouring, motion of gas bubbles, applied magnetic fields, stirring, rotation, vibration; movement of free (equiaxed) grains or solid fragments that have heterogeneously nucleated in the melt, separated from a mould wall or free surface or melted off dendrites, the solid can either flow or settle depending on its density relative to the liquid; deformation of the solid network due to thermal stresses, metallostatic head, shrinkage stresses, or external forces on the solid shell such as those from the rolls in continuous casting of steel.

All efforts to prevent macrosegregation are focused at controlling fluid flow and solid movement. Macrosegregation models are generally focused at understanding the hydrodynamics involved, quantitatively predicting the occurrence and severity of macrosegregation, and performing parametric studies for control and improvement of the solidification process. Macroscopic phenomena to be considered are: heat transfer, solute transport, fluid flow, solid movement, and solid deformation at the scale of the casting. Also micro-phenomena such as phase equilibrium, nucleation, structure formation, segregation and flow at various micro scale must be factored in, since any factors that affect the flow and the microstructure also influence macrosegregation, and vice versa. These relationships are shown in Figure 2.14.

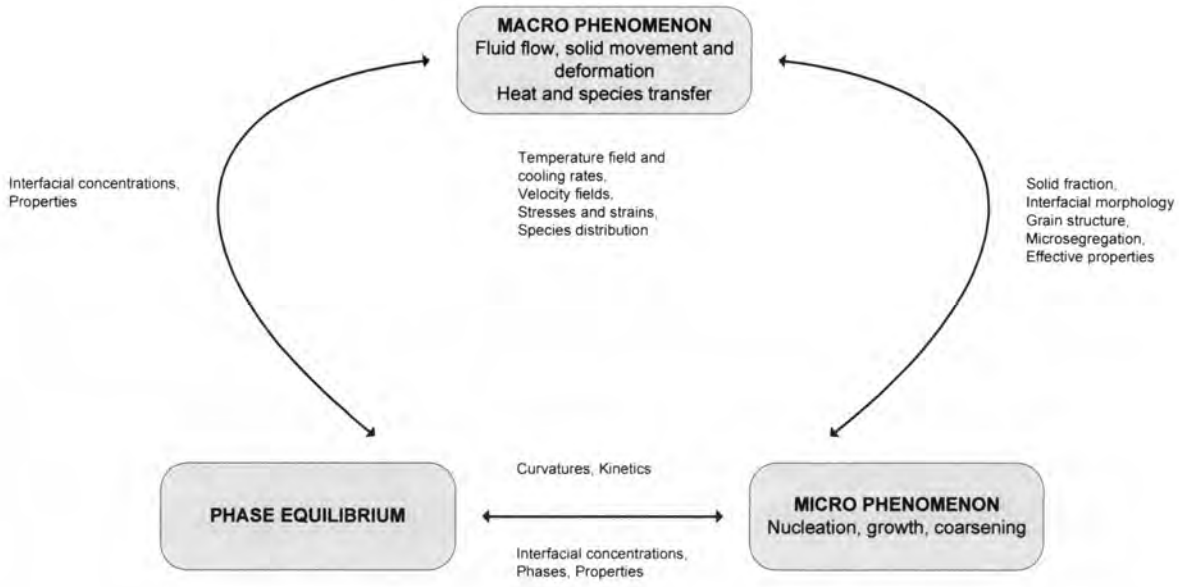


Figure 2.14: Important interactions between macro and micro phenomenon and phase equilibrium

Samanta and Zabaras [2004] modelled the solidification of aluminium on uneven mould surfaces characterised by sinusoids. They studied the effect of different amplitude-wavelength combinations on the solidification process. They concluded that the heat transfer between the mould and the metal was significantly affected which in turn affected the solidification process. Because of this unevenness, fluid flow was also significantly affected near the sinusoids as evidenced from the streamlines distortion, however, these effects were not strong enough to influence the solidification process. Radovic and Lalovic [2004] modelled 2D ingot solidification process. They discovered that their 2D numerical model developed for the solidification process of steel in mould was able to predict the temperature of any position in the ingot section. Using finite difference method, it was possible to describe the temperature distribution, temperature gradient as well as the solid and liquid fraction during ingot solidification. Finally, the cooling curves obtained by empirical method, showed good agreement with those obtained via their model.

### 2.3.1 Filling simulation

The VOF model can be used to successfully track the free surface during pouring [Im et al. 2001; Shepel and Paolucci 2002]. In the model, the introduced function, $F$, which stood for the fractional volume of a mesh cell that was filled with fluid and the value of $F$ was unity in the fluid occupied region and zero in the empty region. The VOF model used by Shepel and Paolucci [2002] was based on the single-fluid algorithm where the fluid displaced a region of the void. It was assumed that there was no interaction between the fluid and the void. Because of that, the void region was not part of the equations to be solved, and that significantly saved them computational time. They mentioned that in reality the melt displaced air within the mould and they felt that the effect of air on the melt motion was negligible except in the vicinity of air entrapment zones. In this research work, they were interested in locating the air entrapment zones, rather than accurately resolving the flow of melt around them, thus they felt that using one fluid algorithm was sufficient. Their results showed good qualitative agreement with available experimental data. They concluded that the numerical modelling of permanent castings and moulds can be a viable tool which can be utilised to predict temperature distributions in both the mould and the melt and possible casting macrodefects occurring during pouring such air entrapment zones.

### 2.3.2 Instantaneous filling

Wu et al. [2003] did not factor in the mould filling phenomena, rather their research was based on instantaneous filling, focused on investigating the influence of crystal movement and melt convection on solidification process. By modelling and simulating the nucleation, crystal evolution, grain movement, sedimentation, melt convection, solute transport and macrosegregation using two-phase volume averaging approach, they studied three scenarios, namely:

- Scenario 1: melt convection, solid movement and no-slip condition for the solid phase at the mould interface, meaning crystals nucleated in the bulk melt were allowed to move and crystals nucleated on the mould surface adhere to the wall

- Scenario 2: melt convection and no solid movement, meaning crystals were not allowed to move, no matter whether they nucleated on the wall or in the bulk melt

- Scenario 3: melt convection, crystal movement and slip condition for the solid phase at the mould walls, meaning the crystal no matter whether they nucleate on the wall or in the bulk melt, were allowed to move. They concluded that crystal movement and sedimentation influenced the solidification process

In the scenario where the crystals did not move, solidification process and the isotherms proceeded equally from the bottom and side walls. In contrast, the solidification process and the isotherm proceeded faster in the bottom regions than in the side wall regions in scenario if the crystals moved. As for the flow patterns, without crystal movement, feeding flow is symmetrical. With crystal movement, the crystals sinking along the mould wall induced vortices, which in turn influenced solid movement and brought grains to the bulk belt. Crystal settlement was believed to be responsible for the negative segregation in globular equiaxed solidification. In scenarios (1) and (2), settlement was found near upper corners, near lower corners and in the middle bottom region, where negative segregations occur. They attributed the formation of positive macrosegregation to the feed of segregated melt to packed zones and the squeezing out of segregate melt by settling crystals. Crystal movement and convection influenced the crystal size distribution. In scenario (3), some crystal sunk from the upper corners towards the lower corners, some move to the casting centre following the strong melt flow, hence raising crystal density in the lower corners and the central regions. Finally, they also discovered that large crystals in the central area for scenarios (1) and (3) were transported from other regions. Some grains nucleate near the wall, sink and move inwards or then towards the casting centre and crystals continue to grow even when they are moving about.

As mentioned, the modelling and simulation of solidification can be confined to filling and solidification or just solidification per se, that is, instantaneous filling assumption, which ignores the phenomenon associated with the filling process. Conservation equations for instantaneous filling will be much simpler than modelling that takes account of the filling process, thereby significantly simplifying the computational effort in modelling solidification. In the case of instantaneous filling assumption, the initial conditions are a full mould cavity and uniform temperature in the molten mixture and mould. However,

according to Barkhudarov [1997], by ignoring filling process, information about the temperatures in the molten mixture and mould at the end of the filling process will be lost. Temperature distribution depends on the sequence in which the mould cavity surface becomes wetted by the hot molten mixture, the filling rate and the mould geometry. In addition, this assumption also ignores residual flow after filling is completed. This residual flow plays an important role in the redistribution of heat in the molten mixture during the first stages of solidification. Finally, fluid flow modelling is excluded in most solidification models even when a complete filling simulation is carried out.

Other similar studies on the modelling and simulation of solidification process include:

- Mathematical modelling of crystallisation processes that occur during polymer processing [Eder 1996],
- Development of a framework for modelling the overall microstructure evolution during equiaxed solidification [Grong et al. 1998],
- Development of a thermodynamic description of the Nb-Si-Ti ternary system by modelling the Gibbs energies of the individual phases in the system [Liang and Chang 1999],
- Computational modelling of CdZnTe crystal growth from the bulk melt [Cerny et al. 2000],
- Modelling of temperature distributions in the moulding of chocolate [Tewkesbury et al. 2000],
- Influence of solidification variables on the microstructure, macrosegregation, and porosity of directionally solidified Mar-M247 [Whitesell and Overfelt 2001],
- Coupling of conductive, convective and radiative heat transfer in Czochralski crystal growth process [Nowak et al. 2002],
- Effects of crystal growth rate and heat and mass transfer on solute distribution Fukui and Maeda 2002] and
- Analysis of fluid flow and energy transport in Czochralski crystal growth process [Nowak et al. 2002; Nowak et al. 2003]

## 2.4 Statistical process control

Growing and stricter requirements coming from customers have resulted in a stiffer competition within the manufacturing sector. Manufacturing companies around the globe have embarked on endless pursuit to consistently achieve a higher throughput, lower reject rate and lower level of rework with a view to delighting their customers and to enhance their shareholders value. For example, many manufacturers even struggle to meet basic manufacturer's obligation, which is, meeting customers' specifications. In this manufacturing era, it is not often a question of whether the manufacturer can meet their customers' specification, rather, the question is how much effort or cost does it take this manufacturer to meet their customers' specification. This affects the bottom line profit which then distinguished the successful from the not so successful manufacturer. To excel, the same group of manufactures became proactive by launching long-ranging practice of process improvement that has a profound effect on their final products.

Over the past decade, different strategies were launched by different manufacturers and among them were the just-in-time approach, poka-yoke, reengineering, theory of constraints, agile manufacturing and lean manufacturing. Unfortunately, most of these strategies devoted far too little attention to variability reduction. It is virtually impossible to reduce the in-process inventory or operate an agile or lean production system when a large and unpredictable fraction of the process output is defective. Consequently, such efforts will not achieve their full potential without a major focus on statistical methods for process improvement and variability reduction to accompany them. However, it must be noted that process improvement must not be carried out prior to understanding the existing process performance. Once the process behavior is understood, the direction to move forward becomes apparent. To understand the cyclotol manufacturing process, ADI characterises the process using statistical method, via statistical process control (SPC). SPC is a group of effective problem-solving techniques which, when applied correctly, effective in achieving process stability and capability through the minimisation of variations and can be used in any processes.

According to Sematech [2005], process characterisation is defined as an activity that aims to identify the key inputs and outputs of a process, collect data on their behaviour over the entire operating range, estimate the steady-state behaviour at optimal operating conditions and build models describing the parameter relationships across the operating range. The result of this activity is a set of mathematical process models that can be used to monitor and improve the process. Best practice requires that any new process or when a process has undergone significant engineering changes to have it characterised. However, process characterisation is also required throughout the life of a process to estimate the process stability and capability when the process is running under normal conditions. For any process to be improved via the reduction of variations and to subsequently produce consistent quality products, process characterisation should be carried out first irregardless of whether it is statistically stable or not [Srikaeo et al. 2005]. Characterised process will provide the research direction that will help to prevent overstretching of limited resources or to prevent investing in the wrong process improvement research project.

Apart from using process characterisation as a starting point for process improvement, it is useful for a situation that involves the introduction of a new process or unit operation, the start-up of a process after scheduled or unscheduled maintenance, the comparison of two processes or unit operations, the checking of process capability and troubleshooting of bad process. In this work, no mathematical model will be proposed, instead, SPC through process capability studies will be used to assess the performance of the cyclotol manufacturing process. Hitherto, there has not been anything written on the systematic characterisation of high explosive manufacturing processes via SPC. Therefore, the objective of this work is to fill this knowledge gap.

For the purpose of process of characterisation, out-of-control situation due to only a point falling outside the control limits will be considered. All other rules mentioned previously will not be considered. In addition, to facilitate its implementation, those points which indicated out-of-control situations were removed and the control limits recalculated. This simulates the situation where the process is in statistical control. This measure is necessary because the true process capability of a process is one where data from the steady-state statistically stable process are acquired. An out of control process is unpredictable and hence any measurement of its capability is useless. In reality, any point that indicates an out-of-control situation shall be investigated promptly, assign its root cause and have it

eliminated. After all the special causes of variation have been eliminated, the process becomes statistically stable. It is only at this stage that the process capability and its index can be meaningfully measured. All the SPC analysis results were then interpreted and the process characterisation conducted based on statistically stable results.

Since the scope of this research work is confined to the existing unit operations currently operating in the production line, process variations must be taken into consideration. To monitor process variations, statistical process control (SPC) control charts were set up at strategic locations [Lee Y-H et al. 2004]. The locations included feed and outlet streams of the unit operation to be modelled and simulated. SPC charts were also used to support model validations by signalling process deviation as a consequence of varying certain crucial variables, as shown in the Ishikawa diagram of Figure 2.15, while at the same time indicating that other variables were being kept constant.

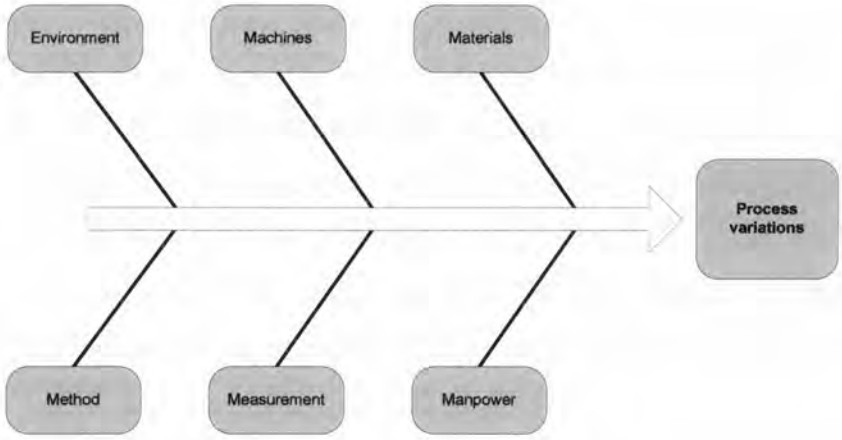


Figure 2.15: Ishikawa diagram showing the causes of variation

The history of modern SPC started at Bell Laboratories in the mid 1920s when Walter Shewhart was requested to study how variation in production processes caused quality problems and to determine its remedy [Kolesar 1993]. This research was prompted by variation in Western Electric production processes so severe that components used in AT&T's emerging U.S. national telephone network were not meeting specifications consistently. What eventually happened was Shewhart invented the control chart, known today as the Shewhart charts, and used it to reduce variation in processes. This method was made known to the rest of the world by three Americans, Edwards Deming, Joseph Juran and Armand Feigenbaum.

SPC is known to be process focused and a proactive way of producing consistent products. Instead of segregating products that meet customer's specification from those that do not, SPC aims to prevent the fabrication of non-conformance products in the first place. This is achieved by reducing variation in different part of the processes. By reducing process variations, it is envisaged that the resulting product will consistently meet the specification. There are two types of variation in SPC, special causes of variation and common causes of variation. The special causes of variations are those that occur when a perturbation to the process happens, while the common causes of variation are those inherent to any processes. Shewhart control chart aims to detect the special causes of variation with a view to eliminating them. The common causes of variation are not like special causes of variation and can only be eliminated by a fundamental change in the process. It is clear that in-process control is more desirable than final product control since early detection of lack of control leads to fewer defective items being produced.

Shewhart suggested several rules of thumb for setting up the control chart, namely: the control limits should be at 3 standard deviations from the centre line on both the mean and range charts, the subgroup sizes should be 4 to 6, the subgroup should usually consist of items essentially adjacent in order of production, and at least 20 subgroups should be used to estimate the grand mean and average range. In later developments, supplementary rules were invented to increase the chances of detecting out-of-control situations. The drawback of such rules is the increase in complexity and higher false alarm rates.

In this study, among the seven SPC tools, only Shewhart control charts will be discussed.

There are two main types of control charts, variables and attributes. Variables charts are applicable to variable that can be measured while attributes applicable to those that can be counted. For this study, most of the work will be carried out using variable charts.

The conventional mean and range chart is suitable for monitoring processes which provide data that fall into natural subgroups.

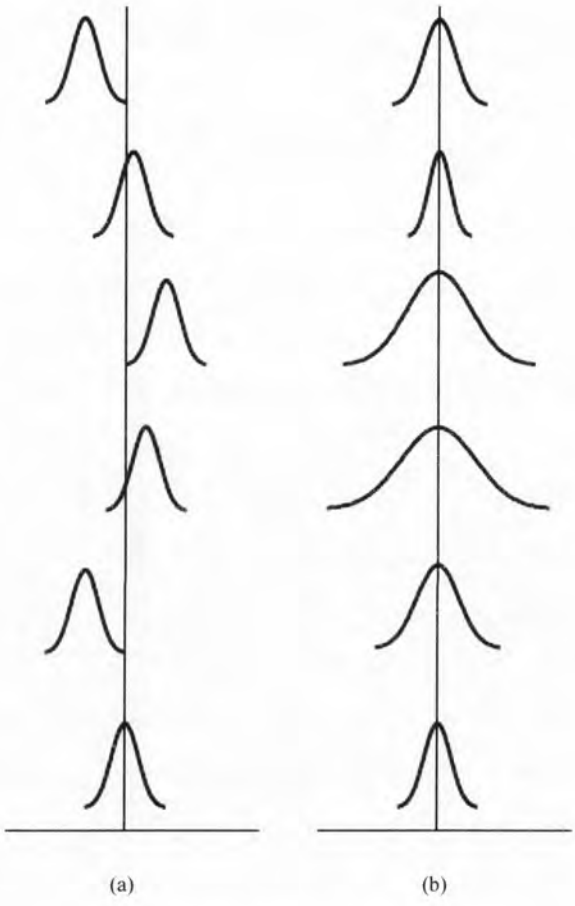


Figure 2.16: Accuracy and precision

The mean chart displays the accuracy of the process. Accuracy in SPC is defined as how centred the process is. Figure 2.16(a) shows a process having accuracy variation. The range chart shows the standard deviation of the process and Figure 2.16(b) shows unpredictability in the process due to the broadening and narrowing of the process data distribution due to presence of variations. Both types show that in the presence of process variations, the process becomes unpredictable.

$$UCL = \overline{\overline{X}} + 3\frac{\sigma}{\sqrt{n}} \quad \text{or} \quad \overline{\overline{X}} + 3\frac{\overline{R}}{d_2\sqrt{n}}$$

$$CL = \overline{\overline{X}}$$

$$LCL = \overline{\overline{X}} - 3\frac{\sigma}{\sqrt{n}} \quad \text{or} \quad \overline{\overline{X}} - 3\frac{\overline{R}}{d_2\sqrt{n}}$$

- 2.8

$$UCL = \overline{R}D_4$$

$$CL = \overline{R}$$

$$LCL = \overline{R}D_3$$

The individuals chart or mean and moving range chart is better suited to monitor processes that provide one-at-a-time data such as in most chemical processing plants.

$$UCL = \overline{X} + 3\sigma \quad \text{or} \quad \overline{X} + 3\frac{\overline{MR}}{d_2}$$

$$CL = \overline{X}$$

$$LCL = \overline{X} - 3\sigma \quad \text{or} \quad \overline{X} - 3\frac{\overline{MR}}{d_2}$$

- 2.9

$$UCL = \overline{MR}D_4$$

$$CL = \overline{MR}$$

$$LCL = \overline{MR}D_3$$

However, for post-mortem analysis of a process, the conventional mean and range charts may be used with any process Oakland [2003]. Table 2.1 shows the values of the constants *D3*, *D4* and *d2* [Montgomery 2005].

Table 2.1: Statistical constants

| *N* | *D3* | *D4* | *d2* |
|---|---|---|---|
| 2 | 0.000 | 3.267 | 1.128 |
| 3 | 0.000 | 2.574 | 1.693 |
| 4 | 0.000 | 2.282 | 2.059 |
| 5 | 0.000 | 2.114 | 2.326 |
| 6 | 0.000 | 2.004 | 2.534 |
| 7 | 0.076 | 1.924 | 2.704 |
| 8 | 0.136 | 1.864 | 2.847 |
| 9 | 0.184 | 1.816 | 2.970 |
| 10 | 0.223 | 1.777 | 3.078 |

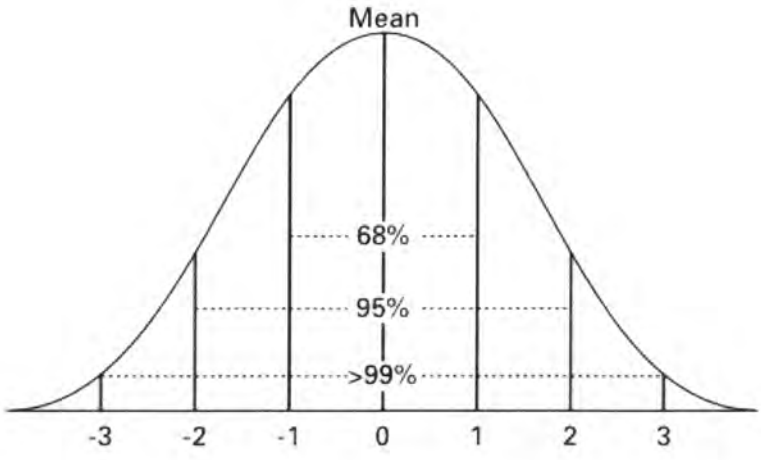


Figure 2.17: Normal curve

There are many statistically valid patterns of instability. Every pattern of instability is based on the properties of the normal curve and the 68-95-99 rule, as shown in Figure 2.17.

- Most are based on the Western Electric Handbook first published in 1954
- All are based on the probabilities and properties of the normal curve
- Most data exhibit normal curve characteristics because of the central limit theorem

The central limit theorem (CLT) states that even when the individual values are not normally distributed, the distribution of their means will tend to have a normal distribution, and the larger the sample size the greater will this tendency be. This theorem makes it possible to apply Shewhart control chart to many situations since for it to function properly, the data should be normal. In this study, accuracy refers to the centring or process mean while precision refers to the spread, standard deviation or range of a process.

Variable chart rules are given below.

*Western Electric Rules:*
- Point outside the control limits
- 2 of 3 points between $2\sigma$ and $3\sigma$ from the mean
- 4 of 5 points between $1\sigma$ and $3\sigma$ from the mean
- 8 points in a row on one side of the centreline

*AIAG Rules:*
- Point outside the control limits
- Run of 7 points on one side of the mean
- Trend up or down of 7 points in a row
- Recurring cycles
- Other non-random patterns

*Nelson Rules:*
- Point outside the control limits
- 2 of 3 points between $2\sigma$ and $3\sigma$ from the mean
- 4 of 5 points between $1\sigma$ and $3\sigma$ from the mean
- Run of 9 on one side of the mean
- 15 in a row near the centreline
- Trend of 6 points in a row increasing or decreasing
- 8 in a row not within $1\sigma$ of the mean
- 14 points in a row that alternate up and down

*Boeing's Advanced Quality System Rules:*
- Point outside the control limits
- 2 of 3 points between $2\sigma$ and $3\sigma$ from the mean
- 4 of 5 points between $1\sigma$ and $3\sigma$ from the mean
- 8 points in a row on one side of the centreline
- Lumping
- Mixtures
- Trend
- Recurring cycles
- Strays
- Process shift
- Few points within limits
- Too few discrete levels

*Six Sigma Rules:*
- Point outside the control limits
- 2 of 3 points between $2\sigma$ and $3\sigma$ from the mean
- 4 of 5 points between $1\sigma$ and $3\sigma$ from the mean
- 8 points in a row on one side of the centreline
- Trend

Example of charts that show an out-of-control situation is given in Figure 2.18.

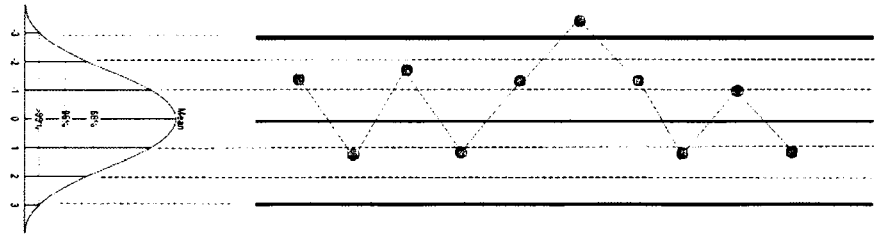

Point outside the control limits

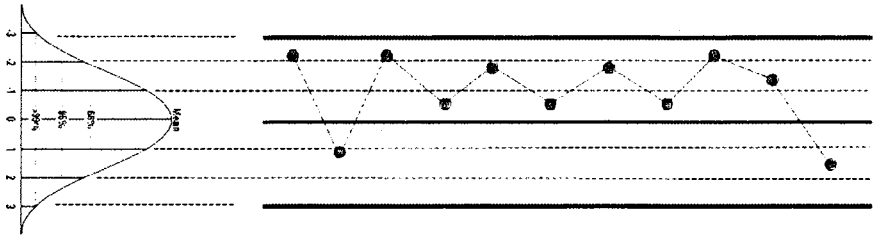

8 points in a row on one side of the centreline

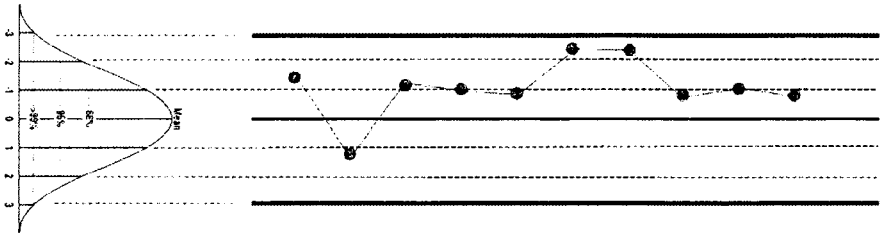

2 of 3 points between 2σ and 3σ from the mean

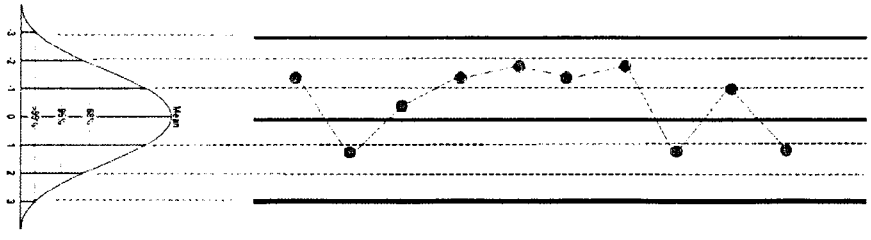

4 of 5 points between 1σ and 3σ from the mean

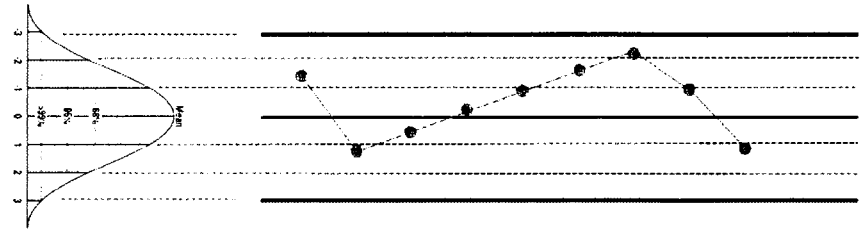

Trends: upward, downward or cyclic

Figure 2.18: Example of charts that constitutes an out-of-control situation

### 2.4.1 Process capability analysis

Process capability analysis refers to the comparison of process performance against its specifications. Its relationship with the upper specification limit (USL) and lower specification limit (LSL) is given by [Thomson and Koronacki 2002]:

$$Cp = \frac{USL - LSL}{6\sigma} \qquad \text{- 2.10}$$

A process is deemed capable if all the possible variable values fall within the specification limits. The *Cp* measurement aims to indicate the proportion of process variation that is covered by the process specifications. The equation includes measuring the process variation by $6\sigma$ ($\pm$ on each side of the mean) using equation above. If Cp $\geq$ 1, then 99.7% process variations fall within the specification. Where *USL* and *LSL* stand for upper specification limit and lower specification limit respectively. The symbol $\sigma$ refers to the standard deviation.

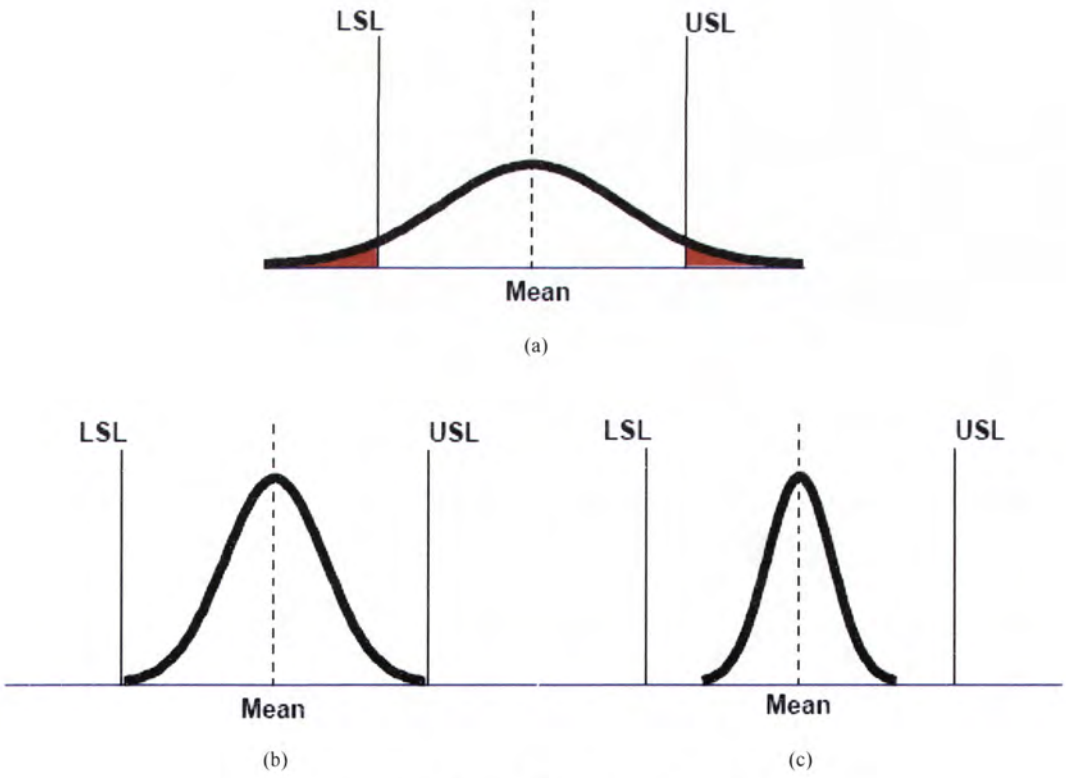


Figure 2.19: Concept of process capability, Cp

Figure 2.19(a) shows an incapable process due to its large standard deviation. In this process, the process could not meet the required specification. In other words, most of the times, many products will be produced outside the customer's specifications. Figure 2.19(b) shows that the process performs better relative to those in Figure 2.19(a), nevertheless, it just barely meet the specification. In other words, all it takes is a worn out part or a slight difference in operation procedure to increase this standard deviation and produce products outside the specification limits. Figure 2.19(c) has a high process capability because it has a narrower base than the first two cases and that makes it located well within the specification limits. If there is any situation that causes the standard deviation to increase, there is buffer gap between the distribution tails and the upper and lower specification limits.

Despite the benefit of measuring the *Cp*, its measurement does not indicate whether the process is centred. The process capability index, *CpK*, aims to overcome this shortcoming. *CpK* is defined mathematically as [Thomson and Koronacki 2002]:

$$CpK = \min\left\{\frac{USL-\mu}{3\sigma}, \frac{\mu-LSL}{3\sigma}\right\} \qquad \text{- 2.11}$$

Where $\mu$ is the mean and the true *CpK* value is the lower value.

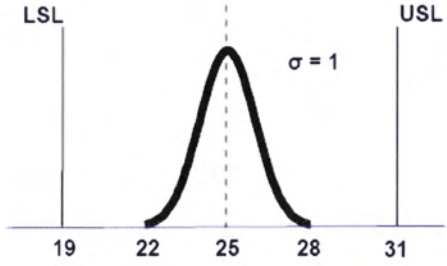


Cp = 2.0
CpK = 2.0

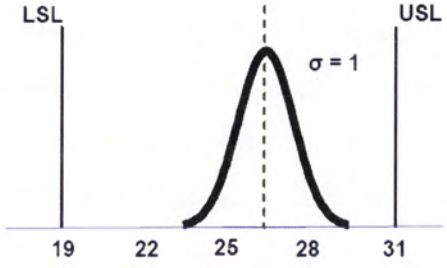


Cp = 2.0
CpK = 1.5

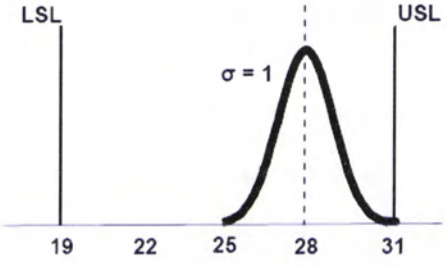


Cp = 2.0
CpK = 1.0

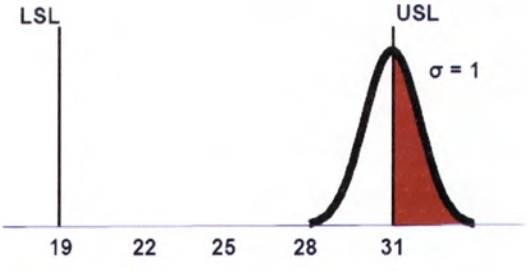


Cp = 2.0
CpK = 0

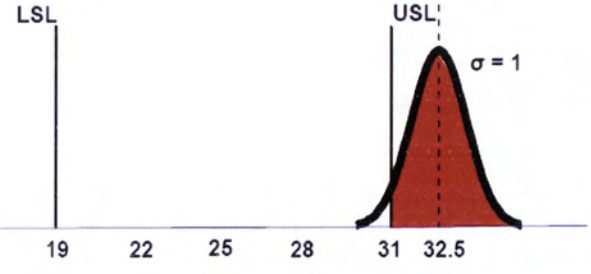


Cp = 2.0
CpK = - 0.5

Figure 2.20: Relationship between Cp and CpK

Figure 2.20 shows that the relationship between *Cp* and *CpK*. In the top most diagram, the process, having a standard deviation of 1, is centred at a mean of 25. Under this process condition, the $Cp = 2.0$ and $CpK = 2.0$. The next few diagrams shows that even though the process having the same standard deviation shifted towards the upper specification limit, the *Cp* value remained the same while the *CpK* value decreases the moment the process departed from the centre line. Centre line is defined as the mid-point between the lower and upper specification limits. This shows that while calculating the *Cp* provides insight into the capability of the process, knowing the *CpK* value determine whether the process is centred, if not, whether it is leaning toward the lower or upper specification limits. This will provide the necessary optimisation direction, that is, to shift the process towards the lower or upper specification limit. Although the *CpK* is important, its use does not invalidate the use of *Cp* because before process shifting is carried out based on the *CpK* value, it is important to reduce the standard deviation, which is reflected by the value of *Cp*.

In general, most modern industrial manufacturers require *Cp* and *CpK* values of at least 1.33. This study uses a value of 1.33 as a benchmark for process capability studies. Process capability study is frequently the prerequisite to a process improvement initiative, particularly when it is found that process capability is low. To achieve a high value of *Cp* and *CpK*, it is desirable to reduce the standard deviation of the process and to increase its accuracy or centring.

It must be noted that to conduct a process capability study, the process of interest must be in statistical control. This is because if the process in not in statistical control, the output is unpredictable therefore negating the benefit of knowing the *Cp* or *CpK* values since they can change along with the next batch of products.

### 2.4.2 Gauge repeatability and reproducibility

Repeatability (equipment variation) is the ability of the measurement system to provide consistent readings when used by a single technician or operator on a given sample. Reproducibility (appraiser variation) is the ability for multiple technicians or operators to achieve consistent results on a given sample. Since the measurement system may also contribute to the overall process variation, a measurement system analysis must be conducted. Such study is a pre-requisite prior to any process characterisation study. However, since the plant has a good calibration system, the accuracy of equipment may be considered acceptable since only data obtained from capable measurement system should be used for capability studies.

### 2.4.3 Plant data analysis

After gauge R&R has been conducted; data analysis must be conducted prior to constructing the control charts. This analysis aims to determine whether the data exhibit Gaussian distribution. This is important because for the control charts to work effectively, the data must exhibit normal distribution. Such method is not applicable for skewed data where different statistical tools will be required.

## 2.5 Photocatalysis technology

Like other manufacturing plants, the munition plants covered in this study produces several aqueous organic wastes. Some of these wastes contain energetic compounds which make them too toxic to be discharged into the environment untreated, too dangerous to be treated by municipal councils or external waste management companies and too risky to be stored underground.

Destroying these wastes via conventional method using activated carbon or bioreactor does not provide an acceptable level of industrial practicality. This is because treatment by activated carbon does not actually destroy the wastes, rather, it merely transfer the waste from liquid or gas phase to solid phase. The spent activated carbon must then be treated via incineration, encapsulated then land-filled or subjected to other methods of secondary treatment. Destruction via a bioreactor is possible but will normally take a significant amount of time for the toxic concentration to drop to an acceptable level.

A method currently employed by ADI involves incinerating such aqueous organic wastes. However, such method is very inefficient because in the process of incineration, massive amounts of energy are consumed and a significant amount of gaseous wastes is discharge into the atmosphere. In contrast, a photoreactor only consumes a fraction of the energy consumes by the existing incinerator, discharges a very small amount of carbon dioxide into the atmosphere and decrease the toxic concentration to an acceptable level within hours of operation [Lea 1998]. This makes photocatalysis an attractive way of treating aqueous wastes produced in these munition plants.

For this reason, the photocatalysis technology has become popular and is the preferred method over other conventional methods of treating aqueous wastes [Hirakawa et al. 2007]. Thus, photocatalysis is proposed to replace the current obsolete method of treating the waste products.

### 2.5.1 Principle of operation

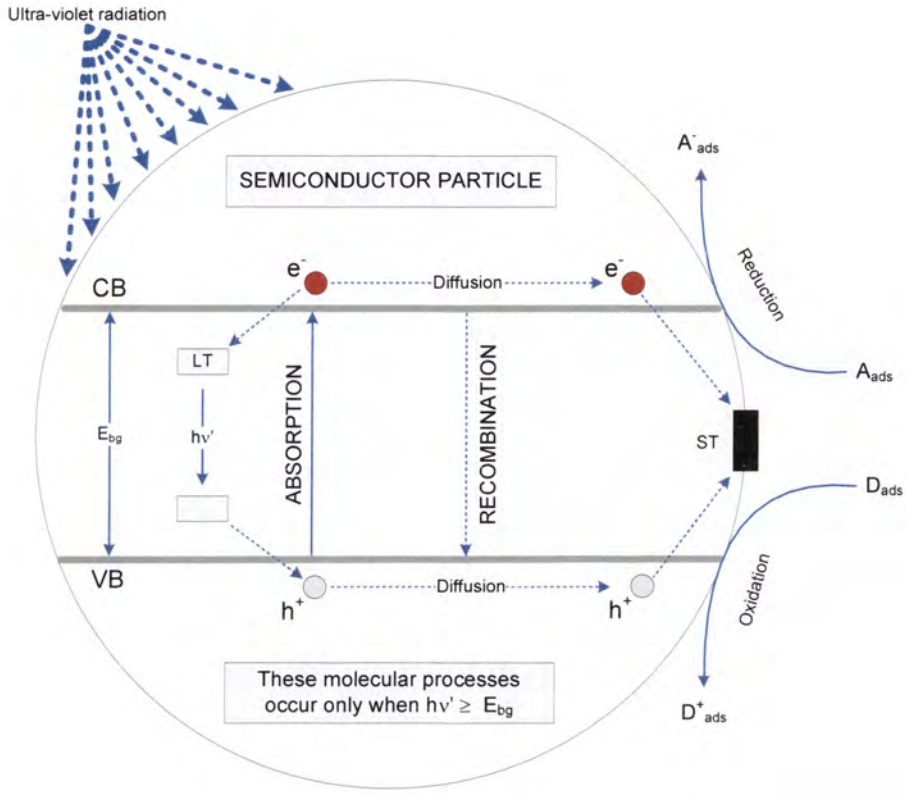


Figure 2.21: Principle of the activation of a photocatalyst particle

Figure 2.21 shows that when a semiconductor particle absorbs a photon with energy equal to or exceeding the energy band-gap, $E_{gb}$, an electron is promoted from the valence to the empty conduction band, thus, creating an electron deficiency in the valence band, also called a positive hole, $h^{+}_{vb}$. This electron-hole pair formed is called an exciton. Moreover, these charge carriers, (photoelectron $e^{-}_{cb}$ and hole $h^{+}_{vb}$), can recombine rapidly by different mechanisms and decay channels. To migrate to the semiconductor particle surface, these charge carriers must compete with non-radiative mechanism such as lattice trapping (LT) or surface trapping (ST) and radiative deactivation mechanisms.

At the surface, an adsorbed acceptor substrate $A_{ads}$ is reduced by transfer of the photoelectron $e^{-}_{cb}$ to an unoccupied molecular orbital of the acceptor molecule. Concurrently, an adsorbed donor substrate $D_{ads}$ is oxidised by a transfer of a donor electron to $h^{+}_{vb}$ of the semiconductor particle. Therefore, the radiation of a semiconductor particle with ultra-violet radiation ultimately initiates redox chemistry at its surface. For example, the positive hole $h^{+}_{vb}$ will split a water molecule according to $H_2O + h^{+}_{vb} = OH\cdot + H^{+}$. One

of the products of this water splitting process, the hydroxy radical $OH\cdot$, plays a vital role in oxidising organic compounds that comes into contact with it.

### 2.5.2 Photocatalyst technology

The band-gap energy of $TiO_2$ is 3.2 eV and this energy is equivalent to the wavelenth $\lambda$ of 387.5 nm. Thus, $TiO_2$ particles are able to absorb parts of the solar UV-A and the solar UV-B radiation, thereby making it one of the most widely used semiconductors for heterogeneous photocatalysis [Oppenlander 2003]. Its popularity is also due to its activity, photostability, non-toxicity and commercial availability and corrosion stability. $TiO_2$ is found in nature and can exist in three crustal modifications: rutile, anatase and brookite. Its composition is temperature dependent because at calcination temperatures above 627 $^{o}C$, the anatase modification is transformed into rutile.

$TiO_2$ is insoluble in water and in diluted acids, but dissolves slowly in hot sulphuric acid. Among the three modifications, only the anatase modification is sufficiently active in photocatalysis. According to Oppenlander [2003], most investigations on $TiO_2$ were conducted using Degussa P-25 $TiO_2$. This material consists of about 80% anatase and 20% rutile and has a BET (Brunauer-Emmett-Teller) specific surface area of 55 $m^2\ g^{-1}$. The particle diameter lies between 25 nm and 35 nm. Thus, the separation of $TiO_2$ nano-particles from its aqueous suspensions represents a serious problem for practical engineering and eventually commercialisation. Because of this, many researchers have experimented with immobilising $TiO_2$ by coating the particles on substrates such as glass sheets and tiles.

The bulk density of this photocatalyst is about 3,900 kg $m^{-3}$. Although the density is relatively heavy, it is easy to suspend these particles owing to its nano size.

### 2.5.3 Wavelength

The wavelength range, λ, generally used in photocatalysis lies between 170 nm and 1,000 nm. This is because light within this wavelength range can electronically excite organic and inorganic molecules. The photochemically active region of the electromagnetic spectrum is divided into five sub-bands: the vacuum-UV (VUV: 100 – 200 nm), UV-C (200 – 280 nm), UV-B (280 – 315 nm) and UV-A (315 – 380 nm) [Oppenlander 2003].

Ionising electromagnetic radiation, such as deep VUV is of such high energy that electrons are expelled from molecules which ultimately lead to photoionisation. Since VUV radiation is absorbed by almost all substances including $H_2O$, $CO_2$ and $O_2$, the spectroscopic measurements of wavelength below 200 nm have to be performed under vacuum or at least under non-absorbing gas conditions.

Absorption of UV-C radiation by cellular constituents of organisms may lead to severe cell mutations and cell death. Therefore, this wavelength band is often called the germicidal range and is used in UV disinfection processes to inactivate bacteria, viruses and other micro-organisms. VUV and UV-C are not present at the earth's surface because of their efficient absorption by $O_2$ and ozone.

Solar UV-B and UV-A radiation reach the earth's surface and may induce sunburn, skin cancer and sun tanning. These two bands are used in the photocatalysis processes.

Wavelength above 380 nm is classified as visible light. Finally, the energy of photons with wavelength > 1,000 nm is too small to reach electronic states of atoms or molecules.

The main advantage of heterogeneous photocatalysis over traditional water treatment methods is that the organic pollutants can be totally degraded to $CO_2$, $H_2O$ and mineral acids [Ollis et al. 1991 and Lea 1998]. Pollutants such as herbicides, pesticides, aliphatics, aromatics, polymers and dyes have been either partially or totally broken down into $CO_2$, $H_2O$, mineral acids [Mills and Le Hunte 1997], galic acid and Escherichia coli [Gumy et al. 2006], dyes such as Acridine Orange and Ethidium Bromide [Faisal et al. 2007] and Triphenylmethane [Chen et al. 2006].

Petroleum derivatives such as benzene, toluene and mixed xylenes are classified into the group of most dangerous compounds to the environment due to their large migration abilities, both in land and aquatics environments, and their acute and chronic toxicities. Recent study showed that the metabolic transformation of benzene, which is caused by specific enzyme, can lead to toxicity in human, damaging the blood formation cells that can ultimately progress to leukaemia. Such derivatives were successfully destroyed by photocatalysis method [Tiburtius et al. 2005]. Whilst Tiburtius et al. [2005] conducted the destruction of such volatile organic compounds (VOCs) on liquid sample, Lam et al. [2007] and Zou et al. [2006] successfully conducted similar destruction on these VOCs in gas phase. Zou et al. [2006] felt that this study can be used to address VOCs generated from motor vehicle exhaust and solvent utilisation.

A detailed study on the key variables governing the performance of a slurry photoreactor was conducted by Lea and Adesina [2001] on 4-nitrophenol; Lea and Adesina [1999] on sodium oxalate and Lea and Adesina [1998] on sodium dodecyl sulphate. These variables consisted of the initial pH of slurry, UV light intensity, percent of oxygen, flowrate of oxygen, catalyst loading, slurry temperature, and pollutant's concentration. In addition, successful photodegradation of organic pollutant was achieved in batch and continuous photoreactors [Lea 1998]. In addition, according to Lea [1998], the quantum yield of a slurry reactor is higher than an immobilised catalyst reactor but a secondary catalyst recovery system must be employed for such reactor.

Three different catalyst configurations for the photodegradation of formic acid were compared in a tubular reactor by Dijkstra [2001]. The key performance indicator (KPI) employed was the quantum yield. The result shows that in the suspended system and the packed bed reactor the degradation appeared to follow pseudo-zero-order kinetics and both

of these systems were free of mass transfer limitations. In contrary, the tubular reactor with the catalyst coated on the wall experienced mass transfer limitation. Oxygen addition directly into this reactor increased the activity by reducing the mass transfer limitation. In the packed bed reactor, two bead diameters are compared. They discovered that for low amounts of catalyst coated on the glass beads the activity of the system with the small beads is comparable to that with the large beads. However, the performance with high amounts of catalyst present in the reactor was better using the large glass beads.

Prieto and Irusta [2005] studied the removal of colour of a synthetic textile effluent at pilot plant scale. The pilot plant scale photoreactor had a volume of 40L and was equipped with flow, pH, $O_2$, radiation and temperature meters. In addition, to study the interactions between controllable and uncontrollable parameters, they employed Taguchi's statistical technique. They also used this technique to determine the top most important parameters. The results show that the most important control factor was $H_2O_2$ concentration, flowrate, and pH. Their kinetic study shows that decolouration photocatalytic process is described well by Langmuir-Hinshelwood kinetic model in the first part of the reaction but an important decrease in photocatalytic rate at last stage of the process causes a change in the trend line. Another group that conducted their study at pilot plant scale were Oller et al. [2006]. In this study, they have successfully demonstrated the technical feasibility and performance of photocatalytic degradation of six water-soluble pesticides, namely: cymoxanil, methomyl, oxamyl, dimethoate, pyrimethanil and telone, at pilot plant scale.

Despite the successes in the destruction of organic chemicals illustrated above using photocatalysis technique, due to the poor absorption of $TiO_2$ in the visible region, the utilisation of solar energy has been limited to the UV portion which is only about 5% of the solar photons. Because of this, a large number of studies have focused on bandgap modification of $TiO_2$, such as doping it with transition metal ion, and attempting to extend its photoresponse into the visible region. Xu and Khan [2006] showed that carbon modified n-$TiO_2$ calcined in Argon at the optimum temperature of 500°C, containing 3.8% carbon showed higher photoresponse in both UV and visible region. As shown in the literature study above, only a very handful of modelling and simulation work have been done on photoreactor, thereby justifying the CFD modelling and simulation of a photoreactor with a view to improving its performance.

## 2.6 Concluding remarks

This chapter has reviewed the literature on the use of CFD technique to model chemical reactors and mixing tanks. This initial study on the development of this technique and its applications has helped to determine the research gap. A small section was also dedicated to the study of the significance of employing baffles in a cylindrical-shaped tank. This chapter has also addressed a literature study in the field of the rheology of fluids to provide a complete picture on the behaviour of different type of fluids. An in-depth study on the rheology of high explosives was also presented to gain a better understanding of their behaviours. Although a study on the solidification of high explosive materials inside a bomb shell was outside the scope of this thesis, nevertheless, a literature study on solidification process in general was included to provide an insight into the process occurring at a downstream plant.

The majority of this thesis was based on a unit operation located in an actual explosive manufacturing plant. As such, it was economically prohibitive to control the input variables to such an extent that their variations were similar to those found under laboratory settings. Because of this, SPC technique was applied to visualise the amount of variations present in the process under study, and to avoid confusion as to the source of the variations. SPC technique was also used to conduct process capability study to determine the statistical stability of the process at the time the unit operations concerned was modelled. This justified the need to conduct a literature review on SPC.

Finally, a literature review on photocatalysis was conducted because this technique was chosen to destroy wastes produced from explosives manufacturing activities.

Nitrocellulose (NC) is a highly flammable compound manufactured by esterification of shredded cellulose (paper) with $HNO_3$, in the presence of $H_2SO_4$ [Urbanski 1964, 1965, 1967 and 1984; and Fordham 1980]. The reaction is given as:

$$C_6H_{10}O_5 + xHNO_3 \Leftrightarrow C_6H_{10-x}O_{5-x}(ONO_2)_x + xH_2O$$

This nitration process adds a large amount of $O_2$ to the chemical structure of the cellulose, as shown in Figure 3.1, and such molecular structure change makes NC useful as a propellant. However, NC can be dangerous to handle without proper care.

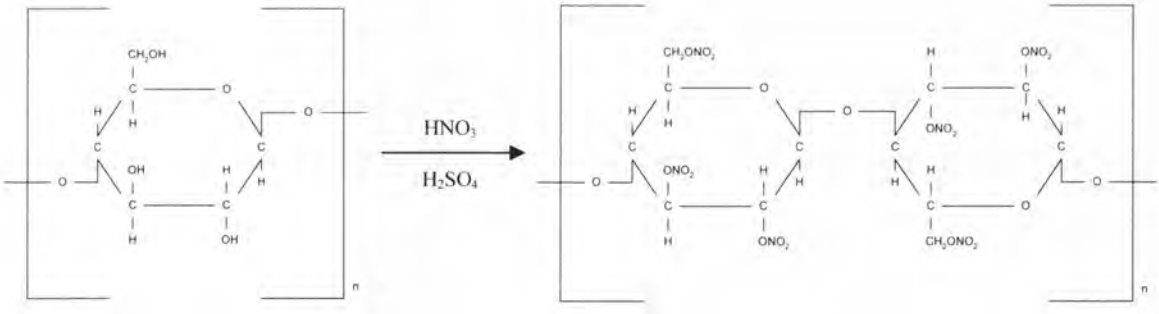


Figure 3.1: Change in molecular structure from cellulose to nitrocellulose

The addition of $O_2$ molecules into the cellulose molecular structure means that:

- $O_2$ is no longer required from air when NC is converted by burning from solid to gas
- The conversion from solid to gas will occur spontaneously once the NC is ignited
- Only a small activation energy is required to initiate the conversion of NC from solid to large quantities of heat and gas

NC which is classified as a secondary explosive, is the basis of most artillery, tank, mortar, and small rocket propellant. It is relatively insensitive, and in most cases requires a detonator to explode. The customary way to define its composition is to express its nitrogen content as a percentage by weight. In theory, NC containing 3 nitrate groups [$C_6H_7O_2(ONO_2)_3$] will contain 14.14%. In practice, the NC compositions used in explosive applications vary from 10 to 13.5% of nitrogen. NC materials prepared from paper are fluffy white solids, which do not melt but has an ignition temperature of 180°C. The thermal stability of NC decreases with increasing nitrogen content. As outlined in later section, the chemical stability of NC depends on the removal of all traces of acid in the manufacturing process. While cellulose is not soluble in organic solvents, NC dissolves in organic solvents to form a gel. This gel will then be converted to propellant in the plant downstream.

The principal classes of explosives using NC are:

- Single base propellant: 100% NC
- Double base propellant: 50% NC, balance nitroglycerine or other similar nitroester
- Triple base propellant: 25% NC, 25% nitroglycerine and 50% nitroguanidine

The NC manufactured is then converted into propellant that is filled into ammunition such as a projectile's cartridge. In operation, the propellant is ignited when the primer is fired by striking pin of the rifle. This ignition causes a massive gas expansion that propels the projectile forward in a spiral fashion.

## 3.1 Process description

This section will describe in brief, aided by a simplified process flow diagram (PFD) as shown in Figure 3.2, the process of manufacturing High Grade NC.

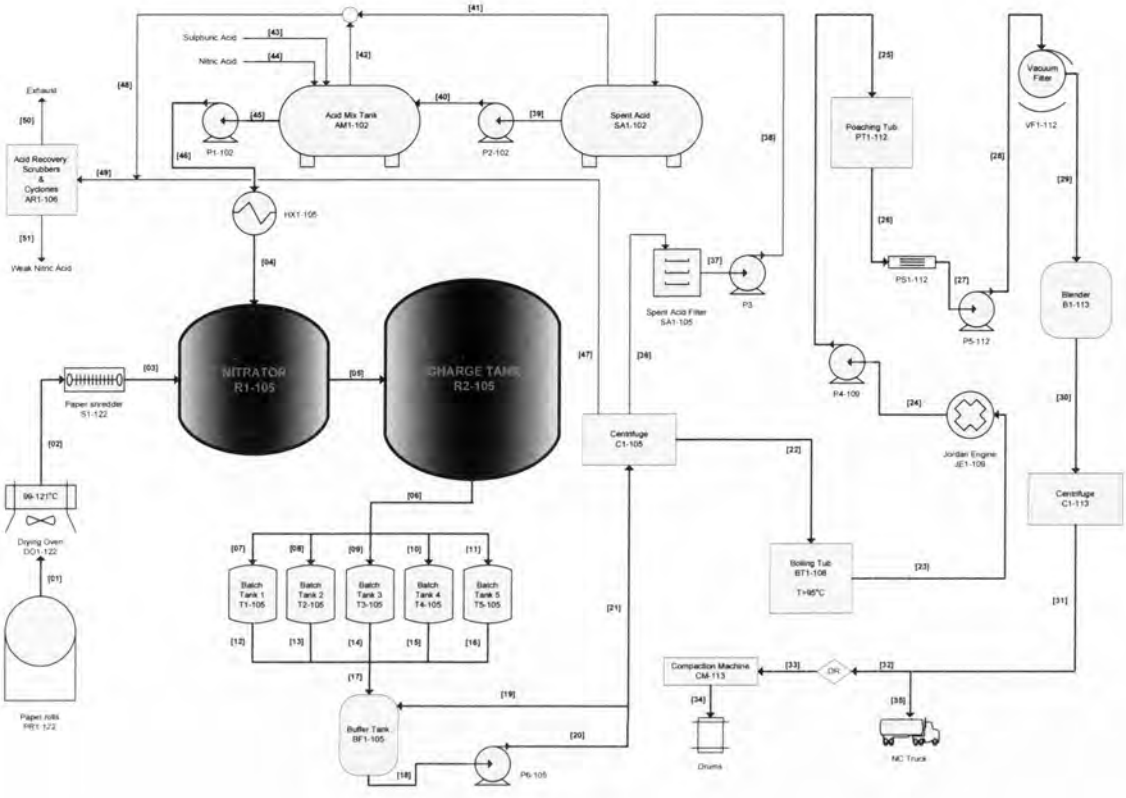


Figure 3.2: Process flow diagram for the manufacture of NC

Drying oven (DO1-122): The alpha cellulose board (ACB) received from supplier normally has a moisture level averaging 4.83%, which for effective nitration is reduced to 0.5%-1% although up to 2% has been successfully nitrated. Referring to the process flow diagram provided, ACB in the form of continuous sheet (PR1-122) will be fed into the drying oven for total duration not more than 15 mins. This reduction of moisture is achieved by blowing air at 165-170°C directly onto the sheets inside the drying chamber. The temperature of the chamber itself is kept between 99-121°C. To prevent the breakdown of the cellulose molecule, the oven temperature must not exceed 175°C and the duration of exposure to temperature above 165°C should not exceed 15 mins. It is understood that excessive temperature also reduces the cellulose viscosity.

Paper shredder (S1-122): Demoisturised ACB will then be shredded using a paper shredder. The process of shredding renders ACB to a suitable condition and size, both for acid penetration and for mobility through pumps and pipe lines after nitration. The characteristics of a particular pulp consignment must meet US military specification (MIL-C-216B). A compromise should be reached between large unopened shreds and fine broken shreds, the former allowing poor penetration and partial nitration, the latter causing loss of pulp from the wringer baskets, boiling tubs and dewatering units. The faster the feed roll speed, the coarser the final shred will be. Other factors determining the quality of shredded cellulose are the conditions of both the shredder rotor and bed plate knifes.

The acid mix tank (AM1-102) has the composition tabulated in Table 3.1.

Table 3.1 Acid Mix Tank Composition

| Chemicals | Values |
|---|---|
| $HNO_3$ | $28.72\% \pm 0.1\%$ |
| $H_2SO_4$ | $60.98\% \pm 0.1\%$ |
| Dilution | 10.3% |

Heat exchanger (HX1-105): Mixed acid from acid mix tank is fed into the heat exchanger to raise the temperature to 32°C prior to feeding it into the charge tank. Excessive acid temperature leads to low viscosities and exert a hydrolysing and oxidising effect on the cellulose as well as a saponifying effect on the ester. On the other hand, low acid temperatures lead to low nitrogen level.

Nitrator (R1-105 & R2-105): Mixed acid and demoisturised ACB will then be fed into the nitrator and charge tank, as shown in Figure 3.3, in the ratio of 40:1, where it will be nitrated to NC. The feeds to nitrator R1-105 has the composition shown in Table 3.2.

Table 3.2: Composition of streams 3 and 4

| Parameter | Stream 03 | Stream 04 |
|---|---|---|
| $[HNO_3]$ , % | - | 28.85 |
| $[H_2SO_4]$ , % | - | 60.65 |
| Dilution, % | 1.5 | 10.50 |
| Nitrous acid, % | - | 0.25 |
| Flowrate, kg $hr^{-1}$ | 450 | 16,920 |
| Temperature, °C | 30 | 32 |

Figure 3.3: Nitrator (left) and charge tank (right)

With $HNO_3$:$H_2SO_4$ in 1:4 ratio, the rate of reaction is more rapid than the rate of diffusion of the acid into the micelle so that the reaction proceeds from the surface of the micelle into the interior, giving a micellar heterogeneous surface reaction production (D tri) which has low solubility. However, as the nitric acid increases the rate of diffusion exceeds the rate of reaction and there is a tendency for hydrated type intermediates (Knecht type) to form with an ultimate zone reaction giving (D tri) type which is fairly soluble. NC leaving the nitrator and charge tank will flow into the batch tank (T1-105 to T5-105) to ensure complete nitration. After about 17 mins, the contents of the batch tanks are discharged into the buffer tanks (BF1-105). The contents are then pumped into the continuous centrifuge (C1-105) for deacidification, by spinning off the excess acid.

Products leaving C1-105 has the composition shown in Table 3.3.

Table 3.3: Composition of stream 36

| Parameter | Stream 36 |
|---|---|
| [$HNO_3$] , % | 25.55 |
| [$H_2SO_4$] , % | 62.65 |
| Dilution, % | 11.85 |
| Nitrous acid, % | 0.28 |
| Temperature, $^{o}C$ | 43 |

Boiling tub (BT1-108): NC leaving this centrifuge via stream 22 will then be fed into the boiling tubs. When the tub is full, the NC is washed until the acidity is between 0.25 and 0.5%. Inside these tubs, the NC should be prevented from coming into direct contact with the steam coming from these coils. It is imperative that during the boiling process the NC should be entirely submerged in boiling water and the temperature inside the tub should not be less than 95°C. The preliminary boiling treatment should be at least 40 hours, with water changes repeated at least 3 times.

Jordan engine (JE1-109): This unit operation role is to pulp the NC. In this process, the NC will be pulped in water to which just enough sodium carbonate solution may be added to preserve a slight alkaline reaction to phenolphthalein. The pulping process should continue until the NC is thoroughly and evenly pulped to a satisfactory degree of fineness.

Poaching tub (PT1-112): Pulped NC will then be fed into the poaching tub where it is boiled for 4 hours at minimum of 95°C, in alkaline condition followed by 1×2 hr and 2×1 hr water poaches with change of water between poaches. After poaching, the NC will be washed 8 times with cold water in the same tub. The effectiveness of each washing will be assured by subjecting the NC to agitation by mechanical impeller for one hour in a sufficient amount of fresh water, accompanied by a thorough settling and decantation of the clear water. In decanting, at least 1/3 of the total contents will be drawn off the tub.

Particle grit screen (PS1-112): The NC will be screened to remove fibres which are not properly pulped. The width of the slits should not be greater than 558 μm. Only those materials that passed through the slits will be offered in the finished product.

Vacuum filter (VF1-112): At the vacuum rotary filter, the NC slurry is dewatered and the resultant cake is additionally washed with water sprays. From here the screened and washed high grade NC is transferred into a blender (B1-113) where it is mixed with pyro NC in a certain ratio to achieve desired nitrogen content. The desired nitrogen content for high grade NC is 13.35-13.70% with sG of 1.66.

Centrifuge (C1-113): The stabilised NC is kept as slurry in the blender for safety reason and will be fed into this continuous centrifuge for dewatering when required. The NC leaves the centrifuge as a fluffy material and contains nominally 30-31% water. If dehydration of NC is required, 95% ethanol is introduced into the centrifuge via the 3 sets of sprays after the bulk of the water has been removed from the NC. Dehydrated NC, circa 3% water and 28% ethanol, is stored in sealed containers to avoid drying out. Finally, compaction, which increases the bulk density of NC, is carried out on the dehydrated NC, if required by the customer.

Acid recovery: scrubbers and cyclone (AR1-106): The acid recovery unit employs cyclone to separate fine liquid droplets from the bulk fume before feeding it to the scrubbers to scrub off the gaseous $HNO_3$, producing weak nitric acid. Fume fed into the acid recovery unit consists almost entirely of $HNO_3$ in the form of liquid droplets, smaller acid mist, gaseous $HNO_3$ and small amounts of nitric oxide and nitrogen dioxide.

## 3.2 Objectives of research

There is always an inherent risk in the manufacture of military products such as nitrocellulose (NC). Because of such risk, it is not always convenient to optimise the nitrator by building a pilot-scale version or to conduct physical experiments in the actual plant. Inept experiments causing small incidents in such a conservative industry often lead to losses of a catastrophic magnitude. Apart from the safety aspect, an equally important motivation is the economic aspect where stopping production to conduct experiments, may be economically prohibitive. Despite such obstacles, to prevent the obsolescence of ADI manufacturing technology due to the lack of optimisation or the failure of keeping up with advances in technology, there was little choice but to harness current and future technologies and apply them to the plant.

*The primary objective of this study was to characterise the nitrator so that relevant information to optimise the performance of this unit was made available. Besides using the results from this study to optimise the unit, having the unit characterised means this unit operation could be understood thoroughly so that in the event a new plant is desired, the transfer of operation knowledge from the existing plant to the proposed plant will have less setbacks.*

Most of the work was conducted at the ADI-Land Ordnance manufacturing facility, located at New South Wales, Australia.

Firstly, the quantitative and qualitative characterisation of this nitrator must occur before its optimisation can begin. To characterise the nitration process, a cutting-edge CFD technology was applied which when used judiciously, is known to have innocuous impact on human safety, the environment and economic factors. In this research work, steady-state and transient simulations were conducted using commercially available Fluent® CFD processor/post-processor V6.2.16 and Gambit V2.2.30 pre-processor [Lea et al. 2005]. This software is based on the finite volume (FV) method which uses the integral form of the conservation of equations as its starting point to ensure global conservation. A differential equation was integrated over the volume of each cell to obtain algebraic equations. Variable values were stored at the cell centres and interpolated using Taylor series expansion which was used to express variable values at cell faces in terms of the cell

centre values. Surface and volume integrals were estimated using appropriate quadrature formulae. As a consequence, all algebraic equations per cell were obtained in which a number of neighbouring cell centre values appeared as unknowns. As FV method can accommodate any type of grid it was therefore suitable for handling complex geometry such as the nitrator. In addition, the multiple reference frame (MRF) approach was used to model and simulate the rotation of the impeller inside the nitrator.

CFD will provide velocity flow fields that enable the prediction of whether the nitrator can be optimised. The validation of CFD simulation results with the 7-equations Reynolds stress models (RSM) was achieved by comparing them to physical experimental results obtained through the use of PIV technology. In general, many researchers reported great success with laminar flow modelling. However, other researchers claimed that although CFD accurately predicted, both qualitatively and quantitatively, the axial-radial mean flow fields under- or over-predicted the tangential velocity component and turbulent quantities such as the turbulent kinetic energy, $k$ and the turbulent energy dissipation rate, $\varepsilon$. Hitherto, most of the research was conducted on bench scale equipment confined to studies involving solids suspension, liquid-liquid mixing or gas dispersion. Very few studies studied the draw-down of floating solids, even though such a process is important in food processing, polymerisation reactions and fermentation processes. The study aims are to fill this research gap and to use the available information for the subsequent optimisation of nitrator.

Chemicals consisting of 61% concentrated nitric acids ($HNO_3$), 29% concentrated sulphuric acid ($H_2SO_4$) and 10% $H_2O$ were being used to nitrate the alpha cellulose boards (ACB), 2% w/w to NC. NC is a highly flammable energetic compound manufactured by nitration of ACB with $HNO_3$, in the presence of $H_2SO_4$, that is:

$$C_6H_{10}O_5 + xHNO_3 \Leftrightarrow C_6H_{10-x}O_{5-x}(ONO_2)_x + xH_2O$$

This nitration process adds a large amount of $O_2$ to the chemical structure of the cellulose. Most chemical reactor designs are greatly dependent on mixing and contacting, which are very fundamental steps in any chemical reaction. Reactants must first be brought together for a chemical reaction to occur since without mixing and contacting no chemical reaction

can take place. The primary design objective for chemical reactors from a mixing and contacting perspective is to obtain a kinetically controlled or equilibrium-controlled reactor and to eliminate all limitations due to transport. Similarly, to enhance the rate of nitration, it is essential that any mass transfer limitation be eliminated or minimised. For nitration to take place, mass transfer from the bulk liquid to the immediate region surrounding the ACB particles must occur. The fluid surrounding the particles will react with the ACB and be depleted. To ensure continuous high nitration rate is maintained, these depleted mixed acids must be replaced with fresh acid from the bulk fluid. Thus, an obvious way to maintain high nitration rate is to increase the relative velocity between the mixed acids and the ACB particles. This in turn can be achieved by investigating methods to induce high turbulence and minimise zones of low turbulence. It is well known from physical experiment measurements and CFD simulations that the turbulence flow profile is far from homogeneous. Significant variations exist in the state of turbulence at different positions within the nitration tank, from the impeller region to the bulk liquid. These variations will affect the local mass transfer rate which eventually affects the global rate of nitration.

It is therefore the intention of this study to model and simulate this nitrator where nitration process is occurring with a view to quantify its performance using parameters such as the power number, flow number, flow efficiency, blending time, percentage deviation from ideality and to provide qualitative information pertaining to the flow field for velocity, turbulence kinetic energy and its dissipation rates.

This chapter presents the following results:

- Simulation results of a scaled-down version of the nitrator validated using PIV;
- Simulation results obtained using the same approach, on the actual nitrator
- Simulation results obtained from proposed optimum design configuration

The validation of CFD results is important to instil confidence among the stakeholders and to prove that the models employed were robust and reliable enough to capture the hydrodynamics behaviour. Thus validation study was conducted prior to modelling and simulating the actual industrial size nitrator. Most validated mixing tank was set on baffled system using liquid water as the medium. Very few studies have been conducted on unbaffled mixing tank. Besides accommodating commercial need, the aim of this work was also to fill existing research gap. To ensure the integrity of the models employed, a validation was conducted by means of using a scaled-down version of the nitrator and applying advanced physical experiments utilising PIV technology. Validation of CFD results using PIV for the purpose of thorough analysis using the existing industrial scale version was not possible owing to its opaque wall which blocks laser light transmission.

## 3.3 Numerical setup

Fluent® solver was used to create a numerical solution that matches the governing conservation equations. In this study, the focus was on solving the conservation of mass, momentum, turbulence transport and species equations with a view to generating a steady-state 3D hydrodynamics profile and transient results [Lea and Adesina 2005].

To simulate impeller rotations, separate rotational zones in the immediate vicinity of the impellers were created and an MRF approach was employed. This method involved solving the flow characteristics of the inner region using a rotating framework. These results were then used to provide boundary conditions for the outer region which employed a stationary framework to secure solution to the flow characteristics. The results from the outer region were then re-supplied as boundary conditions for the inner region. This iterative procedure was repeated until a convergent solution was obtained for both regions. The MRF method provides accurate results yet falls within the confinement of reasonable computational effort [Kerdous et al. 2006].

Because of the nonlinearity of the equation set being solved by Fluent®, it is necessary to control the change of $\phi$. The solver uses under-relaxation to control the update of computed variables at each iteration. This typically reduces the change of $\phi$ produced during each iteration. In a simple form, the new value of the variable $\phi_{new}$ within a cell depends upon the old value, $\phi_{old}$, the computed change in $\phi$, that is $\Delta\phi$, and the under-relaxation factor $\alpha$ as follows:

$$\phi_{new} = \phi_{old} + \alpha\Delta\phi \qquad -3.1$$

Fluent's default under-relaxation values for all variables were set to values that are near optimal for the largest possible number of cases. Default values can be used as the starting point for any iteration and the values can be increased for faster convergence or in the case where the residuals begin to increase, the under-relaxation values should be decreased.

The segregated solution approach was used where the governing equations were solved sequentially unlike the coupled solution approach where the variables are solved in all cells simultaneously [Fluent 2006]. In both the segregated and coupled solution approaches, the discrete, non-linear governing equations are linearised to produce a system of equations for dependent variables in every computational cell and the resultant linear system is solved to yield an updated flow-field solution. However, the manner in which the governing equations are linearised may take an 'implicit' or 'explicit' form with respect to the dependent variable of interest.

In this context, the term implicit refers to a given variable where the unknown value in each cell is computed using a relation that includes both existing and unknown values from neighbouring cells. Thus, each unknown will appear in more than one equation in the system, and these equations must be solved simultaneously to give the unknown quantities. In contrast, the term explicit refers to a given variable where the unknown value in each computational cell is computed using a relation that includes only existing values. Therefore, each unknown will appear in only one equation in the system and the equations for the unknown value in each cell can be solved one at a time to yield the unknown quantities.

In Fluent® solver, there is no explicit option for the segregated solver. Therefore, in the segregated-implicit approach, a single variable field, for example $p$, is solved by considering all cells at the same time. On the other hand, the coupled-implicit approach solves for all variables such as $p$, $u$, $v$, $w$, $T$ in all cells at the same time while in the coupled-explicit approach, all the variables such as $p$, $u$, $v$, $w$, $T$ are solved in one cell at a time. In this simulation, the segregated-implicit approach was adopted.

The simulations were started from a first-order accuracy using the first-order upwind scheme where quantities at cell faces were determined by assuming that the cell-centre values of any field variable represent a cell-average value and hold throughout the entire cell, that is, the face quantities are identical to the cell quantities. Therefore, when the first-order upwind scheme was used, the face value $\phi_f$ is set equal to the cell-centre value of $\phi$ in the upstream cell. Once the residual values stabilised or even converged, a higher order scheme was selected to obtain a higher level of accuracy. To obtain a higher degree of accuracy, all solutions were obtained via the second-order upwind scheme. In this scheme, higher order accuracy was obtained at the cell surfaces where the values at the cell centroid were subjected to multidimensional linear reconstruction using the Taylor series expansion. The following section provides a brief outlines of Taylor series method [Hoffman 2001].

A power series in powers of $x$ is a series of the form:

$$\sum_{n=0}^{\infty} a_n x^n = a_0 + a_1 x + a_2 x^2 + \ldots \qquad \text{- 3.2}$$

A power series in powers of $(x\text{-}x_0)$ is given by:

$$\sum_{n=0}^{\infty} a_n (x - x_0)^n = a_0 + a_1 (x - x_0) + a_2 (x - x_0)^2 + \ldots \qquad \text{- 3.3}$$

Within its radius of convergence, $r$, any continuous function $f(x)$ can be represented exactly by a power series in the form:

$$f(x)=\sum_{n=0}^{\infty} a_n(x-x_0)^n \qquad -3.4$$

is continuous for $(x_0-r) < x < (x_0+r)$

If the coefficients in Equation (3.4) are given by the rule:

$$a_0 = f(x_0),\ \ a_1 = \frac{1}{1!}f'(x_0),\ \ a_2 = \frac{1}{2!}f''(x_0)...$$

Then Equation (3.4) becomes the Taylor series of $f(x)$ at $x=x_0$ and is given by:

$$f(x)=f(x_0)+\frac{1}{1!}f'(x_0)(x-x_0)+\frac{1}{2!}f''(x_0)(x-x_0)^2+... \qquad -3.5$$

Equation (3.5) can be written in the simpler appearing form:

$$f(x)=f_0+f_0'\Delta x+\frac{1}{2}f_0''\Delta x^2+...+\frac{1}{n!}f_0^{(n)}\Delta x^n+... \qquad -3.6$$

where $f_0 = f(x_0),\ \ f^{(n)}=\frac{df^{(n)}}{dx^{(n)}},\ \ \Delta x=(x-x_0)$.

Equation (3.6) can be written in a more compact form as:

$$f(x)=\sum_{n=0}^{\infty}\frac{1}{n!}f_0^{\,n}(x-x_0)^n \qquad -3.7$$

Because it is impractical to evaluate an infinite Taylor series term by term, the Taylor series is written as the finite Taylor series, also known as Taylor formula or Taylor polynomial with remainder and the equation is given by:

$$f(x)=f(x_0)+\frac{1}{1!}f'(x_0)(x-x_0)+\frac{1}{2!}f''(x_0)(x-x_0)^2+\ldots+\frac{1}{n!}f^n(x_0)(x-x_0)^n+R^{n+1} \quad -3.8$$

The term $R^{n+1}$ is the remainder term and is given by:

$$R^{n+1}=\frac{1}{(n+1)!}f^{(n+1)}(\xi)(x-x_0)^{n+1} \quad -3.9$$

$\xi$ lies between $x_0$ and $x$. Approximation of $f(x)$ in Equation (3.8) is obtained by truncating the remainder term.

For functions of more than one independent variable, such as two independent variables, $f(x,y)$, the Taylor series $f(x,y)$ at $(x_0,y_0)$ is given by:

$$\begin{aligned} f(x,y)=f_0+&\frac{\partial f}{\partial x}|_0(x-x_0)+\frac{\partial f}{\partial y}|_0(y-y_0) \\ &+\frac{1}{2!}\left(\frac{\partial^2 f}{\partial x^2}|_0(x-x_0)^2+2\frac{\partial^2 f}{\partial x\partial y}|_0(x-x_0)(y-y_0)+\frac{\partial^2 f}{\partial y^2}|_0(y-y_0)^2\right)+\ldots \end{aligned} \quad -3.10$$

Equation (3.10) can be written in the general form as:

$$f(x,y)=\sum_{n=0}^{\infty}\frac{1}{n!}\left((x-x_0)\frac{\partial}{\partial x}+(y-y_0)\frac{\partial}{\partial y}\right)^n f(x,y)|_0 \quad -3.11$$

where the term $(\ldots)^n$ is expanded by the binomial expansion and the resulting expansion operates on the function $f(x)$ and is evaluated at $(x_0,y_0)$. The Taylor formula with remainder for a function of two independent variables is obtained by evaluating the derivatives in the (n+1) term at the point $(\xi,\eta)$, where $(\xi,\eta)$ lies in the region between points $(x_0,y_0)$ and $(x,y)$.

When the second-order upwind scheme was selected, the face value $\phi_f$ was computed using the following expression:

$$\phi_f = \phi + \nabla\phi \cdot \Delta\vec{s} \qquad \text{- 3.12}$$

where

$\phi$ : cell-centred value

$\nabla\phi$ : gradient in the upstream cell

$\Delta\vec{s}$ : displacement vector from the upstream cell centroid to the face centroid

The formulation involving $\Delta\vec{s}$ required the determination of the gradient $\nabla\phi$ in each cell. This gradient was computed using the divergence theorem, which in discrete form is written as:

$$\nabla\phi = \frac{1}{V}\sum_{f}^{N_{faces}} \tilde{\phi}_f \vec{A} \qquad \text{- 3.13}$$

The face values $\tilde{\phi}_f$ were computed by averaging $\phi$ from the two cells adjacent to the face. Finally, the gradient $\nabla\phi$ was limited so that no new maximum or minimum were introduced. Specifying appropriate initial and boundary conditions are necessary to solve the closed set of governing equations. To solve reactor engineering problem, it is necessary to select an appropriate solution domain, which isolates the system being modelled from the surrounding environment. The effect of the environment on the flow processes concerned within the solution domain is represented by suitable formulation of boundary conditions. It follows that the solution domain, the coordinate system used to formulate the governing equations and the characteristics of the governing equations determine the boundary conditions requirements.

In this study, the solution domain was restricted to the tanks and that flow within the feed pipes was not modelled. This can be assumed as although the volumetric flowrates in the pipes are known accurately, the velocity distribution at the inlet was not known accurately. For the outlet boundary conditions, gradients normal to the outlet boundary are zero for all variables except pressure and it was not necessary to specify pressure at the outlet boundary. At the impermeable wall boundaries of the solution domain, a 'no slip'

boundary condition was employed. This was achieved by setting the transverse fluid velocity equal to that of the surface and setting the normal velocity to zero.

Due to the absence of baffles, significant uninterrupted rotational flow existed inside the nitrator. Because of this, large body forces existed, thus the body-force-weighted algorithm was used to compute the pressure value at the cell surface by interpolating the value at cell centroid.

The SIMPLE (semi-implicit method for pressure linked equations) scheme was used for the pressure-velocity coupling where a relationship between the pressure and velocity corrections was used to enforce conservation of continuity in order to obtain the pressure field [Letellier et al. 2002]. This scheme was employed on all steady-state calculations. On the other hand, for transient calculations such as determining the blending time in the nitrator, the PISO (pressure-implicit with splitting of operators) scheme, which is part of the SIMPLE family of algorithms that is based on a higher degree of the approximate relation between the corrections for pressure and velocity was used. One of the drawbacks of the SIMPLE algorithm is that new velocities and corresponding fluxes do not satisfy the momentum balance after the pressure-correction equation is solved. As a consequence, the calculation must be repeated until the balance is satisfied.

To improve the efficiency of this calculation, the PISO algorithm performs two additional corrections, namely, the neighbour correction and skewness correction. The principle underlying this algorithm is to move the repeated calculations required SIMPLE scheme inside the solution stage of the pressure-correction equation. After one or more additional PISO loops, the corrected velocities satisfy the continuity and momentum equations more closely. This iterative process is called momentum correction or neighbour correction. Although more computational time is required per solver iteration when using the PISO scheme, it compensates by significantly decreasing the number of iterations required for convergence, especially for transient calculations. The other feature of PISO scheme, the skewness correction, allows the solver to obtain a solution on a highly skewed mesh in approximately the same number of iterations as required for a more orthogonal mesh.

Simulations were generally considered converged when the residuals for mass, momentum and turbulence kinetic energy and its dissipation rate fell below $1\times10^{-4}$. Further checks for convergence were made by creating a monitoring point inside the tank and ensuring that the value monitored remained constant with repeated iterations.

To speed up the iteration process, a convergence acceleration technique called full multigrid method (FMG) was employed. The principle of multigrid is based on the observation that iterative schemes usually eliminate high-frequency errors (local) in the solution. On the other hand, they perform rather poor in mitigating low-frequency errors (global) in the solution. Therefore, after advancing the solution on a given grid, it is transferred to a coarser grid, where the low frequency errors become partly high-frequency ones and where they are again effectively dampened by an iterative solver. This manoeuvre is repeated recursively on a sequence of progressively coarser grids where each multigrid level helps to eliminate a certain bandwidth of error frequencies. After the coarsest grid is reached, the solution corrections are consecutively collected and interpolated back to the initial fine grid, where the solution is then updated. This complete multigrid cycle is repeated until the solution changes less than a given threshold. In Fluent® solver, in order to hasten the convergence even further, the multigrid process starts on a coarse grid, carries out a number of cycles and then transfers the solution to a finer grid, where the multigrid cycles are performed again. The procedure is then successively repeated until the finest grid is reached. Since FMG initialisation does most of the work on coarse levels, this initialisation procedure is computationally inexpensive and, for large problems, a good initial solution can be obtained in a fraction of the time spent to converge on a final solution. However, there a limitation on the applicability of this method. They are:

- FMG initialisation is not available for unsteady flows
- FMG will not initialise turbulence or other transport equations field variables
- FMG cannot not be used with multiphase flow

In addition, to further speed up the iteration process, a dual-processor capability computer (3.20GHz and 8GB RAM) operated on Linux 4 Redhat Enterprise was used, and Fluent® parallel processing software was employed to split the total number of cells equally, and assign them to each processor.

## 3.4 Modelling turbulence

Turbulent flows are generally characterised by fluctuating velocity fields. These fluctuations mix transported quantities such as momentum, energy and species concentration, and cause the transported quantities to fluctuate as well. Since these fluctuations can be of small scale and high frequency, they are too computationally demanding to simulate directly to be of any benefits in practical engineering calculations. Instead, the instantaneous governing equations are time-averaged or otherwise manipulated to remove the small scales, resulting in a modified set of equations that are computationally less demanding to solve. However, in doing so, the modified equations contain additional unknown variables, and turbulence models are required to ascertain these variables in terms of known quantities.

The Reynolds averaged Navier-Stokes (RANS) based turbulence models available in Fluent® and considered in this research were [Fluent 2006]:

- Spalart-Allmaras

- $k$-$\varepsilon$ models:
  - $\Rightarrow$ standard $k$-$\varepsilon$ model,
  - $\Rightarrow$ renormalisation-group (RNG) $k$-$\varepsilon$ model,
  - $\Rightarrow$ realisable $k$-$\varepsilon$ model

- $k$-$\omega$ models:
  - $\Rightarrow$ standard $k$-$\omega$ model
  - $\Rightarrow$ shear-stress transport (SST) $k$-$\omega$ model

- Reynolds stress model (RSM)

### 3.4.1 Spalart-Allmaras model

This model is a single conservation equation model that solves directly a modified turbulent viscosity. It is economical [Ranade 2002] for large meshes but performs poorly for 3D flows, free shear flows, flows with strong separation. This model is suitable for mildly complex (quasi-2D) internal/external flows and boundary layer flows under pressure gradient, for example, airfoils, wings, airplane fuselage, missiles and ship hulls.

### 3.4.2 Standard $k$-$\varepsilon$ model

This is the baseline two transport equations model solving for $k$ and $\varepsilon$, set as default in Fluent®. It is the simplest two-equation models in which the solution of two separate transport equations allows the turbulent velocity and length scales to be independently determined. Coefficients are empirically derived but valid for fully turbulent flows only. Options are available to account for viscous heating, buoyancy and compressibility that are shared with other $k$-$\varepsilon$ models. The advantages of using this model are its simplicity, robustness and economy. It is widely used despite the known limitations of the model [Sommerfeld and Decker 2004]. It provides excellent performance for many industrial flows and is the most widely validated model [Ranade 2002]. However, its disadvantages are that it is more expensive than zero equation models, assumes isotropic eddy viscosity, performs poorly for unconfined flows, rotating flows, non-circular ducts and curved boundary layers. This model is suitable for initial iterations, initial screening of alternative designs and parametric studies. Several researchers have employed this model in their study of stirred tanks [Sahu et al. 1999; Montante et al. 2001; and Kumaresan and Joshi 2006].

### 3.4.3 RNG $k$-$\varepsilon$ model

This is a variant of the standard $k$-$\varepsilon$ model, where equations and coefficients are analytically derived. The RNG $k$-$\varepsilon$ model was derived using a statistical technique called renormalisation group theory. It is similar to the standard $k$-$\varepsilon$ model but includes modifications which enable it to outperform the standard $k$-$\varepsilon$ model in separated flows. The significant change in the $\varepsilon$ equation improves the ability to model highly strained flows. Additional options assist in predicting swirling and low Reynolds flows. The effect

of swirl on turbulence is included in the RNG model thereby enhancing accuracy for swirling flows [Ranade 2002]. This model is suitable for complex shear flows involving rapid strain, moderate swirl, vortices and locally transitional flows, for example, boundary layer separation, massive separation and vortex-shedding behind bluff bodies, stall in wide-angle diffusers and room ventilation. While the standard $k$-$\varepsilon$ model is a high Reynolds number model, the RNG theory provides an analytically-derived differential formula for effective viscosity that accounts for low Reynolds number effects. However, effective use of this feature requires appropriate treatment of the near-wall region. Similarly, the disadvantage of this model is that it assumes isotropic eddy viscosity. In addition, a significant drawback of this model is that, hitherto, it has not been sufficiently validated. Overall, the improvements made to RNG $k$-$\varepsilon$ model makes it more accurate and reliable for a wider class of flows than the standard $k$-$\varepsilon$ model. Montante et al. [2005] employed this model to predict the flow pattern for Newtonian and pseudoplastic fluid.

### 3.4.4 Realisable $k$-$\varepsilon$ model

This is a variant of the standard $k$-$\varepsilon$ model where changes that allow certain mathematical constraints to be obeyed, ultimately improve the performance of this model. The realisable $k$-$\varepsilon$ model was developed recently and differs from the standard $k$-$\varepsilon$ model in two ways: it contains a new formulation for the turbulent viscosity and a new transport equation for the dissipation rate has been derived from an exact equation for the transport of the mean-square vorticity fluctuation. An obvious advantage of this model is that it offers the same benefits and has similar applications to RNG $k$-$\varepsilon$, but can be more accurate and easier to converge than the RNG $k$-$\varepsilon$ model. Moreover, it can predict the spreading rate of both planar and round jets more accurately and is also more likely to provide superior performance for flows that involve rotation, boundary layers under strong adverse pressure gradients, separation and recirculation [Fluent 2006]. The disadvantage is that this model produces non-physical turbulent viscosities in cases where the computational domain contains both rotating and stationary fluid zones such as the multiple reference frame and sliding meshes.

### 3.4.5 Standard $k$-$\omega$ model

It is a two conservation equations model (default $k$-$\omega$) solving for $k$-$\omega$, the specific dissipation rate ($\varepsilon/k$) based on Wilcox [1998]. It demonstrates superior performance for wall bounded and low Reynolds number flows. In addition, this model shows potential for predicting transition flow and includes options to account for transitional, free shear and compressible flows. This model is suitable for complex boundary layer flows under adverse pressure gradient and separation, for example, external aerodynamics and turbomachinery.

### 3.4.6 SST $k$-$\omega$ model

This is a variant of the $k$-$\omega$ model where it combines the original Wilcox model [1998] for use near walls and standard $k$-$\varepsilon$ model away from walls using a blending function. This model limits turbulent viscosity to guarantee that $\tau_t \sim k$. In addition, the transition and shearing options were borrowed from standard $k$-$\omega$ and this model does not come with compressibility option. Similar benefits to standard $k$-$\omega$ but its dependency on wall distance makes this less suitable for free shear flows.

### 3.4.7 Reynolds stress model

Reynolds stresses are solved directly with transport equations avoiding isotropic viscosity assumption of other models. The availability of quadratic pressure-strain option improves performance for many basic shear flows. This is the most physically sound RANS model is suitable for complex 3D flows with strong streamline curvature, strong swirl, for example, curved duct, rotating flow passages, swirl combustors with large inlet swirl and cyclones.

The RSM model accounts for the effects of streamline curvature, rotation, swirl, rapid changes in the rate of strain, in a more rigorous manner than the one-equation and two-equation models, therefore the RSM model [Launder et al. 1975; Launder 1989; and Fletcher and Hardesty 1992] has a greater potential to provide a more accurate prediction for complex flow. Thus, to model the existing unbaffled-nitrator, the Reynolds stress models (RSM), despite being the most computationally expensive model, was the most suitable model for this application and the aim for accuracy. This model involves the

calculation of the individual Reynolds stresses, $u_i'u_j'$, using differential transport equations. The individual Reynolds stresses are then used to obtain closure of the Reynolds-averaged momentum equation. The exact form of the Reynolds stress transport equations may be derived by taking moments of the exact momentum equation. This is a process where the exact momentum equations are multiplied by a fluctuating property, the product then being Reynolds-averaged. However, several of the terms in the exact equation are unknown and modelling assumptions are required in order to close the equations.

The RSM transport equation is given by:

$$\underbrace{\frac{\partial}{\partial t}(\rho\overline{u_i'u_j'})}_{\text{Local time derivative}} + \underbrace{\frac{\partial}{\partial x_k}(\rho u_k\overline{u_i'u_j'})}_{C_{ij}\equiv\text{Convection}} = \underbrace{\frac{\partial}{\partial x_k}\left[\rho\overline{u_i'u_j'u_k'} + \overline{p(\delta_{kj}u_i' + \delta_{ik}u_j')}\right]}_{D_{T,ij}\equiv\text{Turbulent diffusion}}$$

$$+\underbrace{\frac{\partial}{\partial x_k}\left[\mu\frac{\partial}{\partial x_k}(\overline{u_i'u_j'})\right]}_{D_{L,ij}\equiv\text{Molecular diffusion}} - \underbrace{\rho(\overline{u_i'u_k'}\frac{\partial u_j}{\partial x_k} + \overline{u_j'u_k'}\frac{\partial u_i}{\partial x_k})}_{P_{ij}\equiv\text{Stress production}} - \underbrace{\rho\beta(g_iu_j'\theta + g_ju_i'\theta)}_{G_{ij}\equiv\text{Buoyancy production}} \qquad \text{- 3.14}$$

$$+\underbrace{\overline{p(\frac{\partial u_i'}{\partial x_j} + \frac{\partial u_j'}{\partial x_i})}}_{\phi_{ij}\equiv\text{Pressure strain}} - \underbrace{2\mu\overline{\frac{\partial u_i'}{\partial x_k}\frac{\partial u_j'}{\partial x_k}}}_{\varepsilon_{ij}\equiv\text{Dissipation}} - \underbrace{2\rho\Omega_k(\overline{u_j'u_m'}\varepsilon_{ikm} + \overline{u_i'u_m'}\varepsilon_{jkm})}_{F_{ij}\equiv\text{Production by system rotation}}$$

$$+ \underbrace{S_{\text{user}}}_{\text{User-defined source term}}$$

Of the various terms in these exact equations, $C_{ij}$, $D_{L,ij}$, $P_{ij}$ and $F_{ij}$ do not require any modelling. However, $D_{T,ij}$, $G_{ij}$, $\phi_{ij}$ and $\varepsilon_{ij}$ need to be modelled to close the equations. $D_{T,ij}$ can be modelled by the generalised-diffusion model [Daly and Harlow 1970]:

$$D_{T,ij} = C_s\frac{\partial}{\partial x_k}\left(\rho\frac{\overline{ku_k'u_l'}}{\varepsilon}\frac{\overline{\partial u_i'u_l'}}{\partial x_l}\right) \qquad \text{- 3.15}$$

However, this equation can result in numerical instabilities, so it has been simplified in Fluent® to use a scalar turbulent diffusitivity [Lien and Leschziner 1994]:

$$D_{T,ij} = \frac{\partial}{\partial x_k}\left(\frac{\mu_t}{\sigma_k}\frac{\overline{\partial u_i' u_j'}}{\partial x_k}\right) \quad \text{- 3.16}$$

$\sigma_k = 0.82$ [Lien and Leschziner 1994]

The turbulent viscosity, $\mu_t$ is defined as:

$$\mu_t = \rho C_\mu \frac{k^2}{\varepsilon} \quad \text{- 3.17}$$

where $C_\mu = 0.09$

The production terms due to buoyancy $G_{ij}$ can be modelled as:

$$G_{ij} = \beta \frac{\mu_t}{\mathrm{Pr}_t}\left(g_i \frac{\partial T}{\partial x_j} + g_j \frac{\partial T}{\partial x_i}\right) \quad \text{- 3.18}$$

where $Pr_t$ is the turbulent Prandtl number for energy, with a default value of 0.85.

$$\beta = \frac{1}{\rho}\left(\frac{\partial \rho}{\partial T}\right)_p \quad \text{- 3.19}$$

From the above equation, expression for $G_{ij}$ is given by:

$$G_{ij} = -\frac{\mu_t}{\rho\,\mathrm{Pr}_t}\left(g_i \frac{\partial \rho}{\partial x_j} + g_j \frac{\partial \rho}{\partial x_i}\right) \quad \text{- 3.20}$$

In general, when the turbulence kinetic energy is needed for modelling a specific term, it is obtained by taking the trace of the Reynolds stress tensor given by:

$$k = \frac{1}{2}\overline{u_i' u_i'} \quad \text{- 3.21}$$

An option is available in Fluent® to solve a transport equation for the turbulence kinetic energy in order to obtain boundary conditions for the Reynolds stresses. In such case, the following model is used:

$$\frac{\partial}{\partial t}(\rho k)+\frac{\partial}{\partial xi}(\rho k u_i)=\frac{\partial}{\partial x_j}\left[\left(\mu+\frac{\mu_t}{\sigma_k}\right)\frac{\partial k}{\partial x_j}\right]+\frac{1}{2}[P_{ii}+G_{ii}]-\rho\varepsilon\left(1+2M_t^2\right)+S_k \qquad -3.22$$

where $\sigma_k = 0.82$ and $S_k$ is a user-defined source term. Although this equation is solved globally throughout the flow domain, the values of $k$ obtained are used only for boundary conditions. In every other case, $k$ is obtained from Equation (3.21).

The dissipation tensor, $\varepsilon_{ij}$ is modelled as:

$$\varepsilon_{ij}=\frac{2}{3}\delta_{ij}\left(\rho\varepsilon+Y_M\right) \qquad -3.23$$

where the additional 'dilatation dissipation' term is given by:

$$Y_M=2\rho\varepsilon M_t^2 \qquad -3.24$$

and the turbulent Mach number in this term is defined as:

$$M_t=\sqrt{\frac{k}{a^2}} \qquad -3.25$$

where $a\equiv\sqrt{\gamma RT}$ is the speed of sound and this compressibility modification always takes effect when the compressible form of the ideal gas law is used. The scalar dissipation rate, $\varepsilon$, is computed with a model transport equation similar to that used in the standard $k$-$\varepsilon$ model:

$$\frac{\partial}{\partial t}(\rho\varepsilon)+\frac{\partial}{\partial xi}(\rho\varepsilon u_i)=\frac{\partial}{\partial t_j}\left[\left(\mu+\frac{\mu_t}{\sigma_\varepsilon}\right)\frac{\partial\varepsilon}{\partial x_j}\right]C_{\varepsilon 1}\frac{1}{2}[P_{ii}+C_{\varepsilon 3}G_{ii}]\frac{\varepsilon}{k}-C_{\varepsilon 2}\rho\frac{\varepsilon^2}{k}+S_\varepsilon \qquad -3.26$$

where $\sigma_\varepsilon$ = 1.0, $C_{\varepsilon 1}$ = 1.44, $C_{\varepsilon 2}$ = 1.92, $C_{\varepsilon 3}$ is evaluated as a function of the local flow direction relative to the gravitational vector.

In Fluent®, by default the pressure-strain term $\phi_{ij}$ is model as [Gibson and Launder 1978; Fu et al. 1987; Launder 1989; Launder 1989].

$$\phi_{ij} = \phi_{ij,1} + \phi_{ij,2} + \phi_{ij,w} \qquad -3.27$$

where $\phi_{ij,1}$ is the slow pressure-strain term, also known as the return-to-isotropy term while $\phi_{ij,2}$ is called the rapid pressure-strain term and finally $\phi_{ij,w}$ is the wall-reflection term. The slow pressure-strain term $\phi_{ij,1}$ is modelled as:

$$\phi_{ij} \equiv -C_1 \rho \frac{\varepsilon}{k}\left[\overline{u_i' u_j'} - \frac{2}{3}\delta_{ij} k\right] \qquad -3.28$$

where $C_1$ = 1.8. On the other hand, the rapid pressure-strain term, $\phi_{ij,2}$ is modelled as:

$$\phi_{ij,2} \equiv -C_2\left[P_{ij} + F_{ij} + G_{ij} - C_{ij}\right] - \frac{2}{3}\delta_{ij}\left(P + G - C\right) \qquad -3.29$$

where $C_2$ = 0.60, $P = 0.5P_{kk}$, $G = 0.5G_{kk}$ and $C = 0.5C_{kk}$.

The wall-reflection term, $\phi_{ij,w}$ is responsible for the redistribution of normal stresses near the wall. It tends to damp the normal stress perpendicular to the wall, while enhancing the stresses parallel to the wall. This term is modelled as:

$$\phi_{ij,w} = C_1' \frac{\varepsilon}{k}\left(\overline{u_k'u'}_m n_k n_m \delta_{ij} - \frac{3}{2}u_i'u_k'n_j n_k - \frac{3}{2}u_j'u_k'n_i n_k\right)\frac{k^{3/2}}{C_{l\varepsilon d}} + C_2'\left(\phi_{km,2}n_k n_m \delta_{ij} - \frac{3}{2}\phi_{ik,2}n_j n_k - \frac{3}{2}\phi_{jk,2}n_i n_k\right)\frac{k^{3/2}}{C_{l\varepsilon d}} \quad \text{- 3.30}$$

where $C_1' = 0.5$, $C_2' = 0.3$, $n_k$ is the $x_k$ component of the unit normal to the wall, d is the normal distance to the wall, and $C_l = \frac{C_\mu^{3/4}}{k}$ where $C_\mu$ = 0.09 and $k$ is the von Karman constant = 0.4187. $\phi_{ij,w}$ is included by default in the Reynolds stress model.

When the RSM model is applied to near-wall flows using the enhanced wall treatment, the pressure-strain model needs to be modified. The modification used in Fluent® specifies the values of $C_1, C_2, C_1', C_2'$ as functions of the Reynolds stress invariants and the turbulent Reynolds number, as proposed by Launder and Shima [1989]:

$$C_1 = 1 + 2.58A\sqrt{A_2}\left(1 - \exp\left(-\left(0.0067\,\mathrm{Re}_t\right)^2\right)\right) \quad \text{- 3.31}$$

$$C_2 = 0.75\sqrt{A} \quad \text{- 3.32}$$

$$C_1' = -\frac{2}{3}C_1 + 1.67 \quad \text{- 3.33}$$

$$C_2' = \max\left[\frac{\frac{2}{3}C_2 - \frac{1}{6}}{C_2}, 0\right] \quad \text{- 3.34}$$

with the turbulent Reynolds number defined as:

$$\mathrm{Re}_t = \left( \frac{\rho k^2}{\mu \varepsilon} \right) \qquad \text{- 3.35}$$

The parameter $A$ and the tensor invariants $A_2$ and $A_3$ are defined as:

$$\begin{aligned} A &\equiv \left[ 1 - \frac{9}{8}(A_2 - A_3) \right] \\ A_2 &\equiv a_{ik} a_{ki} \\ A_3 &\equiv a_{ik} a_{kj} a_{ji} \end{aligned} \qquad \text{- 3.36}$$

$a_{ij}$ is the Reynolds-stress anisotropy tensor, defined as:

$$a_{ij} = -\left( \frac{-\rho u_i' u_j' + \frac{2}{3} \rho k \delta_{ij}}{\rho k} \right) \qquad \text{- 3.37}$$

The modifications detailed above are employed only when the enhanced wall treatment is activated. Another optional pressure-strain model available in Fluent® is that proposed by Speziale et al. [1991]. This model has been demonstrated to give superior performance in a range of basic shear flows, including plane strain, rotating plane shear , and axisymmetric expansion or contraction. This improved accuracy is beneficial for a wider class of complex engineering flows, particularly those with streamline curvature. It is given as:

$$\begin{aligned} \phi_{ij} = &-\left(C_1 \rho \varepsilon + C_1^*\right) b_{ij} + C_2 \rho \varepsilon \left( b_{ik} b_{kj} - \frac{1}{3} b_{mn} b_{mn} \delta_{ij} \right) + \left( C_3 - C_3^* \sqrt{b_{ij} b_{ij}} \right) \rho k S_{ij} \\ &+ C_4 \rho k \left( b_{ik} S_{jk} + b_{jk} S_{ik} - \frac{2}{3} b_{mn} S_{mn} \delta_{ij} \right) + C_5 \rho k \left( b_{ik} \Omega_{jk} + b_{jk} \Omega_{ik} \right) \end{aligned} \qquad \text{- 3.38}$$

where $b_{ij}$ is the Reynolds-stress anisotropy tensor defined as:

$$b_{ij} = -\left( \frac{-\rho\overline{u_i'u'}_j + \frac{2}{3}\rho k\delta_{ij}}{2\rho k} \right) \quad \text{- 3.39}$$

The mean strain rate, $S_{ij}$, is defined as:

$$S_{ij} = \frac{1}{2}\left( \frac{\partial u_j}{\partial x_i} + \frac{\partial u_i}{\partial x_j} \right) \quad \text{- 3.40}$$

The mean rate of rotation tensor $\Omega_{ij}$ is defined as:

$$\Omega_{ij} = \frac{1}{2}\left( \frac{\partial u_i}{\partial x_j} - \frac{\partial u_j}{\partial x_i} \right) \quad \text{- 3.41}$$

The constants are given by:

$C_1 = 3.4,\ C_1^* = 1.8,\ C_2 = 4.2,\ C_3 = 0.8,\ C_3^* = 1.3,\ C_4 = 1.25,\ C_5 = 0.4$

The quadratic pressure-strain model does not require a correction to account for the wall-reflection effect in order to obtain a satisfactory solution in the logarithmic region of a turbulent boundary layer. This model is not available when the enhanced wall treatment is selected.

## 3.5 Boundary layer

Figure 3.4 shows the development of a boundary layer near a flat plate of negligible thickness when a fluid approaches the plat with unit velocity, $\upsilon_\infty$.

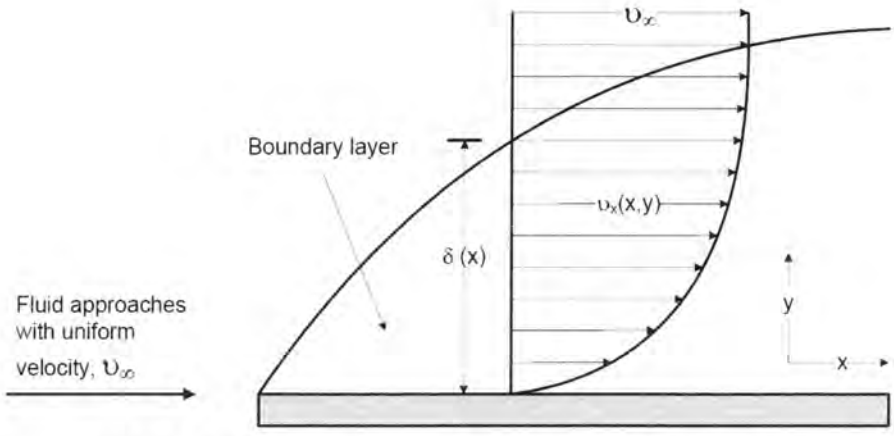


Figure 3.4: Development of a boundary-layer near a flat plate of negligible thickness

Numerous experiments have demonstrated that the near-wall region, especially inside the boundary layer, can be largely subdivided into three layers [Ranade 2002]. The innermost layer is called the viscous sublayer and the flow profile is almost laminar with the molecular viscosity playing a significant role in momentum and heat or mass transfer. The outer layer is called the fully-turbulent layer where turbulence plays a major role. The region between these two layers is where the effects of molecular viscosity and turbulence are equally important.

There are two approaches to modelling the near-wall region, where in one approach the viscous sublayer is not resolved; instead, semi-empirical formulas called wall function are used to bridge the viscous sublayer region and the fully turbulent region. An advantage of using wall functions is that it renders the need to modify the turbulence models to account for the presence of the wall redundant. The other approach involves solving the viscous sublayer with a mesh all the way to the wall. Both of these approaches are illustrated in Figure 3.5.

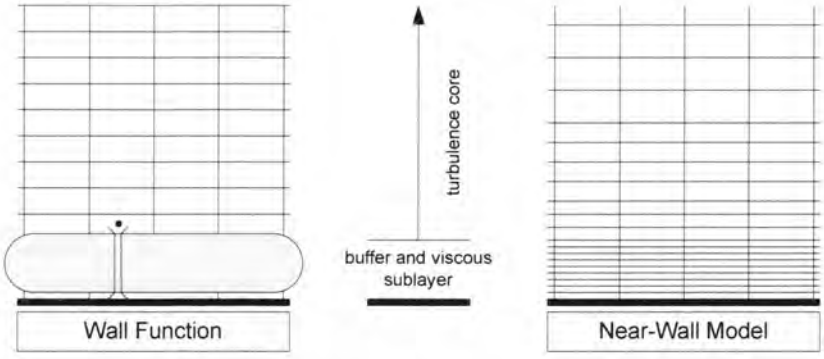


Figure 3.5: Near-wall treatments

In most cases involving high Reynolds number flows, the wall function approach significantly saves computational resources since the viscous sublayer and the buffer region where the solution variables change most rapidly, does not need to be resolved. The wall function approach is more practical because it is economical, robust and reasonably accurate. It is a pragmatic approach for near-wall treatments for industrial flow simulations.

There are two types of wall function approach, namely the *standard wall functions* and the *non-equilibrium wall functions*. Due to the capability to partly factor in the effects of pressure gradients and departure from equilibrium, the non-equilibrium wall functions are recommended for use in complex flows that involve separation, reattachment, and impingement where the mean flow and turbulence are subjected to severe pressure gradients and change rapidly which means improvements can be obtained such as in the prediction of wall shear (skin-friction coefficient) and heat transfer (Nusselt or Stanton number). Despite its advantages, the wall function approach becomes less reliable when the flow conditions depart too much from the ideal conditions underlying the wall functions such as:

- Pervasive low Reynolds number or near-wall effects, for example flow through a small gap or highly viscous, low-velocity fluid flow
- Massive transpiration through the wall such as flowing or suction
- Severe pressure gradients leading to boundary layer separations
- Strong body forces, for example flow near rotating disks, buoyancy-driven flows
- High three-dimensionality in the near-wall region, for example Ekman spiral flow, strongly skewed 3D boundary layers

For such cases, the near-wall models that are valid in the viscous sublayer region are required. The enhanced wall treatment is a near-wall modelling method that combines a two-layer model with enhanced wall functions. In this approach, the whole domain to be resolved is subdivided into a viscosity-affected region and a fully-turbulent region.

Taking the above theory into consideration means that for unbaffled system such as the existing nitrator, the wall function approach is not applicable while for baffled system such as the proposed nitrator, the wall function is sufficient to provide a reasonably accurate result.

## 3.6 Model validation using PIV technology

Particle image velocimetry (PIV) is an advance experimental technique that employs optical technology to measure velocities of fluid movement. In operation, the fluid is seeded with particles that have similar density to the fluid medium and have good light reflection property. Because of the close density between the particles and fluid medium, it is assumed that the particles faithfully follow the fluid flow pattern. The motion of these seeding particles are captured by the optical device and then used to calculate velocity trajectory and map the 2-D flow pattern. An important advantage of the PIV technique is its ability to obtain accurate qualitative and quantitative data without altering the flow pattern. The CFD-predicted flow pattern inside a batch stirred tank that employed four Ekato Intermig impellers, operating at laminar regime, were found to have an excellent agreement with the flow pattern obtained via PIV [Szalai et al. 2004]. Whilst Szalai et al. [2004] employed PIV technique to validate a single phase CFD-predicted flow pattern, Aubin et al. [2004] began using PIV to measure flow pattern in an aerated vessel agitated by a 6-bladed 45° PBT. To achieve this, the liquid phase was seeded with using 30μm hollow glass particles with fluorescent rhodamine implanted on the surface. These particles diffuse light at a wavelenth of 575nm which is greater than the wavelenth of light diffused by the air bubbles, 550nm. By fitting a filter, only light with a wavelenth greater than 550nm were captured. Other authors whose study involved mechanically agitated tanks have also successfully validated their CFD results against PIV results [Sheng et al. 1998; Lamberto et al. 1999, 2001; Zalc et al. 2001 and Matonis et al. 2002].

Despite its repeated successes, major drawback of PIV technique is that it can only provide 2-D velocity vector fields, which risks presenting misleading representations about flows that are highly 3-D [Aubin and Xuereb 2006].

### 3.6.1 Pilot-scale nitrator

To overcome the tank opacity in this study, the industrial unit was scaled down by 50% and a pilot-scale version was built. It was made from perspex which allows PIV to capture any insidious flow profile and to measure the mean velocity components inside the tank, as shown in Figure 3.6. The tank used was a 100L unbaffled dished-bottom tank surrounded by transparent rectangular perspex wall. The rectangular tank was filled with water and its

role in this validation study was to minimise light refraction. Two impellers, attached to a single top-entry shaft were used. The top impeller was a standard pitch-blade turbine (PBT) while the bottom impeller consisted of two 90° vertical blades and two 45° blades. In the industrial nitrator, two impellers were required due to the multiple objectives, that is, to draw down floating particles and to keep particles fully suspended. The top impeller promoted ACB draw-down while the bottom impeller ensured the wetted ACB, having density heavier than its continuous medium, remained completely suspended. The industrial nitrator has the following exact geometrical configuration: $D/T$= 0.6, $C/T$= 0.162, blade width= 135mm (vertical blades) 185mm (pitch blades), impeller rotational speed= 73 rpm, tank diameter= 500mm.

Figure 3.6: The scaled-down unit made from perspex

Figure 3.7: Meshed model of nitrator

Gambit (grid and mesh building intelligent toolkit) was used to build and mesh the geometrical configuration of this scaled-down nitrator [Alliet-Gaubert 2006]. The meshed geometry consisted of 760,944 cells, as shown in Figure 3.7. To ensure solution convergence and to obtain highly accurate results, structured mesh consisting of mainly hexahedral cells was employed which allowed the flow direction to align with the cells. Since most of the cells employed were hexahedral, no size function was employed.

### 3.6.2 PIV validation equipment setup

Particle image velocimetry (PIV) is an advance physical experiment that involves a pair of pulsed laser light sheets used to illuminate a flow field seeded with tracer particles small enough to accurately follow the flow.

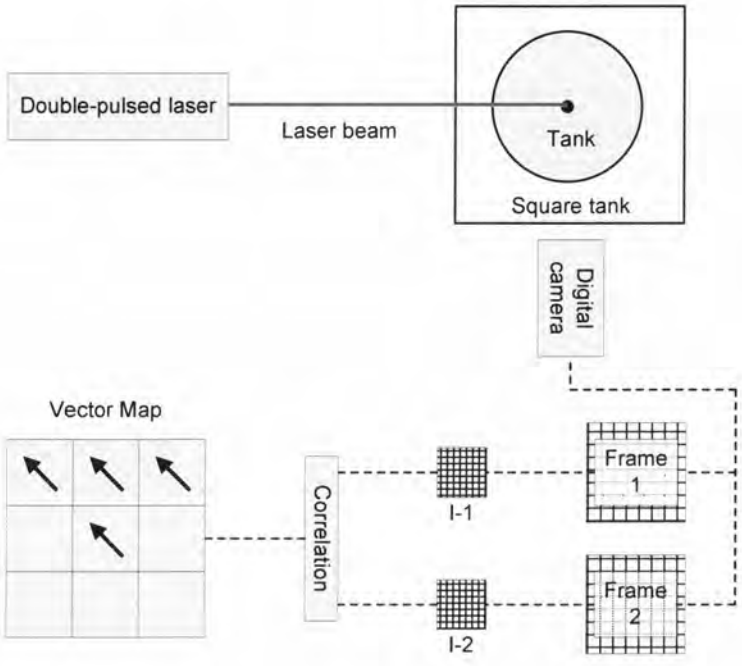


Figure 3.8 Shows the setup of advance experiment utilising PIV technology.

Figure 3.8 shows the setup of PIV experiment where a pair of pulsed lasers (532nm) emitted by laser generator (New Wave Research), separated by 3 milliseconds, were used to provide the pulsed light sheet illumination. When a pair of laser pulses was beamed to the target area, only the tracer particles became illuminated since other structures have been treated to prevent laser beam reflection. A digital camera (Nikon Sensicam, 12-bit cooled imaging charged-coupled device) located perpendicular to the plane of the light sheet was used to capture and transform the target area onto the camera array. This enabled the camera to capture each light pulse in separate image frames. Once a sequence of 400 light pulses was recorded, the images were divided into small subsections called the interrogation areas (I). Each interrogation area (I-1 & I-2) was cross-correlated with each other, pixel by pixel. The correlation produced a signal peak, identifying a particle displacement, $\Delta x$. A velocity vector map over the whole target area was obtained by repeating the cross-correlation for each interrogation area over the 400 image frames

captured by the camera. The velocity magnitude was obtained by averaging the velocity registered by each frame over the entire 400 frames.

### 3.6.3 Charge-coupled device

Charge-coupled device (CCD) is a silicon chip whose surface is divided into light-sensitive pixels. When a photon hits a pixel, it registers a tiny electric charge that can be counted. With large pixel arrays and high sensitivity, CCD can create high-resolution images under a variety of light conditions. A CCD digital camera incorporates a CCD to take such pictures. A CCD camera uses the same technology as the popular digital cameras used for everyday photography. However, regular digital cameras have some drawbacks which make them unsuitable for astrophotography. Astronomical CCD digital cameras are cooled to remove electronic noise which, in a digital camera, can hide the image of faint celestial objects. CCD is becoming more popular than film photography because they are much more sensitive than film and therefore images can be taken much faster and more easily.

### 3.6.4 PIV tracer material

Capturing both light pulses in the same image frame to track the movements of the particles gives a clear visual sense of the flow structure. For air flows, the seeding particles are typically oil drops in the range of 1 μm to 5 μm. For liquid applications, the seeding employed is generally polystyrene, polyamide or hollow glass spheres in the range of 5 μm to 100 μm. Any particle that follows the flow satisfactorily and scatters enough light to be captured by the CCD camera can be used. Finally, the number of particles in the flow is of some importance in obtaining a good signal peak in the cross-correlation. As a rule of thumb, 10 to 25 particle images should be seen in each interrogation area.

In this technology, multiple images of tracer materials (20 μm Rhodamine B-based fluorescent particles) distributed homogeneously (3 mg/100L) in the water medium were captured. Since the tracer particles having density of 1,050 kg $m^{-3}$ have almost similar physical properties to that of $H_2O$, they did alter the flow field. Because of this, local fluid velocity was calculated by measuring the fluid displacement from multiple particle images and dividing that displacement by the time interval between the exposures.

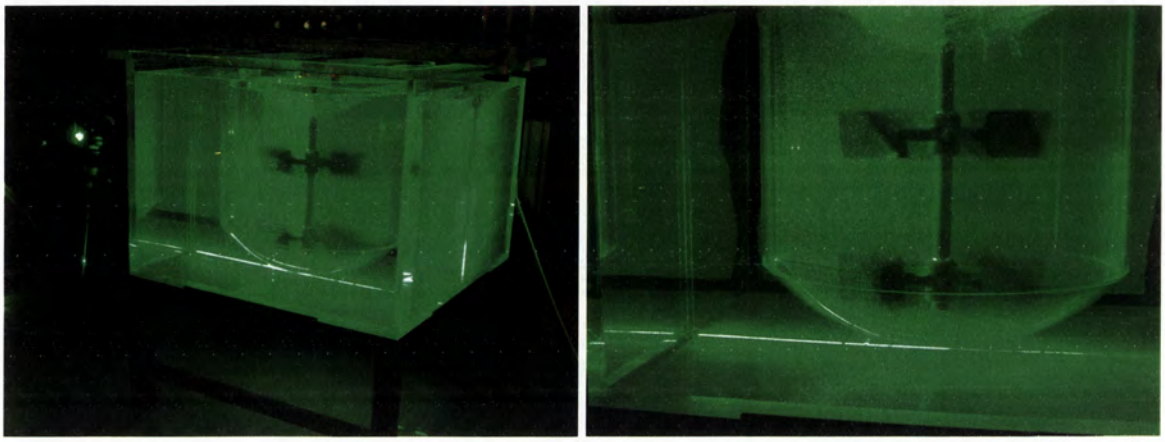

Figure 3.9: Scaled-down unit under laser illumination

Figure 3.9 shows a laser illuminated scale-down unit with the impeller rotating at 33 rpm, surrounded by a rectangular tank filled with water, needed to minimise laser refraction.

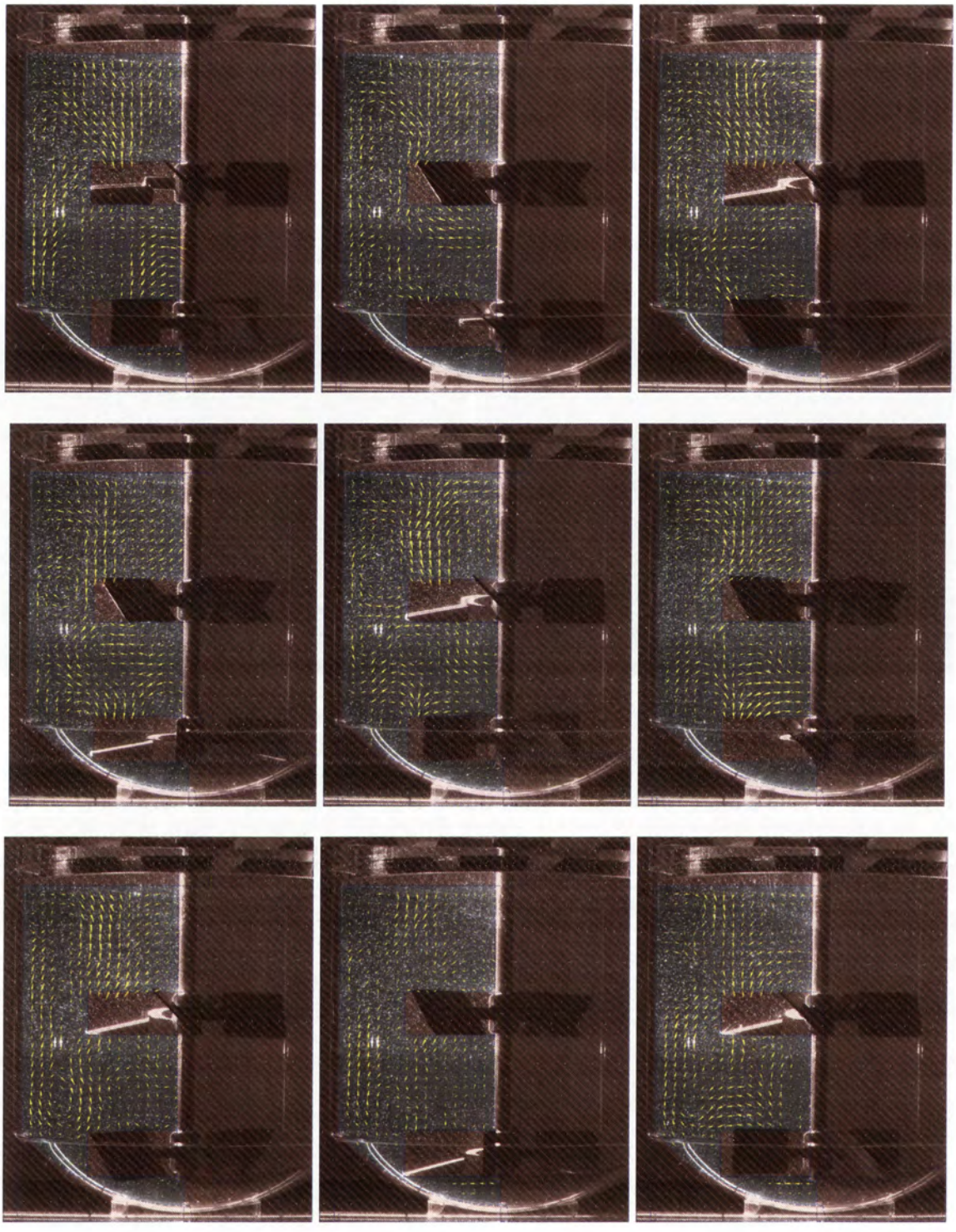

Figure 3.10: Individual snapshots of flow pattern using PIV technology

Figure 3.10 represents individual snapshots of flow pattern, captured by CCD. These snapshots were combined to produce an averaged flow pattern, and were compared to CFD prediction.

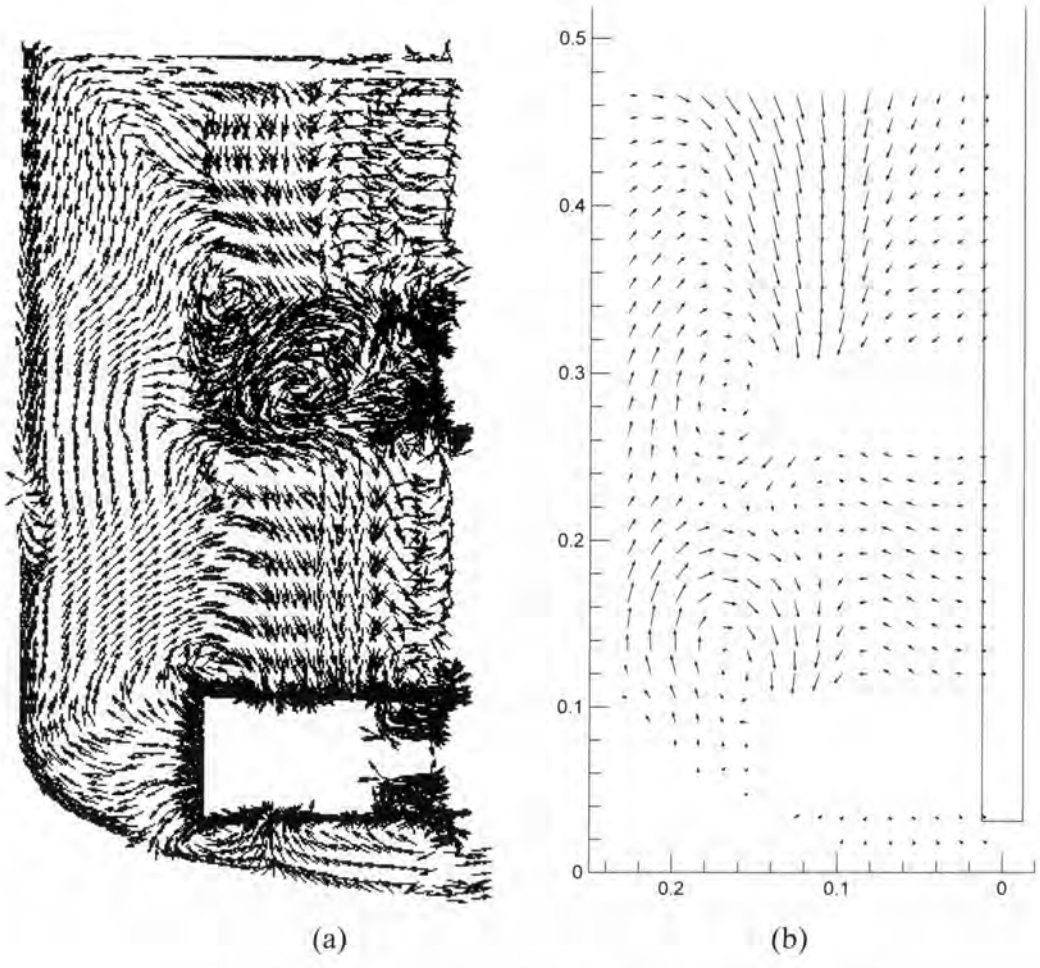


Figure 3.11: CFD velocity prediction (a) versus PIV velocity measurements (b)

Figure 3.11(a) and 3.11(b) show the flow field obtained via CFD simulation and PIV measurements respectively. On each axis, every major scale represents a 0.2m interval. Both results show that the region of high flow was located next to the central vortex where the fluid, starting from the nitrator wall, was drawn down to the top impeller. Two circulation loops were noticeable, one just immediately next to the top impeller, and another just next to the bottom impeller. Both results also showed the existence of dead zones at the tank bottom and low velocity flow at tank lower side and along the entire top-entry shaft. Therefore, this comparison work shows that the CFD models were able to accurately predict the flow field produced by PIV measurements.

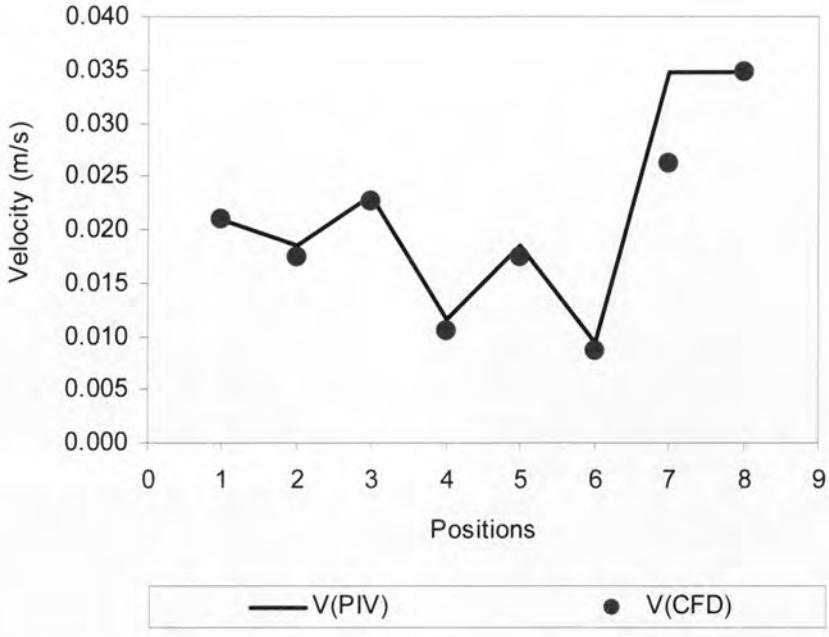


Figure 3.12: Velocity comparison between CFD predictions and PIV measurements

Table 3.4: Coordinates of various positions

| Positions | Coordinates |
|---|---|
| 1 | 0.2, 0.1 |
| 2 | 0.2, 0.2 |
| 3 | 0.2, 0.3 |
| 4 | 0.2, 0.4 |
| 5 | 0.2, 0.45 |
| 6 | 0.1, 0.2 |
| 7 | 0.1, 0.4 |
| 8 | 0.1, 0.45 |

Figure 3.12 shows that with exception of position 7, the CFD results were in close agreement with those obtained via PIV experiment. Position 7, with coordinates shown in Table 3.4, shows that CFD underpredicted the PIV results by as much as 25%. This discrepancy might be due to a combination of these possibilities: (a) the close promixity of this region to the fluid free surface such that during draw-down, some bubbles were entrained, thus affecting the results, (b) due to the high local draw-down velocity in this region and (c) due to a calculation error. Overall, the qualitative and quantitative analysis of the data obtained from CFD predictions and PIV measurements revealed close agreement between the two technologies.

After the successful validation of the scaled-down nitrator which proved the model robustness and reliability, using the same approach, the actual industrial size nitrator was modelled and simulated. The nitrator had geometry identical to that used in the validation study. The only differences were: the actual unit has a volume 5 times larger, the tank wall was made of stainless steel and the fluid used was the process chemicals.

Figure 3.13. Existing NC nitrator geometrical configuration

Figure 3.14: Impellers type in the nitrator

Figure 3.13 shows the nitrator (left) modelled. A dished bottom was used since the just suspended speed, $N_{js}$ is a function of tank bottom and that a flat bottom requires 10-20% higher $N_{js}$ to suspend solid particles. Moreover, for solid suspension in flat-bottomed tank, the solids tend to accumulate in the corners. Figure 3.14 shows the internal geometrical configurations of the nitrator which consisted of two impellers, attached to a single top-shaft were used in the existing NC nitrator. The top impeller was a standard pitch-blade turbine (PBT) while the bottom impeller consisted of two 90° vertical blades and two 45° blades.

Exact geometric dimensions and the unit operating parameters are given in Table 3.5 below.

Table 3.5: Geometrical configuration and physical properties

| Parameter | Values |
|---|---|
| *D/T* | 0.6 |
| *C/T* | 0.162 |
| *W/D* | 0.135 ($90^{o}$) & 0.185 ($45^{o}$) |
| *T* | 1,000 mm |
| *S/D* | 0.7 |
| *V/D* | 0.5 |
| Fluid | $HNO_3$-$H_2SO_4$-$H_2O$ |
| Density @ $32^{o}$C | 1,713 kg $m^{-3}$ |
| Viscosity @ $32^{o}$C | 0.010577 kg $m^{-1}s^{-1}$ |
| Gravity | 9.81 m $s^{-2}$ |
| Operating pressure | 101,325 Pa |
| Impeller speeds | 73 rpm |
| Rotation direction | clockwise |
| Batch volume | 676 L |

## 3.7 Characterisation parameters

The characterisation consisted of the identification of the key attributes governing the performance of the nitrator. These attributes included power number, flow number, flow efficiency, blending time and the deviation from ideality number since they were related to the hydrodynamics and mixing properties of the unit. Knowing these values greatly enhanced the understanding of this unit performance and therefore provided a benchmark for optimisation.

### 3.7.1 Power number

The dimensionless power number $N_P$, provides an indication of the power requirement to operate this impeller. It is given as [Alliet-Gaubert 2006]:

$$N_P = \frac{P}{\rho N^3 D^5} \qquad \text{- 3.42}$$

Equation (3.42) shows the relationship between the power number $N_P$ and power applied to the impeller ($P$) having diameter $D$, agitating fluid with density $\rho$ at $N$ rotational speed. For shaft with multiple impellers, the power delivered to the shaft is the combined power for all impellers. Power can be obtained via the following expression:

$$P = 2\pi N \tau \qquad \text{- 3.43}$$

Where $N$ is the impeller rotational speed in rev $s^{-1}$ and $\tau$ is the torque in Nm.

Flow number is given by [Alliet-Gaubert 2006]:

$$N_Q = \frac{Q}{\rho N D^3} \qquad \text{- 3.44}$$

The flow number $N_Q$, provides a measure of the pumping capability of an impeller. In practical terms, this dimensionless number is the flowrate that crosses the impeller plane and is an important parameter for evaluating circulation effectiveness in the nitrator. To compute $Q$ for an impeller, a surface was created for the discharge region. The surface was circular for the axial flow impeller and a section of cylinder wall for the radial flow impeller. By integrating the total flow discharge through this surface, it was possible to obtain $Q$ and hence, the flow number.

### 3.7.2 Flow efficiency

The third parameter used to characterise the nitrator is the flow efficiency number.

$$\eta = \frac{N_Q}{N_P} \times 100\% \qquad \text{- 3.45}$$

Equation (3.45) shows that $\eta$ can be defined as the pumping capability of the impeller per unit of power consumed by the impeller.

### 3.7.3 Blending time

A transient calculation was conducted to determine the blending time. Virtual tracer material, having identical physical properties with the fluid continuum was injected in the nitrator at the point in time when the impellers were at rest. Its volume fraction as a function of time was then detected by 10 probes strategically located inside the nitrator, as shown in Figure 3.15.

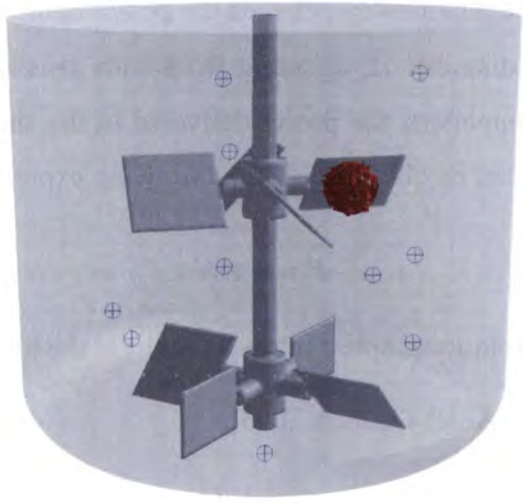

Figure 3.15: Relative position of tracer material and probes inside the nitrator

The use of tracer material identical to those of the fluid continuum assured that the tracer material did not alter the flow pattern of the bulk fluid. Injecting the tracer material when the impellers were at rest means that the time taken for the impeller to reach steady-state speed was taken into consideration. This procedure was essential to simulate start-up operation.

Since the properties of the tracer material was identical to the fluid continuum properties, conservation equations for continuity, momentum and turbulence was not recalculated, but only the transient species calculation was performed. With the available transient data from each probe, the mean of the tracer concentration detected by the monitoring probe, along with its standard deviation ($\delta$) was computed to determine whether the tracer has fully blended.

$$\delta_{n-1} = \sum_{i=1}^{n} \left[ \frac{C_i - C_\infty}{n-1} \right]^{0.5} \quad \text{- 3.46}$$

Blending process is regarded as accomplished when the concentration of tracer measured by a particular probe has a coefficient of variance (COV) less than 1%, and:

$$COV = \frac{\delta_{n-1}}{C_\infty} \times 100\% \quad \text{- 3.47}$$

The blending time was therefore the average blending time detected in multiple locations in the tank.

$$t_{arithmetic,av} = \frac{\sum_{i=1}^{n} t_i}{n} \quad \text{- 3.48}$$

However, since the position of the probe also influences the value of $t_i$, a weighted average blending time for the nitrator was needed and this can be expressed as:

$$t_{weighted,av} = \sum_{i=1}^{n} w_i t_i \quad \text{- 3.49}$$

where

$$w_i = \frac{t_i}{\sum_{i=1}^{n} t_i} \quad \text{- 3.50}$$

### 3.7.4 Deviation from ideality

The deviation from the ideality number determines how far away the mixing performance is from perfect mixing, $t_{ideal}$. Since for a completely uniform mixing, $t_{arithmetic,av} = t_{weighted,av}$, then the deviation from ideality is given by:

$$\xi = \frac{t_{weighted,av} - t_{ideal}}{t_{ideal}} \times 100\% \qquad -3.51$$

For the qualitative analysis, parameters of concern include the flow field for velocity, turbulence kinetic energy and its dissipation rates. This was achieved by exploiting the post-processing feature of the CFD solver. The analysis of flow field solutions was achieved via plotting velocity vectors and the contours. To yield practical useful results, the vectors and contours were plotted on the planes of interest.

### 3.7.5 Grid independence

A preliminary grid convergence study was carried out to verify that the solution obtained from using the second-order upwind discretisation scheme was mesh independent. The number of cells inside the rotational zones was systematically increased in the x-, y- and z-directions throughout the tank. When refining the mesh, care was taken to assign most additional cells in the regions of high gradient on the impeller blades and discharge regions. Again, the RSM model was employed for this mesh independence study. The mass flowrate traversing the plane of each impeller were computed to provide a basis of comparison between the solutions obtained using coarse (696,641), medium (760,944) and high (910,694) density mesh. The result shows that mass flowrate increased by 1.656% when high density mesh was used in place of medium density mesh. The computational cost however, increased by an additional of 10 hours when the high density mesh was employed. Based on this, the medium density mesh was chosen over the high density mesh because of the acceptable level of accuracy and affordable computational cost. Since most of the cells employed were hexahedral, no size function was employed.

### 3.7.6 Number of probes independence test

Monitoring probes located at various positions inside the tank will yield different results from one another. This means that the number of probes employed will influence the value of blending time. Thus a probes independence test was conducted to determine the minimum number of probes to be used to produce unbiased results. Care was taken to ensure that the placing of probes inside the nitrator would not lead to biased results. For instant, when a probe was placed in a region of high flow, an identical probe was placed in a region of low flow. The results show that a minimum of 10 probes was required to obtain unbiased results.

Figure 3.16: Axial flow

Figure 3.17: Radial flow

### 3.7.7 Surface integrations

To obtain the axial or radial flow rate, surface integrations were carried out on the plane or surfaces (shaded in red) where the flow directions are desired. Figure 3.16 shows that the planes where axial flow crosses. As such, only flow that crossed this plane was computed and taken into consideration, eliminating the radial flow altogether. In contrast, Figure 3.17 shows the radial component being computed and in this case, the axial flow component was eliminated altogether.

### 3.7.8 Convergence criteria

Simulations were generally considered converged when the residuals for mass, momentum and turbulence transport and volumetric fraction fell below $1\times10^{-4}$ [Kerdouss et al. 2006]. Further checks for convergence were made by creating a monitoring point inside the tank and ensuring that the value monitored remained constant with repeated iterations.

## 3.8 Characterisation results and discussion

Results from blending time simulation are tabulated in Table 3.6 shown below.

Table 3.6: Blending time data

| Probe No | Time (s) | $w_i$ | $t_{weighted,\ av}$ |
|---|---|---|---|
| 1 | 19 | 0.0809 | 1.536 |
| 2 | 17 | 0.0723 | 1.230 |
| 3 | 19 | 0.0809 | 1.536 |
| 4 | 23 | 0.0979 | 2.251 |
| 5 | 22 | 0.0936 | 2.060 |
| 6 | 20 | 0.0851 | 1.702 |
| 7 | 26 | 0.1106 | 2.877 |
| 8 | 49 | 0.2085 | 10.22 |
| 9 | 21 | 0.0894 | 1.877 |
| 10 | 19 | 0.0809 | 1.536 |
| Total | 235 | - | 26.82s |
| $t_{arithmetic,\ av}$ = 23.5s | | | |

From the simulation results, the performance index values for this nitrator operating at 73 rpm are provided in Table 3.7. By themselves, they did convey meaningful results. However, the objective of these results was to provide a platform of benchmarking by which meaningful comparison of any proposed geometrical configuration can be made against it.

Table 3.7: NC nitrator performance index values

| Parameters | Value |
|---|---|
| Power number, $N_P$ | 0.6089 |
| Flow number, $N_Q$ | 0.2615 |
| Flow efficiency, $\eta$ | 0.4295 |
| Blending time, $t_B$ | 26.82s |
| Deviation from ideality, $\xi$ | 14.13% |

Any process that consumes power greater than 0.2 W $L^{-1}$ should be investigated for a possible reduction in power consumption. In this unbaffled nitrator, the power requirement is healthy since its consumption was only 146 W per 676 L (0.2162 W $L^{-1}$). The flow efficiency for this unit was rather low and was attributed to the unbaffled feature of the tank fitted with impellers employing 90° blades.

Table 3.8 shows the impeller efficiency as a function of the speed for this unit. Similarly, by themselves, they do not convey meaningful results. However, the objective of these results was to provide a platform of benchmarking by which meaningful comparison of any proposed geometrical configuration can be made against it.

Table 3.8: Impeller efficiency as a function of speed

| rpm | $\eta$ |
|---|---|
| 33 | 0.3006 |
| 53 | 0.2922 |
| 73 | 0.4295 |
| 93 | 0.3906 |
| 113 | 0.4548 |
| 133 | 0.4858 |

Table 3.9: Blending time detected by each probe at various impellers rotational speed

| PROBES | 33 rpm | 53 rpm | 73 rpm | 93 rpm | 113 rpm | 133 rpm |
|---|---|---|---|---|---|---|
| P1 | 45 | 22 | 19 | 16 | 11 | 14 |
| P2 | 19 | 17 | 17 | 17 | 9 | 15 |
| P3 | 15 | 28 | 19 | 19 | 10 | 13 |
| P4 | 25 | 33 | 23 | 21 | 13 | 17 |
| P5 | 85 | 49 | 22 | 17 | 22 | 17 |
| P6 | 45 | 24 | 20 | 18 | 12 | 12 |
| P7 | 32 | 40 | 26 | 16 | 18 | 24 |
| P8 | 18 | 25 | 49 | 54 | 43 | 24 |
| P9 | 17 | 19 | 21 | 17 | 14 | 11 |
| P10 | 21 | 22 | 19 | 18 | 13 | 14 |

Table 3.9 shows the blending time, in seconds, detected by each probe at various impellers rotational speed.

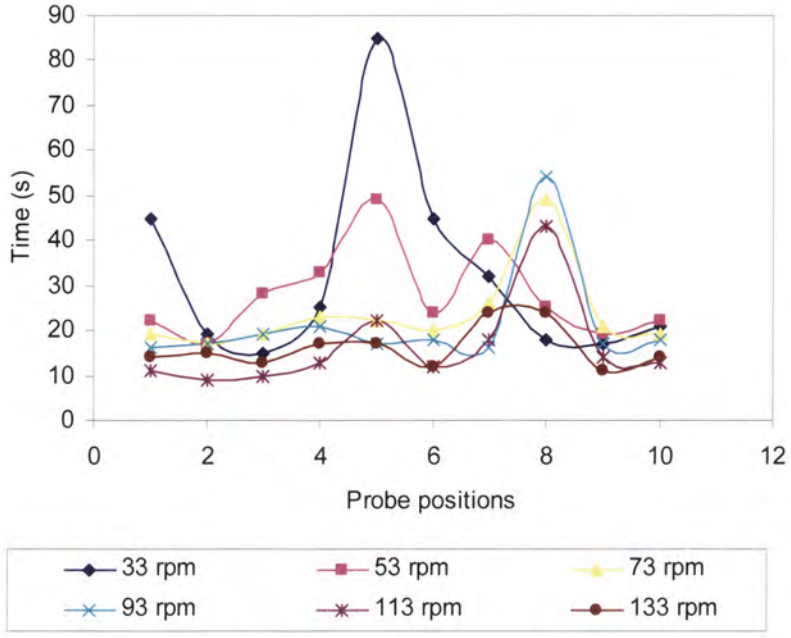


Figure 3.18: Blending time versus probe positions at various impellers rotational speed

Figure 3.18, plotted from result in Table 3.9, shows that the results for each probe were consistent thereby increasing the credibility of the average blending time. Probe 5 and 8 took a longer period of time to achieve homogeneity than other probes. This was attributed to their unfavourable locations. Probe 5 was located immediately below the shaft whilst probe 8 was located above the top impeller, just beside the shaft.

Table 3.10: Weighted average blending time as a function of impeller speed

| rpm | $t_{weighted,\ av}$ (s) |
|---|---|
| 0 | 5,000 |
| 33 | 48.71 |
| 53 | 29.19 |
| 73 | 26.82 |
| 93 | 19.56 |
| 113 | 12.49 |
| 133 | 9.86 |

Table 3.10 shows the weighted average blending time as a function of impellers rotational speed. A simulation was also conducted when the impellers were at rest and it took 5,000 s to achieve a homogeneous mixture.

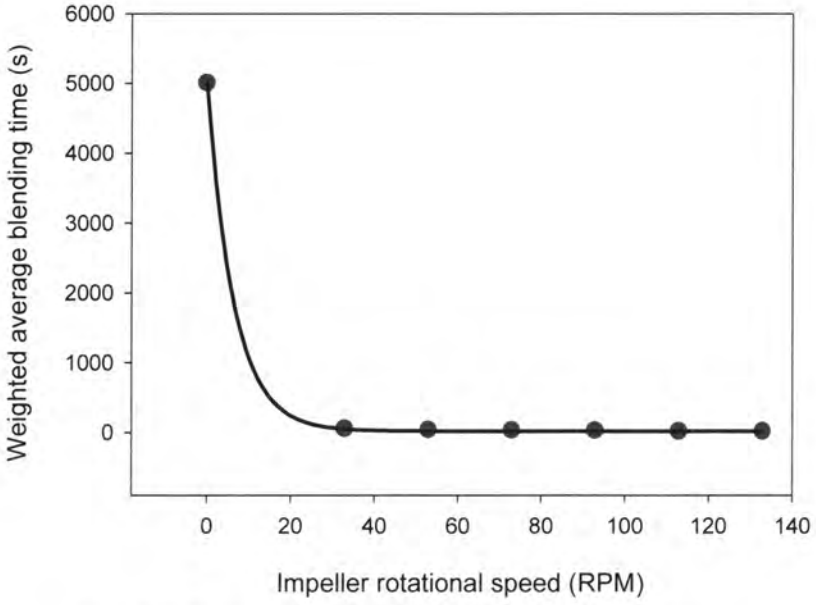


Figure 3.19: Weighted average blending time versus impeller rotational speeds

Figure 3.19 shows the plot of weighted average blending time versus various impeller rotational speeds. It can be seen that when the impeller rotational speed increased, the weighted average blending time decreased in the form of an exponential decay with a perfect regression of 1. The model can be represented mathematically as:

$$t_{weighted} = 19.16 + 4981e^{-0.1547N} \qquad \text{- 3.52}$$

From the practical viewpoint, knowing this correlation will make it easier to predict the minimum time required to achieve a state of homogeneity if the impeller speed were to change.

Table 3.8 shows that although increasing the speed from 73 rpm to 133 rpm increased the flow efficiency of the impellers, this action will result in an increase of power consumption. In contrast, reducing the speed from 73 to 33 resulted in a reduction in power consumption but doing so will compromise the process objective. In practical terms, this means that increasing the efficiency of the system by increasing its rotational speed is possible but comes at a higher operating cost.

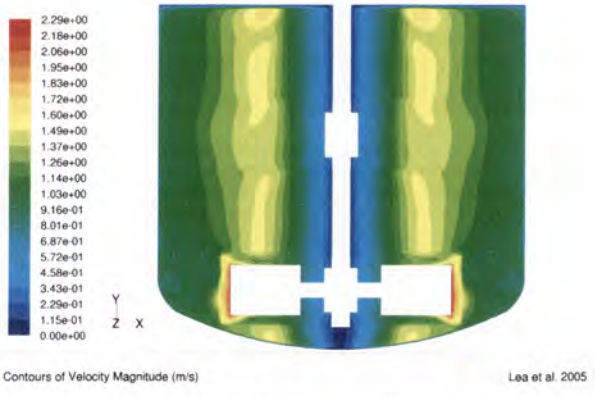


Figure 3.20: Contours of velocity magnitude

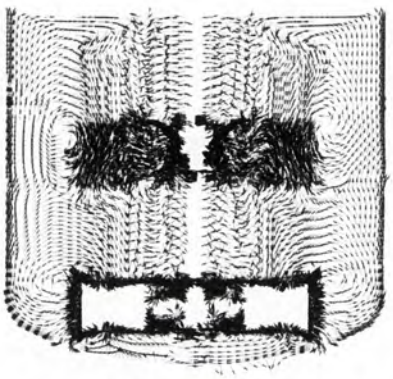

Figure 3.21: Flow field, axial plane

Figure 3.20 shows that the two impellers mounted on the same shaft directed the flow downwards towards the tank bottom. The profile shows the axial nature of the flow profile which reflected the type of impellers used. Figure 3.21 shows that fluid was drawn down by the top impeller and discharged to the bottom impeller. At the bottom impeller, because of the 90° vertical blades and the close proximity of this impeller to the tank bottom, the discharge was directed radially towards the tank wall. The fluid along the wall moved upward where it is drawn down again.

Ideally, only one large swirl loop should exist but due to the employment of two impellers in a tank with an aspect ratio, $H/T \leq 1.2$, two visible swirl loops existed, one located next to the bottom blade and the other located next to the top impeller. Current nitrator design utilised two impellers since there were multiple objectives such as floating solids draw-down and wetted solids suspension. Employing two impellers means the flow complexity was greatly increased especially when there was interaction between the flows generated by the two impellers. The extent of interaction depends on the impeller spacing. Since the impeller spacing ratio, $S/D < 1$, higher shear zone was expected in the region between the two impellers. However, it is worthwhile to consider and investigate ways to reduce this to one impeller. The impeller top clearance, $V/D = 0.5$ may not yield an optimum process

result since the surface vortex is deep enough to cause air entrainment. Ideally, $V/D \geq 0.5$ for a system that employs standard baffle ($T/10$) and $V/D \geq 1.0$ for a system employing narrow baffles ($T/50$).

The axial mass flowrate discharged by both the top and bottom impellers were 60.93 kg $s^{-1}$ and 56.85 kg $s^{-1}$ respectively. Although this calculation indicated that the bottom impeller flow discharged almost the same amount of fluid axially, it was noted that that much of the fluid discharged from the top impeller went through the bottom impeller thus producing a higher impeller discharge value for the bottom impeller.

To demystify this, cylindrical surfaces surrounding each impeller were integrated and the radial mass flowrate discharged by the top and bottom impellers were calculated to be 32.23 kg $s^{-1}$ and 83.39 kg $s^{-1}$ respectively. This shows that while the value for the top impeller was satisfactory, the bottom impeller values indicated otherwise. The value from the bottom impeller was unsatisfactory because it was always desirable to have more axial flow, instead of radial flow, flowing toward the tank bottom to sweep the tank bottom off the solid particles.

However in this case, not only did the 90° vertical blades reduce the axial flow component, they also contributed to the unnecessary excess fluid body rotation where in the absence of baffles, led to a marked reduction in turbulence kinetic energy. Although the pitch blade turbine is a mixed flow impeller, at $D/T > 0.55$, the flow discharge becomes radial. Thus, one way to increase the axial flow discharge of both impellers is to reduce the $D/T$ ratio. But a balance must be achieved between low $D/T$ ratio and power consumption since impellers with a small $D/T$ ratio often require higher rotational speed, thus requiring higher power to achieve the process objective.

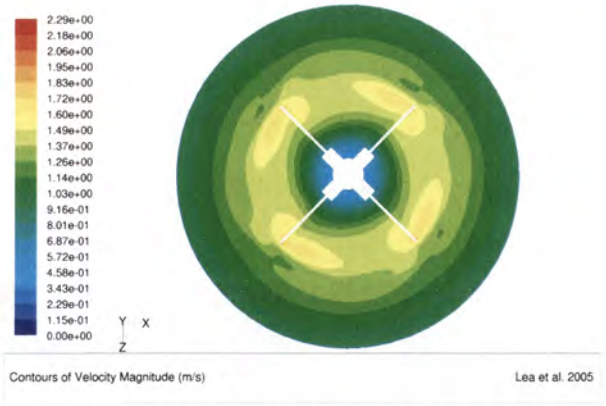


Figure 3.22: Contours of velocity magnitude

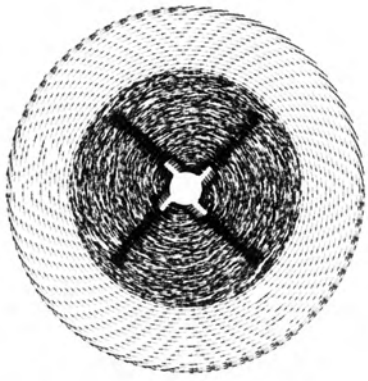

Figure 3.23: Flow field, radial plane

Figure 3.22 shows that the highest flow region occurs around the axial discharge of the impellers. The velocity magnitude initially increased with distance from the shaft and decreased as it moved, in a radial direction, farther away from the blades towards the wall. Figure 3.23 shows that although the process took place at turbulence regime, the flow exhibited 'laminar' like characteristics due to the absence of wall baffles.

This analysis led to the conclusion that increasing the impeller rotational speed may not necessarily increase the turbulence value especially in the region of low turbulence value such as near wall region and therefore will not necessarily improve the reaction. Thus, it was noted that increasing the impeller speed increased the rotational speed but not the relative velocity between fluid and solid particles. To increase the relative velocity between the two phases, the turbulence kinetic energy at the low turbulence region must be increased by employing narrow baffles.

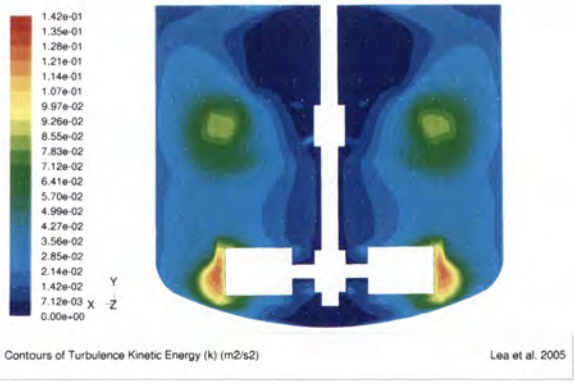


Figure 3.24: Contour of turbulence kinetic energy, axial plane

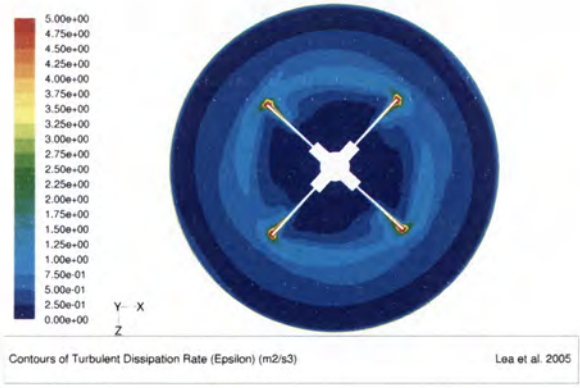


Figure 3.25: Contour of turbulence dissipation rate, radial plane

Figure 3.24 shows that the turbulence kinetic energy, at 73 rpm, varied from one region of the tank to another. It also shows that the turbulence kinetic energy around the wall was lowest due to the lack of baffles, thus leading to high rotational flow [Myers et al. 2002]. Unbaffled tank which normally causes high rotational flow, minimises turbulence and inhibits top-to-bottom turnover, rarely finds industrial application except in situation that demands high rate of heat transfer from the unit to the atmosphere. As such, this rotational flow coupled with the fact that the nitrator was unjacketed, acted counter-productive to one of the process objectives of keeping a constant operating fluid bulk temperature.

The region just above the top impeller represented a deep central vortex and the region just below the bottom impeller represented a zone of low velocity flow. These undesired zones were attributed to the overly close bottom impeller clearance which caused the flow to become radial [Paul et al. 2004] although two of the four blades were supposed to produce axial flow pattern. In addition, the impeller design that incorporated a bridge linking the blades to the hub may partly be the reason for the existence of this zone. Figure 3.25 shows that most of the energy was dissipated around the impeller tips and that very little energy was imparted to the fluid starting from the shaft to midway of the impeller. It also shows that the turbulence kinetic energy was found to be highest around impeller region and lowest around the wall due to the lack of baffling.

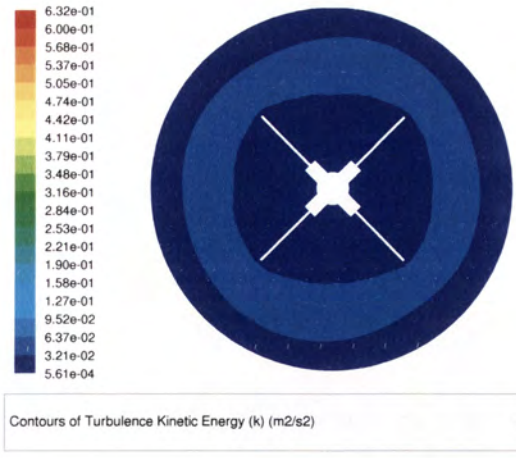


Figure 3.26: Contours of turbulence kinetic energy at 33 rpm

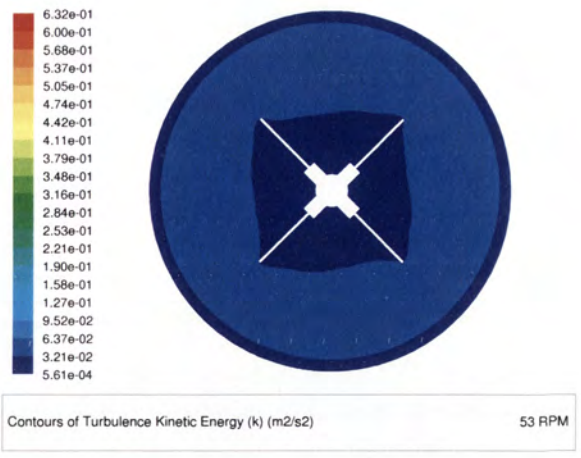


Figure 3.27: Contours of turbulence kinetic energy at 53 rpm

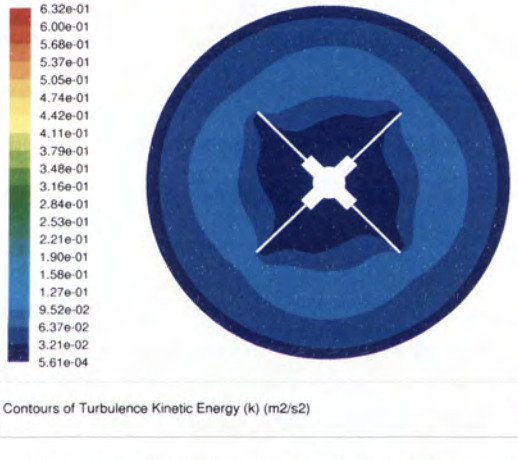


Figure 3.28: Contours of turbulence kinetic energy at 73 rpm

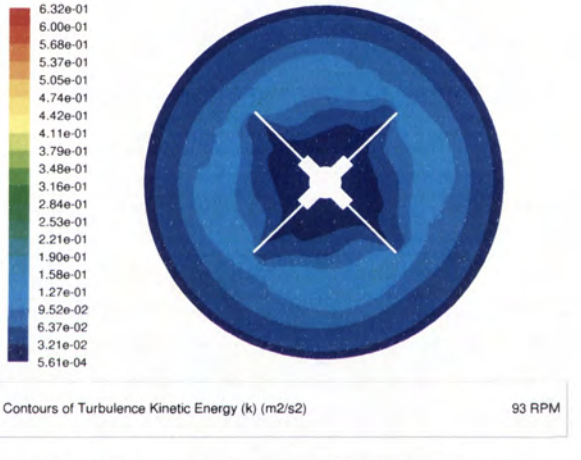


Figure 3.29: Contours of turbulence kinetic energy at 93 rpm

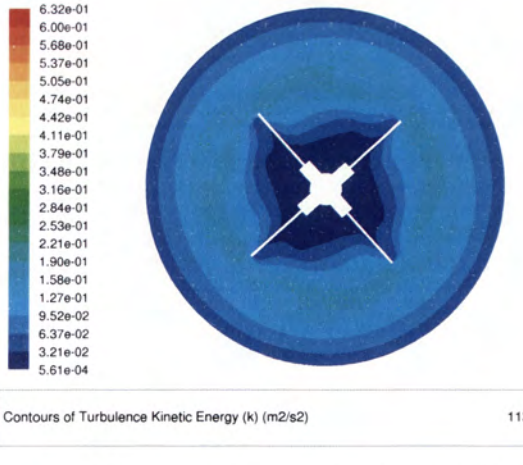


Figure 3.30: Contours of turbulence kinetic energy at 113 rpm

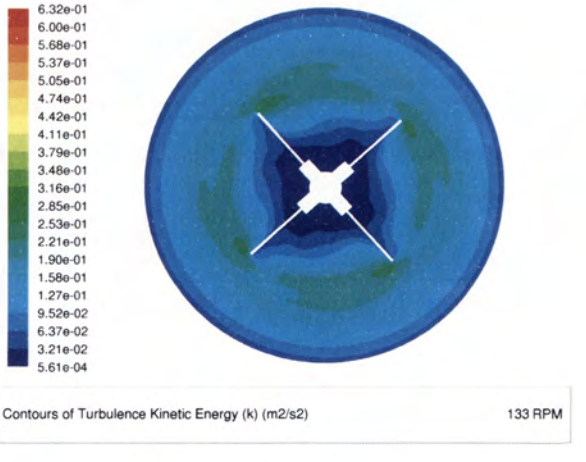


Figure 3.31: Contours of turbulence kinetic energy at 133 rpm

Table 3.11: Effect of turbulence kinetic energy and power requirement as a function of impeller speed

| $N$ (rpm) | $k$ ($m^2s^{-2}$) | % ↑ in $k$ | % ↑ in $P$ |
|---|---|---|---|
| 33 | 0.0845 | - | - |
| 53 | 0.101 | 19.53 | 405 |
| 73 | 0.118 | 39.64 | 2,500 |
| 93 | 0.135 | 59.76 | 6,966 |
| 113 | 0.152 | 79.88 | 8,804 |
| 133 | 0.169 | 100.00 | 17,880 |

Figures 3.26-3.31 show that in an unbaffled system, increasing the impeller rotational speeds from 33 rpm to 133 rpm resulted in only a slight increase of turbulence kinetic energy. Moreover, the percentage increase in turbulence kinetic energy decreased with each increment in speed as shown in Table 3.11. This shows that increasing the speed per se was not an effective approach to increase the turbulence and may not necessarily increase the turbulence value especially in the region of low turbulence value such as near wall regions and consequently will not necessarily improve the nitration process. More importantly, such an approach was not economically feasible considering that to double the turbulence kinetic energy, the power consumption had to increase by 17,880%.

Although increasing the impeller speed increased the rotation speed of the fluid body, the relative velocity between fluid and solid particles only increased slightly. To increase the relative velocity between the two phases, the turbulence kinetic energy at the low turbulence region must be increased. Figures 3.26-3.31 also show that high turbulence was confined to the impeller discharge zone while low turbulence regions was found near the wall and within the diameter of the impeller. The low turbulence region within the diameter of the impeller did not improve much at higher rotational speed. This was attributed to the impeller design that incorporated a bridge between the blades and the impeller hub. This study led to the conclusion that increasing the impeller rotational speed may not necessarily increase the turbulence value especially in the region of low turbulence value such as near wall region and therefore will not necessarily improve the reaction. Thus, it should be noted that increasing the impeller speed increased the rotational speed but not the relative velocity between fluid and solid particles. This study shows that to increase the relative velocity between the two phases, the turbulence kinetic energy at the low turbulence region must be increased by employing narrow baffles.

## 3.9 Numerical setup for multiphase modelling and simulation

Particle interactions:

Volume loading (volume fraction of secondary phase)

Dilute loading (<10%) particle-particle interactions can be neglected

Particulate loading (mass density ratio of discrete to continuous phase)

1. Low particle loading: coupling between phases is one-way since discrete phase does not affect continuous phase flow
2. Moderate particle loading: coupling between phases is two-way and the discrete phase affect the continuous phase flow
3. High particle loading: coupling between phases is four-way. In this situation, individual particles in the discrete phase develop their own pressure and stress, therefore creating particle-particle interaction

The multiphase models available in Fluent® can be summarised as follow:

### 3.9.1 Eulerian-Lagrangian: discrete phase model (DPM)

In this model, trajectories of discrete phase are computed in a Lagrangian frame which means the particles can exchange mass, momentum and energy with the continuous phase. Each trajectory represents a group of particles having the same initial properties. However, particle-particle interaction is neglected.

| | |
|---|---|
| Flow regime | : Bubbly, droplet or particle-laden flow |
| Volume loading | : Must be dilute (volume fraction < 12%) |
| Particulate loading | : Low to moderate |
| Turbulence modelling | : Weak to strong coupling between phases |
| Stokes number | : All ranges of Stokes number |

This model is suitable for: cyclones, spray dryers, particle separation and classification, aerosol dispersion, liquid fuel and coal combustion.

### 3.9.2 Eulerian-Eulerian: volume of fluid (VOF) model

This model has been designed to track the position of the interface between two or more immiscible fluids. A single momentum equation is solved and the resulting velocity field is shared by all phases. In this model, the surface tension and wall adhesion effects can be taken into account. In addition, this model solves the transport equation for volume fraction of each secondary phase. It has been recommended that simulation be performed in unsteady mode when using this model.

| | |
|---|---|
| Flow regime | : Slug flow, stratified or free-surface flow |
| Volume loading | : Dilute to dense |
| Particulate loading | : Low to high |
| Turbulence modelling | : Weak to moderate coupling between phases |
| Stokes number | : All ranges of Stokes number |

This model is suitable for large slug flow, filling, off-shore oil tank sloshing, boiling and coating.

### 3.9.3 Eulerian-Eulerian: mixture model

This is the simplified Eulerian approach for modelling Newtonian phase flows. Full multiphase model depends greatly on the reliability of closure relations and is therefore impractical to model wide distributions in particle size. It solves the mixture momentum equation, albeit for mass-averaged mixture velocity and prescribes relative velocities to describe the dispersed phases. Interphase exchange terms depend on relative (slip) velocities which are algebraically determined. In addition, turbulence and energy equations can be solved for the mixture. However, only one of the phases may be defined as compressible. Finally, it solves the transport equation of volume fraction for each secondary phase.

| | |
|---|---|
| Flow regime | : Bubbly, droplet or slurry flow |
| Volume loading | : Dilute to moderately dense |
| Particulate loading | : Low to moderate |
| Turbulence modelling | : Weak coupling between phases |
| Stokes number | : Stokes number $<< 1$ |

This model is suitable for hydrocyclones, bubble column reactors, solid suspensions and gas sparging.

### 3.9.4 Eulerian-Eulerian: Eulerian model

This is the most sophisticated and general purpose multiphase model, used to model multiple interpenetrating phases. It solves continuity, momentum and energy equations for each phase where the volume fractions characterise equation set for each phase and coupling among phases achieved through interphase exchange terms. The strong coupling makes this model more difficult to use than the mixture model. Finally, it uses single pressure field for all phases. This model includes the granular option.

| | |
|---|---|
| Flow regime | : Bubbly, droplet or slurry flow, fluidised beds |
| Volume loading | : Dilute to dense |
| Particulate loading | : Low to high |
| Turbulence modelling | : Weak to strong coupling between phases |
| Stokes number | : All ranges of Stokes number |

This model is suitable for high particle loading flows, slurry flows, sedimentation, hydro-transport, fluidised beds, risers and packed bed reactors.

Model selection:

The four models elaborated have each their applicability and limitations. The selection of an appropriate model very much depends on: flow regime, volume loading, particulate loading, turbulent or laminar flow and Stokes number. The following guidelines are provided by Fluent®:

| | |
|---|---|
| Free surface and stratified flows | : VOF |
| High particle loading | : Eulerian-Granular model |

Low to moderate loading depends on Stokes number

| | |
|---|---|
| Stokes > 1 | : mixture model is not applicable, choose DPM or Eulerian |
| Stokes < 1 | : both models are applicable |

Strong coupling among phase equations solve better with lowered under-relaxation factors.

### 3.10 Multiphase modelling using volume of fluid model

To simulate the air draw-down, the multiphase model using volume of fluid (VOF) approach was employed. This model was designed for two or more immiscible fluids where the position of the interface between the fluids is of interest and depends on the fact that the air and liquid are not interpenetrating. Each phase is represented by its volume fraction therefore in each control volume the volume fraction representing air and the liquid phase equals to unity. Moreover, the fields for all variables and properties are shared by the phases and represent volume-averaged values. This is valid only if the volume fraction of each of the phases is known at each location. This means the variables and properties in any given cell either purely represents one of the phases or represents a mixture of the phases, depending upon the volume fraction values. For example if a fluid $q$ volume fraction in a cell is represented by $\alpha_q$, then three scenarios are possible, namely:

$\alpha_q = 0$ : cell is void of $q$ fluid

$\alpha_q = 1$ : cell is full of the $q$ fluid

$0 < \alpha_q < 1$ : cell contains the interface between the $q$ fluid and one or more other fluids

Based on the local value of $\alpha_q$ the appropriate properties and variables will be assigned to each control volume within the domain. The tracking of the interface between the phases is achieved by the solving of the continuity equation for the volume fraction of one (or more) of the phases. For example, for the $q$ phase, the continuity equation is:

$$\frac{1}{\rho_q}\left[\frac{\partial}{\partial t}(\alpha_q \rho_q) + \nabla \cdot (\alpha_q \rho_q \vec{v}_q) = S_{\alpha q} + \sum_{p=1}^{n}(\dot{m}_{pq} - \dot{m}_{qp})\right] \qquad -3.53$$

where

$\dot{m}_{qp}$ : mass transfer from phase $q$ to phase $p$

$\dot{m}_{pq}$ : mass transfer from phase $p$ to phase $q$

$S_{\alpha q}$ : source term and is zero by default but a constant or user-defined mass source can be specified for each phase

The volume fraction equation was not solved for the primary phase, rather, it was solved based on the following constraint:

$$\sum_{q=1}^{n} \alpha_q = 1 \qquad \text{- 3.54}$$

The properties that appear in the transport equation are determined by the presence of the component phases in each control volume. For instant, in a two-phase system, if the phases are represented by the subscripts 1 and 2 and if the volume fraction of the second phase is being solved, the density in each cell is given by:

$$\rho = \alpha_2 \rho_2 + (1 - \alpha_2)\rho_1 \qquad \text{- 3.55}$$

Moreover, for an n-phase system, the volume-fraction-averaged density has the following expression:

$$\rho = \sum \alpha_q \rho_q \qquad \text{- 3.56}$$

All other properties, for example, viscosity were computed in this manner.

As for the momentum equation, a single equation was solved throughout the domain which resulted in shared velocity field among the phases. The momentum equation is dependent on the volume fractions of all phases through the properties $\rho$ and $\mu$.

$$\frac{\partial}{\partial t}(\rho \vec{v}) + \nabla \cdot (\rho \vec{v} \vec{v}) = -\nabla_p + \nabla \cdot [\mu(\nabla \vec{v} + \nabla \vec{v}^T)] + \rho \vec{g} + \vec{F} \qquad \text{- 3.57}$$

A limitation of the shared-fields approximation is that in situations where large velocity differences exist between the phases, the accuracy of the velocities calculated near the interface can be severely affected.

There are three schemes available in the VOF model which includes: Geometric reconstruction scheme, donor-acceptor scheme, Euler explicit scheme and implicit scheme.

*Geometric reconstruction scheme* – the standard interpolation schemes that are used in Fluent® are used to obtain the face fluxes whenever a cell is completely filled with one phase or another. When the cell is near the interface between two phases, the geometric reconstruction scheme is used. This scheme represents the interface between fluids using a piecewise-linear approach and in Fluent®, this scheme has the highest accuracy which is

applicable for general unstructured meshes [Youngs 1982]. It assumes that the interface between two fluids has a linear slope within each cell, and uses this linear shape for calculation of the advection of fluid through the cell faces. The first step in this reconstruction scheme is calculating the position of the linear interface relative to the centre of each partially-filled cell, based on the information about the volume fraction and its derivatives in the cell. The second step involves the calculation of the advecting amount of fluid through each face using the computed linear interface representation and information about the normal and tangential velocity distribution on the face. The third step is calculating the volume fraction in each cell using the balance of fluxes calculated during the previous step. It must be noted that when this scheme is employed, a transient simulation must be computed.

*Donor-acceptor scheme* – the standard interpolation schemes that are used in Fluent® are used to obtain the face fluxes whenever a cell is completely filled with one phase or another. When the cell is near the interface between two phases, the donor-acceptor scheme is used to determine the amount of fluid advected through the face [Hirt and Nichols 1981]. This scheme identifies one cell as a donor of an amount of fluid from one phase and another neighbouring cell as the acceptor of that identical amount of fluid, and is used to prevent numerical diffusion at the interface. The amount of fluid from one phase that can be convected across a cell boundary is limited by the minimum of two values: the filled volume in the donor cell or the free volume in the acceptor cell. The orientation of the interface is also used in determining the face fluxes. The interface orientation is either horizontal or vertical, depending on the direction of the volume fraction gradient of the $q^{th}$ phase within the cell, and that of the neighbour cell that shares the face in question. Depending on the interface's orientation as well as its motion, flux values are obtained by pure upwinding, pure down-winding or some combination of the two. Similarly, when this scheme is used, transient simulation must be computed. It must be noted however, this scheme can only be used with quadrilateral or hexahedral meshes.

*Euler explicit approach* – Fluent's standard finite-difference interpolation schemes are applied to the volume fraction values that were computed at the previous time step.

$$\frac{\alpha_q^{n+1}\rho_q^{n+1}-\alpha_q^n\rho_q^n}{\Delta t}V+\sum_f(\rho_q U_f^n\alpha_{q,f}^n)=\left[\sum_{p=1}^{n}(\dot{m}_{pq}-\dot{m}_{qp}\right]V \qquad -3.58$$

where

$n+1$ : index for new (current) time step

$n$ : index for previous time step

$\alpha_{q,f}$ : face value of the qth volume fraction, computed from the first or second-order upwind, QUICK, or modified HRIC

$V$ : volume of cell

$U_f$ : volume flux through the face, based on normal velocity

Similarly, when this scheme is used, a transient simulation must be computed.

*Implicit interpolation method* – Fluent's standard finite-difference interpolation scheme, including the modified HRIC scheme, are used to obtain the face fluxes for all cells, including those near the interface.

$$\frac{\alpha_q^{n+1}\rho_q^{n+1}-\alpha_q^n\rho_q^n}{\Delta t}V+\sum_f(\rho_q^{n+1}U_f^{n+1}\alpha_{q,f}^{n+1})=\left[S_{\alpha_q}\sum_{p=1}^{n}(\dot{m}_{pq}-\dot{m}_{qp}\right]V \qquad -3.59$$

Since this equation requires the volume fraction values at the current time step (rather than at the previous step, as for the Euler explicit scheme), a standard scalar transport equation is solved iteratively for each of the secondary-phase volume fractions at each time step. An advantage of this scheme is its applicability to both the transient and steady-state simulations. Since the draw-down of air in this research work involved steady-state modelling, therefore, this scheme was selected. The VOF model can also capture the effects of open channel flows. Such flows involve the existence of a free surface between the flowing fluid and the fluid above it which is generally the atmosphere. In such cases, the wave propagation and free surface behaviour becomes important. Flow is generally governed by the forces of gravity and inertia. Since none of the model in this work involves open channel flows, this feature will not be discussed further.

The following results were derived from a multiphase modelling using VOF approach. The aim of this modelling was to snapshoot the air draw-down occurring in the nitrator during start-up and steady-state operation; and subsequently to convey this snapshot in the form of the contours of air volume fraction.

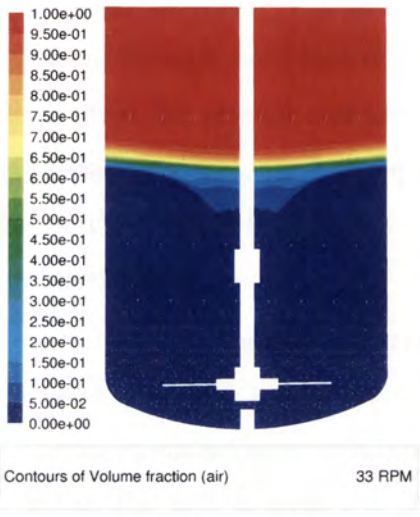


Figure 3.32: Air volume fraction at 33 rpm

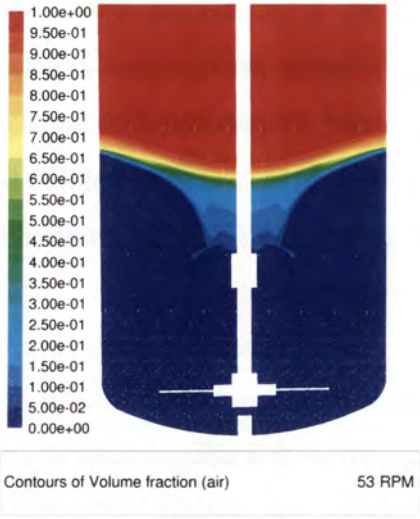


Figure 3.33: Air volume fraction at 53 rpm

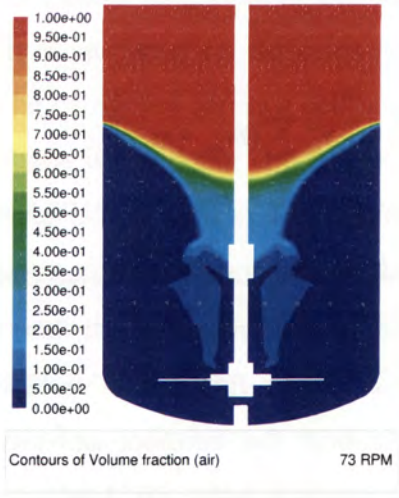


Figure 3.34: Air volume fraction at 73 rpm

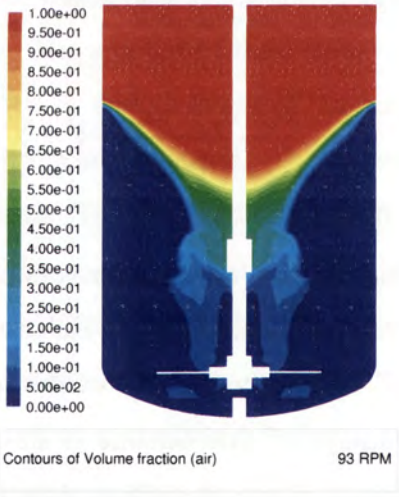


Figure 3.35: Air volume fraction at 93 rpm

As shown in Figure 3.32, the central vortex was already prevalent even when the impellers were rotating at 33 rpm. This phenomenon was attributed to the absence of baffles that reduced bulk fluid rotation inside the nitrator.

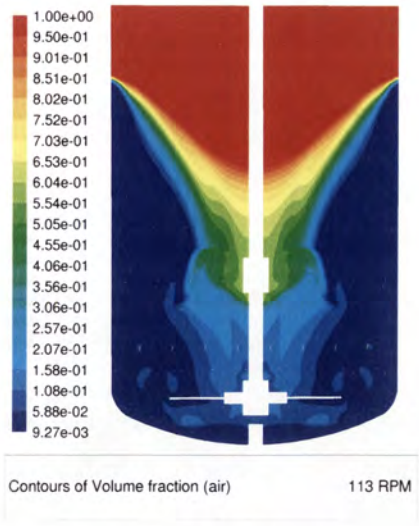


Figure 3.36: Air volume fraction at 113 rpm

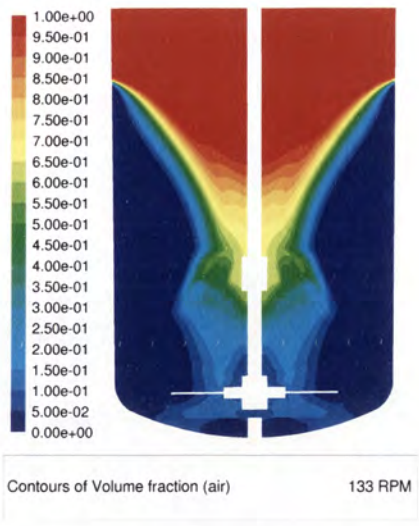


Figure 3.37: Air volume fraction at 133 rpm

The central vortex deepened as the speed was increased, as shown in Figures 3.33-3.37. Air entrainment, defined as the situation when the air pocket hits the impeller hub, partly occurred even at 73 rpm. In the absence of baffles, the vortex formed promoted the draw-down of floating solids, however, the drawn down solids have the tendency of concentrating in the central vortex which normally leads to its poor distribution throughout the nitrator. This concentration of floating solids will eventually leads to a significant reduction in mass transfer, thus lowering reaction rate. In addition, even after the solids have been incorporated into the liquid media, the lack of baffles generally promotes solid body rotation which was shown to minimise turbulence and eventually prevents effective mixing. To remedy this problem, narrow baffles were recommended because besides being able to incorporate floating solids they also have the ability to distribute floating solids homogeneously.

### 3.10.1 Impeller geometry analysis

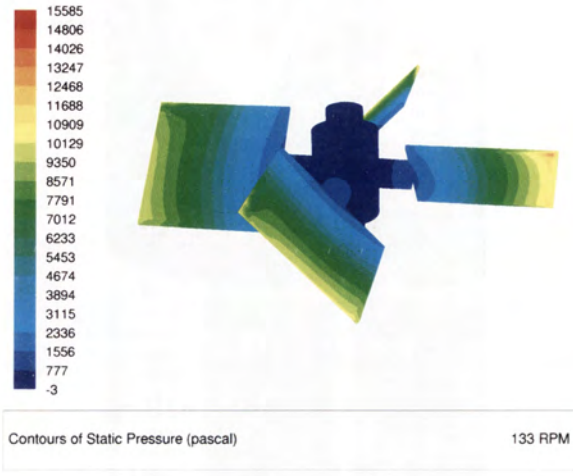


Figure 3.38: Contours of static pressure for the top impeller

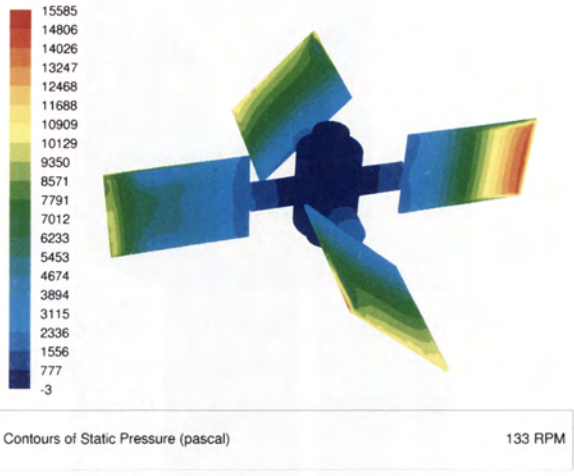


Figure 3.39: Contours of static pressure for the bottom impeller

Figure 3.38 shows that the static pressure was greatest at the blade tips. Figure 3.39 shows that the static pressure was greater in a $90^{o}$ vertically mounted blade than those found in the $45^{o}$ pitched blades. In both cases, the static pressure decreased as the region moved from the blade tips to the impeller hub.

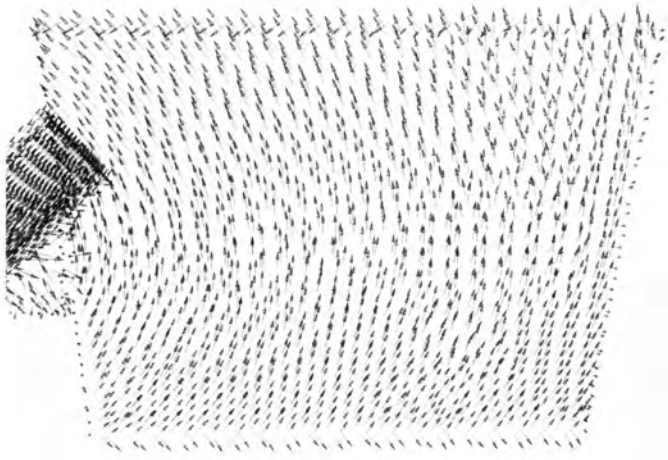

Figure 3.40: Vector plot of 45° pitched blade

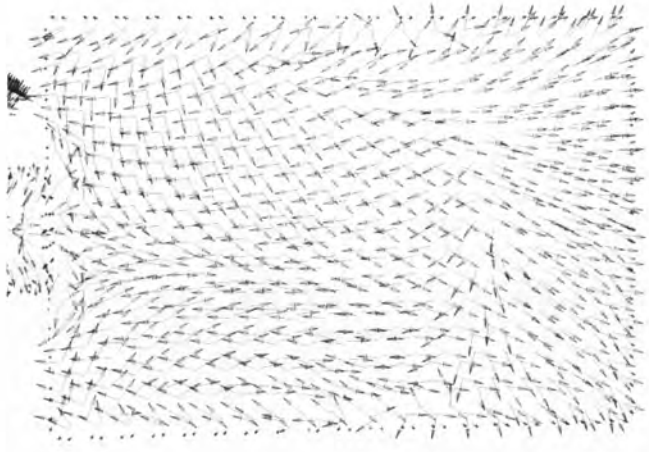

Figure 3.41: Vector plot of a vertical mounted blade

The vector plots shown in Figure 3.40 shows that the flow is axially oriented for the 45° pitched blades whereas the flow is radially oriented for the 90° vertically mounted blade shown in Figure 3.41.

## 3.11 Proposed nitrator geometrical configuration

### 3.11.1 Numerical setup

Except where mentioned, the numerical setup for the improved nitrator is similar to that used for the existing unit.

Due to presence of baffles, significant interrupted rotational flow existed inside the nitrator thereby creating steep pressure gradient. Because of this, PRESTO (pressure staggering option) was employed to compute the pressure value at the cell surface by interpolating the value at cell centroid. SIMPLE (semi-implicit method for pressure linked equations) scheme was used for the pressure velocity coupling where a relationship between the pressure and velocity corrections was used to enforce conservation of continuity in order to obtain the pressure field [Kerdouss 2006].

On the other hand, to model the improved nitrator fitted with four narrow baffles, Realizable $k$-$\varepsilon$ model [Rahimi 2005] was used to capture the hydrodynamics. The term 'realisable' means that the model satisfies certain mathematical constraints on the normal stresses, consistent with the physics of turbulent flows. As mentioned previously, it aims to overcome the weakness poses by the standard $k$-$\varepsilon$ or other conventional $k$-$\varepsilon$ models.

The Realizable $k$-$\varepsilon$ transport equation is given by:

$$\frac{\partial}{\partial t}(\rho k)+\frac{\partial}{\partial x_j}(\rho k u_j)=-\frac{\partial}{\partial x_i}\left[(\mu+\frac{u_t}{\sigma_k})\frac{\partial k}{\partial x_j}\right]+G_k+G_b-\rho\varepsilon-Y_M+S_k \qquad -3.60$$

and

$$\frac{\partial}{\partial t}(\rho\varepsilon)+\frac{\partial}{\partial x_j}(\rho\varepsilon u_j)=\frac{\partial}{\partial x_j}\left[(\mu+\frac{u_t}{\sigma_\varepsilon})\frac{\partial \varepsilon}{\partial x_j}\right]+\rho C_1 S_\varepsilon-\rho C_2\frac{\varepsilon^2}{k+\sqrt{v\varepsilon}}+C_{1\varepsilon}\frac{\varepsilon}{k}C_{3\varepsilon}G_b+S_\varepsilon \qquad -3.61$$

where

$$C_1=\max\left[0.43,\frac{\eta}{\eta+5}\right] \qquad -3.62$$

$$\eta = S\frac{k}{\varepsilon} \qquad \text{- 3.63}$$

$$S = \sqrt{2S_{ij}S_{ij}} \qquad \text{- 3.64}$$

In the two equations above, $G_k$ represents the turbulence kinetic energy generated due to the mean velocity gradients whereas $G_b$ is the turbulence kinetic energy due to buoyancy. $Y_M$ represents the contribution of the fluctuating dilation in compressible turbulence to the overall dissipation rate. $C_2$ and $C_{1\varepsilon}$ are constants while $\sigma_k$ and $\sigma_\varepsilon$ are the turbulent Prandtl numbers for $k$ and $\varepsilon$ respectively. In this model, except for the value of the constants, the $k$ equation is identical to those found in the standard $k$-$\varepsilon$ and the RNG $k$-$\varepsilon$ models. The $\varepsilon$ equation on the other hand, is different from those found in the standard $k$-$\varepsilon$ and the RNG $k$-$\varepsilon$ models.

The $\varepsilon$ equation found in the standard $k$-$\varepsilon$ model is given as:

$$\frac{\partial}{\partial t}(\rho\varepsilon) + \frac{\partial}{\partial x_i}(\rho\varepsilon u_i) = \frac{\partial}{\partial x_j}\left[(\mu + \frac{u_t}{\sigma_\varepsilon})\frac{\partial \varepsilon}{\partial x_j}\right] + C_{1\varepsilon}\frac{\varepsilon}{k}(G_k + C_{3\varepsilon}G_b) - C_{2\varepsilon}\rho\frac{\varepsilon^2}{k} + S_\varepsilon \qquad \text{- 3.65}$$

The $\varepsilon$ equation found in the RNG $k$-$\varepsilon$ model is given as:

$$\frac{\partial}{\partial t}(\rho\varepsilon) + \frac{\partial}{\partial x_i}(\rho\varepsilon u_i) = \frac{\partial}{\partial x_j}\left[\alpha_\varepsilon \mu_{eff}\frac{\partial \varepsilon}{\partial x_j}\right] + C_{1\varepsilon}\frac{\varepsilon}{k}(G_k + C_{3\varepsilon}G_b) - C_{2\varepsilon}\rho\frac{\varepsilon^2}{k} - R_\varepsilon + S_\varepsilon \qquad \text{- 3.66}$$

One of the differences found between the two $\varepsilon$ equations is that the production term in the Realisable model $\varepsilon$ equation does not involve the production of $k$, that is, it does not contain the same $G_k$ term as those found in other $k$-$\varepsilon$ models. It is believed that this difference provides better spectral energy transfer representation. Another difference is that the destruction term does not have any singularity, that is, its denominator never vanishes, even if $k$ vanishes or becomes smaller than zero. On the other hand, there is a singularity due to the $k$ in the denominator present in other $\varepsilon$ equation in other k-$\varepsilon$ models.

The turbulent viscosity, $\mu_t$, is computed by combining $k$ and $\varepsilon$ as follows:

$$\mu_t = \rho C\mu \frac{k^2}{\varepsilon} \quad \text{-3.67}$$

While the $C_\mu$ is a constant for the other $k$-$\varepsilon$ models, it is not constant for this model and can be computed via:

$$C_\mu = \frac{1}{A_0 + A_s \frac{kU^*}{\varepsilon}} \quad \text{-3.68}$$

where

$$U^* \equiv \sqrt{S_{ij}S_{ij} + \tilde{\Omega}_{ij}\tilde{\Omega}_{ij}} \quad \text{-3.69}$$

$$\tilde{\Omega}_{ij} = \Omega_{ij} - 2\varepsilon_{ijk}\omega_k \quad \text{-3.70}$$

$$\Omega_{ij} = \overline{\Omega}_{ij} - \varepsilon_{ijk}\omega_k \quad \text{-3.71}$$

The term $\overline{\Omega}_{ij}$ is the mean rate of rotation tensor viewed in a rotating reference frame with the angular velocity $\omega_k$. The model constants $A_0$ and $A_s$ are given as: $A_0 = 4.04$ and $A_s = \sqrt{6}\cos\phi$ respectively.

$$\phi = \frac{1}{3}\cos^{-1}\left(\sqrt{6}W\right), \quad W = \frac{S_{ij}S_{jk}S_{ki}}{S^3}, \quad \tilde{S} = \sqrt{S_{ij}S_{ij}}, \quad S_{ij} = \frac{1}{2}\left(\frac{\partial u_j}{\partial x_i} + \frac{\partial u_i}{\partial x_j}\right) \quad \text{-3.72}$$

It can be seen that $C_\mu$ is a function of the mean strain and rotation rates, the angular velocity of the system rotation, and the turbulence fields ($k$ and $\varepsilon$). However, in Fluent® the term $-2\varepsilon_{ijk}\omega_k$, by default, is not included in the calculation of $\tilde{\Omega}_{ij}$ because it is not compatible with simulations involving sliding meshes or multiple reference frame.

The model constants $C_2$, $\sigma_k$, $\sigma_\varepsilon$ have been established to ensure that the model performs well for certain canonical flows. The model constants are given by:

$$C_{1\varepsilon} = 1.44, \quad C_2 = 1.9, \quad \sigma_k = 1.0, \quad \sigma_\varepsilon = 1.2$$

### 3.11.2 Impeller selection

Before modifying the nitrator, the right impeller must be employed. In this scenario, an important attribute in selecting impellers is the amount of axial flow discharged by the impellers per unit power consumption [Wu et al. 2006]. Table 3.12 shows six impellers having their performance compared to one another. The impellers tested were a four-bladed high efficiency impeller, ADI-high efficiency three-bladed impeller, standard four-bladed pitch blade turbine, standard four bladed paddle impeller, a four-bladed thirty degree inclination and finally a four-bladed thirty degrees inclination with a bended blade at some point along the blade. The ADI-HE impeller also has decreasing blade width which was shown to promote maximum axial flow [Kumaresan and Joshi 2006].

Table 3.12: Results generated from using impellers

| Impeller | $P$ (W) | $T$ (Nm) | $Q$ (kg s$^{-1}$) | $N_P$ | $N_Q$ | $\eta$ |
|---|---|---|---|---|---|---|
| HE-4 | 85.51 | 8.165 | 49.63 | 0.6056 | 0.1883 | 0.3110 |
| ADI-HE | 68.63 | 6.554 | 44.48 | 0.4860 | 0.1688 | 0.3473 |
| PBT | 118.5 | 11.32 | 44.75 | 0.8392 | 0.1698 | 0.2024 |
| Paddle | 178.3 | 17.03 | 7.69 | 1.263 | 0.0292 | 0.0231 |
| 30° – 4 blades | 84.47 | 8.067 | 43.58 | 0.5982 | 0.1654 | 0.2764 |
| 30° – bended blades | 68.73 | 6.563 | 44.71 | 0.4868 | 0.1697 | 0.3486 |

Judging from the results tabulated, the paddle impeller produced low axial flow ($Q$) and at the same time, promoted high radial flow. Apart from having high power consumption, the paddle impeller did not create turbulence, instead, promoted 'laminar' like rotational flow. Its low axial flow and high power consumption contributed to its very low efficiency relative to the other impellers. Based on this, the paddle impeller was excluded.

The other five impellers have comparable performance from their respective efficiency numbers. The most notable impellers were the ADI-HE and the 30°-bended blades where their performance matches each other. These two were short listed and decision to select one between them depended on qualitative analysis. Although the 30°-bended blades had

similar performance with the two short listed impellers, its performance was much lower under baffled setting. This was attributed to the shallow angle of attack which promoted axial flow and minimum radial flow. For baffle to work well, a fair amount of radial flow component must exist.

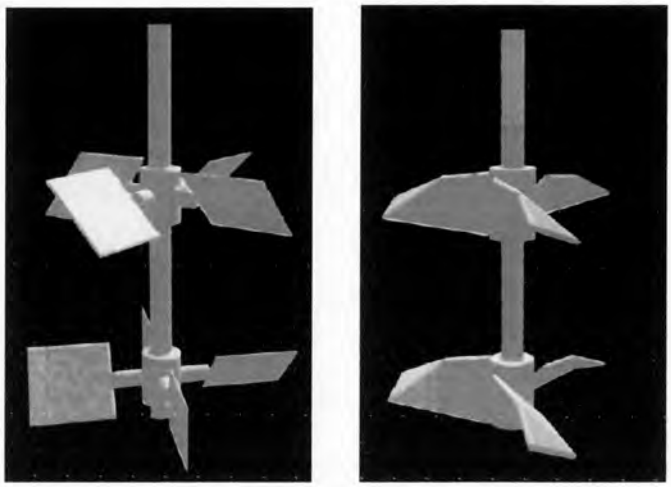

Figure 3.42: Existing impellers setup (left) vs improved new impellers setup (right)

Figure 3.42 shows the existing 4-bladed impellers setup replaced by the improved 3-bladed high-efficiency impeller setup.

### 3.11.3 Designing a nitrator

Table 3.13 shows eight reactor geometrical configurations under investigation. The trial condition was generated using a software called Qualitek-4 which employed the principle of the design of experiment (DOE) by Taguchi. On the other hand, Figure 3.43 shows the diagrammatic representation of each of these variants.

Table 3.13: Variants generated using the design of experiment software

| Variant # | 1 | 2 | 3 | 4 | 5 | 6 | 7 | 8 |
|---|---|---|---|---|---|---|---|---|
| No. of baffles | 2 | 2 | 2 | 2 | 4 | 4 | 4 | 4 |
| Impeller diameter | 0.55T | 0.55T | 0.6T | 0.6T | 0.55T | 0.55T | 0.6T | 0.6T |
| No. of impellers | 1 | 2 | 1 | 2 | 1 | 2 | 1 | 2 |
| Blade width | 0.3D | 0.35D | 0.35D | 0.3D | 0.35D | 0.3D | 0.3D | 0.35D |

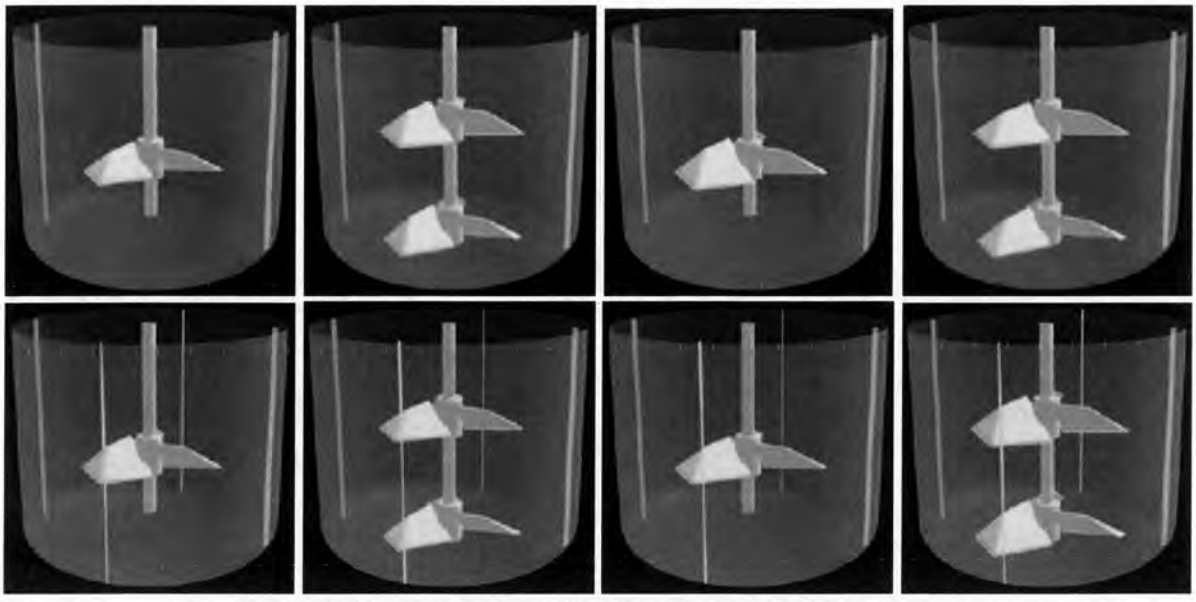

Figure 3.43: Different tank design configurations representing the eight variants

Table 3.14: Results of different geometrical configurations

| Variant # | 1 | 2 | 3 | 4 | 5 | 6 | 7 | 8 |
|---|---|---|---|---|---|---|---|---|
| $\tau$ | 10.86 | 17.41 | 16.99 | 22.5 | 12.38 | 16.74 | 16.85 | 26.82 |
| $Q$ | 93.61 | 155.3 | 107.5 | 171.6 | 126 | 209.1 | 139.3 | 246.6 |
| $N$ | 1.217 | 1.217 | 1.217 | 1.217 | 1.217 | 1.217 | 1.217 | 1.217 |
| $P$ | 83.03 | 133.1 | 129.9 | 172.0 | 94.65 | 128 | 128.8 | 205.1 |
| $D$ | 0.55 | 0.55 | 0.60 | 0.60 | 0.55 | 0.55 | 0.60 | 0.60 |
| $\rho$ | 1713 | 1713 | 1713 | 1713 | 1713 | 1713 | 1713 | 1713 |
| $N_P$ | 0.5348 | 0.8573 | 0.5415 | 0.7171 | 0.6096 | 0.8243 | 0.5370 | 0.8547 |
| $N_Q$ | 0.2700 | 0.4479 | 0.2388 | 0.3812 | 0.3634 | 0.6030 | 0.3094 | 0.5478 |
| $\eta$ | 0.5048 | 0.5244 | 0.4410 | 0.5316 | 0.5961 | 0.7316 | 0.5762 | 0.6409 |

Table 3.14 summarised the performance of each nitrator geometrical configuration. Of these eight variants assessed, variant 6 was chosen as the desired design. To ensure that the results were not influenced by the number of cells, grid independence test were conducted.

A preliminary grid convergence study was carried out on variant 6 to verify that the solution obtained from using the second-order upwind discretisation scheme was mesh independent. The number of cells inside and outside the rotational zones was systematically increased in the x-, y- and z-directions throughout the tank. When refining the mesh, care was taken to assign additional cells to the regions of high gradient around the impeller blades and discharge regions. Simulation results did not show significant changes (<1%) when the number of cells was increased.

### 3.11.4 Comparison of proposed and existing nitrators

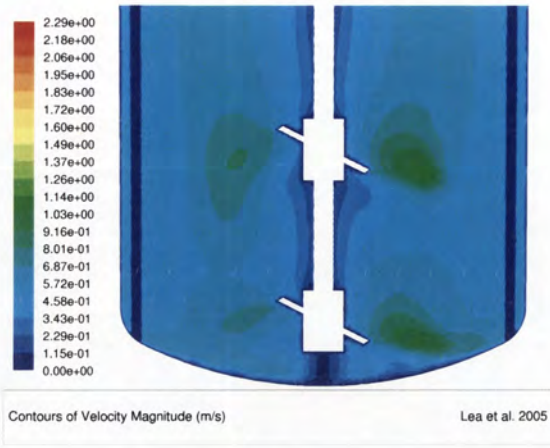


Figure 3.44: Contours of velocity magnitude - axial plane

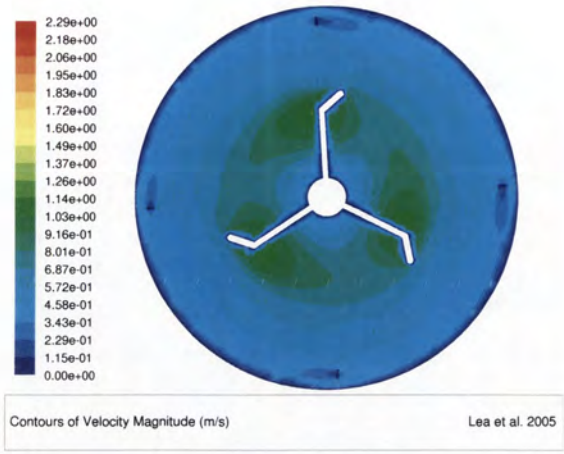


Figure 3.45: Contours of velocity magnitude - radial plane

Referring to Figure 3.44, the axial plane contours of velocity magnitude shows that the velocity in all the directions is less relative to the existing system. The fastest region is located around impeller region and fades with distant from the impeller, as shown in Figure 3.45. Very low velocity can be found along the wall, due to boundary layer effect. The lower overall velocity magnitude was attributed to the conversion of the power dissipated from the impellers to creating turbulence in the nitrator.

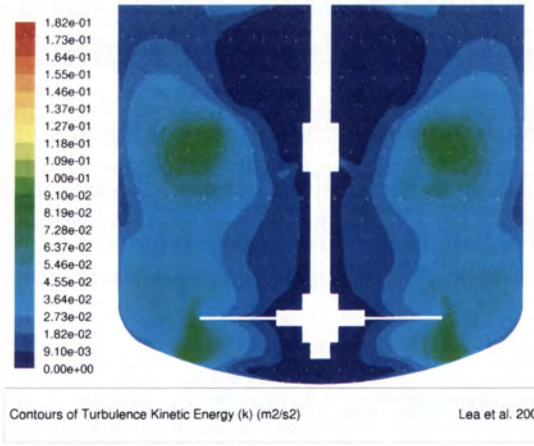


Figure 3.46: Existing nitrator

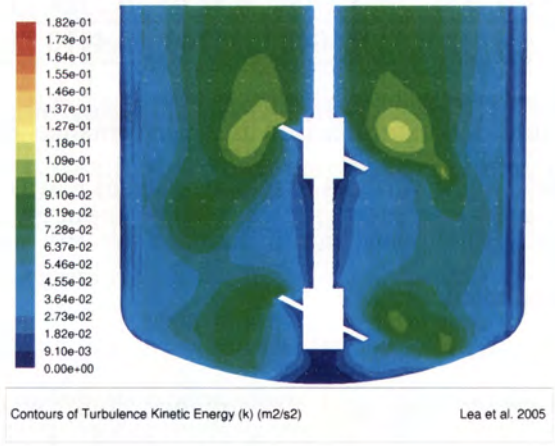


Figure 3.47: Improved nitrator

Figures 3.46 and 3.47 show that the lowest turbulence areas are confined to those above the impellers, around the shaft and at the tank bottom. With the improved system, the areas of low turbulence above shown in the existing system vanished and the low

turbulence region at the tank bottom was significantly minimised. Moreover, turbulence around wall region is higher relative to the existing system.

Figure 3.48: Optimum tank design configuration

Figure 3.48 shows the geometrical configuration of the proposed system that promises optimum performance. Two factors help to convert radial flow to axial flow namely, the implementation of axial-flow ADI-HE impellers and the use of four narrow baffles. This will mix materials having different densities more effectively thereby improving contacting which eventually will increase the reaction rate due to the minimisation of mass transfer limitation.

### 3.11.5 Power requirement

The power requirement of the existing nitrator as measured by a wattmeter was 1.5 kW at full load. Similar reading was obtained at zero loading. This means that the motor size was too big to reflect on the power draw due to the load. Consequently, the power draw of the existing nitrator was taken as 1.5 kW.

The torque of the proposed improved nitrator when the impellers are rotating at 73 rpm is 0.8826 relative to the existing nitrator. Thus, at 73 rpm, the power requirement of this unit was = 0.8826 × 1.5 kW = 1.324 kW

The torque of the proposed improved nitrator when the impellers are rotating at 93 rpm is 1.431 relative to the existing nitrator. Therefore, when the impellers were rotating at 93 rpm, the power requirement of this unit was = 1.431 × 1.5 kW = 2.147 kW

Table 3.15: Geometrical configurations of the nitrator and the charge tank

| Parameter | Nitrator | Charge tank |
|---|---|---|
| Impellers type | ADI high efficiency | ADI high efficiency |
| Top impeller location | 0.582 m | 0.540 m |
| Bottom impeller location | 0.162 m | 0.162 m |
| *S/D* | 0.76 | 0.64 |
| *D/T* | 0.55 | 0.60 |
| *C/T* | 0.162 | 0.162 |
| *V/T* | 0.35 | 0.56 |
| *W/D* (root) | 0.30 | 0.30 |
| *W/D* (tip) | 0.18 | 0.18 |
| Blade angle (root) | 45° | 45° |
| Blade angle (tip) | 20° | 20° |
| *T* | 1.0 m | 1.2 m |
| *H/T* | 1.0 | 1.217 |
| *Z/T* (aspect ratio) | 0.933 | 1.025 |
| Fluids | $HNO_3$-$H_2SO_4$-$H_2O$ | $HNO_3$-$H_2SO_4$-$H_2O$ |
| Bottom style | Klopperboden | Klopperboden |
| Baffle type | Narrow baffle | Narrow baffle |
| *B/T* | 0.02 | 0.02 |
| *b/T* | 0.03 | 0.025 |
| Density of acids @ 32°C | 1,713 kg $m^{-3}$ | 1,713 kg $m^{-3}$ |
| Viscosity of water @ 25°C | 0.010577 Pa.s | 0.010577 Pa.s |
| Impeller speeds | 73 rpm | 37 rpm |
| Rotation direction | Clockwise | Clockwise |

Table 3.15 shows the geometrical configurations for both the nitration and the charge tanks. Although no modelling was performed on the charge tank, its function and size were similar to the nitrator therefore, changes to the impeller types and the addition of narrow baffles can be done via dimensionless extrapolation. The *V/T* of the nitrator was lower than that of the charge tank because in this unit, a controlled central vortex was needed to draw-down floating ACB particles whereas by the time the ACB travelled to the charge tank, the particles were wetted and had little buoyancy property remaining. Although the *b/T* of the charge tank was smaller than the nitrator, it was still wider than the conventional recommended baffle clearance of at least 0.014.

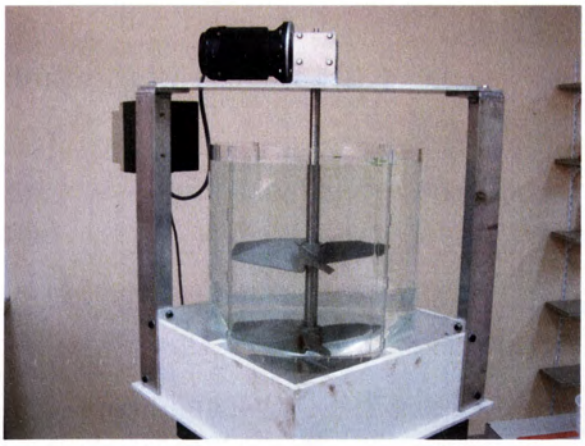

Figure 3.49: General setup

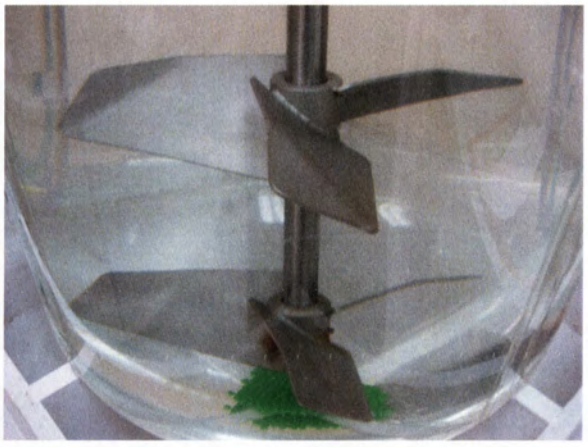

Figure 3.50: Mixing tank at rest

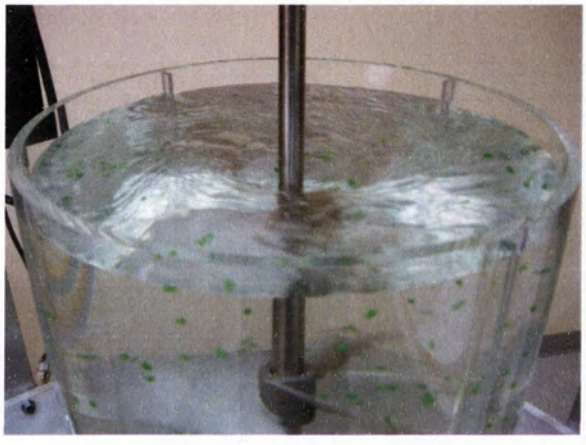

Figure 3.51: Free surface

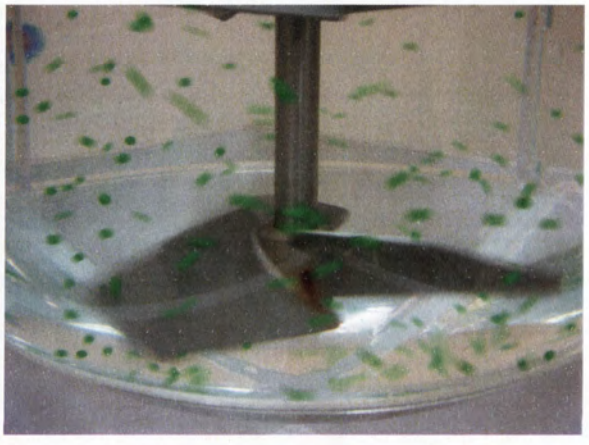

Figure 3.52: Cleared tank bottom

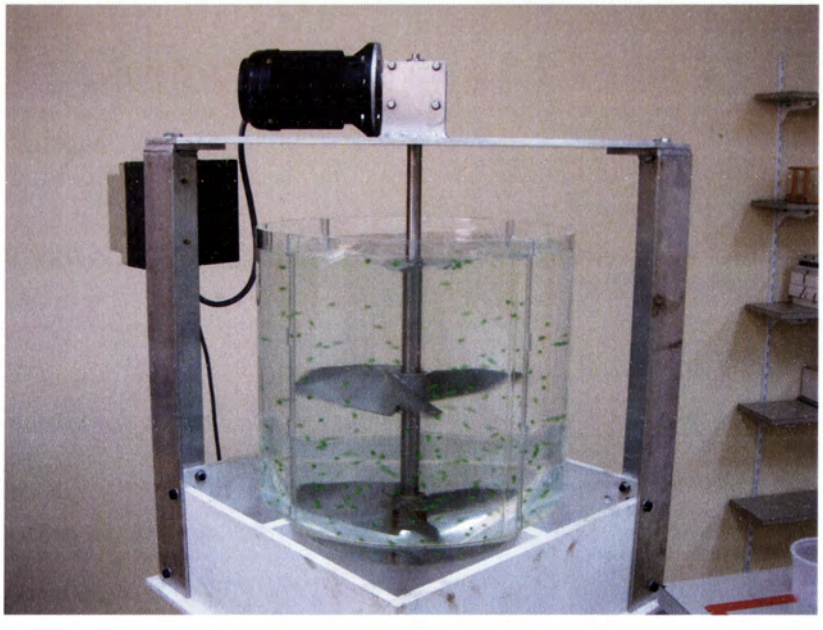

Figure 3.53: Homogeneous suspension

Figure 3.49 shows the general setup of the scaled-down unit installed with the new impellers and four narrow baffles. The assessment criteria used to ascertain whether this design should proceed to the industrial scale nitrator included:

1. The ability to suspend solids heavier than the liquid media, homogeneously
2. The ability to draw-down solids lighter than the liquid media, homogeneously
3. The non-clinging of solids particles on the baffles during reaction process
4. The non-clinging of solid particles on the baffles during emptying of the nitrator

Figures 3.50-3.53 show that this geometrical setup was able to suspend solids easily whereas other experiments (not shown), show that this setup met the other three criteria listed above. Having passed all the criteria above, this design proceeded to the next stage, which included modifying the existing nitrator.

Table 3.16: Improvement expected with the proposed unit

| Parameter | Existing | Proposed | Improvement, % |
|---|---|---|---|
| Power number, $N_P$ | 0.6089 | 0.8243 | 35.38 |
| Flow number, $N_Q$ | 0.2615 | 0.6030 | 130.6 |
| Flow efficiency, $\eta$ | 0.4295 | 0.7316 | 70.34 |
| Flowrate, $kgs^{-1}$ | 117.8 | 209.1 | 77.50 |
| Blending time, $t_B$, s | 26.82 | 15.68 | 41.54 |
| Deviation from ideality, $\xi$, % | 14.13 | 4.53 | 67.92 |
| Global turbulence, $m^2 s^{-2}$ | 37,014 | 51,535 | 39.23 |

Table 3.16 above shows the power number ($P/[\rho \times N^3 \times D^5]$) increased by 35.38% which was attributed to the installation of four narrow baffles. Although it was desirable to minimise power consumption, in some cases, more power was required to achieve process objective. In this case, a higher power consumed means more power was delivered into the process fluid.

The flow number ($Q/[\rho \times N \times D^3]$) was increased by 130.6% at the same rotational speed and using a slightly smaller diameter impeller. The huge increment was attributed to the new impeller design and the installation of four narrow baffles which promoted axial flow. Flow efficiency [$(N_Q/N_P) \times 100\%$] which increased by 70.34%, shows that the proposed system was much more power efficient than the existing system. In general, the draw-

down of floating particles can be achieved via two mechanisms, that is, the intensity of turbulence and the formation of surface vortex. In this case, since the formation of surface vortex was suppressed by four narrow baffles, power consumption, position of the impeller with respect to the free surface, and type of impeller (axial/radial) became the controlling parameters, which means that high liquid velocity and the intensity of the turbulence were responsible for pulling down the buoyant solids.

The proposed system had an axial velocity 77.50% higher than that of the existing system. High axial flowrate, offered by the synergistic cooperation between the proposed impellers and four narrow baffles, will help to promote the draw-down of floating ACB.

Blending time was shortened by 41.54% which can be translated into a higher plant throughput. Deviation from ideality was reduced by 67.92% which means that the room for improving the blending time is now much smaller. Finally, the global turbulence for the proposed system exceeded that of the existing system by 39.23%, thus the mass transfer rate should increase significantly.

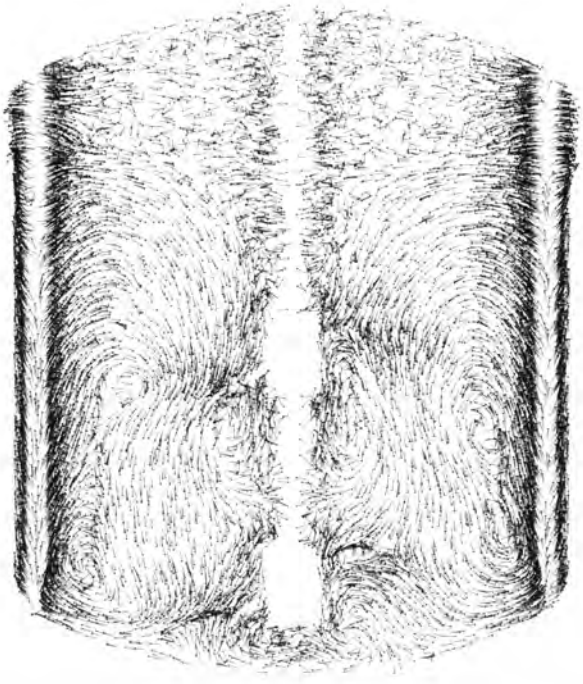

Figure 3.54: Flow pattern inside the optimum tank design

Figure 3.54 exhibits the vector plot inside the optimum tank design. The vectors show that at 73 rpm, there was a strong flow from the free surface to the top impeller. The discharge from the top impeller was then fed to the suction region of the second impeller. The discharge from the second impeller that was somewhat radial in nature because of its close clearance to the tank bottom was then directed upwards by the narrow baffles. Thus it can be seen that the role of the narrow baffles was to convert radial flow into axial flow.

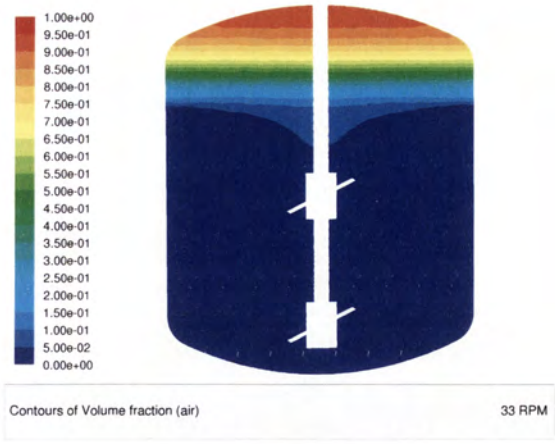


Figure 3.55: Air volume fraction at 33 rpm

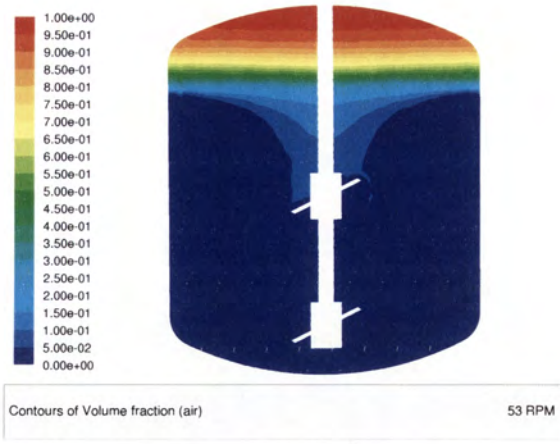


Figure 3.56: Air volume fraction at 53 rpm

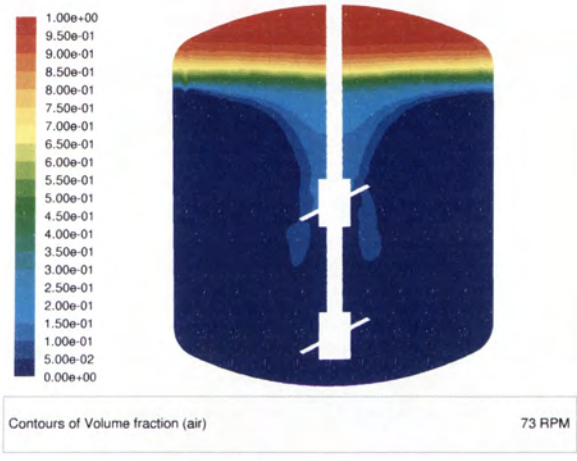


Figure 3.57: Air volume fraction at 73 rpm

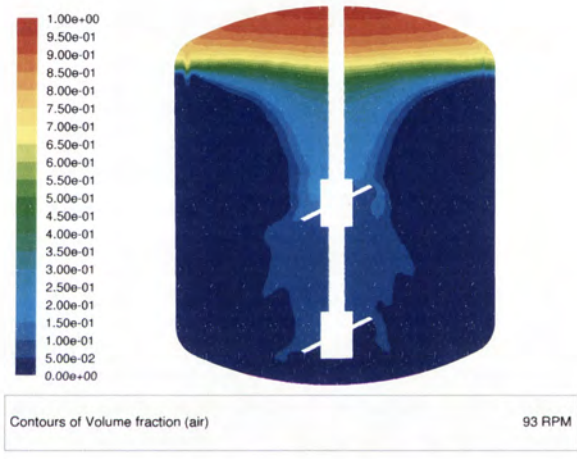


Figure 3.58: Air volume fraction at 93 rpm

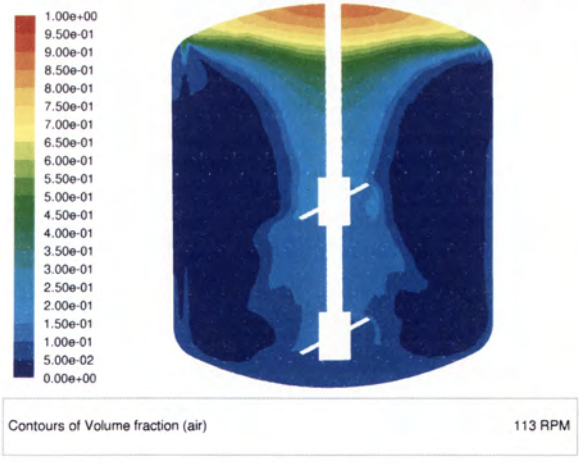


Figure 3.59: Air volume fraction at 113 rpm

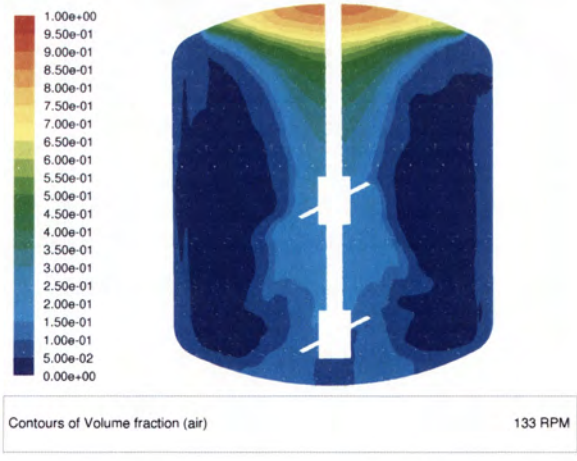


Figure 3.60: Air volume fraction at 133 rpm

At 33 rpm, 10% of air reached halfway through between the top impeller and the free surface but there was not the slightest vortex on the free surface. At 53 rpm, 15% of the air reached the top impeller and a slight vortex was seen on the free surface. Similarly, at 73 rpm, the vortex went deeper and slightly exceeded the top impeller hub. At 93 rpm, not only did the vortex pass through the top impeller, about 5% of air reached to the bottom impeller. At 113 rpm, the vortex hit the tank bottom and finally at 133 rpm, 15% of air reached the tank bottom. This sequence of processes was represented in graphical format from Figures 3.55-3.60.

Table 3.17: Blending time detected by each probe at various impellers rotational speed

| Probes | 33 rpm | 53 rpm | 73 rpm | 93 rpm | 113 rpm | 133 rpm |
|---|---|---|---|---|---|---|
| P1 | 17 | 13 | 14 | 13 | 12 | 10 |
| P2 | 22 | 18 | 15 | 9 | 10 | 9 |
| P3 | 26 | 12 | 12 | 12 | 10 | 9 |
| P4 | 26 | 13 | 13 | 11 | 10 | 9 |
| P5 | 29 | 13 | 22 | 11 | 9 | 8 |
| P6 | 18 | 13 | 14 | 9 | 11 | 10 |
| P7 | 22 | 17 | 17 | 10 | 9 | 8 |
| P8 | 24 | 27 | 19 | 16 | 17 | 14 |
| P9 | 20 | 26 | 12 | 9 | 7 | 6 |
| P10 | 16 | 21 | 12 | 12 | 10 | 9 |

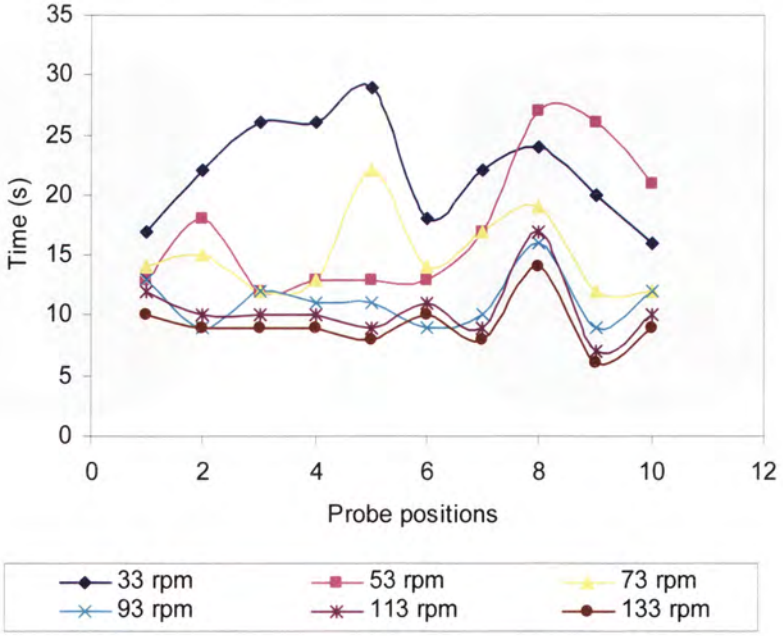


Figure 3.61: Blending time versus probe positions at various impellers rotational speed

Figure 3.61, plotted from result in Table 3.17, shows that the results for each probe were consistent thereby increasing the credibility of the average blending time. Similarly, probes 5 and 8 took a longer time than the rest to achieve homogeneity due to their unfavourable locations. This also means that the individual time required to achieve homogeneity as recorded by each probe was more location dependent than impeller dependent in this scenario. This was attributed to the nature of the fluid flow, that is, both were designed with axial flow in mind. The individual blending time will change dramatically if a set of impeller is axial-focus while another set is radial-focus. The weighted average blending time as a function of impeller speed from 33 rpm to 133 rpm was tabulated in Table 3.18.

Table 3.18: Weighted average blending time as a function of impeller speed

| rpm | $t_{weighted,\ av}$ (s) |
|---|---|
| 33 | 27.97 |
| 53 | 18.35 |
| 73 | 15.68 |
| 93 | 9.97 |
| 113 | 7.08 |
| 133 | 5.47 |

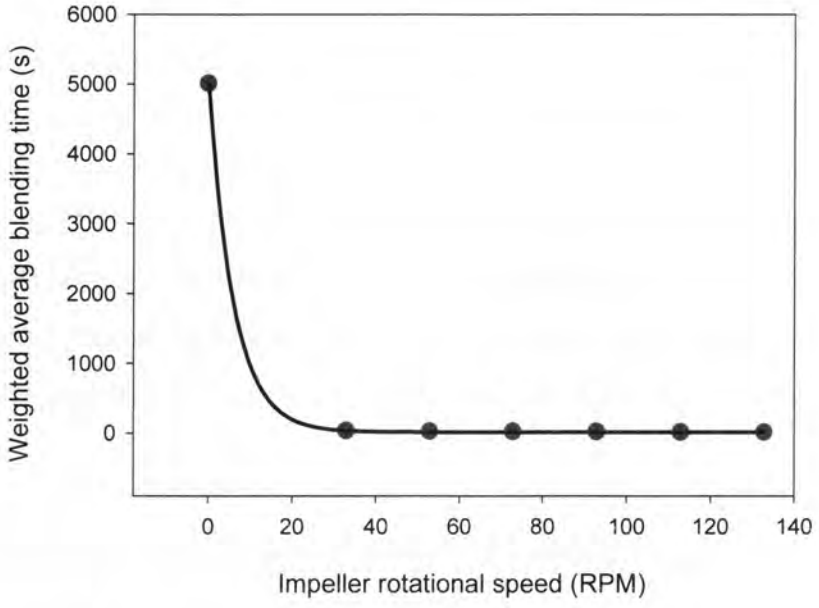


Figure 3.62: Weighted average blending time versus impeller rotational speed

Figure 3.62 shows the plot of weighted average blending time versus various impeller rotational speeds. It can be seen that when the impeller rotational speed increased, the weighted average blending time decreased in the form of an exponential decay with a perfect regression of 1. The model can be represented mathematically as:

$$t_{weighted} = 13.81 + 4986e^{-0.1650N} \qquad \text{- 3.73}$$

From the practical viewpoint, knowing this correlation will make it easier to predict the minimum time required to achieve a state of homogeneity if the impeller speed were to change. In addition, this model also shows a significant improvement in the blending effectiveness, relative to the existing system.

Figures 3.63-3.68 show the changes in the contours of turbulence kinetic energy on a plane section of the nitrator when the impeller speed was increased from 33 rpm to 133 rpm.

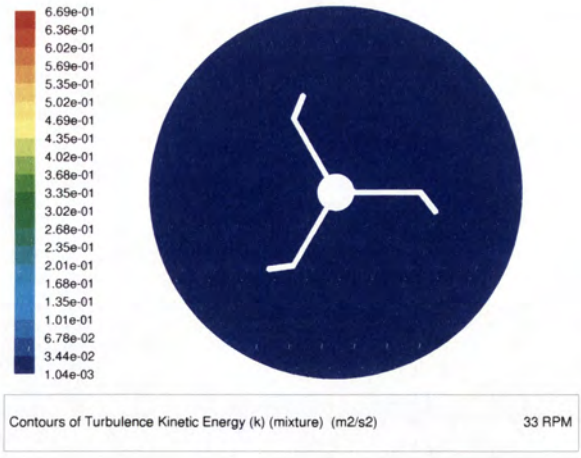


Figure 3.63: Turbulence kinetic energy at 33 rpm

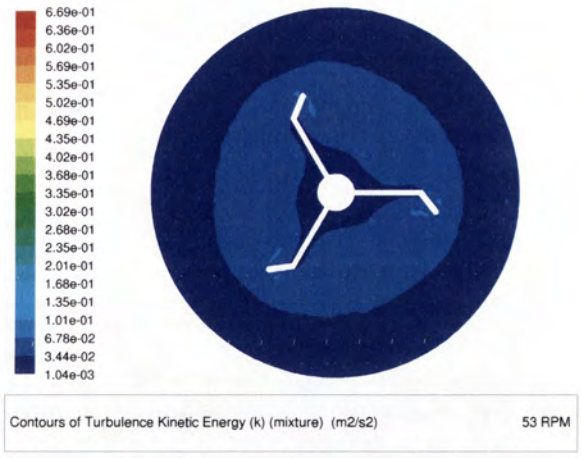


Figure 3.64: Turbulence kinetic energy at 53 rpm

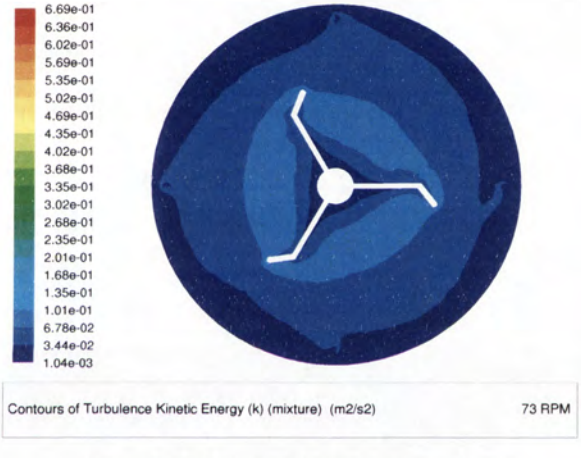


Figure 3.65: Turbulence kinetic energy at 73 rpm

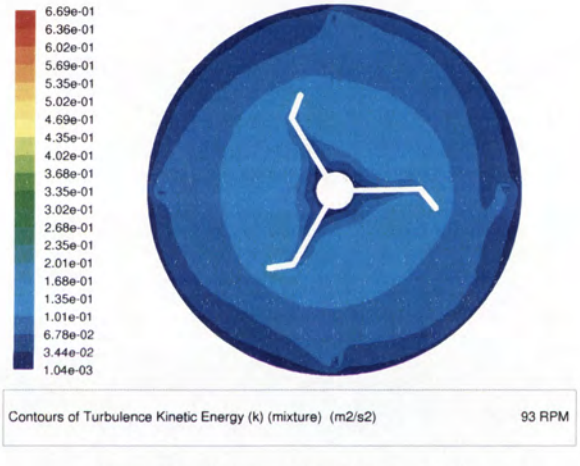


Figure 3.66: Turbulence kinetic energy at 93 rpm

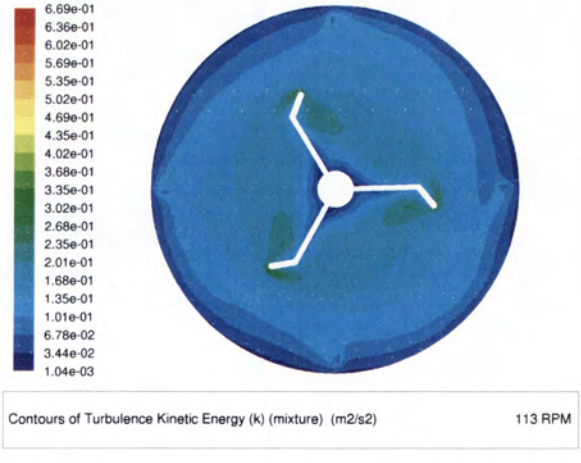


Figure 3.67: Turbulence kinetic energy at 113 rpm

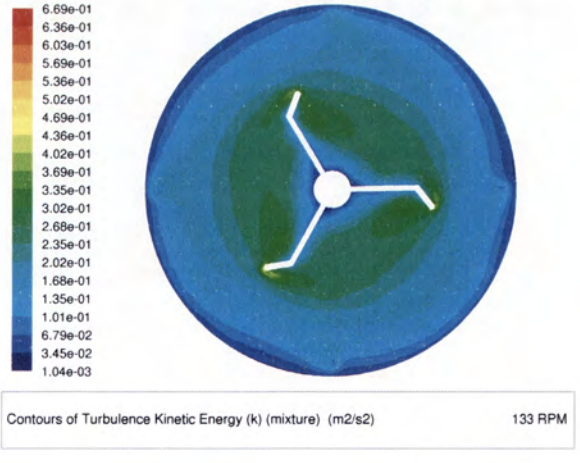


Figure 3.68: Turbulence kinetic energy at 133 rpm

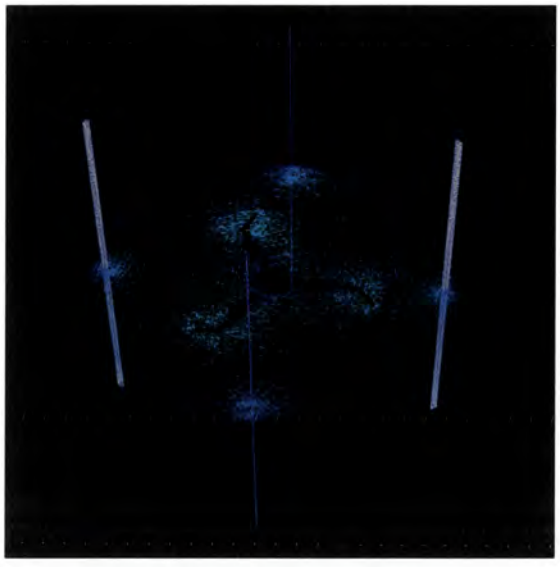

Figure 3.69: Vectors showing turbulence regions

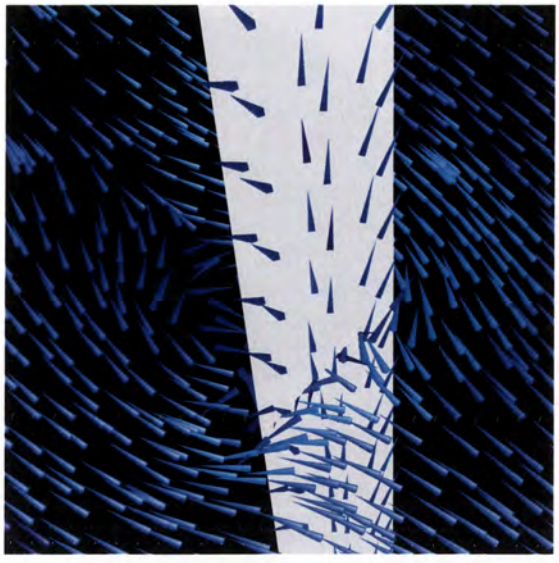

Figure 3.70: Flow pattern around narrow baffles

Figure 3.69 shows that region of high turbulence were those surrounding the impeller blades and the four narrow baffles. Figure 3.70 shows the flow pattern around each of these narrow baffles. The baffles observed to convert the high rotational flow into axial flow. Moreover, the vortex shedding behind this baffle shows that the 'laminar' like flow was interrupted and turbulence was induced as a consequence.

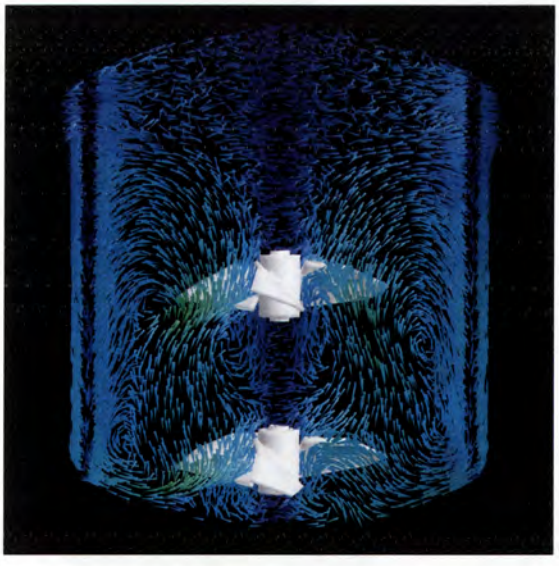

Figure 3.71: Flow pattern inside narrow-baffled tank

Figure 3.72: Flow pattern around ADI-HE impellers

Figure 3.71 shows the general flow pattern inside the optimised nitrator. The flow was axially-oriented and originated from the free-surface, flowed through the blades, diverted by the tank bottom and returned to the top of the tank, aided by the narrow baffles. Figure 3.72 shows the flow pattern surrounding the ADI-HE impeller. The blades promoted

downward-flow rather than horizontal-flow discharge, aided the incorporation of the floating ACB and suspension of the wetted ACB.

### 3.11.6 Impeller geometry analysis

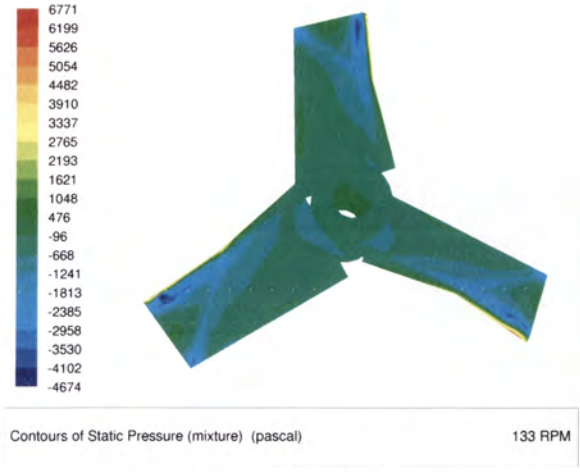


Figure 3.73: Contour plot from top view

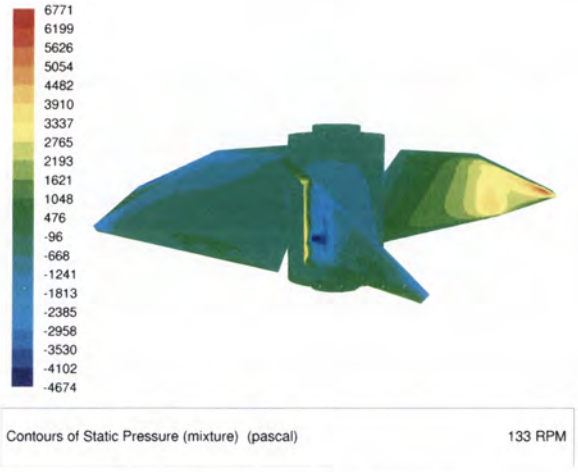


Figure 3.74: Contour plot from side view

The blade width at impeller tip is 0.6 times the blade width at the impeller hub, as shown in Figure 3.73. This was in place to promote uniform flow across the impeller diameter because the speed was highest at the blade tip and lowest at the blade hub. The secret to high pumping was the arch which is geometrically shaped to provide a low angle of attack at the leading edge, while enabling the trailing edge to direct powerful flow downward. Figure 3.74 shows that the contour of static pressure was highest inside the arch which mean it was this region that trapped and directed the fluid downward.

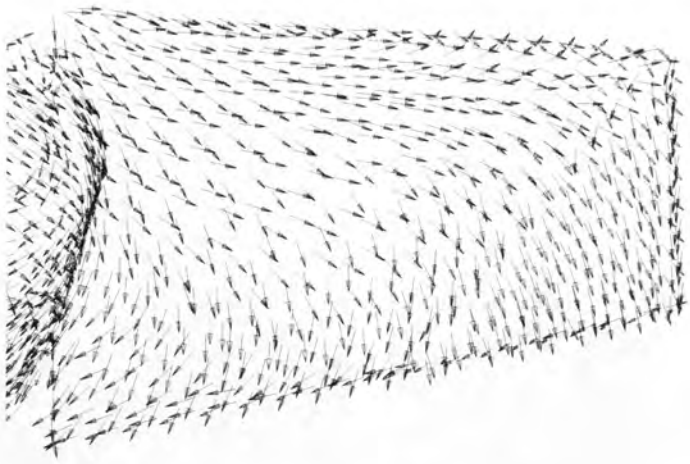

Figure 3.75: Vector plot from top view

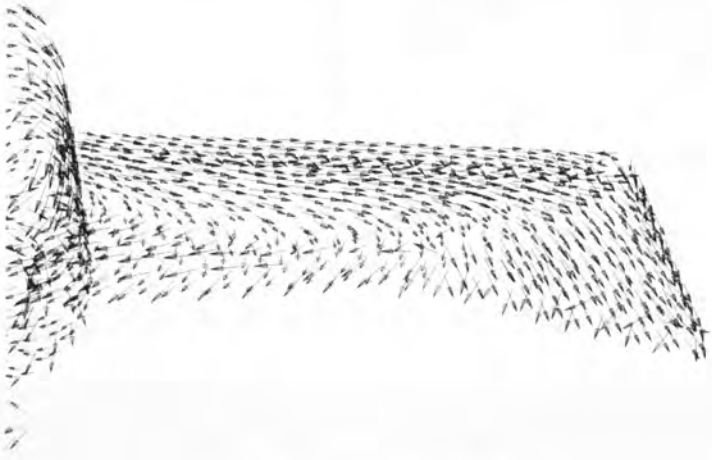

Figure 3.76: Vector plot from side view

Figure 3.75 and 3.76 show that a major component of the vectors starting from the hub, was travelling in the radial direction but as it approached the arched region, it was directed downwards. This shows that the arched region played a significant role in ensuring that the radial flows were converted to axial flow which aided in the draw-down of floating particles as well as the suspension of denser particles.

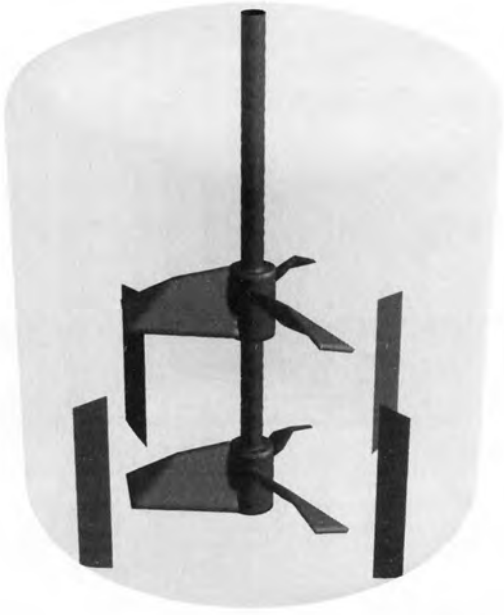

Figure 3.77: Partial-baffled tank design configuration

Figure 3.77 shows the nitrator that utilised four partial baffles. Such baffles consisted of four standard baffles ($T/12$) that extended vertically from the tank bottom to the middle of the tank. Such arrangement produced central vortex that in turn facilitated floating solid draw-down, and yet at the same time promoting solids suspension by using the four baffles to convert rotational flow to axial flow.

Figures 3.78-3.83 shows that while the draw-down depth was the same as those produced by the narrow baffles tank, the mass fraction of air was higher in these configurations for most speeds.

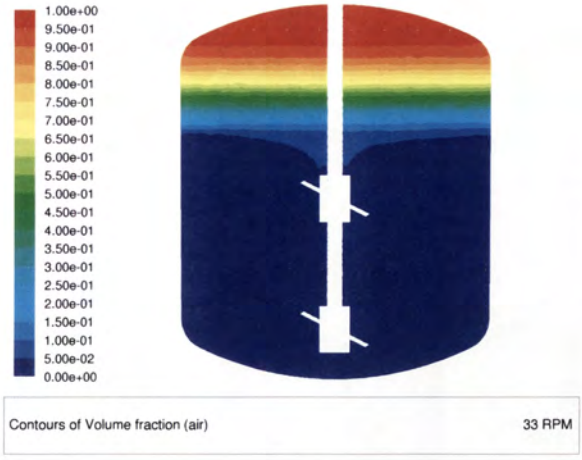


Figure 3.78: Air volume fraction at 33 rpm

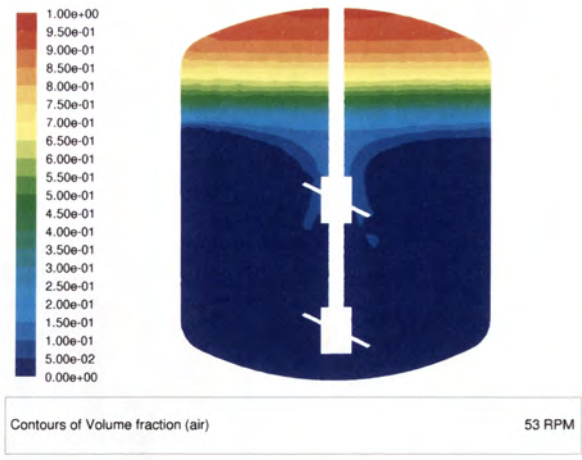


Figure 3.79: Air volume fraction at 53 rpm

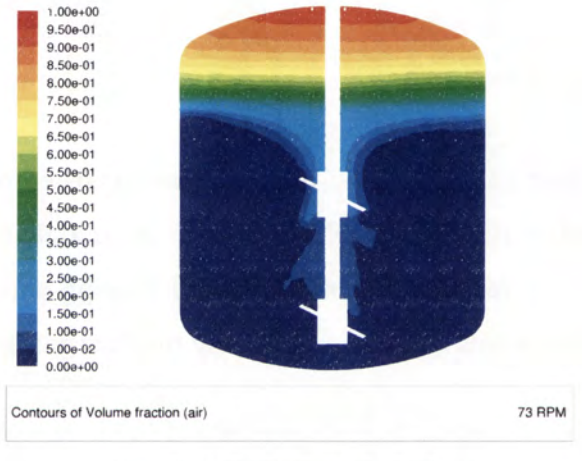


Figure 3.80: Air volume fraction at 73 rpm

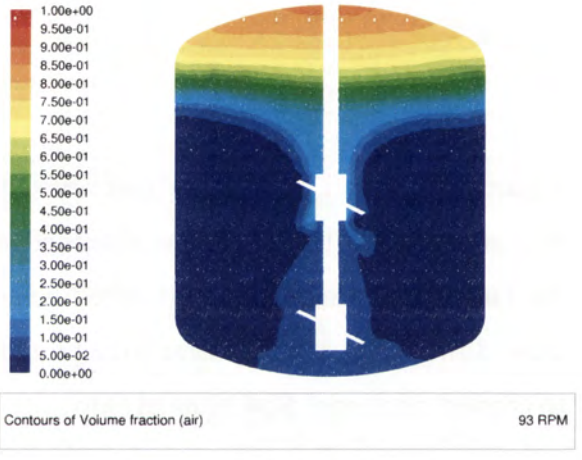


Figure 3.81: Air volume fraction at 93 rpm

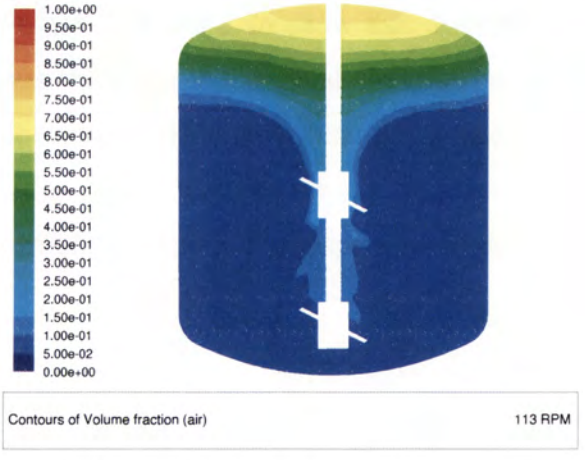


Figure 3.82: Air volume fraction at 113 rpm

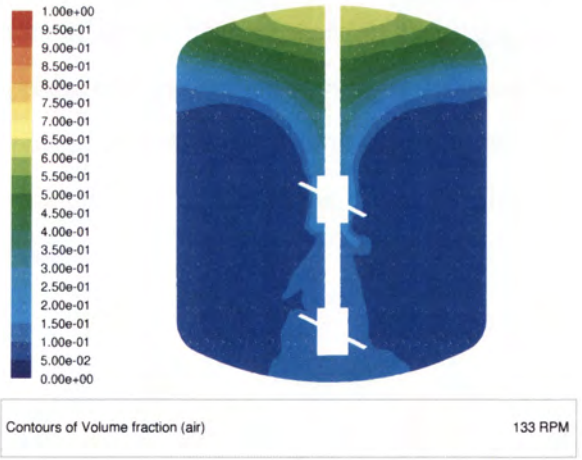


Figure 3.83: Air volume fraction at 133 rpm

Table 3.19: Comparison of liquid draw-down using different baffles configuration

| Impeller speed | Existing (%) | Narrow (%) | Partial (%) |
|---|---|---|---|
| 33 | 2.50 | 2.55 | 2.74 |
| 53 | 2.50 | 7.0 | 8.14 |
| 73 | 17.5 | 12.44 | 12.93 |
| 93 | 32.5 | 17.19 | 17.43 |
| 113 | 57.5 | 20.69 | 20.83 |
| 133 | 62.5 | 25.68 | 23.15 |

Table 3.19 shows that at 73 rpm, the percentage of air drawn down to the top impeller hub was around 17.5% for the existing nitrator and hovered around 12% for the proposed narrow-baffled and the partial-baffled tank. The table also shows that to achieve the level of draw down achieved by the existing nitrator, the speed of the proposed units must be at least 93 rpm. In brief, there was little difference in the performance between the narrow and partial baffles.

Figure 3.84 shows the plot of air volume fraction versus impeller rotational speed for various configuration systems.

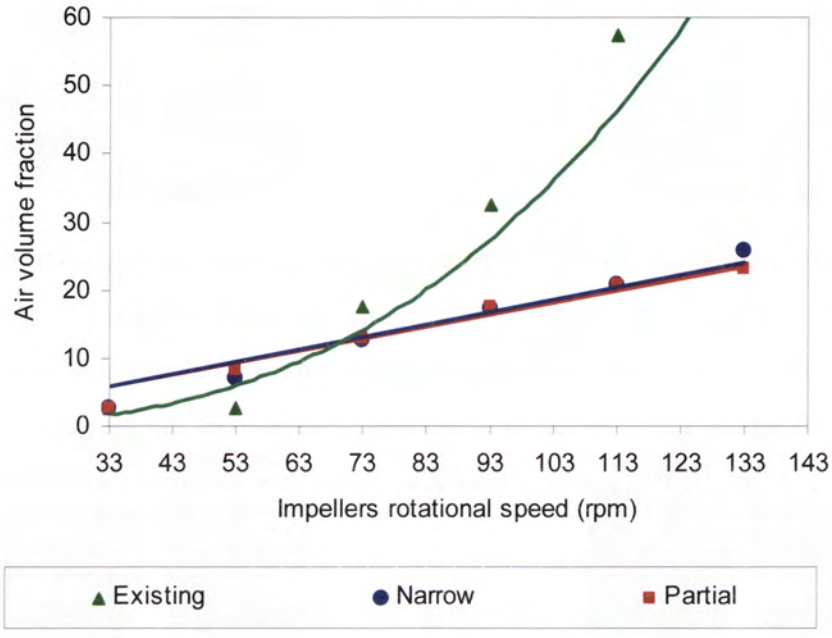


Figure 3.84: Plot of air volume fraction versus impeller speeds on different baffle configurations

Existing system, correlation fit of 0.9019:

$$VF_{air} = 0.0001N^{2.7087} \quad \text{- 3.74}$$

Narrow baffled system, correlation fit of 0.9417:

$$VF_{air} = 0.1803N \quad \text{- 3.75}$$

Partial baffled system, correlation fit of 0.9576:

$$VF_{air} = 0.1763N \quad \text{- 3.76}$$

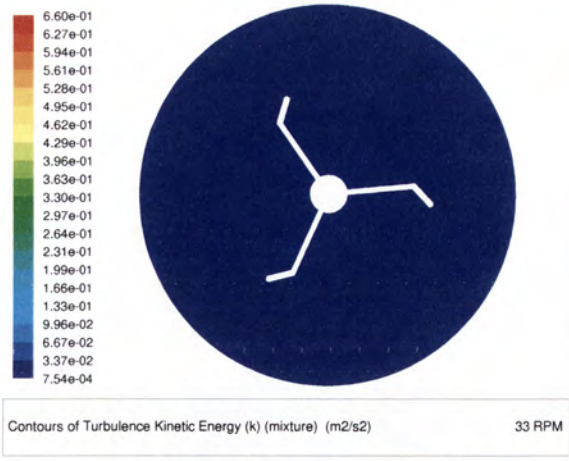


Figure 3.85: Turbulence kinetic energy at 33 rpm

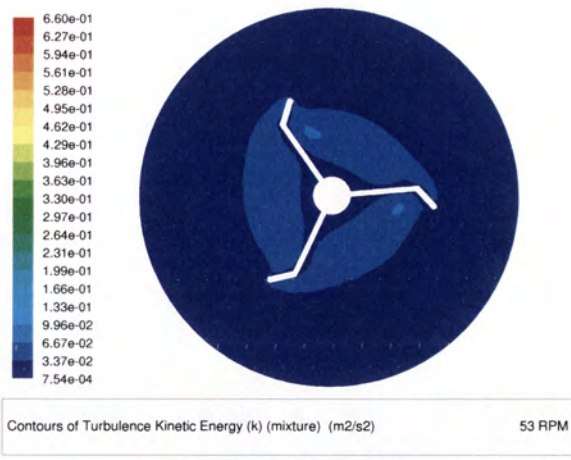


Figure 3.86: Turbulence kinetic energy at 53 rpm

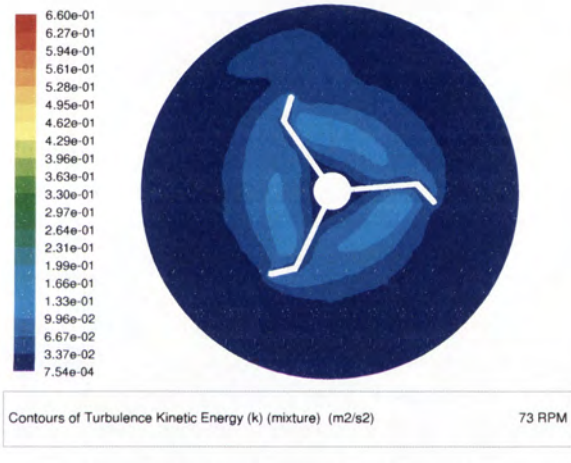


Figure 3.87: Turbulence kinetic energy at 73 rpm

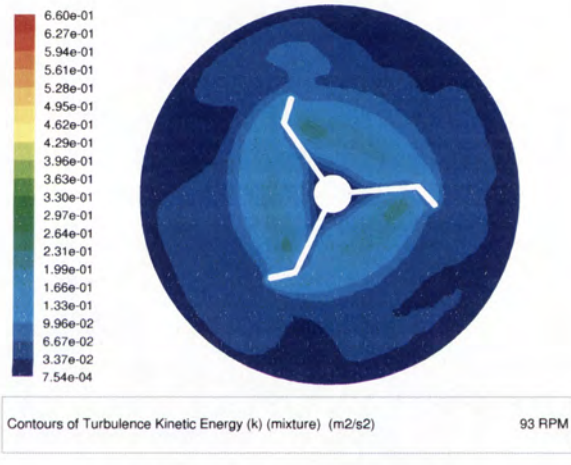


Figure 3.88: Turbulence kinetic energy at 93 rpm

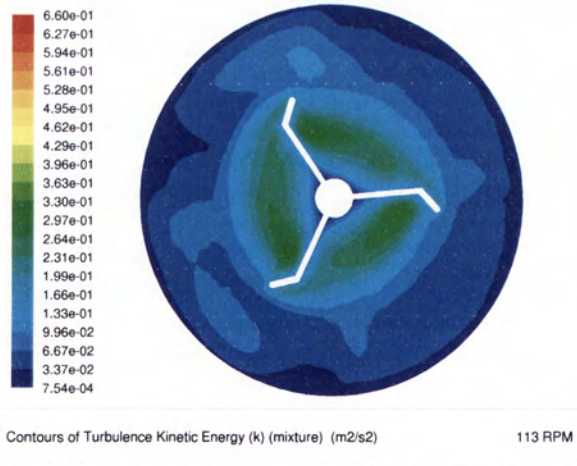


Figure 3.89: Turbulence kinetic energy at 113 rpm

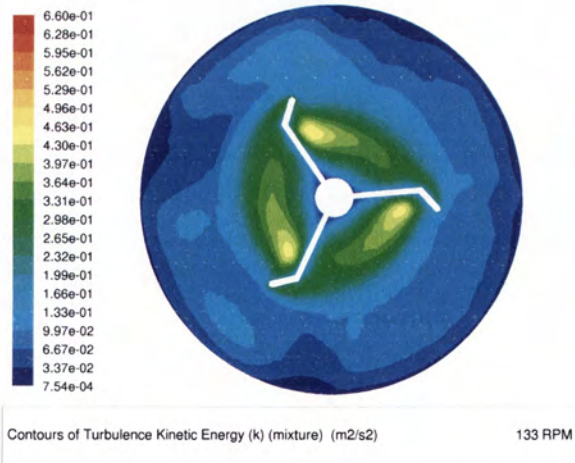


Figure 3.90: Turbulence kinetic energy at 133 rpm

The contours shown in Figures 3.85-3.90 were obtained by creating a surface at the cross-section area of the tank, located at the top impeller. It shows turbulence region was confined to impeller region. This is due to the fact that the four partial baffles also extend up to the middle of the tank. At 73 rpm, turbulence around wall region is almost absent as shown, giving rise to high rotational flow thereby creating the central vortex to incorporate floating particles. This is the underlying principle of this type of baffling configuration.

## 3.12 Implementation

### 3.12.1 Modifying existing nitrator

Figure 3.91: Fabrication of impellers

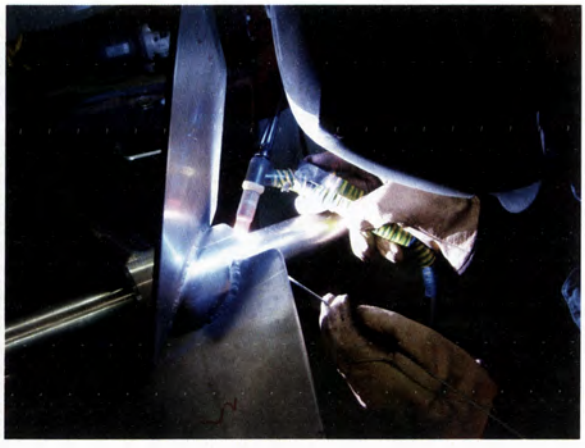

Figure 3.92: Impellers being welded to the shaft

Figure 3.93: Nitrators disassembled

Figure 3.94: Position four narrow baffles

Figure 3.95: Baffles being welded to the tank wall

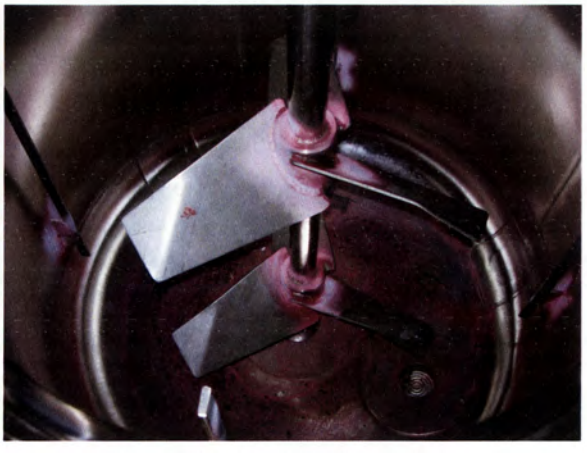

Figure 3.96: Assembling the impellers

Figures 3.91-3.96 show the stages in the modification of the existing nitrator which included fabricating the new impellers, disassembling the existing nitrator, welding the four narrow baffles onto the wall, assembling the nitrator and incorporating the new impellers.

### 3.12.2 Nitrator performance observations

From the sight glass attached to the nitrator, it was observed that solid body rotation had ceased to exist, instead, random ACB particles movement, displaying a sign of turbulence, was observed. This was because the baffles and the new impellers had converted massive swirling flow to axial flow. ACB particles were seen to traverse in the upward direction reflecting the nature of the new geometrical configuration where ACB particles were drawn down at the middle of the unit and directed upwards along the wall. In addition, a sudden stationary fluid immediately next to the sight glass, located behind one of the baffles, was noticed. This can be explained with the aid of the contour of velocity magnitude of the new geometrical nitrator. In this contour plot (Figure 3.45), wall region has very low flow relative to the previous design so at times, about 10-30mm thick of fluid will remain stagnant momentarily due to vortex shedding. This can also imply a sudden increase in load from the fluctuating ACB feed. At the point when there were extra amount of ACB fed, most of the power was consumed at the impeller region to disperse these particles. As the particles were dispersed, power distribution to the wall was restored and ACB particles resumed moving. This means that the geometrical configuration could be operating at the edge of its mixing capability, therefore, a slightly higher rotational speed will ease this shortcoming.

On the first production run, a decomposition of the ACB occurred which indicated that the draw-down might not have been quick enough to prevent this from occurring. In addition, running the proposed impellers at existing speed of 73 rpm caused a higher than normal amount of ACB particles being trapped in the extraction duct which clogged it and posed safety issue. From the plot of air volume versus impeller speed, the previous design has better floating objects draw-down ability than the existing design by about 3%. Increasing impellers rotational speed to 87 rpm will increase the draw-down ability of the proposed design. No decomposition of the ACB was observed at 87 rpm which means this was the minimum speed on the proposed design required to draw-down the particles. However, a

higher speed than 87 rpm was recommended to further increase the rate of draw-down so that the ACB will not remain above the liquid free surface long enough to be caught in the extraction duct.

From Figure 3.84, it can be seen that to match the draw-down ability of the previous design, the impellers on the proposed design must rotate at least 93 rpm. Laboratory analysis on the NC indicated that it has a $\%N_2$ value lower than the minimum specification limit. These newly designed impellers were the prime suspect and the impellers were immediately removed and the old impellers reinstated. However, even after the previous impellers were reinstated, laboratory analysis still indicated an out-of-specification value. It was later discovered that the ACB used, supplied from another supplier, caused this problem because when the paper supplied by the existing supplier was used, the $\%N_2$ was within the specification value but as soon as they were switched to the paper supplied by the new supplier, the $\%N_2$ dropped and fell outside the lower specification limit. Finally, it was felt that the proposed nitrator performed as designed but an impellers rotational speed of 93 rpm was recommended to match the rate of ACB draw-down.

## 3.13 Concluding remarks

This chapter encompassed the modelling and simulation on the nitrator currently used to manufacture NC. NC, classified as a secondary explosive, is the basis of most artillery, tank, mortar, and small rocket propellants. NC was relatively insensitive, and in most cases required a detonator to explode. NC manufacturing process description, aided by a process flow diagram was included to give the modelling of this nitrator a sense of perspective. The objectives of this chapter were firstly to provide detailed characterisation of the nitrator, followed by a recommendation to optimise the nitrator performance. Volume of fluid (VOF) multiphase approach was explained and applied to model the drawdown of air into the bulk mixture inside the nitrator. In addition, the type of turbulence models and boundary layer treatment adopted were also explained.

An experimental study (section 3.6) was devoted to the validation of CFD results using particle image velocity (PIV). PIV results showed that experimental and numerical results showed good agreement. PIV-validated quantitative and qualitative results uncovering valuable unknown information were presented. For the quantitative characterisation, the power number, flow number, flow efficiency, blending time and deviation from ideality were presented. For the qualitative characterisation, the turbulence kinetic energy profile, turbulence dissipation rate, velocity magnitude profile and air draw-down were presented. This study showed that the geometrical configuration of the existing nitrator was not effective in promoting effective mass transfer, thus, from the work covered in this chapter, a more effective nitrator was proposed. Finally, a preliminary implementation was conducted to test the impellers recommended but the test had to be stopped because a crucial raw material (ACB) that meets in-coming product specifications was unvailable. Thus, until such raw material is available, the implementation could not be continued.

# CHAPTER 4: SUSPENSION MIXING TANK

In the process industry, suspension of particles denser than its fluid media is one of the most common and important goal to be achieved. Achieving complete suspension of the particles leads to homogeneous suspension while achieving partial success leads to inhomogeneity and eventually product quality issues. In spite of the industrial relevance of this operation, especially in high explosive manufacturing facilities, the impact on the performance of the suspension mixing tank through changing several crucial variables had received little research attention. Moreover, in many instances, the design of a mixing tank for suspending particles was largely based on empirical data. Consequently, operators had to work with sub-optimum process conditions which inevitably led to poor product quality, consistency and yield.

Significant improvements in the design capability and reliability of suspension mixing tank may be expected from advances in CFD simulation technology. Hitherto, CFD offers a cost-effective means of capturing the hydrodynamic phenomena and the ability to quantify the performance of a suspension mixing tank [Sommerfeld and Decker 2004]. The results of this study are applicable across the broad spectrum of the manufacturing study. For example, not only can the results of this study be applied to the manufacture of high explosives and bombs, it can also be applied across a broad range of industries such as but not limited to the chemical, bioprocess, pharmaceutical, petrochemical and mineral processing industries. Despite the broad applicability of these results, they are only applicable to popular cylindrical suspension mixing tank and do not apply to square mixing tanks [Kresta et al. 2006 and Kilander et al. 2007].

## 4.1 Objective of research

Ten crucial variables that have profound effect on the ability of a mixing tank to suspend particles were investigated, namely: [1] shaft to impeller diameter (*d/D*), [2] blade width to impeller diameter (*W/D*), [3] impeller to tank diameter (*D/T*), [4] number of blades ($N_B$), [5] impeller clearance to tank diameter ratio (*C/T*), [6] impeller rotational speed (*N*), [7] baffle width to tank diameter ratio (*B/T*) and [8] baffle off-wall spacing to tank diameter ratio (*b/T*), [9] number of baffles ($N_{BF}$) and [10] number of impellers ($N_I$). Overall, these ten variables constitute the crucial parameters that govern the success of a given geometrical configuration in suspending particles. The impeller employed was a standard 6-bladed 45° pitch blade turbine. The quantitative performance of each trial condition was captured via surface integration of the plane where the flow passed through. Integrated values were plotted as a function of each variable [Lea et al. 2007].

*The aim of this chapter was to provide a design approach based on the fundamental equations governing the hydrodynamics of multiphase solid-liquid system. This was achieved using computational fluid dynamic investigation of the effect of the key variables on mixing performance.*

The trial conditions for all ten variables are shown in Table 4.1.

Table 4.1: One-factor-at-a-time trial conditions and results

| Trials | $d/D$ | $W/D$ | $D/T$ | $N_B$ | $C/T$ | $N$ | $B/T$ | $b/T$ | $N_{BF}$ | $N_I$ | $\dot{m}$ | $P$ |
|---|---|---|---|---|---|---|---|---|---|---|---|---|
| 1 | 0.080 | 0.23 | 0.5 | 6 | 0.76 | 80 | 0.071 | 0.0187 | 4 | 1 | **1,251** | **5,858** |
| 2 | 0.094 | 0.23 | 0.5 | 6 | 0.76 | 80 | 0.071 | 0.0187 | 4 | 1 | **1,245** | **5,800** |
| 3 | 0.131 | 0.23 | 0.5 | 6 | 0.76 | 80 | 0.071 | 0.0187 | 4 | 1 | **1,238** | **5,741** |
| 4 | 0.169 | 0.23 | 0.5 | 6 | 0.76 | 80 | 0.071 | 0.0187 | 4 | 1 | **1,229** | **5,683** |
| 5 | 0.200 | 0.23 | 0.5 | 6 | 0.76 | 80 | 0.071 | 0.0187 | 4 | 1 | **1,225** | **5,624** |
| 6 | 0.08 | 0.1 | 0.5 | 6 | 0.76 | 80 | 0.071 | 0.0187 | 4 | 1 | **943** | **3,398** |
| 7 | 0.08 | 0.3 | 0.5 | 6 | 0.76 | 80 | 0.071 | 0.0187 | 4 | 1 | **1,328** | **6,796** |
| 8 | 0.08 | 0.4 | 0.5 | 6 | 0.76 | 80 | 0.071 | 0.0187 | 4 | 1 | **1,401** | **8,143** |
| 9 | 0.08 | 0.5 | 0.5 | 6 | 0.76 | 80 | 0.071 | 0.0187 | 4 | 1 | **1,455** | **9,608** |
| 10 | 0.08 | 0.7 | 0.5 | 6 | 0.76 | 80 | 0.071 | 0.0187 | 4 | 1 | **1,496** | **12,712** |
| 11 | 0.08 | 0.25 m | 0.15 | 6 | 0.76 | 80 | 0.071 | 0.0187 | 4 | 1 | **4.042** | **26.50** |
| 12 | 0.08 | 0.25 m | 0.30 | 6 | 0.76 | 80 | 0.071 | 0.0187 | 4 | 1 | **488** | **586** |
| 13 | 0.08 | 0.25 m | 0.35 | 6 | 0.76 | 80 | 0.071 | 0.0187 | 4 | 1 | **651** | **1,172** |
| 14 | 0.08 | 0.25 m | 0.40 | 6 | 0.76 | 80 | 0.071 | 0.0187 | 4 | 1 | **866** | **2,109** |
| 15 | 0.08 | 0.25 m | 0.55 | 6 | 0.76 | 80 | 0.071 | 0.0187 | 4 | 1 | **1,255** | **9,432** |
| 16 | 0.08 | 0.25 m | 0.60 | 6 | 0.76 | 80 | 0.071 | 0.0187 | 4 | 1 | **1,150** | **14,821** |
| 17 | 0.08 | 0.25 m | 0.70 | 6 | 0.76 | 80 | 0.071 | 0.0187 | 4 | 1 | **861** | **28,845** |
| 18 | 0.08 | 0.23 | 0.5 | 0 | 0.76 | 80 | 0.071 | 0.0187 | 4 | 1 | **0** | **202** |
| 19 | 0.08 | 0.23 | 0.5 | 2 | 0.76 | 80 | 0.071 | 0.0187 | 4 | 1 | **991** | **2,519** |
| 20 | 0.08 | 0.23 | 0.5 | 3 | 0.76 | 80 | 0.071 | 0.0187 | 4 | 1 | **1,105** | **3,398** |
| 21 | 0.08 | 0.23 | 0.5 | 4 | 0.76 | 80 | 0.071 | 0.0187 | 4 | 1 | **1,160** | **4,394** |
| 22 | 0.08 | 0.23 | 0.5 | 8 | 0.76 | 80 | 0.071 | 0.0187 | 4 | 1 | **1,257** | **6,913** |
| 23 | 0.08 | 0.23 | 0.5 | 6 | 0.15 | 80 | 0.071 | 0.0187 | 4 | 1 | **1,170** | **7,206** |
| 24 | 0.08 | 0.23 | 0.5 | 6 | 0.20 | 80 | 0.071 | 0.0187 | 4 | 1 | **1,215** | **6342** |
| 25 | 0.08 | 0.23 | 0.5 | 6 | 0.30 | 80 | 0.071 | 0.0187 | 4 | 1 | **1,272** | **5,331** |
| 26 | 0.08 | 0.23 | 0.5 | 6 | 0.4 | 80 | 0.071 | 0.0187 | 4 | 1 | **1,284** | **5,335** |
| 27 | 0.08 | 0.23 | 0.5 | 6 | 0.50 | 80 | 0.071 | 0.0187 | 4 | 1 | **1,280** | **5,565** |
| 28 | 0.08 | 0.23 | 0.5 | 6 | 0.60 | 80 | 0.071 | 0.0187 | 4 | 1 | **1,271** | **5,858** |
| 29 | 0.08 | 0.23 | 0.5 | 6 | 0.68 | 80 | 0.071 | 0.0187 | 4 | 1 | **1,260** | **5,855** |
| 30 | 0.08 | 0.23 | 0.5 | 6 | 0.76 | 20 | 0.071 | 0.0187 | 4 | 1 | **312** | **88** |
| 31 | 0.08 | 0.23 | 0.5 | 6 | 0.76 | 100 | 0.071 | 0.0187 | 4 | 1 | **1,565** | **11,424** |
| 32 | 0.08 | 0.23 | 0.5 | 6 | 0.76 | 120 | 0.071 | 0.0187 | 4 | 1 | **1,878** | **19,772** |
| 33 | 0.08 | 0.23 | 0.5 | 6 | 0.76 | 140 | 0.071 | 0.0187 | 4 | 1 | **2,191** | **31,474** |
| 34 | 0.08 | 0.23 | 0.5 | 6 | 0.76 | 80 | 0.063 | 0.0187 | 4 | 1 | **1,215** | **5,725** |
| 35 | 0.08 | 0.23 | 0.5 | 6 | 0.76 | 80 | 0.083 | 0.0187 | 4 | 1 | **1,273** | **6,173** |
| 36 | 0.08 | 0.23 | 0.5 | 6 | 0.76 | 80 | 0.100 | 0.0187 | 4 | 1 | **1,298** | **6,371** |
| 37 | 0.08 | 0.23 | 0.5 | 6 | 0.76 | 80 | 0.110 | 0.0187 | 4 | 1 | **1,300** | **6,420** |
| 38 | 0.08 | 0.23 | 0.5 | 6 | 0.76 | 80 | 0.115 | 0.0187 | 4 | 1 | **1,292** | **6,390** |
| 39 | 0.08 | 0.23 | 0.5 | 6 | 0.76 | 80 | 0.125 | 0.0187 | 4 | 1 | **1,266** | **6,348** |
| 40 | 0.08 | 0.23 | 0.5 | 6 | 0.76 | 80 | 0.071 | 0.0167 | 4 | 1 | **1,249** | **5,858** |
| 41 | 0.08 | 0.23 | 0.5 | 6 | 0.76 | 80 | 0.071 | 0.0250 | 4 | 1 | **1,252** | **5,893** |
| 42 | 0.08 | 0.23 | 0.5 | 6 | 0.76 | 80 | 0.071 | 0.0350 | 4 | 1 | **1256** | **5,917** |
| 43 | 0.08 | 0.23 | 0.5 | 6 | 0.76 | 80 | 0.071 | 0.0500 | 4 | 1 | **1,247** | **5,917** |
| 44 | 0.08 | 0.23 | 0.5 | 6 | 0.76 | 80 | 0.071 | 0.0750 | 4 | 1 | **1,211** | **5,800** |
| 45 | 0.08 | 0.23 | 0.5 | 6 | 0.76 | 80 | 0.071 | 0.0900 | 4 | 1 | **1,197** | **5,741** |
| 46 | 0.08 | 0.23 | 0.5 | 6 | 0.76 | 80 | 0.071 | 0.1000 | 4 | 1 | **1,193** | **5,683** |
| 47 | 0.08 | 0.23 | 0.5 | 6 | 0.76 | 80 | 0.071 | 0.0187 | 0 | 1 | **903** | **5,003** |
| 48 | 0.08 | 0.23 | 0.5 | 6 | 0.76 | 80 | 0.071 | 0.0187 | 2 | 1 | **1,094** | **5,414** |
| 49 | 0.08 | 0.23 | 0.5 | 6 | 0.76 | 80 | 0.071 | 0.0187 | 3 | 1 | **1,189** | **5,598** |
| 50 | 0.08 | 0.23 | 0.5 | 6 | 0.76 | 80 | 0.071 | 0.0187 | 5 | 1 | **1,290** | **6,110** |
| 51 | 0.08 | 0.23 | 0.5 | 6 | 0.76 | 80 | 0.071 | 0.0187 | 6 | 1 | **1,313** | **6,261** |
| 52 | 0.08 | 0.23 | 0.5 | 6 | 0.76 | 80 | 0.071 | 0.0187 | 12 | 1 | **1,399** | **7,342** |
| 53 | 0.08 | 0.23 | 0.5 | 6 | 0.76 | 80 | 0.071 | 0.0187 | 20 | 1 | **1,438** | **7,543** |
| 54 | 0.08 | 0.23 | 0.5 | 6 | 0.76 | 80 | 0.071 | 0.0187 | 4 | 0 | **0** | **200** |
| 55 | 0.08 | 0.23 | 0.5 | 6 | 0.76 | 80 | 0.071 | 0.0187 | 4 | 2 | **1,295** | **5,858** |
| 56 | 0.08 | 0.23 | 0.5 | 6 | 0.76 | 80 | 0.071 | 0.0187 | 4 | 3 | **1,323** | **8,498** |
| 57 | 0.08 | 0.23 | 0.5 | 6 | 0.76 | 80 | 0.071 | 0.0187 | 4 | 4 | **1,346** | **10,761** |
| 58 | 0.08 | 0.23 | 0.5 | 6 | 0.76 | 80 | 0.071 | 0.0187 | 4 | 5 | **1,360** | **12,303** |

where

$d/D$ : shaft diameter to impeller diameter ratio

$W/D$ : blade width to impeller diameter ratio

$D/T$ : impeller diameter to tank diameter ratio

$N_B$ : number of blades in the impeller

$C/T$ : impeller bottom clearance

$N$ : impeller rotational speed, rpm

$B/T$ : baffle width to tank diameter ratio

$b/T$ : baffle spacing to tank diameter ratio

$N_{BF}$ : number of baffles

$N_I$ : number of impellers

$\dot{m}$ : mass flowrate across plane, kg $s^{-1}$

$P$ : power consumed, W

## 4.2 Key performance indicator

A horizontal plane across the impeller was created so that surface integration can be conducted to determine the axial flow passing through the impeller (Figure 4.1). Because of such arrangement, the computation excluded the radial flow component. The amount of axial flow generated is the key performance indicator (KPI) and is compared from one variable to another [Lea et al. 2007].

Figure 4.1: Key performance indicator

## 4.3 Grid independence test

Grid independence tests were carried out on trials 1 and 14. For trial 1, the results show that at 447,495 cells, the mass flowrate was 1,251 kg $s^{-1}$ while at 639,693 cells, the mass flowrate was 1,255 kg $s^{-1}$. In other words, an increase in 42.95% in the number of cells will change the mass flowrate value by 0.3197%. For trial 14, the results show that at 467,436 cells the mass flowrate was 1,255 kg $s^{-1}$ and at 646,744 cells, the mass flowrate was 1,259 kg $s^{-1}$. This translates into a 0.3187% increase for an increase of 38.36% in the number of cells. These grid independence tests show that the economical number of cells suitable for this variable study is anything between 400,000 and 500,000, which will not compromise the results integrity. Figure 4.2 shows a typical geometry meshed with tetrahedral cells.

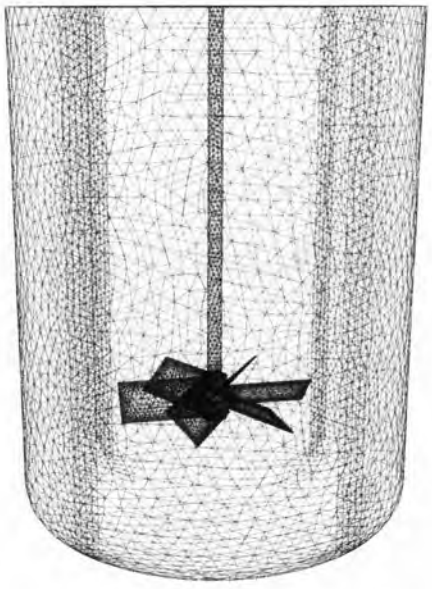

Figure 4.2: Meshed suspension mixing tank geometry

## 4.4 Discussion on crucial variables

### 4.4.1 Shaft diameter to impeller diameter ratio

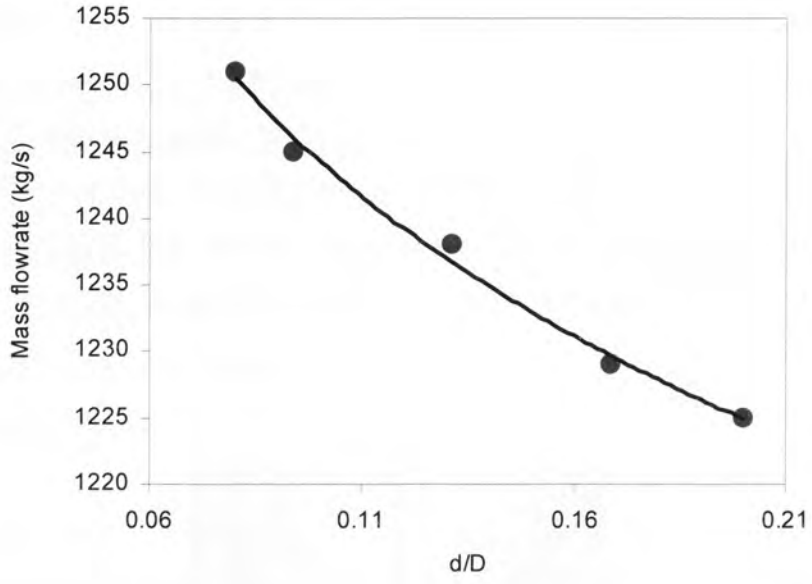


Figure 4.3: Mass flowrate vs d/D

Figure 4.3 shows a power relationship between the mass flowrate of flow passing through the plane and the shaft diameter to impeller diameter ratio. It is obvious that *d/D* is inversely proportional to the mass flowrate and follows a power function with a good regression of 0.9923, in the form:

$$\dot{m} = 1181\left(\frac{d}{D}\right)^{-0.0226} \qquad \text{- 4.1}$$

A 150% increment in *d/D* will reduce the mass flowrate of fluid passing through the plane by 2.0%. That is, a 1% increase in *d/D* will decrease the flowrate by 0.01333%.

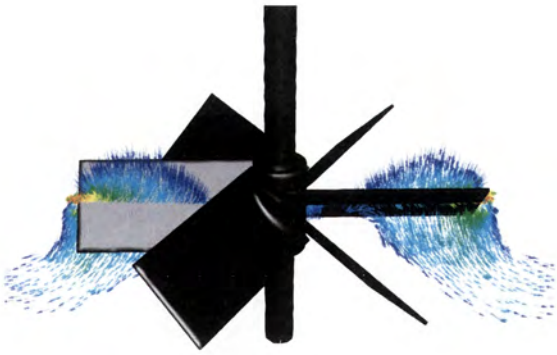

Figure 4.4: Vector plot of d/D = 0.08

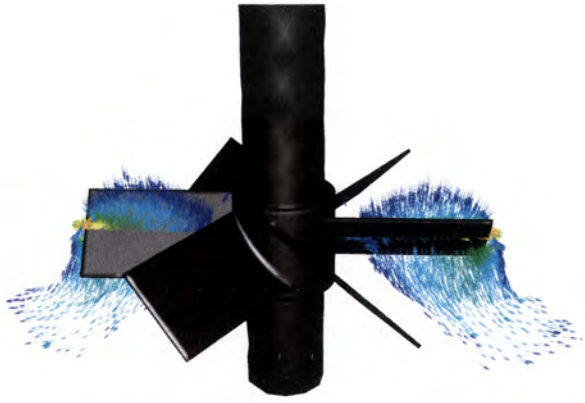

Figure 4.5: Vector plot of d/D = 0.2

Figure 4.4 and 4.5 shows that although the shaft diameter has been increased by 150%, the flow profile remains the same. The slight reduction in the mass flowrate when the shaft diameter was increased gradually was attributed to the high flow discharge being located at the blade tip and low flow discharge in the vicinity of the shaft hub.

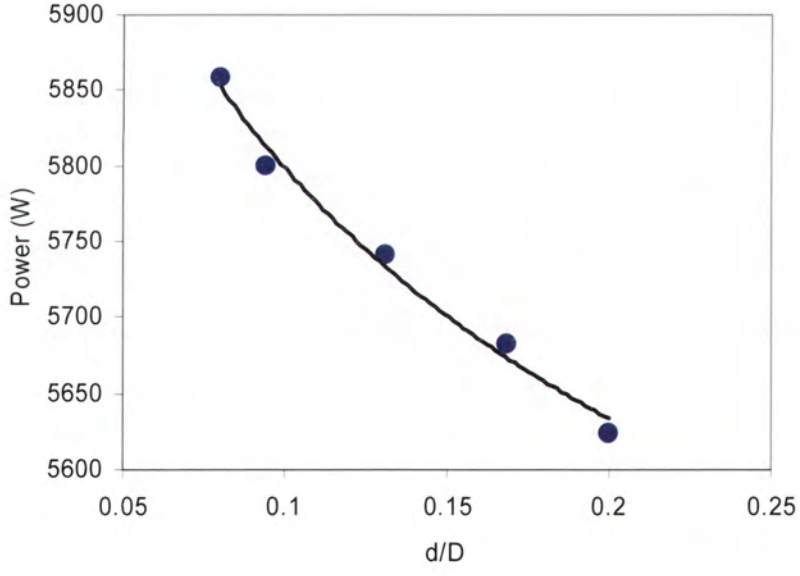


Figure 4.6: Power consumed in kilowatts vs d/D

The power consumption in kilowatts as a function of shaft diameter to impeller diameter ratio, as shown in Figure 4.6, follows a power relationship with good regression of 0.9867, in the form:

$$P = 5268\left(\frac{d}{D}\right)^{-0.0416} \qquad \text{- 4.2}$$

An increase in *d/D* from 0.08 to 0.2 reduced the power consumption by only 3.742%. That is, for every 1% increment in *d/D*, the power consumption will reduce by 2.5%. From a practical perspective, it is more beneficial to minimise the shaft diameter without compromising the minimum shaft diameter and maximise the blade length within a given impeller diameter.

### 4.4.2 Blade width to impeller diameter ratio

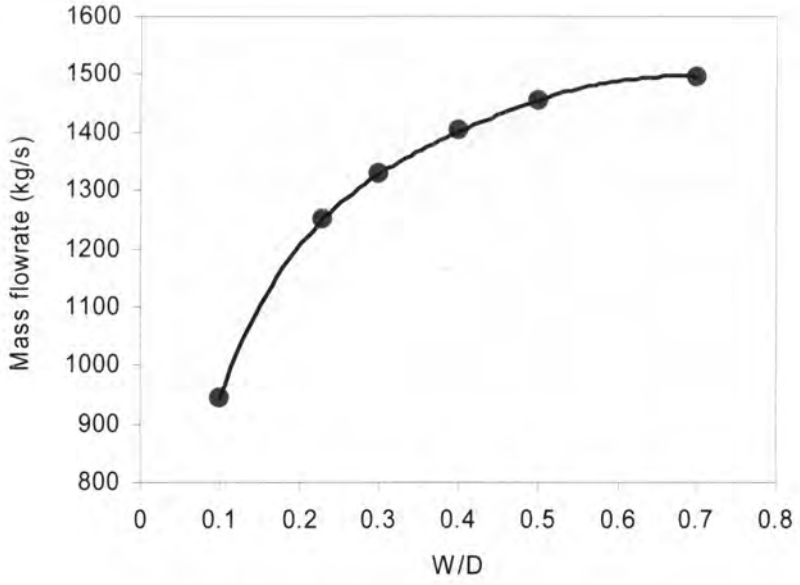


Figure 4.7: Mass flowrate vs W/D

Figure 4.7 shows the relationship between the mass flowrate and the blade width to impeller diameter ratio.

The behaviour is described by the model:

$$\dot{m} = \frac{a\left(\frac{W}{D}\right)}{1 + b\left(\frac{W}{D}\right)} \qquad \text{- 4.3}$$

$\dot{m}$ represented mass flowrate and *W/D* represented the blade width to impeller diameter ratio.

Data regression to Equation (4.3) yielded $a$=20,000 kg $s^{-1}$ and $b$=12 with an excellent correlation fit of 1.

When *W/D* was increased by 200% from 0.1 - 0.3, the increase in flowrate was 43.44%, that is, a 1% increase in *W/D* increased the flowrate by 0.2172%.

When *W/D* was increased by 25% from 0.4 - 0.5, the increase in flowrate was only 3.595%, that is, a 1% increase in *W/D* increased the flowrate by 0.1438%.

Beyond this range, the percentage increase in the axial flowrate decreased as the graph levelled. A 400% increase in *W/D* from 0.5 - 0.7, resulted in an increase of 4.199%, that is, a 1% increase in *W/D* increased the flowrate by a 0.01050%

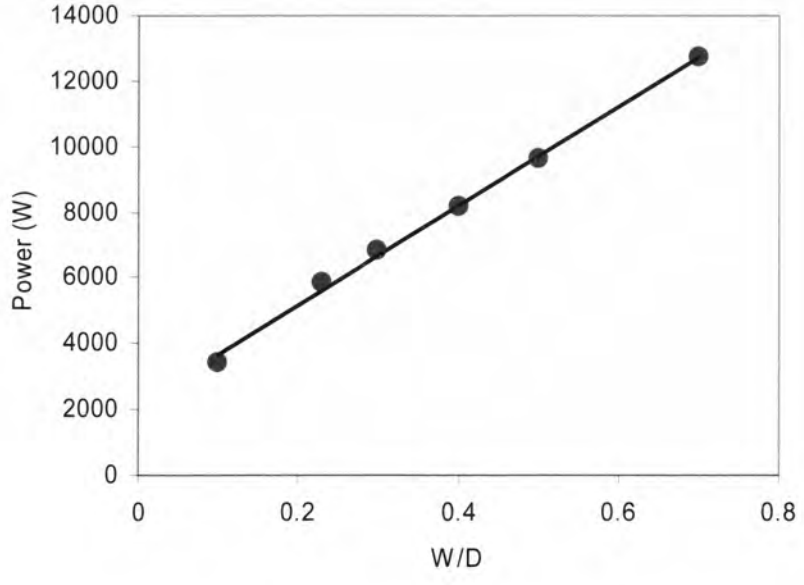


Figure 4.8: Power consumed in kilowatts vs W/D

The power consumption as a function of the blade width to impeller diameter ratio, as shown in Figure 4.8, has a linear relationship, with a good regression of 0.9972. The expression is given by:

$$P = 15162\left(\frac{W}{D}\right) + 2117 \qquad \text{- 4.4}$$

Equation (4.4) shows that a 1% increase in *W/D* will increase the power consumption by 0.5890%.

Every time the blade width is increased, there will be an increase in the power consumption [Kumaresan and Joshi 2006]. However, beyond *W/D*=0.3, a higher blade width aspect ratio does not render economic feasibility, while below *W/D*=0.1, the flowrate generated may not be sufficient to suspend the particles. Therefore, the optimum performance is $0.1 \leq W/D \leq 0.3$.

### 4.4.3 Impeller diameter to tank diameter ratio

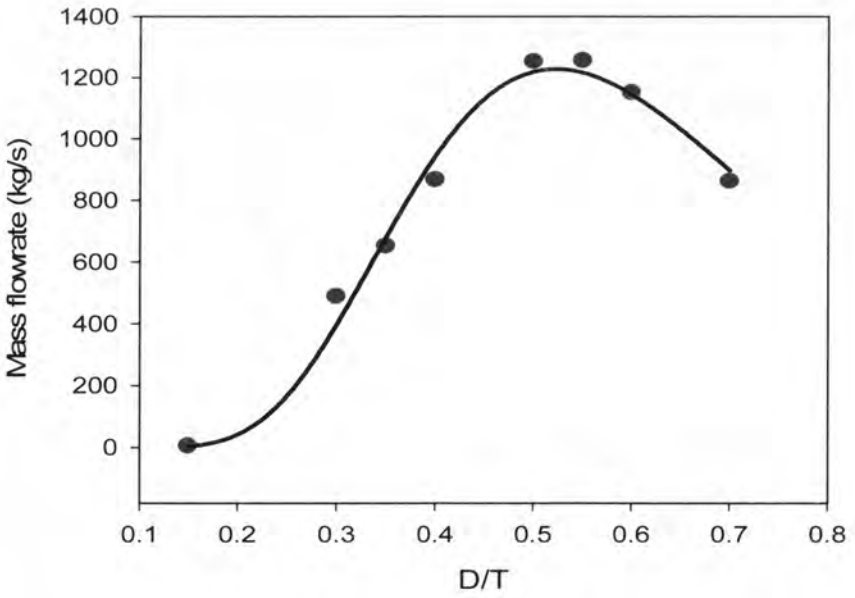


Figure 4.9: Mass flowrate vs *D/T*

Figure 4.9 shows the relationship between the mass flowrate and the impeller diameter to tank diameter ratio and is governed by the following quadratic expression, with a good regression value of 0.9901:

$$\dot{m} = ae^{\left[-0.5\left(\ln\left(\frac{(D/T)}{x_0}\right)/b\right)^2\right]} \qquad \text{- 4.5}$$

Conducting a non-linear regression on Equation (4.5), yielded $a$=1,228 kg $s^{-1}$, $b$=0.3693, $x_0$=0.5226 with excellent regression of R=0.9925.

For maximum values,

$$\frac{dm}{d(D/T)} = -\frac{a}{b^2}\ln\left(\frac{D/T}{x_0}\right)e^{\left\{-\frac{0.5}{b^2}\left[\ln\left(\frac{D/T}{x_0}\right)\right]^2\right\}} = 0 \qquad \text{- 4.6}$$

The maximum value was located at $D/T$ = 0.5226

Increasing the $D/T$ ratio from 0.15 - 0.55 increased the mass flowrate however, increasing the $D/T$ value beyond the maximum value caused a reduction in the mass flowrate.

Between $D/T$ = 0.3 - 0.4 (33% increment), the increase in mass flowrate was 138.1%, between $D/T$ = 0.4 - 0.55 (37.50% increment), the increase was 28.69% and between $D/T$ = 0.55 - 0.6 (9.09% increment), the reduction in flowrate was 5.839%. Between $D/T$ = 0.6 – 0.7 (16.67% increment), there was a sharp decrease in mass flowrate by 21.59%. Thus, for optimum performance: $0.5 \leq D/T \leq 0.55$. This result agrees with those prescribed by Tatterson [1994] and Paul et al. [2004].

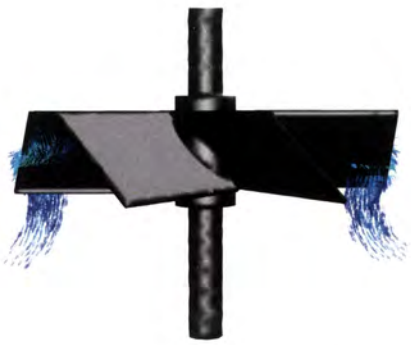

Figure 4.10: Vector plot of $D/T = 0.4$

Figure 4.11: Vector plot of $D/T = 0.55$

The reduction in the mass flowrate when the $D/T$ ratio was increased to value beyond the maximum value, was attributed to the change in the flow profile discharged by the impellers. Figure 4.10 shows that at $D/T = 0.4$, the flow discharge was axial in nature but when $D/T = 0.55$, the flow changed from axial flow to radial flow as shown by the vector plot in Figure 4.11. Obviously, the amount of fluid that passed through the horizontal plane decreased per unit time.

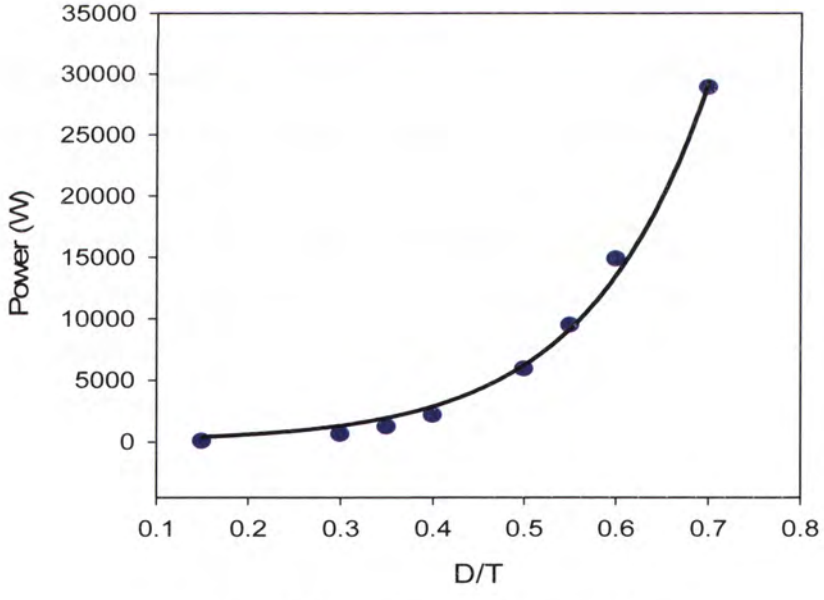


Figure 4.12: Power consumed in kilowatts vs $D/T$

Figure 4.12 shows the power consumed in kilowatts when $D/T$ was increased from 0.15 to 0.7. The plot follows an exponential relationship with a good regression of 0.9971 in the form:

$$P = 130e^{7.74\left(\frac{D}{T}\right)} \quad \text{- 4.7}$$

Between $D/T$ = 0.3 - 0.4, the increase in power consumption was 116.9%, between $D/T$ = 0.4 - 0.55, the increased power consumption was 219.3% and between $D/T$ = 0.55 - 0.6, the increased in power consumption was 47.24%. Finally, from $D/T$ = 0.6 – 0.7, the increase in power consumption was 116.8%. Thus, increasing $D/T$ is always accompanied by the increase in power consumption [Kumaresan and Joshi 2006].

From the mass flowrate and power consumption analyses, it was observed that between $D/T$ = 0.4 - 0.55, there was a huge power consumption increment because this was the effective range to deliver massive flow in the axial direction.

### 4.4.4 Number of blades in the impeller

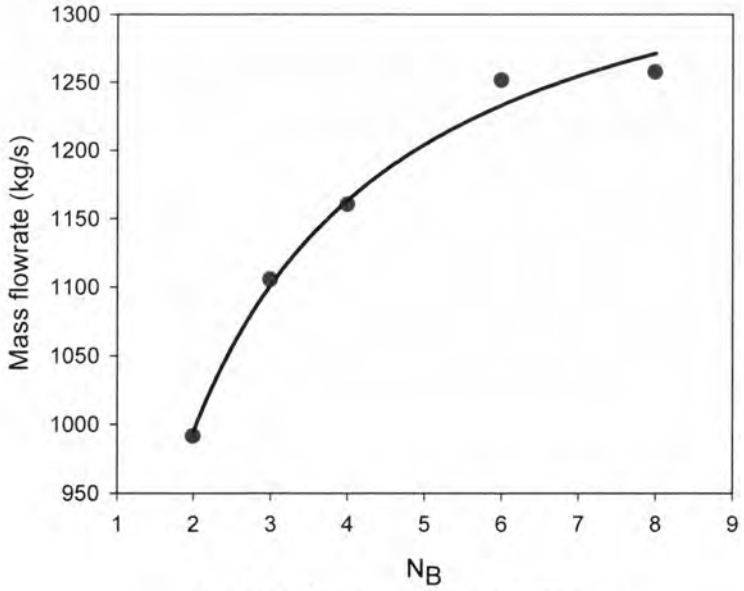


Figure 4.13: Mass flowrate vs number of blades

Figure 4.13 shows the relationship between the mass flowrate and the impeller diameter to tank diameter ratio and is governed by the following model:

$$\dot{m} = \frac{aN_B}{1 + bN_B} \qquad -4.8$$

where $\dot{m}$ represents mass flowrate and $N_B$ represents the number of blades. Data regression to Equation (4.8) yielded $a$=1,717 kg $s^{-1}$ and $b$=1.226 with an excellent correlation fit of 0.9943. The increase in mass flowrate when the number of blades was increased from 2 to 3 blades was 10.65%, from 3 to 4 blades was 5.631%, from 4 to 6 was 6.019% and from 6 to 8 blades was 3.082% [Kumaresan and Joshi 2006]. Increasing the number of blades from 6 to 8 did not return a significantly higher mass flowrate value.

The advantage of using a 6-bladed impeller is that it delivers more axial flow per unit time, attainable at a lower impeller rotational speed. In contrast, to produce the same amount of axial flow per unit time, the speed required from a 4-bladed impeller is higher. This is important for processes where a lower impeller rotational speed is needed, yet a high axial flow is desired to meet the process objective.

Despite such an advantage, the use of a 6-bladed impeller requires a thicker shaft, which means in some plants, may involve overhauling the entire mixing tank rather than simply swapping existing impeller with a 6-bladed impeller.

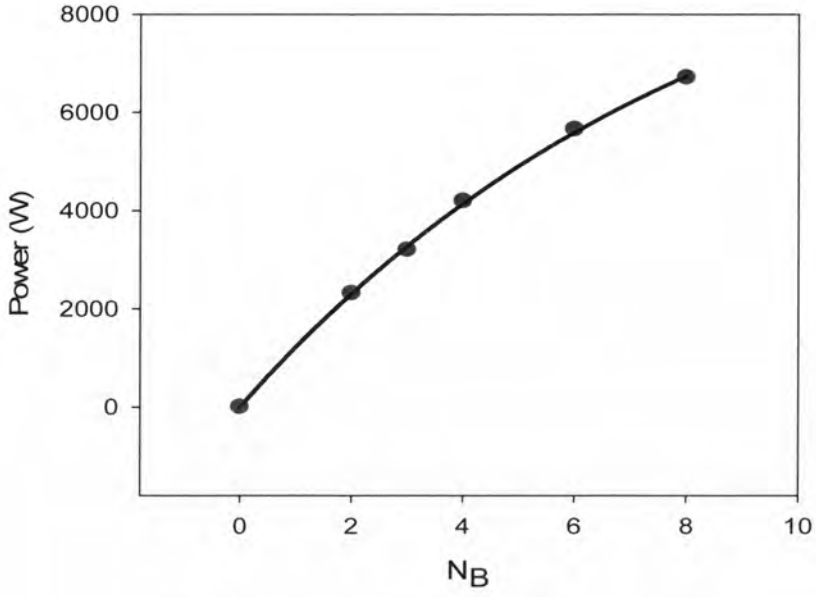


Figure 4.14: Power consumed in kilowatts vs number of blades

The power consumed as a function of the number of blades, shown in Figure 4.14, can be represented by the correlation with good regression of 0.9998, in the form:

$$P = P_0 + a\left(1 - e^{-b(N_B)}\right) \qquad \text{- 4.9}$$

$P$ is the power consumed in W, whereas $P_0$=202 W and is the power consumed when there are no blades on the impeller, that is, no impeller on the shaft. A non-linear regression analysis on Equation (4.9) yielded $a$=11,134 W, $b$=0.1164.

Increasing from 4 to 6 blades will increase the power consumption by 33.38% and 16.35% from 6 to 8 blades [Kumaresan and Joshi 2006].

In addition to the advantages and disadvantages of using 6-bladed impeller outlined above, the use of 6-bladed impeller will increase the power consumption as well. Therefore, the use of either 4 or 6-bladed impeller is dependent on the plant situation and can only be prescribed on a case-by-case basis.

### 4.4.5 Impeller bottom clearance

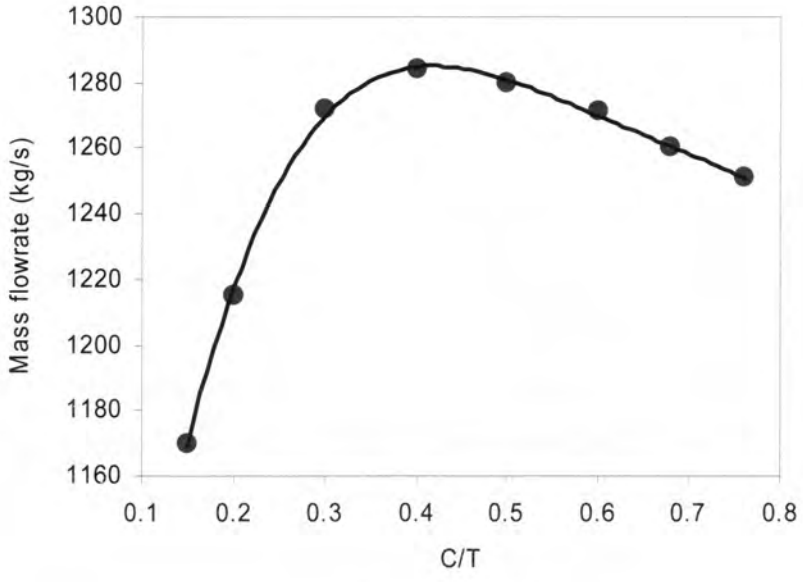


Figure 4.15: Mass flowrate vs C/T

Figure 4.15 shows the relationship between the mass flowrate and the impeller bottom clearance to tank diameter ratio and is governed by:

$$\dot{m} = \frac{a\left(\frac{C}{T}\right)}{\left[1+b\left(\frac{C}{T}\right)\right]^2} \qquad \text{- 4.10}$$

$\dot{m}$ represented mass flowrate and $C/T$ represented the impeller bottom clearance to tank diameter ratio. Data regression to Equation (4.10) yielded $a$ = 13,840 kg $s^{-1}$ and $b$ = 2.565 with a good correlation fit of 0.9943. For maximum values,

$$\frac{d\dot{m}}{d\left(\frac{C}{T}\right)} = \frac{13840 - 91081\left(\frac{C}{T}\right)^2}{\left(1+2.565\left(\frac{C}{T}\right)\right)^4} = 0 \qquad \text{- 4.11}$$

The maximum value was located at $\left(\frac{C}{T}\right) = 0.3898$

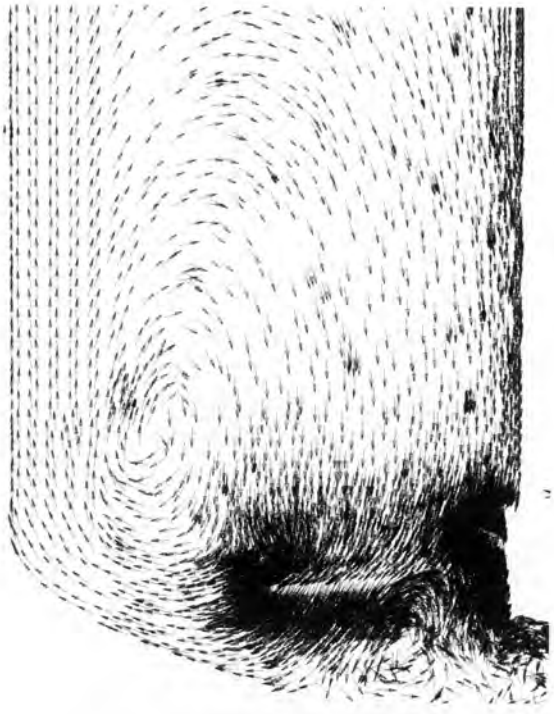

Figure 4.16: Vector plot at C/T=0.15

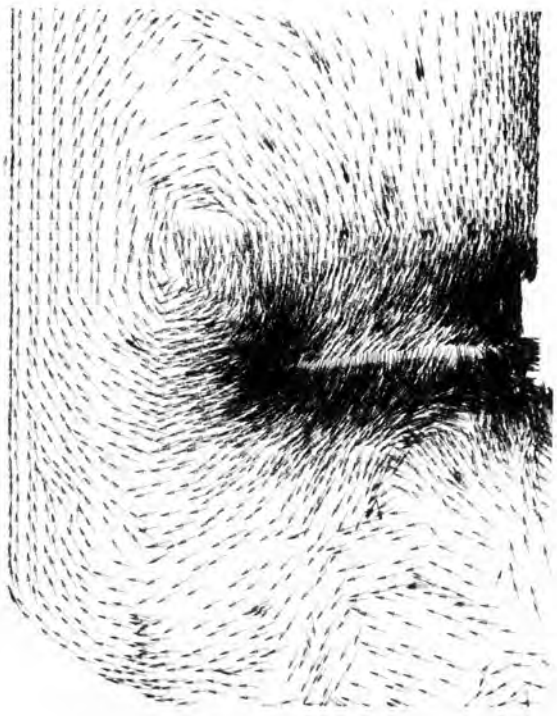

Figure 4.17: Vector plot at C/T=0.40

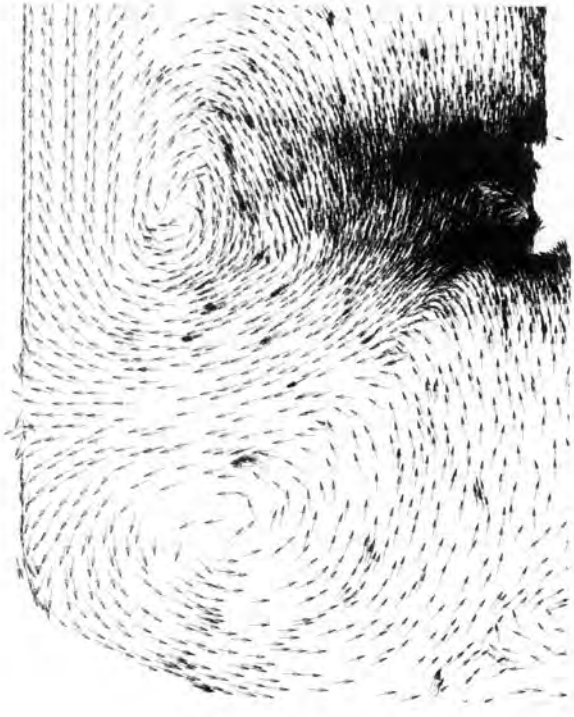

Figure 4.18: Vector plot at C/T=0.50

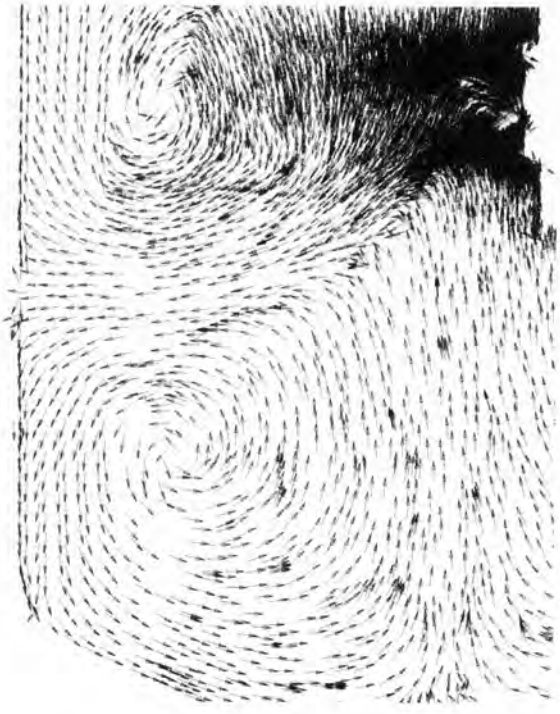

Figure 4.19: Vector plot at C/T=0.60

When the impeller was located too close to the tank bottom, as shown in Figure 4.16, a lower axial flowrate was obtained because of the narrow clearance between the tank bottom and the impeller for the flow to naturally deflect according to the curvature of the tank bottom. The narrow clearance prevented the development of axial discharge from the impellers, forcing the flow discharge to traverse radially. As a result, a significant amount of radial flow was produced in place of axial flow. However, when the *C/T* ratio was increased starting from 0.15 to 0.40 the axial mass flowrate increased by 24.58%. This was because below $C/T = 0.4$, the spherical bottom helped to deflect the axial and radial flow toward the baffles which then directed the flow upwards, as shown in Figure 4.17. The upward flow at some point re-entered the impeller from the top before emerging from the blade tips. Thus, increasing the amount of fluid moving upwards, through the use of a spherical bottom, will help to discharge higher downward axial flow.

Beyond $C/T = 0.4$, increasing the *C/T* ratio will cause a decrease in the mass flowrate. Starting from $C/T = 0.5$, a significant component of the flow discharged from the impeller was travelling downwards along the wall baffle. This downward flow was then directed by the spherical bottom before joining the impeller from the bottom side, as shown in Figures 4.18 and 4.19. This negated the axial flow discharged moving in a downward direction, thus reducing the net axial mass flowrate. This occurred because beyond this maximum value, a major component of the flow discharged came into contact with the baffles first and before being deflected downwards. The ideal situation should consist of having the flow discharge coming into contact with the spherical bottom first before being deflected upwards by the baffles. From here it can be seen that for optimal performance, $0.15 \leq C/T \leq 0.4$.

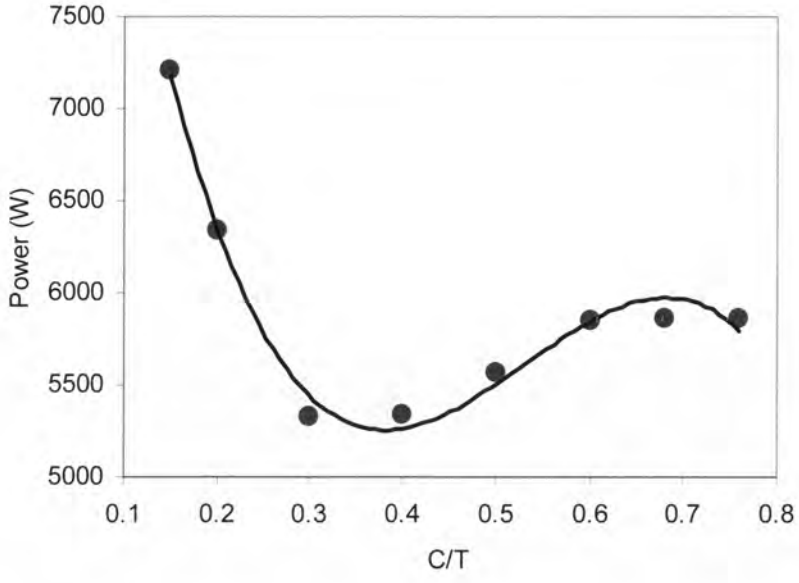


Figure 4.20: Power consumed in kilowatts vs C/T

The power consumed in kilowatts as a function of impeller clearance can be represented by a third-order polynomial expression with a good regression of 0.9854, as shown in Figure 4.20. It can be expressed as:

$$P = -53039\left(\frac{C}{T}\right)^3 + 84461\left(\frac{C}{T}\right)^2 - 41244\left(\frac{C}{T}\right) + 11641 \qquad -4.12$$

For minimum power consumption:

$$\frac{dP}{d\left(\frac{C}{T}\right)} = -159117\left(\frac{C}{T}\right)^2 + 168922\left(\frac{C}{T}\right) - 41244 = 0 \qquad -4.13$$

Minimum power consumption can be obtained at $\left(\frac{C}{T}\right) = 0.38$

Increasing the *C/T* ratio from 0.15 to 0.3 reduced the power consumption rate by 24.23%. Increasing the *C/T* ratio from 0.4 to 0.6 will cause an 11.04% increment in the power consumed. The reduction in power consumption was due to the lack of interference as the impeller was moved further away from the tank bottom. Beyond the minimum point, the power consumption increased again due to the change in the flow pattern where resistance from the baffles was significant.

### 4.4.6 Impeller rotational speed, rpm

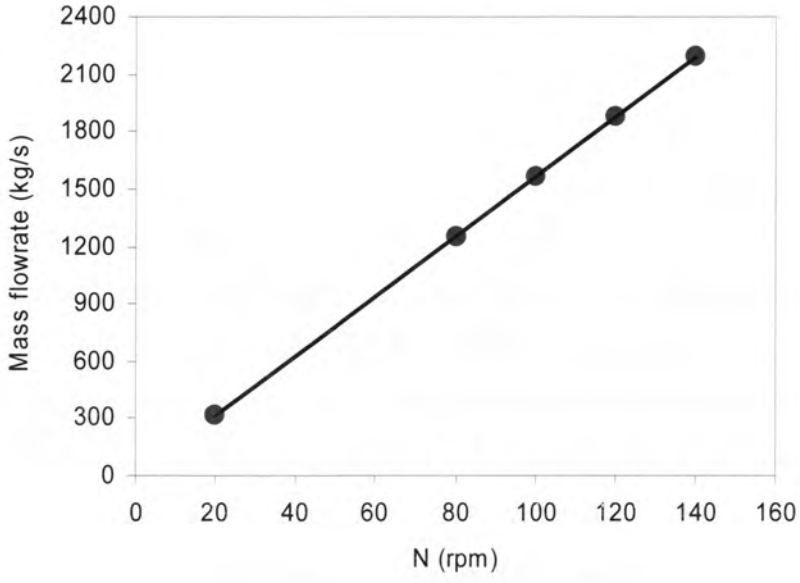


Figure 4.21: Mass flowrate vs impeller rotational speed

Figure 4.21 shows that the mass flowrate increased when the impeller rotational speed was increased. This follows a linear relationship, with regression of 1 and can be expressed in the form:

$$\dot{m} = 15.65N \qquad \text{- 4.14}$$

An increase in the speed by 1% results in 1% increase in the axial mass flowrate. The recommended impeller rotational speed is any speed that is much greater than the just suspended speed, $N_{js}$.

The Zwietering [1958] correlation for determining the minimum rotational speed required to lift the particles from the tank bottom and that no particles remain on the tank bottom for any longer than 1-2 seconds is given by:

$$N_{js} = S\nu^{0.1}\left[\frac{g(\rho_s - \rho_l}{\rho_l}\right]^{0.45} X^{0.13} d_p^{0.2} D^{-0.85} \qquad \text{- 4.15}$$

where

| | | |
|---|---|---|
| $S$ | = Zwietering constant | - |
| $\nu$ | = kinematic viscosity | $m^2\ s^{-1}$ |
| $g$ | = gravitational constant | $m\ s^{-2}$ |
| $\rho_s$ | = density of solid media | $kg\ m^{-3}$ |
| $\rho_l$ | = density of liquid media | $kg\ m^{-3}$ |
| $X$ | = solid loading | - |
| $d_p$ | = diameter of solid particles | m |
| $D$ | = impeller diameter | m |

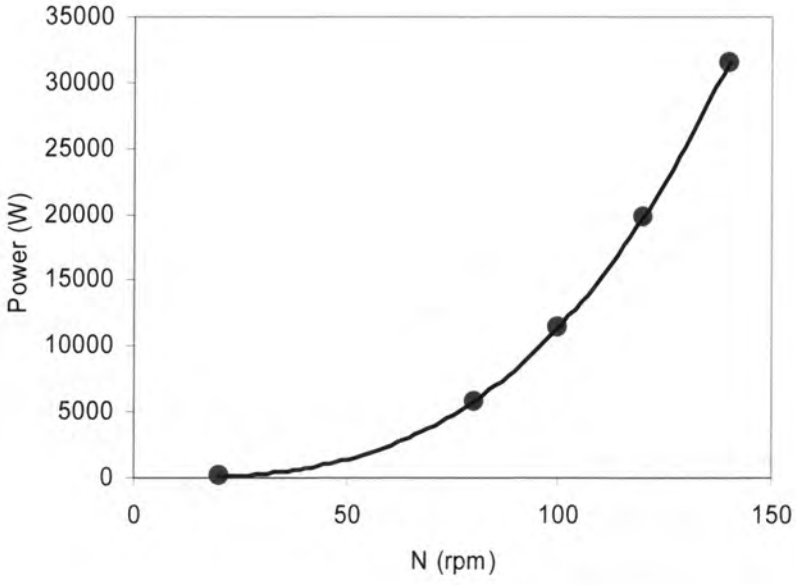


Figure 4.22: Power consumed in kilowatts vs N in revolution per minute

Figure 4.22 shows the power consumed as a function of the impeller rotational speed. The power function with a regression of 1, can be expressed as:

$$P = 0.0103(N)^{3.0222} \qquad \text{- 4.16}$$

Increasing the speed by 300% from 20 rpm to 80 rpm will increase the power consumption by 5,812%, that is, a 1% increase in the speed in this range will increase the power consumption by 19.37%. Increasing the speed from 80 rpm to 140 rpm (75%) will increase the power consumption by 442.7%. Therefore for every percent increase in the speed, the power consumed will increase by 5.902%.

### 4.4.7 Baffle width to tank diameter ratio

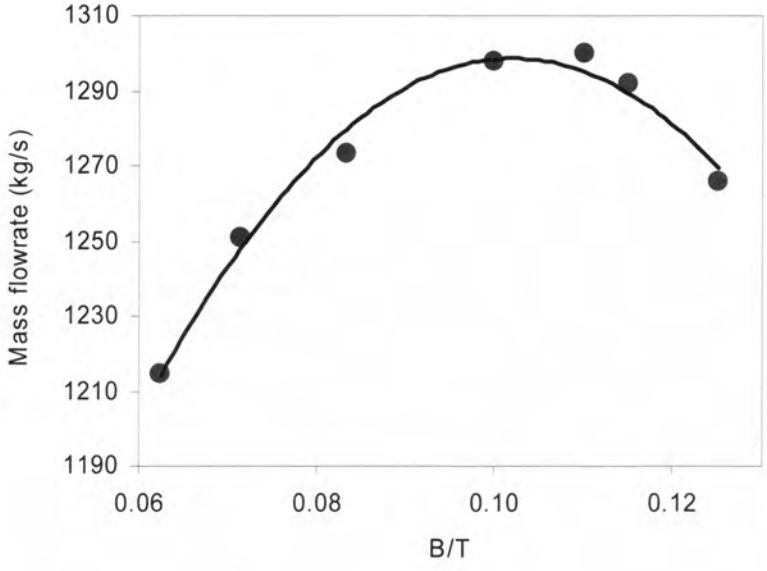


Figure 4.23: Mass flowrate vs B/T

Figure 4.23 shows the relationship between the mass flowrate and the impeller diameter to tank diameter ratio. Its behaviour is governed by a quadratic expression, having a good regression of 0.9823. The mathematical expression is given by:

$$\dot{m} = -54270\left(\frac{B}{T}\right)^2 + 11064\left(\frac{B}{T}\right) + 734.7 \qquad \text{- 4.17}$$

For maximum values,

$$\frac{d\dot{m}}{d\left(\frac{B}{T}\right)} = -108540\left(\frac{B}{T}\right) + 11064 = 0 \qquad \text{- 4.18}$$

For optimum performance, $B/T = 0.1019$

The purpose of baffles is to convert radial flow into axial flow. The maximum value is at $B/T = 0.1019$, which explains why most baffles in the industry have widths ranging from 1/12 to 1/10 because beyond 1/10, the mass flowrate started to drop. When the baffle widths were too small, the flow resistance was small which means the amount of radial flow converted to axial flow was minimal. An increase in the conversion can be achieved by widening the baffle width since doing so will increase the amount of flow resistance. But as baffle width was further widened, too much flow resistance was provided by the baffles to such an extent that not much radial flow was available to be converted to axial flow. As a consequence beyond $B/T = 0.1019$, the mass flowrate started to drop. From here it can be seen that for standard wall baffles, the optimum $B/T$ ratio is 1/10.

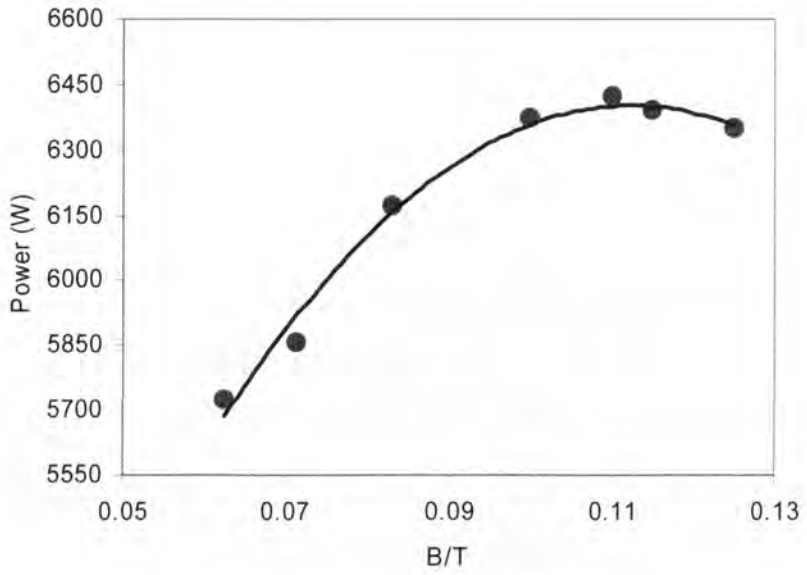


Figure 4.24: Power consumed in kilowatts vs B/T

As shown in Figure 4.24, the power consumption as a function of the baffle widths can be expressed with a good regression of 0.9872 as:

$$P = -288907\left(\frac{B}{T}\right)^2 + 64864\left(\frac{B}{T}\right) + 2762 \qquad -4.19$$

Increasing $B/T$ value from 0.063 to 0.10 (58.73%) will increase the power consumption by 369.6%. Increasing the $B/T$ value from 0.10 to 0.15 (50%) will cause a reduction in the flowrate by 44.07%.

### 4.4.8 Baffle spacing to tank diameter ratio

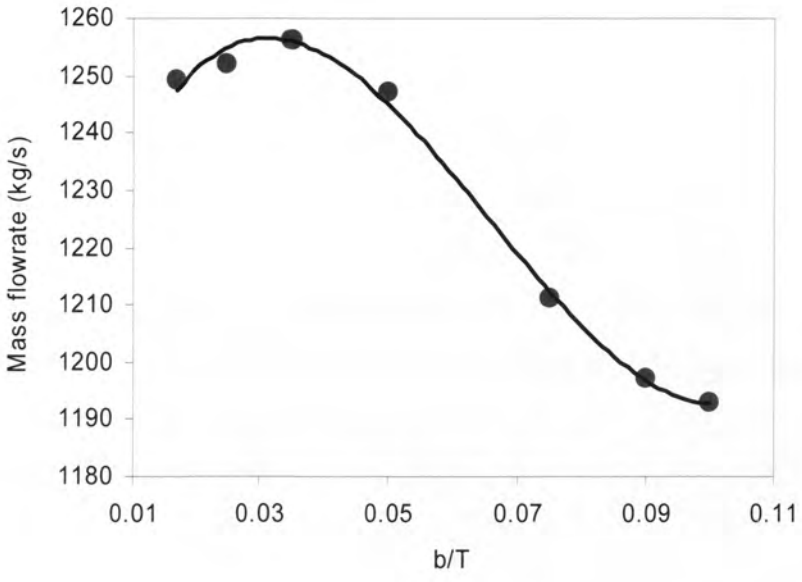


Figure 4.25: Mass flowrate vs b/T

Figure 4.25 shows the relationship between the mass flowrate and the impeller diameter to tank diameter ratio and is governed by the following third-order polynomial expression with good regression of 0.9961:

$$\dot{m} = 376766\left(\frac{b}{T}\right)^3 - 74426\left(\frac{b}{T}\right)^2 + 3529\left(\frac{b}{T}\right) + 1207 \qquad \text{- 4.20}$$

For maximum values,

$$\frac{d\dot{m}}{d\left(\frac{b}{T}\right)} = 1130298\left(\frac{b}{T}\right)^2 - 148852\left(\frac{b}{T}\right) + 3529 = 0 \qquad \text{- 4.21}$$

The maximum value is at $b/T = 0.031$

From the maximum value, baffle clearance produced peak mass flowrate at 1/32 ($b/T$=0.031). At small $b/T$ value, the baffles were located rather far way from the impellers therefore, not much flow resistance was contributed by them. This means that not much radial flow was converted to axial flow. As the clearance widened, the baffles were closer to the impellers thereby converting most of the radial flow to axial flow. This automatically maximised the mass flowrate traversing in the axial direction.

However, as the clearance was further widened, the flow resistance dropped because the clearance was large enough for the fluid to flow pass behind the baffles with minimal interruption. This means that placing the baffles too far away from the tank wall will cause a reduction in the axial flowrate because the baffles do not convert enough radially oriented flow to axially oriented flow.

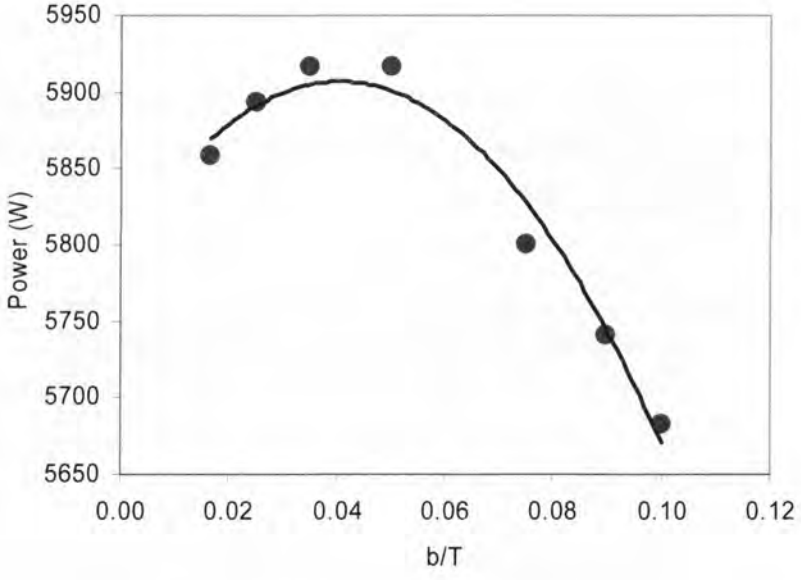


Figure 4.26: Power consumed in kilowatts vs b/T

The power consumption as a function of various values of $b/T$, shown in Figure 4.26, can be expressed by a quadratic expression with a good regression of 0.9715 as:

$$P = -66405\left(\frac{b}{T}\right)^2 + 5356\left(\frac{b}{T}\right) + 5799 \qquad \text{- 4.22}$$

For peak power consumption,

$$\frac{dP}{d\left(\frac{b}{T}\right)} = -132810\left(\frac{b}{T}\right)^2 + 5356 = 0 \qquad \text{- 4.23}$$

The peak power consumption occurred at $b/T = 0.04033$

The power increased from 1/60 to 1/30 but beyond this $b/T$ value, the power consumption started to decrease. At small $b/T$ value, the baffles were located rather far way from the impellers therefore, little flow resistance was created. As the spacing widened, the baffles were closer to the impellers therefore contributing more flow resistance. However, as the spacing was further widened, the flow resistance dropped because the spacing was large enough for the fluid to flow behind the baffles with minimal interruption. This phenomenon caused a reduction in the power consumption.

### 4.4.9 Number of baffles

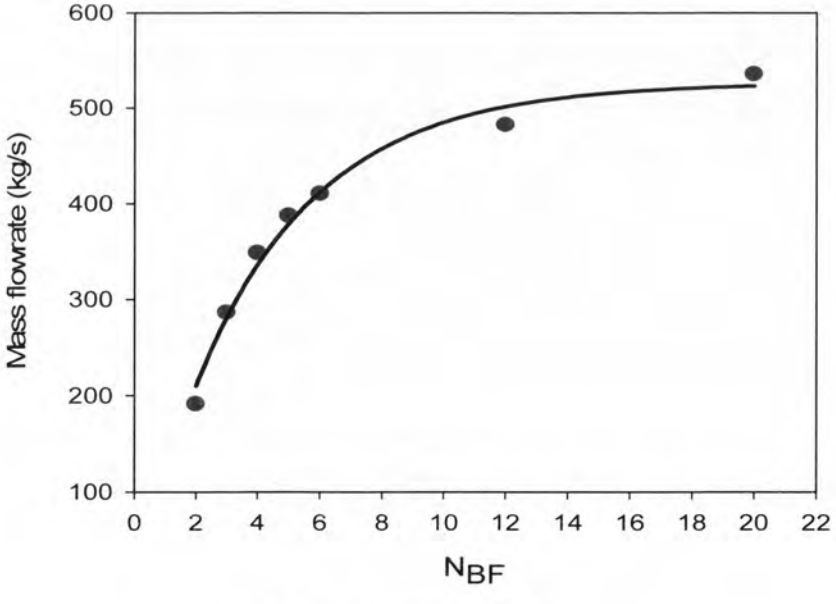


Figure 4.27: Mass flowrate vs $N_{BF}$

Figure 4.27 shows the relationship between the mass flowrate and number of baffles, which is governed by the following expression:

$$\dot{m} = \dot{m}_0 + a\left(1 - e^{-b(N_{BF})}\right) \qquad \text{- 4.24}$$

where $\dot{m}$ represents mass flowrate and $\dot{m}_0$ =903 kg $s^{-1}$ and is the mass flowrate when there are no baffles employed, and $N_{BF}$ represents the number of blades. A non-linear regression performed on Equation (4.24) yielded $a$=526.3 kg $s^{-1}$ and $b$=0.2546 with an excellent correlation fit of 0.9931. Increasing the number of baffles from 2-3, 3-4, 4-5 and 5-6 resulted in an increase in axial flowrate by 6.379%, 4.645%, 3.471% and 2.574% respectively. In addition, increasing the number of baffles beyond 30 baffles did not result in any increase in the mass flowrate.

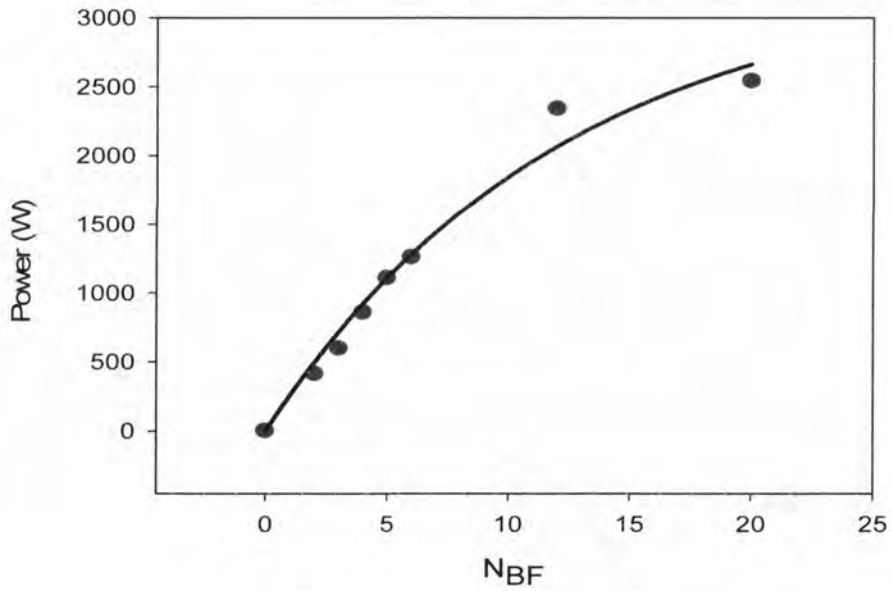


Figure 4.28: Power consumed in kilowatts vs $N_{BF}$

The power consumed as a function of the number of baffles, shown in Figure 4.28, can be represented by the correlation with good regression of 0.9895, in the form:

$$P = P_0 + a\left(1 - e^{-b(N_{BF})}\right) \qquad \text{- 4.25}$$

$P$ is the power consumed in W, whereas $P_0$=5,003 W and is the power consumed when there are no baffles installed. A non-linear regression analysis on Equation (4.25) yielded $a$=3,310 W, $b$=0.0817. This shows that if the number of baffles is increased from 30-35, the power consumption will increase by 1.020% although no increase in mass flowrate will be attained.

### 4.4.10 Number of impellers

Figure 4.29: Five mixing tanks each showing a different number of impellers

A simulation was conducted to determine the effect of the number of impellers on the axial mass flowrate. Five geometrical models each having a different number of impellers were created for this purpose, as shown in Figure 4.29.

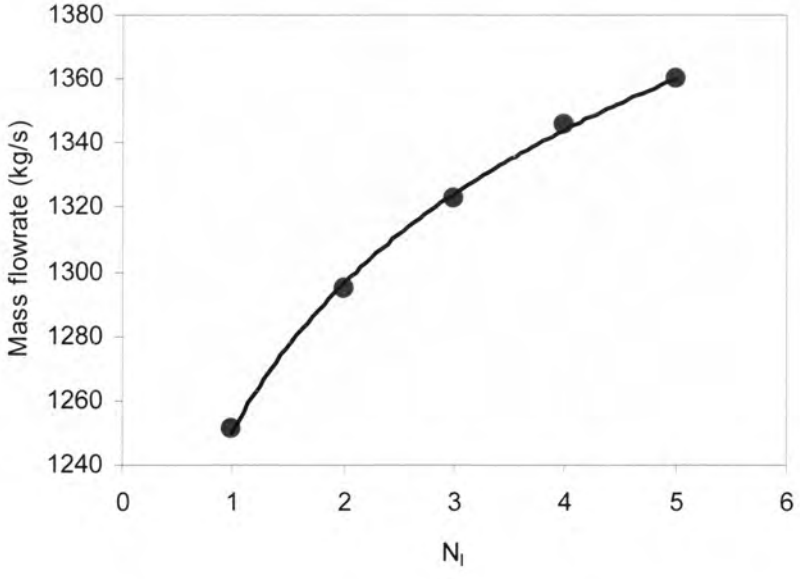


Figure 4.30: Mass flowrate vs number of impellers

Figure 4.30 shows the relationship between the axial mass flowrate and the number of impeller installed on the same shaft. The relationship can be expressed as:

$$\dot{m} = 1250 N_I^{0.0524} \qquad \text{- 4.26}$$

A good correlation fit of 0.9991 was obtained for this expression.

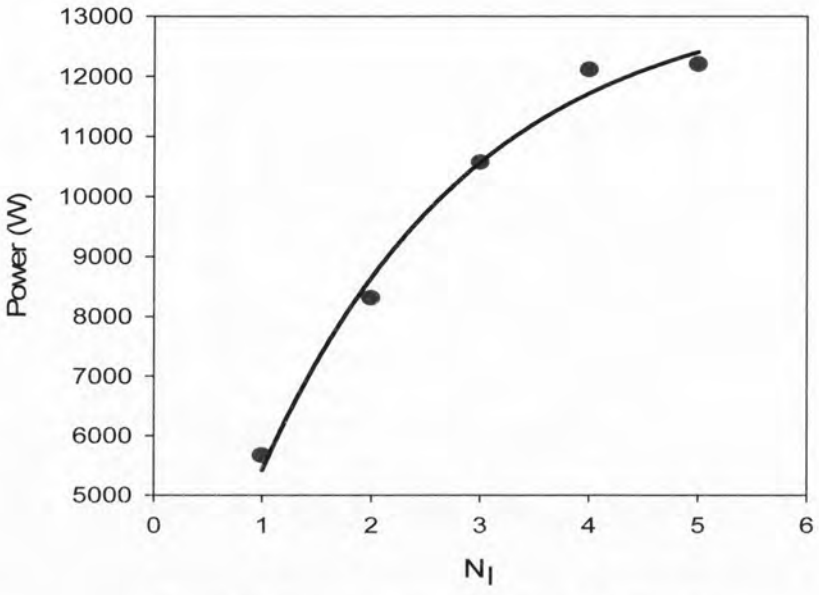


Figure 4.31: Power consumed in kilowatts vs number of impeller

Figure 4.31 shows the relationship between the power consumed by the process and the number of impellers installed on the same shaft. It can be represented by the following correlation having an excellent regression of 0.9940:

$$P = P_0 + a\left(1 - e^{-b(N_I)}\right) \qquad \text{- 4.27}$$

$P$ is the power consumed in W, whereas $P_0$=200 W and is the power consumed when there is no impeller installed. A non-linear regression analysis on Equation (4.27) yielded $a$=13,417 W, $b$=0.5172. The percentage increment in the power consumed as a function of the increment in the number of impellers is best represented by the bar chart as shown in Figure 4.32.

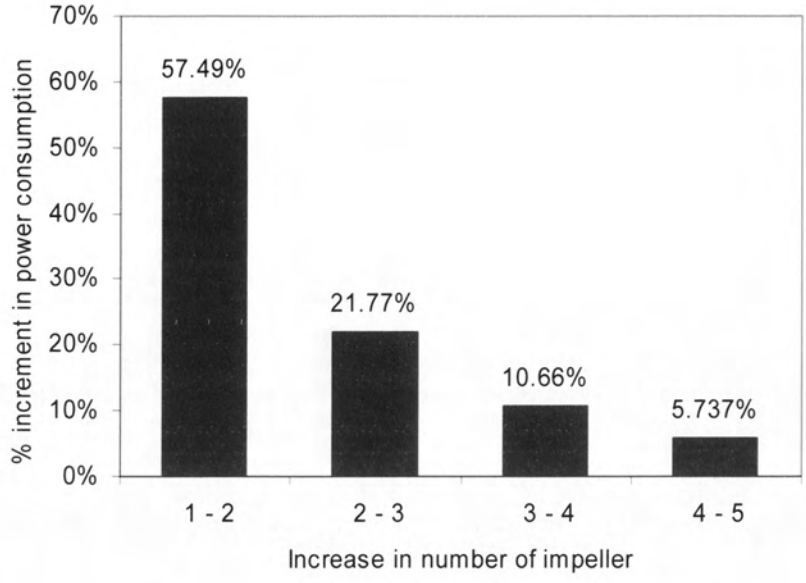


Figure 4.32: Percentage increment in power consumption vs increase in number of impellers

For $Z/T \leq 1.4$, $N_I = 2$ since beyond this number, the increase in the flowrate did not warrant the increase in the power consumption.

## 4.5 Application range

To prove that the results presented in previous sections are applicable at different speeds, the trials were repeated but at speeds ranging from 120 rpm to 200 rpm.

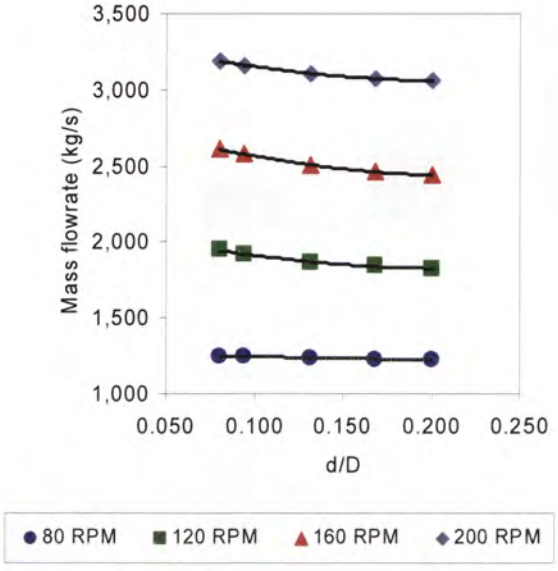


Figure 4.33: Mass flowrate vs d/D

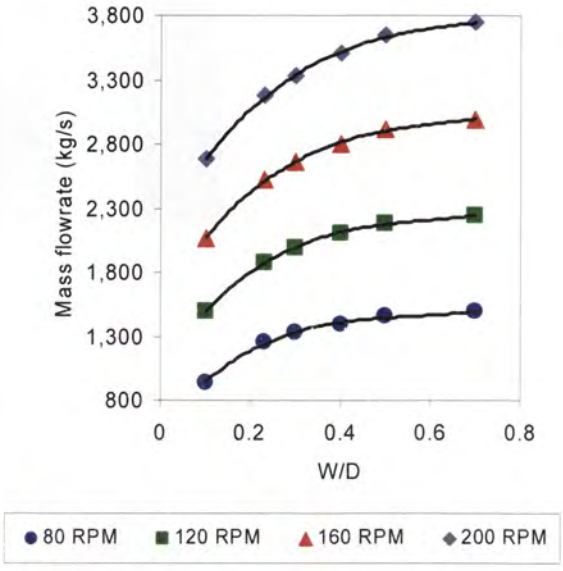


Figure 4.34: Mass flowrate vs W/D

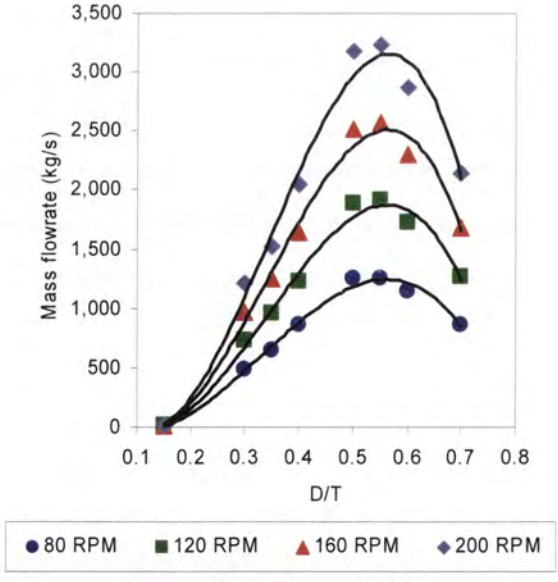


Figure 4.35: Mass flowrate vs D/T

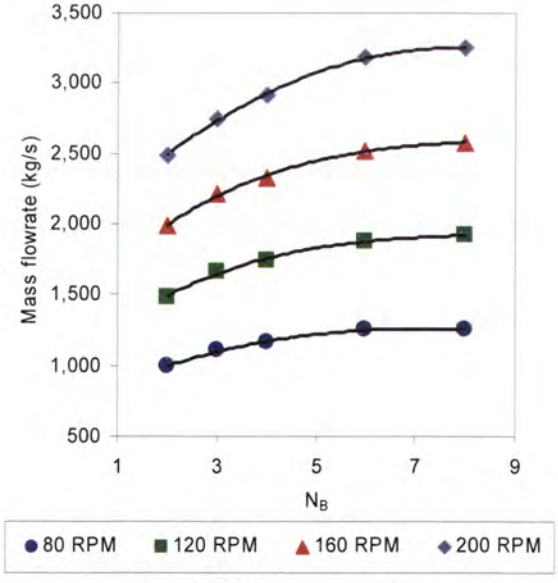


Figure 4.36: Mass flowrate vs $N_B$

Figures 4.33-4.36 each represents a plot of the mass flowrate versus a crucial variable. In each plot, the four curves represent impeller speed at 80 rpm (blue circles), 120 rpm, 160 rpm and 200 rpm, starting from the bottom most curve moving upwards as the impeller

speed increased. From these studies, it can be concluded that the results discussed previously on these four variables are valid from 80 to 200 rpm.

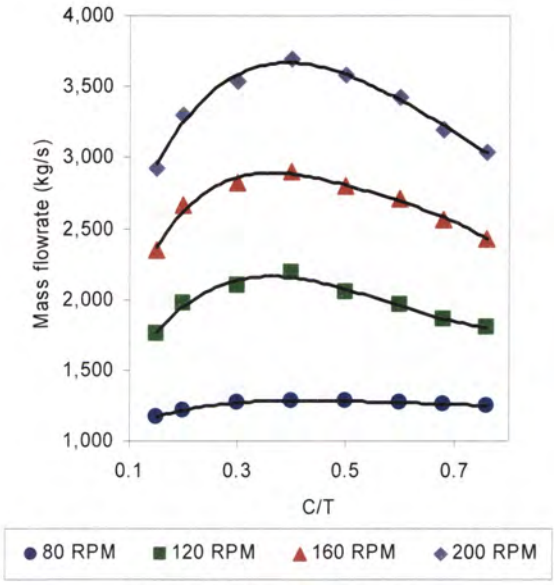


Figure 4.37: Mass flowrate vs C/T

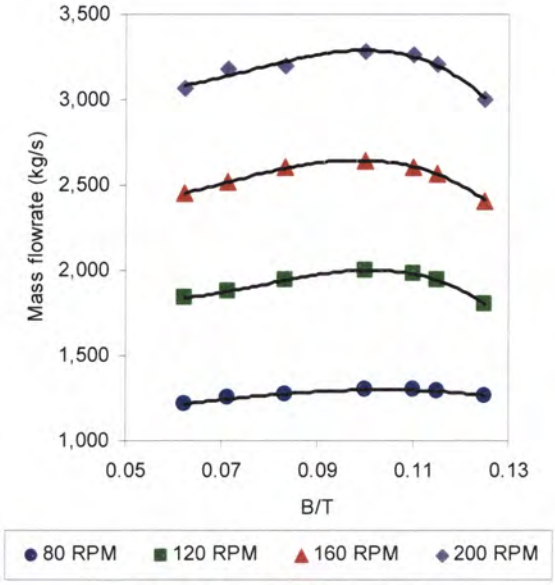


Figure 4.38: Mass flowrate vs B/T

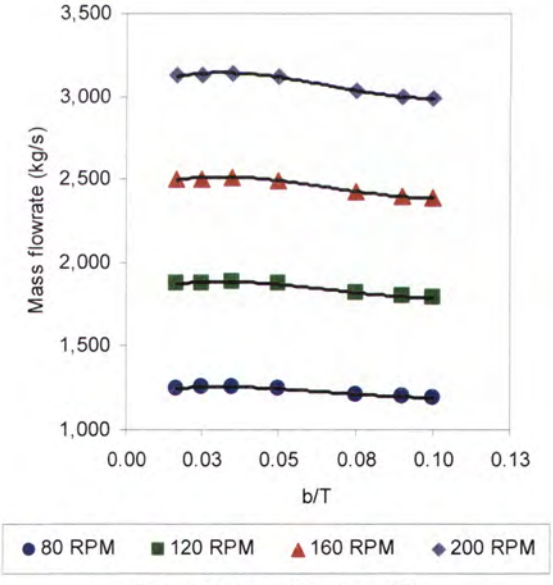


Figure 4.39: Mass flowrate vs b/T

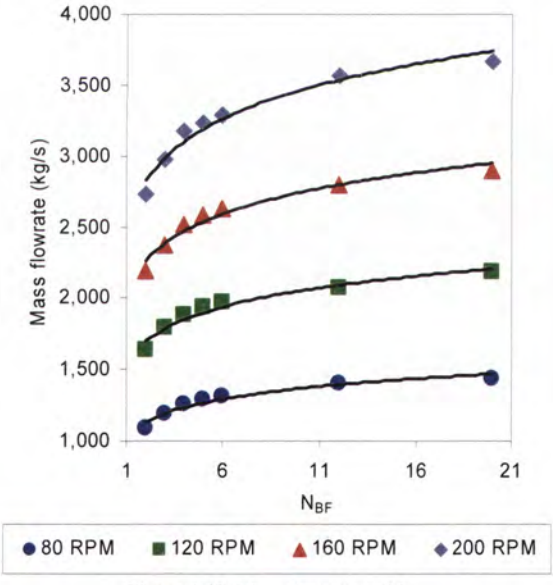


Figure 4.40: Mass flowrate vs $N_{BF}$

Similarly, Figures 4.37-4.40 each represents a plot of the mass flowrate versus a crucial variable. In each plot, the four curves represent impeller speed at 80 rpm (blue circles), 120 rpm, 160 rpm and 200 rpm, starting from the bottom most curve moving upwards as the impeller speed increased. From these studies, it can be concluded that the results discussed previously on these four variables are valid from 80 to 200 rpm.

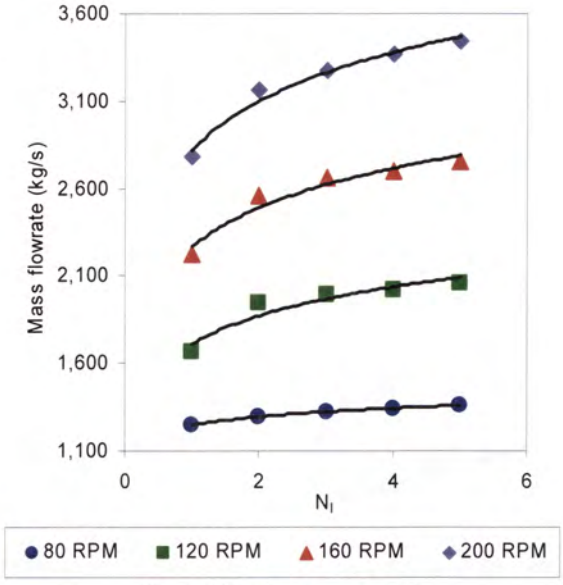


Figure 4.41: Mass flowrate vs $N_I$

Unlike the eight variables discussed previously, Figure 4.41 shows that the curve representing impeller speed at 80 rpm (blue circles) is almost linear whereas the curve representing impeller speeds at 120 rpm, 160 rpm and 200 rpm assume a polynomial expression. In conclusion, for a tank having aspect ratio of about 1 and impeller speed ≥ 120 rpm, having more than two impellers are not recommended. This is because any system that employs more than two impellers will consume more power but deliver a marginal increase in the axial mass flowrate. Thus, the resultant benefit per unit power is insignificant when there are more than two impellers employed on the same shaft.

## 4.6 Design template

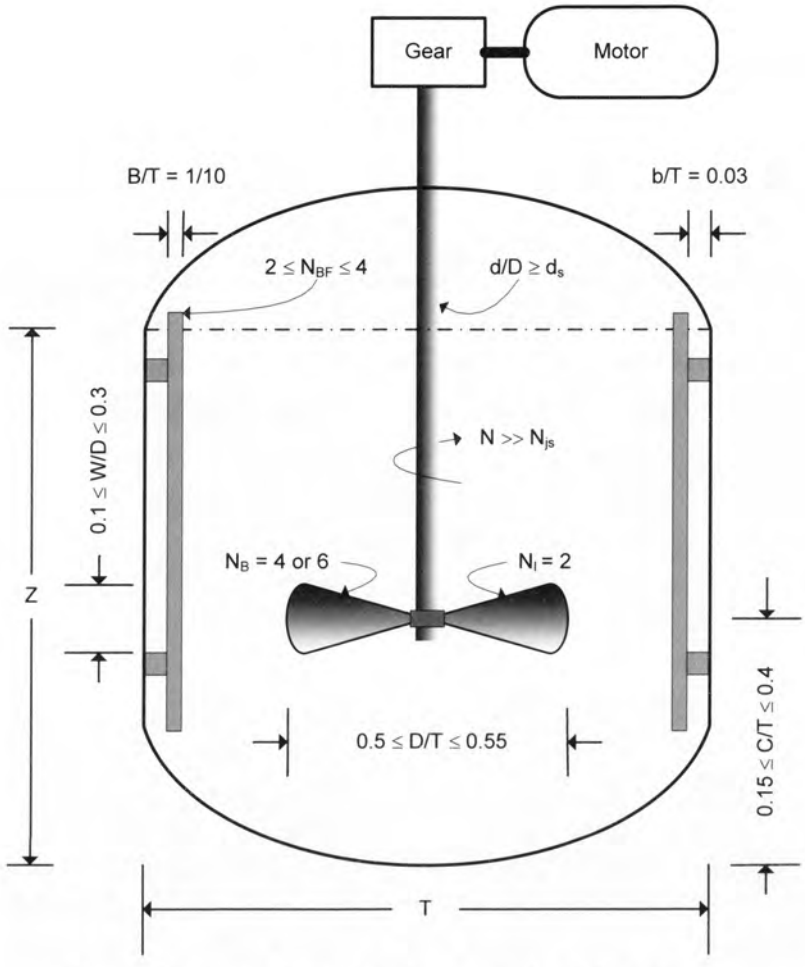


Figure 4.42: Summary of values for optimum suspension mixing performance

Figure 4.42 presents a summary of the values recommended for optimum suspension mixing performance. By being aware of such maximum and minimum values, engineers can avoid pitfalls and concurrently optimise the mixing tank performance to produce a more homogeneous suspension or, in the case of multiphase reactors involving solid-liquid phases, to increase the global mass transfer rate.

## 4.7 Multivariable analysis

The objective of this section is to determine which two variables out of the ten variables investigated have a significant impact on the performance of a suspension mixing tank. This is achievable by conducting factorial experiments since the one-factor-at-a-time experiment is not suitable for this purpose. A full-factorial experiment involving 10 factors carried out at 5 levels requires 9,765,625 trials. Because of the economically prohibitive nature of full-factorial experiment, the partial-factorial experiment was adopted instead. Qualitek-4 software that employs the design of experiment (DOE) by Taguchi technique and this was used to create the trial condition as shown in Table 4.2. This technique is able to reduce a full factorial experiment to a partial factorial experiment while ensuring each trial condition is given a fair exposure.

Table 4.2: Trial conditions

| Trials | $d/D$ | $W/D$ | $D/T$ | $N_B$ | $C/T$ | $N$ | $B/T$ | $b/T$ | $N_{BF}$ |
|---|---|---|---|---|---|---|---|---|---|
| 1 | 0.08 | 0.20 | 0.25 | 2 | 0.20 | 20 | 0.080 | 0.020 | 2 |
| 2 | 0.08 | 0.25 | 0.35 | 3 | 0.30 | 80 | 0.100 | 0.025 | 3 |
| 3 | 0.08 | 0.30 | 0.45 | 4 | 0.40 | 120 | 0.110 | 0.030 | 5 |
| 4 | 0.08 | 0.35 | 0.55 | 6 | 0.50 | 140 | 0.115 | 0.035 | 6 |
| 5 | 0.09 | 0.20 | 0.25 | 3 | 0.30 | 120 | 0.110 | 0.035 | 6 |
| 6 | 0.09 | 0.25 | 0.35 | 2 | 0.20 | 140 | 0.115 | 0.030 | 5 |
| 7 | 0.09 | 0.30 | 0.45 | 6 | 0.50 | 20 | 0.080 | 0.025 | 3 |
| 8 | 0.09 | 0.35 | 0.55 | 4 | 0.40 | 80 | 0.10 | 0.020 | 2 |
| 9 | 0.10 | 0.20 | 0.35 | 4 | 0.50 | 20 | 0.10 | 0.030 | 6 |
| 10 | 0.10 | 0.25 | 0.25 | 6 | 0.40 | 80 | 0.080 | 0.035 | 5 |
| 11 | 0.10 | 0.30 | 0.55 | 2 | 0.30 | 120 | 0.115 | 0.020 | 3 |
| 12 | 0.10 | 0.35 | 0.45 | 3 | 0.20 | 140 | 0.110 | 0.025 | 2 |
| 13 | 0.11 | 0.20 | 0.35 | 6 | 0.40 | 120 | 0.115 | 0.025 | 2 |
| 14 | 0.11 | 0.25 | 0.25 | 4 | 0.50 | 140 | 0.110 | 0.020 | 3 |
| 15 | 0.11 | 0.30 | 0.55 | 3 | 0.20 | 20 | 0.10 | 0.035 | 5 |
| 16 | 0.11 | 0.35 | 0.45 | 2 | 0.30 | 80 | 0.080 | 0.030 | 6 |
| 17 | 0.08 | 0.20 | 0.55 | 2 | 0.50 | 80 | 0.110 | 0.025 | 5 |
| 18 | 0.08 | 0.25 | 0.45 | 3 | 0.40 | 20 | 0.115 | 0.020 | 6 |
| 19 | 0.08 | 0.30 | 0.35 | 4 | 0.30 | 140 | 0.080 | 0.035 | 2 |
| 20 | 0.08 | 0.35 | 0.25 | 6 | 0.20 | 120 | 0.10 | 0.030 | 3 |
| 21 | 0.09 | 0.20 | 0.55 | 3 | 0.40 | 140 | 0.08 | 0.030 | 3 |
| 22 | 0.09 | 0.25 | 0.45 | 2 | 0.50 | 120 | 0.10 | 0.035 | 2 |
| 23 | 0.09 | 0.30 | 0.35 | 6 | 0.20 | 80 | 0.110 | 0.020 | 6 |
| 24 | 0.09 | 0.35 | 0.25 | 4 | 0.30 | 20 | 0.115 | 0.025 | 5 |
| 25 | 0.10 | 0.20 | 0.45 | 4 | 0.20 | 80 | 0.115 | 0.035 | 3 |
| 26 | 0.10 | 0.25 | 0.55 | 6 | 0.30 | 20 | 0.110 | 0.030 | 2 |
| 27 | 0.10 | 0.30 | 0.25 | 2 | 0.40 | 140 | 0.10 | 0.025 | 6 |
| 28 | 0.10 | 0.35 | 0.35 | 3 | 0.50 | 120 | 0.080 | 0.020 | 5 |
| 29 | 0.11 | 0.20 | 0.45 | 6 | 0.30 | 140 | 0.10 | 0.020 | 5 |
| 30 | 0.11 | 0.25 | 0.55 | 4 | 0.20 | 120 | 0.080 | 0.025 | 6 |
| 31 | 0.11 | 0.30 | 0.25 | 3 | 0.50 | 80 | 0.115 | 0.030 | 2 |
| 32 | 0.11 | 0.35 | 0.35 | 2 | 0.40 | 20 | 0.110 | 0.035 | 3 |

From the trial condition shown in Table 4.2, the two most important variables are:

- Diameter of impeller to diameter of tank ratio ($D/T$)
- impeller rotational speed ($N$)

## 4.8 Power requirement

The power requirement to operate the impellers in the turbulence regime is given by:

$$N_P = \frac{P}{\rho N^3 D^5} \qquad \text{- 4.28}$$

$N_P$ : power number (dimensionless)

$D$ : diameter of impeller (m)

$\rho$ : density of fluid (kg $m^{-3}$)

$N$ : impeller rotational speed (rev $s^{-1}$)

From Equation (4.28) and taking into consideration $P \alpha N^3$ and $P \alpha D^5$, increasing $D$ from 0.2 to 0.5 will increase the power by $(2.5)^3 = 97.66$ times. In contrast, increasing $N$ from 1 rev $s^{-1}$ to 6.54 rev $s^{-1}$ will increase the power consumption by $(6.54)^3 = 280$ times. According to Tatterson [1994], the above changes resulted in the same reduction in mixing times.

In brief, increasing the $D/T$ ratio is more energy efficient at reducing mixing times than increasing the value of $N$. Thus, where practical, changes to $D/T$ must be given first priority.

## 4.9 Concluding remarks

Suspension of particles via mechanical agitation in the process industry is a common goal. This paper has investigated the influence of ten industrially-recognised important variables in the design of suspension mixing tanks using a CFD model of the commercial vessel. The performance of the suspension mixing tank as a function of these crucial variables was discussed in detail. For the mass flowrate investigation, out of the ten variables investigated, nine followed a non-linear relationship and one followed a linear relationship. Similarly, for the power consumed as a function of the variables, nine followed a non-linear relationship and the remaining variable obeyed a linear correlation. The derived relationships were used to optimise the vessel design with respect to the variables. A design template incorporating the optimum operating range to suspend particles was developed as a result of this study. It is applicable for impeller speed rotating between 80 to 200 rpm. This practical design template can be applied across a broad range of industries such as the chemical, biochemical, pharmaceutical, petrochemical, explosives and mineral processing industries. Finally, from the multivariable analysis, the two most important variables that affected the performance of mixing tank in suspending particles were determined as the diameter of impeller to diameter of tank ratio ($D/T$) and the impeller rotational speed ($N$). Even so, from an industrial standpoint, changing the $D/T$ must be given priority over $N$.

RDX, cyclonite, cyclo-1,3,5-trimethylene-2,4,6-trinitramine or hexogen or trimethylentrinitramin or dexogene or more commonly known as research department explosive (RDX) exists in the form of white crystalline solids. Its molecular structure is given in Figure 5.1. Because of its high melting point, its use as a poured filling has been precluded. RDX is manufactured by nitration process via a process called the continuos Woolwich process. Its melting point is about 204°C and its detonation velocity is about 8,750 m $s^{-1}$. It is soluble in acetone, insoluble in water and sparingly soluble in ether and ethanol. RDX dissolves in cyclohexanone, nitrobenzene and glycol at elevated temperatures. RDX is probably the most important high-brisance explosive where its high explosive nature comes from the high density and detonation velocity. It is relatively insensitive and stable. Overall, its performance is slightly inferior to those of octogen (HMX). Usually, for use as a high explosive, RDX is normally mixed with other high explosive such as molten 2,4,6 trinitrotoluene (TNT) in a ratio of 60:40 to form cyclotol (Composition B) [Kohler and Meyer 1993].

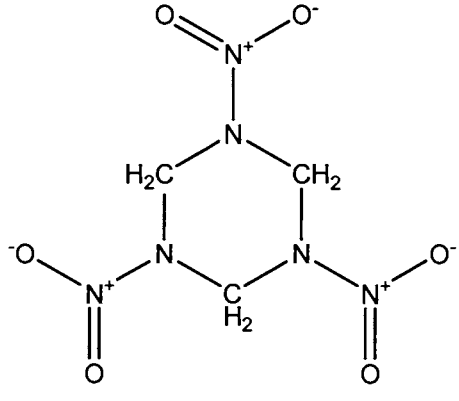


Figure 5.1: Research department explosive (RDX)

## 5.1 Objective of research

Figure 5.2: RDX slurry holding tank

The objective of this research was to solve a process issue associated with the RDX slurry holding tank as shown in Figure 5.2. The RDX holding tank could not attain homogeneous RDX particle suspension. As a consequence, the RDX particles volume fraction discharged from this unit was not consistent. Moreover, it was observed that at 46% tank height, the content was homogeneous and some RDX particles, due to trapped air, started to float at about 56% tank height. At 80% tank height, the water at the top half of the tank contained insignificant amount of RDX particles.

*The purpose of this study was therefore to conduct a research with a view to designing a better system which effectively suspends the RDX particles homogeneously.*

To achieve this, the design template incorporating the optimum operating range to suspend particles, formulated in Chapter 4, was applied in this chapter.

## 5.2 Process description

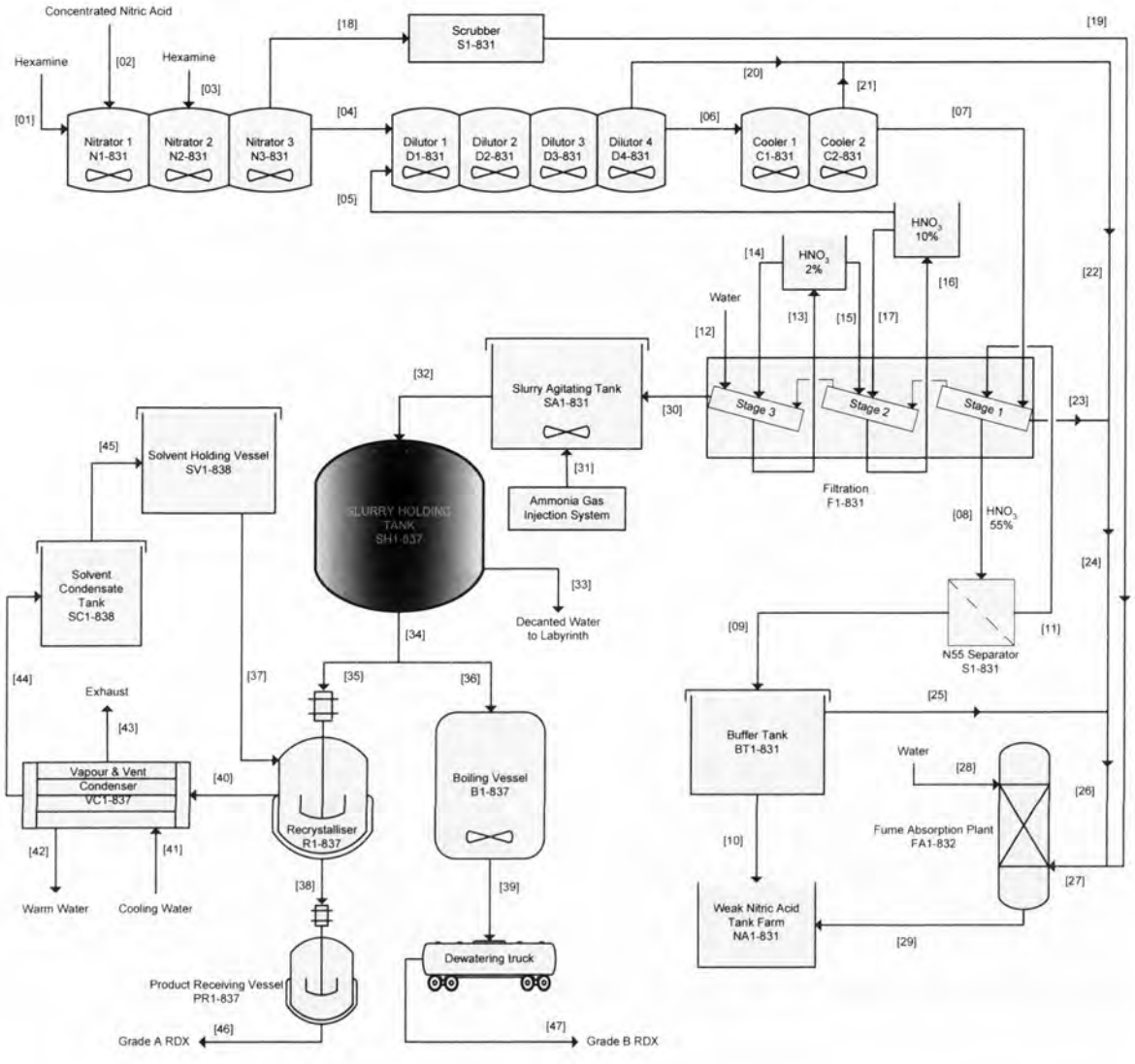


Figure 5.3: RDX manufacturing process flow diagram

Figure 5.3 shows the RDX manufacturing process flow diagram. The RDX process is divided into two sub-processes: nitration and purification. The main major unit operations of the nitration process consist of the nitrator, the dilutor, the cooler, the filtration unit, the slurry agitation tank and the fume absorption plant. The nitration process is a continuous process and takes approximately 8 hours to complete. The purification process is a batch process and consists of the following unit operations: the slurry holding tank, the recrystalliser and the boiler.

Nitrator (N1-831 to N3-831): The nitrator comprises of three interconnected compartments. 99% concentrated nitric acid (CNA) with a flowrate of 14 L $min^{-1}$ and hexamine with a flowrate of 100 kg $hr^{-1}$ (80% of total hexamine flowrate) are fed in the first compartment (N1-831). The ratio of nitric acid to hexamine is about 10:1 and only about 22% of the nitric acid reacts with hexamine. The hexamine dissolves in the concentrated nitric acid and a clear solution consisting of dissolved crude RDX, unstable by-products and unused nitric acid is produced. The remaining acid is returned to the weak nitric acid tank farm (NA1-831) after the process of dilution, cooling and filtration in the first filter bed. The reaction of hexamine and concentrated nitric acid is vigorous and exothermic, therefore cooling coils fed with chilled brine at -5 °C are placed within the compartment to maintain a temperature of about 23-25 °C.

Compartments two and three (N2-831 and N3-831) are also fitted with smaller cooling coils. The product formed in N1-831 overflows into N2-831 which has a feed of the remaining 20% hexamine flowrate and the temperature in N2-831 is maintained at about 26-28 °C. Nitric acid from N1-831 is reacted with the hexamine in N2-831. $CO_2$ gas is used for fire suppression and is injected through the fume ducts into the nitrator if a fire is detected.

Compartment three (N3-831) contains the overflow from N2-831 and the temperature maintained at 30-33 °C. The product from N3-831 flows into the dilutor (D1-831). Drowning valves are fitted in N1-831 and N2-831 to release nitrator contents into a drowning tank in case of a problem or cleaning the compartments at the end of a run. The impellers are operated at high speeds in all the compartments. Fume from the nitrator is removed and scrubbed before being ducted into the stream 19 towards the fume absorption plant (FA1-832). The fume absorption plant is a five column absorption plant using water to absorb nitrous fumes. The fume temperature in the duct downstream of the nitrator is monitored to provide early warning on potential hazard situation.

Dilutor (D1-831 to D4-831): The dilutor comprises of four interconnected compartments. Product from N3-831 contains 90% concentrated nitric acid and RDX solution which flows into D1-831 where it is diluted with N10 (10% nitric acid). The N10 acid is obtained as filtrate from the second stage of the raked filtration unit (F1-831). The filtrate is pumped to the $HNO_3$ 10% tank from where it flows into the dilutor at 6 L $min^{-1}$. The density of

N55 filtrate from the first stage of the raked filter is measured since the flowrate and quantity of N10 introduced into the dilutor is controlled. The temperatures in each of the compartments of the dilutor are maintained as follows: 80 °C in D1-831, 75 °C in D2-831, 75 °C in D3-831 and 75 °C in D4-831. The dilutor is enclosed by a cooling water jacket and has a cooling coil for each compartment. Cooling water is recirculated from a cooling tower through the cooling coils and cooling jacket in parallel. The steam sparges in the dilutor are used to increase the temperature of the contents during initial start and if there is a nitrator drown or feed hold. During drown or feed hold, the temperature set points of the dilutor is raised. This stops cooling water through the cooling coils and introduces steam through the sparges, ensuring continuation of the reaction at a controlled rate. This ensures that unstable reaction by-products are driven off from the slurry (spent acid).

The impellers are operated at high speeds in all the compartments. The impellers in D1-831 and D3-831 rotate in clockwise direction so the solution is drawn down in these two compartments while the impellers in D2-831 and D4-831 operate in the anti-clockwise direction drawing the solutions up in compartments 2 and 4. Thus ensuring adequate dwell time and ordered flow through the dilutor. The product from D4-831 is transferred to the cooler (C1-831). The RDX slurry flows from the dilutor into the RDX cooler through a covered channel. The channel also carries fumes in the opposite direction, sucked into the dilutor from the cooler. The dilutor is fitted with a drain valve, which drains through an open gutter into the filter unit. The drain valve is used to empty the dilutor during cleaning after the steam ejector removes the bulk of the contents but the drain valve is prone to blockage with RDX crystals.

Unstable reaction by-products are decomposed and driven off in the dilutor as abundant quantities of $NO_x$ fume by maintaining the dilutor temperature above 75 °C. The $NO_x$ fumes are removed through the ducts mounted on the dilutor cover to the Fume Absorption Plant (FA1-832) by fans. A damper in the duct is automatically controlled to maintain a fixed suction pressure in the dilutors. After passing through the damper, the fumes enter a solids arrester which traps RDX solids and entrained condensate borne in the fumes. These particles are released to the bottom of the arrester and into a seal pot which is filled with water and prevents fumes or air from escaping the arrester or entering the pot. Fumes from the arrester pass through a vapour cooler which has cooling water circulating through and any condensate from the fumes collects in the bottom and drained into the seal pot.

Cooler (C1-831 to C2-831): The cooler comprises of two interconnected compartments. The temperatures in each of the compartments of the cooler are maintained as follows: 15 °C in C1-831 and 12 °C in C2-831. The cooler is fitted with four chilled brine cooling coils, two in each compartment. The chilled brine flow through each pair of coils is controlled to maintain a temperature of 12 °C in the compartments so that when the slurry of RDX and N55 is cooled, solution losses are minimised.

Product from D4-831 containing 55% concentrated nitric acid and RDX solution overflows to C1-831 for cooling. Each compartment is fitted with an impeller. Each impeller has two propellers, one mounted at the base; the second mounted about 470 mm above. Both impellers are driven by one motor and operated at high speeds. The slurry of RDX and N55 overflows to the first stage of the filtration unit (F1-831). Fumes from the cooler pass back into the dilutor along the supply channel and are then extracted with the fumes from the dilutor to the fume absorption plant.

Filtration (F1-831): Filtration is a three stage process which progressively decreases the concentration of nitric acid in the RDX-acid slurry from C2-831. Initially all the three stages are approximately 50% filled with water. The concentration of nitric acid is approximately 55% and suitable for use in reconcentrating nitric acid back to 99%. Therefore when the RDX slurry is deposited into the base of the first stage, reciprocating rakes push the RDX solids up a sloping filter bed and the liquid is drawn through the filter by a vacuum pump and flows to the N55 separator (S1-831). Any RDX solids that are drawn with the acid to the separator are transferred back to the first stage. The acid overflows from the separator into a buffer tank (BT1-831). From the buffer tank, the acid is pumped into the weak nitric acid tank farm (NA1-831). The filtered RDX is passed from the top of the first stage to the base of the second stage.

The main objective of the second and third stages is to remove the acid from the RDX crystals. The second stage uses N2 acid wash solution from the third stage and the water to dilute the concentration of the RDX/acid slurry as the RDX is pushed from the base of the second stage to the top by the rakes. The filtrate that is obtained has a concentration of 10% nitric acid. This filtrate is stored in the $HNO_3$ 10% tank which supplies the diluted acid to the dilutor compartment one (D1-831). In case of overflow in the $HNO_3$ 10% tank, the extra filtrate flows back into the second stage. The RDX is filtered and then released to

the base of the third stage. The third stage uses water from the process water head tank to wash the RDX. The filtrate that is obtained has a concentration of 2% nitric acid. This filtrate is stored in the $HNO_3$ 2% tank which supplies the diluted acid to the second stage. In case of overflow in the $HNO_3$ 2% tank, the extra filtrate flows back into the first stage. The RDX is mixed with water to form RDX-water slurry which is washed from the discharge chute into the slurry agitation tank (SA1-831).

The first stage of the filtration is covered to contain fumes given off by the N55 acid. The fumes are ducted up and follow the same route as the fumes from the dilutor and are passed to the fume absorption plant (FA1-832). A damper in the filter fume duct is used to control the suction from the first stage into the absorption plant. Fumes from the buffer tank and the vacuum pump are passed to the fume absorption plant via the vapour cooler. Some weak nitric acid (N55) can also be obtained from the condensate from fumes of the dilutor compartment four (D4-831) and the first stage of the filtration (F1-831). This acid is sent to the weak nitric acid tank farm.

Slurry agitation tank (SA1-831): Before the slurry is pumped to the slurry holding tank (SH1-837), residual nitric acid is neutralised with ammonia bubbled through the slurry using an ammonia gas injection system providing a pH of approximately 7 and minimising the formation of cyclohexanone condensation dimer (CCD) during subsequent purification. The pH of the slurry is used to determine the amount of ammonia passed into the tank and monitored to ensure neutralisation of the crude RDX is completed prior to pumping over to slurry holding tank. Ammonia gas injection system is a distributor which is attached to ammonia gas storage bottles and a compressed air line. A small amount of compressed air is continuously bled into the distributor to prevent slurry being drawn back into the distributor when there is a low ammonia flow.

RDX from the third filter unit and water from process water head tank in a ratio of 1:3 are mixed and agitated by a continuous impeller in the agitation tank which also serves as a pumping tank. The density of the slurry in the tank is measured to determine if the slurry is in the range suitable for pumping to the purification process with respect to the ratio of RDX and water. The density is reduced by manually adding water to the slurry if necessary. The agitation tank is emptied on a batch basis when the level of the tank reaches approximately 80%.

Slurry holding tank (SH1-837): Slurry holding tank acts as a buffer tank and has an impeller to homogenise the RDX/water slurry transferred from the slurry agitation tank (SA1-831). The amount of slurry transferred from the holding tank to either the recrystalliser (R1-837) or the boiling vessel (B1-831), is monitored by a mass flowmeter. The slurry is first recycled back to the holding tank through a pump until the desired mass is achieved. The slurry is then pumped to either the recrystalliser or the boiling vessel when a control valve is opened. Excess water is decanted off to a clean labyrinth and this is also done when the mass flowmeter is not in use. Any RDX found with decanted water in the labyrinth settles to the bottom and is removed by an air operated diaphragm pump.

Recrystalliser (R1-837): The purification of RDX by recrystallisation results in Grade A RDX and involves dissolving RDX from the slurry in a mixture of cyclohexanone and water. A blank distillation is carried out prior to recrystallisation in order to minimise the formation or concentration of CCD. RDX slurry is not introduced in the recrystalliser and only cyclohexanone/water mixture is present. This distillation is simply the purification of cyclohexanone and the recrystalliser is heated to an azeotropic boiling point temperature of 97.1°C for 75 mins. The solvent vapours condense in a vapour & vent condenser (VC1-837) with circulating cooling water (streams 41 and 42) and collected in the solvent condensate tank (SC1-838) and then pumped into a solvent holding vessel (SV1-838) ready for recrystallisation process. As the temperature reaches 99°C, the condensate is diverted to a waste tank and steam from a steam sparge is used to strip the CCD. When the temperature reaches 101°C, it is an indication that the CCD removal is completed.

Cyclohexanone from the solvent holding vessel is added to the RDX/water mixture that is pumped from the slurry holding tank (SH1-831). The RDX/water mixture transfer time from the slurry holding tank to the recrystalliser is approximately 45 mins. The cyclohexanone transfer time from the solvent holding tank to the recrystalliser is also approximately 45 mins, but the solvent transfer is conducted after the RDX/water mixture is transferred in the recrystalliser. The recrystalliser is heated using steam at 200 kPa from the steam jacket and a coil and steam at 150 kPa from a steam sparge. At a temperature of 92 °C, RDX dissolves in the cyclohexanone-water mixture in 30 mins and the minimum ratio between RDX, cyclohexanone and water is 1: 3.4: 9, therefore 900 kg of RDX would equate to 3,000 kg of cyclohexanone and 8,000 kg of water. The cyclohexanone/water mixture is then distilled off at a temperature of 97.1°C in 75 mins leaving recrystallised and

purified RDX in water with an average particle size of 200 μm and is largely free of nitric acid. The solution is continually heated, boiling off the cyclohexanone/water azeotrope and leaving RDX and water.

The cyclohexanone/water vapour is collected and condensed in the condenser. From the condenser, it is collected in a pumping solvent condensate tank and is pumped to the solvent holding vessel for reuse. The condensate may also be stored in the cyclohexanone tank. When the solution has been boiled off, the RDX slurry contains purified crystals of RDX and contaminated water. This slurry is pumped into the product receiving vessel (PR1-837) where excess water is decanted off using vacuum probes. The dewatered RDX slurry is normally transferred to the cyclotol plant building 841 in dewatering trucks. The RDX may also be stored or set aside for waxing.

Boiling vessel (B1-837): The purification of RDX by boiling results in Grade B RDX and involves passing the RDX crystals through a mill to break down agglomerations of crystals and subsequent washing and boiling to physically break up the crystals and allow the occluded nitric acid to escape. RDX slurry from the slurry holding tank (SH1-831) is pumped to a mill where crystal agglomerates are broken into smaller particles. The water level in the boiler is 50%. The RDX is then boiled at 100°C to complete the breakdown and removal of by-products and to minimise acid retention in the interstices of the RDX crystals. When boiling is completed, the RDX slurry is cooled to 40°C and either dewatered and stored in dewatering trucks or greased, dewatered and stored in dewatering trucks.

The RDX slurry holding tank has the following geometrical configuration and operating condition, as shown in Table 5.1.

Table 5.1: Summary of geometrical and operating condition

| Parameter | Values |
|---|---|
| *D/T* | 0.5 |
| *C/T* | 0.26 |
| *W/D* | 0.23 |
| *T* | 2.134m |
| *H* | 3.336 |
| *Z* | 2.669 (80% of H) |
| *Z/T* | 1.25 |
| Fluid | RDX suspended in water |
| Density of water @ 25°C | 998.2 kg $m^{-3}$ |
| Density of RDX @ 25°C | 1,770 kg $m^{-3}$ |
| Viscosity of water @ 25°C | 0.001003 kg $m^{-1}s^{-1}$ |
| Gravity | 9.81m $s^{-2}$ |
| Operating pressure | 101,325 Pa |
| Impeller speeds | 60 rpm |
| Rotation direction | clockwise |
| Batch volume | 10,860L |

## 5.3 Just suspended speed

The Zwietering [1958] correlation for determining the minimum rotational speed required to lift particles from the tank bottom and maintain that no particles remain on the tank bottom for any longer than 1 - 2 s is given by:

$$N_{js} = S\nu^{0.1}\left[\frac{g(\rho_s - \rho_l)}{\rho_l}\right]^{0.45} X^{0.13} d_p^{0.2} D^{-0.85} \qquad \text{- 5.1}$$

where

| | | |
|---|---|---|
| $S$ | = Zwietering constant | - |
| $\nu$ | = kinematic viscosity | $m^2\ s^{-1}$ |
| $g$ | = gravitational constant | $m\ s^{-2}$ |
| $\rho_s$ | = density of solid media | $kg\ m^{-3}$ |
| $\rho_l$ | = density of liquid media | $kg\ m^{-3}$ |
| $X$ | = solid loading | - |
| $d_p$ | = diameter of solid particles | m |
| $D$ | = impeller diameter | m |

In the case of the RDX slurry holding tank, the $N_{js}$ is approximated to be:

$$5.2\times(0.000001005)^{0.1}\times\left[\frac{9.81(1{,}770-998.2)}{998.2}\right]^{0.45}\times 0.189^{0.13}\times 0.00015^{0.2}\times 1.067^{-0.85}$$

$= 0.4757\ rev\ s^{-1}$ or 28.5 rpm

For a single PBT at $Z/T = 1$, the cloud height is 70% of slurry height at $N_{js}$ and exceeds 95% of slurry height at 1.5 times of $N_{js}$. However, at $Z/T = 1.75$, the cloud height is only 40%. At $Z/T = 1.75$, the cloud height never went above 70% of tank height even at three times $N_{js}$ [Paul et al. 2004]. This means that for $Z/T >>> 1$, the cloud height will not exceed 70% of tank height for a single PBT even if the rotational speed is $>>> N_{js}$. In this case of $Z/T$=1.25, the maximum cloud height attainable was $(0.7\times 2.669)\div 3.336 = 0.56$ or 56%. This value was reflected in control panel output for a single PBT rotating at 60 rpm.

To achieve a homogeneous suspension of solid particles, Paul et al. [2004] specifies the number of impellers to be 1 for $Z/T \leq 1.2$, 2 for $1.2 \leq Z/T \leq 1.8$ and 3 for $Z/T > 1.8$, although it must be emphasised that a tank with such a high aspect ratio is not a good system for suspending solid particles. An ideal aspect ratio is 1 because of the impeller's proximity to all regions of the tank. Moreover, any tank with a high aspect ratio is undesirable because some regions are too far away from the impeller to have any influence on its discharge. Thus, another PBT must be installed to increase the cloud height in this RDX slurry holding tank.

## 5.4 Numerical setup

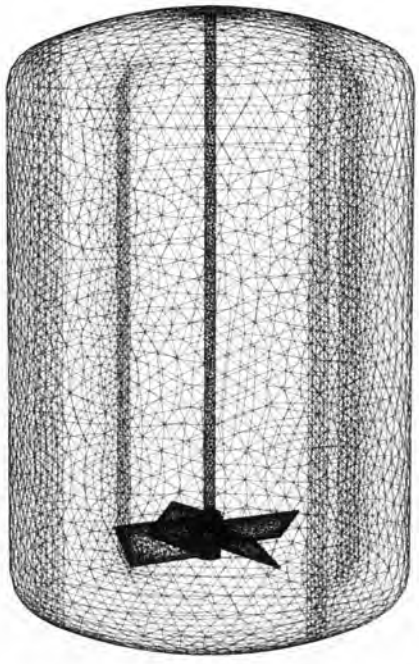

Figure 5.4: Meshed geometry of the RDX slurry holding tank

Figure 5.4 shows the meshed geometry of the RDX slurry holding tank created using MixSim 2.0. The top and bottom styles used were Klopperboden. Initial mesh size used on the tank volume was 0.1067 m, mesh strategy employed was CurvOnly, mesh normal angle was 35°. Size function on volume was not activated. Initial mesh size used on the flat wall baffles was 0.04 m, initial mesh size from width and thickness was 0.06096 m, initial mesh size correction for off wall was 0.02096 m and the growth rate employed was 1.4. As for the shaft, the initial mesh size was 0.01579 m and the growth rate used was 1.4. For the PBT, the initial mesh size used was 0.07113 m.

Tetrahedral cells were used instead of hexahedral due to prevalent turbulence induced by the presence of standard wall baffles. The meshed geometry of the mixing tank consisted of 404,524 tetrahedral cells shown in Figure 5.4. A significantly higher number of cells were allocated to area of high velocity and pressure gradient, notably the rotating zones. The baffles were assumed to have zero thickness in order to eliminate additional meshing within the tank. Meshing baffles with non-zero thickness means that very small cells will be required and this can lead to an unnecessarily prohibitive large number of cells with attendant computational costs. To minimise the total number of cells while retaining

accuracy, size function was applied to region of high velocity changes. These regions were identified as those immediately surrounding the impeller.

Figure 5.5: Mesh geometry at axial plane

Figure 5.6: Mesh geometry at z-plane

Figure 5.5 exhibits the meshed cells via a cut plane positioned at the impeller axial location. It shows the difference in cell sizes between the rotational zone and the rest of the tank volume. This was due to the size function employed inside the rotational zone that stipulated a maximum cell size value. The rotational zone has much finer cells than the rest of the tank volume. Figure 5.6 shows a cut plane positioned at the hub of the impeller along the z-plane to further illustrate the impact of assigning size function to the domain concerned.

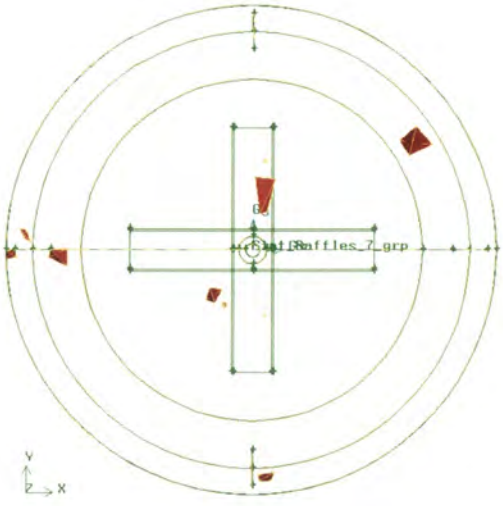

Figure 5.7: Mesh geometry at axial plane

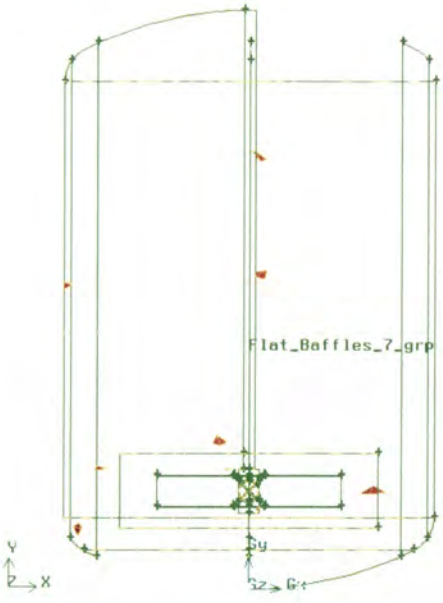


Figure 5.8: Mesh geometry at z-plane

To ensure convergence and obtain accurate results, the quality of the cells must be examined prior to starting the simulation [Kerdouss et al. 2006]. The worst element lay in the tank with an EquiAngle Skew quality value of 0.82. To be specific, only 10 elements had an EquiAngle Skew quality value $\geq 0.80$. These elements were scattered around as shown in Figures 5.7 and 5.8. For tetrahedral cells, the EquiAngle Skew quality value must not exceed 0.9 because exceeding this value will give rise to convergence difficulty and inaccurate results.

Fluent® solver was used to create a numerical solution that matched the governing conservation equations. In this study, the focus was on solving the conservation of mass, momentum, and turbulence transport with a view to generating a steady-state 3D hydrodynamics profile.

To simulate impeller rotations, separate rotational zones in the immediate vicinity of the impellers were created and an MRF approach was employed. This method involved solving the flow characteristics of the inner region using a rotating framework. These results were then used to provide boundary conditions for the outer region which employed a stationary framework to secure solution to the flow characteristics. The results from the outer region were then re-supplied as boundary conditions for the inner region. This iterative procedure was repeated until a convergent solution was obtained for both regions.

The segregated-implicit approach was used where the governing equations were solved sequentially unlike the coupled-implicit approach where the variables are solved in all cells simultaneously. To obtain a higher degree of accuracy, starting from first-order upwind scheme, all solutions were obtained via the second-order upwind scheme or the QUICK scheme for the volume fraction solution. In this scheme, higher order accuracy was obtained at the cell surfaces where the values at the cell centroid were subjected to multidimensional linear reconstruction using the Taylor series expansion.

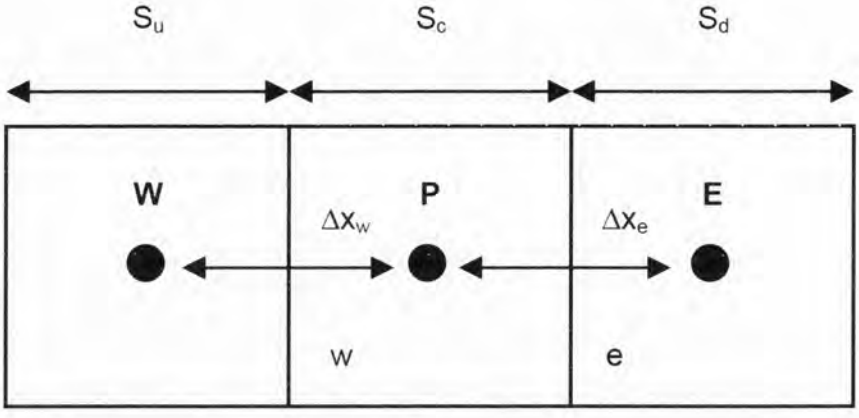


Figure 5.9: One-dimensional control volume

Referring to Figure 5.9 [Fluent 2006], if the flow is from left to right, such a value can be written as:

$$\phi_e = \theta\left[\frac{S_d}{S_c+S_d}\phi_P + \frac{S_c}{S_c+S_d}\phi_E\right] + (1-\theta)\left[\frac{S_u+2S_c}{S_u+S_c}\phi_P - \frac{S_c}{S_u+S_c}\phi_W\right] \quad -5.2$$

Where $\theta = 1$ in Equation (5.2) results in a central second-order interpolation while $\theta = 0$ yields a second-order upwind value. The traditional QUICK scheme is obtained by setting $\theta = 1/8$.

While the QUICK scheme (third-order accuracy) is more accurate on structured grids, nevertheless, it is also applicable to unstructured grids such as tetrahedral mesh. In such cases, the usual second-order upwind discretisation scheme was used at the faces of non-hexahedral cells. Due to presence of baffles, significant interrupted rotational flow existed inside the nitrator thereby creating steep pressure gradient. Because of this, PRESTO

(pressure staggering option) was employed to compute the pressure value at the cell surface by interpolating the value at cell centroid.

SIMPLE scheme was used for the pressure velocity coupling where a relationship between the pressure and velocity corrections was used to enforce conservation of continuity in order to obtain the pressure field [Rahimi 2005]. The under-relaxation factors used were the default settings namely, pressure = 0.3, density = 1, body forces = 1, momentum = 0.7, volume fraction = 0.2, turbulence kinetic energy = 0.8, turbulence dissipation rate = 0.8 and turbulent viscosity = 1.

To model the multiphase phenomena associated with the suspension of RDX particles in the holding tank, an appropriate model must be selected from the models available in *Euler-Lagrange* or the *Euler-Euler* approach [Fluent 2006]. The three different models available in the Euler-Euler approach include the VOF model, the mixture model and the Eulerian model. While the VOF model is more suitable for simulating phenomena such as the draw-down of air or water into the primary phase, the mixture and Eulerian models are suitable for simulating the suspension of particles in the primary phase. As a general guide, there are two parameters that assist in the identification of an appropriate multiphase model for those situations where the use of VOF model is inappropriate. The first is the particulate loading, denoted by $\beta$ and the second is the Stokes number, denoted by *St*.

Particulate loading has a major impact on phase interactions. The particulate loading is defined as the mass density ratio of the dispersed phase *d* to that of the carrier phase *c* and is given by:

$$\beta = \frac{\alpha_d \rho_d}{\alpha_c \rho_c} \qquad \text{- 5.3}$$

where

$\alpha_d$ : volumetric fraction of dispersed phase

$\alpha_c$ : volumetric fraction of carrier phase

$\rho_d$ : density of dispersed phase, kg $m^{-3}$

$\rho_c$ : density of carrier phase, kg $m^{-3}$

The material density ratio is defined as

$$\gamma = \frac{\rho_d}{\rho_c} \qquad \text{- 5.4}$$

where

$\gamma > 1000$ : gas-solid flows

$\gamma \sim 1$ : liquid-solid flows

$\gamma < 0.001$ : gas-liquid flows

Using these parameters, the average distance between the individual particles of the particulate phase can be estimated via Crowe et al. [1998] model and is given by:

$$\frac{L}{d_d} = \left(\frac{\pi + k}{6k}\right)^{1/3} \qquad \text{- 5.5}$$

where

$$k = \frac{\beta}{\gamma} \qquad \text{- 5.6}$$

Depending on the particulate loading, the degree of interaction between the phases can be divided into three categories:

*Low loading* (solids volume fraction, $\alpha_d \leq 10\%$) – the coupling between the phases is one-way. In this case, the fluid carrier influences the particles via drag and turbulence, but the particles have no influence on the fluid carrier. The discrete phase, mixture and Eulerian models can all handle this type of problem correctly. Since the Eulerian model is the most computationally expensive, the discrete phase or mixture model is preferable.

*Intermediate loading* (solids volume fraction, $\alpha_d \geq 10\%$) – the coupling is two-way. In this case, the fluid carrier influences the particulate phase via drag and turbulence, but the particles in turn influence the carrier fluid via reduction in mean momentum and turbulence. The discrete phase, mixture, and Eulerian models are all applicable here. The

Stokes number can be used to distinguish the most suitable model to be used under such scenario.

*High loading* (solids volume fraction, $\alpha_d \geq 70\%$) – there is two-way coupling plus particle pressure and viscous stresses due to particles (four-way coupling). Only the Eulerian model will handle this type of problem correctly.

In this modelling work involving the suspension of RDX particles in water,

$\rho_d$ : 1,770 kg $m^{-3}$ (bulk density of RDX particles)

$\alpha_d$ : 0.3 (volume fraction of RDX particles)

$\rho_c$ : 998.2 kg $m^{-3}$ (density of water)

$\alpha_c$ : 0.6 (volume fraction of water)

$\beta(25°C) = 0.75$ $\gamma(25°C) = 1.773$ $k = 0.4230$

$\frac{L}{d_d}$(RDX-water at 25°C) = 1.120

Since the inter-particle distance was larger than the diameter of the particle, the packing was considered as intermediate loading.

For intermediate loading, the mixture model will provide the same level of accuracy as the Eulerian model provided the Stokes number is < 1. If the Stokes number is calculated to be < 1, generally, it is the model of choice over the Eulerian model owing to its less computational demand.

The Stokes number can be defined as the relation between the particles response time and the system response time:

$$St = \frac{\tau_d}{t_s} \qquad \text{- 5.7}$$

where

$$\tau_d = \frac{\rho_d d_d^2}{18\mu_c} \quad \text{- 5.8}$$

and

$$t_s = \frac{L_s}{V_s} \quad \text{- 5.9}$$

$\rho_d$ : density of secondary phase (kg $m^{-3}$)

$d_d^2$ : diameter of secondary phase (m)

$\mu_c$ : absolute viscosity of primary phase (kg $m^{-1}s^{-1}$)

$L_s$ : characteristic length (m) of the system of interest

$V_s$ : characteristic velocity (m $s^{-1}$) of the system of interest

For Stokes number < 1, the particle under investigation will follow the flow closely and any of the three models (discrete phase from Euler-Lagrange, mixture and Eulerian from Euler-Euler) is applicable and the least expensive model, which is the mixture model in most cases, or the most appropriate model considering other factors, can be used. For $St$ > 1, the particles will move independently of the flow and either the discrete phase model or the Eulerian model is applicable. For $St \sim 1$, again any of the three models is applicable, the least expensive or the most appropriate model considering other factors can be used.

In this modelling work, at 25°C:

$\rho_d$ : 1,770 kg $m^{-3}$ (bulk density of RDX particles)

$d_d^2$ : 0.00024 m (median diameter of RDX particles)

$\mu_c$ : 0.001003 Pa.s or kg $m^{-1}s^{-1}$ (viscosity of water at 25°C)

$L_s$ : 1.067 m (diameter of mixing tank)

$V_s$ : 0.9114 m $s^{-1}$ at 80 rpm (volume-weighted average)

From the Stokes number equation, $St$ (80 rpm) = 0.004823

Clearly, the mixture model was applicable in this modelling work.

## 5.5 Multiphase modelling: mixture model

The mixture model is a simplified Eulerian approach for modelling n-phase flows. This model uses a single-fluid approach and it allows phases to be interpenetrating. In addition, the model allows phases to move at different velocities, using the concept of slip velocities. This model solves the continuity equation for the mixture, the momentum equation for the mixture, the energy equation for the mixture, the volume fraction equation for the secondary phases and the algebraic expressions for the relative velocities if the slip velocity option is activated. However, since no heat transfer was modelled, the energy equation was not solved or discussed.

The continuity equation for the mixture model is:

$$\frac{\partial}{\partial t}(\rho_m) + \nabla \cdot (\rho_m \vec{v}_m) = 0 \qquad \text{- 5.10}$$

where the mass-averaged velocity is given by:

$$\vec{v}_m = \frac{\sum_{k=1}^{n} \alpha_k \rho_k \vec{v}_k}{\rho_m} \qquad \text{- 5.11}$$

and the mixture density is given by:

$$\rho_m = \sum_{k=1}^{n} \alpha_k \rho_k \qquad \text{- 5.12}$$

where $\alpha_k$ is the volume fraction of phase $k$.

The momentum equation for the mixture model is:

$$\frac{\partial}{\partial t}(\rho_m \vec{v}_m) + \nabla \cdot (\rho_m \vec{v}_m \vec{v}_m) = -\nabla p + \nabla \cdot [\mu_m (\nabla \vec{v}_m + \nabla \vec{v}_m^T)] + \rho_m \vec{g} + \vec{F} + \nabla \cdot (\sum_{k=1}^{n} \alpha_k \rho_k \vec{v}_{dr,k} \vec{v}_{dr,k}) \quad - 5.13$$

where $n$ is the number of phases, $\vec{F}$ is the body force, and $\mu_m$ is the mixture viscosity and is given by:

$$\mu_m = \sum_{k=1}^{n} \alpha_k \mu_k \quad - 5.14$$

and the drift velocity, $\vec{v}_{dr,k}$ for secondary phase $k$ is given by:

$$\vec{v}_{dr,k} = \vec{v}_k - \vec{v}_m \quad - 5.15$$

Slip velocity is defined as the velocity of the secondary phase $p$ relative to the velocity of the primary phase $q$:

$$\vec{v}_{pq} = \vec{v}_p - \vec{v}_q \quad - 5.16$$

It follows that the drift velocity and the slip velocity are interrelated by this expression:

$$\vec{v}_{dr,p} = \vec{v}_{pq} - \sum_{k=1}^{n} \frac{\alpha_k \rho_k}{\rho_m} \vec{v}_{qk} \quad - 5.17$$

The mixture model utilises algebraic slip formulation in which the fundamental assumption of the algebraic slip mixture model is that to prescribe an algebraic relation for the slip velocity, a local equilibrium between the phases should be reached over short spatial length scale. The form of the relative velocity is given by:

$$\vec{v}_{pq} = \frac{\tau_p (\rho_p - \rho_m)}{f_{drag} \rho_p} \vec{a} \quad - 5.18$$

where

$$\tau_p = \frac{\rho_p d_p^2}{18\mu_q} \qquad \text{- 5.19}$$

$d_p$ : diameter of the particles, droplets or bubbles of secondary phase $p$

$\vec{a}$ : secondary-phase particle's acceleration

Finally, $f_{drag}$ is the drag function which is taken from Schiller and Naumann [1935] and is given by:

$$f_{drag} = \begin{cases} 1 + 0.15\,\mathrm{Re}^{0.687} & \text{for } \mathrm{Re} \le 1000 \\ 0.0183\,\mathrm{Re} & \text{for } \mathrm{Re} > 1000 \end{cases}$$

and the acceleration $\vec{a}$ comes in the form of:

$$\vec{a} = \vec{g} - (\vec{\upsilon}_m \cdot \nabla)\vec{\upsilon}_m - \frac{\partial \vec{\upsilon}_m}{\partial t} \qquad \text{- 5.20}$$

The simplest algebraic slip formulation is the drift flux model, in which the acceleration of the particle is given by gravity and/or a centrifugal force and the particulate relaxation time is modified to take into account the presence of other particles. In turbulent flows the relative velocity should contain a diffusion term due to the dispersion appearing in the momentum equation for the dispersed phase. Fluent® added this dispersion to the relative velocity:

$$\vec{\upsilon}_{pq} = \frac{(\rho_p - \rho_m)d_p^2}{18\mu_q f_{drag}}\vec{a} - \frac{\nu_m}{\alpha_p \sigma_D}\nabla\alpha_q \qquad \text{- 5.21}$$

$\nu_m$ : mixture turbulent viscosity

$\sigma_D$ : Prandtl dispersion coefficient

When the multiphase calculation is done with slip velocity, the formulation for the drag function can be prescribed directly. The available choices in Fluent® includes: Schiller and Naumann [1935], being the default formulation, Morsi and Alexander [1972], symmetric, constant and user-defined drag function formula. If the slip velocity is not solved, the mixture model is reduced to a homogeneous multiphase model.

The volume fraction equation for the secondary phase $p$ can be obtained from the continuity equation for secondary phase $p$. It is given by:

$$\frac{\partial}{\partial t}(\alpha_p \rho_p) + \nabla \cdot (\alpha_p \rho_p \vec{v}_m) = -\nabla \cdot (\alpha_p \rho_p \vec{v}_{dr,p}) \quad \text{- 5.22}$$

Since the concentration of particles is an important factor in the calculation of the effective viscosity for the mixture, the granular viscosity can be used to get a value for the viscosity of the suspension. The volume weighted averaged for the viscosity would now contain shear viscosity arising from particle momentum exchange due to translation and collision. The collisional, kinetic parts and the optional frictional part are added to give the solids shear viscosity.

$$\mu_s = \mu_{s,collision} + \mu_{s,kinetic} + \mu_{s,friction} \quad \text{- 5.23}$$

The collisional part of the shear viscosity is modelled as Gidaspow [1992] and Syamlal et al. [1993] and is given by:

$$\mu_{s,collision} = \frac{4}{5}\alpha_s \rho_s d_s g_{0,ss}(1+e_{ss})\left(\frac{\Theta_s}{\pi}\right)^{1/2} \quad \text{- 5.24}$$

Two expressions for the kinetic part are provided by Fluent® where the default expression is from Syamlal et al. [1993] and is given by:

$$\mu_{s,kinetic} = \frac{\alpha_s d_s \rho_s \sqrt{\Theta_s \pi}}{6(3-e_{ss})}\left[1+\frac{2}{5}(1+e_{ss})(3e_{ss}-1)\alpha_s g_{0,ss}\right] \quad \text{- 5.25}$$

Expression from Gidaspow [1992] is given by:

$$\mu_{s,kinetic} = \frac{10\rho_s d_s \sqrt{\Theta_s \pi}}{96\alpha_s (1+e_{ss}) g_{0,ss}} \left[1 + \frac{4}{5} g_{0,ss} \alpha_s (1+e_{ss})\right]^2 \quad \text{- 5.26}$$

and

$e_{ss}$ : coefficient of restitution for particle collisions

$g_{0,ss}$ : radial distribution function

$\Theta_s$ : granular temperature

Apart from Syamlal et al. [1993] and Gidaspow [1992] expressions, a constant value can be specified for the granular viscosity or user-defined granular viscosity formulation can be used.

The various viscosity formulations due to collision and kinetic, need the specification of the granular temperature $\Theta_s$ for the $s^{th}$ solids phase. The transport equation proposed by Syamlal et al. [1993] that represents the algebraic model set as default model in Fluent®, was obtained by neglecting convection and diffusion in the transport equation from the Ding and Gidaspow [1990] kinetic theory:

$$0 = \left(-p_s \bar{\bar{I}} + \bar{\bar{\tau}}_s\right) : \nabla \vec{v}_s - \gamma_{\Theta_s} + \phi_{ls} \quad \text{- 5.27}$$

with

$\left(-p_s \bar{\bar{I}} + \bar{\bar{\tau}}_s\right) : \nabla \vec{v}_s$ : generation of energy by the solid stress tensor

$\gamma_{\Theta_s}$ : collisional dissipation of energy

$\phi_{ls}$ : energy exchange between the $l^{th}$ fluid or solid phase and the $s^{th}$ solid phase

The collisional dissipation of energy $\gamma_{\Theta_s}$ represents the rate of energy dissipation within the $s^{th}$ solids phase due to collisions between particles. This term is represented by the expression derived by Lun et al. [1984] and is given by:

$$\gamma_{\Theta m} = \frac{12(1-e_{ss}^2)g_{0,ss}}{d_s\sqrt{\pi}}\rho_s\alpha_s^2\Theta_s^{3/2} \qquad -5.28$$

The transfer of the kinetic energy of random fluctuations in particle velocity from the $s^{th}$ solids phase to the $l^{th}$ fluid or solid phase is represented by $\phi_{ls}$ and is given by:

$$\phi_{ls} = -3K_{ls}\Theta_s \qquad -5.29$$

The following granular temperature options are available, namely: algebraic formulation, being the default setting. This algebraic expression was obtained by neglecting convection and diffusion in the transport equation. Constant granular temperature for those very dense situations where the random fluctuations are small and finally user-defined function for granular temperature.

The total solid pressure is calculated and included in the mixture momentum equations. It is given by:

$$P_{s,total} = \sum_{q=1}^{N} p_q \qquad -5.30$$

Simulations were generally considered converged when the residuals for mass, momentum and turbulence kinetic energy and its dissipation rate fell below $1\times10^{-4}$. To speed up the iteration process, a dual-processor capability computer (3.20GHz and 8GB RAM) operated on Linux 4 Redhat Enterprise was used, and Fluent® parallel processing software to split the total number of cells equally, and assign them to each processor. In addition, the second-order upwind scheme was used at partition boundaries.

### 5.5.1 Summary of drag function options

When the mixture multiphase model is selected, the drag functions available are:

*Schiller-Naumann* – this is the default method and is acceptable for general use in all fluid-fluid multiphase calculations

*Morsi-Alexander* – this is the most complete, adjusting the function definition frequently over a large range of Reynolds numbers, but calculations with this model may be less stable than with the other models

*Symmetric* – this is recommended for flows in which the secondary (dispersed) phase in one region of the domain becomes the primary (continuous) phase in another. For example, if air is injected into the bottom of a container filled halfway with water, then the air which is originally the dispersed phase at the bottom half of the container becomes the continuous phase when it reaches the top half of the container

*Wen and Yu* – this is applicable for dilute phase flows, in which the total secondary phase volume fraction is significantly lower than that of the primary phase

*Gidaspow* – this is recommended for dense fluidised beds

*Syamlal-O'Brien* – this is recommended for use in conjunction with the Syamlal-O'Brien model for granular viscosity

## 5.6 Characterisation results and discussion

### 5.6.1 Existing geometrical configuration

Figure 5.10: Existing geometrical configuration

Figure 5.10 shows the geometrical configuration of the RDX slurry holding tank. It consisted of a top 4-bladed PBT and a bottom retreat curve. Originally, the two impellers were located next to each other, located at the bottom of the tank where the current retreat curve impeller was positioned. To mitigate the ineffectiveness of this configuration, the pitched blade turbine was shifted to a higher position along the shaft. Moreover, the bottom outlet was originally located at the bottom of the tank. When the impeller was rotating at 60 rpm, nothing came out from the outlet. To induce an outlet of the product, the speed must be reduced to 30 rpm, however, in doing so, the homogeneity of the product was compromised. This research work recommended that the outlet position be shifted to the bottom-side outlet because immediately below the impeller, most vectors were travelling upwards toward the bottom impeller, thus preventing the slurry from leaving the tank when the impellers were rotating at 60 rpm. The problem was resolved when the bottom outlet was shifted to the bottom-side outlet position.

This multiphase simulation was initiated by patching the tank bottom with RDX particles, leaving the rest as water [Ochieng and Lewis 2006], as shown in Figure 5.11. The simulation results to be followed were carried out on the assumption that the tank was

completely filled with 30% v/v slurry. The packing limit which specifies the maximum volume fraction for the granular phase was set at 0.80. Although the RDX particle size analysis revealed a normal curve particle size distribution, its particle size was taken as 0.00015 m or 150 μm. Modelling based on the largest particle size will inadvertently lead to over-design while modelling the smallest particle will lead to under-design.

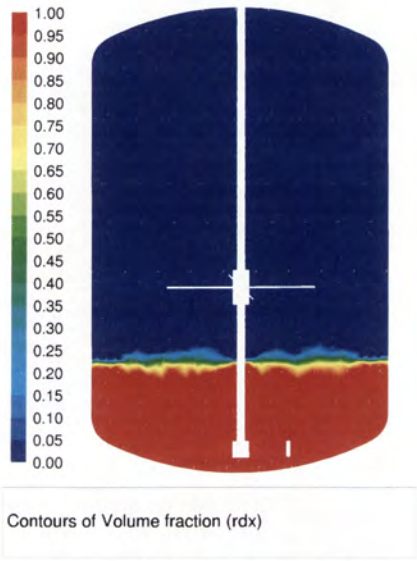


Figure 5.11: RDX volume fraction at 0 rpm

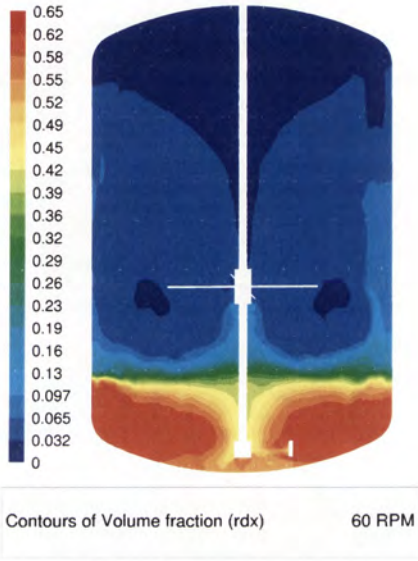


Figure 5.12: RDX volume fraction at 60 rpm

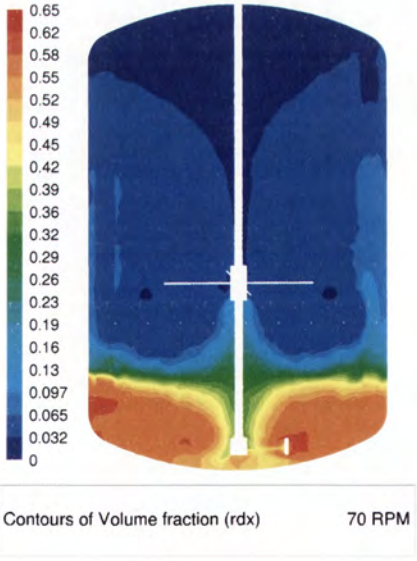


Figure 5.13: RDX volume fraction at 70 rpm

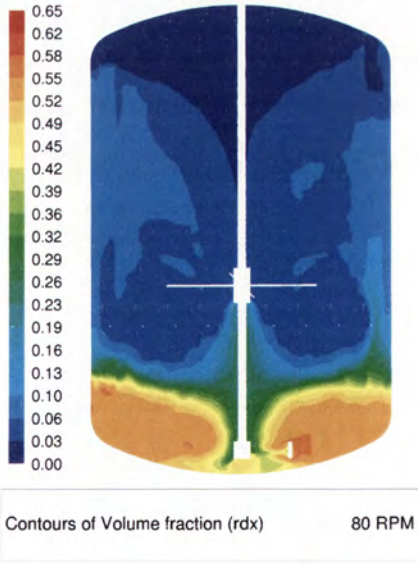


Figure 5.14: RDX volume fraction at 80 rpm

Figures 5.12-5.14 show that increasing the impeller speed did not produce significant benefit to towards the homogeneity of the slurry. This confirms the ineffectiveness of the existing geometrical configuration.

## 5.7 Proposed geometrical configuration

### 5.7.1 Various setups

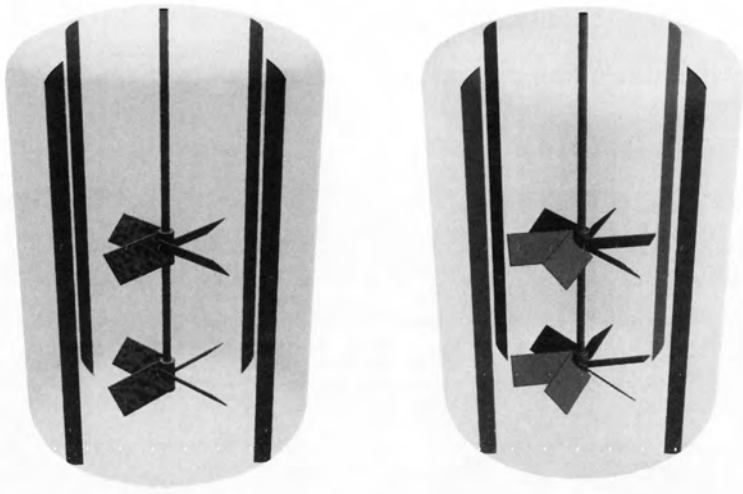

Variant 1 Variant 2

Figure 5.15: Two variants modelled and simulated

The two variants shown in Figure 5.15 consisted of, starting from the left hand side:

Variant 1: A pair of top and bottom 4-bladed PBTs

Variant 2: A pair of top and bottom 6-bladed PBTs (*S/D* = 1.0)

Variant 3: As per variant 2 but *S/D* ratio = 1.1 at 80 rpm

Variant 4: As per variant 2 but *S/D* ratio = 1.3 at 80 rpm

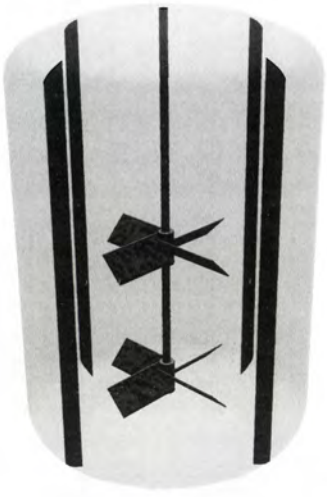

Figure 5.16: Variant 1

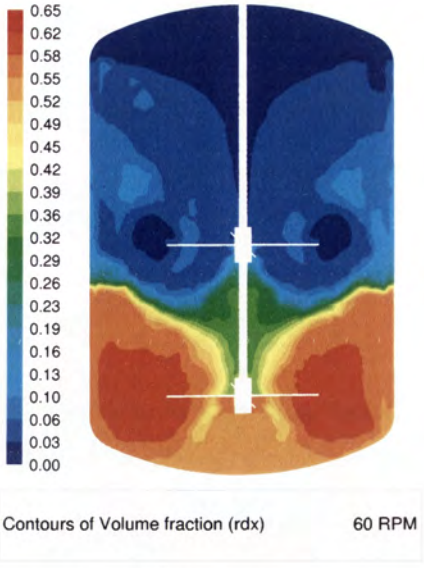


Figure 5.17: Variant 1 at 60 rpm

Figure 5.16 shows the geometrical configuration of the RDX slurry holding tank (*S/D*=1.0, *D/T*=0.5) while Figure 5.17 shows the contours of volume fraction when the impellers were rotating at 60 rpm. In this diagram, the cloud height only reached 40% of the liquid height although the contours indicated that the concentration was lower than that obtained from a single PBT. This agreed with previous studies that discovered adding a second impeller enhances homogeneity of the bulk fluid.

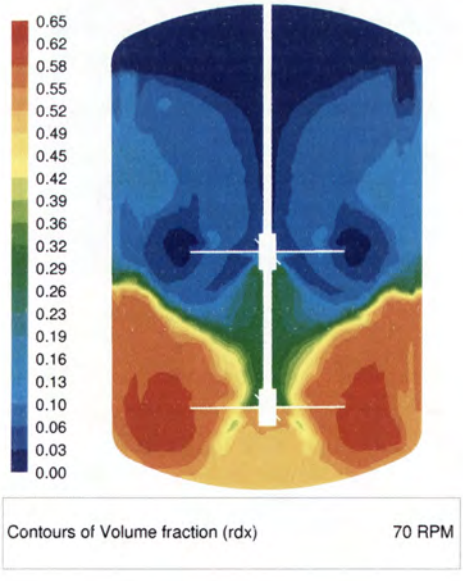


Figure 5.18: Variant 1 at 70 rpm

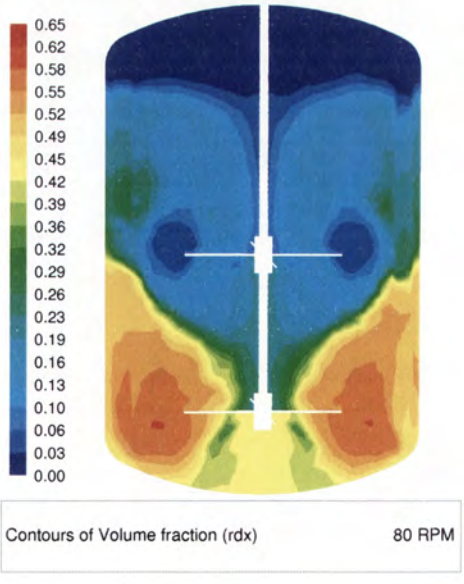


Figure 5.19: Variant 1 at 80 rpm

Increasing the impellers rotational speed from 60 rpm to 70 rpm and from 70 rpm to 80 rpm achieved a slight improvement in the suspension of RDX, as shown in Figures 5.18 and 5.19.

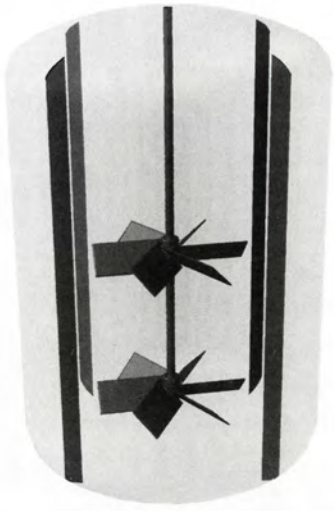

Figure 5.20: Variant 2 at 60 rpm

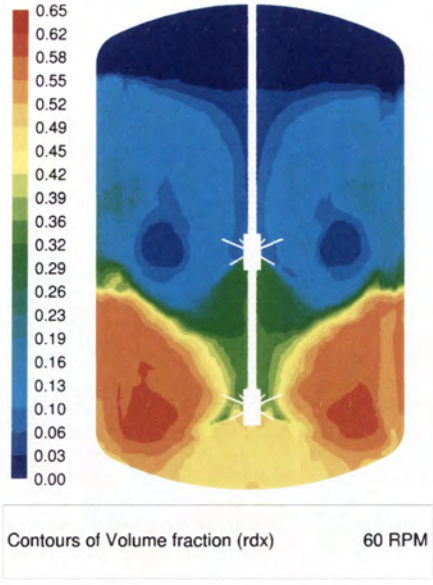


Figure 5.21: Variant 2 at 60 rpm

Figure 5.20 shows the geometrical configuration consisting of a 6-bladed PBT designed to increase the cloud height at low speed and improves homogeneity. Figure 5.21 shows that at 60 rpm, the cloud height reached 50% of the liquid height only. The contours profile was similar to that obtained from a 4-bladed PBT.

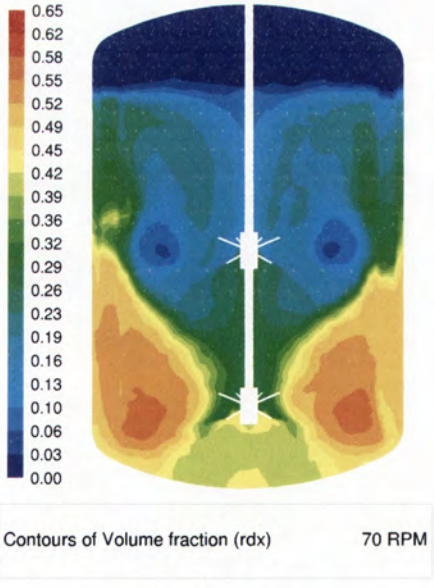


Figure 5.22: Variant 2 at 70 rpm

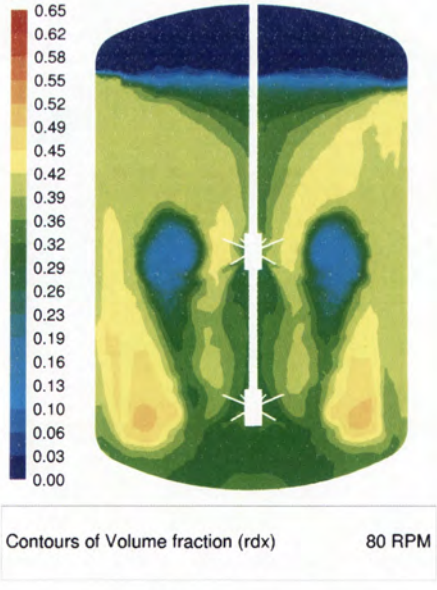


Figure 5.23: Variant 2 at 80 rpm

Figure 5.22 shows that at a minimum speed of 70 rpm, the cloud height reached 60% of the tank height. Contours profile showed that the RDX suspension was not homogeneous. A

good result was obtained when the impeller speed was increased to 80 rpm where the cloud height attained 90% of the liquid height, shown in Figure 5.23.

Overall, from the impeller effectiveness in creating a homogenous RDX suspension, the 6-bladed PBT outperformed the 4-bladed PBT.

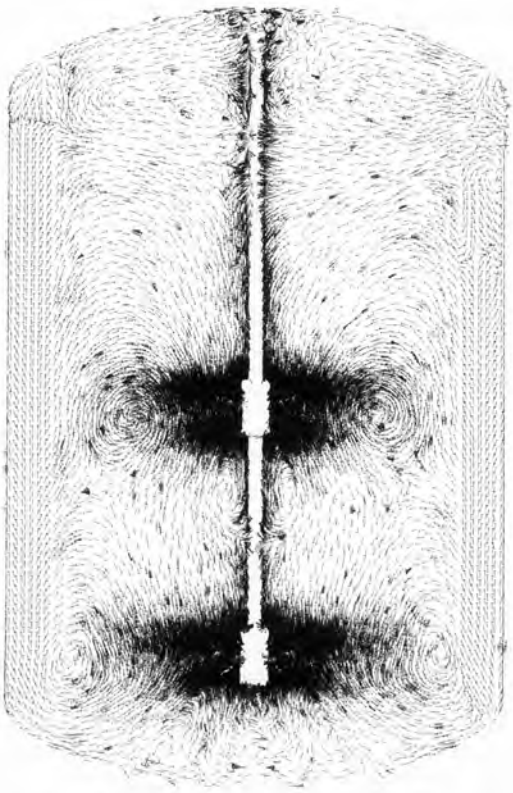

Figure 5.24: Velocity vector of variant 4 at 70 rpm

Figure 5.24 shows the velocity vectors of the tank having geometrical configuration consisting of the two 6-bladed PBT rotating at 80 rpm. It shows that a large loop starting from the top impeller which extended past the bottom impeller before being directed upward by the standard baffles. No compartmentalisation, which is known to hinder the achievement of good cloud height, was observed. It must be noted that on the region which lay directly below the bottom impeller has the flow moving upwards toward the impellers. This is the reason why the outlet must not be located directly below the bottom impellers if, during discharge, the impellers are required to be kept in motion.

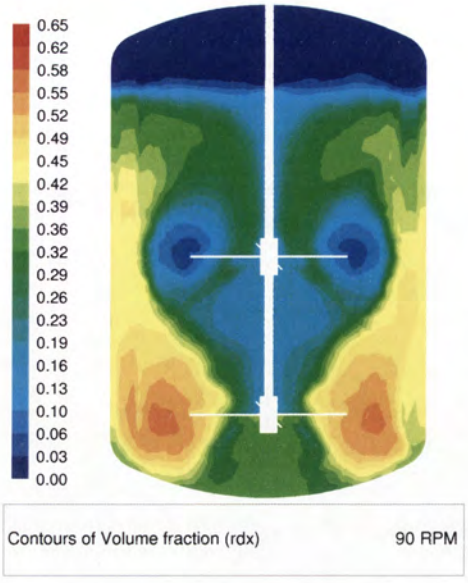


Figure 5.25: Variant 1 at 90 rpm

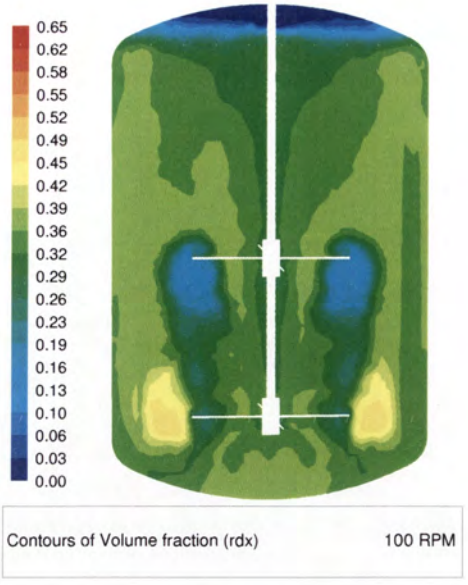


Figure 5.26: Variant 1 at 100 rpm

Figure 5.25 shows that for a pair of 4-bladed PBT, the performance was still unsatisfactory relative to that using 6-bladed PBT even when the impeller rotational speed was increased to 90 rpm. Figure 5.26 shows that for it to match the performance of 6-bladed PBT, the rotational speed must be increased to 100 rpm. At 100 rpm, the power consumption was 16.78 kW. This figure was calculated by first obtaining the torque using Fluent® post-processing feature, and multiplied it by 2, $\pi$ and impeller's speed [Alliet-Gaubert 2006].

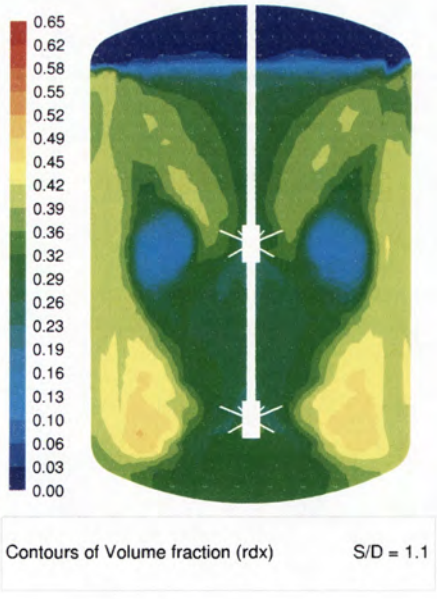


Figure 5.27: Variant 3 at 80 rpm

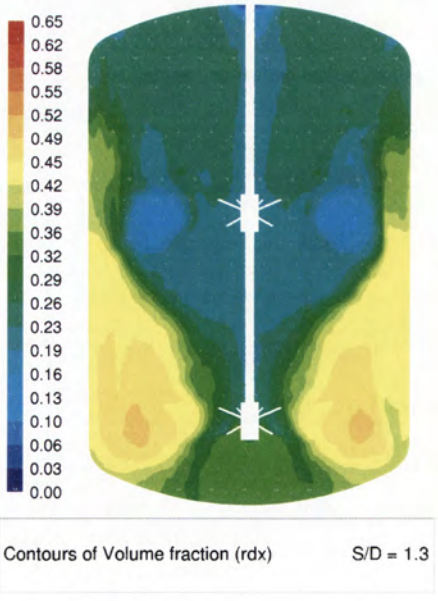


Figure 5.28: Variant 4 at 80 rpm

Figure 5.27 shows the contour plot of the RDX particles achieving a higher level of cloud height at the expense of a more homogeneous RDX suspension when the *S/D* ratio was increased to 1.1. When the *S/D* ratio was further increased to 1.3, the cloud height dropped immediately to the top impeller level, as shown in Figure 5.28.

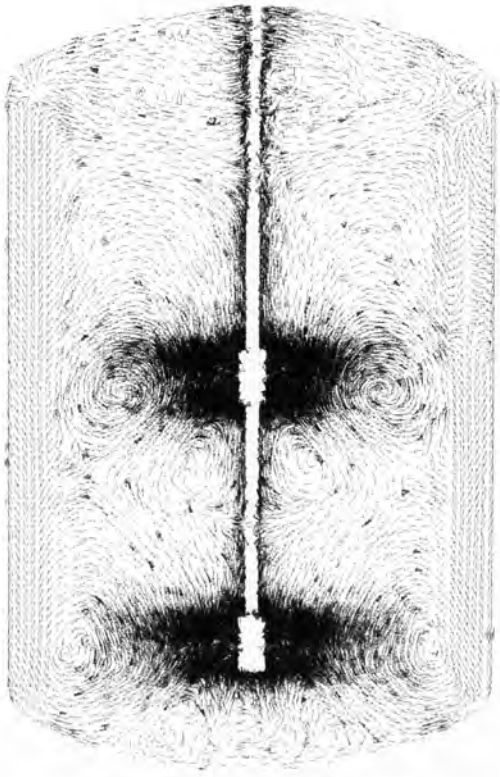

Figure 5.29: Vector plot of S/D = 1.1

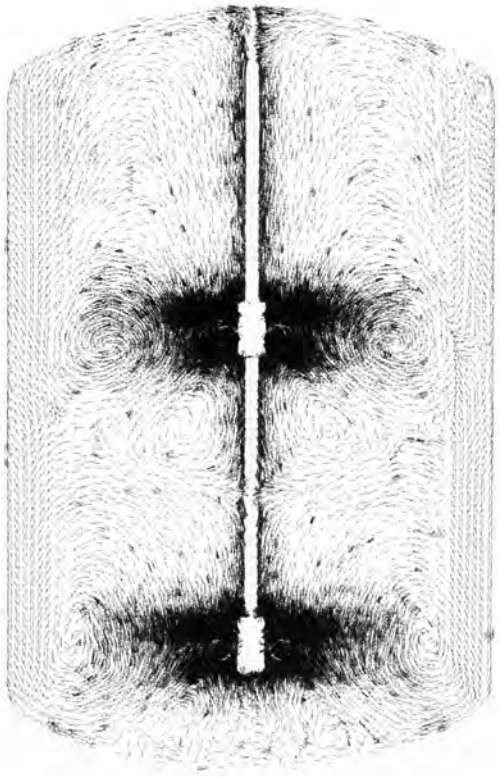

Figure 5.30: Vector plot of S/D = 1.3

The decrease in the cloud height attained when the *S/D* ratio was increased to 1.3 can be explained by studying the vector plots generated using *S/D* = 1.1 and *S/D* = 1.3. Figure 5.29 shows that compartmentalisation started to occur at *S/D*=1.1 and the large circulation loop present in *S/D* = 1.0 started to diminish. At *S/D* = 1.3 as shown in Figure 5.30, there were two distinct compartments, each surrounding the impellers. The failure to achieve a cloud height above the top impeller was attributed to the formation of such compartments. This observation agreed with the findings of Bakker et al. [2000] which concluded that adding a second impeller will assist in producing a more homogeneous suspension however, the impellers must not be placed too far apart otherwise the cloud height may never reach the top impeller.

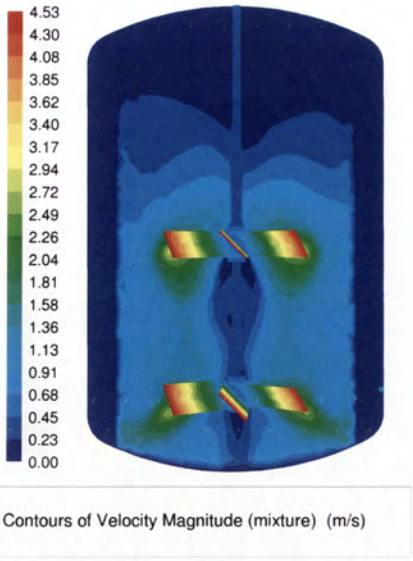


Figure 5.31: Velocity contours of variant 3 at 80 rpm

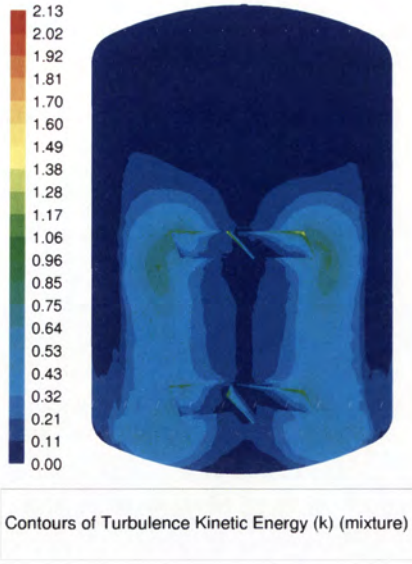


Figure 5.32: Turbulence contours of variant 3 at 80 rpm

Figure 5.31 shows velocity contours of the 6-bladed geometrical configuration rotating at 80 rpm. In there, the slurry was still moving at acceptable speed even at the top of the tank. This accounted for the fact that the cloud height obtained was high. In addition, velocity was at its highest around the impellers region especially along the downward path. This phenomenon was attributed to the axial flow nature of the impellers. Figure 5.32 exhibits the turbulence contour plot at 80 rpm which shows that turbulence region reached nearly the top of the tank. It was obvious that the dead region on this geometrical configuration had been minimised. Moreover, because of the far reaching influence of the impellers discharge, the RDX particles were suspended homogenously.

### 5.7.2 Power requirement

Existing drive motor was rated at 7 kW and it was anticipated that the power requirement for the recommended geometrical configuration was higher than the existing geometrical configuration. This extra power was needed to accommodate the changes made to the impellers.

The power requirements to operate the impellers in the turbulence regime are given by:

$$N_P = \frac{P}{\rho N^3 D^5} \qquad \text{- 5.31}$$

$N_P$ : power number (dimensionless)

$D$ : diameter of impeller (m)

$\rho$ : density of fluid (kg $m^{-3}$)

$N$ : impeller rotational speed (rev $s^{-1}$)

Flow regime and mixing mechanism is usually dependent on the impeller Reynolds number, defined as [Chopey 2004]:

$$N_{\mathrm{Re}} = \frac{\rho N D^2}{\mu} \qquad \text{- 5.32}$$

$\rho$ : density of fluid, kg $m^{-3}$

$N$ : impeller rotational speed, rev $s^{-1}$

$D$ : impeller diameter, m

$\mu$ : absolute viscosity, kg $m^{-1}s^{-1}$ or Pa.s

For Reynolds number ranging from 10 to 100, the mixing regime is laminar. For turbulent mixing regime, the Reynolds number is greater than 10,000. Transition mixing regime falls between the laminar and turbulent mixing regime, that is, 100 < transition < 10,000. Besides correlating the type of flow regime to the impeller Reynolds number, the mixing time, impeller pumping rate, impeller power consumption, heat and mass transfer coefficients can also be correlated to this dimensionless group.

In this case when:

$\rho$ : $(0.6667 \times 998.2\ kg\ m^{-3}) + (0.3333 \times 1{,}770\ kg\ m^{-3}) = 1{,}255\ kg\ m^{-3}$

$N$ : $1.333\ rev\ s^{-1}$ (impeller rotational speed at 70 rpm)

$D$ : 1.067 m (impeller diameter)

$\mu$ : $0.001261\ kg\ m^{-1}s^{-1}$ or Pa.s

*Re* was found to be 1,510,762 which mean the mixing was carried out at fully turbulence regime.

For shaft with multiple impellers, the power delivered to the shaft is the combined power for all impellers. For a 6-bladed PBT, $W/D = 0.2$, $D/T = 0.3333$, $C/T = 0.3333$, installed in a mixing tank with four standard wall baffles, $N_P = 1.64$ [Paul et al. 2004]. For the proposed geometrical configuration, $W/D = 0.23$ and using $W/D$ as the reference value, $N_P = 1.886$

Power per impeller $= 1.886 \times 1{,}255\ kg\ m^{-3} \times (1.333\ rev\ s^{-1})^3 \times (1.067\ m)^5 = 7.753\ kW$

Power requirement for two impellers on a single shaft $= 7.753\ kW \times 2 = 15.507\ kW$

Therefore, proposed motor size required to drive this geometrical configuration is $15\ kW \times 1.2 = 18\ kW$ at 80 rpm.

### 5.7.3 Minimum shaft diameter

To compute the shaft diameter for both allowable shear and tensile stress, the rotational speed of the mixer, the type of impeller, diameter of impeller, power, location of impellers and the process service the impellers were designed to deliver, must be known. For top-entry overhung shaft, the maximum torque will occur above the uppermost impeller. The maximum torque can be determined from the following equation:

$$T_{Q(\max)} = \frac{P}{2\pi N} \qquad \text{- 5.33}$$

where

$T_{Q(max)}$ : torque, Nm

$P$ : motor power, W

$N$ : impeller rotational speed, rev $s^{-1}$

To ensure that any process upset does not exceed shaft design limits, the motor power was used instead of impeller power. Individual fractions of motor power were required for the following bending moment equation because the impellers were at different height on the shaft.

$$P_i = P_{i(calculated)} \frac{P_{motor}}{\sum_{i=1}^{n} P_{i(calculated)}} \qquad \text{- 5.34}$$

The maximum bending moment, $M_{\max}$, for a top-entry overhung shaft is the sum of the products of the hydraulic forces and the distance from the individual impellers to the bottom bearing in the mixer drive.

The following expression computes an empirical hydraulic force related to the impeller torque acting as a load at a distance related to the impeller diameter.

$$M_{\max} = \sum_{i=1}^{n} \frac{0.048 P_i L_i f_{H_i}}{N D_i} \qquad - 5.35$$

where

$M_{max}$ : bending moment, Nm

$L_i$ : distance from the drive bearing to the $i^{th}$ impeller location, m

$N$ : impeller rotational speed, rev $s^{-1}$

$D$ : $i^{th}$ impeller diameter, m

$f_{Hi}$ : hydraulic service factor

The hydraulic service factor is related to the impeller type and process operating conditions. Approximate hydraulic service factors for various impellers and conditions are given in Table 5.2.

Table 5.2: Hydraulic service factor

| Condition | HE impeller | PBT |
|---|---|---|
| Standard | 1.5 | 1.0 |
| Significant time at the free surface | 2.5-3.5 | 2.0-3.0 |
| Operating in boiling system | 2.0-3.0 | 1.5-2.5 |
| Operation in gas sparged systems | 2.5-3.5 | 2.0-3.0 |
| Large volume solid additions | 3.0-5.0 | 3.0-5.0 |
| Inspecting of large solids | 5.0-7.0 | 5.0-7.0 |
| Startup in settled solids | 5.0-7.0 | 5.0-7.0 |
| Operating in a flow stream | 1.5-7.0 | 1.0-7.0 |

Since the bending moment and the torque act simultaneously, these loads must be combined and resolved into a combined shear stress and combined tensile stress acting on the shaft.

The minium shaft diameter for the allowable tensile and shear stresses can be calculated by the following equations:

$$d_t = \left( \frac{16(M_{\max} + \sqrt{T_{Q(\max)}^2 + M_{\max}^2})}{\pi \sigma_t} \right)^{1/3} \quad \text{- 5.36}$$

where

$d_t$ : minimum shaft diameter, m

$\sigma_t$ : allowable tensile stress limit, N $m^{-2}$

$$d_s = \left( \frac{16\sqrt{T_{Q(\max)}^2 + M_{\max}^2}}{\pi \sigma_s} \right)^{1/3} \quad \text{- 5.37}$$

where

$d_s$ : minimum shaft diameter, m

$\sigma_s$ : allowable shear stress limit, N $m^{-2}$

The minimum shaft diameter is the greater of the two values calculated from Equations (5.36) and (5.37).

Limits for shear and tensile stresses are functions of shaft material, operating temperature and processing environment. It is important to determine the allowable stresses in the condition of operation. Besides strength, the shaft straigthness is also important to avoid creating unnecessary loads and strength.

In this scenario,

$P$ : 18,000 W

$N$ : 1.33 rev $s^{-1}$

$T_{Q(\max)} = 2{,}154$ Nm

It is assumed that the calculated $P_{bottom} = 10$ kW and the calculated $P_{top} = 5$ kW

Thus, $P_{bottom} = 12$ kW while $P_{top} = 6$ kW total $P = 18$ kW

$L_{bottom}$ : 2.781, m

$L_{top}$ : 1.714, m

$N$ : 1.33, rev $s^{-1}$

$D_{bottom}$ : 1.067, m

$D_{top}$ : 1.067, m

$f_{H_{bottom}}$ : 10

$f_{H_{top}}$ : 1.5

For the bottom impeller, service factor for startup in settled solids is 7 but this value is applicable for 4-bladed PBT. For 6-bladed PBT, the value is estimated as 10.5 owing to an additional of two blades. For the top blade, service factor for standard application is 1.0. Similarly, the value is estimated as 1.5 for 6-bladed PBT.

The bending moment, $M_{\max}$, is determined to be 11.80 Nm

Table 5.3: Allowable stresses for shaft and impeller design

| Metal type | Shaft Design Tensile Stress ($N\ m^{-2}$) $\times 10^6$ | Shaft Design Shear Stress ($N\ m^{-2}$) $\times 10^6$ | Impeller Design Stress ($N\ m^{-2}$) $\times 10^6$ |
|---|---|---|---|
| Carbon steel | 62.1 | 37.2 | 75.2 |
| Stainless steel 304 | 66.2 | 40.0 | 80.0 |
| Stainless steel 304L | 57.9 | 35.2 | 70.3 |
| Stainless steel 316 | 68.9 | 41.4 | 83.4 |
| Stainless steel 316L | 60.0 | 35.9 | 72.4 |
| Hastelloy C | 91.0 | 54.5 | 109.6 |
| Hastelloy B | 98.6 | 59.3 | 118.6 |
| Monel 400 | 63.4 | 37.9 | 76.5 |
| Inconel 600 | 71.0 | 42.7 | 85.5 |
| Nickel 200 | 50.3 | 30.3 | 60.7 |
| Carpenter 20 | 76.5 | 45.5 | 91.7 |

The shaft will be made from stainless steel 316 and from Table 5.3,

$\sigma_t$ : $68.9 \times 10^6$, $N\ m^{-2}$

$\sigma_s$ : $41.4 \times 10^6$, $N\ m^{-2}$

Thus,

$d_t$ was calculated as 0.0543 m

$d_s$ was calculated as 0.06423 m

Since $d_s$ had a larger value, therefore the minimum shaft diameter was 0.06423 m.

The existing geometry employs shaft with diameter = 0.1016 m. Since the proposed system has a shaft diameter requirement smaller than the shaft diameter employed by the existing system, thus the existing shaft can be used on the proposed system.

### 5.7.4 Calculating the critical Speed

It is however, important to determine that 80 rpm is not close to the critical speed due to natural frequency. Natural frequency is a dynamic characteristic of a mechanical system. An important concern to a reactor or mixer design is the first lateral natural frequency, which is defined as the lowest frequency at which a shaft will vibrate as a function of length and mass. The concern about natural frequency is that an excitation such as mixer operating speed could cause undamped vibrations. Undamped vibrations occur when no resisting forces are present to diminish the amplitude of vibration. Such vibrations could result in sudden and catastrophic failure of the mixer shaft and the most dangerous conditions usually occur when the mixer is operated in air. Large mixers normally operate below the first natural frequency, while small portable mixers, which accelerate quickly, often operate above the first natural frequency. In either case, operating at or near the natural frequency must be avoided for both mechanical reliability and safety. The general rule used to design a mixer shaft and impeller systems is to keep operating speed 20% less than or more than the critical speed. This rule applies to the first, second and third natural frequencies. However, higher-order natural frequencies are seldom encountered in mixer applications. Large mixers running at less than 150 rpm usually operate below the first critical speed while small mixers operating above 250 rpm usually operate between first and second critical, $1.2N_c$ to $0.8N_{c2}$, where $N_{c2}$ is the second lateral natural frequency [Paul et al. 2004]. The factors that determine the lateral natural frequency are the magnitudes and locations of concentrated and distributed masses, the tensile modulus of elasticity of the material and the moment of inertia of the shaft.

The equation that estimates the first lateral natural frequency or critical speed, in revolution per second (rev $s^{-1}$), is given by:

$$N_c = \frac{5.33d^2\sqrt{\frac{E_m}{\rho_m}}}{L\sqrt{L+S_b}\sqrt{W_e+\frac{wL}{4}}} \qquad \text{- 5.38}$$

where

$N_c$ : critical speed, rev $s^{-1}$

$d$ : shaft diameter, m

$E_m$ : modulus of elasticity, N $m^{-2}$

$\rho_m$ : density of the shaft material, kg $m^{-3}$

$L$ : length of shaft, m

$S_b$ : bearing spacing supporting the shaft, m

$W_e$ : equivalent mass of the impellers at the bottom of the shaft, kg

$w$ : specific mass of the shaft, kg $m^{-1}$

$W_e$ is the equivalent mass of each impeller resolved to the bottom of the shaft, and is defined mathematically as:

$$W_e = \sum_{i=1}^{n} W_i\left(\frac{L_i}{L}\right)^3 \qquad \text{- 5.39}$$

$W_i$ is the mass of the individual impellers (kg) and $L_i$ is the shaft length to each impeller (m) and $L$ is the total shaft length (m). A single impeller at the bottom of the shaft results in an equivalent mass equal to the actual impeller mass.

Table 5.4: A few common metals properties

| Metal type | Modulus of elasticity, $E_m$ (N m$^{-2}$) × 10$^{12}$ | Density, $\rho_m$ (kg m$^{-3}$) |
|---|---|---|
| Carbon steel | 0.205 | 7,833 |
| Stainless steel, 304/316 | 0.197 | 8,027 |
| Hastelloy C | 0.213 | 8,941 |
| Hastelloy B | 0.212 | 9,245 |
| Monel 400 | 0.179 | 8,830 |
| Inconel 600 | 0.214 | 8,415 |
| Nickel 200 | 0.205 | 8,913 |
| Carpenter 20 | 0.193 | 7,999 |

The shaft will be made of stainless steel 316 and with the aid of Table 5.4:

$d$ : 0.1016 m

$E_m$ : 0.197E12 N m$^{-2}$

$\rho_m$ : 8,027 kg m$^{-3}$

$L$ : 2.781 m (3.336 m - 0.26 × 2.134 m)

$S_b$ : 0.3 m

$W_e$ : 49.36 kg (taking the mass of each impeller as 40 kg)

$w$ : 65.08 kg m$^{-1}$ (181 kg ÷ 2.781 m)

The critical speed, $N_c$, in this scenario = 5.708 rev s$^{-1}$ or 342 rpm

Since the recommended speed of 80 rpm will be operating at least 20% below the critical speed, shaft vibration due to the natural frequency will be avoided.

### 5.7.5 Recommendation

Figure 5.33: Proposed RDX slurry holding tank

Figure 5.33 shows the proposed RDX slurry holding tank that incorporated existing standard baffles, employed two sets of 6-bladed PBT where the top impeller will be fitted with stabilizers at a rotational speed of 80 rpm, driven by an 18 kW motor. This proposed tank promised > 95% homogeneous RDX suspension.

Table 5.5: Geometrical configuration and operating condition

| Parameter | Values |
|---|---|
| Impellers type | Two 6-bladed PBTs |
| Impellers diameter | 1.067 |
| *S/D* | 1 |
| *D/T* | 0.5 |
| *C/T* | 0.26 |
| *W/D* | 0.23 |
| *T* | 2.134 m |
| *H* | 3.336 |
| *Z* | 2.6688 (80% of H) |
| *Z/T* | 1.25 |
| Fluid | RDX suspended in water |
| Density of water @ 25°C | 998.2 kg $m^{-3}$ |
| Density of RDX @ 25°C | 1,770 kg $m^{-3}$ |
| Viscosity of water @ 25°C | 0.001003 kg $m^{-1}s^{-1}$ |
| Gravity | 9.81 m $s^{-2}$ |
| Operating pressure | 101,325 Pa |
| Impeller speeds | 80 rpm |
| Rotation direction | clockwise |
| Batch volume | 10,860L |

Table 5.5 shows the geometrical configuration and operating condition.

### 5.7.6 Pilot-scale physical trial

A physical trial to determine the effectiveness of the proposed impellers operating at the condition specified was conducted using a pilot-scale size perspex tank fitted with four standard wall baffles. As a general rule of thumb, stabilisers are not required for impellers whose diameters exceed the shaft diameter by a factor of 10 or more. The only exception to this rule is that mixed-flow impellers such as the PBTs, benefit from stabilisers when operating at or near the liquid free surface. Stabilisers, welded to the blades as shown in Figure 5.34, were required to damp the vibration caused by unbalance hydraulic loads when the impeller operates at or near the free liquid surface since during the process of draining the tank content, a few blades will hit air while others will hit the liquid media. It should be noted that the uneven load or forces acting on the shaft might not pose any problem in the absence of the stabilisers in the pilot-scale size that was because of the relatively short shaft length. However, in the actual size slurry holding tank, the shaft was nearly two metres long therefore the impact of uneven forces acting on the shaft was more prominent.

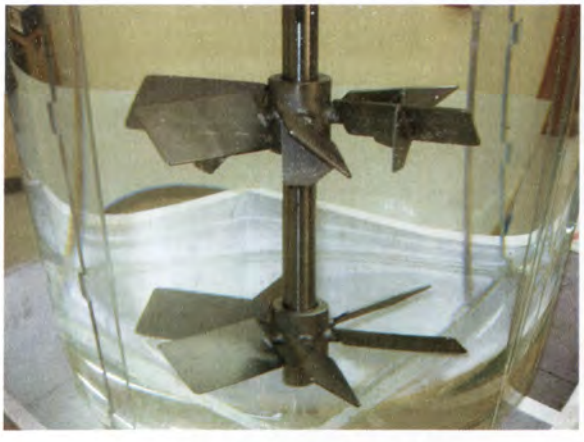

Figure 5.34: Proposed impellers design

Figure 5.35: Suspension of sands-water slurry

Figure 5.35 shows the suspension of sand in water at 80 rpm. No unsuspended sand was observed at the tank bottom therefore it can be safely assumed that $N_{js}$ had been attained. The cloud height attained was greater than 90% of liquid height which means successful suspension of sand was achieved.

Upon the successful completion of the trial involving sand-water system, the same trial was conducted using real high explosive RDX particles. Figure 5.36 shows that 33% volume fraction of RDX was introduced into the pilot-scale perspex tank filled with water. The picture shows that majority of the RDX particles sunk to the bottom of the tank while a small portion of RDX floated along the liquid free surface. These floating RDX particles were actually very fine RDX particles clustered together. Its buoyancy property was attributed to the presence of trapped air inside these clustered particles.

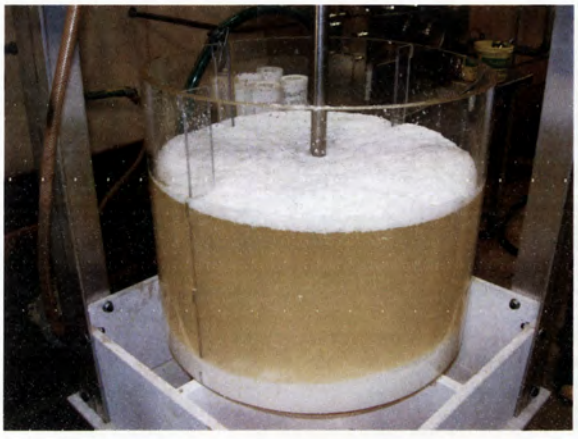

Figure 5.36: Suspension of RDX-water slurry (t = 0s)

Figure 5.37: Suspension of RDX-water slurry (t = 3 mins)

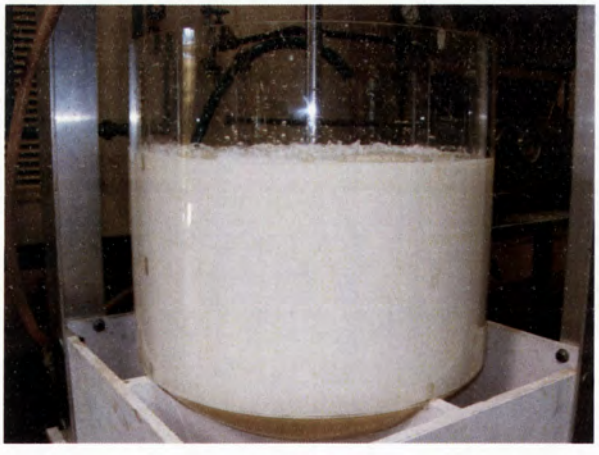

Figure 5.38: Suspension of RDX-water slurry (t = 3 mins)

After 3 mins of impellers rotation, RDX-water stratification layers have disappeared and what remaining was a homogeneous mixture of RDX suspended in water. Figures 5.37 and 5.38 show that the suspension achieved a good cloud height (almost 100%), as evidenced by the lack of a clear fluid/milky fluid interface. This mixture was drained via a bottom outlet into four containers, each with the volume known. By weighing each

container filled with RDX-water slurry obtained from the pilot-testing, a good density estimate of the content in the container was obtained, as presented in Table 5.6.

Table 5.6: Results from the pilot-testing

| Container | A | B | C | D |
|---|---|---|---|---|
| Height of slurry, m | 0.320 | 0.314 | 0.243 | 0.318 |
| Diameter of container, m | 0.290 | 0.290 | 0.290 | 0.290 |
| Volume of slurry, $m^3$ | 0.02114 | 0.02074 | 0.01605 | 0.02101 |
| Mass of slurry-filled container, kg | 23.5 | 22.5 | 16.5 | 22 |
| Density of slurry, kg $m^{-3}$ | 1,112 | 1,085 | 1,028 | 1,047 |

From Table 5.6, it was found that:

Average density of slurry = 1,068 kg $m^{-3}$

Standard deviation = 37.54

Coefficient of variation from one container to another = 3.515%

A simple statistical analysis shows that the coefficient of variation from one container to another was only 3.5%. This leads to the conclusion that using the proposed impellers rotating at a minimum speed of 70 rpm will achieve a homogeneous RDX particles suspension.

## 5.8 Concluding remarks

In this chapter, CFD modelling and simulation was conducted on the suspension of RDX particles inside the slurry holding tank. A process description aided by a process flow diagram was provided to convey a sense of perspective to this modelling work. The objectives were to resolve current issues associated with operating this RDX slurry holding tank and to optimise its performance. To achieve this multiphase modelling successfully, the mixture multiphase model approach was employed and an outline of the mathematics underlying this approach was also given. From the CFD characterisation results, it was discovered that the existing slurry holding tank was performing at sub-optimal level. Additional CFD modellings and simulations were conducted with a view to optimising and improving the performance of this slurry holding tank. The emphasis of the optimisation was placed on the type of impellers, the rotational speed, the impellers spacing, the motor size and the shaft size. From the numerical-based optimisation study, a pilot-scale slurry holding tank was fabricated and a trial to assess its performance was conducted. The trial, conducted using actual RDX particles, showed that the proposed geometrical configuration was successful in suspending RDX particles homogeneously.

# CHAPTER 6: RDX/TNT MIXING TANK

The RDX particles described in Chapter 5 are transported to another manufacturing facility for further processing, in this case, to be made into a composite high explosive called RDX/TNT. RDX/TNT also known as cyclotol is a military high explosive widely-used for bombs filling. It is manufactured by combining RDX (white powder) and TNT (yellow flakes, shown in Figure 6.1, in specified ratio.

Figure 6.1: RDX (white) and TNT (yellow)

The ratio of RDX to TNT ranges from 60/40 to 75/25. RDX/TNT 60/40 is generally known as Composition B. However, in this study, since only RDX/TNT 60/40 is studied, the term cyclotol is also used to refer to Composition B. Cyclotol, shown in Figure 6.2, is produced by mixing cyclo-1,3,5-trimethylene-2,4,6-trinitramine (RDX) and 2,4,6-trinitrotoluene (TNT) at 59.5/39.5 w/w%. 1% Beeswax is added to desensitise the explosive mixture to enable safer handling.

Figure 6.2: RDX/TNT

2,4,6 trinitrotoluene ($C_7H_5N_3O_6$) or trinitrotoluol or trinitrotoluene or trotyl or totile or more commonly known as TNT, usually comes in the form of a pale yellow crystalline solid or flake, Figure 6.1. Its molecular structure is given in Figure 6.3.

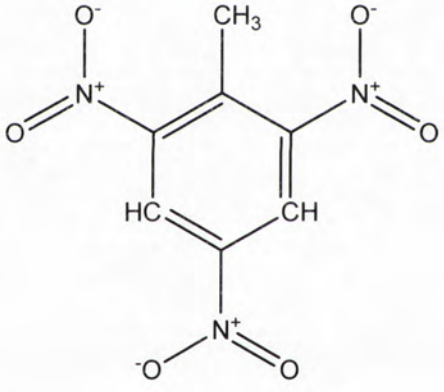


Figure 6.3: Molecular structure of TNT

TNT is almost insoluble in water, sparingly soluble in alcohol, soluble in benzene, toluene and acetone. It is the most important explosive for blasting charges of all weapons, is very stable, neutral and does not react with metals. Apart from being a relatively insensitive powerful high explosive with a detonation velocity of 6,950 m $s^{-1}$, its low melting point renders it suitable for cast filling. Its purity is determined by its solidification point and the minimum value for military purposes is 80.2°C. Although it can be used on its own, it is normally mixed with other more powerful and more sensitive high explosives such as ammonium nitrate to form amatol, with aluminium powder to form tritonal, with RDX to form cyclotol [Kohler and Meyer 1993].

## 6.1 Process description

This process description is given in order to understand the relevance of the CFD study to process operation and help put CFD interpretation into perspective. RDX slurry (water and RDX solid particles) is fed into molten TNT in a mixing tank equipped with a double-impeller and maintained at constant temperature. Typically, an 800 kg batch of cyclotol may be manufactured from 310 kg TNT; 490 kg RDX and > 490 kg $H_2O$. When TNT is being melted, the impeller speed is set at 40 rpm, and is increased to 58 rpm while the RDX slurry is being charged. Mixing process takes place for 10 mins at 40 rpm. After that, the speed is reduced to 10 rpm whereupon the product is recirculated to achieve the desired density which normally takes 5-10 mins to accomplish. There are several factors contributing to homogeneous suspensions and one of them is the impeller speed. For instant, if the impeller speed is set too high, vortex formed will draw-down water. However, if the impeller speed is set too low to mitigate water draw-down, the suspension will not be homogeneous since RDX particles are heavier than molten TNT. The mixing is carried out at the temperature between 85–100 °C. On completion of the mixing process, the content is transferred to the drying tank for further processing where most of the water is removed.

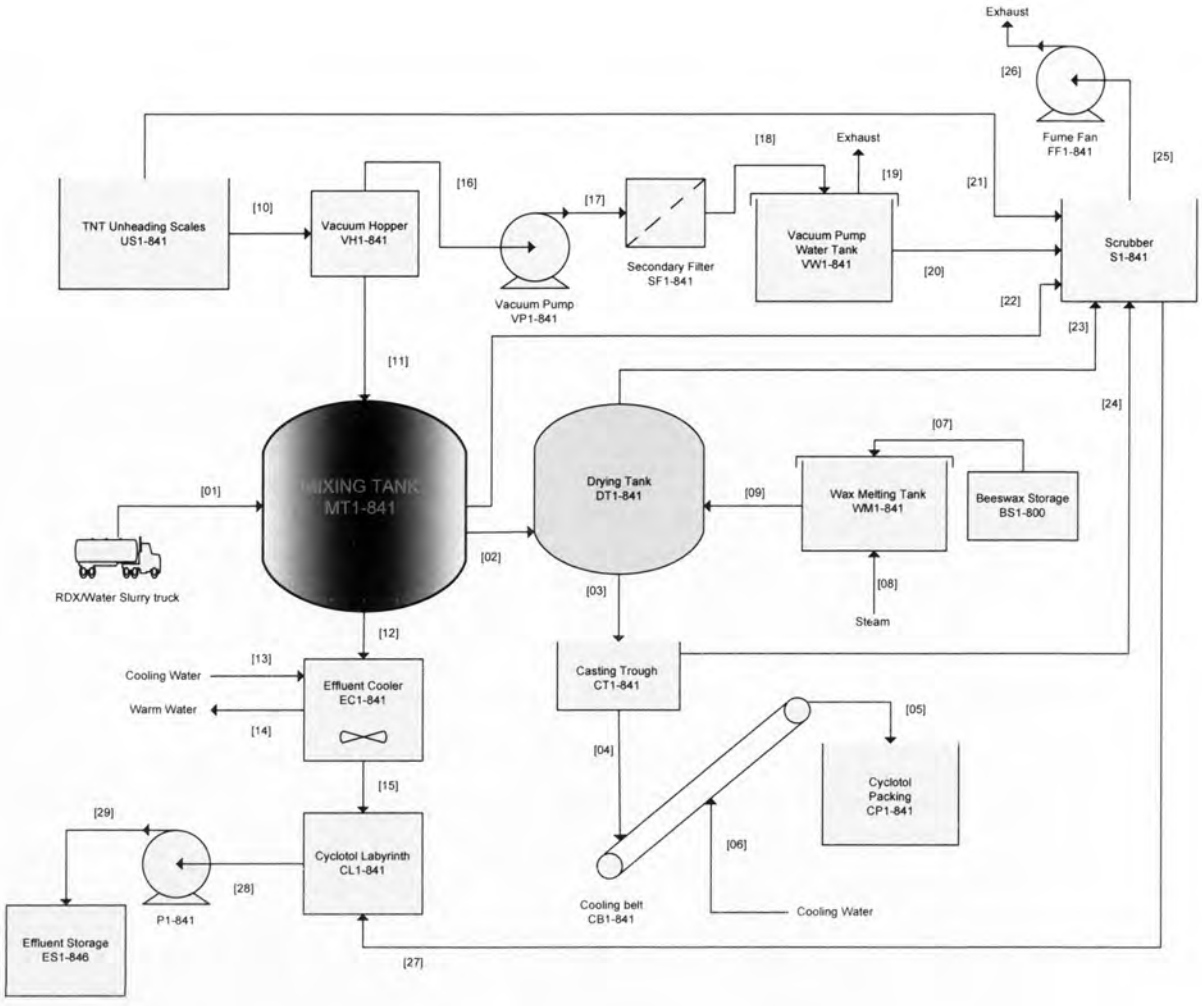


Figure 6.4: Cyclotol manufacturing process flow diagram

Figure 6.4 shows the cyclotol manufacturing process flow diagram and the shaded unit operation, labelled as 'mixing tank, MT1-841' is the focus of this CFD modelling and simulation.

TNT unheading scales (US1-841): A pallet of 2 boxes weighing a total of 310 kg is positioned on the scales below the fume duct. The fume duct is used to transfer dust to the scrubber (S1-841). A pneumatic conveyor is used to transfer the TNT flakes to the mixing tank (MT1-841). The pneumatic conveyor consists of a probe for drawing TNT flakes from the boxes and a vacuum hopper (VH1-841) for filtering the TNT from the air flow. A pump is used to generate vacuum in the probe. An inline metal detector is placed in order to detect any metals mixed with the TNT flakes.

Vacuum hopper (VH1-841): TNT flakes are removed from the air stream by filter socks in the vacuum hopper. Any TNT deposited on the filter sock is removed by a reverse pulse of compressed air that is passed into the socks. This pulse dislodges the TNT which falls to the base of the vacuum hopper and then by opening a flap valve on the base, falls into the mixing tank (MT1-841). The dust with very minute quantity of TNT is passed via a vacuum pump (VP1-841) to a secondary filter (SF1-841) which is no longer used in practice. The vacuum pump is a liquid (water) ring seal type. The liquid seal ensures that there is no mechanical contact with the working mechanism of the pump. The dust is then transferred to a vacuum pump water tank (VW1-841) which entrains the dust particles. The water tank acts as a separator as well as a reservoir for the water used in the vacuum pump. Air is released to the atmosphere while excess water with dust and TNT overflows to the scrubber (S1-841).

Mixing tank (MT1-841): The steam jacketed tank is heated until it reaches a temperature indication of 90 °C. Steam at 100 kPa is used to maintain constant temperature in the tank. Around this temperature, TNT is dropped into the tank from the vacuum hopper (VH1-841) and is melted using a steam sparge and agitation at impeller speed of 40 rpm for 8 – 10 mins. 25 kg – 80 kg of rework may be added to the tank prior to TNT. The steam from the sparge at 400 kPa is used to heat water and melt TNT. RDX (470 kg dry weight) is supplied from the RDX purification plant and hot water is added in large quantities to prepare RDX/$H_2O$ slurry (RDX:$H_2O$ of 1:3). The transfer time for the slurry is approximately 10 mins. This slurry is added to the molten TNT in the mixing tank to achieve a homogeneous mixture (cyclotol). The impeller is operated at 58 rpm during the RDX incorporation stage.

After 2 mins of mixing, the impeller speed is reduced to 10 rpm to pump cyclotol to a drying tank (DT1-841). The amount of cyclotol transferred from the mixing tank to the drying tank (DT1-841) is monitored by a mass flowmeter with a density indication. The cyclotol mixture is first recycled back to the mixing tank through a pump a few times until the desired density between 1,650 and 1,680 kg $m^{-3}$ is achieved. The average density of cyclotol is 1,670 kg $m^{-3}$. A control valve to the drying tank is opened and the mixture is then pumped to the drying tank. The transfer time of 800 kg of cyclotol from the mixing tank to drying tank is approximately 6 – 8 mins.

Crude mixture consisting of hot water, cyclotol and non-homogenous RDX particles and molten TNT that could not be transferred to the drying tank due to unsuitable density is left behind in the tank. The control valve to the drying tank is closed off and the crude mixture is decanted through a decant pump to an effluent cooler (EC1-841) with circulating cooling water (streams 13 and 14). The cooled product from the cooler is released to the cyclotol labyrinth (CL1-841). In the labyrinth, the crude solid part of the product settles to the bottom and the liquid effluent is pumped out (P1-841) to effluent storage (ES1-846) for treatment. The liquid effluent can be reused in the process. The settled crude product mixes with incoming TNT traces from the scrubber (S1-841) and this final mixture is removed by a steam ejector. The liquid effluent can be reused in the process. Any fume created from the process in the mixing tank is transferred to the scrubber.

Drying tank (DT1-841): The steam jacketed tank uses steam from a sparge at 105 °C and 100 kPa to vaporise any residual water. An impeller in the tank is used to dry the mixture transferred from the mixing tank (MT1-841). The impeller is operated at a constant speed of 35 rpm during the drying phase and the casting phase. Once the tank is heated up to the temperature indication of 105 °C, the drying cycle is completed and all the water has evaporated. The duration for the drying cycle is between 30 and 180 mins, 60 mins average. Then 9 kg of molten beeswax from the wax melting tank (WM1-841) is added to the drying tank. The minimum mixing duration is 5 mins minimum and the average mixing duration is 10 mins. The impeller speed can be increased to 40 or 45 rpm during the casting phase only if necessary to lower the viscosity of cyclotol mixture so that the mixture flows properly and at a faster rate into the casting trough (CT1-841) or to achieve a homogeneous state. The bottom tank geometry of the drying tank is spherical. Again fume or vapour created from the tank is transferred to the scrubber (S1-841).

Wax melting tank (WM1-841): Beeswax from storage (BS1-800) is poured in the tank and steam jacketed tank is heated with steam at 35 kPa. About 9 kg of molten beeswax is then pumped to the drying tank (DT1-841) via a wax measure pot. The transfer line between the wax melting tank and the drying tank (DT1-841) has a steam jacket which prevents the wax from solidifying.

Casting trough (CT1-841) and cooling belt (CB1-841): The cyclotol mixed with beeswax from the drying tank (DT1-841) is cast into a trough. The casting duration is between 30 and 60 mins, 40 mins average. Similarly fume or vapour created is transferred to the scrubber (S1-841). The trough has a line of dies through which the mixture is poured on the upper surface of a cast and cooled conveyor. This cast and cooled conveyor is a stainless steel conveyor belt. As the rows of molten cyclotol from the trough land on the cooling belt and start moving upwards, cooling water is sprayed on the under surface of the belt to solidify the molten cyclotol. Hot compressed air is also applied on molten cyclotol at the lower end causing the rows to flatten providing more surface area, better cooling and flaking. When the rows reach the top end of the conveyor belt, the solid cyclotol is broken off with a doctor knife arrangement and packed in cardboard boxes (CP1-841). The solid cyclotol leaving the cooling belt has the following composition, as shown in Table 6.1:

Table 6.1: Results from the pilot-testing

| Items | Stream 05 |
|---|---|
| RDX, % | 59.5 |
| TNT, % | 39.5 |
| Beeswax, % | 1 |
| Temperature, °C | Ambient |

For a total weight of 800 kg of the solid cyclotol, the finished product should have an RDX content of 59.5% ± 2%. The viscosity of the cyclotol that is acceptable should be 7 seconds or less and this is measured by a viscometer.

Scrubber (S1-841): The scrubber treats streams 20 – 24. Air is released to the atmosphere via a fume fan (FF1-841). Scrubbed water containing trace TNT (stream 27) is fed into the cyclotol labyrinth (CL1-841) where TNT and RDX settle to the bottom of the labyrinth and the reusable liquid effluent is pumped out (P1-841) to effluent storage (ES1-846). The settled cyclotol is removed by a steam ejector.

## 6.2 Objective of research

There are four non-penetrating phases in this mixing tank, shown in Figure 6.5: the heaviest component, RDX particles, molten TNT, water and the lightest, air, as the free surface.

Figure 6.5: Cyclotol mixing tank

Once the cyclotol mixture is homogeneous, it is transferred to another unit operation for further processing. It is desirable to transfer only water-free cyclotol, at high rotational speeds (58 rpm) which ensures homogeneity. It is also a process requirement that the RDX particles are homogeneously suspended. This problem is further complicated by the fact that when the mixture level drops during the transfer, the water/cyclotol interface may be lowered to a level where the distance between the interface and the top impeller causes water, by the action of central vortex, to be incorporated into the cyclotol mixture. This will result in water being transferred to the next stage as well. Therefore, modification to this mixing tank is necessary to achieve quality RDX suspension without water incorporation into the cyclotol mixture.

However, improvement in the design of the mixing tank does not lend itself to physical experimentation due to the explosive nature of the cyclotol mixture. As a result, an accurate fluid dynamics modelling of the mixing process must be conducted to characterise the present operation and subsequently employed to optimize the mixing tank for new geometrical and operational specifications to satisfy process safety and profitability. It is in

this respect that a CFD modelling and simulation approach that captures the complex turbulent phenomena occurring during mixing becomes judicious and attractive.

*Thus, the objective of this study was to characterise this mixing tank using CFD, and to render visible any process issue that interfered with its successful operation.*

A CFD model validation study was successfully carried out via PIV experiment and the details can be obtained in Lea et al. [2005]. The same validated-model was employed for the simulations described in this work. This ensures the reliability of the models used in this investigation and hence, the integrity of the results presented.

To elucidate the complex phenomena associated with the mixing process taking place in the mixing tank shown in Figure 6.5, the study of interest were the flow pattern, water draw-down, turbulence transport, velocity magnitude, RDX particles suspension and water entrainment.

The characterisation can be categorised into:

- Flow pattern profiling using vectors
- Water draw-down profiling at different impellers speed
- RDX particles suspension profiling
- Water entrainment profiling at different liquid level
- Product recirculation profiling
- Impeller's contribution analysis

Table 6.2: Summary of geometrical configuration and physical properties

| Parameter | Values |
|---|---|
| Top impeller type | Hydrofoil |
| Bottom impeller type | Semi-anchor |
| Top impeller diameter | 0.990 m |
| Bottom impeller diameter | 1.015 m |
| *S/D* (bottom reference) | 0.6404 |
| *D/T* (bottom) | 0.4669 |
| *D/T* (top) | 0.4554 |
| *C/T* | 0.0092 |
| *W/D* (top) | 0.1010 |
| *W/D* (bottom) | 0.0985 |
| *B/T* | 0.0690 |
| *T* | 2.174 m |
| *H* | 2.087 m |
| *Z* | 2.087 m |
| *Z/T* | 0.9600 |
| Viscosity of water @ 85 °C | 0.001003 Pa.s |
| Molecular weight of TNT | 227.1 amu |
| Density of solid TNT @ 80°C | 1,654 kg $m^{-3}$ |
| Density of liquid TNT @ 80°C | 1,461 kg $m^{-3}$ |
| Density of liquid TNT @ 85°C | 1,460 kg $m^{-3}$ |
| Density of liquid TNT @ 90°C | 1,455 kg $m^{-3}$ |
| Density of liquid TNT @ 140°C | 1,406 kg $m^{-3}$ |
| Density of RDX @ 80.8°C | 1,770 kg $m^{-3}$ |
| Maximum density of RDX/TNT @ 80°C | 1,737 kg $m^{-3}$ |
| Viscosity of RDX/TNT @ 83°C | 0.31 Pa.s |
| Viscosity of RDX/TNT @ 90°C | 0.30 Pa.s |
| Viscosity of RDX/TNT @ 95°C | 0.27 Pa.s |
| Batch volume | 6,386 L |

Table 6.2 provides a summary of geometrical configuration and the physical properties of the system being studied in this chapter.

## 6.3 Theoretical considerations

CFD analysis generally consists of (a) meshing of the vessel (or system) in question, (b) the numerical solution of the governing partial differential equations, for example Navier-Stokes and (c) post-processing of the results in the context of the physical system and possible model refinement. This 3-step procedure was effected using Fluent® 6.2, a commercial CFD package [Lea and Adesina 2006].

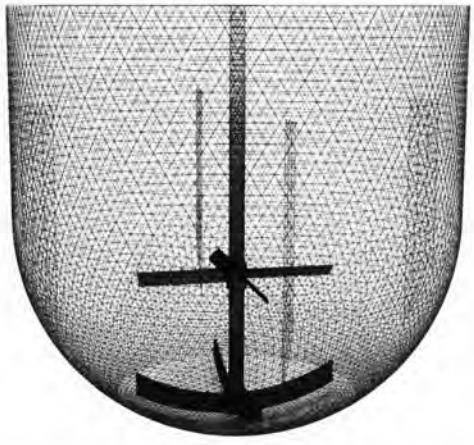

Figure 6.6: Meshed cyclotol mixing tank

The mixing tank geometry was created using Gambit 2.3 and care was taken to ensure that the dimensions of the geometry created represented the dimensions of the actual mixing tank in the plant. The tank thickness was not taken into consideration because no heat transfer equation was solved in this modelling work. In addition, the shaft and impellers blades were created as hollow objects because no heat transfer took place from these objects to the fluid. The meshed geometry of the mixing tank consisted of 1,332,701 tetrahedral cells, as shown in Figure 6.6, using Gambit 2.3 in the Fluent® software package.

For unbaffled mixing tank, there is no physical object to disrupt the 'laminar' like flow, thus a solid body rotation often occur. Because of this, to obtain accurate simulation results, the flow of the fluid must be aligned with the grid. Such condition requires structured mesh, for example, the hexahedral mesh. In contrast, for baffled tank such as the one use in this study, the use of tetrahedral unstructured mesh was acceptable since the baffles disrupt the flow so it was not necessary to align the flow with the grid.

From previous modelling and simulation works conducted, it was shown that the use of unstructured mesh did not significantly prolong the time required for the solution to converge. The use of structured mesh on the other hand is labour intensive due to the necessity in decomposing the mixing tank. Based on this, the unstructured mesh was chosen over the structured mesh. A significantly higher number of cells were allocated to areas of high velocity and pressure gradient, notably the rotating zones. The baffles were assumed to have zero thickness in order to eliminate additional meshing within the tank. Meshing baffles with non-zero thickness means that very small cells will be required and this can lead to an unnecessarily prohibitive large number of cells with attendant computational costs.

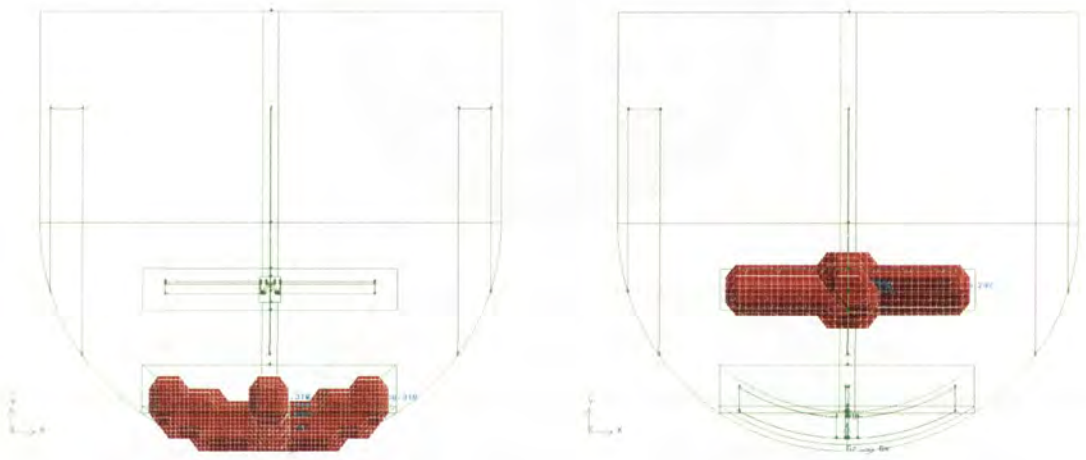

Figure 6.7: Cells highlighting size function application

To minimise the total number of cells while retaining accuracy, size-function was applied to the region of high velocity gradient. These regions were identified as those immediately surrounding each impeller. For the top impeller, the start size was 10mm, growth factor of 1.4 (generally this value is recommended as being aggressive in rapidly reaching the required number of cells) and size limited to 30 mm. On the other hand, for the bottom impeller, start size was taken as 5 mm, growth factor 1.4 and size limit being 20 mm. The size-functions for both impellers are depicted in Figure 6.7. The bottom impeller needed smaller start size and size limit due to the close clearance of the rotating zone to the tank bottom. A growth rate factor of 1.4 was selected to further minimise the total number of cells in the domain since this growth factor is aggressive in reaching the size limit.

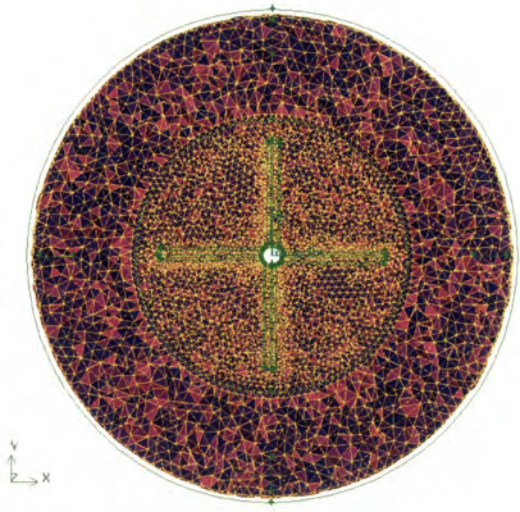

Figure 6.8: Meshed top rotational zone

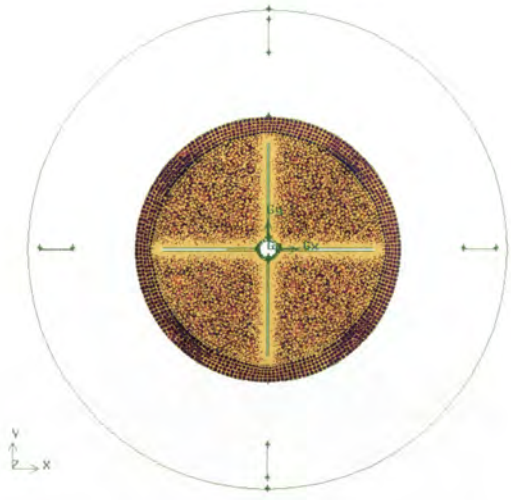

Figure 6.9: Meshed bottom rotational zone

Figures 6.8 and 6.9 exhibit the meshed cells via a cut plane positioned at different axial locations. Figure 6.8 shows the difference in cell sizes between the top rotational zone and the rest of the tank volume. This was due to the size function employed inside the rotational zone that stipulated a maximum cell size value. The rotational zone has much finer cells than the rest of the tank volume. Figure 6.9 shows that the cells inside the bottom rotational zone were even smaller than those located inside the top rotational zone. This was mainly due to the necessary smaller cells start size value assigned in the size function.

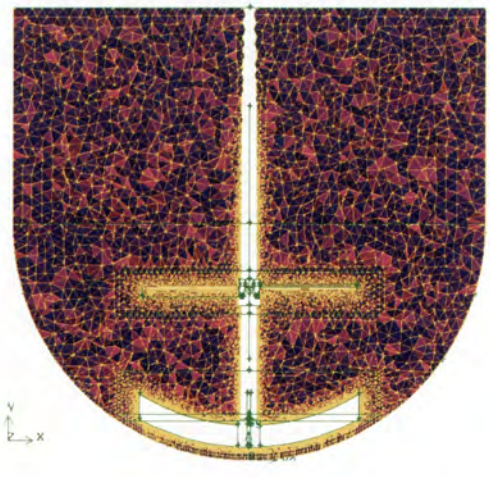

Figure 6.10: Meshed geometry showing both rotational zones

Figure 6.10 exhibits meshed cells via a cut plane positioned at different radial locations. This shows the relative size of the cells located inside the rotational zones relative to the cells assigned to rest of the tank volume.

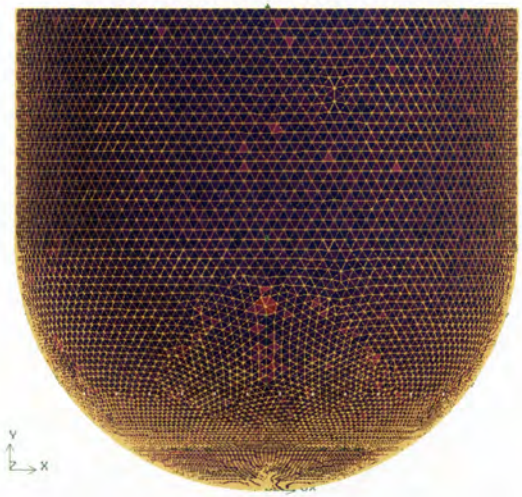

Figure 6.11: Meshed tank

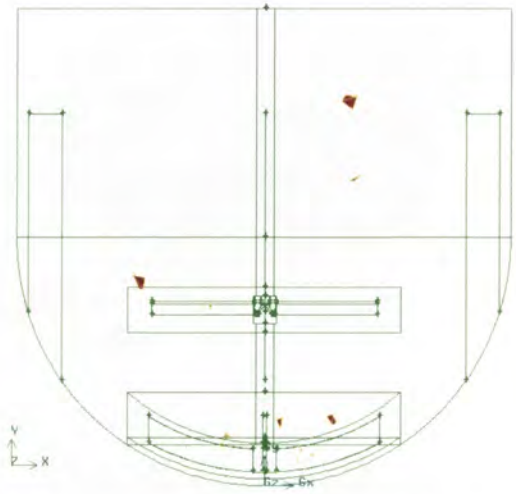

Figure 6.12: Cells with EquiAngle skew ≥ 0.8

Figure 6.11 presented a total of 1,332,701 tetrahedral cells for quality examination. Out of these 1,332,701 cells, only 23 elements shown in Figure 6.12 had EquiAngle Skew value ≥ 0.8 and among these, the worst quality cell had an EquiAngle Skew value of 0.8185. For mixing simulation such as this, the EquiAngle Skew should not exceed 0.85 for hexahedral and 0.9 for tetrahedral cells. Based on this guideline, it was safe to assume that the overall cells had quality high enough to promote convergence and accuracy during computation.

A preliminary grid convergence study was carried out to verify that the solution obtained from using the second-order upwind discretisation scheme was mesh-independent. The number of cells inside and outside the rotational zones was systematically increased in the x-, y- and z-directions throughout the tank. When refining the mesh, care was taken to assign additional cells to the regions of high gradient around the impeller blades and discharge regions. A horizontal plane equivalent to the top impeller's diameter was created so that a surface integration can be carried out to determine the axial mass flow rate passing through this plane. Simulation was conducted on single-phase operating condition at 85°C and impeller speed set to 40 rpm. The results show that the mass flow rate obtained from using a 1,332,701 cells model was 657.9 kg $s^{-1}$ whereas the mass flow rate obtained

from using a 1,501,200 was 660.2 kg $s^{-1}$. This shows that the results are not mesh-dependent since the changes implicated were less than 1%.

For the boundary zone allocation, the impellers blades were defined as wall, both rotational boundary zones were defined as interior. Assigning interior to both rotational zones made the modelling easier, however, it precluded the use of sliding mesh modelling [Mousavi et al. 2006] which means that transient simulation could not be carried out. Baffles, shaft and tank wall were defined as wall. Tank top was defined as symmetry to model open top tank while tank volume and both rotational zone volumes were defined as fluid.

Fluent® solver was used to create a numerical solution that matches the governing conservation equations. In this study, the focus was on solving the conservation of mass, momentum, turbulence transport and volumetric fraction with a view to generating a steady-state 3D hydrodynamics profile.

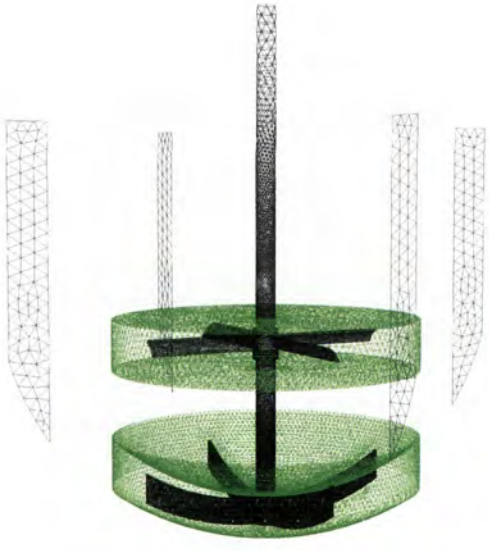

Figure 6.13: MRF created for both impellers

To simulate impeller rotations, separate rotational zones in the immediate vicinity of the impellers were created and a multiple reference frame (MRF) approach was employed, as shown in Figure 6.13. This method involved solving the flow characteristics of the inner region using a rotating framework. These results were then used to provide boundary conditions for the outer region which employs a stationary framework to secure solution to the flow characteristics. The results from the outer region were then re-supplied as

boundary conditions for the inner region. This iterative procedure was repeated until a convergent solution was obtained for both regions.

The segregated-implicit method where the governing equations were solved sequentially was used. To obtain a higher degree of accuracy, all solutions were obtained via the second-order upwind scheme or the QUICK scheme for the volume fraction solution. In this scheme, higher order accuracy was obtained at the cell surfaces where the values at the cell centroid were subjected to multidimensional linear reconstruction using the Taylor series expansion. While the QUICK scheme (third-order accuracy) is more accurate on structured grids, it is also applicable to unstructured grids such as tetrahedral mesh. In such cases, the usual second-order upwind discretisation scheme was used at the faces of non-hexahedral cells.

Due to the presence of baffles, significant interrupted rotational flow existed inside the mixing tank unit thus creating steep pressure gradient. As a result, PRESTO (pressure staggering option) was employed to compute the pressure value at the cell surface by interpolating the values at cell centroid. SIMPLE (semi-implicit method for pressure linked equations) scheme was used for the pressure-velocity coupling [Alliet-Gaubert et al. 2006]. This applies a correlation between the pressure and velocity to enforce conservation of continuity in order to obtain the pressure field. The under-relaxation factors used were the default settings namely, pressure = 0.3, density = 1, body forces = 1, momentum = 0.7, volume fraction = 0.2, turbulence kinetic energy = 0.8, turbulence dissipation rate = 0.8 and turbulent viscosity = 1.

Due to the lack of solid body rotation, the Realizable $k$-$\varepsilon$ turbulent model was used to capture the hydrodynamics phenomena. The corresponding transport equations are:

$$\frac{\partial}{\partial t}(\rho k)+\frac{\partial}{\partial x_i}(\rho k u_j)=-\frac{\partial}{\partial x_i}\left[(\mu+\frac{u_t}{\sigma_k})\frac{\partial k}{\partial x_j}\right]+G_k+G_b-\rho\varepsilon-Y_M+S_k \qquad -6.1$$

and

$$\frac{\partial}{\partial t}(\rho\varepsilon)+\frac{\partial}{\partial x_j}(\rho\varepsilon u_j)=-\frac{\partial}{\partial x_j}\left[(\mu+\frac{u_t}{\sigma_\varepsilon})\frac{\partial\varepsilon}{\partial x_j}\right]+$$

$$\rho C_1 S_\varepsilon-\rho C_2\frac{\varepsilon^2}{k+\sqrt{v\varepsilon}}+C_{1\varepsilon}\frac{\varepsilon}{k}C_{3\varepsilon}G_b+S_\varepsilon \qquad \text{- 6.2}$$

In the two equations above, $G_k$ represents the turbulence kinetic energy generated due to the mean velocity gradients whereas $G_b$ is the turbulence kinetic energy due to buoyancy. $Y_M$ represents the contribution of the fluctuating dilation in compressible turbulence to the overall dissipation rate. $C_2$ and $C_{1\varepsilon}$ are constants; $\sigma_k$ and $\sigma_\varepsilon$ are the turbulent Prandtl numbers for $k$ and $\varepsilon$ respectively.

To simulate the air draw-down, the multiphase model using volume of fluid (VOF) approach was employed. This model was designed for two or more immiscible fluids where the position of the interface between the fluids is of interest. This approach assumes that the air and liquid are not interpenetrating. Each phase is represented by its volume fraction therefore in each control volume the volume fraction representing air and the liquid phase equals to unity. The fields for all variables and properties are shared by the phases and represent volume-averaged values. For example, in a fluid, $q$, with volume fraction, $\alpha_q$, three scenarios are possible in the cell, namely:

$\alpha_q = 0$ : cell is void of $q$ fluid

$\alpha_q = 1$ : cell is full of the $q$ fluid

$0 < \alpha_q < 1$ : cell contains the interface between the $q$ fluid and one or more other fluids

Based on the local value of $\alpha_q$ the appropriate properties and variables will be assigned to each control volume within the domain. The tracking of the interface between the phases is achieved by the solving of the continuity equation for the volume fraction of one (or more) of the phases. For example, for the $q$ phase, the continuity equation is:

$$\frac{1}{\rho_q}\left[\frac{\partial}{\partial t}(\alpha_q\rho_q)+\nabla\cdot(\alpha_q\rho_q\vec{v}_q)=S_{\alpha q}+\sum_{p=1}^{n}(\dot{m}_{pq}-\dot{m}_{qp})\right] \qquad \text{- 6.3}$$

where

$\dot{m}_{qp}$ : mass transfer from phase $q$ to phase $p$

$\dot{m}_{pq}$ : mass transfer from phase $p$ to phase $q$

$S_{\alpha q}$ : source term and is zero by default but a constant or user-defined mass source can be specified for each phase

The volume fraction equation was not solved for the primary phase, rather, it was solved based on the following constraint:

$$\sum_{q=1}^{n} \alpha_q = 1 \qquad \text{- 6.4}$$

The properties appeared in the transport equation were determined by the presence of the component phases in each control volume. For instant, in a two-phase system, if the phases are represented by the subscripts 1 and 2 and if the volume fraction of the second phase is being solved, the density in each cell is given by:

$$\rho = \alpha_2 \rho_2 + (1 - \alpha_2)\rho_1 \qquad \text{- 6.5}$$

Moreover, for an n-phase system, the volume-fraction-averaged density has the following expression:

$$\rho = \sum \alpha_q \rho_q \qquad \text{- 6.6}$$

All other properties, for example, viscosity were computed in this manner.

As for the momentum equation, a single equation was solved throughout the domain which resulted in shared velocity field among the phases. The momentum equation is dependent on the volume fractions of all phases through the properties $\rho$ and $\mu$.

$$\frac{\partial}{\partial t}(\rho \vec{v}) + \nabla \cdot (\rho \vec{v} \vec{v}) = -\nabla_p + \nabla \cdot [\mu(\nabla \vec{v} + \nabla \vec{v}^T)] + \rho \vec{g} + \vec{F} \qquad \text{- 6.7}$$

A limitation of the shared-fields approximation is that in situations where large velocity differences exist between the phases, the accuracy of the velocities calculated near the interface can be severely affected.

To model the multiphase phenomena associated with the suspension of RDX particles in the holding tank, an appropriate model must be selected from the models available in Euler-Lagrange or the Euler-Euler approach. The three different models available in the Euler-Euler approach include the VOF model, the mixture model and the Eulerian model. While the VOF model is more suitable for simulating phenomena such as the draw-down of air or water into the primary phase, the mixture and Eulerian models are suitable for simulating the suspension of particles in the primary phase. As a general guide, there are two parameters that may assist in the identification of an appropriate multiphase model for situations where the use of VOF model is inappropriate. The first is the particulate loading, denoted by $\beta$ and the second is the Stokes number, denoted by *St*.

Particulate loading has a major impact on phase interactions. The particulate loading is defined as the mass density ratio of the dispersed phase *d* to that of the carrier phase *c* and is given by:

$$\beta = \frac{\alpha_d \rho_d}{\alpha_c \rho_c} \qquad \text{- 6.8}$$

where

$\alpha_d$ : volumetric fraction of dispersed phase

$\alpha_c$ : volumetric fraction of carrier phase

$\rho_d$ : density of dispersed phase, kg $m^{-3}$

$\rho_c$ : density of carrier phase, kg $m^{-3}$

The material density ratio is defined as

$$\gamma = \frac{\rho_d}{\rho_c} \qquad \text{- 6.9}$$

where

$\gamma > 1000$ : gas-solid flows

$\gamma \sim 1$ : liquid-solid flows

$\gamma < 0.001$ : gas-liquid flows

Using these parameters, the average distance between the individual particles of the particulate phase can be estimated via Crowe et al. [1998] model and is given by:

$$\frac{L}{d_d} = \left( \frac{\pi + k}{6k} \right)^{1/3} \qquad \text{- 6.10}$$

where

$$k = \frac{\beta}{\gamma}. \qquad \text{- 6.11}$$

Depending on the particulate loading, the degree of interaction between the phases can be divided into three categories:

*Low loading* (solids volume fraction, $\alpha_d \leq 10\%$) – the coupling between the phases is one-way. In this case, the fluid carrier influences the particles via drag and turbulence, but the particles have no influence on the fluid carrier. The discrete phase, mixture and Eulerian models can all handle this type of problem correctly. Since the Eulerian model is the most computationally expensive, the discrete phase or mixture model is preferable.

*Intermediate loading* (solids volume fraction, $\alpha_d \geq 10\%$) – the coupling is two-way. In this case, the fluid carrier influences the particulate phase via drag and turbulence, but the particles in turn influence the carrier fluid via reduction in mean momentum and turbulence. The discrete phase, mixture, and Eulerian models are all applicable here. The Stokes number can be used to distinguish the most suitable model to be used under such scenario.

*High loading* (solids volume fraction, $\alpha_d \geq 70\%$) – there is two-way coupling plus particle pressure and viscous stresses due to particles (four-way coupling). Only the Eulerian model will handle this type of problem correctly.

In this situation involving the suspension of RDX particles in molten TNT,

$\rho_d$ : 1,770 kg m$^{-3}$ (bulk density of RDX particles)

$\alpha_d$ : 0.5661 (volume fraction of RDX particles)

$\rho_c$ : 1,461 kg m$^{-3}$ (density of molten TNT)

$\alpha_c$ : 0.4338 (volume fraction of molten TNT)

$\beta(85^{\circ}C) = 1.581$; $\gamma(85^{\circ}C) = 1.211$; $k = 1.305$

Thus, $\frac{L}{d_d}$ (RDX-molten TNT at 85°C) = 0.8281

Since the inter-particle distant was only slightly less than the diameter of the particles, this system can still be considered as intermediate loading.

The Stokes number can be defined as the relation between the particles response time and the system response time:

$$St = \frac{\tau_d}{t_s} \qquad \text{- 6.12}$$

where

$$\tau_d = \frac{\rho_d d_d^2}{18\mu_c} \qquad \text{- 6.13}$$

and

$$t_s = \frac{L_s}{V_s} \qquad \text{- 6.14}$$

$\rho_d$ : density of discrete phase (kg $m^{-3}$)
$d_d$ : diameter of discrete phase (m)
$\mu_c$ : absolute viscosity of continuous phase (Pa.s or kg $m^{-1}s^{-1}$)
$L_s$ : characteristic length (m) of the system of interest
$V_s$ : characteristic velocity (m $s^{-1}$) of the system of interest

For Stokes number < 1, any of the three models (discrete phase from Euler-Lagrange, mixture and Eulerian from Euler-Euler) is applicable and the least expensive model, which is the mixture model in most cases may be used. For $St$ > 1, the particles will move independently of the flow and either the discrete phase model or the Eulerian model is applicable. For $St$ ~ 1, again any of the three models is applicable.

In this modelling work, at 85°C:

$\rho_d$ : 1,770 kg $m^{-3}$ (bulk density of RDX particles)

$d_d^2$ : 0.00024 m (median diameter of RDX particles)

$\mu_c$ : 0.01122 Pa.s or kg $m^{-1}s^{-1}$ (viscosity of TNT at 85°C)

$L_s$ : 0.5355 m (diameter of mixing tank)

$V_s$ : 0.7299 m $s^{-1}$ at 10 rpm and 0.8405 m $s^{-1}$ at 80 rpm (volume-weighted average)

From the Stokes number equation, *St* (10 rpm) = 0.00069 and *St* (80 rpm) = 0.00078

Clearly, the mixture model was applicable in this modelling work. The mixture model is a simplified Eulerian approach for modelling n-phase flows. This model uses a single-fluid approach and it allows phases to be interpenetrating. In addition, the model allows phases to move at different velocities, using the concept of slip velocities.

To model the fluid-fluid interaction between TNT and $H_2O$, the Schiller-Naumann correlation [1935] was employed. This model is the default method whenever the mixture model is selected, and is acceptable for general use for all fluid-fluid multiphase calculations. Although Morsi and Alexander [1972] model is more complete because it adjusts the function definition frequently over a large range of Reynolds number, computation involving this model is less stable. The drag function for the Schiller-Naumann [1935] model is given as:

$$C_D = \begin{cases} \dfrac{24\left(1 + 0.15\,\mathrm{Re}^{0.687}\right)}{\mathrm{Re}} & \text{for } \mathrm{Re} \le 1000 \\ 0.44 & \text{for } \mathrm{Re} > 1000 \end{cases} \qquad \text{- 6.15}$$

To model the fluid-solid interaction between TNT-$H_2O$ and RDX particles [Mousavi et al. 2006], the slip velocity function was activated and the Syamlal-O'Brien [1989] drag function was invoked. The model is given as:

$$C_D = \left( 0.63 + \frac{4.8}{\sqrt{\mathrm{Re}_s / \upsilon_{r,s}}} \right)^2 \qquad \text{- 6.16}$$

This model is based on measurements of the terminal velocities of particles in fluidised or settling beds, with correlations that are a function of the volume fraction and relative Reynolds number. The mixing process taking place inside this mixing tank resembles that of settling bed where if the impellers were stopped, the RDX particles will sink to the tank bottom. This is the justification on the use of this drag function model.

Simulations were generally considered converged when the residuals for mass, momentum, turbulence $k$-$\varepsilon$, and volumetric fraction fell below $1\times10^{-4}$ [Kerdouss et al. 2006]. Further checks for convergence were made by creating a monitoring point inside the tank and ensuring that the value monitored remained constant with further iterations. This further assisted to ensure results integrity. To increase the iteration speed, a dual-processor capability computer (3.20GHz and 8GB RAM) operated on Linux 4 Redhat Enterprise was used, and Fluent® parallel processing software to split the total number of cells equally, and assign them to each processor. In addition, the second-order upwind scheme was used at partition boundaries.

## 6.4 Results and discussion

### 6.4.1 Flow pattern profiling using vectors

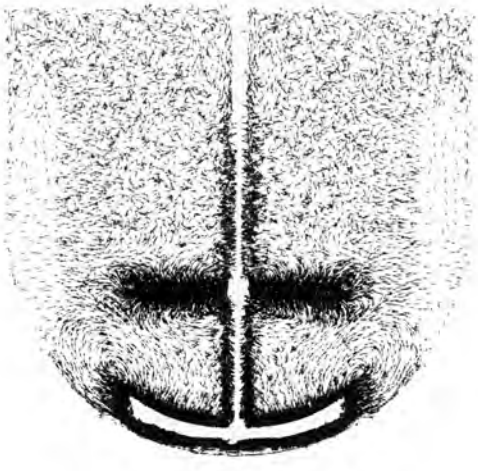

Figure 6.14: Vectors at 10 rpm

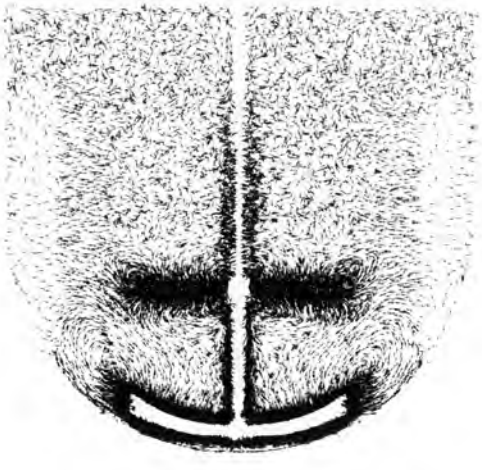

Figure 6.15: Vectors at 15 rpm

Vector profiling provided microscopic insight into the flow pattern inside the tank during mixing and hence complemented the analysis from water draw-down profiling and RDX particles suspension analysis. Results above show the hydrodynamics when the impellers were rotating at 10 and 15 rpm as displayed in Figures 6.14 and 6.15 respectively. Although a hydrofoil impeller was known to be an axial-flow impeller [Wu et al. 2006], the results show that axial flow in the vicinity of the top hydrofoil impeller was not obvious as evidenced by the lack of upward moving vectors from the top region to the hub or vectors moving away from the bottom of the top impeller towards the bottom impeller. As a result, the quantity of downward axial flow arising from the top to the bottom impeller was very little [Lea and Adesina 2006].

The bottom semi-anchor impeller produced predominantly radial flow which was immediately deflected upwards by the spherical tank bottom. In other words, the use of close proximity semi-anchor impeller coupled with a spherical tank bottom induced a significant amount of radial to axial flow. In spite of this, such low impeller rotational speed did not have enough kinetic energy to sustain significant upward flow from the bottom impeller travelling along the axis of the standard flat baffles, as evidenced by the lack of aligned vectors moving up along the baffles. From a practical perspective, the lack of downward and upward axial flow means that the current operation did not generate enough energy within the mixing tank to suspend solid particles from the tank bottom or to keep the solid particles in homogeneous circulation.

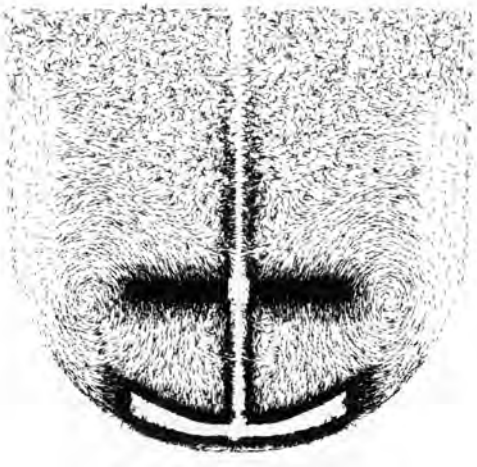

Figure 6.16: Vectors at 20 rpm

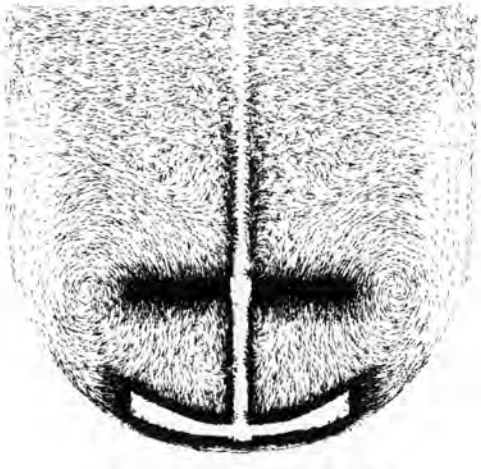

Figure 6.17: Vectors at 30 rpm

When the impellers rotational speed was increased to 20 rpm as shown in Figure 6.16, the flow pattern changed dramatically with the hydrofoil impeller executing its role through promoting flow from the top, passing through the blades and exiting from the bottom of the impeller. This axial flow terminated at the bottom impeller where the flow was diverted radially by the semi-anchor impeller. Radial flow was further promoted due to the closeness of this impeller to the tank bottom. These actions created a big circulation loop inside the cyclotol mixing tank. It was also seen that the vectors were more aligned and moving upward starting from the radial discharge of the bottom impeller. These radial flow vectors were directed to the top by the four standard wall baffles before being drawn down by the top impellers. Although more vectors were pointing upwards, a significant number of vectors still pointed sideways, indicating that the flow was not predominantly axial at 20 rpm. Even so, axial flow became more established when the speed was increased to 30 rpm as shown by the decrease in the number of vectors pointing sideways, as shown in Figure 6.17.

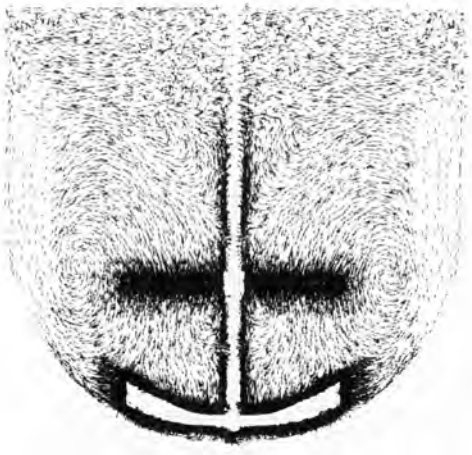

Figure 6.18: Vectors at 40 rpm

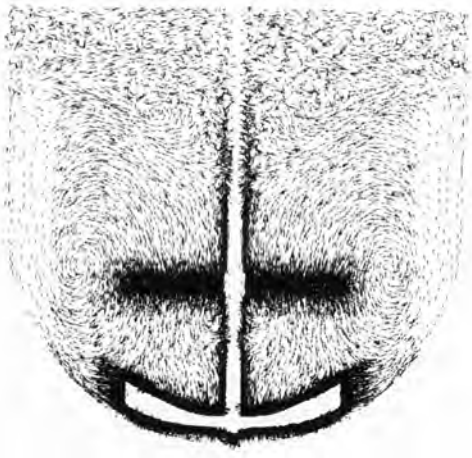

Figure 6.19: Vectors at 60 rpm

Figure 6.18 shows that at 40 rpm, all the vectors on the baffles pointed upwards which suggested that axial flow was fully established. Moreover, the vectors moving downward from the top towards the top impeller's hub were more aligned and originated from a source higher along the baffle axis. This was the basis for the RDX particle suspension at this impeller speed. At 60 rpm, not only did this source along the baffle axis shifted to a higher vertical position, more vectors was seen converging around the top impeller in the region between hub and the shaft position located above the hydrofoil impeller, as shown in Figure 6.19.

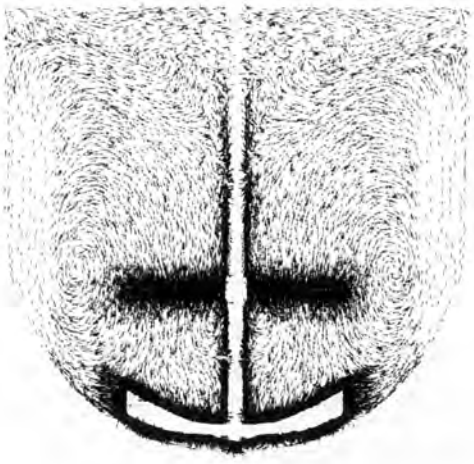

Figure 6.20: Vectors at 80 rpm

Finally, at 80 rpm shown in Figure 6.20 the vectors pointing upwards travelled farther along the baffle. In addition, more vectors converged on the top hub. It was this phenomenon that helped to increase the cloud height of suspended particles. This was attributed to the higher kinetic energy made available by the impellers rotating at this speed which helped to induce higher downward flow, but deflected radially by the bottom impeller and directed upwards by the spherical tank bottom and baffles. It was therefore clear that the minimum bottom impeller's clearance, the use of semi-anchor contributed significantly towards generating upward axial flow which enabled the suspension of RDX particles.

Figure 6.21: Vectors along tank wall at 10 rpm

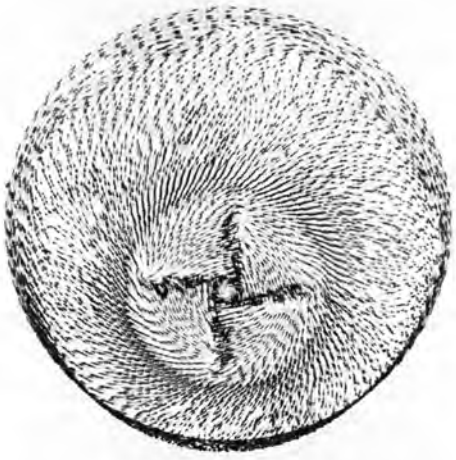

Figure 6.22: Vectors along tank wall at 80 rpm

Figure 6.21 represents the vector plot along the tank wall at 10 rpm. At the tank bottom, the vectors were rotating about the hub of the bottom impeller. As the vector plot shows, these vectors were travelling in the same direction, that is, rotational direction. Along the

wall, the vectors were still travelling along the same direction but as the height increased, the vectors started to move in different directions. In addition, very few vectors were seen travelling in an upward direction. This assessment agreed with previous discussion where at 10 rpm, insufficient axial flow was generated resulting in the failure to suspend RDX particles.

Figure 6.22 also displays the vector plot along the tank wall at the impeller speed of 80 rpm. At the tank bottom, all the vectors were rotating around the hub of the bottom impeller similar to those produced at 10 rpm. As the vector plot shows, these vectors were travelling in the same rotating direction. Along the wall, the vectors were still travelling at the same but pointed in upward instead of tangential direction. This differed significantly from the vectors produced at 10 rpm. Even as the height increased, the vectors remained travelling at the same upward direction. Unlike those vectors produced when the impellers were rotating at 10 rpm, very few vectors were seen travelling in a tangential direction.

### 6.4.2 Water draw-down

The objective of these simulations was to characterise the cyclotol mixing tank water draw-down as a function of the impeller rotational speed. This would reveal the minimum impeller rotational speed at which water draw-down did occur [Lea and Adesina 2006].

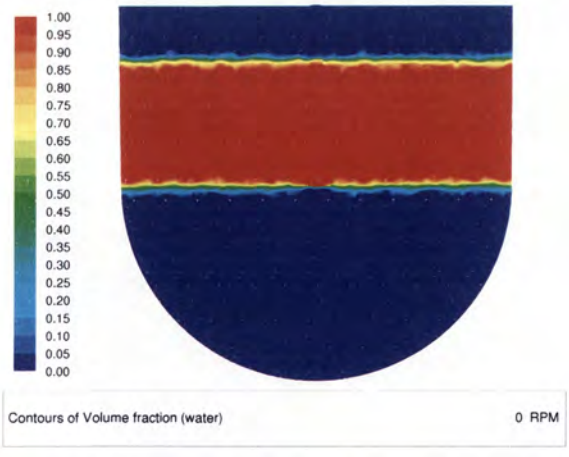


Figure 6.23: Contours of volume fraction of water at 0 rpm

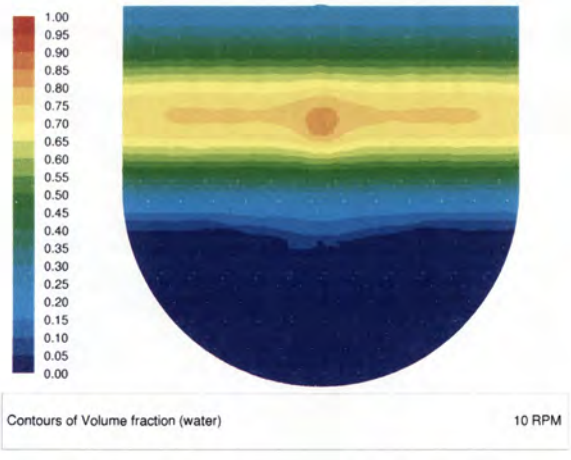


Figure 6.24: Contours of volume fraction of water at 10 rpm

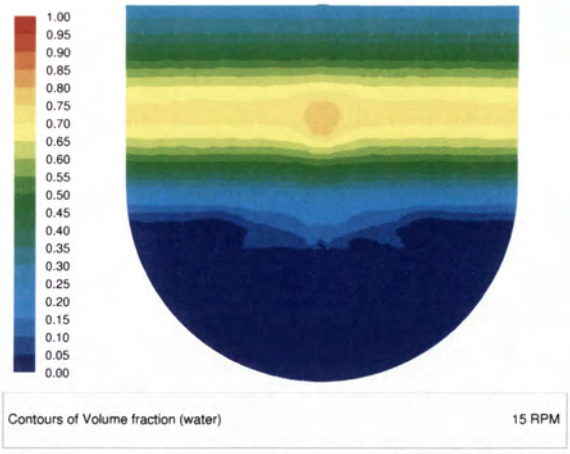


Figure 6.25: Contours of volume fraction of water at 15 rpm

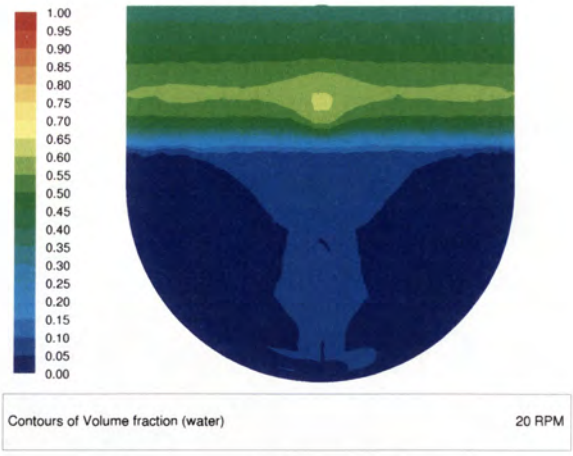


Figure 6.26: Contours of volume fraction of water at 20 rpm

Figure 6.23 shows the 3-phase system in the cyclotol mixing tank consisting of cyclotol mixture as the bottom layer (1.067m) with water floating above it (1.067m-1.787m) and air as the uppermost layer (1.787m-2.087m). The three layers were at equilibrium (non-penetrating) when the impellers were at rest as evidenced by the lack of water and air draw-down. Figure 6.24 shows that about 10% water was drawn down and reached the top impeller immediately, the impellers started rotating at 10 rpm. Increasing the speed to 15 rpm revealed that the same amount of water was further drawn down to the top impeller and deeper into the tank (cf. Figure 6.25). Figure 6.26 shows that at 20 rpm, water penetrated further down through the top hydrofoil and the bottom semi-anchor impellers. The ease of water draw-down was attributed to the close densities between cyclotol and water (density ratio of about 1.7).

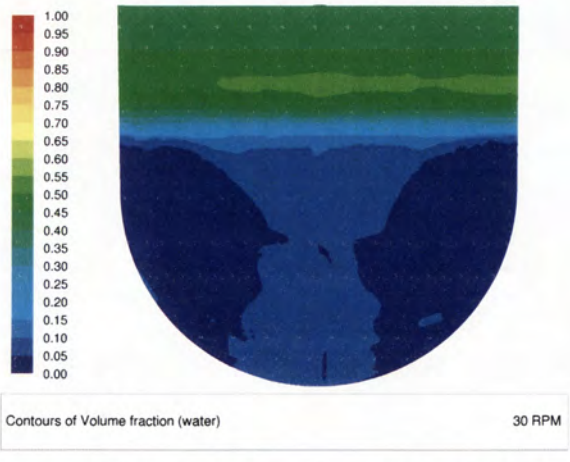


Figure 6.27: Contours of volume fraction of water at 30 rpm

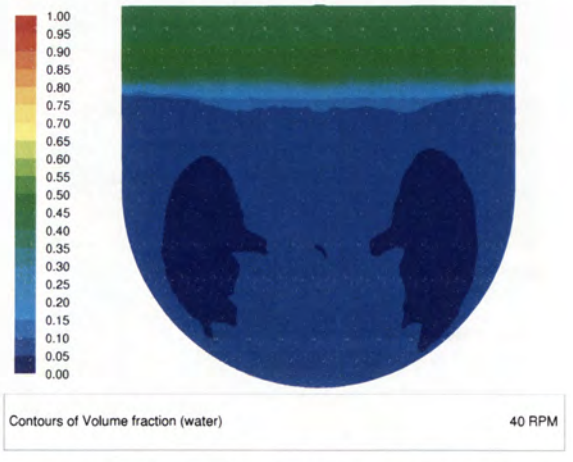


Figure 6.28: Contours of volume fraction of water at 40 rpm

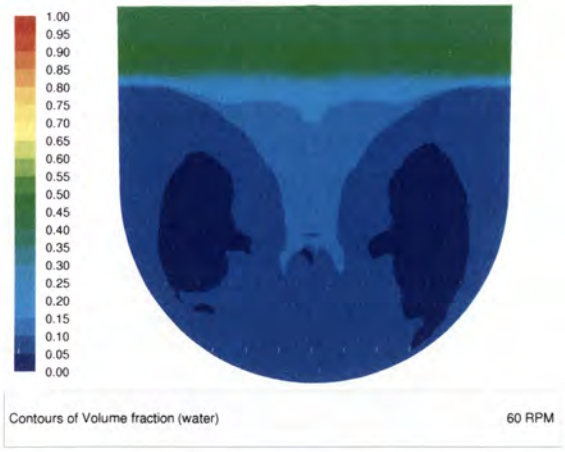


Figure 6.29: Contours of volume fraction of water at 60 rpm

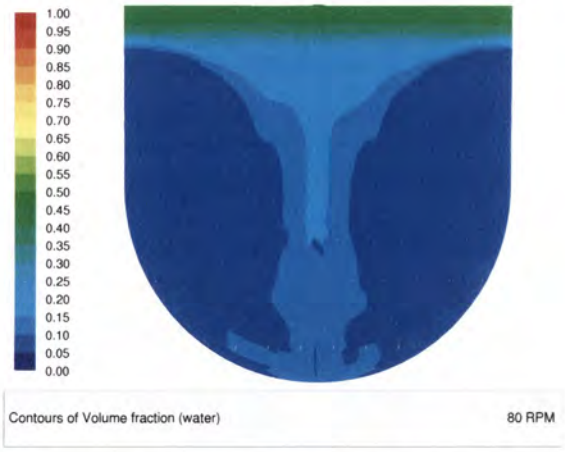


Figure 6.30: Contours of volume fraction of water at 80 rpm

At 30 rpm, although the volume fraction of water draw-down remained at 10%, the total volume in the tank occupied by water increased rapidly and a small second wave of water drawn down began to appear, as shown in Figure 6.27. Figure 6.28 shows that the 10% water draw-down at 40 rpm had started to infiltrate a large portion of the mixing tank. At 60 rpm, the volume fraction of water drawn down to the top hydrofoil impeller increased to 15% and not only was water distributed to the rest of the mixing tank, as shown in Figure 6.29, but also a third wave of water draw-down started to occur. By this time, the second wave formed at 30 rpm had reached the top impeller. Obviously, above 60 rpm, the infiltration was deeper, as shown in Figure 6.30.

In order to appreciate the significance of these CFD results, it is important to recall the manner in which the cyclotol mixing is carried out in practice. In the actual operation, when TNT is being melted, the impellers are rotating at 40 rpm speed. From the preceding analysis, it is evident that at this speed, water left over from the previous batch would have been drawn down and distributed as shown in Figure 6.28. Since the speed is increased to 58 rpm when the RDX slurry is charged to the tank, this would also cause the mass fraction of water drawn down to increase significantly. After the charge in, mixing is then carried out for 10 mins at 40 rpm. At this speed and during this period, water from the slurry would have been drawn down and well distributed throughout the mixing tank as explained earlier.

Subsequently, the impeller speed is reduced to 10 rpm and the mixture is recirculated via a bottom outlet and top inlet to obtain the right density using a density meter. Normally it takes about 5-10 mins to achieve the desired density of cyclotol. This means if water is

also carried along with the cyclotol mixture, this might pose a problem for the density meter placed immediately at the exit line of the mixing tank. These CFD results uncover one of the underlying reasons for the fluctuation in the density readings observed during product recirculation at 40 rpm (for the purpose of obtaining the right product density). Indeed, Figures 6.31-6.42 show the 3D imaging as water progressively infiltrated to different extents in the tank as impeller speed increased even for an initial water content of 5%. Clearly, above 20 rpm the risk of water being drawn out with the cyclotol product mixture is virtually assured. This matter will be addressed in greater detail in a later section.

10 rpm – 5%

Figure 6.31: 3D display of 5% v/v $H_2O$ drawdown at 10 rpm

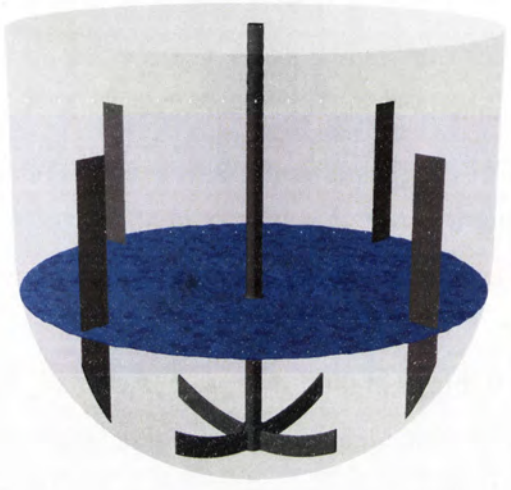

10 rpm – 10%

Figure 6.32: 3D display of 10% v/v $H_2O$ drawdown at 10 rpm

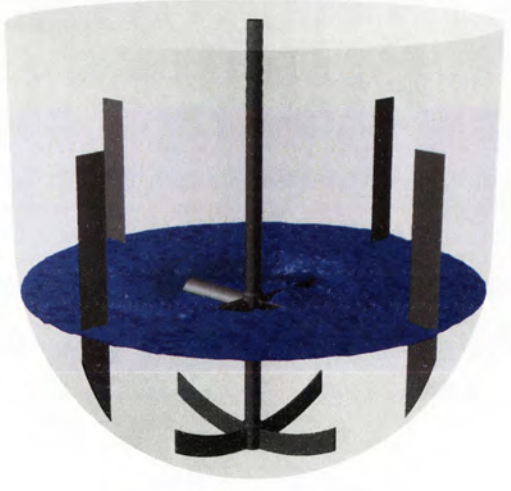

15 rpm – 5%

Figure 6.33: 3D display of 5% v/v $H_2O$ drawdown at 15 rpm

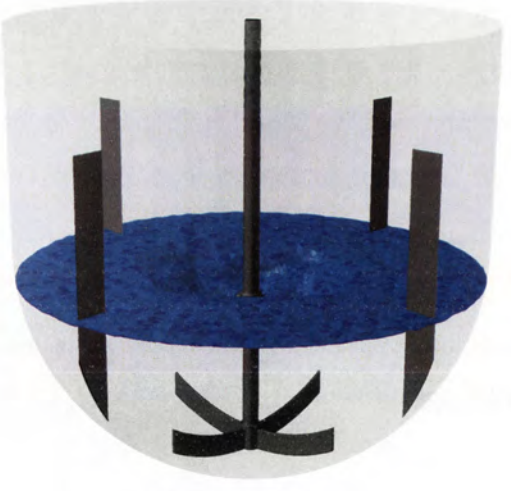

15 rpm – 10%

Figure 6.34: 3D display of 15% v/v $H_2O$ drawdown at 15 rpm

20 rpm – 5%

Figure 6.35: 3D display of 5% v/v $H_2O$ drawdown at 20 rpm

20 rpm – 10%

Figure 6.36: 3D display of 10% v/v $H_2O$ drawdown at 20 rpm

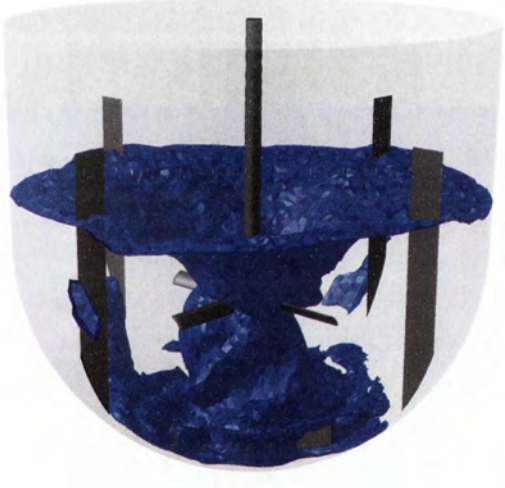

30 rpm – 5%

Figure 6.37: 3D display of 5% v/v $H_2O$ drawdown at 30 rpm

30 rpm – 10%

Figure 6.38: 3D display of 10% v/v $H_2O$ drawdown at 30 rpm

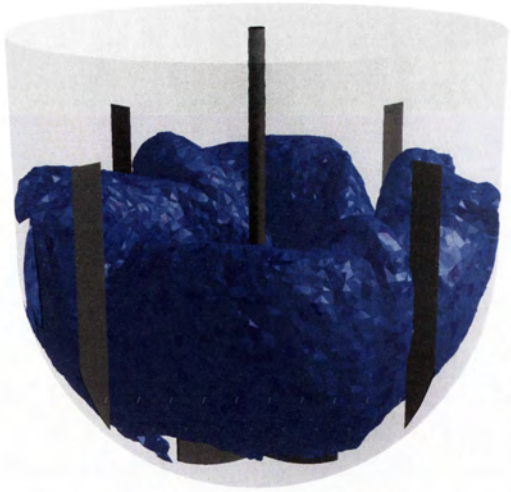

40 rpm – 5%

Figure 6.39: 3D display of 5% v/v $H_2O$ drawdown at 40 rpm

40 rpm – 10%

Figure 6.40: 3D display of 10% v/v $H_2O$ drawdown at 40 rpm

60 rpm – 10%

Figure 6.41: 3D display of 10% v/v $H_2O$ drawdown at 60 rpm

80 rpm – 10%

Figure 6.42: 3D display of 10% v/v $H_2O$ drawdown at 80 rpm

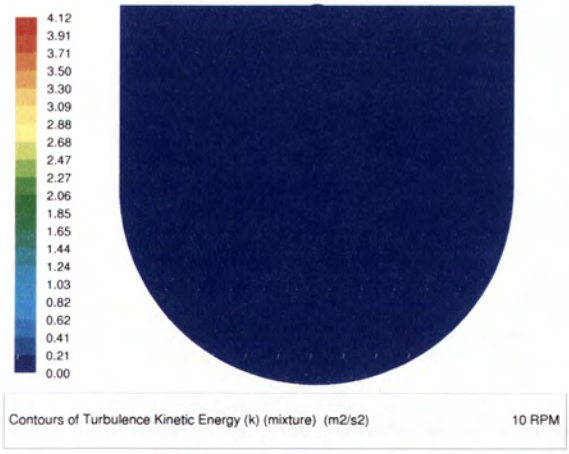


Figure 6.43: Turbulence kinetic energy at 10 rpm

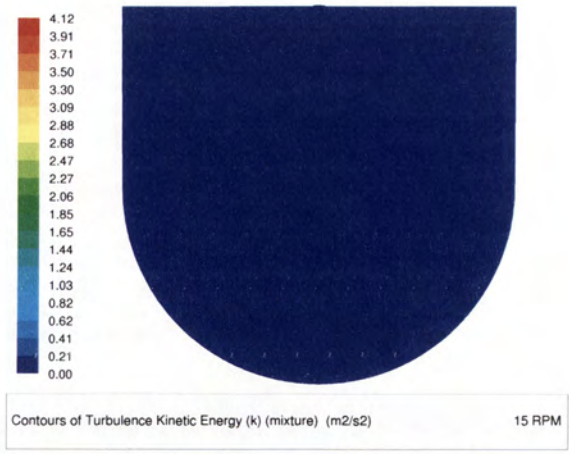


Figure 6.44: Turbulence kinetic energy at 15 rpm

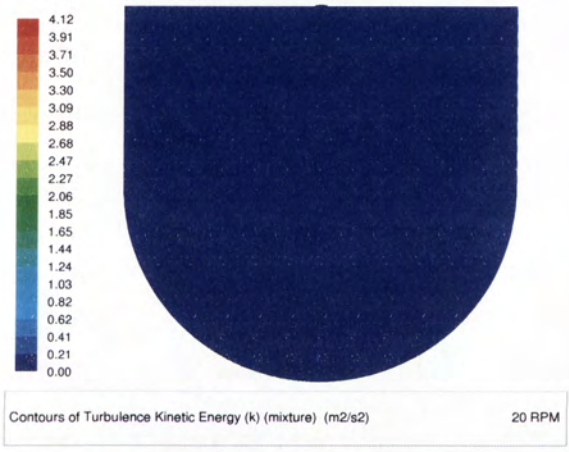


Figure 6.45: Turbulence kinetic energy at 20 rpm

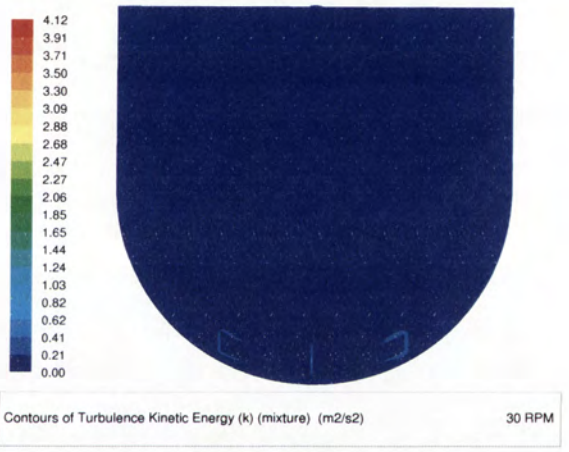


Figure 6.46: Turbulence kinetic energy at 30 rpm

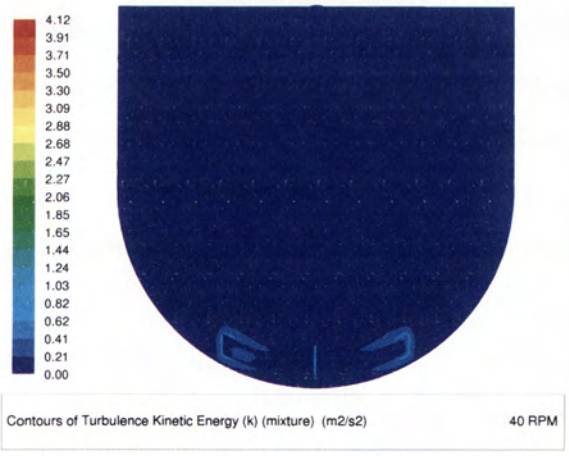


Figure 6.47: Turbulence kinetic energy at 40 rpm

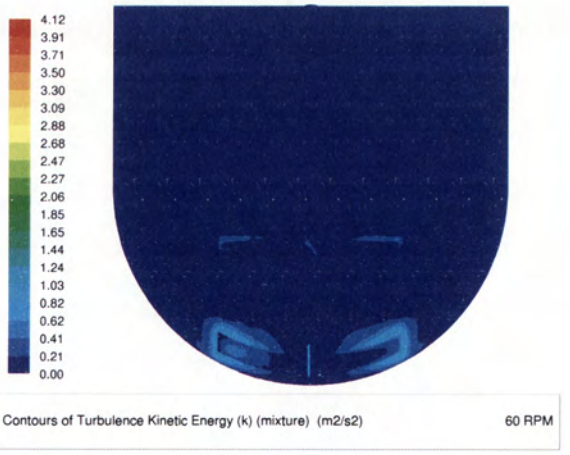


Figure 6.48: Turbulence kinetic energy at 60 rpm

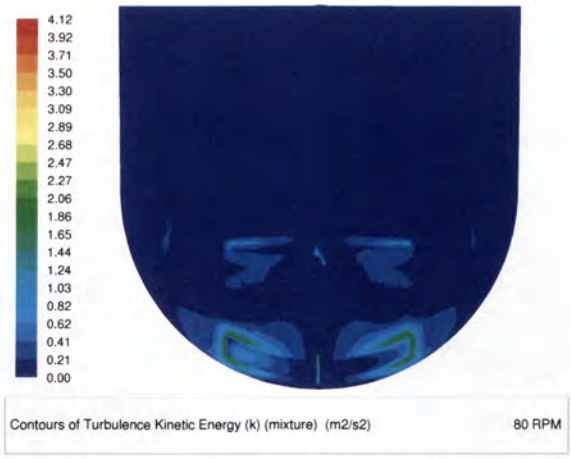


Figure 6.49: Turbulence kinetic energy at 80 rpm

Figures 6.43-6.49 show that turbulence kinetic energy levels increased with increasing impellers rotational speed but below 60 rpm, the turbulence kinetic energy influence extended to around the bottom blade area only, that is, local turbulence. Obviously, the bottom impeller, having blades parallel to the axis of the shaft, induced more local turbulence than the top hydrofoil impeller. In practice when the cyclotol is being mixed, the impellers are rotating at 40 rpm. From Figure 6.47, it was observed that turbulence was confined to region around the bottom impeller therefore the mixture might not be homogeneous owing to the lack of turbulence in regions away from both impellers. This was important because the homogeneity of cyclotol mixture affected the viscosity distribution inside the tank which eventually affected the mobility of RDX particles.

Indeed, this lack of homogeneity will translate to inefficient heat transfer from the jacketed wall to the bulk fluid. The associated variation in temperature distribution will further accentuate viscosity and density gradients in the tank which also contributes to non-uniform mobility of RDX particles in the molten TNT. Variation in RDX concentration will affect its dissolution rate thereby influencing its re-crystallisation behaviour. In a nutshell, the lack of homogeneity in the cyclotol tank due to poor turbulence kinetic energy distribution will eventually affect the rheological behaviour of cyclotol mixture. Figure 6.49 shows that at 80 rpm, turbulence kinetic energy extended throughout the tank bottom and but did not extend much beyond the top impeller.

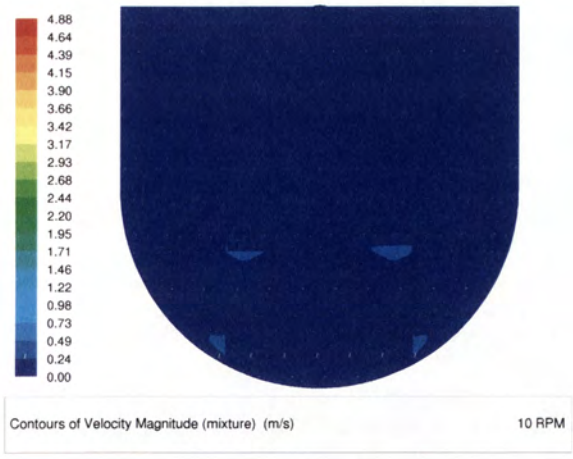


Figure 6.50: Velocity magnitude at 10 rpm

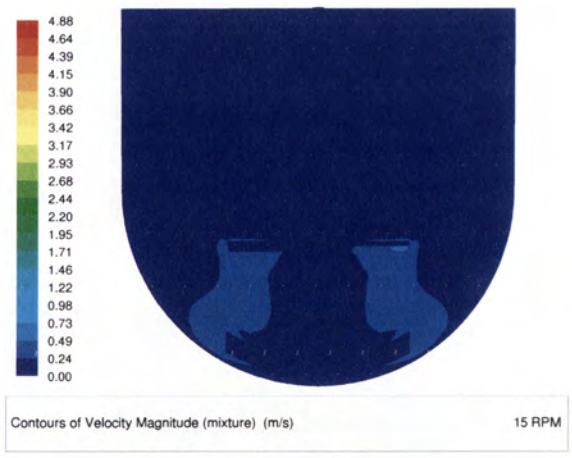


Figure 6.51: Velocity magnitude at 15 rpm

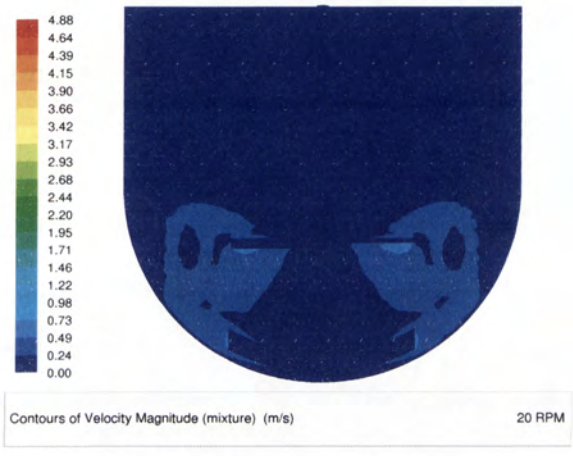


Figure 6.52: Velocity magnitude at 20 rpm

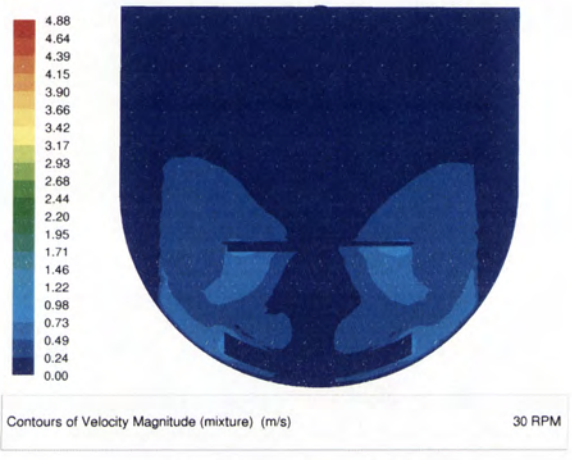


Figure 6.53: Velocity magnitude at 30 rpm

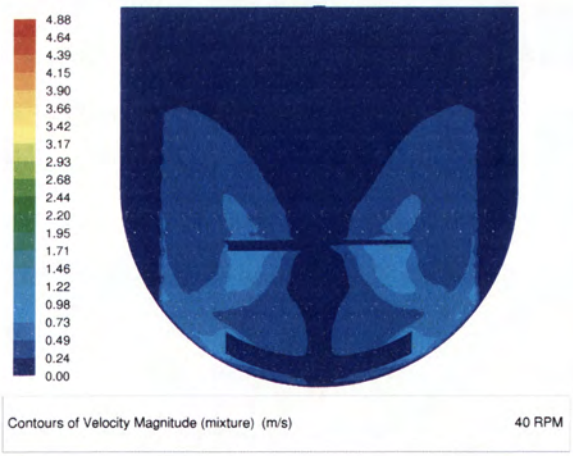


Figure 6.54: Velocity magnitude at 40 rpm

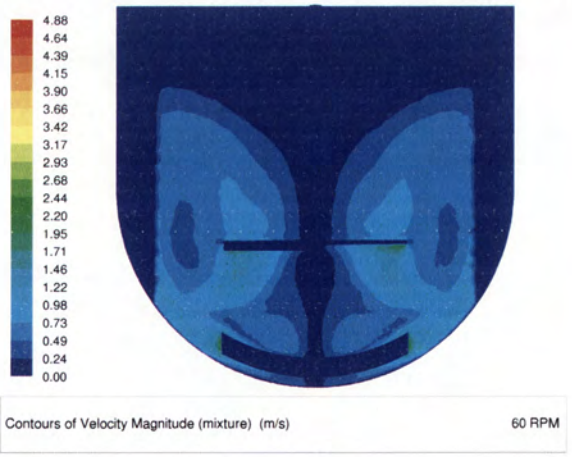


Figure 6.55: Velocity magnitude at 60 rpm

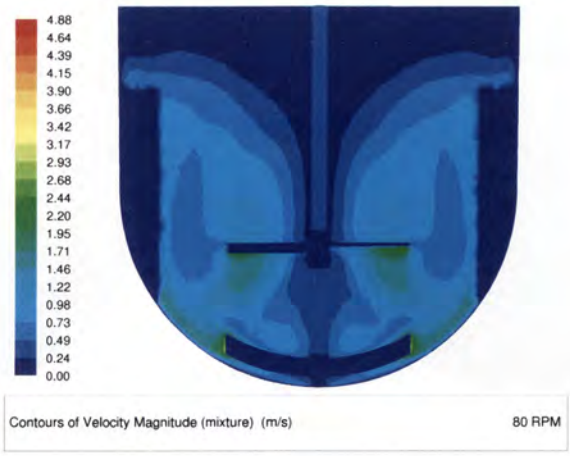


Figure 6.56: Velocity magnitude at 80 rpm

Due to the design of the semi-anchor impeller and its proximity to the tank bottom, the discharge from this impeller was significantly radial in nature, whereas the top hydrofoil impeller discharged flow axial in nature. Both of these phenomena were shown in Figures 6.50-6.56. Very little fluid movement was recorded at 10 and 15 rpm, relative to those at 80 rpm, as shown in Figure 6.56. This might give rise to insignificant downward forces leading to a failure in solid suspension. Successful mixing was attained at 40 rpm due to sufficient fluid movement, as shown in Figure 6.54. An even better mixing takes place during RDX particles charge in, as evidenced by the contours of velocity magnitude shown in Figure 6.55.

Previous chapters show that the hydrofoil impeller imparted more axial flow than radial flow. In contrast, the bottom semi-anchor impeller imparted more radial flow than axial flow. From the analysis above, it was assumed at this point that to prevent water draw-down into the cyclotol mixture, the use of axial flow impeller was not recommended. Radial flow impeller apart from discharging flows radial in nature will induce more turbulence in region further away from the impeller. Figure 6.50 shows that relative to the mixing process, the velocity magnitude achieved was very low during transfer, which was operated at 10 rpm. Due to the heavier density of RDX to molten TNT, the lack of fluid movement caused the RDX particles to sink and created segregation that consisted of a lighter density mixture above and heavier density mixture below.

When TNT is being melted, impellers speed is set to rotate at 40 rpm (50% in DCS system), and is increased to 58 rpm (80%) when the RDX slurry is charged in. Mixing takes place for 10 mins at 40 rpm. After that, speed is reduced to 10 rpm (15%) where the product is recirculated to achieve the right density which normally takes 5-10 mins to accomplish.

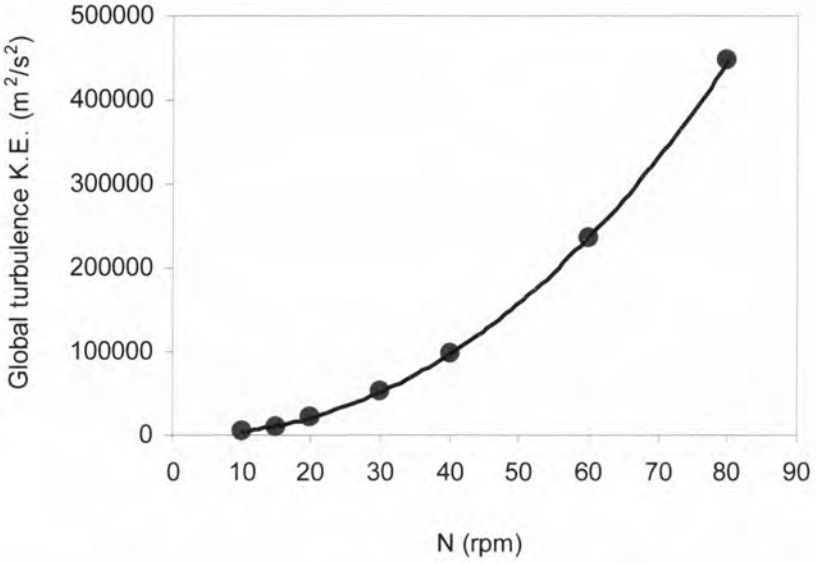


Figure 6.57: Relationship of global turbulence kinetic energy with impeller rotational speeds

Figure 6.57 illustrates the nonlinear dependency of global turbulence kinetic energy on the impeller rotational speed, and may be described by:

$$G_{KE} = 29.954N^{2.192} \qquad \text{- 6.17}$$

Since the viscosity of cyclotol was higher single-phase molten TNT, it was apparent that if the mixing tank could not deliver sufficient global turbulence for molten TNT, it would not be able to achieve enough turbulence for cyclotol suspension as well since in theory, turbulence dampening occurs at higher viscosity values.

### 6.4.3 Suspension of RDX particles

There are several factors contributing to homogeneous suspensions and one of them is the impeller speed. In this particular case, the impeller speed could not be set too high because vortex formed will draw-down water. However, if the impeller speed is set too low to mitigate water draw-down, then the suspension will not be homogeneous since RDX particles are heavier than molten TNT [Lea and Adesina 2006].

In this section, simulations were conducted to simulate the suspension of RDX particles in molten TNT at 85°C, as a function of different impellers rotational speed. The rotational speeds investigated were: 0, 10, 15, 20, 30, 40, 60, and 80 rpm. These simulations were based on model consisting of 490 kg of RDX particles occupying 0.2768 $m^3$ of space. Using the volume of sphere formula, $(\pi/3)\ y^2\ (1.5d\text{-}y)$ where $y$ is the height of RDX level and $d$ is the diameter of the sphere, the RDX particles level reached up to a height of 0.4791 m in the mixing tank, as shown in Figure 6.58.

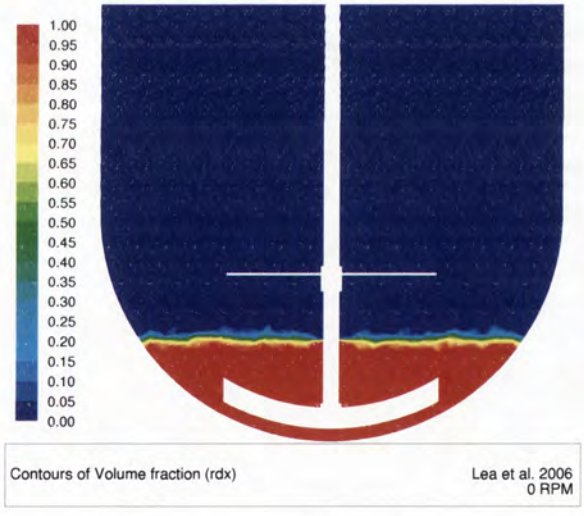


Figure 6.58: RDX volume fraction at 0 rpm

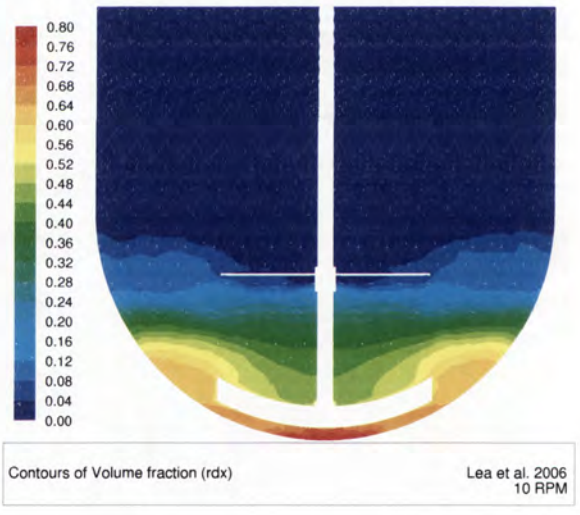


Figure 6.59: RDX volume fraction at 10 rpm

Figure 6.59 shows that at 10 rpm, there was a small increase in RDX particles level but high RDX particles concentration was located immediately below the bottom impeller's blade. Similar high RDX concentration was found in the vicinity of the bottom impeller, along the tank wall. Relatively low concentration of RDX particles was found around the top impeller. Cloud height was only slightly higher than that obtained when the impeller speed was zero. Overall, at this speed, effective suspension did not take place, and it can be

safely assumed that at 10 rpm, the speed, $N_{js}$, necessary to just suspend the RDX particles, had not been attained.

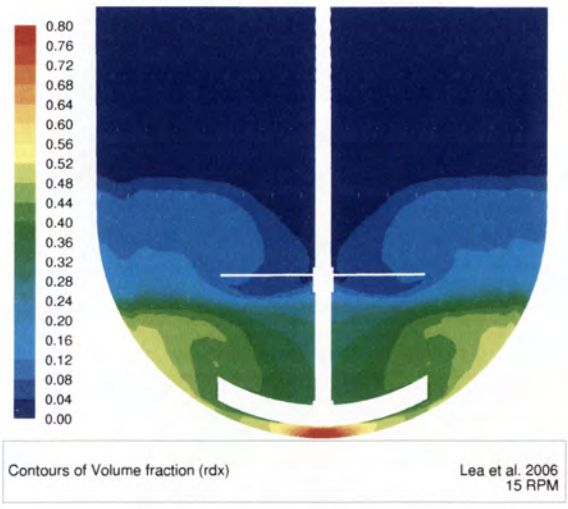


Figure 6.60: RDX volume fraction at 15 rpm

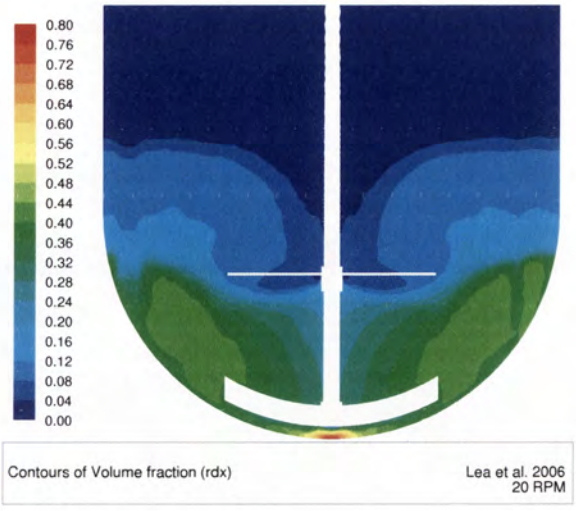


Figure 6.61: RDX volume fraction at 20 rpm

Figure 6.60 shows that at 15 rpm, suspension of RDX particles was improved. The accompanying faint cloud height was also noticeably higher. However, a high concentration of RDX particles was located at the bottom of the semi-anchor impeller, albeit at a lower concentration than when the speed was set to 10 rpm. Less solids build up was seen around the bottom impeller region. Figure 6.61 shows that at 20 rpm, the high concentration of RDX particles located immediately below the semi-anchor impeller had virtually disappeared. Moreover, it was observed that the region with higher concentration of RDX particles was smaller in size. As expected, the faint cloud height had also increased. In spite of this observed improvement, homogeneous dispersion of RDX particles in molten TNT was attained.

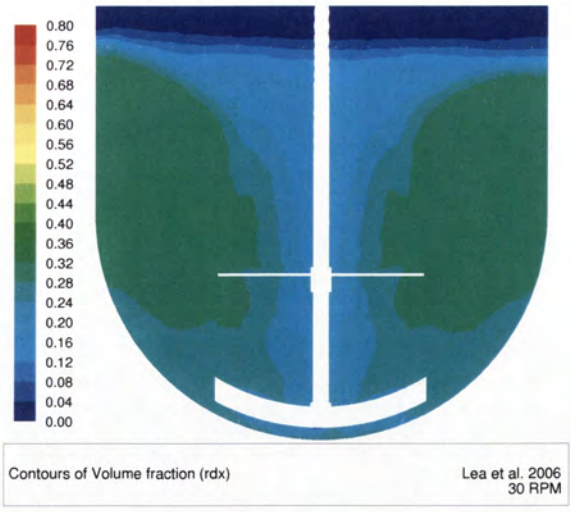


Figure 6.62: RDX volume fraction at 30 rpm

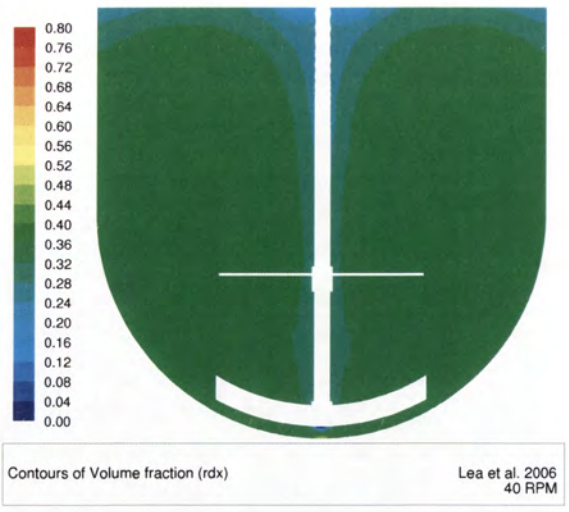


Figure 6.63: RDX volume fraction at 40 rpm

Significant improvement was seen when the impeller speed was increased to 30 rpm, as shown in Figure 6.62. At this speed, localised build-up of RDX particles ceased to exist and cloud height reached 80% of the tank level. Water sits above this level. In this case, although a marked improvement was noticed, further improvement to the homogeneity of cyclotol mixture was achieved above 40 rpm, as shown in Figures 6.63. However, even at the good homogeneity obtained, a further improvement in the homogeneity of cyclotol was achieved at 60 rpm and 80 rpm, as shown in Figures 6.64 and 6.65 respectively, judging by the spatially-uniform volume fraction of RDX particles in the tank.

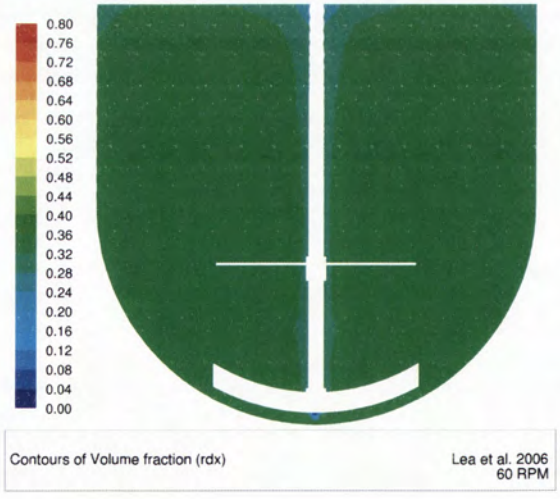


Figure 6.64: RDX volume fraction at 60 rpm

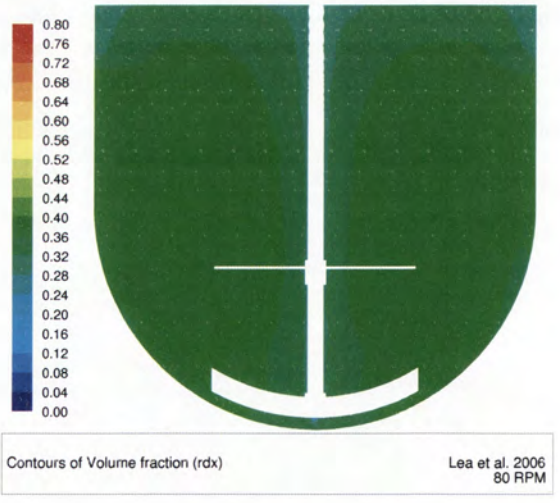


Figure 6.65: RDX volume fraction at 80 rpm

This provided an explanation as to why production personnel experienced product variations from batch to batch which, from the CFD results was attributed to the inability of the mixing tank to suspend the RDX particles homogeneously when the impellers were rotating at 10 rpm. From this process analysis, it was manifested that the production of explosive mixture having consistent density from batch to batch would be a challenge. Currently, production personnel are experiencing statistical product composition reproducibility, which was reflected by the plant data recorded over a period of time, as displayed in later section. On the basis of CFD simulation, it observed that good RDX particles suspension was achievable with a minimum speed of 40 rpm. However, based on CFD simulation for water draw-down profiling, the maximum speed allowable to prevent water draw-down was about 20 rpm. This suggested that with the current tank operating procedure and design, it was impossible to achieve homogeneous mixing concurrently with minimal water draw-down. This jeopardised the quality of the product cyclotol for bomb-filling. Consequently, a change in the design of the mixing tank was required to both prevent water draw-down and achieve a homogeneous RDX suspension in the molten TNT.

In summarising these results, good RDX particles suspension was achievable with a minimum speed of 40 rpm. However, this recommendation was at odds with the previous simulations carried out on the draw-down of water as a function of impellers rotational speed. In those simulations, the maximum impeller rotational speed allowable to prevent water draw-down was 20 rpm. Consequently, a change in the design of the mixing tank is required to prevent water draw-down and achieve a homogeneous RDX suspension in the molten TNT.

### 6.4.4 Water entrainment

Table 6.3: Liquid level at various stages of tank transfer

| Level % | Cyclotol level (m) | Water level (m) | Air level (m) |
|---|---|---|---|
| 100 | 0 – 1.087 | 1.087 – 1.787 | 1.787 – 2.087 |
| 80 | 0 – 0.870 | 0.870 – 1.570 | 1.570 – 2.087 |
| 70 | 0 – 0.761 | 0.761 – 1.461 | 1.461 – 2.087 |
| 60 | 0 – 0.652 | 0.652 – 1.352 | 1.352 – 2.087 |
| 40 | 0 – 0.435 | 0.435 – 1.135 | 1.135 – 2.087 |
| 20 | 0 – 0.217 | 0.217 – 0.917 | 0.917 – 2.087 |

Table 6.3 shows the cyclotol, water and air levels at different stages in tank transfer. While the volume of cyclotol decreased, the volume of air increased but the volume of water trapped between these two components remained constant throughout the entire cyclotol transferring process [Lea and Adesina 2007].

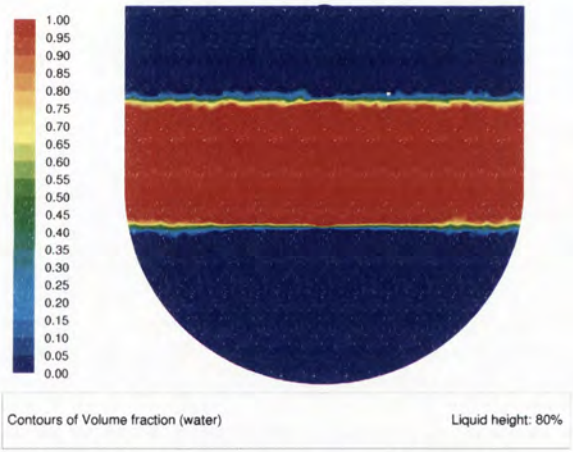


Figure 6.66: Volume fraction at 80% liquid height – 0 rpm

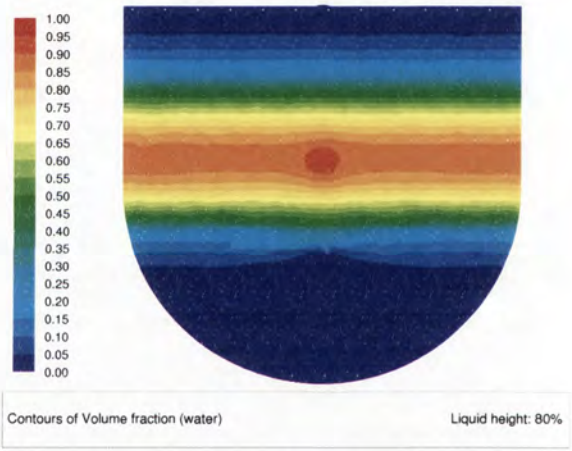


Figure 6.67: Volume fraction at 80% liquid height – 10 rpm

Figure 6.66 shows the volume fraction of three non-penetrating components when the impellers were at rest, namely: cyclotol at the bottom, water in the middle and air as the top layer where water draw-down was found to be negligible. During the high explosive content transfer, the impeller rotational speed was set to 10 rpm and Figure 6.67 shows that some water was drawn down into the cyclotol mixture at 80% of initial liquid height (ILH). This draw-down of water was attributed to the closeness of the density of water and cyclotol. In addition, because vortex was not apparent in this case, the draw-down was most likely caused by the similarity in the density of the two fluid components. At the rotational speed of 10 rpm, the downward force of the blades could not provide enough energy to generate a significant central vortex.

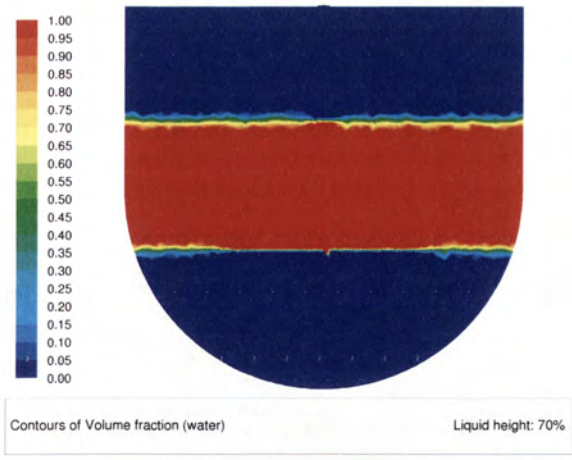


Figure 6.68: Volume fraction at 70% liquid height – 0 rpm

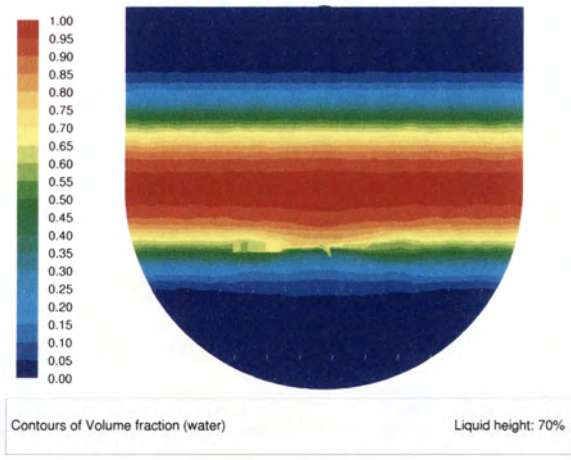


Figure 6.69: Volume fraction at 70% liquid height – 10 rpm

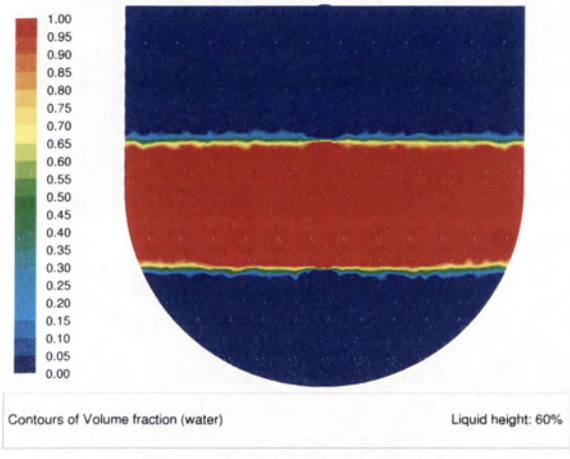


Figure 6.70: Volume fraction at 60% liquid height – 0 rpm

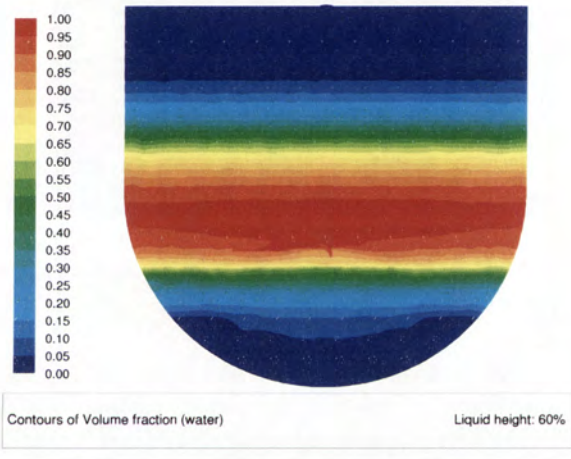


Figure 6.71: Volume fraction at 60% liquid height – 10 rpm

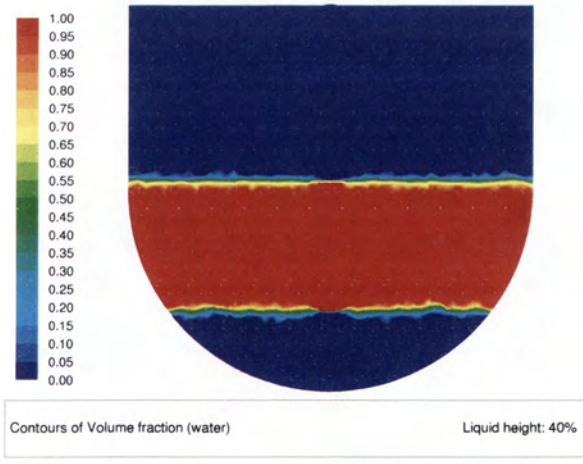


Figure 6.72: Volume fraction at 40% liquid height – 0 rpm

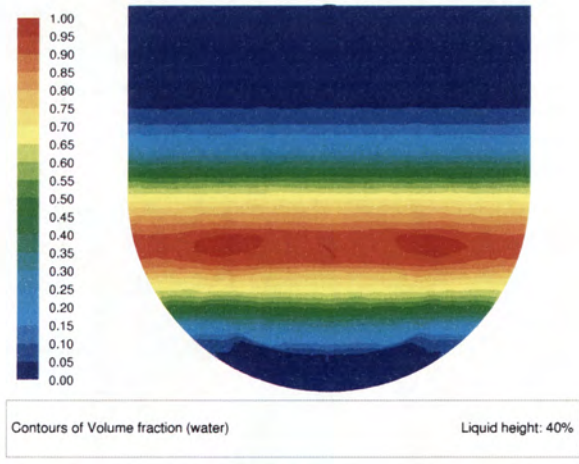


Figure 6.73: Volume fraction at 40% liquid height – 10 rpm

Figures 6.68-6.73 show the tank composition distribution as the cyclotol mixture was further withdrawn from the bottom (i.e. height decrease). Up to 40% of the ILH, this water draw-down did not have any negative impact on the process of tank emptying because only the cyclotol mixture was leaving the tank and most of the water was left behind. However, at 20% of ILH, a mixture containing 16% of $H_2O$ was predicted to be sitting immediately above the bottom outlet as shown in Figures 6.75 and 6.76. Thus, during the explosive mixture transfer, this water was conveyed out in the manner shown in vector plot on Figure 6.77. Stopping the impellers created liquid segregation, reflected on the contour plot shown in Figure 6.74.

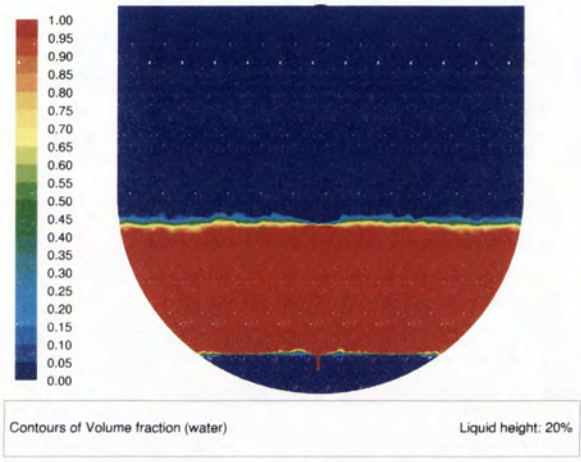


Figure 6.74: Volume fraction at 20% liquid height – 0 rpm

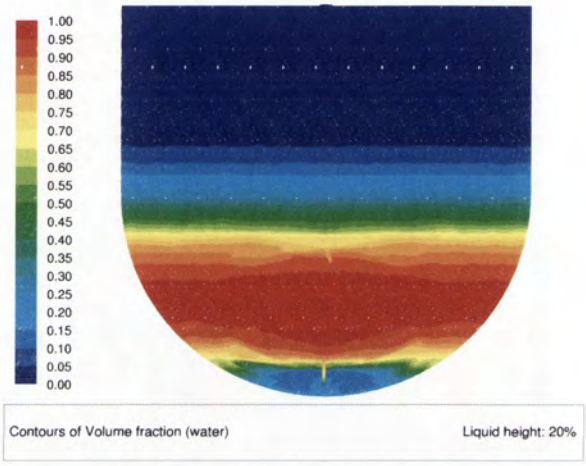


Figure 6.75: Volume fraction at 20% liquid height – 10 rpm

Figure 6.76 : 16% by volume of $H_2O$

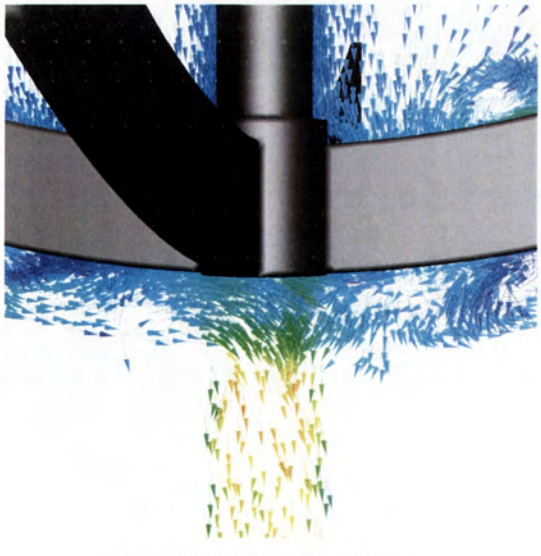

Figure 6.77 : Water entrainment

This implies that, during the transfer of cyclotol mixture, the level of water must not fall below 20% of initial liquid height or 0.217m from the tank bottom. This finding explained a possible source of product quality variation during cyclotol transfer to the next unit. This clearly justified the use of the CFD simulation in product and process analysis especially in a situation where, due to the explosive nature of the chemicals, direct experimentation is impractical and unsafe.

The CFD results showed that the maximum impeller speed allowable to avoid water draw-down was 20 rpm while the minimum speed required to suspend the RDX particles homogeneously was 40 rpm. These conflicting requirements necessitate a fundamental change in the design and operation of the mixing tank. In addition, during the transfer of cyclotol mixture to the next unit operation, the level of water must not fall 0.217m from the tank bottom, failing which water entrainment to the next unit operation was inevitable. These results agreed with production data, visualised using statistical process control technique and plant observations. Overall, this section of the research work shows that process diagnosis via numerical method had provided production personnel with information not previously possible. This enhanced their understanding of the process and hence shed some light on an ongoing problem of excessive variation in final product composition.

### 6.4.5 Product recirculation

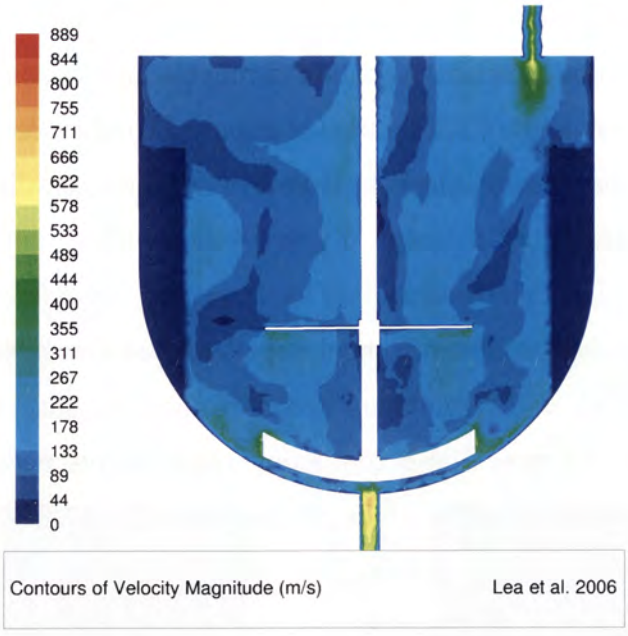


Figure 6.78: Contour of flow pattern during transferring of cyclotol

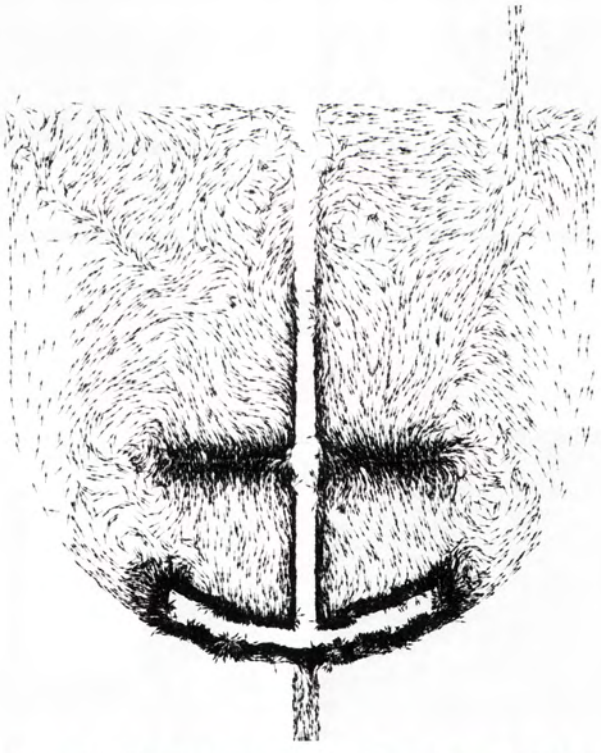

Figure 6.79: Vectors of flow pattern during transferring of cyclotol

During recirculation of cyclotol mixture to obtain the desired density, the flow from the top inlet pipe created a slight higher velocity region at the pipe opening, as shown in Figure 6.78. Besides that, the flow pattern was not influenced significantly by the recirculation of the explosive mixture, as shown in Figure 6.79.

### 6.4.6 Impellers contribution analysis

The aim of this section of the study was to determine whether by removing the top axial flow impeller in the mixing tank, water draw-down could be mitigated without compromising its ability to suspend the RDX particles.

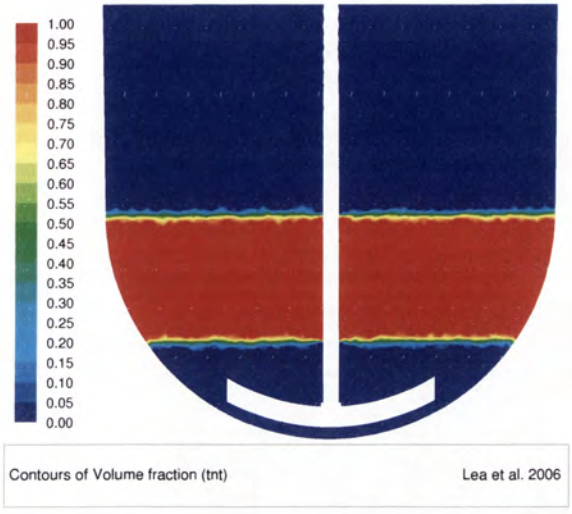


Figure 6.80: RDX-TNT-$H_2O$ system

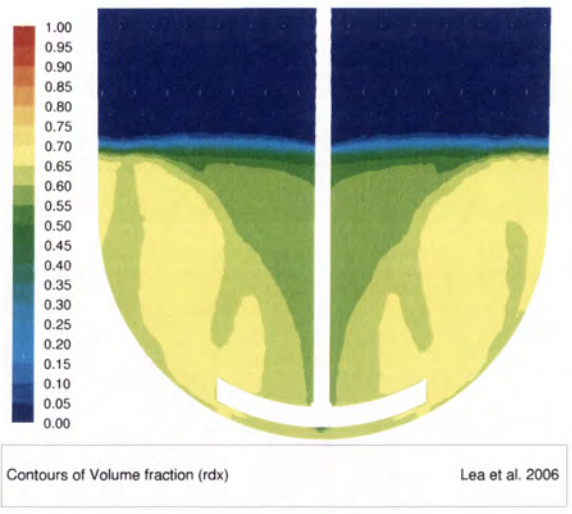


Figure 6.81: Volume fraction of RDX at 40 rpm

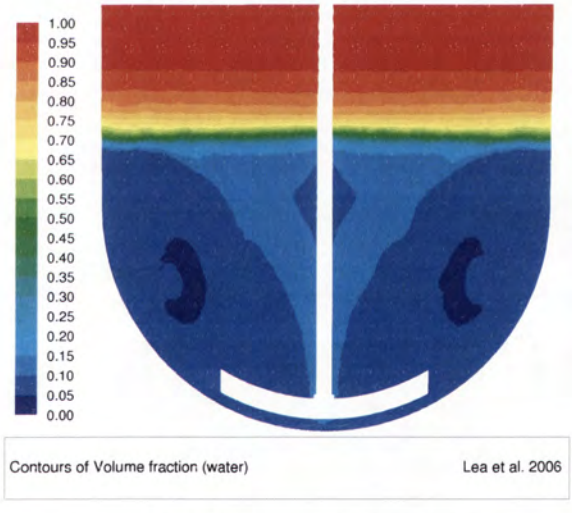


Figure 6.82: Volume fraction of water at 40 rpm

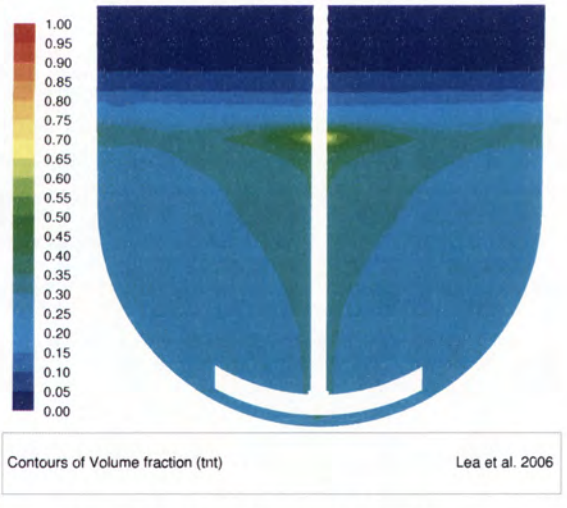


Figure 6.83: Volume fraction of TNT at 40 rpm

To study the contribution of the semi-anchor impeller, simulations were conducted in which the top hydrofoil impeller was removed. The simulations were conducted when the bottom impeller was rotating at 40 rpm. Figure 6.80 shows a multiphase system consisting of the bottom RDX layer, TNT middle layer and top water layer. As shown in Figure 6.81, the RDX particles were suspended although its homogeneity was compromised. The

contour plot shows that around the shaft, the volume fraction of RDX was lower than that near the wall.

Figure 6.82 which shows the volume fraction of water at this speed indicated that a significant amount of water was drawn down, thus proving that removing the top impeller did not help to prevent the infiltration of water. Even so, TNT in the middle layer was dispersed uniformly although with smaller volume fraction along the wall than around the shaft as shown in Figure 6.83. This result agreed with plant observations, which revealed the presence of higher RDX concentration along the wall.

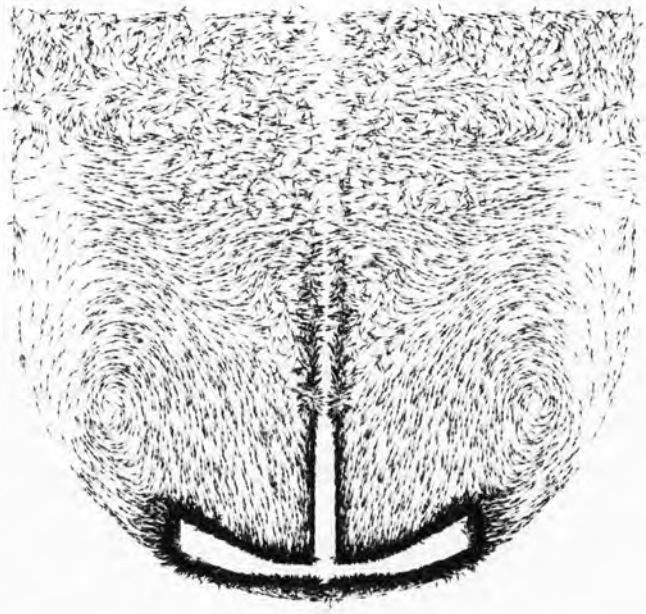

Figure 6.84: Vector plot of the RDX-TNT-$H_2O$ system

Without the top hydrofoil impeller, the cloud height attained was much lower than if the top hydrofoil impeller was present. The vector plot shown in Figure 6.84, also revealed that the bottom impeller generated mostly radial flow which was deflected upward by the spherical tank bottom and by wall baffles. A vortex surrounding the shaft was also seen under these conditions. Although cloud height reached up to the top of the baffle, there was a steep central vortex which converged just above the hub of the impeller. This indicated that even though a high cloud height was achieved, it might not be homogeneous because there was not enough vertical recirculation within the tank to push the RDX particles toward to the tank bottom and toward the baffles.

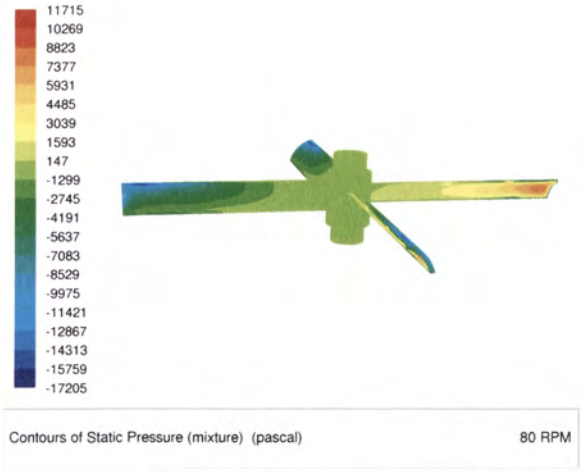


Figure 6.85: Top impeller

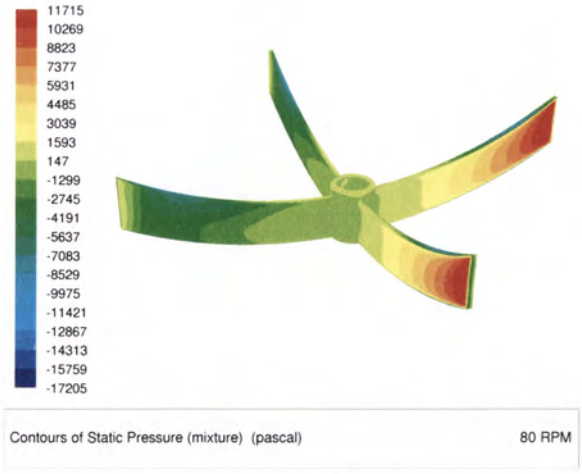


Figure 6.86: Bottom impeller

Figure 6.85 shows that the blade tips were subjected to the highest pressure while the lowest pressure was experienced around the hub region. Figure 6.86 also shows that the highest pressure experienced by the bottom semianchor impeller occurred around the blade tip. When the two impellers were compared, it was seen that the bottom semianchor impeller experienced a higher pressure at the blade tip than the top impeller. This was attributed to the semianchor $90^{o}$ upright blade as opposed to the inclined top impeller.

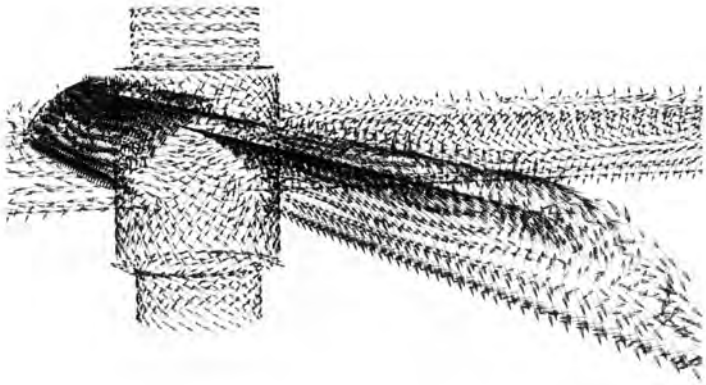

Figure 6.87: Vector plot for top impeller

Figure 6.87 shows that for the top impeller, most of the vectors were directed downward towards the tank bottom. This reflected the nature of the axial-flow hydrofoil impeller.

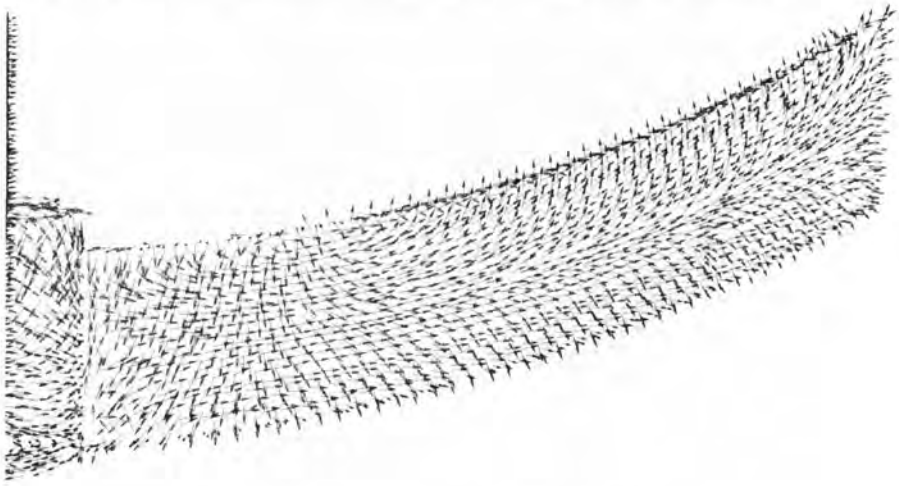

Figure 6.88: Vector plot for bottom impeller

Figure 6.88 shows that most of the vectors were directed toward the blade tip, thus reflecting the radial-flow nature of a $90^{o}$ upright blade. This, combined with the spherical-bottom tank, impeller close clearance and wall baffles, helped to ensure that denser particles were propelled to a higher elevation in the tank. It must be noted that in the absence of any of the abovementioned factors, the effectiveness of this impeller design in suspending particles would be severely compromised.

## 6.5 Multiphase flow in general

The description of multiphase flow as interpenetrating continuous incorporates the concept of phasic volume fractions, denoted as $\alpha_q$. Volume fractions represent the space occupied by each phase. The laws of conservation of mass and momentum are satisfied by each phase individually. The derivation of the conservation equations can be done by ensemble averaging the local instantaneous balance for each of the phases [Anderson and Jackson 1967] or by using the mixture theory approach [Bowen 1976].

The volume of phase $q$ denoted by $V_q$ is defined as

$$V_q = \int_V \alpha_q dV \qquad \text{- 6.18}$$

and

$$\sum_{q=1}^{N} \alpha_q = 1 \qquad \text{- 6.19}$$

The effective density of phase $q$ is given:

$$\hat{\rho}_q = \alpha_q \rho_q \qquad \text{- 6.20}$$

where $\rho_q$ is the physical density of phase $q$.

The conservation of mass equation in general from which the equation solved by Fluent® was derived, is as follow:

$$\frac{\partial}{\partial t}(\alpha_q \rho_q) + \nabla \cdot (\alpha_q \rho_q \vec{v}_q) = \sum_{p=1}^{N} \left(\dot{m}_{pq} - \dot{m}_{qp}\right) + S_q \qquad \text{- 6.21}$$

where

$\vec{\upsilon}_q$ : velocity of phase $q$

$\dot{m}_{pq}$ : characterises the mass transfer from the $p^{th}$ to $q^{th}$ phase

$\dot{m}_{qp}$ : characterises the mass transfer from phase $q$ to phase $p$

$S_q$ : source term, zero by default but a constant or user-define mass source for each phase can be specified

The conservation of momentum equation in general, from which the equation solved by Fluent® was derived is as follow:

$$\frac{\partial}{\partial t}(\alpha_q \rho_q \vec{\upsilon}_q) + \nabla \cdot (\alpha_q \rho_q \vec{\upsilon}_q \vec{\upsilon}_q) = -\alpha_q \nabla p - \nabla \cdot \overline{\overline{\tau}}_q + \alpha_q \rho_q \vec{g} + \sum_{p=1}^{N} \left( \vec{R}_{pq} + \dot{m}_{pq} \vec{\upsilon}_{pq} - \dot{m}_{qp} \vec{\upsilon}_{qp} \right) + \left( \vec{F}_q + \vec{F}_{lift,q} + \vec{F}_{vm,q} \right) \quad \text{- 6.22}$$

where $\overline{\overline{\tau}}_q$ is the $q^{th}$ phase stress-strain tensor and is given by:

$$\overline{\overline{\tau}} = \alpha_q \mu_q \left( \nabla \vec{\upsilon}_q + \nabla \vec{\upsilon}_q^T \right) + \alpha_q \left( \lambda_q - \frac{2}{3} \mu_q \right) \nabla \cdot \vec{\upsilon}_q \overline{\overline{I}} \quad \text{- 6.23}$$

where

$\mu_q$ : shear viscosity of phase $q$

$\lambda_q$ : bulk viscosity of phase $q$

$\vec{F}_q$ : external body force

$\vec{F}_{lift,q}$ : lift force

$\vec{F}_{vm,q}$ : virtual mass force

$\vec{R}_{pq}$ : interaction force between phases

$p$ : pressure shared by all phases

$\vec{v}_{pq}$ is the interphase velocity and is defined as follows:

If $\dot{m}_{pq} > 0$ (phase $p$ mass is being transferred to phase $q$), then $\vec{v}_{pq} = \vec{v}_p$

If $\dot{m}_{pq} < 0$ (phase $q$ mass is being transferred to phase $p$), $\vec{v}_{pq} = \vec{v}_q$

Likewise, if $\dot{m}_{qp} > 0$ then $\vec{v}_{qp} = \vec{v}_q$ but if $\dot{m}_{qp} < 0$, then $\vec{v}_{qp} = \vec{v}_p$

The conservation of momentum shown above must be closed with appropriate expressions for the interphase force $\vec{R}_{pq}$. This force depends on the friction, pressure, cohesion and other effects and is subject to the conditions that $\vec{R}_{pq} = -\vec{R}_{qp}$ and $\vec{R}_{qq} = 0$

$$\sum_{p=1}^{n} \vec{R}_{pq} = \sum_{p=1}^{n} K_{pq}\left(\vec{v}_p - \vec{v}_q\right) \qquad \text{- 6.24}$$

where $K_{pq}$ or $K_{qp}$ is the interphase momentum exchange coefficient.

For multiphase flows, Fluent® can include the effect of lift forces on the secondary phase particles, droplets or bubbles. These lift forces act on a particle mainly due to velocity gradients in the primary-phase flow field. The lift force will be more significant for larger particles, but the Fluent® model assumes that the particle diameter is much smaller than the interparticle spacing. Therefore, the inclusion of lift force is not appropriate for closely packed particles or for very small particles. The lift force acting on a secondary phase $p$ in a primary phase $q$ is computed from Drew and Lahey [1993] and is given by:

$$\vec{F}_{lift} = -0.5\rho_q \alpha_p \left(\vec{v}_q - \vec{v}_p\right) \times \left(\nabla \times \vec{v}_q\right) \qquad \text{- 6.25}$$

The lift force $\vec{F}_{lift}$ will be added to the right-hand side of the momentum equation for both phases, that is $\vec{F}_{lift,q} = -\vec{F}_{lift,p}$. In most cases, the lift force is insignificant compared to the drag force, so there is no reason to include this extra term. If the lift force is significant as in the case when the phase separate quickly, it may be appropriate to include this term. By default, $\vec{F}_{lift}$ is not included. The lift force and lift coefficient can be specified for each pair of phases, if required.

Fluent® also includes the 'virtual mass effect' that occurs when a secondary phase $p$ accelerates relative to the primary phase $q$. The inertia of the primary phase mass encountered by the accelerating particles, droplets or bubbles exerts a 'virtual mass force' on the particles [Drew and Lahey 1993]. This is given in mathematical expression as:

$$\vec{F}_{vm} = 0.5\alpha_p \rho_q \left( \frac{d_q \vec{v}_q}{dt} - \frac{d_p \vec{v}_p}{dt} \right) \quad \text{- 6.26}$$

The term $\frac{d_q}{d_t}$ denotes the phase material time derivative of the form:

$$\frac{d_q(\phi)}{dt} = \frac{\partial(\phi)}{\partial t} + (\vec{v}_q \cdot \nabla)\phi \quad \text{- 6.27}$$

The virtual mass force $\vec{F}_{vm}$ will be added to the right-hand side of the momentum equation for both phases, that is $\vec{F}_{vm,q} = -\vec{F}_{vm,p}$. The virtual mass effect is significant when the secondary phase density is much smaller than the primary phase density, such as in the case of a transient bubble column. By default, the $\vec{F}_{vm}$ is not included in the calculation.

## 6.6 Eulerian multiphase model for fluid-fluid system

Although the Eulerian model was not used in this section, nevertheless, an overview of this model was provided here for future reference in case the need arises. The equations for fluid-fluid and granular multiphase flows solved by Fluent® are given here for the general application to n-phase flow.

### 6.6.1 Continuity equation

The volume fraction of each phase is calculated from a continuity equation in the form of:

$$\frac{1}{\rho_{rq}}\left(\frac{\partial}{\partial t}(\alpha_q\rho_q)+\nabla\cdot(\alpha_q\rho_q\vec{v})=\sum_{p=1}^{N}\left(\dot{m}_{pq}-\dot{m}_{qp}\right)\right) \qquad \text{- 6.28}$$

where $\rho_{rq}$ is the phase reference density or the volume averaged density of the $q^{th}$ phase in the solution domain. The solution of this equation for each secondary phase, subject to the condition that the volume fractions sum to one, enables the calculation of the primary-phase volume fraction.

### 6.6.2 Fluid-fluid momentum equation

Conservation of momentum for a fluid phase $q$ is given by:

$$\frac{\partial}{\partial t}(\alpha_q\rho_q\vec{v}_q)+\nabla\cdot(\alpha_q\rho_q\vec{v}_q\vec{v}_q)=-\alpha_q\nabla p-\nabla\cdot\overline{\overline{\tau}}_q+\alpha_q\rho_q\vec{g}+$$
$$\sum_{p=1}^{N}\left(K_{pq}\left(\vec{v}_p-\vec{v}_q\right)+\dot{m}_{pq}\vec{v}_{pq}-\dot{m}_{qp}\vec{v}_{qp}\right)+\left(\vec{F}_q+\vec{F}_{lift,q}+\vec{F}_{vm,q}\right) \qquad \text{- 6.29}$$

Here $\vec{g}$ is the acceleration due to gravity

### 6.6.3 Fluid-fluid exchange coefficient

For fluid-fluid flows, each secondary phase is assumed to form droplets or bubbles. This has an impact on how each of the fluids is assigned to a particular phase. For example, in flows where there are unequal amounts of two fluids, the predominant fluid should be modelled as the primary fluid, because the sparser fluid is more likely to form droplets or bubbles. The fluid-fluid exchange coefficient for these types of bubbly, liquid-liquid or gas-liquid mixtures is written in the following general form:

$$K_{pq} = \frac{\alpha_q \alpha_p \rho_p f}{\tau_p} \qquad \text{- 6.30}$$

where the term $f$, being the drag function, is defined differently for various exchange-coefficient models and $\tau_p$ being the 'particulate relaxation time' is defined as,

$$\tau_p = \frac{\rho_p d_p^2}{18\mu_q} \qquad \text{- 6.31}$$

where $d_p$ is the diameter of particles of phase $p$. All definitions of $f$ include a drag coefficient $C_D$ that is based on the relative Reynolds number $Re$. It is this drag function that differs among the various exchange-coefficient models. For all these situations, $K_{pq}$ approaches zero whenever the primary phase is not present within the domain to be modelled. To enforce this, the drag function $f$ is always multiplied by the volume fraction of the primary phase $q$ as shown in the definition of $K_{pq}$ above.

Three drag coefficient models available are, namely: Schiller and Naumann [1935]; Morsi and Alexander [1972] and the symmetric model.

For the model of Schiller and Naumann [1935],

$$f = \frac{C_D \mathrm{Re}}{24} \qquad \text{- 6.32}$$

where

$$C_D = \begin{cases} \dfrac{24\left(1 + 0.15\,\mathrm{Re}^{0.687}\right)}{\mathrm{Re}} & \text{for } \mathrm{Re} \le 1000 \\ 0.44 & \text{for } \mathrm{Re} > 1000 \end{cases} \qquad \text{- 6.33}$$

and Re is the relative Reynolds number. The relative Reynolds number for the primary phase $q$ and secondary phase $p$ is obtained from

$$\mathrm{Re} = \frac{\rho_q \left|\vec{v}_p - \vec{v}_q\right| d_p}{\mu_q} \qquad \text{- 6.34}$$

The relative Reynolds number for secondary phases $p$ and $r$ is obtained from:

$$\mathrm{Re} = \frac{\rho_{rp} \left|\vec{v}_r - \vec{v}_q\right| d_{rp}}{\mu_{rp}} \qquad \text{- 6.35}$$

where the mixture viscosity of the phases $p$ and $r$ is given by:

$$\mu_{rp} = \alpha_p \mu_p + \alpha_r \mu_r \qquad \text{- 6.36}$$

In Fluent®, this model is set as the default calculation method and is applicable for general use on all fluid-fluid pairs of phases. Another model available for selection in Fluent® includes the Morsi and Alexander [1972] model and is given by:

$$f = \frac{C_D \mathrm{Re}}{24} \qquad \text{- 6.37}$$

where

$$C_D = a_1 + \frac{a_2}{\mathrm{Re}} + \frac{a_3}{\mathrm{Re}^2} \qquad \text{- 6.38}$$

and Re is defined by

$$\mathrm{Re} = \frac{\rho_q \left|\vec{v}_p - \vec{v}_q\right| d_p}{\mu_q} \qquad \text{- 6.39}$$

or

$$\mathrm{Re} = \frac{\rho_{rp} \left|\vec{v}_p - \vec{v}_q\right| d_{rp}}{\mu_{rp}} \qquad \text{- 6.40}$$

The constants $a_1$, $a_2$ and $a_3$ are defined as:

| $a_1$ | $a_2$ | $a_3$ | Re |
|---|---|---|---|
| 0 | 24 | 0 | $0 < \mathrm{Re} < 0.1$ |
| 3.690 | 22.73 | 0.0903 | $0.1 < \mathrm{Re} < 1$ |
| 1.222 | 29.1667 | -3.8889 | $1 < \mathrm{Re} < 10$ |
| 0.6167 | 46.50 | -116.67 | $10 < \mathrm{Re} < 100$ |
| 0.3644 | 98.33 | -2,778 | $100 < \mathrm{Re} < 1{,}000$ |
| 0.357 | 148.62 | -47,500 | $1{,}000 < \mathrm{Re} < 5{,}000$ |
| 0.46 | -490.546 | 578,700 | $5{,}000 < \mathrm{Re} < 10{,}000$ |
| 0.5191 | -1,662.5 | 5,416,700 | $\geq 10{,}000$ |

The Morsi and Alexander [1972] models is the most complete, adjusting the function definition frequently over a large range of Reynolds numbers, however, calculations with this model may be less stable relative to the stability of other models.

The third model available for selection is the symmetric model and the exchange-coefficient given by:

$$K_{pq} = \frac{\alpha_p \left(\alpha_p \rho_p + \alpha_q \rho_q\right) f}{\tau_{pq}} \qquad \text{- 6.41}$$

where

$$\tau_{pq} = \frac{\left(\alpha_p \rho_p + \alpha_q \rho_q\right) \left(\frac{d_p + d_q}{2}\right)^2}{18(\alpha_p \mu_p + \alpha_q \mu_q)} \qquad \text{- 6.42}$$

similarly,

$$f = \frac{C_D \mathrm{Re}}{24} \qquad \text{- 6.43}$$

$$C_D = \begin{cases} \dfrac{24\left(1 + 0.15\,\mathrm{Re}^{0.687}\right)}{\mathrm{Re}} & \text{for } \mathrm{Re} \le 1000 \\ 0.44 & \text{for } \mathrm{Re} > 1000 \end{cases} \qquad \text{- 6.44}$$

and similarly, *Re* is defined by

$$\mathrm{Re} = \frac{\rho_q \left|\vec{v}_p - \vec{v}_q\right| d_p}{\mu_q} \qquad \text{- 6.45}$$

or

$$\mathrm{Re} = \frac{\rho_{rp} \left|\vec{v}_r - \vec{v}_q\right| d_{rp}}{\mu_{rp}} \qquad \text{- 6.46}$$

For a single disperse phase, $d_p$=$d_q$ for the definition of $\tau_{pq}$. This model is recommended for flows in which the secondary phase in one region of the domain becomes the primary phase in another. Therefore, for a single secondary phase, $d_p$=$d_q$ and $\frac{d_p + d_q}{2} = d_p$. This model can also be used for the interaction between secondary phases. Different exchange coefficients can be specified for each pair of phases. It is also possible to use user-defined functions to define exchange coefficients for each pair of phases. If the exchange coefficient is equal to zero, such as in the case when no exchange coefficient is specified, the flow fields for the fluids will be computed independently, with the only interaction being their complementary volume fractions within each computational cell. Since the Eulerian model was used in this work involving the modelling and simulation of the RDX/TNT mixing tank, then the components were molten TNT, being the primary fluid phase and the water being the secondary fluid phase. When the Eulerian multiphase model is used, Fluent® uses the phase coupled SIMPLE (PC-SIMPLE) algorithm for the pressure-velocity coupling. The PC-SIMPLE is an extension of the SIMPLE algorithm for multiphase flows where the velocities are solved coupled by phases, but in a segregated fashion.

### 6.6.4 Multiphase turbulence modelling

Three methods for modelling turbulence in multiphase flows within the context of the $k$-$\varepsilon$ models and two turbulence options within the context of the Reynolds stress models (RSM).

The three $k$-$\varepsilon$ models available are:

- Mixture turbulence model
- Dispersed turbulence model
- Turbulence model for each phase

The RSM turbulence models available are:

- Mixture turbulence model
- Dispersed turbulence model

The mixture turbulence model is the default multiphase turbulence model and represents the first extension of the single-phase $k$-$\varepsilon$ models. It is applicable when phases separate for stratified multiphase flows and when the density ratio between phases is close to 1. In these cases, using mixture properties and mixture velocities is sufficient to capture important features of the turbulent flow. The dispersed turbulence model is the appropriate model when the concentrations of the secondary phases are dilute. In such cases, the interparticle collisions are negligible and the dominant process in the random motion of the secondary phases is the influence of the primary phase turbulence. Fluctuating quantities of the secondary phases can therefore be given in terms of the mean characteristics of the primary phase and the ratio of the particle relaxation time and eddy-particle interaction time.

This model is applicable when there is clearly one primary continuous phase and the rest are dispersed dilute secondary phases. The most general multiphase turbulence model solves a set of $k$-$\varepsilon$ transport equations for each phase. This turbulence model is the appropriate choice when the turbulence transfer among the phases plays a dominant role. If this model is selected, Fluent® will be solving two additional transport equations for each secondary phase rendering this model more computationally intensive than the other models.

In this research work involving cyclotol mixing tank, the turbulence model for each phase is selected because cyclotol:water = 1,737 kg $m^{-3}$ ÷ 998.2 kg $m^{-3}$ = 1.740

The transport equations are given by:

$$\frac{\partial}{\partial t}\left(\alpha_q \rho_q k_q\right)+\nabla\cdot\left(\alpha_q \rho_q \vec{U}_q k_q\right)=\nabla\cdot\left(\alpha_q \frac{\mu_{t,q}}{\sigma_k}\nabla k_q\right)+\left(\alpha_q G_{k,q}-\alpha_q \rho_q \varepsilon_q\right)+$$
$$\sum_{l=1}^{n} K_{lq}\left(C_{lq}k_l - C_{ql}k_q\right)-\sum_{l=1}^{n} K_{lq}\left(\vec{U}_l-\vec{U}_q\right)\cdot\frac{\mu_{t,l}}{\alpha_l\sigma_l}\nabla\alpha_l+\sum_{l=1}^{n} K_{lq}\left(\vec{U}_l-\vec{U}_q\right)\cdot\frac{\mu_{t,q}}{\alpha_q\sigma_q}\nabla\alpha_q \quad \text{- 6.47}$$

and

$$\frac{\partial}{\partial t}\left(\alpha_q \rho_q \varepsilon_q\right)+\nabla\cdot\left(\alpha_q \rho_q \vec{U}_q \varepsilon_q\right)=\nabla\cdot\left(\alpha_q \frac{\mu_{t,q}}{\sigma_\varepsilon}\nabla\varepsilon_q\right)+\frac{\varepsilon_q}{k_q}\left[\ C_{1\varepsilon}\alpha_q G_{k,q}-C_{2\varepsilon}\alpha_q \rho_q \varepsilon_q+\right.$$
$$\left. C3\varepsilon\left(\sum_{l=1}^{n} K_{lq}\left(C_{lq}k_l - C_{ql}k_q\right)-\sum_{l=1}^{n} K_{lq}\left(\vec{U}_l-\vec{U}_q\right)\cdot\frac{\mu_{t,l}}{\alpha_l\sigma_l}\nabla\alpha_l+\sum_{l=1}^{n} K_{lq}\left(\vec{U}_l-\vec{U}_q\right)\cdot\frac{\mu_{t,q}}{\alpha_q\sigma_q}\nabla\alpha_q\right)\ \right] \quad \text{- 6.48}$$

The terms $C_{lq}$ and $C_{ql}$ can be approximated as:

$$C_{lq}=2,\ \ C_{ql}=2\left(\frac{\eta_{lq}}{1+\eta_{lq}}\right) \quad \text{- 6.49}$$

## 6.7 Statistical process characterisation

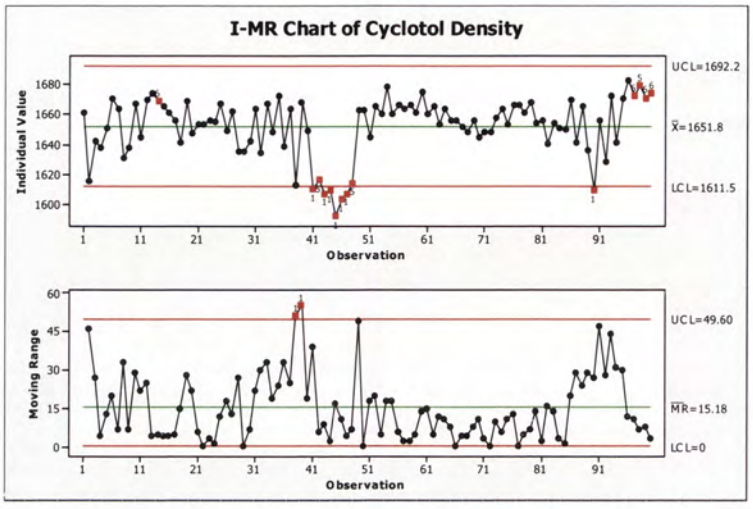


Figure 6.89: Individual moving range chart for Cyclotol density

Analysing the mean chart in Figure 6.89 above shows that the cyclotol density (January 2005 – October 2005) is not in statistical control due to several observations that breached the control chart rules, namely:

- Point outside the control limits
- 2 of 3 points between 2σ and 3σ from the mean
- 4 of 5 points between 1σ and 3σ from the mean
- 8 points in a row on one side of the centreline
- Trend

The range chart also shows an out of control situations for two observations because both of these points exceeded the 3σ standard deviation control limits. Despite this, 5 points resided on the LCL reflected very low standard deviation and therefore worth investigating to determine what caused these excellent results with a view to repeating the causes. Both the process mean and range deviated at some point in the process. To stabilise the process, the special causes of variation for the range must be identified and eliminated before shifting the process mean to the central line.

Figure 6.90 shows a snapshot of the process capability of the cyclotol density after removing those points that fall outside the control limits, defined as $3\sigma$ from the central line, and ignoring all run rules.

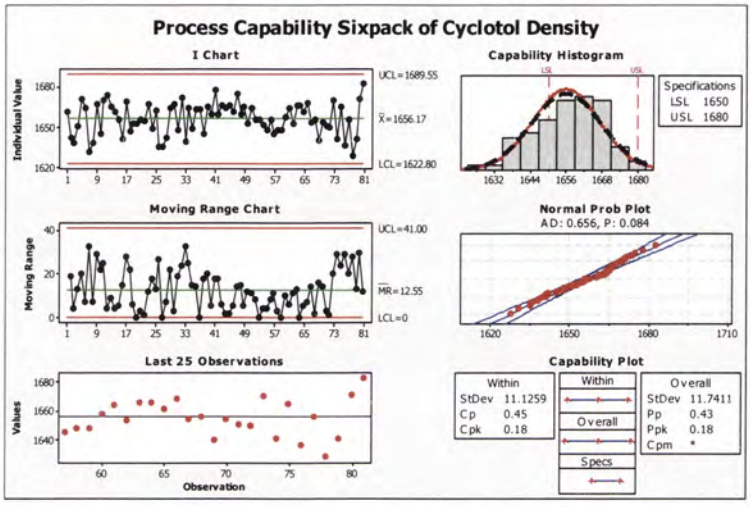


Figure 6.90: Process capability study

Firstly, the normal probability plot shows a linear correlation which indicated that the data followed a normal distribution, therefore SPC technique was applicable to these sets of data. In this snapshot, the mean and range charts above shows that the process was in statistical control. In reality the points representing out of control situations can only be removed after the special causes of variation have been identified and eliminated.

It is only after the process achieves statistical control that the true process capability and its index can be measured. The capability plot shows that the *CpK* was 0.18 and from the capability histogram, the process was seen to exceed both the upper (USL) and lower specification limits (LSL). The histogram also shows that a big portion of it exceeded LSL. The *CpK* value simply indicated that the process was not capable of meeting its objective most of the time. Moreover, even if the mean had shifted to the centre, the process capability would achieve its full potential of only 0.45.

A very important aspect point is that, apart from having low potential process capability (*Cp*), the process was not capable even after the out-of-specification points had been removed, to simulate a process in statistical control. The interpretation was that even though the special causes of variations had been removed, the common causes of variations that remained were too significant.

A fundamental change in the process must be carried out to eliminate these commons causes of variations. It was felt that this fundamental change consisted of but not limited to improving the mixing tank performance and effectiveness. The justification for this action was based on the results of earlier CFD simulation conducted to determine the ability of this unit operation in carrying out its duty to produce a homogeneous mixture of cyclotol.

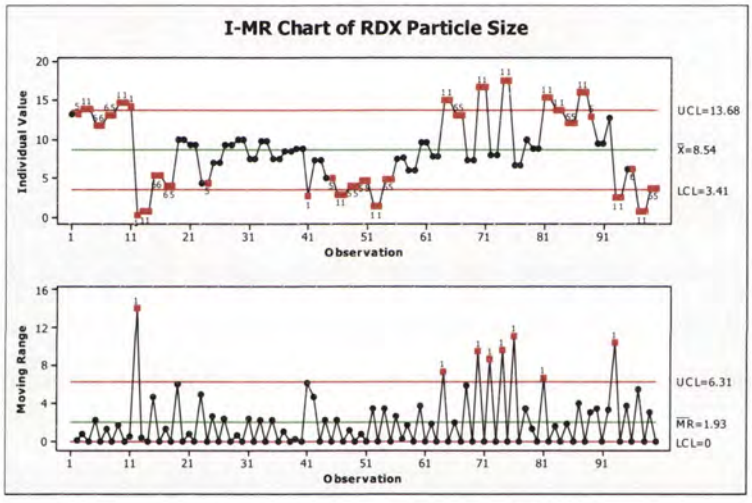


Figure 6.91: Individual moving range chart for RDX particle size

Figure 6.91 shows the moving range chart of RDX particle size. The chart shows that the RDX particle size was not in statistical control. This would cause the mixture viscosity to vary because as previously mentioned in the literature review, the mixture viscosity was particle-size dependent.

Table 6.4: Process capability

| Variables | Specification | Best running range | Cp | CpK | Comment |
|---|---|---|---|---|---|
| Cyclotol density | 1,650-1,680 | 1,623-1,690 | 0.45 | 0.18 | Not capable |
| % of RDX in cyclotol | 57.5-61.5 | 55.1-64.5 | 0.43 | 0.37 | Not capable |

The new control limits representing $3\sigma$ on each side of the central limits when the process was in statistical control was assumed as the range by which the current process was best running.

Using similar technique, the process capability index of the percentage of RDX in cyclotol was computed. In general, it was summarised that the process was not capable in the variables studied since the CpK were lower than the benchmark value of 1.33 [Montgomery 2005]. Table 6.4 shows the process capability summary of these results.

## 6.8 Concluding remarks

The CFD results showed that the maximum impeller speed allowable to avoid water draw-down is 20 rpm while the minimum speed required to suspend the RDX particles homogeneously is 40 rpm. These conflicting requirements necessitate a fundamental change in the design and operation of the mixing tank. In addition, during the transfer of cyclotol mixture to the next unit operation, the level of water must not fall below 20% of the ILH (0.217m from the tank bottom for the industrial operation), failing that, water entrainment to the next unit operation is inevitable. These results agreed with historical production data, statistical process evaluation and current plant observations. In addition, removing the top hydrofoil impeller did not help to mitigate the water draw-down, instead, it reduced the tank effectiveness in suspending the RDX particles homogeneously.

Overall, this chapter shows that process diagnosis via numerical simulation has provided production personnel with information not previously possible. This has enhanced their understanding of the process and hence shed some light on the on-going problem of excessive variation in final product composition.

# CHAPTER 7: BOMB INCORPORATOR

A significant amount of the high explosive cyclotol manufactured and described in Chapter 6 is transported to another part of the plant to be used to fill bomb shells. Bombs produced included but not limited to the MK-82, a free-fall, nonguided general purpose 500-pound bomb and the MK-84, a free-fall, nonguided general purpose 2,000-pound bomb. The MK-80 series low drag general purpose (LDGP) bombs are used in the majority of bombing operations where maximum blast and explosive effects are desired. The bomb shells are relatively light and approximately 45% of their complete weight is cyclotol.

The bomb MK-82, comes with filling having the following composition as shown in Table 7.1.

Table 7.1: Composition of MK82 by mass

| Components | Mass (kg) | Mass % |
|---|---|---|
| D2 (wax) | 15 | 4.403 |
| RDX/TNT | 252 | 73.97 |
| Aluminium | 72 | 21.13 |
| Calcium Chloride | 1.70 | 0.4990 |
| Total | 340.7 | 100 |

Impeller speed : 45 - 46 rpm

Temperature : 90 - 92°C

## 7.1 Objective of research

Currently, the production rate for the manufacture of MK82 bombs is 20 bombs per 8-hour production shift and 40 bombs within 2 production shifts. The Department of Defence (DoD) had just placed an order for ADI to manufacture 5,000 MK82 bombs. This translated into 25 weeks of continuous manufacturing to fulfil this order. To shorten the delivery date, it was desired to increase the production rate to a higher level without impacting on the quality of bombs produced.

*Therefore, the objective of this study was to increase the bombs production rate via:*

1. *Reducing reject rate by ensuring better quality bombs were produced each time*
2. *Increasing the mixing effectiveness, thus reducing the residence time*

To improve the throughput of bombs production rate, different geometrical configurations of mixing tank were generated with a view to assessing their performance with respect to a set of assessment criteria. The assessment criteria included qualitative and quantitative analysis, namely:

Qualitative analysis

1. Having sufficient axial flow to lift particles from the tank bottom
2. Having flow moving in the right focused direction
3. Having sufficient level of turbulence kinetic energy

Quantitative analysis

1. Having the highest axial flow
2. Having the highest global turbulence kinetic energy

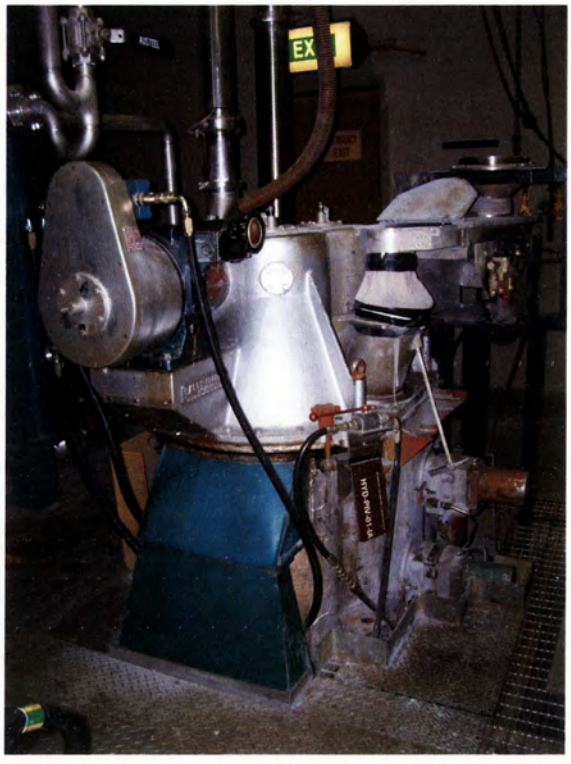


Figure 7.1: Bomb incorporator unit operation

Figure 7.1 shows the external casing of the bomb incorporator in which modelling and simulation was conducted.

Figure 7.2: Feeding the solidified RDX/TNT mixture

Figure 7.2 shows the RDX/TNT flakes being fed into the bomb incorporator along with aluminium particles and calcium chloride.

Figure 7.3: Bomb filling operation

Figure 7.3 shows the setup up of the plant to fill empty bomb shells with molten H6.

Figure 7.4: Manual topping-up of the bomb fill

Figure 7.4 shows an H6 manual filling of a bomb to ensure any cracks and crevices produced due to contraction during solidification, is fully covered. The presence of air in any cracks or crevices will make the bomb more sensitive thus increasing the risk of handling.

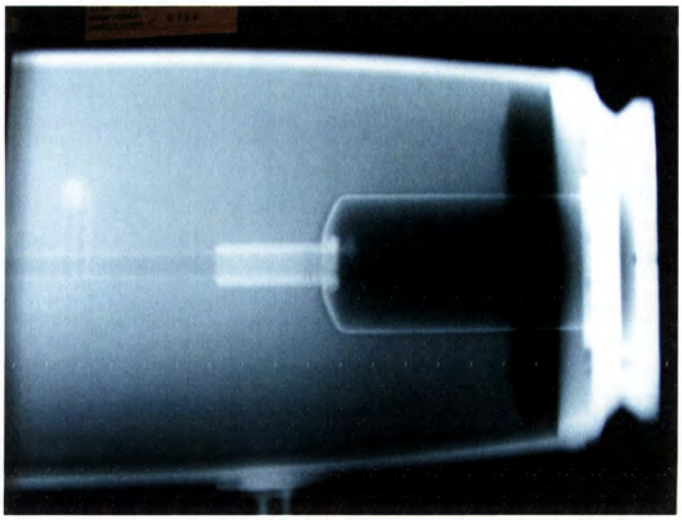

Figure 7.5: Quality control using X-ray to determine the presence of any cracks

Once the explosive mixture has fully solidified, the bombs are sent for x-ray to determine whether cracks or other undesirable features are present. Figure 7.5 present one of those x-ray photos taken. The presence of undesirable features is dependent on the rate of solidification which in turn depends on the homogeneity of the molten explosive mixtures. Obviously, the homogeneity of the molten explosive mixture depends on the performance and effectiveness of the bomb incorporator.

Figure 7.6: Finished products ready to be despatched for next line assembly

Bombs that do not have undesirable features will then be packed, as shown in Figure 7.6, and sent to the next stage where features such as fins to increase the drag coefficient will be fitted.

## 7.2 Numerical setup

The numerical setups involved in this part of the study were similar to those employed and elaborated in earlier sections. Hence, elaboration on the approaches were not provided but listed. Fluent® solver was used to create a numerical solution that matches the governing conservation equations. To simulate impeller rotations, separate rotational zones in the immediate vicinity of the impellers were created and a multiple reference frame (MRF) approach was employed. Fluent's default under-relaxation values were used in all simulation runs. In this simulation, the segregated-implicit approach was adopted. All simulations were started using the first-order upwind scheme and upon convergence of the results, were switched to second-order upwind scheme or QUICK scheme in the case of the volume fraction.

PRESTO (pressure staggering option) was employed to compute the pressure value at the cell surface by interpolating the value at cell centroid. SIMPLE algorithm was used for the pressure-velocity coupling. VOF model was used to simulate the hydrodynamics of air draw-down while the Mixture and Eulerian models were used to capture the hydrodynamics of RDX particles to be suspended and aluminium particles to be drawn down. Simulations were generally considered converged when the residuals for mass, momentum and turbulence kinetic energy and its dissipation rate fell below $1\times10^{-4}$.

To model the multiphase phenomena associated with the suspension of RDX particles in the holding tank, an appropriate model must be selected from the models available in Euler-Lagrange or the Euler-Euler approach. The three different models available in the Euler-Euler approach include the VOF model, the mixture model and the Eulerian model. While the VOF model is more suitable for simulating phenomena such as the draw-down of air or water into the primary phase, the mixture and Eulerian models are suitable for simulating the suspension of particles in the primary phase. As a general guide, there are two parameters that assist in the identification of an appropriate multiphase model for those situations where the use of VOF model is inappropriate. The first is the particulate loading, denoted by $\beta$ and the second is the Stokes number, denoted by $St$.

Particulate loading has a major impact on phase interactions. The particulate loading is defined as the mass density ratio of the dispersed phase *d* to that of the carrier phase *c* and is given by:

$$\beta = \frac{\alpha_d \rho_d}{\alpha_c \rho_c} \qquad \text{- 7.1}$$

where

$\alpha_d$ : volumetric fraction of dispersed phase

$\alpha_c$ : volumetric fraction of carrier phase

$\rho_d$ : density of dispersed phase, kg $m^{-3}$

$\rho_c$ : density of carrier phase, kg $m^{-3}$

The material density ratio is defined as

$$\gamma = \frac{\rho_d}{\rho_c} \qquad \text{- 7.2}$$

where

$\gamma > 1000$ : gas-solid flows

$\gamma \sim 1$ : liquid-solid flows

$\gamma < 0.001$ : gas-liquid flows

Using these parameters, the average distance between the individual particles of the particulate phase can be estimated via Crowe et al. [1998] model and is given by:

$$\frac{L}{d_d} = \left( \frac{\pi + k}{6k} \right)^{1/3} \qquad \text{- 7.3}$$

where

$$k = \frac{\beta}{\gamma} \qquad \text{- 7.4}$$

Depending on the particulate loading, the degree of interaction between the phases can be divided into three categories:

*Low loading* (solids volume fraction, $\alpha_d \leq 10\%$) – the coupling between the phases is one-way. In this case, the fluid carrier influences the particles via drag and turbulence, but the particles have no influence on the fluid carrier. The discrete phase, mixture and Eulerian models can all handle this type of problem correctly. Since the Eulerian model is the most computationally expensive, the discrete phase or mixture model is preferable.

*Intermediate loading* (solids volume fraction, $\alpha_d \geq 10\%$) – the coupling is two-way. In this case, the fluid carrier influences the particulate phase via drag and turbulence, but the particles in turn influence the carrier fluid via reduction in mean momentum and turbulence. The discrete phase, mixture, and Eulerian models are all applicable here. The Stokes number can be used to distinguish the most suitable model to be used under such scenario.

*High loading* (solids volume fraction, $\alpha_d \geq 70\%$) – there is two-way coupling plus particle pressure and viscous stresses due to particles (four-way coupling). Only the Eulerian model will handle this type of problem correctly.

To shortlist the models that can be used in this modelling work involving H6 which consists of the suspension of RDX particles and aluminium particles in molten TNT,

$\rho_d$ : 1,770 kg $m^{-3}$ (bulk density of RDX particles)

$\alpha_d$ : 0.4018 (volume fraction of RDX particles)

$\rho_c$ : 1,740 kg $m^{-3}$ (density of molten H6)

$\alpha_c$ : 0.5982 (volume fraction of aluminium particles and molten TNT)

$\beta(90°C) = 0.6833$ $\gamma(90°C) = 1.017$ $k = 0.6717$

$\frac{L}{d_d}$(RDX - molten H6 at 90°C) = 0.9818

Since the inter-particle distant of RDX particles is only slightly less than the diameter of the RDX particles, this system can still be considered as intermediate loading.

$\rho_d$ : 1,250 kg $m^{-3}$ (bulk density of aluminium particles)

$\alpha_d$ : 0.2713 (volume fraction of aluminium particles)

$\rho_c$ : 1,740 kg $m^{-3}$ (density of molten H6)

$\alpha_c$ : 0.7287 (volume fraction of RDX particles and molten TNT)

$\beta(90°C) = 0.2675$ $\gamma(90°C) = 0.7184$ $k = 0.3724$

$\frac{L}{d_d}$(aluminium – molten H6 at 90°C) = 1.163

Since the inter-particle distant of the aluminium particles was larger than the diameter of the aluminium particles, this system was considered as intermediate loading. To select either the simplified mixture model or the Eulerian model, the Stokes number must be determined.

The Stokes number can be defined as the relation between the particles response time and the system response time:

$$St = \frac{\tau_d}{t_s} \qquad -7.5$$

where

$$\tau_d = \frac{\rho_d d_d^2}{18\mu_c} \qquad -7.6$$

$$t_s = \frac{L_s}{V_s} \qquad -7.7$$

$\rho_d$ : density of secondary phase (kg $m^{-3}$)

$d_d^2$ : diameter of secondary phase (m)

$\mu_c$ : absolute viscosity of primary phase (Pa.s or kg $m^{-1}s^{-1}$)

$L_s$ : characteristic length (m) of the system of interest

$V_s$ : characteristic velocity (m $s^{-1}$) of the system of interest

For Stokes number < 1, the particle under investigation will follow the flow closely and any of the three models (discrete phase from Euler-Lagrange, mixture and Eulerian from Euler-Euler) is applicable and the least expensive model, which is the mixture model in most cases, or the most appropriate model considering other factors, can be used. For $St >$ 1, the particles will move independently of the flow and either the discrete phase model or the Eulerian model is applicable. For $St \sim 1$, again any of the three models is applicable, the least expensive or the most appropriate model considering other factors can be used.

In this modelling work, at 90°C:

$\rho_d$ : 1,770 kg $m^{-3}$ (bulk density of RDX particles)

$d_d^2$ : 0.00024 m (median diameter of RDX particles)

$\mu_c$ : 0.00972 Pa.s or kg $m^{-1}s^{-1}$ (viscosity of TNT at 90°C)

$L_s$ : 0.6 m (diameter of mixing tank)

$V_s$ : 0.87340 m $s^{-1}$ at 100 rpm (volume-weighted average)

$\rho_d$ : 1,250 kg $m^{-3}$ (bulk density of aluminium particles)

$d_d^2$ : 0.000075 m (median diameter of aluminium particles)

$\mu_c$ : 0.00972 Pa.s or kg $m^{-1}s^{-1}$ (viscosity of TNT at 90°C)

$L_s$ : 0.6 m (diameter of mixing tank)

$V_s$ : 0.87340 m $s^{-1}$ at 100 rpm (volume-weighted average)

From the Stokes number equation:

$St_{RDX}$ (100 rpm) = 0.00084

$St_{Al}$ (100 rpm) = 0.00004

Clearly, the mixture model was applicable in this modelling work. The mixture model was a simplified Eulerian approach for modelling n-phase flows. This model used a single-fluid approach and it allowed phases to be interpenetrating. In addition, the model allowed phases to move at different velocities, using the concept of slip velocities. However, to assess the qualitative and quantitative differences between the mixture model and the full Eulerian multiphase model, a few simulations were repeated using the Eulerian model.

## 7.3 Eulerian multiphase model for fluid-solid system

Several parameters having paramount importance which were employed when using the full Eulerian multiphase model were discussed. These parameters were:

- Fluid-solid momentum equation
- Fluid-solid exchange coefficient
- Solid-solid exchange coefficient
- Radial distribution function
- Maximum packing limit in binary mixtures
- Solids shear stresses
- Solids pressure
- Granular temperature

From the work of Alder and Wainwright [1960]; Chapman and Cowling [1990]; Ding and Gidaspow [1990]; Gidaspow et al. [1992]; Lebowitz [1964]; Lun et al. [1984]; Ogawa et al. [1980] and Syamlal et al. [1993], Fluent® uses a multi-fluid granular model to describe the flow behaviour of a fluid-solid mixture. The solid-phase stresses were derived by making an analogy between the random particle motion arising from particle-particle collision and the thermal motion of the molecules in a gas, taking into account the inelasticity of the granular phase. As is the case for a gas, the intensity of the particle velocity fluctuations determines the stresses, viscosity, and pressure of the solid phase. The kinetic energy associated with the particle velocity fluctuations is represented by a 'pseudothermal' or granular temperature which is proportional to the mean square of the random motion of the particles.

### 7.3.1 Fluid-solid momentum equation

The conservation of momentum for the fluid phases for $s^{th}$ solid phase is given by:

$$\frac{\partial}{\partial t}(\alpha_s \rho_s \vec{\upsilon}_s) + \nabla \cdot (\alpha_s \rho_s \vec{\upsilon}_s \vec{\upsilon}_s) = -\alpha_s \nabla p - \nabla p_s + \nabla \cdot \overline{\overline{\tau}}_s + \alpha_s \rho_s \vec{g} + \sum_{l=1}^{N} \left( K_{ls}(\vec{\upsilon}_l - \vec{\upsilon}_s) + \dot{m}_{ls}\vec{\upsilon}_{ls} - \dot{m}_{sl}\vec{\upsilon}_{qsl} \right) + \left( \vec{F}_s + \vec{F}_{lift,s} + \vec{F}_{vm,s} \right) \quad \text{- 7.8}$$

where

$p_s$ : $s^{th}$ solids pressure

$K_{ls}=K_{sl}$ : momentum exchange coefficient

$N$ : to number of phases

### 7.3.2 Fluid-solid exchange coefficient

The fluid-solid exchange coefficient $K_{sl}$ can be written in the following general form:

$$K_{sl} = \frac{\alpha_s \rho_s f}{\tau_s} \quad \text{- 7.9}$$

where the term $f$ is defined differently for various exchange-coefficient models and $\tau_s$ being the 'particulate relaxation time' is defined as,

$$\tau_s = \frac{\rho_s d_s^2}{18\mu_l} \quad \text{- 7.10}$$

where $d_s$ is the diameter of particles of phase $s$. All definitions of $f$ include a drag function $C_D$ that is based on the relative Reynolds number $Re_s$. It is this drag function that differs among the various exchange-coefficient models. There are currently three $C_D$ models available, namely: Syamlal-O'Brien [1989], Wen and Yu [1966], Gidaspow [1992].

$$f = \frac{C_D \mathrm{Re}_s \alpha_l}{24 \upsilon_{r,s}^2} \qquad \text{- 7.11}$$

For the model proposed by Syamlal-O'Brien [1989], the drag function has the form:

$$C_D = \left( 0.63 + \frac{4.8}{\sqrt{\mathrm{Re}_s / \upsilon_{r,s}}} \right)^2 \qquad \text{- 7.12}$$

This model is based on measurements of the terminal velocities of particles in fluidised or settling beds, with correlations that are a function of the volume fraction and relative Reynolds number given by:

$$\mathrm{Re}_s = \frac{\rho_l d_s \left| \vec{\upsilon}_s - \vec{\upsilon}_l \right|}{\mu_l} \qquad \text{- 7.13}$$

where the subscript $l$ is for the $l^{th}$ fluid phase, $s$ is for the $s^{th}$ solid phase, and $d_s$ is the diameter of the $s^{th}$ solid phase particles.

$$K_{sl} = \frac{3 \alpha_s \alpha_l \rho_l}{4 \upsilon_{r,s}^2 d_s} C_D \left( \frac{\mathrm{Re}_s}{\upsilon_{r,s}} \right) \left| \vec{\upsilon}_s - \vec{\upsilon}_l \right| \qquad \text{- 7.14}$$

where $\upsilon_{r,s}$ is the terminal velocity correlation for the solid phase and is given by:

$$\upsilon_{r,s} = 0.5 \left( A - 0.06 \mathrm{Re}_s + \sqrt{(0.06 \mathrm{Re}_s)^2 + 0.12 \mathrm{Re}_s (2B - A) + A^2} \right) \qquad \text{- 7.15}$$

with

$$A = \alpha_l^{4.14}, \; B = 0.8 \alpha_l^{1.28} \text{ (for } \alpha_l \leq 0.85) \text{ and } B = \alpha_l^{2.65} \text{ (for } \alpha_l \geq 0.85)$$

This model is suitable when the solids shear stresses are defined according to Syamlal et al. [1993].

For the model proposed by Wen and Yu [1966], the fluid-solid exchange coefficient has the following form:

$$K_{sl} = \frac{3}{4} C_D \frac{\alpha_s \alpha_l \rho_l |\vec{v}_s - \vec{v}_l|}{d_s} \alpha_l^{-2.65} \quad \text{- 7.16}$$

where

$$C_D = \frac{24}{\alpha_l \mathrm{Re}_s} \left[1 + 0.15(\alpha_l \mathrm{Re}_s)^{0.687}\right] \quad \text{- 7.17}$$

This model is suitable for dilute systems.

For the model proposed by Gidaspow [1992], which is the combination of the Wen and Yu [1966] and Ergun [1952] models, the fluid-solid exchange coefficient has the following form:

For $\alpha_l \geq 0.8$, the fluid-solid exchange coefficient has the following form:

$$K_{sl} = \frac{3}{4} C_D \frac{\alpha_s \alpha_l \rho_l |\vec{v}_s - \vec{v}_l|}{d_s} \alpha_l^{-2.65} \quad \text{- 7.18}$$

where

$$C_D = \frac{24}{\alpha_l \mathrm{Re}_s} \left[1 + 0.15(\alpha_l \mathrm{Re}_s)^{0.687}\right] \quad \text{- 7.19}$$

Whereas for $\alpha_l \leq 0.8$, the fluid-solid exchange coefficient has the following form:

$$K_{sl} = 150 \frac{\alpha_s (1 - \alpha_l) \mu_l}{\alpha_l d_s^2} + 1.75 \frac{\rho_l \alpha_s |\vec{v}_s - \vec{v}_l|}{d_s} \quad \text{- 7.20}$$

This model is recommended for dense fluidised bed.

The mixing process taking place inside the bomb incorporator resembles that of settling bed where if the impellers were stopped, the RDX particles will sink to the tank bottom. As such, the fluid-solid exchange coefficient selected was Syamlal-O'Brien [1989].

### 7.3.3 Solid-solid exchange coefficient

The solid-solid exchange coefficient proposed by Syamlal-O'Brien [1989] has the following form:

$$K_{ls} = \frac{3(1+e_{ls})\left(\frac{\pi}{2} + C_{fr,ls}\frac{\pi^2}{8}\right)\alpha_s\rho_s\alpha_l\rho_l(d_l+d_s)^2 g_{0,ls}}{2\pi(\rho_l d_l^3 + \rho_s d_s^3)}\left|\vec{\upsilon}_l - \vec{\upsilon}_s\right| \qquad \text{- 7.21}$$

$e_{ls}$ : coefficient of restitution

$C_{fr,ls}$ : coefficient of friction between the $l^{th}$ and $s^{th}$ solid-phase particles ($C_{fr,ls} = 0$)

$d_l$ : diameter of the particles of solid $l$

$g_{0,ls}$ : radial distribution of coefficient

Since there was more than one solid phase being mixed inside the bomb incorporator, there was inter-particles interaction where the RDX particles would have collided and interacted with the aluminium particles. As such the Syamlal-O'Brien [1989] expression was used to account for this inter-particles interaction phenomenon.

### 7.3.4 Radial distribution function

The radial distribution function is a correction factor that modifies the probability of collisions between grains when the solid granular phase becomes dense. This function may also be interpreted as the non-dimensional distance between spheres:

$$g_0 = \frac{s + d_p}{s} \qquad \text{- 7.22}$$

where $s$ is the distance between grains. From the above equation, it can be seen that for a dilute solid phase, as $s \to \infty$, $g_0 \to 1$. In the limit when the solid phase compacts, as $s \to 0$, $g_0 \to \infty$. The radial distribution function is closely connected to the factor $\chi$ of Chapman and Cowling [1990] theory of non-uniform gases. $\chi$ is equal to 1 for a rare gas, increases and tends to approach infinity when the molecules are so close together that motion is not possible.

For a single solids phase, Ogawa et al. [1980] proposes that:

$$g_0 = \left[1 - \left(\frac{\alpha_s}{\alpha_{s,\max}}\right)^{1/3}\right]^{-1} \quad \text{- 7.23}$$

This is an empirical function and does not extend easily to $n$ phases. For two identical phases with the property that $\alpha_q = \alpha_1 + \alpha_2$, the above function is not consistent for the calculation of the partial pressures $p_1$ and $p_2$, $p_q = p_1 + p_2$. To correct this problem, Fluent® uses the following consistent formulation:

$$g_{0,ll} = \left[1 - \left(\frac{\alpha_s}{\alpha_{s,\max}}\right)^{1/3}\right]^{-1} + \frac{1}{2} d_l \sum_{k=1}^{N} \frac{\alpha_k}{d_k} \quad \text{- 7.24}$$

where

$$\alpha_s = \sum_{k=1}^{N} \alpha_k \quad \text{- 7.25}$$

and $k$ are solids phases only.

The following radial distribution expressions are also available:

Ibdir and Arastoopour [2005]:

$$g_{0,ll} = \frac{1}{\left(1 - \frac{\alpha_s}{\alpha_{s,\max}}\right)} + \frac{3}{2} d_l \sum_{k=1}^{N} \frac{\alpha_k}{d_k} \quad \text{- 7.26}$$

Ma and Ahmadi [1990]:

$$g_{0,ll} = \frac{1 + 2.5\alpha_s + 4.59\alpha_s^2 + 4.52_s^3}{\left(1 - \frac{\alpha_s}{\alpha_{s,\max}}\right)^{0.678}} + \frac{1}{2} d_l \sum_{k=1}^{N} \frac{\alpha_k}{d_k} \quad \text{- 7.27}$$

Syamlal et al. [1993]:

$$g_{0,kl} = \frac{1}{(1-\alpha_s)} + \frac{3\sum_{k=1}^{N}\frac{\alpha_k}{d_k}}{(1-\alpha_s)^2(d_j+d_k)} d_k d_l \qquad \text{- 7.28}$$

when the number of solid phases > 1, equations proposed by Ogawa et al. [1980], Ibdir and Arastoopour [2005]; and Ma and Ahmadi [1990] are extended to:

$$g_{0,lm} = \frac{d_m g_{0,ll} + d_l g_{0,mm}}{d_m + d_l} \qquad \text{- 7.29}$$

### 7.3.5 Maximum packing limit in binary mixtures

The packing limit is not a fixed quantity and may change according to the number of particles present within a given volume and the diameter of the particles. Small particles may accumulate in between larger particles thereby increasing the packing limit. For a binary mixture with diameters $d_1 > d_2$, the mixture composition is defined as

$$X_1 = \frac{\alpha_1}{\alpha_1 + \alpha_2} \qquad \text{- 7.30}$$

where

$$X_1 = \frac{\alpha_{1,\max}}{\left(\alpha_{1,\max} + \left(1-\alpha_{1,\max}\right)\alpha_{2,\max}\right)} \qquad \text{- 7.31}$$

The maximum packing limit for the mixture is given by:

$$\alpha_{s,\max} = \left(\alpha_{1,\max} - \alpha_{2,\max} + \left(1-\sqrt{\frac{d_2}{d_1}}\right)\left(1-\alpha_{1,\max}\right)\alpha_{2,\max}\right) \times \left(\alpha_{1,\max} + \left(1-\alpha_{1,\max}\right)\alpha_{2,\max}\right)\frac{X_1}{\alpha_{1,\max}} + \alpha_{2,\max} \qquad \text{- 7.32}$$

otherwise, the maximum packing limit for the binary mixture is given by:

$$\left(1-\sqrt{\frac{d_2}{d_1}}\right)\left(\alpha_{1,\max}+\left(1-\alpha_{1,\max}\right)\alpha_{2,\max}\right)\left(1-X_1\right)+\alpha_{1,\max} \qquad \text{- 7.33}$$

The packing limit is used for the calculation of the radial distribution function.

### 7.3.6 Solids shear stresses

The solids stress tensor contains shear and bulk viscosities arising from particle momentum exchange due to translation and collision. A frictional component of viscosity can also be included to account for the viscous-plastic transition that occurs when particles of a solid phase reach the maximum solid volume fraction. The collisional, kinetic parts and the optional frictional part are added to give the solids shear viscosity.

$$\mu_s = \mu_{s,collision} + \mu_{s,kinetic} + \mu_{s,friction} \qquad \text{- 7.34}$$

*Collisional viscosity* – the collisional part of the shear viscosity is modelled as Gidaspow [1992] and Syamlal et al. [1993] and is given by:

$$\mu_{s,collision} = \frac{4}{5}\alpha_s\rho_s d_s g_{0,ss}\left(1+e_{ss}\right)\left(\frac{\Theta_s}{\pi}\right)^{1/2} \qquad \text{- 7.35}$$

*Kinetic viscosity* – two expressions for the kinetic part are provided by Fluent® where the default expression is from Syamlal et al. [1993] and is given by:

$$\mu_{s,kinetic} = \frac{\alpha_s d_s \rho_s \sqrt{\Theta_s \pi}}{6\left(3-e_{ss}\right)}\left[1+\frac{2}{5}\left(1+e_{ss}\right)\left(3e_{ss}-1\right)\alpha_s g_{0,ss}\right] \qquad \text{- 7.36}$$

Expression from Gidaspow [1992] is given by:

$$\mu_{s,kinetic} = \frac{10\rho_s d_s \sqrt{\Theta_s \pi}}{96\alpha_s (1+e_{ss}) g_{0,ss}} \left[1 + \frac{4}{5} g_{0,ss} \alpha_s (1+e_{ss})\right]^2 \quad \text{- 7.37}$$

*Frictional viscosity* – in dense flow at low shear where the secondary volume fraction for a solid phase approximates the packing limit, the generation of stress is mainly due to friction between particles. The solids shear viscosity computed by Fluent®, by default, does not take into account the inter-particles friction. If the frictional viscosity is included in the calculation, Fluent® uses Schaeffer [1987] expression, which is given by:

$$\mu_{s,friction} = \frac{p_s \sin\phi}{2\sqrt{I_{2D}}} \quad \text{- 7.38}$$

where

$p_s$ : solids pressure

$\phi$ : angle of internal friction

$I_{2D}$ : second invariant of the deviatoric stress tensor

It is also possible to specify a constant or user-defined frictional viscosity.

*Bulk viscosity* – the solids bulk viscosity accounts for the resistance of the granular particles to compression and expansion. The granular bulk viscosity has the following form from Lun et al. [1984] and is given by:

$$\lambda_s = \frac{4}{3}\alpha_s \rho_s d_s g_{0,ss} (1+e_{ss}) \left(\frac{\Theta_s}{\pi}\right)^{1/2} \quad \text{- 7.39}$$

By default, the bulk viscosity is set to a constant value of zero but it is possible to select the Lue et al. [1984] expression or to use the user-defined granular bulk viscosity formulation.

### 7.3.7 Solids pressure

For granular flows in the compressible regime where the solids volume fraction is less than its maximum allowed value, a solids pressure is calculated independently and used for the pressure gradient term, $\nabla p_s$, in the granular-phase momentum equation. Due to a Maxwellian velocity distribution being used for the particles, a granular temperature is introduced into the model, and appears in the expression for the solids pressure and viscosities. The solids pressure is composed of a kinetic term and a second term due to particles collisions:

$$p_s = \alpha_s \rho_s \Theta_s + 2\rho_s (1+e_{ss}) \alpha_s^2 g_{0,ss} \Theta_s \qquad \text{- 7.40}$$

$e_{ss}$ : coefficient of restitution for particle collisions

$g_{0,ss}$ : radial distribution function

$\Theta_s$ : granular temperature

Fluent® uses a default value of 0.9 for $e_{ss}$ but this value can be adjusted to suit the particle type. The granular temperature $\Theta_s$ is proportional to the kinetic energy of the fluctuating particle motion. The function $g_{0,ss}$ is a distribution function that governs the transition from the 'compressible' condition with $\alpha < \alpha_{s,max}$ where the spacing between the solid particles can continue to decrease, to the 'incompressible' condition with $\alpha = \alpha_{s,max}$ where no further reduction in the spacing can occur. Although a value of 0.63 is the default setting for $\alpha_{s,max}$ in the Fluent® solver, this value can be adjusted to reflect the system to be modelled. Other expressions that are available include those proposed by Syamlal et al. [1993]; Ma and Ahmadi [1990]; Gidaspow [1994].

For Syamlal et al. [1993],

$$p_s = 2\rho_s (1+e_{ss}) \alpha_s^2 g_{0,ss} \Theta_s \qquad \text{- 7.41}$$

For Ma and Ahmadi [1990],

$$p_s = \alpha_s \rho_s \Theta_s + 4\rho_s \alpha_s^2 g_{0,ss} \Theta_s + \frac{1}{2}\left[(1+e_{ss})(1-e_{ss}+2\mu_{friction})\right] \quad - 7.42$$

When more than one solids phase are calculated, the above expression does not take into account the effect of other phases. As such, there is a need to provide a better formulation so that some properties may feel the presence of other phases. A known problem is that $N$ solids phases with identical properties should be consistent when the same phases are described by a single solids phase. Equations derived empirically may not satisfy this property and need to be changed accordingly without deviating significantly from the original form. From Gidaspow [1994], a general solids pressure formulation in the presence of other phases is expressed as:

$$p_q = \alpha_q \rho_q \Theta_q + \sum_{p=1}^{N} \frac{\pi}{3} g_{0,pq} d_{qp}^3 n_q n_p (1+e_{qp}) f(m_p, m_q, \Theta_p \Theta_q) \quad - 7.43$$

where

$d_{pq} = \dfrac{d_p + d_q}{2}$ : average diameter

$n_p, n_q$ : number of particles

$m_p, m_q$ : masses of the particles in phases p and q

$f$ : function of the particles masses and their granular temperatures

$$p_q = \alpha_q \rho_q \Theta_q + \sum_{p=1}^{N} 2\frac{d_{pq}^3}{d_q^3} n_q n_p (1+e_{qp}) g_{0,pq} \alpha_q \alpha_p \rho_q \Theta_q \quad - 7.44$$

Since all the models need to be expressed in the general form, it follows that

$$p_q = \alpha_q \rho_q \Theta_q + \left( \sum_{p=1}^{N} \frac{d_{pq}^3}{d_q^3} p_{c,qp} \right) \rho_q \Theta_q \quad - 7.45$$

where $p_{c,qp}$ is the collisional part of the pressure between phases $q$ and $p$. The above equations reverts to the one solids phase expression when $N = 1$ and $q = p$ but also has the

property of feeling the presence of other phases. Apart from the Syamlal et al. [1993] and the Ma and Ahmadi [1990] models, a user-defined solids pressure can also be specified.

### 7.3.8 Granular temperature

The granular temperature for the $s^{th}$ solids phase is proportional to the kinetic energy of the random motion of the particles. The transport equation proposed by Syamlal et al. [1993] that represents the algebraic model set as default model in Fluent®, was obtained by neglecting convection and diffusion in the transport equation from the Ding and Gidaspow [1990] kinetic theory:

$$\frac{3}{2}\left[\frac{\partial}{\partial t}(\rho_s \alpha_s \Theta_s)+\nabla\cdot(\rho_s \alpha_s \vec{v}_s \Theta_s)\right]=\left(-p_s\bar{\bar{I}}+\bar{\bar{\tau}}_s\right):\nabla\vec{v}_s+\nabla\cdot(k_{\Theta_s}\nabla\Theta_s)-\gamma_{\Theta_s}+\phi_{ls} \qquad \text{- 7.46}$$

where

$\left(-p_s\bar{\bar{I}}+\bar{\bar{\tau}}_s\right):\nabla\vec{v}_s$ : generation of energy by the solid stress tensor

$k_{\Theta_s}\nabla\Theta_s$ : diffusion of energy ( $k_{\Theta_s}$ is the diffusion coefficient)

$\gamma_{\Theta_s}$ : collisional dissipation energy

$\phi_{ls}$ : energy exchange between the $l^{th}$ fluid or solid phase and the $s^{th}$ solid phase

As the above equation contains the term $k_{\Theta_s}\nabla\Theta_s$ describing the diffusive flux of granular energy, when Syamlal et al. [1993] model is used, the diffusion coefficient for granular energy, $k_{\Theta_s}$, is given by:

$$k_{\Theta_s}=\frac{15 d_s \rho_s \alpha_s \sqrt{\Theta_s \pi}}{4(41-33\eta)}\left[1+\frac{12}{5}\eta^2(4\eta-3)\alpha_s g_{0,ss}+\frac{16}{15\pi}(41-33\eta)\eta\alpha_s g_{0,ss}\right] \qquad \text{- 7.47}$$

where

$$\eta=\frac{1}{2}(1+e_{ss}) \qquad \text{- 7.48}$$

If the optional Gidaspow et al. [1992] model is activated, the granular energy is given by:

$$k_{\Theta_s} = \frac{150\rho_s d_s\sqrt{\Theta\pi}}{384(1+e_{ss})g_{0,ss}}\left[1+\frac{6}{5}\alpha_s g_{0,ss}(1+e_{ss})\right]^2 + 2\rho_s\alpha_s^2 d_s(1+e_{ss})g_{0,ss}\sqrt{\frac{\Theta_s}{\pi}} \quad \text{- 7.49}$$

The collisional dissipation of energy, $\gamma_{\Theta_s}$, represents the rate of energy dissipation within the $s^{th}$ solids phase due to collision between particles. This term is represented by the expression derived by Lun et al. [1984] and is given by:

$$\gamma_{\Theta m} = \frac{12(1-e_{ss}^2)g_{0,ss}}{d_s\sqrt{\pi}}\rho_s\alpha_s^2\Theta_s^{3/2} \quad \text{- 7.50}$$

The transfer of the kinetic energy of random fluctuations in particle velocity from the $s^{th}$ solids phase to the $l^{th}$ fluid or solid phase is represented by $\phi_{ls}$ and is given by the Ding and Gidaspow [1990]:

$$\phi_{ls} = -3K_{ls}\Theta_s \quad \text{- 7.51}$$

Apart from the algebraic model, constant granular temperature is also available, which is useful in very dense situations where the random fluctuations are small. In addition, the partial differential equation based on the original equation proposed by the Ding and Gidaspow [1990] kinetic theory is available where choosing different options for its properties is allowed. The user-defined function is also allowed for the granular temperature.

For granular phase $s$, the shear force at the wall can be written as:

$$\vec{\tau}_s = -\frac{\pi}{6}\sqrt{3\phi}\frac{\alpha_s}{\alpha_{s,\max}}\rho_s g_0 \sqrt{\Theta_s \vec{U}_{s,\parallel}} \qquad \text{- 7.52}$$

$\vec{U}_{s,\parallel}$ : particle slip velocity parallel to the wall

$\phi$ : specularity coefficient between the particle and the wall

$\alpha_{s,\max}$ : volume fraction for the particles at maximum packing

$g_0$ : radial distribution function that depends on the model used

The general boundary condition for granular temperature at the wall according to Johnson and Jackson [1987] takes the form:

$$q_s = \frac{\pi}{6}\sqrt{3\phi}\frac{\alpha_s}{\alpha_{s,\max}}\rho_s g_0 \sqrt{\Theta_s \vec{U}_{s,\parallel}} \cdot \vec{U}_{s,\parallel} - \frac{\pi}{4}\sqrt{3}\frac{\alpha_s}{\alpha_{s,\max}}\left(1-e_{sw}^2\right)\rho_s g_0 \Theta_s^{3/2} \qquad \text{- 7.53}$$

### 7.3.9 Summary of drag function options

When the full Eulerian multiphase model is selected, the drag functions available are:

*Schiller-Naumann* – this is the default method and is acceptable for general use in all fluid-fluid multiphase calculations

*Morsi-Alexander* – this is the most complete, adjusting the function definition frequently over a large range of Reynolds numbers, but calculations with this model may be less stable than with the other models

*Symmetric* – this is recommended for flows in which the secondary (dispersed) phase in one region of the domain becomes the primary (continuous) phase in another. For example, if air is injected into the bottom of a container filled halfway with water, then the air which is originally the dispersed phase at the bottom half of the container becomes the continuous phase when it reaches the top half of the container

*Wen and Yu* – this is applicable for dilute phase flows, in which the total secondary phase volume fraction is significantly lower than that of the primary phase

*Gidaspow* – this is recommended for dense fluidised beds

*Syamlal-O'Brien* – this is recommended for use in conjunction with the Syamlal-O'Brien model for granular viscosity

*Syamlal-O'Brien-symmetric* – this is recommended for a pair of solid phases

### 7.3.10 Multiphase turbulence modelling

Three methods for modelling turbulence in multiphase flows within the context of the $k$-$\varepsilon$ models and two turbulence options within the context of the Reynolds stress models (RSM).

The three $k$-$\varepsilon$ models available are:

- Mixture turbulence model
- Dispersed turbulence model
- Turbulence model for each phase

The RSM turbulence models available are:

- Mixture turbulence model
- Dispersed turbulence model

The mixture turbulence model is the default multiphase turbulence model and represents the first extension of the single-phase $k$-$\varepsilon$ models. It is applicable when phases separate for stratified multiphase flows and when the density ratio between phases is close to 1. In these cases, using mixture properties and mixture velocities is sufficient to capture important features of the turbulent flow. The dispersed turbulence model is the appropriate model when the concentrations of the secondary phases are dilute. In such cases, the interparticle collisions are negligible and the dominant process in the random motion of the secondary phases is the influence of the primary phase turbulence. Fluctuating quantities of the secondary phases can therefore be given in terms of the mean characteristics of the primary phase and the ratio of the particle relaxation time and eddy-particle interaction time. This model is applicable when there is clearly one primary continuous phase and the rest are dispersed dilute secondary phases. The most general multiphase turbulence model solves a set of $k$-$\varepsilon$ transport equations for each phase. This turbulence model is the appropriate choice when the turbulence transfer among the phases plays a dominant role. If this model is selected, Fluent® will be solving two additional transport equations for each secondary phase rendering this model more computationally intensive than the other models.

In this research work which models H6 inside the bomb incorporator, the mixture turbulence Eulerian model was selected because the density ratio between the phases was close to 1 considering that the ratio of molten TNT:aluminium = 1,455 kg $m^{-3}$/1,250 kg $m^{-3}$ = 1.164 while RDX:molten TNT = 1,770 kg $m^{-3}$ ÷ 1,455 kg $m^{-3}$ = 1.216

The $k$ and $\varepsilon$ equations describing this mixture turbulence model are as follows:

$$\frac{\partial}{\partial t}(\rho_m k)+\nabla\cdot(\rho_m \vec{\upsilon}_m k)=\nabla\cdot\left(\frac{\mu_{t,m}}{\sigma_k}\nabla k\right)+G_{k,m}-\rho_m\varepsilon \qquad \text{- 7.54}$$

and

$$\frac{\partial}{\partial t}(\rho_m k)+\nabla\cdot(\rho_m \vec{\upsilon}_m k)=\nabla\cdot\left(\frac{\mu_{t,m}}{\sigma_k}\nabla k\right)+C_{1\varepsilon}G_{k,m}-C_{2\varepsilon}\rho_m\varepsilon \qquad \text{- 7.55}$$

where the mixture density and velocity, $\rho_m$ and $\vec{\upsilon}_m$ are computed from:

$$\rho_m=\sum_{i=1}^{n}\alpha_i\rho_i \qquad \text{- 7.56}$$

and

$$\vec{\upsilon}_m=\frac{\sum_{i=1}^{n}\alpha_i\rho_i\vec{\upsilon}_i}{\sum_{i=1}^{n}\alpha_i\rho_i} \qquad \text{- 7.57}$$

the turbulent viscosity, $\mu_{t,m}$ is computed from:

$$\mu_{t,m}=\rho_m C_\mu\frac{k^2}{\varepsilon} \qquad \text{- 7.58}$$

and the production of turbulence kinetic energy, $G_{k,m}$ is computed from

$$G_{k,m}=\mu_{t,m}\left(\nabla\vec{\upsilon}_m+(\nabla\vec{\upsilon}_m)^T\right):\nabla\vec{\upsilon}_m \qquad \text{- 7.59}$$

The constants in these equations are the same as those present in the $k$-$\varepsilon$ model for single phase modelling.

## 7.4 Characterisation of existing H6 bomb incorporator

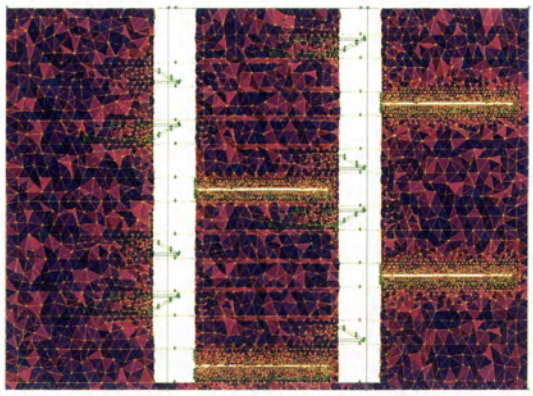

| | | | |
|---|---|---|---|
| Start size | : 5 | *T* (equivalent) | : 680mm |
| Growth rate | : 1.4 | *D/T* | : 0.94 |
| Size limit | : 25 | *W/D* | : 0.1172 |
| Equisize skew | : 0.86 | *C/T* | : 0.0738 |
| Total size | : 1,009,817 | *V/T* | : 0.2941 |

Figure 7.7: Existing geometrical configuration

Figure 7.7 shows the geometrical configuration of the existing geometrical configuration which consisted of two top-entry parallel shafts, each mounted with 6 blades distributed vertically. In the actual operation, half the length of the blade was facing upwards and the other half facing downwards. However, meshing such geometrical configuration gave rise to high Equisize skew value, therefore to prevent this from occurring, all the blades were built downward. It was felt that downward facing blades would perform better than mixed blades and therefore would give a good indication of what the performance of the existing geometrical configuration would be. Figure 7.7 also shows the large *D/T* ratio of this current design which is known to promote radial instead of axial flow. Each blade was assigned a rotating zone and from the meshed geometry shown, extra cells were assigned to region of high flow notably, inside the fluid zones.

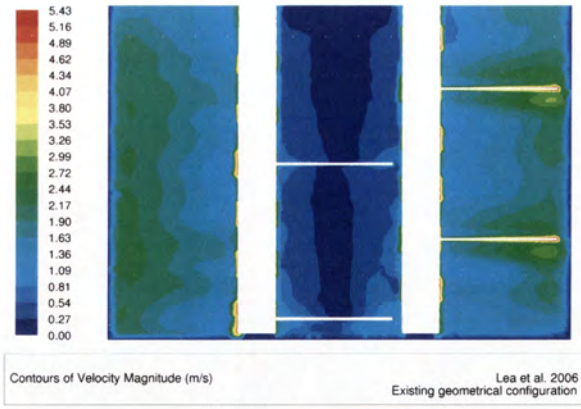


Figure 7.8: Velocity contours – side view

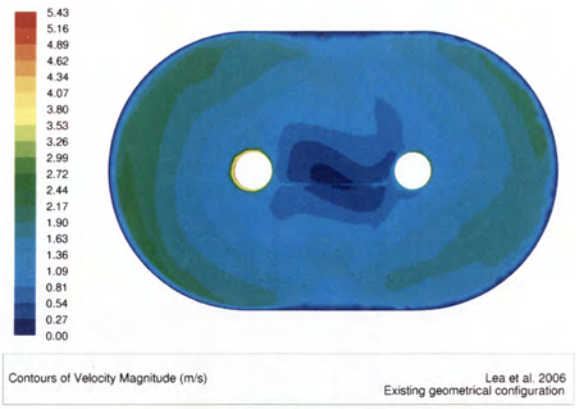


Figure 7.9: Velocity contours – top view

Figure 7.8 shows the velocity contours plot developed at 100 rpm by the existing geometrical configuration. It was seen that due to the nature of the impellers, most of the high velocity region occurred at the tank wall away from the middle of the tank. However, it must be noted that the flow was radially in nature and seriously lacked flow in axial direction. Figure 7.9 confirms that the region of high velocity was that confined to the wall region which was greatly aided by the large *D/T* nature of the impellers.

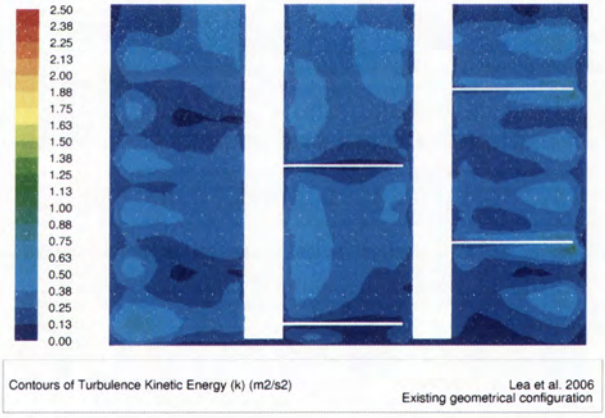


Figure 7.10: Turbulence KE contour plot – existing geometrical configuration

Figure 7.10 shows that there was no region of high turbulence, in fact, most of the turbulent regions were rather well distributed throughout the tank. This was attributed to the vertical distribution of the blades.

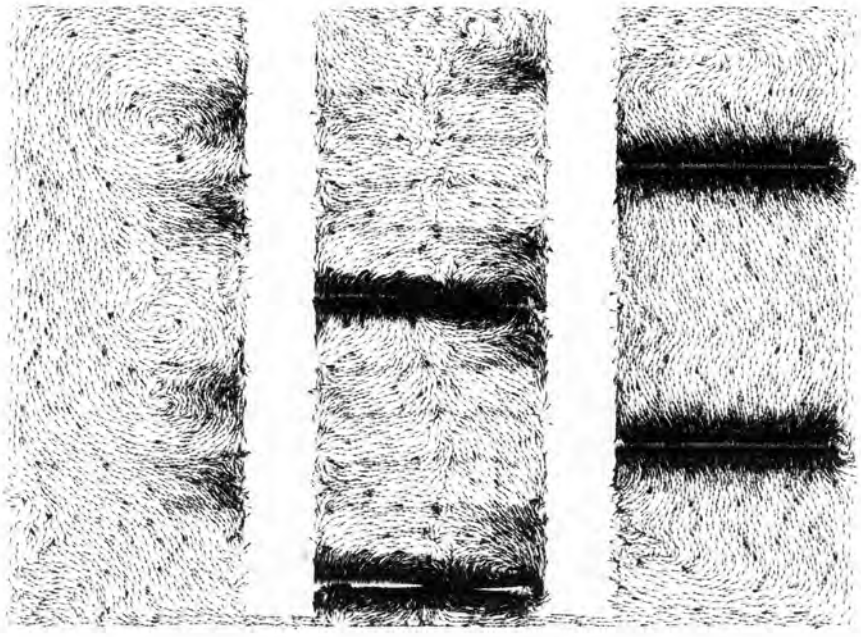

Figure 7.11: Vector plot of existing geometrical configuration – side view

Since the position of the right shaft was shifted upward, it was meaningless to discuss in detail its vector plot. As such, vector plot discussion will be limited to those on the left shaft. As shown in Figure 7.11, the flow consisted of multiple compartmentalisations and not much downward flow, either from the liquid free surface into the impellers or from the impellers directed towards the tank bottom, was seen in the vector plot shown in Figure 7.11. In addition, not much movement was located at the bottom left hand corner of the tank since majority of the flow simply bypassed this region.

The lack of axial flow seriously impeded the draw-down of floating particles or the suspension of denser particles.

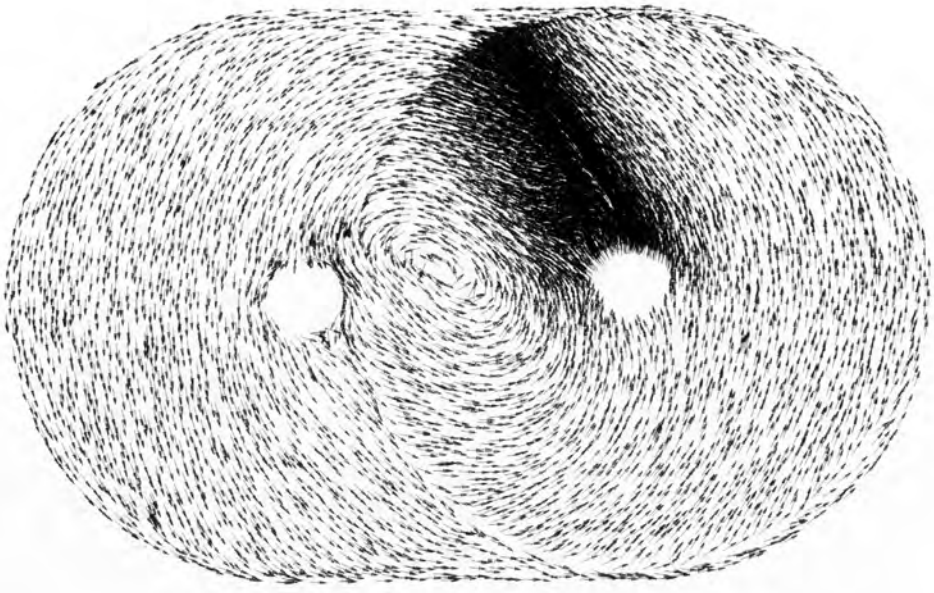

Figure 7.12: Vector plot of existing geometrical configuration – top view

Figure 7.12 shows that the vectors on the left shaft were moving in anti-clockwise direction while the vectors on the right shaft were moving in the clockwise position. No interruption to the rotational movement was observed except in the region between the two shafts.

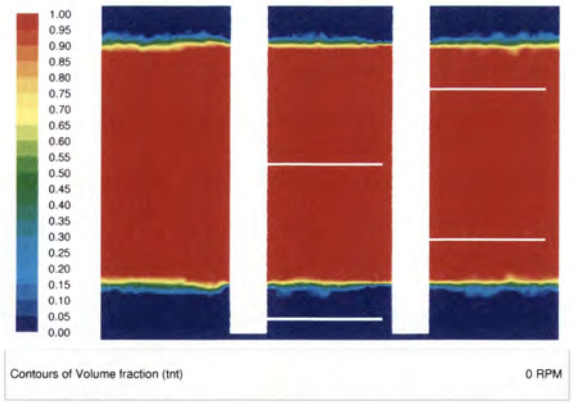


Figure 7.13: Volume fraction of molten TNT – 0 rpm

Figure 7.13 shows the contour plot of the molten TNT volume fraction. 100% aluminium particles were patched to the region bounded by y = 0.3093 to y = 0.4. In contrast, 100% RDX particles were patched to the region bounded by y = -0.4 to y = -0.2666. The remaining region was occupied by 100% molten TNT.

### 7.4.1 Suspension of RDX particles

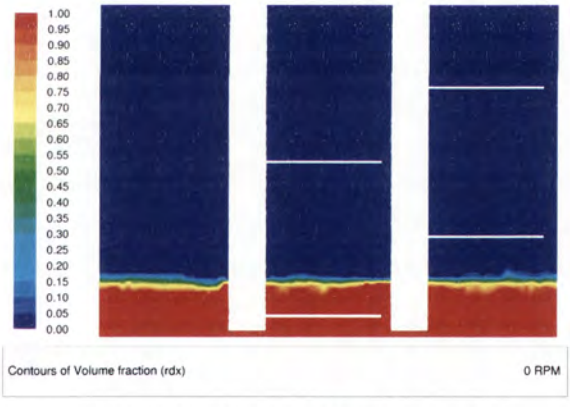


Figure 7.14: Volume fraction of RDX particles – 0 rpm

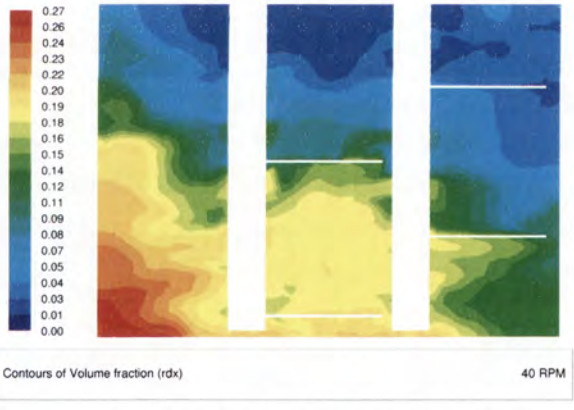


Figure 7.15: Volume fraction of RDX particles – 40 rpm

Figure 7.14 shows the contour map of RDX particles volume fraction when the impellers were at rest. As the rotational speed of the impellers reached 40 rpm, the RDX particles began to be suspended but as shown in Figure 7.15, the cloud height achieved was low and homogeneous suspension of RDX particles was not attained. A dead zone was seen at the side of the tank bottom. Since the height of the right impellers was increased to reduce the computational demand, the results produced by the left and right impellers were not identical. A dead zone should also be located at the right side of the tank bottom as well. This dead zone was attributed to the close clearance of the impellers to the tank bottom and

tank side. Consequently, instead of producing the required axial flow to sweep the particles from the tank bottom [Ochieng and Lewis 2006], the particles were swept radially towards the wall. This, coupled with the poor tank geometry for particles suspension, led to the generation of dead zones or regions of high RDX particles concentration.

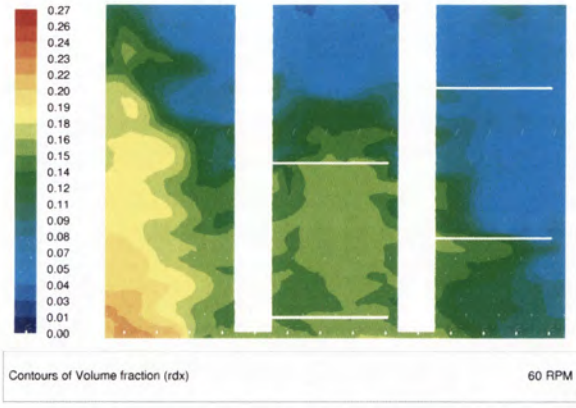


Figure 7.16: Volume fraction of RDX particles – 60 rpm

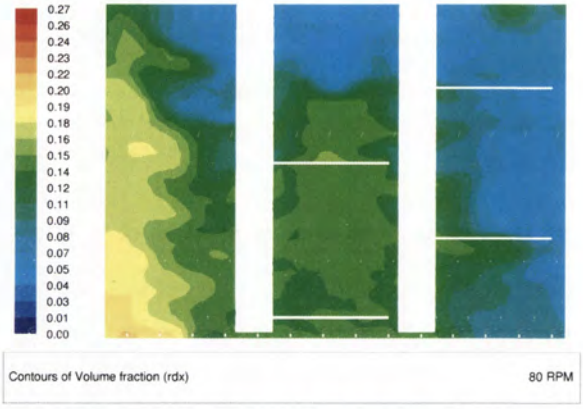


Figure 7.17: Volume fraction of RDX particles – 80 rpm

A 4% reduction in the concentration of the RDX particles at the bottom side of the tank was seen when the impellers rotational speed was increased to 60 rpm, as shown in Figure 7.16. Finally, another 4% reduction in the RDX particles concentration was achieved when the impellers rotational speed was increased to 80 rpm, as shown in Figure 7.17. The lack of process performance was an indication of the failure of this geometrical configuration to suspend the RDX particles homogeneously. This ineffectiveness was attributed to the lack of axial flow generated by the radial impellers.

### 7.4.2 Incorporation of aluminium particles

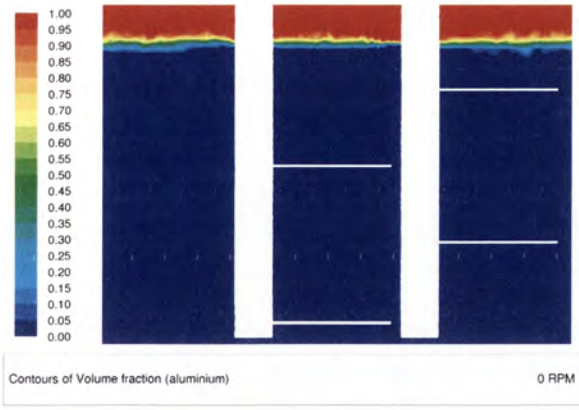


Figure 7.18: Volume fraction of aluminium particles – 0 rpm

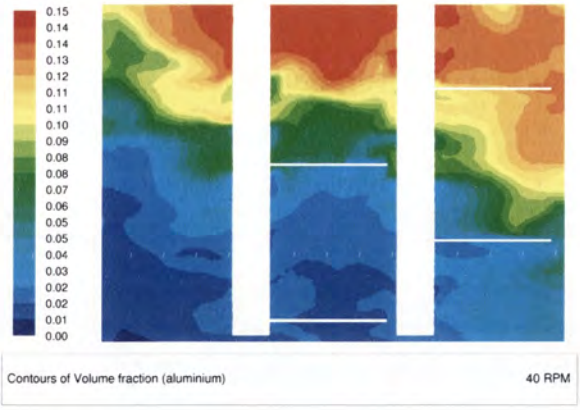


Figure 7.19: Volume fraction of aluminium particles – 40 rpm

Figure 7.18 shows an aluminium powder layer sitting above the molten RDX/TNT mixture. Figure 7.19 shows that a significant proportion of the aluminium particles were still floating when the impellers were rotating at 40 rpm. In addition, the amount of aluminium particles was inversely proportional to the depth of the incorporator. Similarly a dead zone was located at the left side of the tank bottom. In this region which was occupied by mostly TNT and RDX particles, very little aluminium particles was observed. This dead zone should also occur on the right side if it was not for the raised right impellers. The lack of the incorporator to draw-down the aluminium particles was attributed to the inability of the impellers to draw-down and discharge fluid axially. This evidently pointed to the ineffective draw-down of aluminium particles using this geometrical configuration when the impellers were rotating at 40 rpm.

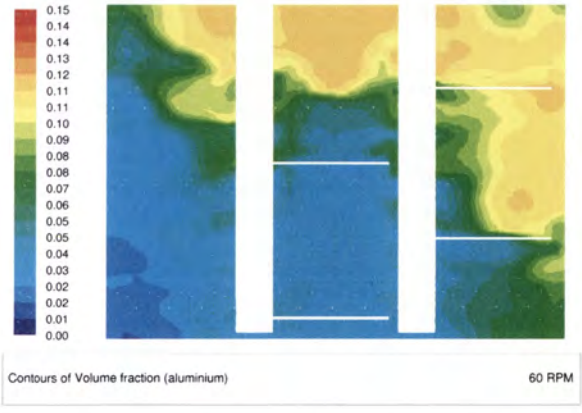


Figure 7.20: Volume fraction of aluminium particles – 60 rpm

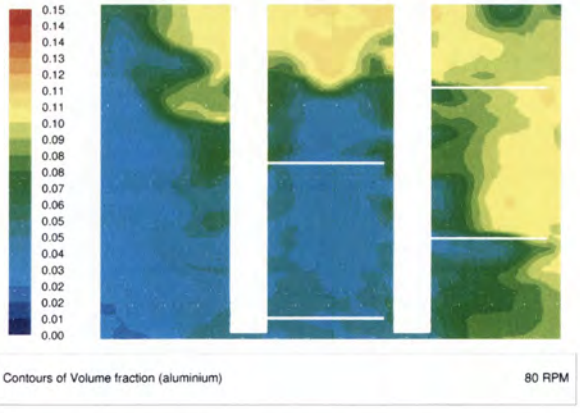


Figure 7.21: Volume fraction of aluminium particles – 80 rpm

When the impellers speed was increased to 60 rpm, as shown in Figure 7.20, a 2% reduction in the amount of aluminium particles floating above the TNT media was seen.

Despite this, not much improvement was seen as the tank depth increased. Finally, at 80 rpm, a further reduction of 2% in the amount of the aluminium particles was achieved. In conclusion, the existing incorporator configuration was not an effective design for drawing down aluminium particles or to suspend RDX particles. This was shown in Figure 7.21.

## 7.5 Impeller study

Figure 7.22: Geometry of the existing impeller (left) and standard pitch blade turbine (right)

For the purpose of studying the impact of a PBT impeller where half the blades was facing the motor and the other half facing the shaft tip, two geometrical configurations were created, as shown in Figure 7.22. The results from this section aimed to illustrate the performance of the existing impellers in the bomb incorporator, relative to blades facing in only one direction.

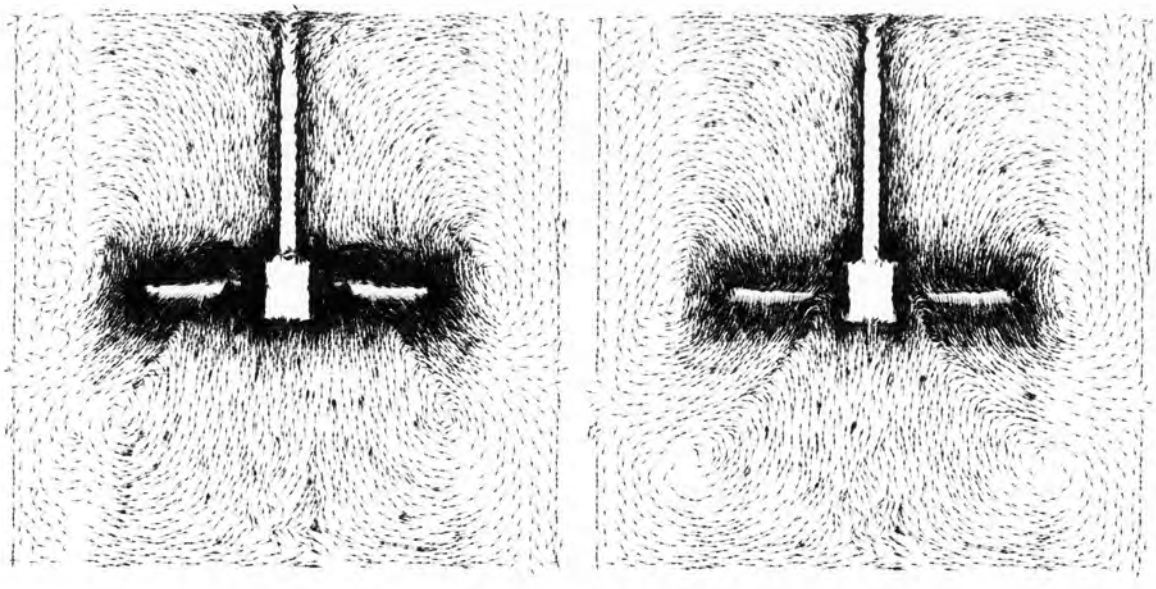

Figure 7.23: Vector plot of the existing impeller (left) and standard pitch blade turbine (right)

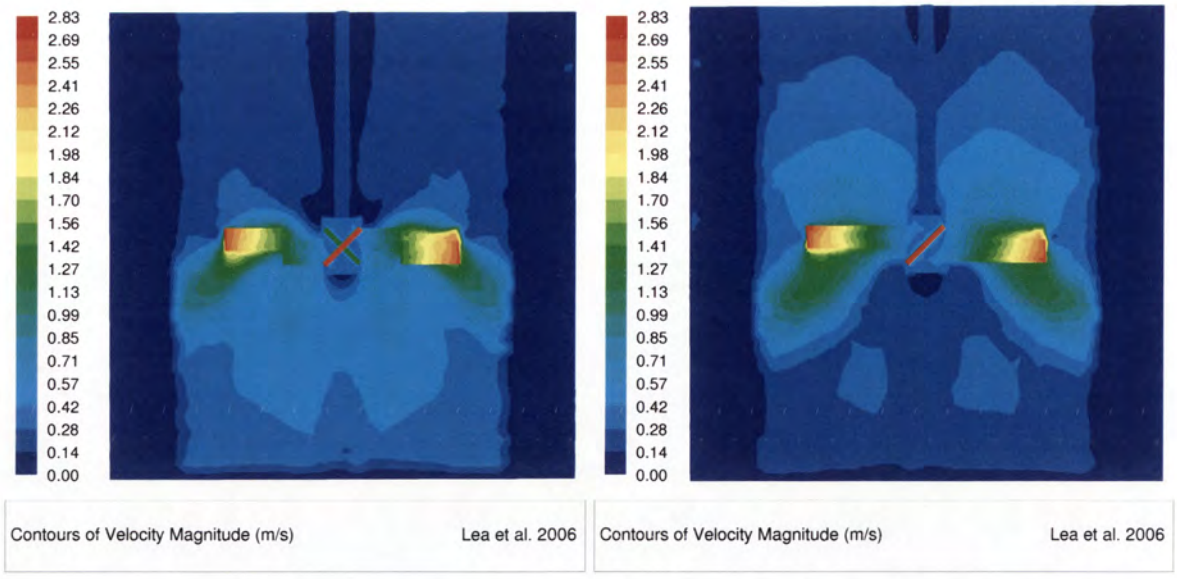


Figure 7.24: Contour plot of the existing impeller (left) and standard pitch blade turbine (right)

Figures 7.23 and 7.24 show the vector plots and contour plots of velocity magnitude respectively. In sets of the figures, the diagrams on the left hand side represented the existing impeller configuration where half of the blade faced upwards while the other half was facing downwards, when the impellers were rotating in the anti-clockwise position looking down from the top. The diagrams on the right hand side represented a 4-bladed PBT impeller which faced downwards when the impeller was rotating in the anti-clockwise direction. From Figure 7.24, it was seen that a higher velocity magnitude in the region immediately below the impeller existed in the existing configuration relative to the same region in the PBT configuration. However, Figure 7.23 indicated that the flow in this region was travelling upwards. Secondly, the discharge from the existing impeller blade tips was lower than that from the PBT blade tips. Similarly, the discharge was facing downwards, as indicated by the vector plots. Thirdly, in the region immediately above each impeller, the velocity magnitude in the existing impeller was much lower than that discovered in the PBT impeller. Vector plot shows that these flows were moving downwards from the liquid free surface towards the impellers hub.

Figure 7.25: Surface integration at three levels

Three planes located at different heights were created for surface integration as shown in Figure 7.25. To further confirm the qualitative analysis performed, analysis was drawn from quantitative analysis as well. This was achieved by creating surfaces at three levels where surface integration was conducted. Table 7.2 shows the results of surface integrations.

Table 7.2: Liquid level at various stages of tank transfer

| Parameters | Existing | PBT |
|---|---|---|
| | | |
| Location: Height = 0.3m | | |
| Axial | 59.07 | 12.67 |
| | | |
| Location: Height = 0.5m | | |
| $\tau$ | 29.74 | 25.71 |
| Axial | 227.7 | 221.7 |
| Radial | 115.6 | 70.49 |
| Turbulence | 49,301 | 11,527 |
| | | |
| Location: Height = 0.7m | | |
| Axial | 12.27 | 47.75 |

Table 7.2 shows that in the regions above the impellers (0.7m), the PBT impeller produced stronger downward axial flow than the existing impeller. Below the impeller region, however, the existing impeller produced a stronger upward axial flow than the existing impeller. At hub level, both impellers have similar axial flow magnitude but the existing impeller registered higher radial flow than the PBT impeller. In addition, due to the non-streamline nature of the flow emanating from the existing impeller, the global turbulence produced by the existing impeller was much higher than that produced by the PBT impeller.

From earlier studies, to draw-down floating particles, the flow from the liquid free surface must be strong enough to overcome the buoyancy force exerted by the less dense particles. In contrast, to suspend denser particles, the flow discharge from the blade tips must be strong enough to sweep these particles from the tank bottom. In brief, to draw-down floating particles and suspend denser particles, impellers producing axial flow were preferred. Based on these criteria and from the qualitative perspective, the PBT impeller performed better than the existing impeller for floating particles incorporation and the suspension of denser particles.

## 7.6 Proposed geometrical configurations

### 7.6.1 Designing a bomb incorporator

Eight variants were created and to be selected as the ideal design, the geometrical configuration generated must meet each and every criterion. The variant with the highest numerical value shall be selected.

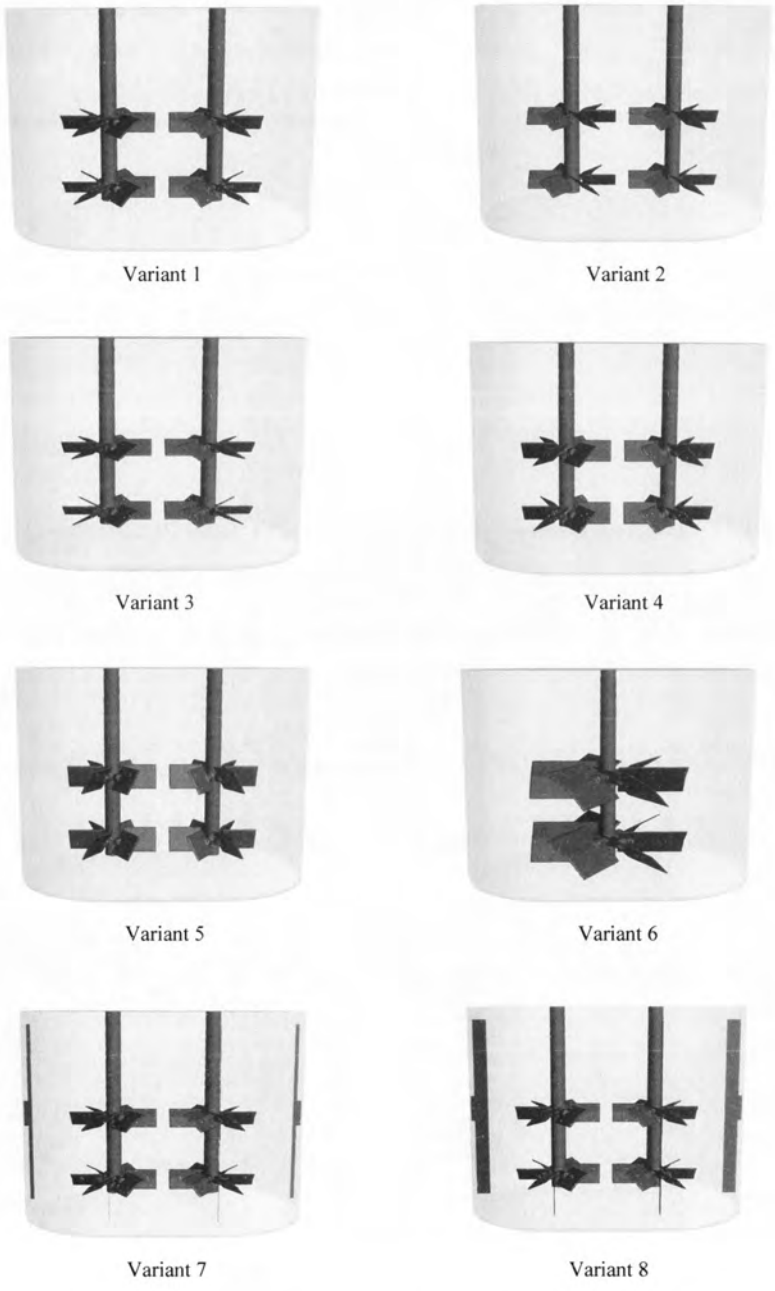


Figure 7.26: Eight geometrical configuration variants

## 7.6.2 Results and discussion on several variants

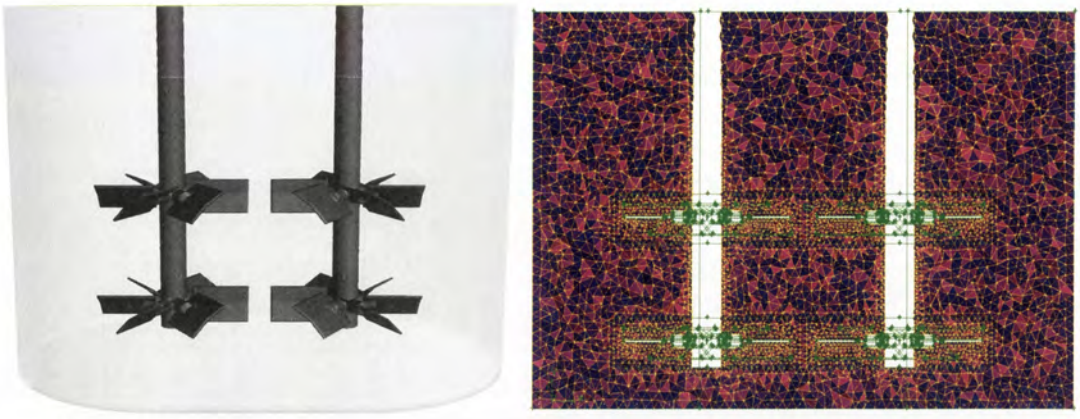

| | | | |
|---|---|---|---|
| Start size | : 8 | *T* (equivalent) | : 680mm |
| Growth rate | : 1.2 | *D/T* | : 0.5 |
| Size limit | : 20 | *W/D* | : 0.3 |
| Equisize skew | : 0.82 | *C/T* | : 0.2 |
| Total size | : 880,631 | *V/T* | : 0.1677 |

Figure 7.27: Variant 1: 30°/45° (Opposite direction)

Figure 7.27 shows the geometrical configuration of variant 1 which consisted of two top-entry parallel shafts, each mounted with a pair of six-bladed impellers. Each blade had half of it tilted at 30° and the other half 45°. It was felt that the 30° angle would impart extra axial flow into the fluid. Looking at the tank from the top, the shaft on the left hand side rotated anti-clockwise while the shaft on the right hand side rotated clockwise. Figure 7.27 also shows the meshed geometry where extra cells were assigned to region of high flow notably, inside the four fluid zones.

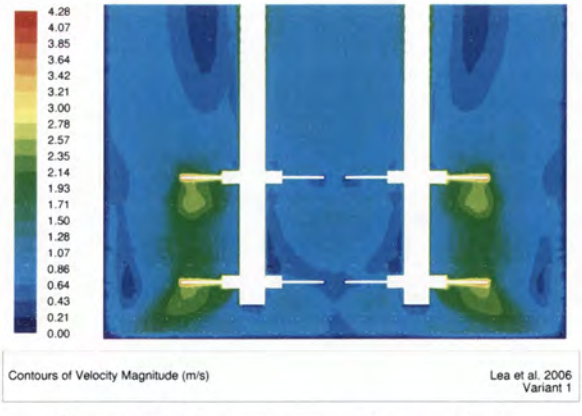


Figure 7.28: Velocity contours of variant 1 – side view

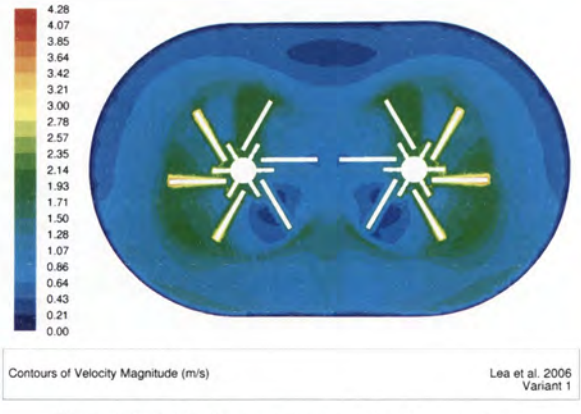


Figure 7.29: Velocity contours of variant 1 – top view

Figure 7.28 shows the velocity contour from the side view when the impellers were rotating at 100 rpm. No dead zones were seen in the contour map. The regions of highest flow include those surrounding the blade tips but confined to those nearest to the tank wall. The flow was seen to extend all the way to the tank bottom. From the top view, the velocity contour again indicated that dead zones were not present. Regions of high flow were located inside the rotational zones that face away from each other, as shown in Figure 7.29.

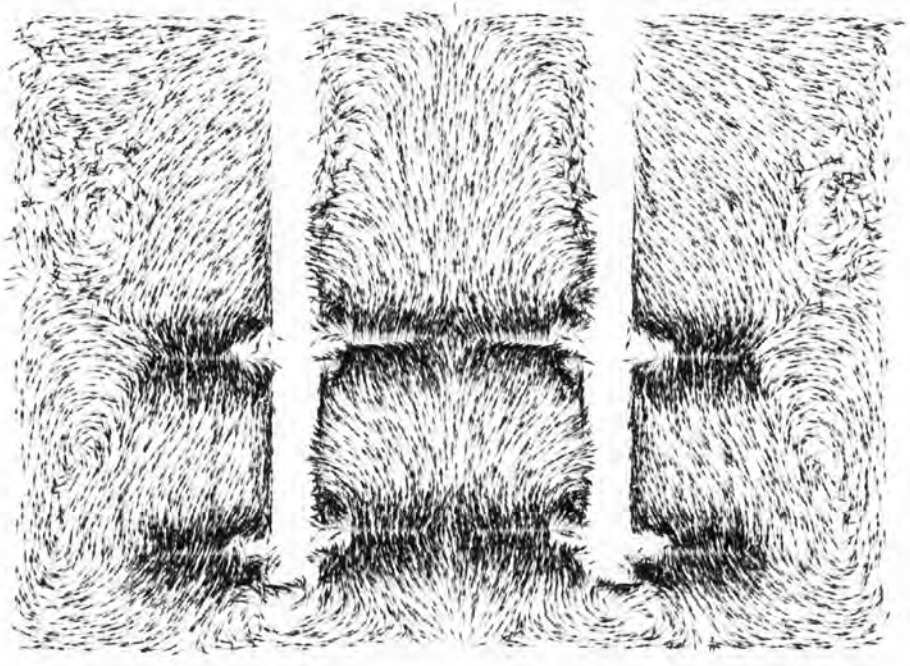

Figure 7.30: Vector plot of variant 1 – side view

Figure 7.30 shows the vector plot from the side view. Most of the vectors were moving in the same direction especially those travelling from the top to the bottom of the tank. These vectors were directed by the top impeller and as they passed by the top impeller, they were then directed by the bottom impeller. The discharge from the bottom impeller was directed towards the tank bottom where they were deflected by the tank bottom before travelling upwards along the wall. It was noticed that along the wall, even though there were axial component, quite a significant portion of the vectors deflected from the tank bottom were converted to side vortex, at the expense of upward flow. This was translated into a lower cloud height achievable potential and was attributed to the lack of wall baffle to help in directing the flow upward. Region between the two shafts indicated that the vectors were moving upward and were focused. This compensated the lack of upward movement along

the wall regions. Overall, the flow pattern included flow moving down from top to bottom inside the rotational zone nearest to the wall and flow moving upward from bottom to top in the region between the two shafts.

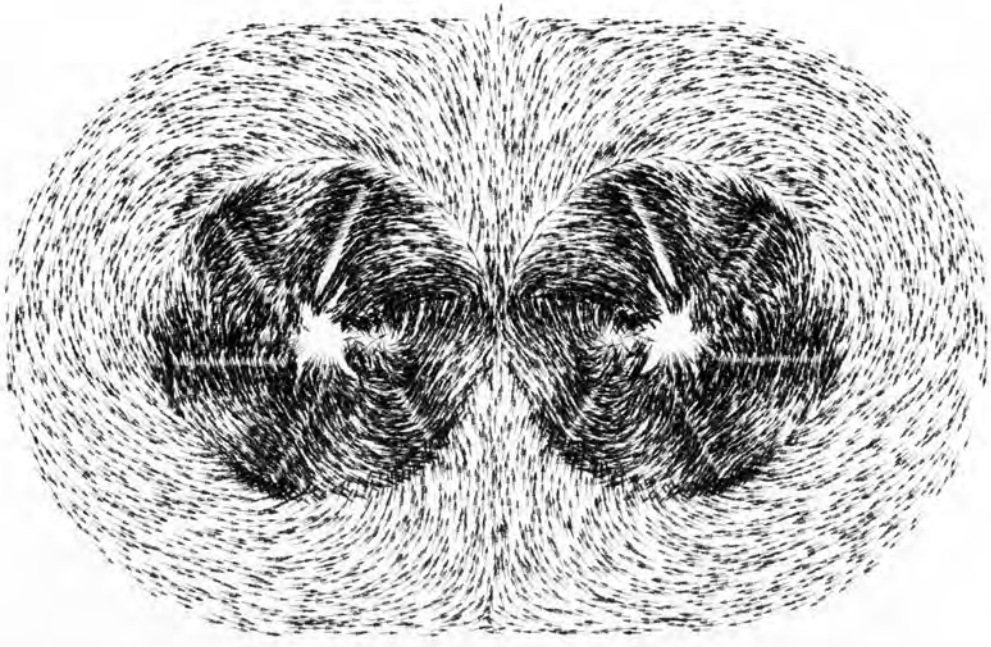

Figure 7.31: Vector plot of variant 1 – top view

From the top view, the vectors were seen rotating anti-clockwise around the left shaft and rotating clockwise around the right shaft. The two regions of vectors then merged in the region between the two shafts, as shown in Figure 7.31. In summary, from the qualitative analysis perspective, variant 1 mixing configuration would be even more effective in mixing and particle suspension duties where sufficient flow moving from the top to bottom and bottom to top must be present, if wall baffles were attached.

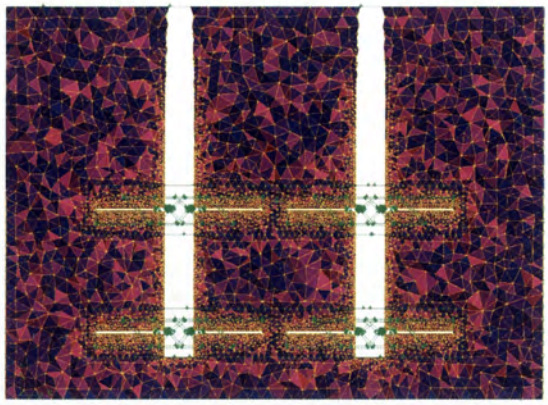

| | | | |
|---|---|---|---|
| Start size | : 5 | *T* (equivalent) | : 680mm |
| Growth rate | : 1.4 | *D/T* | : 0.5 |
| Size limit | : 25 | *W/D* | : 0.3 |
| Equisize skew | : 0.83 | *C/T* | : 0.2 |
| Total size | : 960,723 | *V/T* | : 0.1677 |

Figure 7.32: Variant 2: 30°/45° (Same direction)

Figure 7.32 shows the geometrical configuration of variant 2 which consisted of two top-entry parallel shafts, each mounted with a pair of six-bladed impellers. Each blade has half of it tilted at 30° and the other half 45°. It was felt that the 30° angle would impart extra axial flow into the fluid. From the top view, both shafts rotated clockwise. The figure also shows the meshed geometry where extra cells were assigned to region of high flow notably, inside the four fluid zones.

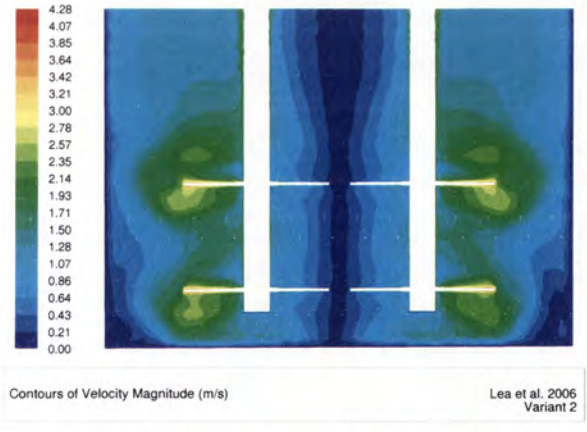


Figure 7.33: Velocity contours of variant 2 – side view

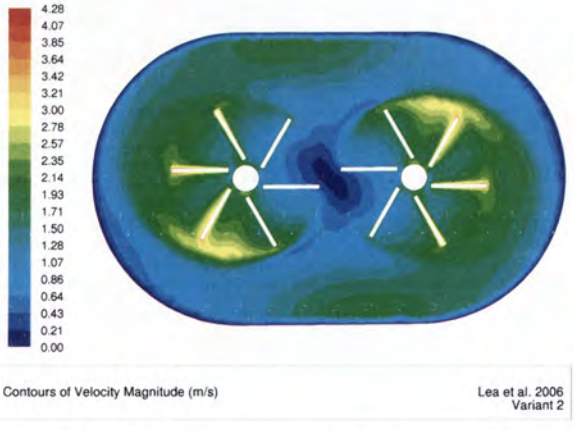


Figure 7.34: Velocity contours of variant 2 – top view

Figure 7.33 shows the velocity contour from the side view when the impellers were rotating at 100 rpm. Dead zones or regions with significant low flow were seen in the contour map. Such flow was seen prevalent in the region between the two shafts and at the bottom corner of the tank. The regions of highest flow included those surrounding the

blade tips but confined to those nearest to the tank wall. However, unlike those produced by variant 1, the flow did not extend all the way to the tank bottom. This gave rise to dead zones located at the bottom corner of the tank. From the top view, as shown in Figure 7.34, the velocity contour obtained by creating a horizontal plane at the hub of the bottom impeller, again indicated that dead zones were present in the region between the two shafts. Regions of high flow were located inside the rotational zones that face away from each other and unlike variant 1, were also located along the tank wall. This shows that variant 2, where both shaft were rotating in clockwise direction, imparted more tangential flow thereby giving rise to a more significant solid body rotation.

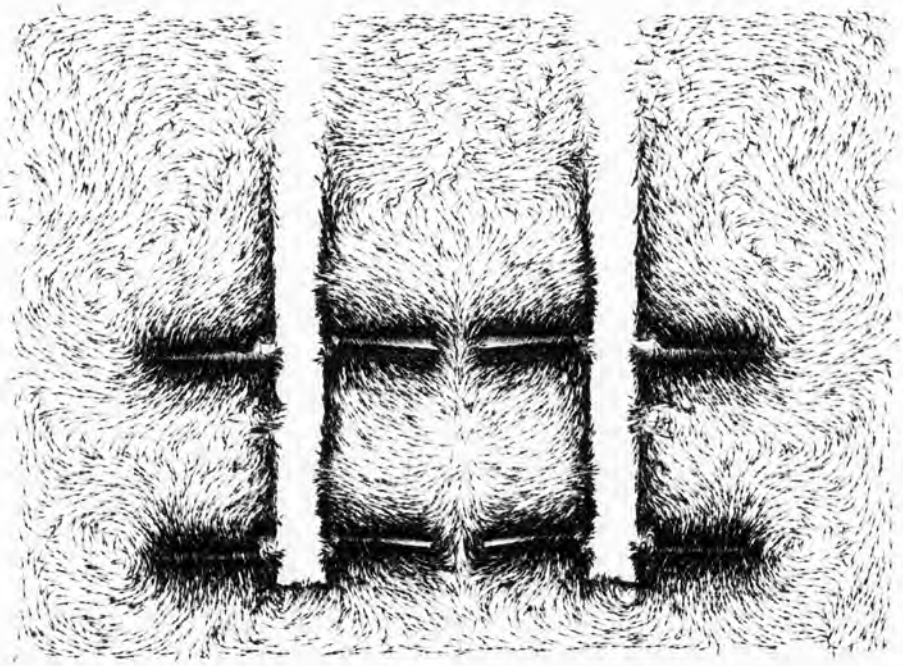

Figure 7.35: Vector plot of variant 2 – side view

Figure 7.35 depicts the vector plot from the side view and unlike those produced by variant 1, shows that most of the vectors were not moving in the same direction. A small component of these vectors was directed by the top impeller and as they passed by the top impeller, they were then directed by the bottom impeller. Majority of these vectors were radially discharged from the top impellers and did not pass through the second impeller. Instead they formed a side vortex and travelled upwards. In other words, the flow was compartmentalised. The discharge from the bottom impeller was directed towards the tank bottom where they were deflected by the tank bottom, but unlike variant 1, instead of travelling upwards along the wall, the majority of the deflected vectors formed side vortex

again and rejoined the bottom impeller from its hub. It was observed that along the wall, those vectors near the bottom impeller were moving towards the tank bottom while those near the top impeller were moving towards the tank top. This was another visible sign that the hydrodynamic of this mixing tank was highly compartmentalised. The presence of baffle might or might not help to improve the mixing performance of this tank because baffles help to convert radial to axial flow. In this case, the performance might worsen if the baffles were to actually convert more radial flow to downward axial flow. Region between the two shafts indicated that while some vectors were moving upward the others were moving radially. This further augmented the lack of overall vectors upward movement. Overall, vector plot from the side view indicated that the hydrodynamics of this mixing tank was highly compartmentalised.

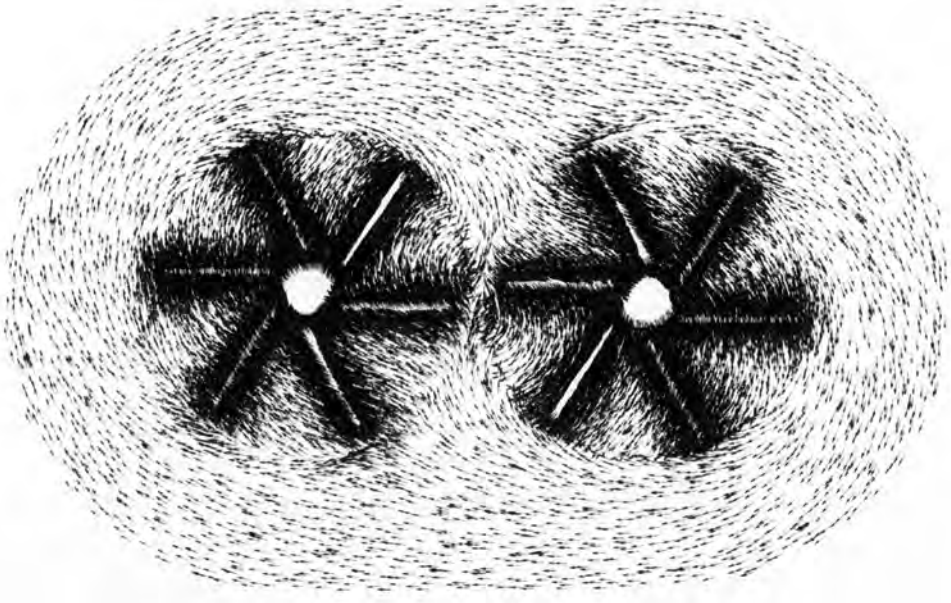

Figure 7.36: Vector plot of variant 2 – top view

From the top view, the vector plot, as shown in Figure 7.36, indicated that solid body rotation in this mixing tank was rather prevalent due to having both shafts rotating in clockwise direction. In summary, from the qualitative analysis perspective, variant 2 mixing configuration was ineffective in mixing and particle suspension duties due to the lack of sufficient non-compartmentalised axial flow that provides the thrust to sweep the particles from the tank bottom and lift them to the top of the tank.

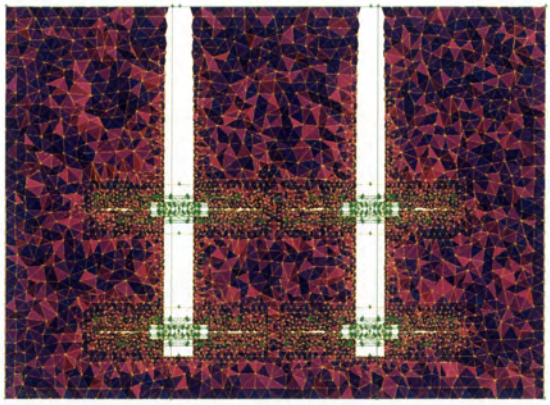

| | | | |
|---|---|---|---|
| Start size | : 8 | *T* (equivalent) | : 680mm |
| Growth rate | : 1.2 | *D/T* | : 0.5 |
| Size limit | : 25 | *W/D* | : 0.3 |
| Equisize skew | : 0.81 | *C/T* | : 0.2 |
| Total size | : 654,566 | *V/T* | : 0.1677 |

Figure 7.37: Variant 3: 30° (Opposite direction)

Figure 7.37 shows the geometrical configuration of variant 3 which consisted of two top-entry parallel shafts, each mounted with a pair of six-bladed impellers. Each blade had a 30° angle. It was felt that the 30° angle would impart extra axial flow into the fluid. Looking into the tank from the top, the shaft on the left hand side rotated anti-clockwise while the shaft on the right hand side rotated clockwise. Figure 7.37 also shows the meshed geometry where extra cells were assigned to region of high flow notably, inside the four fluid zones.

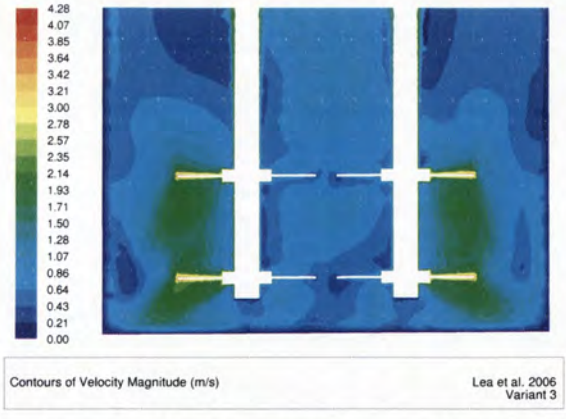


Figure 7.38: Velocity contours of variant 3 – side view

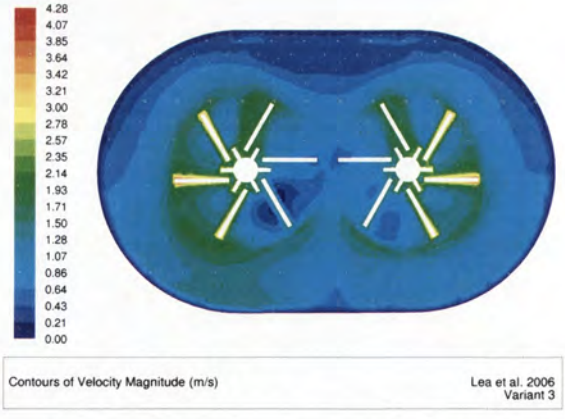


Figure 7.39: Velocity contours of variant 3 – top view

The velocity contour of variant 3 has similar features to those obtained from variant 1. Figure 7.38 shows the velocity contour from the side view when the impellers were rotating at 100 rpm. No dead zones were seen in the contour map. The regions of highest

flow include those surrounding the blade tips but confined to those nearest to the tank wall. The flow was seen to extend all the way to the tank bottom. From the top view, the velocity contour again indicated that dead zones were not present. Regions of high flow were located inside the rotational zones that face away from each other, as shown in Figure 7.39.

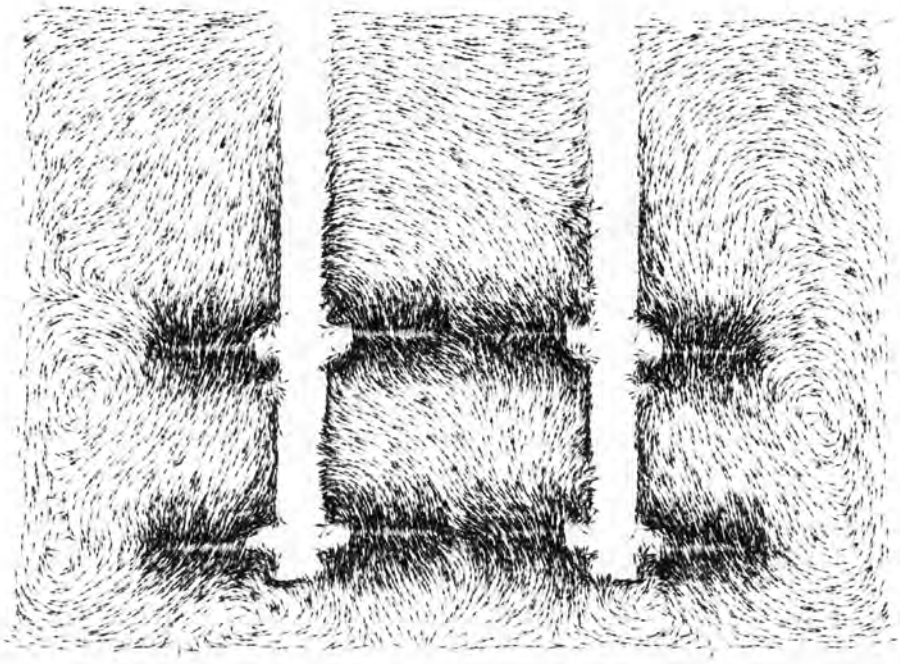

Figure 7.40: Vector plot of variant 3 – side view

Vector plot of variant 3 also show great similarity to those obtained from variant 1. Figure 7.40 shows the vector plot from the side view. Most of the vectors were moving at the same direction especially those travelling from the top to the bottom of the tank. These vectors were directed by the top impeller and as they passed by the top impeller, they were then directed by the bottom impeller. The discharge from the bottom impeller was directed towards the tank bottom where they were deflected by the tank bottom before travelling upwards along the wall. It can be noticed that along the wall, even though there were axial component, quite a significant portion of the vectors deflected from the tank bottom were converted to side vortex, at the expense of upward flow. This was attributed to the lack of wall baffle to help in directing the flow upward. Region between the two shafts indicated that the vectors were moving upward and were focused. However, the vectors were not moving as upright as those seen in variant 1. This compensated the lack of upward movement along the wall regions. Overall, the flow pattern included flow moving down

from top to bottom inside the rotational zone nearest to the wall and flow moving upward from bottom to top in the region between the two shafts.

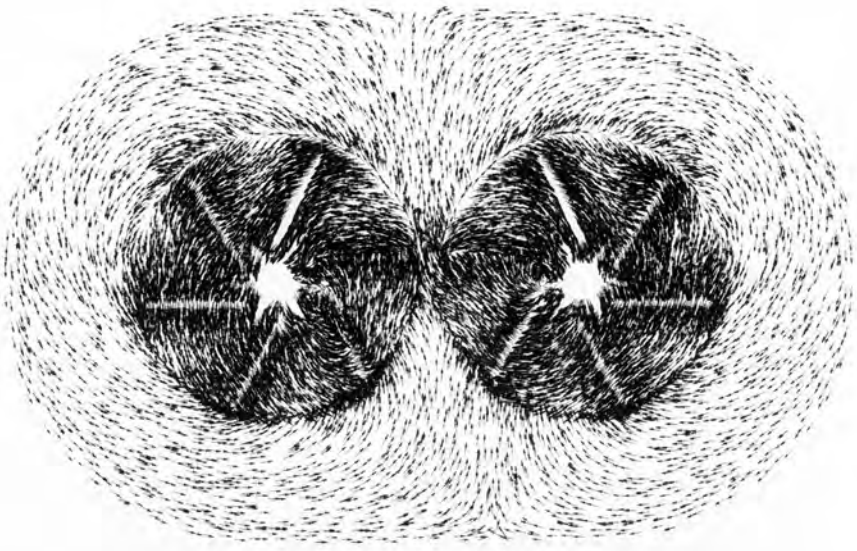

Figure 7.41: Vector plot of variant 3 – top view

From the top view, the vectors were seen rotating anti-clockwise around the left shaft and rotating clockwise around the right shaft. The two regions of vectors then merged in the region between the two shafts, as shown in Figure 7.41. In summary, from the qualitative analysis perspective, variant 3 mixing configuration was effective in mixing and particle suspension duties where sufficient from moving from the top to bottom and bottom to top must be present.

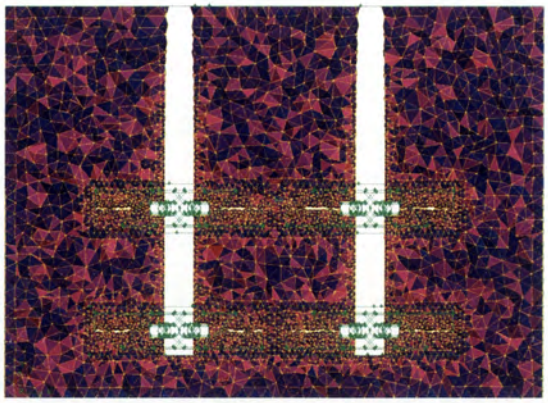

| | | | |
|---|---|---|---|
| Start size | : 8 | *T* (equivalent) | : 680mm |
| Growth rate | : 1.2 | *D/T* | : 0.5 |
| Size limit | : 25 | *W/D* | : 0.3 |
| Equisize skew | : 0.81 | *C/T* | : 0.2 |
| Total size | : 658,499 | *V/T* | : 0.1677 |

Figure 7.42: Variant 4: 45° (Opposite direction)

Figure 7.42 shows the geometrical configuration of variant 4 which consisted of two top-entry parallel shafts, each mounted with a pair of six-bladed impellers. Each blade had a 45° angle. The 45° angle was known to impart mixed radial-axial flow into the fluid. Looking at the tank from the top, the shaft on the left hand side rotated anti-clockwise while the shaft on the right hand side rotated clockwise. Figure 7.42 also shows the meshed geometry where extra cells were assigned to region of high flow notably, inside the four fluid zones.

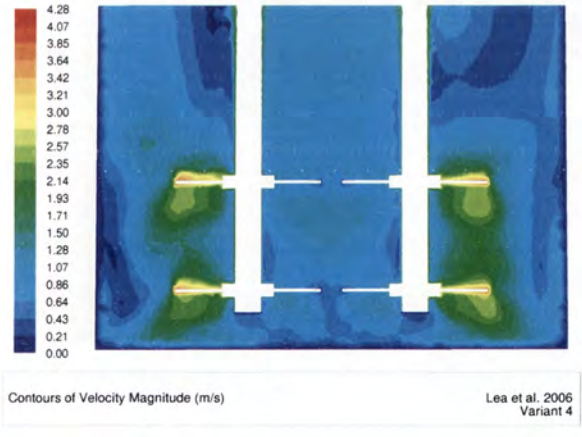


Figure 7.43: Velocity contours of variant 4 – side view

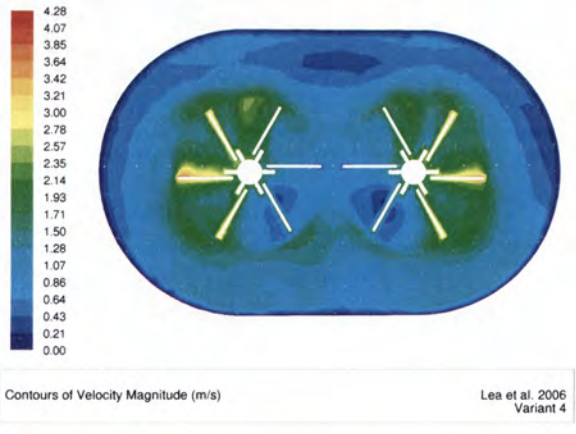


Figure 7.44: Velocity contours of variant 4 – top view

Figure 7.43 shows the velocity contour from the side view when the impellers were rotating at 100 rpm. The velocity contour obtained from this geometrical configuration was similar to those obtained from variant 1 and this included having no dead zones present in the contour map. The regions of highest flow included those surrounding the blade tips but confined to those nearest to the tank wall. Despite the similarity between variant 4 and 1, the axial flow was less than those in variant 1. This was evidenced by the lack of contour depicting high flow in the region connecting the top and bottom impellers, which was present in variant 1. The flow was seen to extend all the way to the tank bottom. From the top view, the velocity contour again indicated that dead zones were not present. Regions of high flow were located inside the rotational zones that face away from each other, as shown in Figure 7.44.

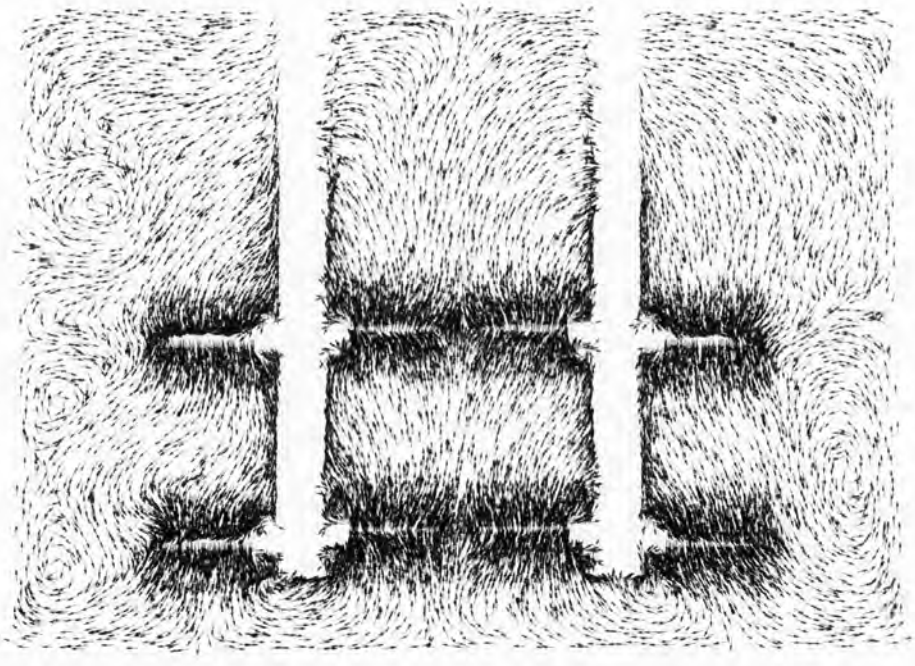

Figure 7.45: Vector plot of variant 4 – side view

Figure 7.45 shows the vector plot from the side view. Like those found in variant 1, most of the vectors were moving in the same direction especially those travelling from the top to the bottom of the tank. These vectors were directed by the top impeller and as they passed by the top impeller, they were then directed by the bottom impeller. The discharge from the bottom impeller was directed towards the tank bottom where they were deflected by the tank bottom before travelling upwards along the wall.

It can be noticed that along the wall, even though there was axial component, quite a significant portion of the vectors deflected from the tank bottom were converted to side vortex, at the expense of upward flow. This was attributed to the lack of wall baffle to help in directing the flow upwards. Region between the two shafts indicated that the vectors were moving upwards and were focused. This compensated the lack of upward movement along the wall regions. Overall, the flow pattern included flow moving down from top to bottom inside the rotational zone nearest to the wall and flow moving upward from bottom to top in the region between the two shafts.

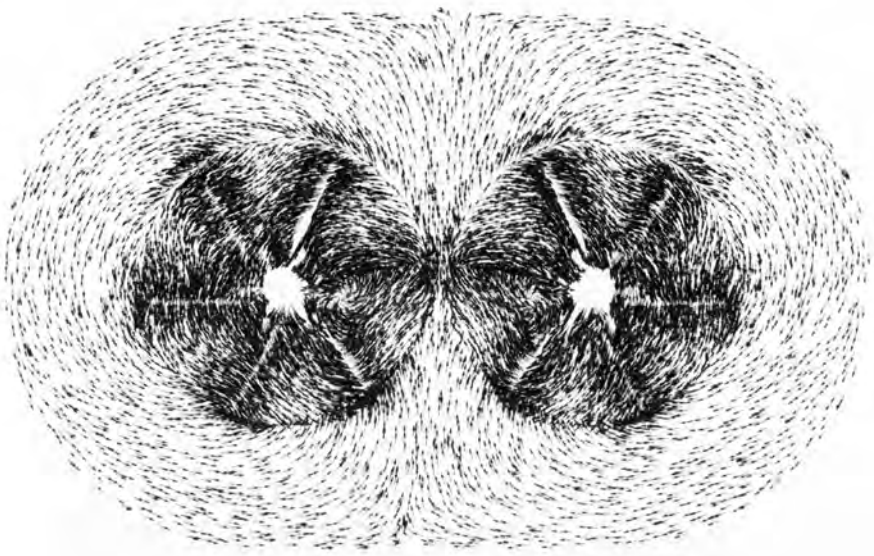

Figure 7.46: Vector plot of variant 4 – top view

From the top view, the vectors were seen rotating anti-clockwise around the left shaft and rotating clockwise around the right shaft. The two regions of vectors then merged in the region between the two shafts, as shown in Figure 7.46. In summary, from the qualitative analysis perspective, variant 4 mixing configuration was effective in mixing and particle suspension duties where sufficient from flow moving from the top to bottom and bottom to top must be present.

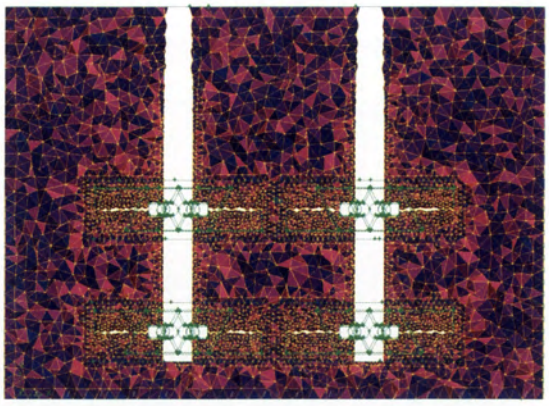

| | | | |
|---|---|---|---|
| Start size | : 8 | *T* (equivalent) | : 680mm |
| Growth rate | : 1.2 | *D/T* | : 0.5 |
| Size limit | : 25 | *W/D* | : 0.3 |
| Equisize skew | : 0.79 | *C/T* | : 0.2 |
| Total size | : 683,572 | *V/T* | : 0.1677 |

Figure 7.47: Variant 5: 60° (Opposite direction)

Figure 7.47 shows the geometrical configuration of variant 5 which consisted of two top-entry parallel shafts, each mounted with a pair of six-bladed impellers. Each blade had 60° angle. The 60° angle would impart more radial flow than axial flow component into the fluid. Looking at the tank from the top, the shaft on the left hand side rotated anti-clockwise while the shaft on the right hand side rotated clockwise. The figure also shows the meshed geometry where extra cells were assigned to region of high flow notably, inside the four fluid zones.

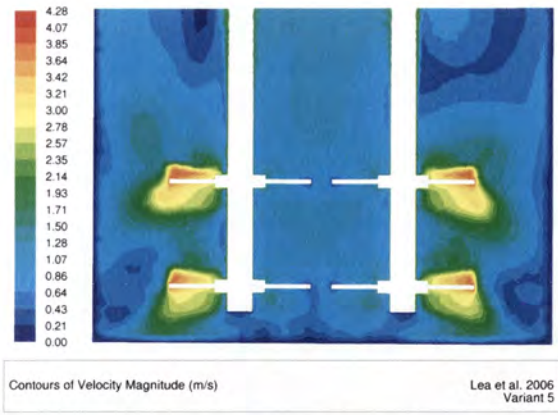


Figure 7.48: Velocity contours of variant 5 – side view

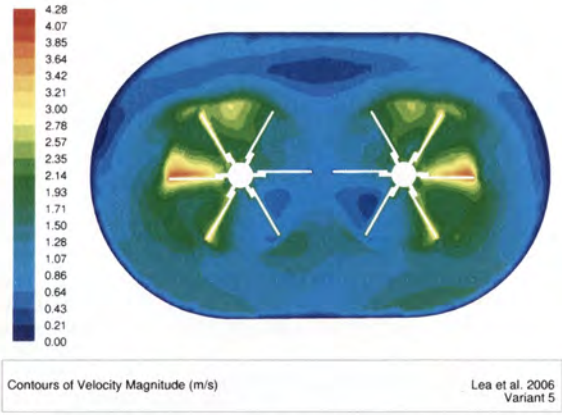


Figure 7.49: Velocity contours of variant 5 – top view

Figure 7.48 shows the velocity contour from the side view when the impellers were rotating at 100 rpm. No dead zones were seen in the contour map. The regions of highest flow included those surrounding the blade tips but confined to those nearest to the tank wall. Despite higher flow being registered at blade tips, relative to those produced in variant 1, the axial flow was much less than those in variant 1. This was evidenced by the lack of contour depicting high flow in the region connecting the top and bottom impellers, which was present in variant 1. The flow was seen to extend all the way to the tank bottom. From the top view, the velocity contour again indicated that dead zones were not present. Regions of higher flow, relative to those in variant 1, were located inside the rotational zones that face away from each other, as shown in Figure 7.49. This was consistent with discharge emanating from radial flow impellers. Moreover, from the contour velocity shown, a higher tangential flow was obtained in this geometrical configuration relative to those obtained from variant 1. The lack of axial flow and the increase in tangential flow relative to those flows in variant 1 was attributed to the radial impellers used in the geometrical configuration of this mixing tank.

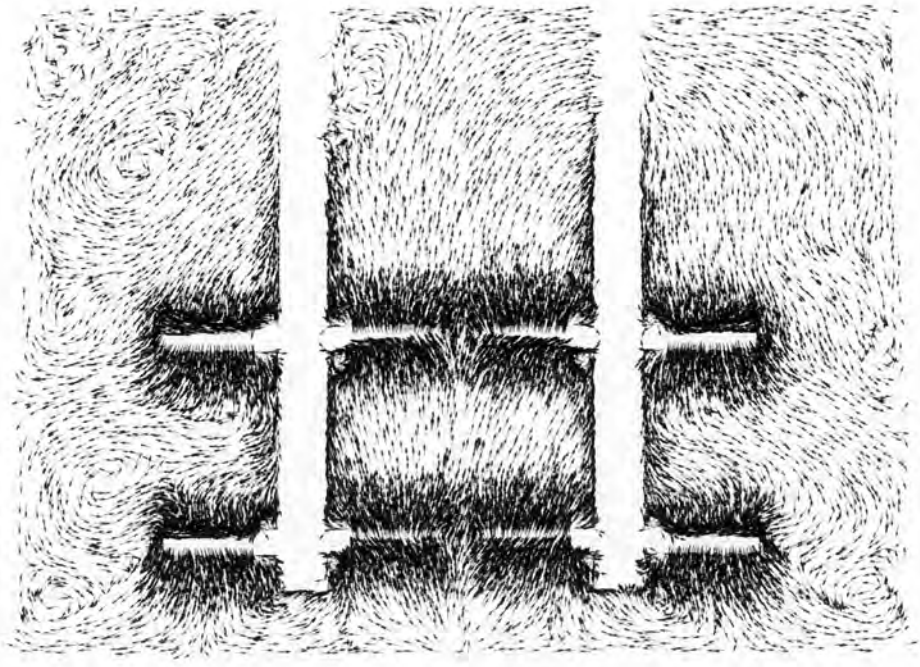

Figure 7.50: Vector plot of variant 5 – side view

Figure 7.50 shows the vector plot from the side view. Like those found in variant 1, most of the vectors were moving in the same direction especially those travelling from the top to the bottom of the tank. These vectors were directed by the top impeller and as they passed by the top impeller, they were then directed by the bottom impeller. However, unlike those in variant 1, a significant component of the flow were seen leaving in radial direction from the top impeller, reflecting the radial nature of any $60^{o}$ tilted blade. The discharge from the bottom impeller was directed towards the tank bottom where they were deflected by the tank bottom before travelling upwards along the wall. It was noticed that along the wall, although there was an axial component, quite a significant portion of the vectors deflected from the tank bottom were converted to side vortex, at the expense of upward flow. This was attributed to the lack of wall baffle to help in directing the flow upward. Region between the two shafts indicated that the vectors were moving upwards and were focused. This compensated the lack of upward movement along the wall regions. Overall, the flow pattern included compartmentalised flow moving down from top to bottom inside the rotational zone nearest to the wall and flow moving upwards from bottom to top in the region between the two shafts.

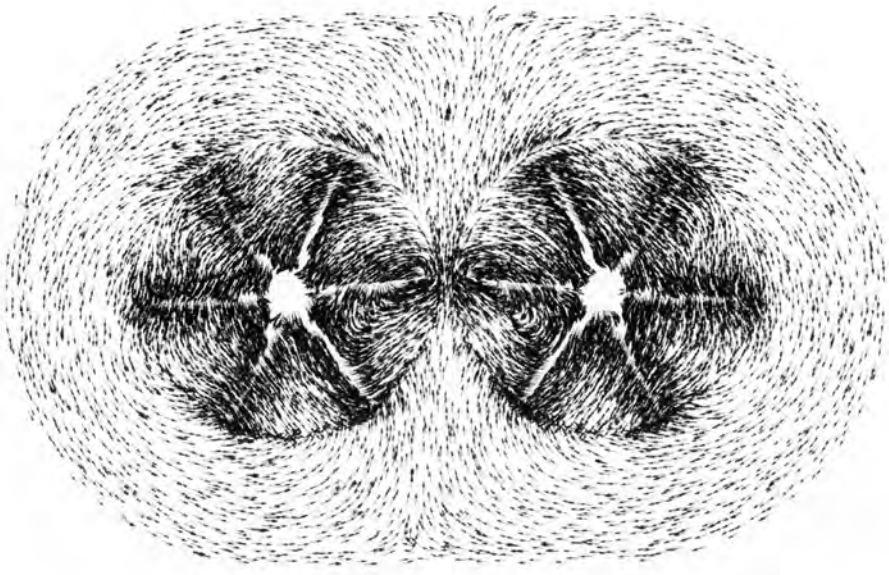

Figure 7.51: Vector plot of variant 5 – top view

From the top view, the vectors were seen rotating anti-clockwise around the left shaft and rotating clockwise around the right shaft. The two regions of vectors then merged in the region between the two shafts, as shown in Figure 7.51. In summary, from the qualitative analysis perspective, due to the lack of significant axial flow, variant 5 geometrical configurations were not very effective for particle suspension. This was simply because to suspend particles effectively, sufficient kinetic energy must be imparted into the fluid to sweep the particles from the tank bottom and lifts them towards the tank top. This kinetic energy could be provided by the axial flow which was lacking in variant 5.

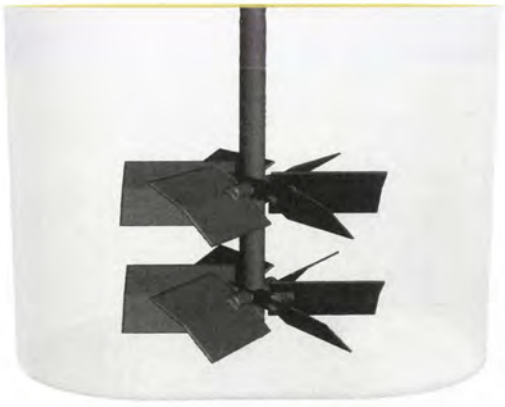

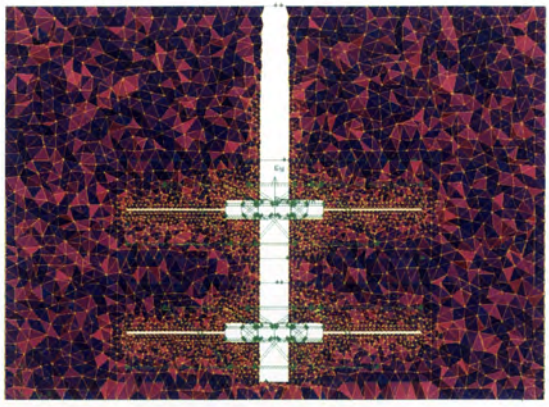

| | | | |
|---|---|---|---|
| Start size | : 8 | *T* (equivalent) | : 680mm |
| Growth rate | : 1.4 | *D/T* | : 0.8824 |
| Size limit | : 25 | *W/D* | : 0.3333 |
| Equisize skew | : 0.86 | *C/T* | : 0.2 |
| Total size | : 671,071 | *V/T* | : 0.1677 |

Figure 7.52: Variant 6: 30°/45° (Single shaft)

Figure 7.52 shows the geometrical configuration of variant 6 which consisted of a single top-entry shaft, mounted with a pair of six-bladed impellers. Each blade had half of it tilted at 30° and the other half 45°. It was felt that the 30° angle would impart extra axial flow into the fluid. Looking into the tank from the top, the impellers rotated in a clockwise direction. The figure also shows the meshed geometry where extra cells were assigned to regions of high flow notably, inside the two fluid zones.

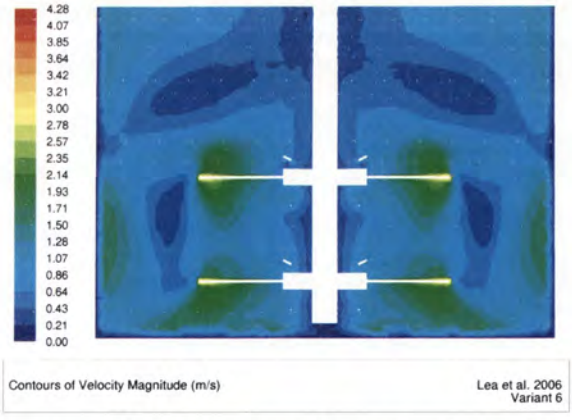


Figure 7.53: Velocity contours of variant 6 – side view

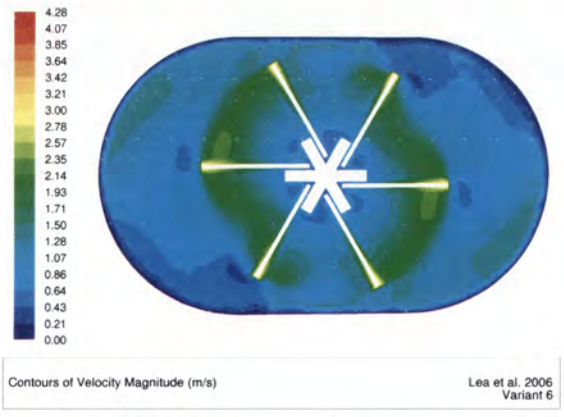


Figure 7.54: Velocity contours of variant 6 – top view

Figure 7.53 shows the velocity contour from the side view when the impellers were rotating at 100 rpm. No dead zones were seen in the contour map. The regions of highest flow include those surrounding the blade tips. The flow discharged by the bottom impeller was seen to extend all the way to the tank bottom. From the top view, the velocity contour

again indicated that dead zones were not present. Regions of high flow were located inside the rotational zones, as shown in Figure 7.54.

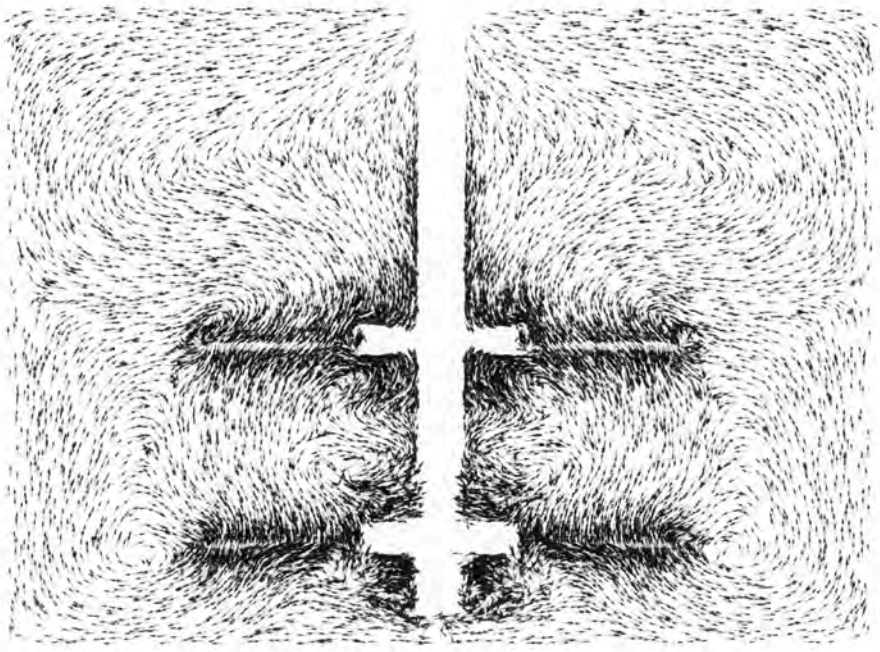

Figure 7.55: Vector plot of variant 6 – side view

Figure 7.55 shows the vector plot from the side view. Most of the vectors were moving in the same direction especially those travelling from the top to the bottom of the tank. These vectors were directed by the top impeller and as they passed by the top impeller, they were then directed by the bottom impeller. The discharge from the bottom impeller was directed towards the tank bottom where they were deflected by the tank bottom before travelling upwards along the wall. It was noticed that along the wall, although there was an axial component, quite a significant portion of the vectors deflected from the tank bottom were converted to side vortex, at the expense of upward flow. This was attributed to the lack of wall baffle to help in directing the flow upwards. Overall, the flow pattern included flow moving down from top to bottom inside the rotational zone and flow moving from the tank bottom towards the tank top along the wall until it reached the height of the top impeller. From there, the vectors were directed by the top impellers towards the bottom impeller.

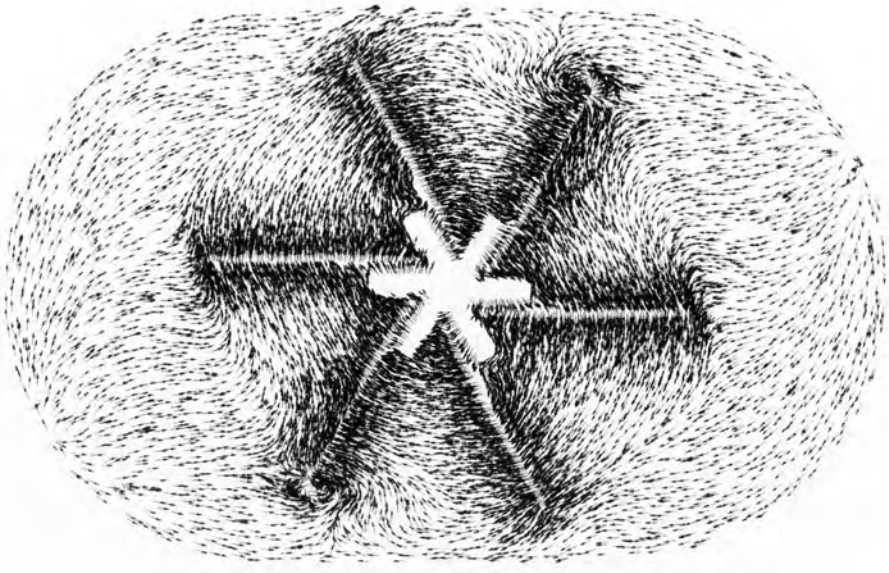

Figure 7.56: Vector plot of variant 6 – top view

From the top view, the vectors were seen rotating clockwise around the impeller. Significant flow was seen moving away from the wall toward the impeller, as shown in Figure 7.56. In summary, from the qualitative analysis perspective, variant 6 mixing configuration was effective in mixing and particle suspension duties where sufficient flow from moving from the top to bottom and bottom to top must be present.

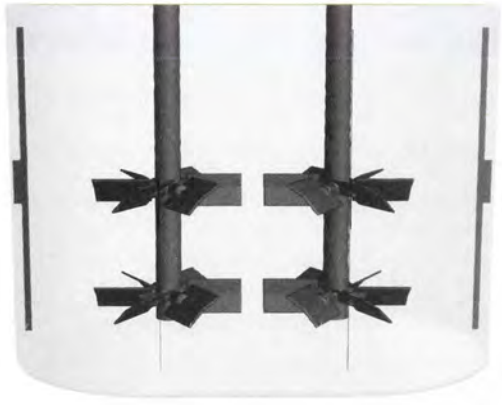

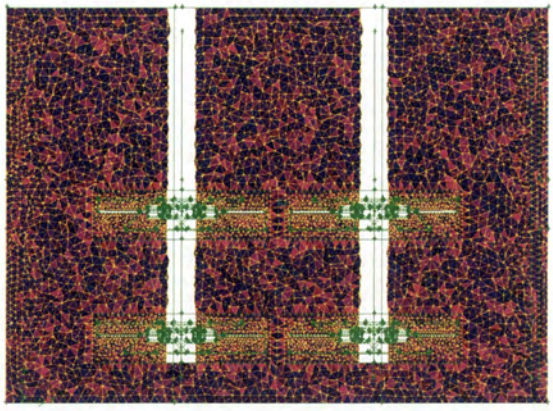

| | | | |
|---|---|---|---|
| Start size | : 7 | *T* (equivalent) | : 680mm |
| Growth rate | : 1.2 | *D/T* | : 0.5 |
| Size limit | : 20 | *W/D* | : 0.3 |
| Equisize skew | : 0.86 | *C/T* | : 0.2 |
| Total size | : 1,179,777 | *V/T* | : 0.1677 |
| No. of baffles | : 6 | *B/T* & *b/T* | : 0.022 |

Figure 7.57: Variant 7 – narrow baffle installed: 30°/45° (Opposite direction)

Figure 7.57 shows the geometrical configuration of variant 7 which consisted of two top-entry parallel shafts, each mounted with a pair of six-bladed impellers. Each blade had its top-half tilted at 30° and the bottom-half at 45°. It was felt that the 30° angle would impart extra axial flow into the fluid. The tank had 6 narrow baffles (*T*/50) strategically assigned to each location in the tank along the tank wall. Looking at the tank from the top, the shaft on the left hand side rotated anti-clockwise while the shaft on the right hand side rotated clockwise. Figure 7.57 also shows the meshed geometry where extra cells were assigned to region of high flow notably, inside the four fluid zones.

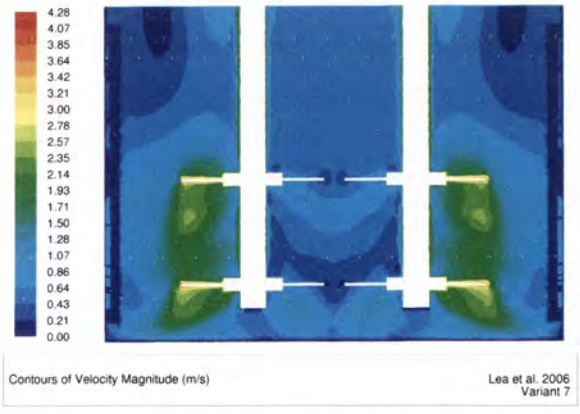


Figure 7.58: Velocity contours of variant 7 – side view

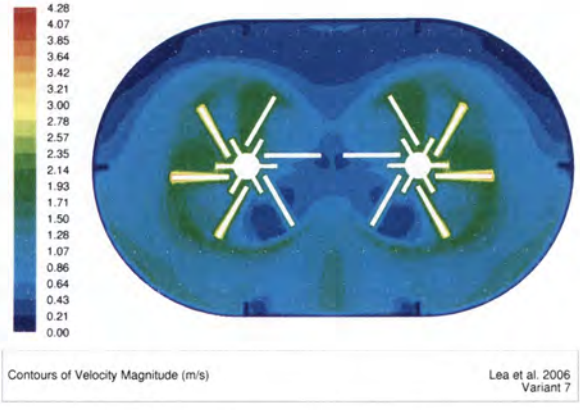


Figure 7.59: Velocity contours of variant 7 – top view

Figure 7.58 shows the velocity contour from the side view when the impellers were rotating at 100 rpm. No dead zones were seen in the contour map. The regions of highest flow included those surrounding the blade tips but confined to those nearest to the tank wall. The flow was seen to extend all the way to the tank bottom. From the top view, the velocity contour again indicated that dead zones were not present. Regions of high flow were located inside the rotational zones that face away from each other, as shown in Figure 7.59.

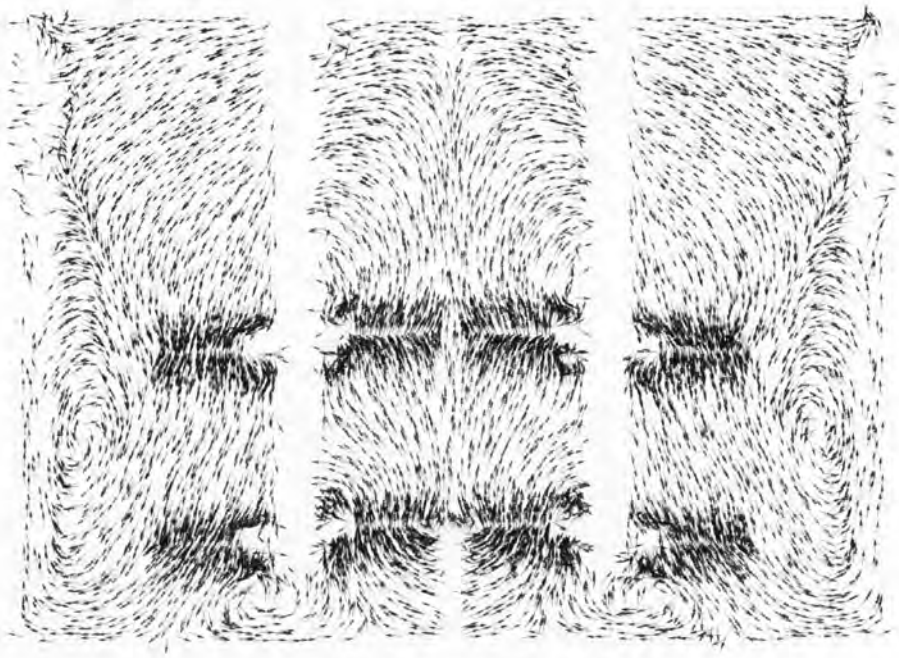

Figure 7.60: Vector plot of variant 7 – side view

Figure 7.60 shows the vector plot from the side view. Most of the vectors were moving in the same direction especially those travelling from the top to the bottom of the tank. These vectors were directed by the top impeller and as they passed by the top impeller, they were then directed by the bottom impeller. The discharge from the bottom impeller was directed towards the tank bottom where they were deflected by the tank bottom before travelling upwards along the wall. It was noticed that along the wall, although there was an axial component, quite a significant portion of flow was converted side vortex.

However, the difference between this design and the unbaffled tank was that the side vertex in this case was larger and extends above the top impeller. This means compartmentalisation was not as serious as in the case of variant 1 and a higher level of cloud height was achievable. Region between the two shafts indicated that the vectors

were moving upwards and were focused. This compensated the lack of upward movement along the wall regions. Overall, the flow pattern included flow moving down from top to bottom inside the rotational zone nearest to the wall and flow moving upwards from bottom to top in the region between the two shafts.

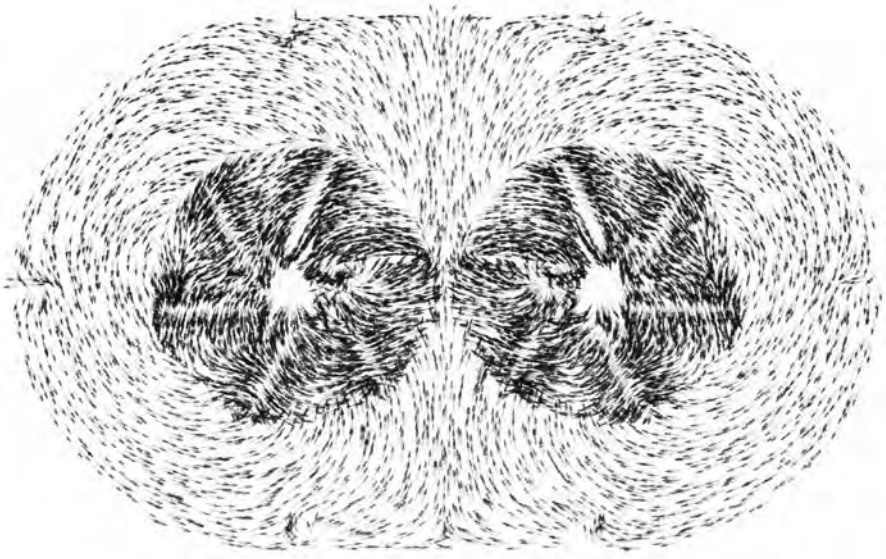

Figure 7.61: Vector plot of variant 7 – top view

From the top view, the vectors were seen rotating anti-clockwise around the left shaft and rotating clockwise around the right shaft. Solid body rotation was slightly interrupted by the presence of 6 narrow baffles. However, due to the gap between the narrow baffles and the wall allocated, dead zone behind the narrow baffles did not occur. This was depicted by the vectors behind the narrow baffles. The two flow regions merged in the region between the two shafts, as shown in Figure 7.61. In summary, from the qualitative analysis perspective, variant 7 mixing configuration was effective in mixing and particle suspension duties where sufficient flow moving from the top to bottom and bottom to top must be present.

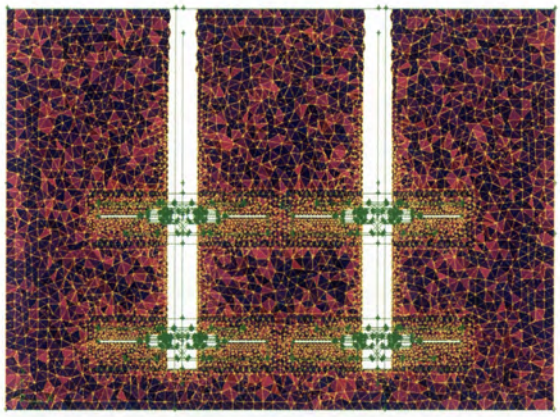

| | | | |
|---|---|---|---|
| Start size | : 7 | *T* (equivalent) | : 680mm |
| Growth rate | : 1.2 | *D/T* | : 0.5 |
| Size limit | : 20 | *W/D* | : 0.3 |
| Equisize skew | : 0.81 | *C/T* | : 0.2 |
| Total size | : 1,024,784 | *V/T* | : 0.1677 |
| No. of baffles | : 6 | *B/T* & *b/T* | : 0.083 & 0.022 |

Figure 7.62: Variant 8 – standard baffles installed: 30°/45° (Opposite direction)

Figure 7.62 shows the geometrical configuration of variant 8 which consisted of two top-entry parallel shafts, each mounted with a pair of six-bladed impellers. Each blade had its top-half tilted at 30° and the bottom-half at 45°. It was felt that the 30° angle will impart extra axial flow into the fluid. The tank had 6 standard baffles (*T*/12) strategically assigned to each location in the tank along the tank wall. Looking at the tank from the top, the shaft on the left hand side rotated anti-clockwise while the shaft on the right hand side rotated clockwise. This figure also shows the meshed geometry where extra cells were assigned to region of high flow notably, inside the four fluid zones.

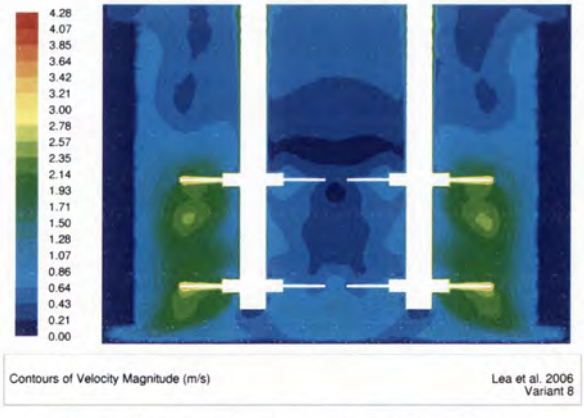


Figure 7.63: Velocity contours of variant 8 – side view

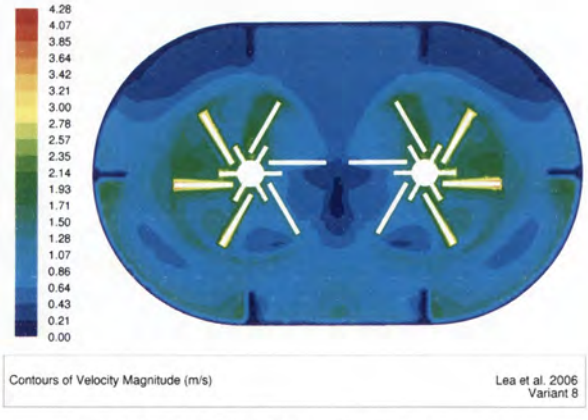


Figure 7.64: Velocity contours of variant 8 – top view

Figure 7.63 shows the velocity contour from the side view when the impellers were rotating at 100 rpm. No dead zones were seen in the contour map. The regions of highest flow included those surrounding the blade tips but confined to those nearest to the tank wall. The flow was seen to extend all the way to the tank bottom. From the top view, the velocity contour again indicated that dead zones were not present. Regions of high flow were located inside the rotational zones that face away from each other, as shown in Figure 7.64.

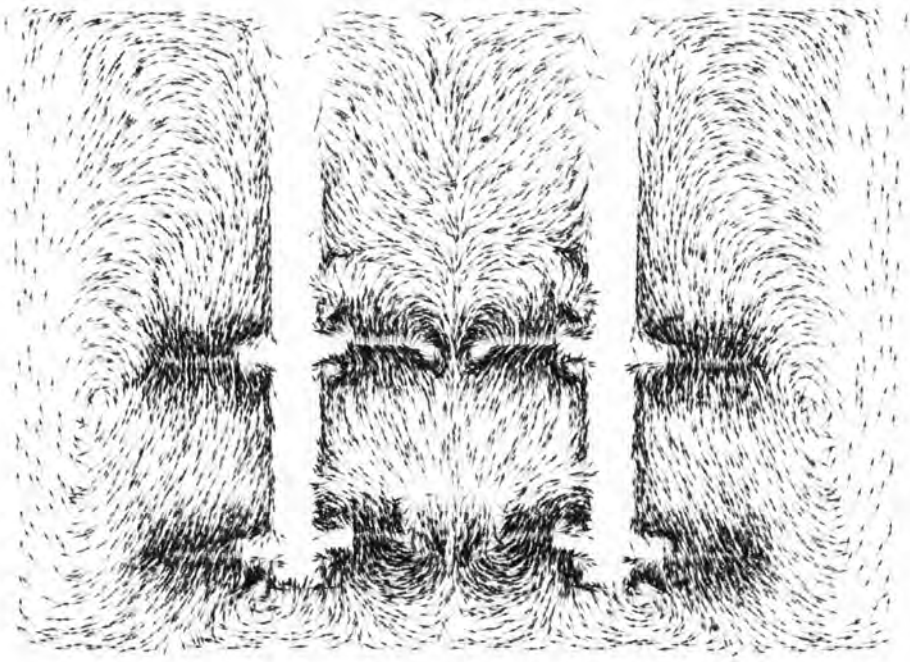

Figure 7.65: Vector plot of variant 8 – side view

Figure 7.65 shows the vector plot from the side view. Most of the vectors were moving in the same direction especially those travelling from the top to the bottom of the tank. These vectors were directed by the top impeller and as they passed by the top impeller, they were then directed by the bottom impeller. The discharge from the bottom impeller was directed towards the tank bottom where they were deflected by the tank bottom before travelling upwards along the wall. It was noticed that along the wall, unlike those produced by variant 7 (narrow baffles), all the vectors were pointing upwards. In addition, no compartmentalisation existed. Region between the two shafts indicated that the vectors were moving upwards and were focused. This analysis shows that the use of standard wall baffles, relative to narrow baffles, was a better choice for task requiring the suspension of heavier particles.

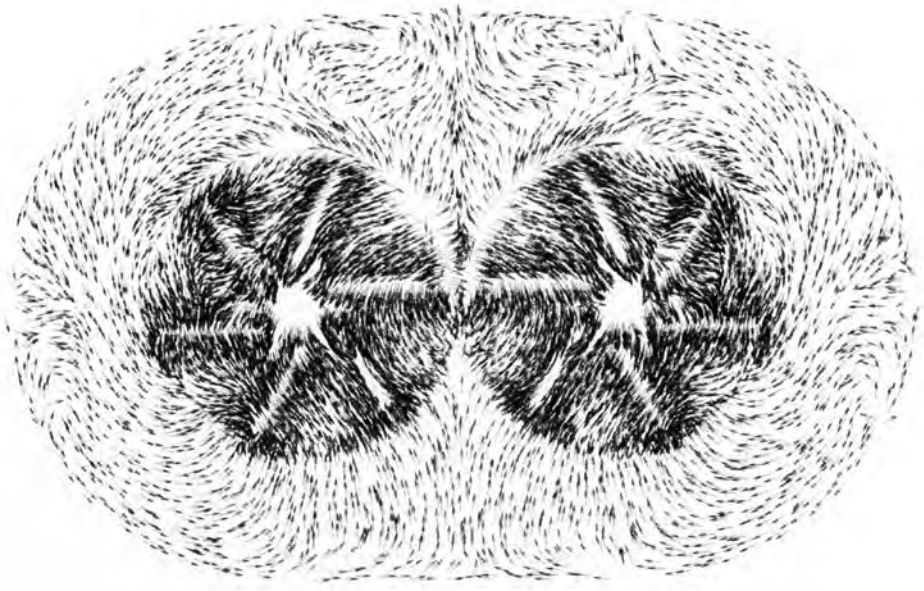

Figure 7.66: Vector plot of variant 8 – top view

From the top view, the vectors were seen rotating anti-clockwise around the left shaft and rotating clockwise around the right shaft. Solid body rotation was significantly interrupted by the presence of 6 standard wall baffles. However, due to the gap between the narrow baffles and the wall allocated, dead zone behind the narrow baffles did not occur. This had depicted by the vectors behind the narrow baffles. The two flow regions merged in the region between the two shafts, as shown in Figure 7.66. In summary, from the qualitative analysis perspective, variant 8 mixing configuration was effective in mixing and particle suspension duties where sufficient flow moving from the top to bottom and bottom to top must be present. However, due to the significant interruption to the solid body rotation caused by the standard wall baffles, this design was not recommended for any task involving the draw down of floating particles. This was because for a tank-centre draw-down to occur, a slight by controlled central vortex must be formed by solid body rotation.

From the contour of velocity plots and the vector plots for all the variants, only variants 1, 3, 4 and 6 were suitable for particle suspension duty whereas variants 2 and 5 were not suitable for such duty due to the lack of axial flow component. Between variants 7 and 8, to draw down aluminium particles and suspend RDX particles concurrently, variant 7 was preferred owing to its superior performance over variant 8.

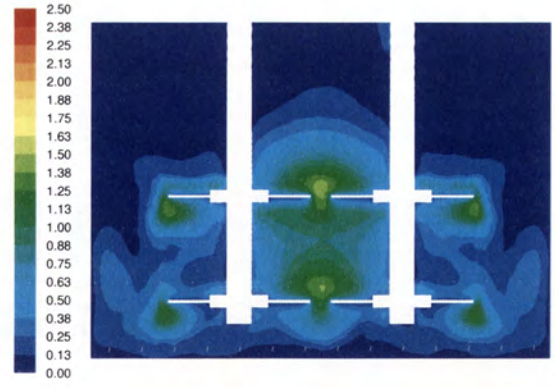


Figure 7.67: Turbulence KE contour plot – variant 1

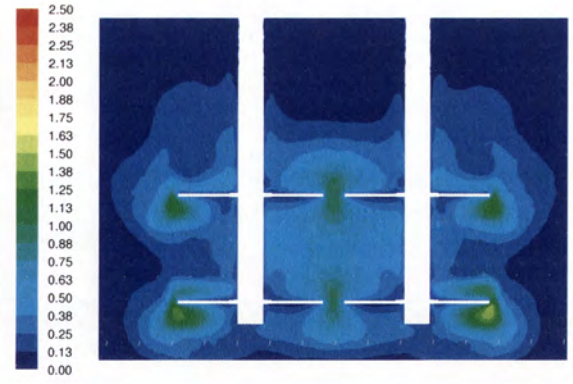


Figure 7.68: Turbulence KE contour plot – variant 2

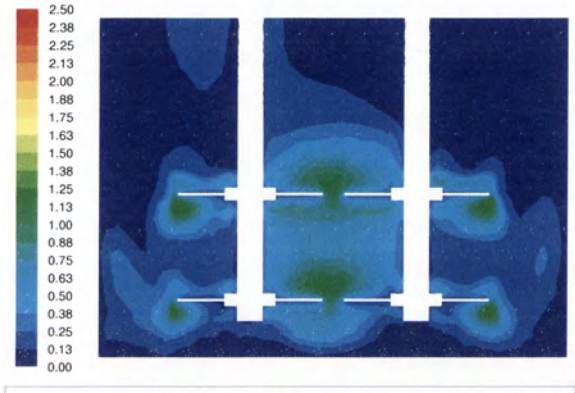


Figure 7.69: Turbulence KE contour plot – variant 3

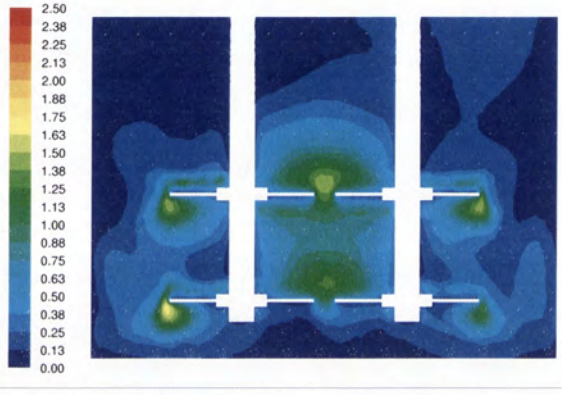


Figure 7.70: Turbulence KE contour plot – variant 4

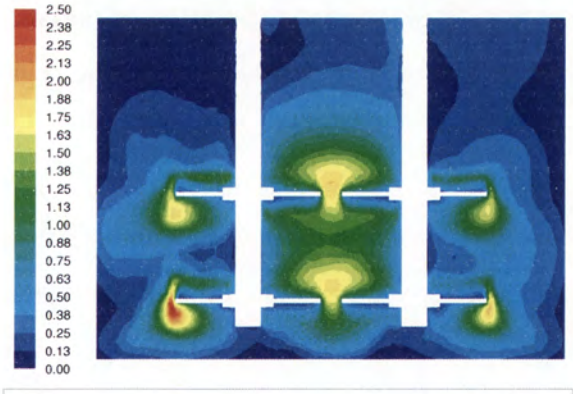


Figure 7.71: Turbulence KE contour plot – variant 5

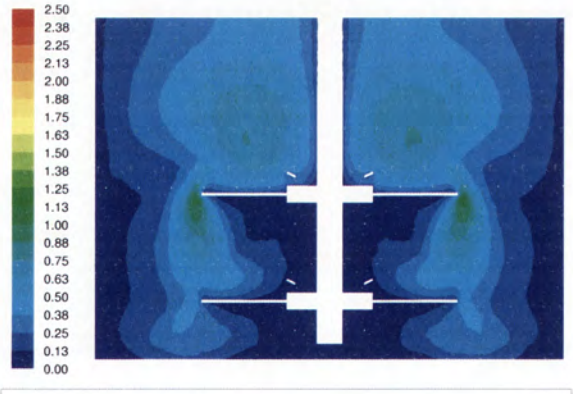


Figure 7.72: Turbulence KE contour plot – variant 6

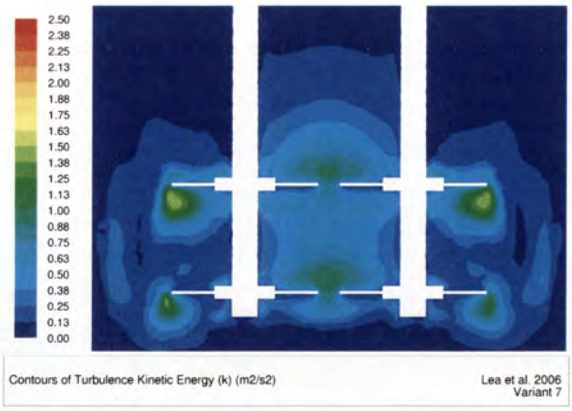


Figure 7.73: Turbulence KE contour plot – variant 7

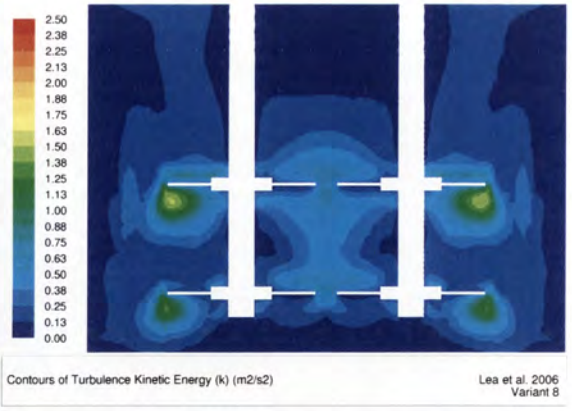


Figure 7.74: Turbulence KE contour plot – variant 8

The contour of kinetic energy plots shows that variants 1, 4, 5, 7 and 8 had similar regions of high turbulence kinetic energy, as shown in Figures 7.67, 7.70, 7.71, 7.73 and 7.74 respectively. This was attributed to the similar geometrical configurations of the impellers employed. Among these three variants, variant 5 depicted the highest turbulence kinetic energy because of the angle of attack of the impellers blades.

Previous study [Lea et al. 2005] shows that a radial impeller will generate more turbulence than an axial impeller. Moreover, between variant 1 and 4, variant 1 depicted a slightly higher local turbulence level in the region between the two shafts and also the blade tips. This was attributed to the $30^{o}/45^{o}$ angle of attack of the impeller blades incorporated in variant 1. Between variant 1 (unbaffled tank) and variant 7 (baffled tank), variant 7 depicted a lower turbulence kinetic energy reading between the two shafts. This was attributed to the streamlining of the flow, aided by the use of 6 narrow baffles in variant 7. Finally, between variants 7 and 8, the turbulence kinetic energy calculated in the region between the two shafts was lower in variant 8 relative to that found in variant 7.

When both impellers were rotating in clockwise direction as in the case of variant 2, the local turbulence level depicted was low as shown in Figure 7.68. When the angle of attack was reduced to $30^{o}$, the level of turbulence further decreased, as shown in Figure 7.69. This was attributed to the low resistance provided by such impellers. At $30^{o}$ angle of attack, the blades could not trap enough fluid and as a consequence failed to impart power into the fluid to induce flow and turbulence.

Except for variant 6, all variants show that the regions of turbulence kinetic energy were confined to those regions in the immediate vicinity of the impellers. Very little turbulence can be found in the region between the fluid free surface and the top impellers. Despite a higher turbulence kinetic energy depicted in this region by variant 6, it depicted very low turbulence level in other regions, as shown in Figure 7.72.

In summary, from the contour of turbulence kinetic energy plotted for all the variants, only variant 1, 4, 5 and 7 depicted enough turbulence level for effective mixing of the three major components of H6, namely RDX, TNT, and aluminium. As studied previously, for effective mixing to take place, the speed at which the fluid was rotating was not of a paramount importance, rather, it was the relative speed among the particles to be mixed [Lea et al. 2005]. At high speed and low turbulence level, this group of RDX merely travelled from one region of the tank to another but failed to be broken up and dispersed to the TNT medium homogeneously.

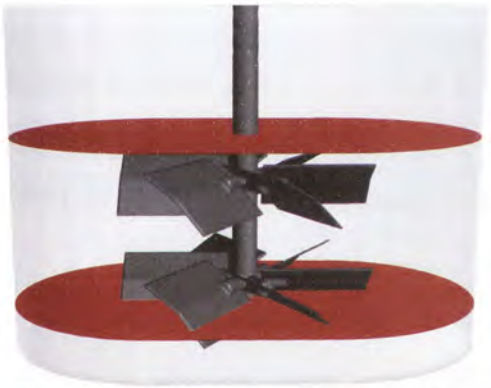

Figure 7.75: Axial flow – across tank horizontal plane

Figure 7.76: Axial flow – impeller diameter

As previously described in [Lea et al. 2005], to suspend particles having density heavier than the primary phase and at the same time draw-down solids having density lighter than the primary phase, the flow orientation must be channelled in axial direction. The ability to produce sufficient axial flow to achieve these dual objectives made an important selection criterion of impeller types. In order to determine as to which impeller produce higher axial flow, surface integration of the appropriate planes must be carried out. Figure 7.75 shows the plane shaded in red where axial flow crosses, located at 0.1 m and 0.5 m from the tank bottom, to calculate the flow required to suspend particles and flow required to draw-down floating particles respectively.

The horizontal planes were reduced to a size where each has a diameter identical to the impeller shown (0.3 m), as shown in Figure 7.76. Flow that crosses this plane were computed and taken into consideration, eliminating the radial flow. Surface integrations were carried out on this plane to determine the summation of axial mass flowrate passing through this plane, irregardless of whether they were flowing upwards or downwards in direction. Previous study also showed that, for flow passing through this plane, most will flow from the top to the bottom of the tank. However, such study also discovered that these downward flows would then be deflected by the tank bottom before flowing upwards along the tank wall [Lea et al. 2005].

In order to keep track of whether the results made sense and consistent, the plane was extended to cover the entire horizontal plane of the bomb incorporator. Surface integration of this plane would reveal the summation of mass flowrate of flows flowing downwards and flows flowing upwards along the tank wall. In addition, having high downward flow might not necessarily mean that the flow would be deflected off the tank bottom and be translated into axial flow travelling upward along the tank wall. Lea et al. [2005] mentioned that for $D/T > 0.55$ the flow tended to favour radial to axial flow. It was possible that the deflected flow had a major radial flow component in a few regions when the $D/T > 0.55$, made possible due to the non-symmetrical geometry of this bomb incorporator.

Figure 7.77: Axial flow – equivalent impeller diameter

Figure 7.78: Axial flow – across tank horizontal plane

Figure 7.77 shows a plane identical in size and shape to that created previously. It was felt that in order to make a meaningful comparison from one impeller to another, an identical plane must be created and integrated. In addition, to assess the interaction of flows from the contribution of each impeller, the plane must include both impellers in its perimeter.

Figure 7.78 shows a plane across the horizontal plane of the bomb incorporator. The result of surface integration of this plane would reveal the mass flowrate of the downward flow which took the flow interaction contributed by each impeller, and the resulting upward flow along the tank wall.

Table 7.3: Summary of assessment results

| Variant no. | 0 | 1 | 2 | 3 | 4 | 5 | 6 | 7 | 8 |
|---|---|---|---|---|---|---|---|---|---|
| Velocity magnitude | No | Yes | No | Yes | Yes | No | Yes | Yes | Yes |
| Vector plots | No | Yes | No | Yes | Yes | No | Yes | Yes | Yes |
| Turbulence kinetic energy | No | Yes | No | No | Yes | Yes | No | Yes | Yes |
| Above impeller flowrate, kg $s^{-1}$ (s) | 58 | 91 | 88 | 89 | 120 | 148 | 150 | 109 | 114 |
| Above impeller flowrate, kg $s^{-1}$ (l) | 192 | 224 | 227 | 216 | 278 | 361 | 416 | 304 | 360 |
| Below impeller flowrate, kg $s^{-1}$ (s) | 98 | 181 | 107 | 143 | 211 | 197 | 183 | 255 | 205 |
| Below impeller flowrate, kg $s^{-1}$ (l) | 283 | 449 | 270 | 376 | 497 | 421 | 445 | 454 | 488 |
| Selection | No | Yes | No | No | Yes | No | No | Yes | No |

Referring to Table 7.3. from the qualitative analysis it was clear only variant 1, 4 and 7 have been shortlisted to be selected as the proposed geometrical configuration for the H6 bomb incorporator. To decide which of the variant would be used as the proposed incorporator, a quantitative analysis must be conducted, achievable by comparing the results of the surface integration.

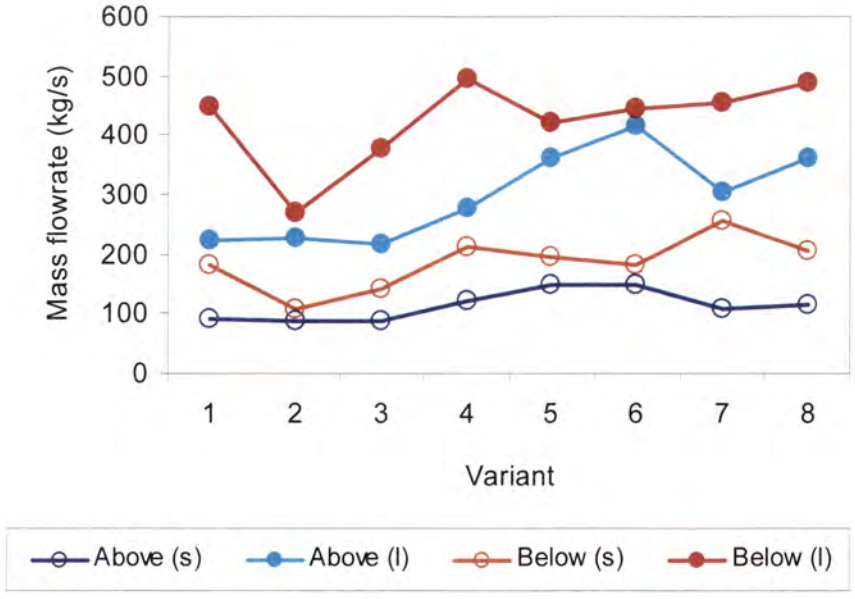


Figure 7.79: Plot of flowrate versus variant numbers

The plot in Figure 7.79 shows that variants 4 and 7 have better draw-down ability than variant 1. As for the small plane below the impellers, variant 7 outperformed variant 4 but for the larger plane, variant 4 outperformed variant 7. Despite this, the larger plane of variant 7 showed a better ability in drawing down floating particles than variant 4 and vice-versa for the smaller plane. This shows that the upward flow was located in the middle of the tank while the draw-down flow was located at the side of the tank for variant 7 but the reverse was true for variant 4. In this scenario, variant 7 was chosen due to its ability in drawing down floating particles across a wider surface area which aided in the distribution of such particles.

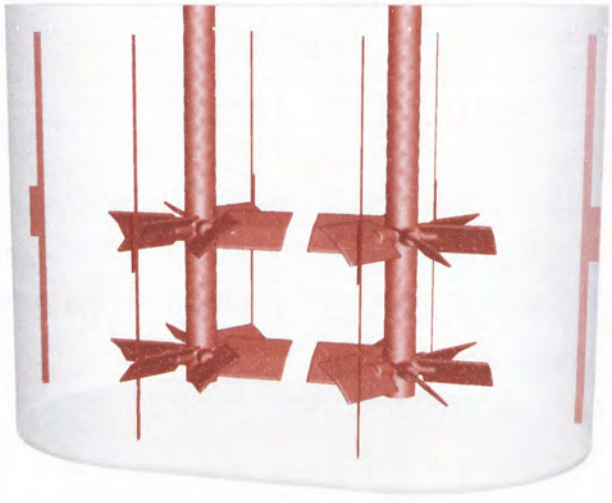

Figure 7.80: Proposed geometrical configuration for the bomb incorporator

Figure 7.80 shows a proposed geometrical configuration for the bomb incorporator. It consisted of six narrow baffles, each attached to the incorporator wall. Excellent fluid movement would be realised by a set of shafts, each installed with a pair of 6-bladed modified PBT. Discussion on the impeller speed and motor size required to operate this proposed bomb incorporator is discussed in the following section.

Table 7.4: Summary of geometrical and physical properties

| Parameter | Values |
|---|---|
| *T* | 680 mm |
| *Top and bottom impeller type* | 6-bladed modified PBT |
| *D/T* | 0.50 |
| *C/T* | 0.2 |
| *W/D* | 0.3 |
| *V/T* | 0.1677 |
| *B/T & b/T* | 0.022 |
| *H* | 600 mm |
| *Z* | 500 mm |
| *Z/T* | 0.7353 |
| Density of solid TNT @ 80°C | 1,654 kg $m^{-3}$ |
| Density of liquid TNT @ 80°C | 1,461 kg $m^{-3}$ |
| Density of liquid TNT @ 85°C | 1,460 kg $m^{-3}$ |
| Density of liquid TNT @ 90°C | 1,455 kg $m^{-3}$ |
| Density of liquid TNT @ 140°C | 1,406 kg $m^{-3}$ |
| Density of RDX @ 80.8°C | 1,770 kg $m^{-3}$ |
| Maximum density of RDX/TNT @ 80°C | 1,737 kg $m^{-3}$ |
| Maximum density of H6 @ 90°C | 1,740 kg $m^{-3}$ |
| Viscosity of RDX/TNT @ 83°C | 0.31 Pa.s |
| Viscosity of RDX/TNT @ 90°C | 0.30 Pa.s |
| Viscosity of RDX/TNT @ 95°C | 0.27 Pa.s |
| Viscosity of H6 @ 90°C (estimated) | 0.34 Pa.s |
| Batch volume | 512.7 L |

Table 7.4 shows the geometrical configuration, operating condition and summary of the physical property of a few energetic products.

### 7.6.3 Power requirement

The power requirement to operate the impellers in the turbulence regime is given by:

$$N_P = \frac{P}{\rho N^3 D^5} \qquad \text{- 7.60}$$

$N_P$ : power number (dimensionless)

$D$ : diameter of impeller (m)

$\rho$ : density of fluid (kg $m^{-3}$)

$N$ : impeller rotational speed (rev $s^{-1}$)

Flow regime and mixing mechanism is usually dependent on the impeller Reynolds number, defined as [Chopey 2004]:

$$N_{\text{Re}} = \frac{\rho N D^2}{\mu} \qquad \text{- 7.61}$$

$\rho$ : density of fluid, kg $m^{-3}$

$N$ : impeller rotational speed, rev $s^{-1}$

$D$ : impeller diameter, m

$\mu$ : absolute viscosity, kg $m^{-1}s^{-1}$ or Pa.s

For *Re* ranging from 10 to 100, the mixing regime is laminar. For turbulent mixing regime, the Reynolds number is greater than 10,000. Transition mixing regime falls between the laminar and turbulent mixing regime, that is, 100 < transition < 10,000. Besides correlating the type of flow regime to the impeller Reynolds number, the mixing time, impeller pumping rate, impeller power consumption, heat and mass transfer coefficients can also be correlated to this dimensionless group.

In this case when:

$\rho$ : 1,740 kg $m^{-3}$ (density of H6)

$N$ : 1.667 rev $s^{-1}$ (impeller rotational speed at 100 rpm)

$D$ : 0.34 m (impeller equivalent diameter)

$\mu$ : 0.34 kg $m^{-1}s^{-1}$ or Pa.s

*Re* was found to be 986.2 which means the mixing was carried out at the transition regime. Due to the lack of study in this regime, the power requirement was taken as those requirements in the turbulence regime.

For shaft with multiple impellers, the power delivered to the shaft was the combined power for all impellers. For a 6-bladed PBT, $W/D = 0.2$, $D/T = 0.3333$, $C/T = 0.3333$, installed in a mixing tank with four standard wall baffles, $N_P = 1.64$ [Paul et al. 2004]. For variant 7, $W/D = 0.3$ and using $W/D$ as the reference value, $N_P = 2.460$

Power required per impeller
$= 2.460 \times 1{,}740 \text{ kg m}^{-3} \times (1.67 \text{ rev s}^{-1})^3 \times (0.34 \text{ m})^5 = 0.09058 \text{ kW}$

Power required for two impellers on a single shaft = 0.09058 kW × 2 = 0.1812 kW at 100 rpm

Power required for two impellers on a single shaft = 0.1556 kW × 2 = 0.3112 kW at 120 rpm

Thus, at the recommended speed of 120 rpm, motor power per shaft recommended is 0.6224 kW. Using motor with 100% overrated power was deemed necessary for safety precaution purpose. This was to prevent overheating during operation which would create a hazardous situation.

### 7.6.4 Minimum shaft diameter

To compute the shaft diameter for both allowable shear and tensile stress, the rotational speed of the mixer, the type of impeller, diameter of impeller, power, location of impellers and the process service the impellers were design to deliver, must be known. For top-entry overhung shaft, the maximum torque will occur above the uppermost impeller. The maximum torque can be determined from the following equation:

$$T_{Q(\max)} = \frac{P}{2\pi N} \qquad \text{- 7.62}$$

where

$T_{Q(max)}$ : torque, Nm

$P$ : motor power, W

$N$ : impeller rotational speed, rev $s^{-1}$

To ensure that process upsets or changes did exceed shaft design limits, the motor power was used instead of impeller power. Individual fractions of motor power were required for the following bending moment equation because the impellers were at different height on the shaft.

$$P_i = P_{i(calculated)} \frac{P_{motor}}{\sum_{i=1}^{n} P_{i(calculated)}} \qquad \text{- 7.63}$$

The maximum bending moment, $M_{max}$, for a top-entry overhung shaft is the sum of the products of the hydraulic forces and the distance from the individual impellers to the bottom bearing in the mixer drive.

The following expression computes an empirical hydraulic force related to the impeller torque acting as a load at a distance related to the impeller diameter.

$$M_{\max} = \sum_{i=1}^{n} \frac{0.048 P_i L_i f_{H_i}}{N D_i} \qquad - 7.64$$

where

$M_{\max}$ : bending moment, Nm

$L_i$ : distance from the drive bearing to the $i^{th}$ impeller location, m

$N$ : impeller rotational speed, rev $s^{-1}$

$D$ : $i^{th}$ impeller diameter, m

$f_{Hi}$ : hydraulic service factor

The hydraulic service factor is related to the impeller type and process operating conditions. Approximate hydraulic service factors for various impellers and conditions are given in Table 7.5.

Table 7.5: Hydraulic service factor

| Condition | HE Impeller | PBT |
|---|---|---|
| Standard | 1.5 | 1.0 |
| Significant time at the free surface | 2.5-3.5 | 2.0-3.0 |
| Operating in boiling system | 2.0-3.0 | 1.5-2.5 |
| Operation in gas sparged systems | 2.5-3.5 | 2.0-3.0 |
| Large volume solid additions | 3.0-5.0 | 3.0-5.0 |
| Inspecting of large solids | 5.0-7.0 | 5.0-7.0 |
| Start-up in settled solids | 5.0-7.0 | 5.0-7.0 |
| Operating in a flow stream | 1.5-7.0 | 1.0-7.0 |

Since the bending moment and the torque act simultaneously, these loads must be combined and resolved into a combined shear stress and a combined tensile stress acting on the shaft.

The minium shaft diameter for the allowable tensile and shear stresses can be calculated by the following equations:

$$d_t = \left( \frac{16(M_{\max} + \sqrt{T_{Q(\max)}^2 + M_{\max}^2})}{\pi \sigma_t} \right)^{1/3} \quad \text{- 7.65}$$

where

$d_t$ : minimum shaft diameter, m

$\sigma_t$ : allowable tensile stress limit, N $m^{-2}$

$$d_s = \left( \frac{16\sqrt{T_{Q(\max)}^2 + M_{\max}^2}}{\pi \sigma_s} \right)^{1/3} \quad \text{- 7.66}$$

where

$d_s$ : minimum shaft diameter, m

$\sigma_s$ : allowable shear stress limit, N $m^{-2}$

The minimum shaft diameter is the greater of the two values calculated from these two equations.

Limits for shear and tensile stresses are function of shaft material, operating temperature and processing environment. It is important to determine the allowable stresses in the condition of operation. Besides strength, the shaft straigthness is also important to avoid creating unnecessary loads and strength.

In this scenario,

$P$ : 0.6224 kW

$N$ : 2.0 rev $s^{-1}$

$T_{Q(\max)} = 49.53$ Nm

It was assumed that the calculated $P_{bottom} = 0.2$ kW and the calculated $P_{top} = 0.1112$ kW

Thus, $P_{bottom} = 0.4001$ kW while $P_{top} = 0.2224$ kW total $P = 0.6224$ kW

$L_{bottom}$ : 0.464, m

$L_{top}$ : 0.214, m

$N$ : 2.0, rev $s^{-1}$

$D_{bottom}$ : 0.340, m

$D_{top}$ : 0.340, m

$f_{H_{bottom}}$ : 7.5

$f_{H_{top}}$ : 7.5

For the top and bottom impeller, service factor for large volume solid additions was 5 but this value was applicable for 4-bladed PBT. For 6-bladed PBT, the value estimated for each impeller was 7.5 owing to an additional of two blades.

The bending moment, $M_{\max}$ was determined to be 0.1117 Nm

Table 7.6: Allowable stresses for shaft and impeller design

| Metal type | Shaft Design Tensile Stress ($Nm^{-2}$) × $10^6$ | Shaft Design Shear Stress ($Nm^{-2}$) × $10^6$ | Impeller Design Stress ($Nm^{-2}$) × $10^6$ |
|---|---|---|---|
| Carbon steel | 62.1 | 37.2 | 75.2 |
| Stainless steel 304 | 66.2 | 40.0 | 80.0 |
| Stainless steel 304L | 57.9 | 35.2 | 70.3 |
| Stainless steel 316 | 68.9 | 41.4 | 83.4 |
| Stainless steel 316L | 60.0 | 35.9 | 72.4 |
| Hastelloy C | 91.0 | 54.5 | 109.6 |
| Hastelloy B | 98.6 | 59.3 | 118.6 |
| Monel 400 | 63.4 | 37.9 | 76.5 |
| Inconel 600 | 71.0 | 42.7 | 85.5 |
| Nickel 200 | 50.3 | 30.3 | 60.7 |
| Carpenter 20 | 76.5 | 45.5 | 91.7 |

The shaft would be made from stainless steel 316 and from Table 7.6,

$\sigma_t$ : $68.9 \times 10^6$, N $m^{-2}$

$\sigma_s$ : $41.4 \times 10^6$, N $m^{-2}$

Thus,

$d_t$ was calculated as 0.01542 m

$d_s$ was calculated as 0.01826 m

Since $d_s$ had the larger value, therefore the minimum shaft diameter was 0.01826 m.

To overcome any process fluctuation, it was recommended that the shaft diameter employed = 0.01826 m × 2 (100% safety margin) = 0.03652 m

### 7.6.5 Shaft critical speed

It was however, important to determine that 120 rpm was not close to the critical speed due to natural frequency. Natural frequency is a dynamic characteristic of a mechanical system. An important concern to a reactor or mixer design is the first lateral natural frequency, which is defined as the lowest frequency at which a shaft will vibrate as a function of length and mass. The concern about natural frequency is that an excitation such as mixer operating speed can cause undamped vibrations.

Undamped vibrations occur when no resisting forces are present to diminish the amplitude of vibration. Such vibrations can result in sudden and catastrophic failure of the mixer shaft and the most dangerous conditions usually occur when the mixer is operated in air. Large mixers normally operate below the first natural frequency, while small portable mixers, which accelerate quickly, often operate above the first natural frequency. In either case, operating at or near the natural frequency must be avoided for both mechanical reliability and safety.

The general rule used to design a mixer shaft and impeller systems is to keep operating the speed at 20% more or less than the critical speed. This rule applies to the first, second and third natural frequencies. However, higher-order natural frequencies are seldom encountered in mixer applications. Large mixers running at less than 150 rpm usually operate below the first critical speed while small mixers operating above 250 rpm usually operate between first and second critical, $1.2N_c$ to $0.8N_{c2}$, where $N_{c2}$ is the second lateral natural frequency [Paul et al. 2004]. The factors that determine the lateral natural frequency are the magnitudes and locations of concentrated and distributed masses, the tensile modulus of elasticity of the material, and the moment of inertia of the shaft.

The equation that estimates the first lateral natural frequency or critical speed, in revolution per second (rev $s^{-1}$), is given by:

$$N_c = \frac{5.33d^2\sqrt{\frac{E_m}{\rho_m}}}{L\sqrt{L+S_b}\sqrt{W_e+\frac{wL}{4}}} \qquad \text{- 7.67}$$

where

$N_c$ : critical speed, rev $s^{-1}$

$d$ : shaft diameter, m

$E_m$ : modulus of elasticity, N $m^{-2}$

$\rho_m$ : density of the shaft material, kg $m^{-3}$

$L$ : length of shaft, m

$S_b$ : bearing spacing supporting the shaft, m

$W_e$ : equivalent mass of the impellers at the bottom of the shaft, kg

$w$ : specific mass of the shaft, kg $m^{-1}$

$W_e$ is the equivalent mass of each impeller resolved to the bottom of the shaft, and is defined mathematically as:

$$W_e = \sum_{i=1}^{n} W_i\left(\frac{L_i}{L}\right)^3 \qquad \text{- 7.68}$$

$W_i$ is the mass of the individual impellers (kg) and $L_i$ is the shaft length to each impeller (m) and $L$ is the total shaft length (m). A single impeller at the bottom of the shaft results in an equivalent mass equal to the actual impeller mass.

Table 7.7: A few common metals properties

| Metal type | Modulus of elasticity, $E_m$ ($Nm^{-2}$) × $10^{12}$ | Density, $\rho_m$ ($kg\ m^{-3}$) |
|---|---|---|
| Carbon steel | 0.205 | 7,833 |
| Stainless steel, 304/316 | 0.197 | 8,027 |
| Hastelloy C | 0.213 | 8,941 |
| Hastelloy B | 0.212 | 9,245 |
| Monel 400 | 0.179 | 8,830 |
| Inconel 600 | 0.214 | 8,415 |
| Nickel 200 | 0.205 | 8,913 |
| Carpenter 20 | 0.193 | 7,999 |

The shaft would be made of stainless steel 316 and with the aid of Table 7.7:

$d$ : 0.03652 m

$E_m$ : 0.197E12 N $m^{-2}$

$\rho_m$ : 8,027 kg $m^{-3}$

$L$ : 0.464 m (0.6 m - 0.2 × 0.68 m)

$S_b$ : 0.3 m

$W_e$ : 16.47 kg (taking the mass of each impeller as 15 kg)

$w$ : 8.408 kg $m^{-1}$ (3.901 kg ÷ 0.464 m)

The critical speed, $N_c$, in this scenario = 20.79 rev $s^{-1}$ or 1,247 rpm

Since the recommended speed of 120 rpm will be operating at least 20% below the critical speed, shaft vibration due to the natural frequency will be avoided.

## 7.7 Comparison between proposed and existing bomb incorporator

### 7.7.1 Suspension of RDX particles

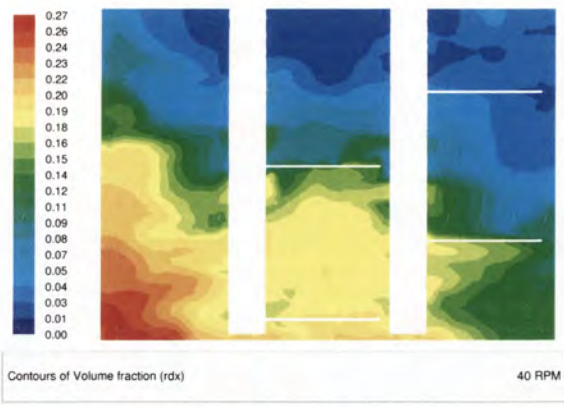


Figure 7.81: Volume fraction of RDX particles - existing

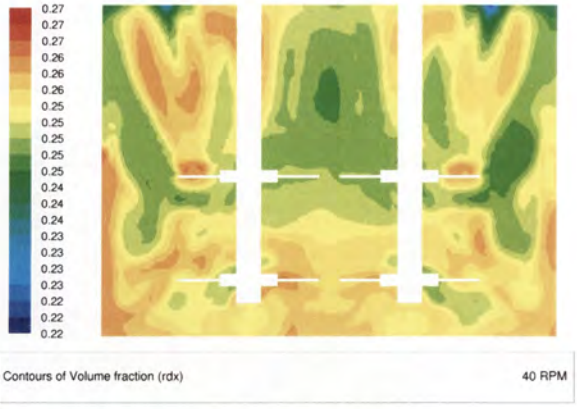


Figure 7.82: Volume fraction of RDX particles - proposed

Figures 7.81 and 7.82 show the contours of volume fraction assigned to the RDX particles for the existing and proposed geometrical configuration respectively. At 40 rpm, a large portion of the RDX particles failed to be suspended as shown by the contour plot. The red zone had a high concentration of RDX because there was not enough bottom clearance for axial flow to develop. Close clearance is known to discharge radial flow and this coupled with the flat bottom tank made it difficult for the RDX particles to flow upward. Consequently, the RDX particles were swept and resided around the corner region [Ochieng and Lewis 2006]. In addition, the range of RDX volume fraction for the RDX particles was rather wide as, shown by the high and low concentration of RDX particles at the bottom and the top of the tank respectively.

In contrast, with the proposed geometrical configuration shown in Figure 7.82, although the RDX particles were not distributed homogeneously, nevertheless, the inhomogeneity was not as bad when compared to the condition experienced in the existing geometrical configuration. This was evidenced from the distribution of RDX particles where no region of highly concentrated RDX particles was observed.

From this comparison, it was concluded that the proposed impellers outperformed the existing geometrical configuration in relation to the suspension of RDX particles. However, the proposed system could not fully suspend the RDX particles due to

insufficient impellers rotational speed. A higher speed will discharge more power into the fluid thereby allocating more kinetic energy to each RDX particles.

A detailed study on the proposed geometrical configuration was conducted where the impellers rotational speed starting from 40 rpm was increased gradually, in step increment of 10 rpm, until it reached a speed of 120 rpm. The contour of volume fraction of RDX particles at each speed was plotted as shown in Figures 7.83-7.88.

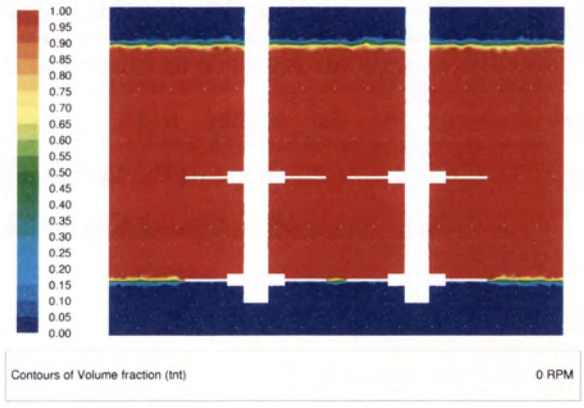


Figure 7.83: Volume fraction of RDX particles – 0 rpm

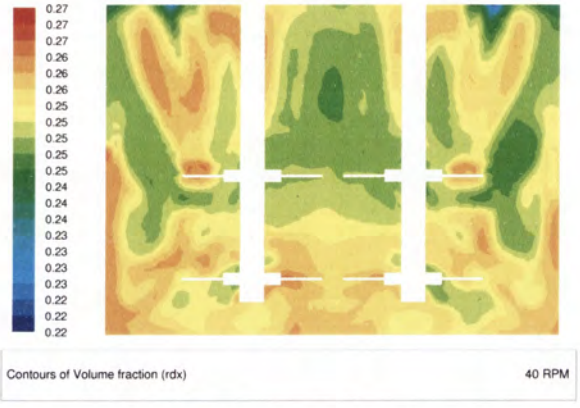


Figure 7.84: Volume fraction of RDX particles – 40 rpm

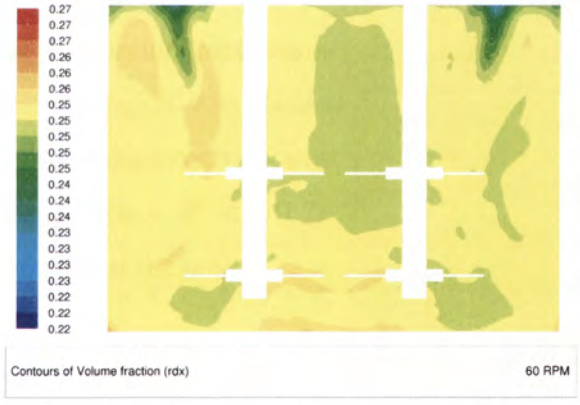


Figure 7.85: Volume fraction of RDX particles – 60 rpm

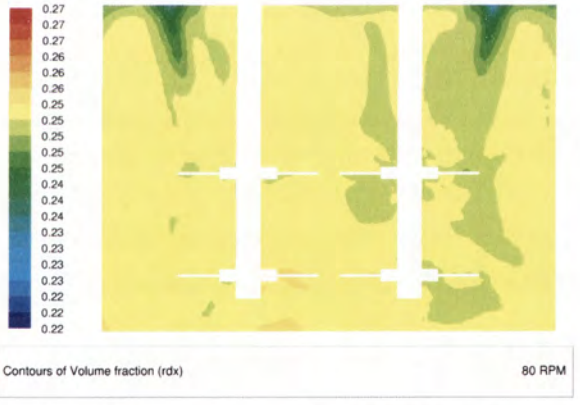


Figure 7.86: Volume fraction of RDX particles – 80 rpm

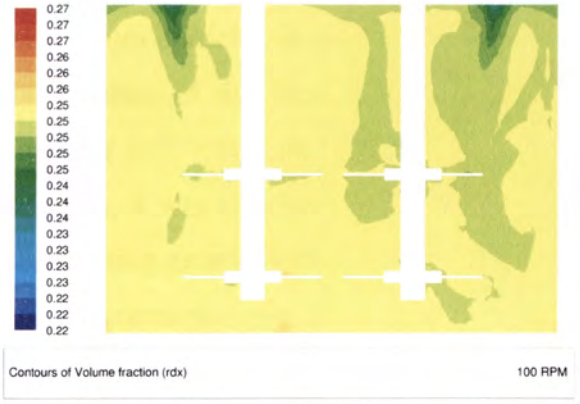


Figure 7.87: Volume fraction of RDX particles – 100 rpm


Figure 7.88: Volume fraction of RDX particles – 120 rpm

From Figures 7.83-7.88, it was observed that significant improvement was derived when the impellers rotational speed was increased from 40 rpm to 60 rpm and from 60 rpm to 80 rpm. At 60 rpm, the RDX particles were quite homogeneously distributed in the molten TNT solution but pockets of higher RDX concentration were concentrated at the tank bottom. This higher concentration of RDX particles was dispersed when the speed was increased from 60 rpm to 80 rpm. Above 80 rpm and up to 120 rpm, the homogeneity of RDX particles improved only slightly. A slightly higher than average concentration of RDX particles was located in the regions such as the tank bottom corner and immediately below the two bottom impellers. A slightly lower RDX particles region was located at the tank top surrounding the left shaft. The existence of the higher RDX particles concentration at the bottom corner was attributed to the flat bottom shape of the tank which did not provide a smooth uninterrupted pathway for the particles to flow upwards [Ochieng and Lewis 2006].

### 7.7.2 Draw-down of aluminium particles

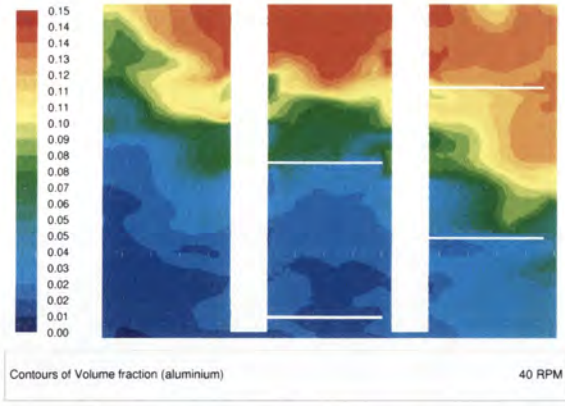


Figure 7.89: Volume fraction of aluminium particles – existing

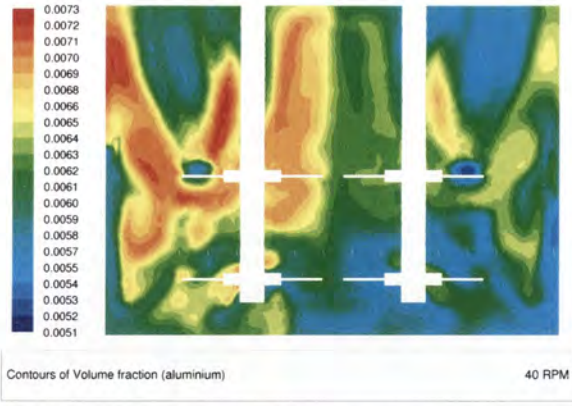


Figure 7.90: Volume fraction of aluminium particles – proposed

Figures 7.89 and 7.90 show the contours of aluminium particles volume fraction in the existing and proposed geometrical configurations respectively. A common feature present in both cases was the gradual reduction in the volume fraction of aluminium particles as the region move from the top to the bottom of the tank, which made logical sense. Despite this common feature, there were a few major differences between these two cases. In the existing geometrical configuration, the contours range was wider and a high concentration of aluminium particles was found at the top of the tank (about 15%) while a very low concentration was located at the bottom of the tank (about 1%). In contrast, with the proposed geometrical configuration, the contours range was much narrower as evidence by the presence of only 0.73% of aluminium particles at the top of the tank and 0.51% at the bottom of the tank.

Obviously, due to the nature of the impellers ($D/T$ = 0.94), which discharged predominantly radial flow, in the existing geometrical configuration, an effective draw-down of aluminium particles could not be realised. The effectiveness draw-down of aluminium particles in the proposed geometrical configuration was attributed to the axial flow nature of the impellers where the $D/T$ = 0.5. As mentioned previously, when an impeller $D/T > 0.5$, the flow transforms from an axial to become radial flow. From this analysis, it was concluded that the proposed geometrical configuration had outperformed the existing geometrical configuration on the draw-down of aluminium particles. What left to be determined was the minimum impellers rotational speed on which the draw-down was most rapid, producing a sustained homogeneous dispersion of aluminium particles in the molten TNT.

A detailed study to determine the minimum impeller speed that resulted in an effective draw-down of aluminium particles was conducted by increasing the impeller speed starting from 40 rpm, gradually in an incremental step of 20 rpm, until it reached 120 rpm. Contours plot of the volume fraction of aluminium particles at each speed was shown in Figures 7.91-7.95.

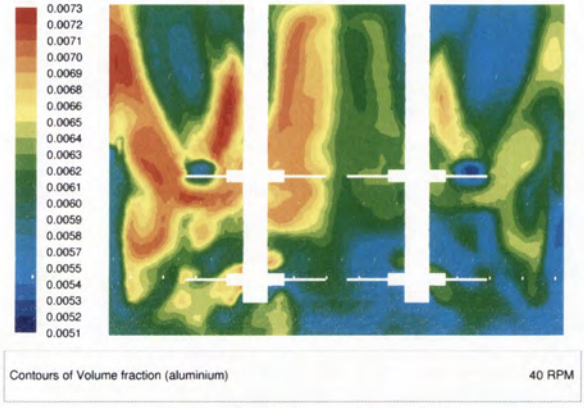


Figure 7.91: Volume fraction of aluminium particles – 40 rpm

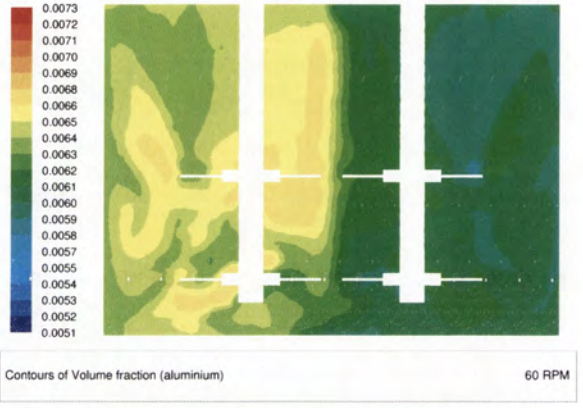


Figure 7.92: Volume fraction of aluminium particles – 60 rpm

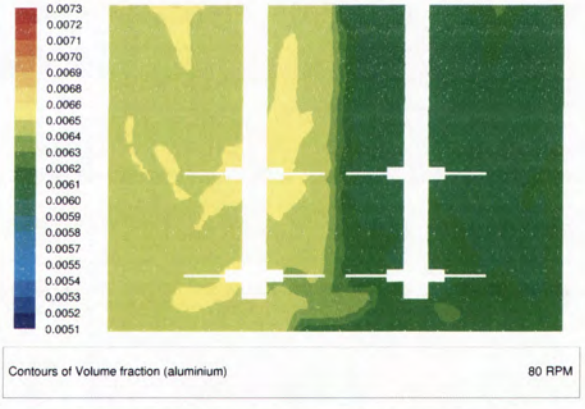


Figure 7.93: Volume fraction of aluminium particles – 80 rpm


Figure 7.94: Volume fraction of aluminium particles – 100 rpm

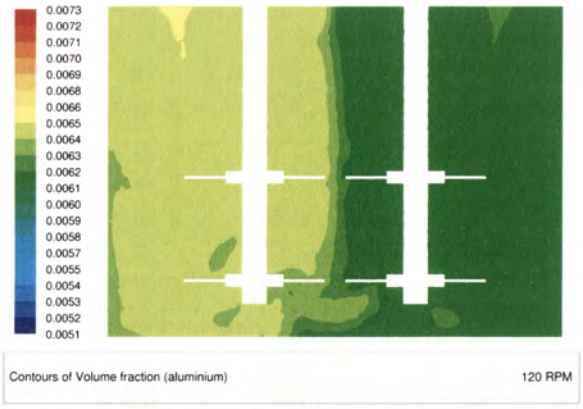


Figure 7.95: Volume fraction of aluminium particles – 120 rpm

Figures 7.91-7.92 show that increasing the impeller rotational speed from 40 rpm to 60 rpm made significant improvement on the draw-down ability and the homogeneity of the aluminium particles. At 80 rpm and above, shown in Figures 7.93-7.95, only slight improvement was achieved as shown by the reduction in the size of the higher concentration region located next to the left shaft. This concluded that a minimum impeller rotational speed of 80 rpm was required to effectively draw-down the aluminium particles.

### 7.7.3 Increasing bomb production rate

Achieving a homogenous mixture with a view to producing better quality bombs was only one of the two objectives of this research work. The other objective was to increase the production rate of the bomb making facility. This objective could be achieved by increasing the draw-down rate of aluminium particles. A way of achieving this was to increase the impeller rotational speed beyond the minimum impeller speed. To determine the increase in the draw-down speed, surface integrations were conducted on three surfaces created as shown in Figure 7.96.

Figure 7.96: Axial flow – across tank horizontal planes

The three horizontal planes shown in Figure 7.96 above were created at 0.1 m, 0.3 m and 0.5 m above the tank bottom. This was to determine the amount of material flowing through the planes below the impellers, in the case of particles suspension, between the impellers and above the impellers, in the case of floating particles draw-down. The plane between the impellers was created to determine whether the flow was axial in nature. For instant, if the flow emanating from the top of the impellers was higher than or even equal to the flow calculated via the plane situated between the impellers, then the majority of the flow must be radial in nature since such flow will not flow past this plane.

Table 7.8: Mass flowrates at various impellers rotational speed.

| N (rpm) | Below impellers (kg $s^{-1}$) | Between impellers (kg $s^{-1}$) | Above impellers (kg $s^{-1}$) |
|---|---|---|---|
| 40 | 178 | 228 | 125 |
| 60 | 275 | 351 | 193 |
| 80 | 363 | 461 | 254 |
| 100 | 440 | 564 | 317 |
| 120 | 542 | 688 | 381 |

Table 7.8 shows the mass flowrates calculated at each plane at various impellers rotational speed. These results were converted into graphical form as shown in Figure 7.97.

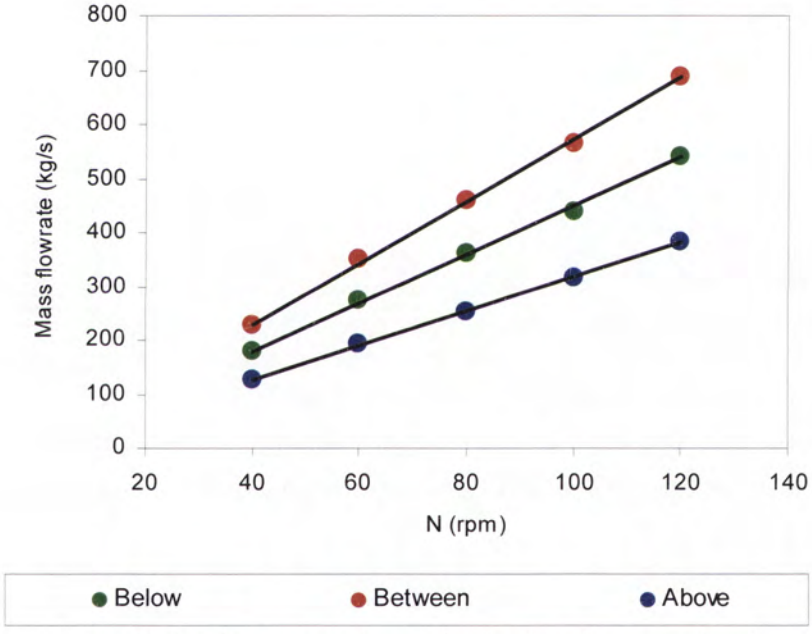


Figure 7.97: Mass flowrate across plane as a function of impellers rotational speed

Figure 7.97 shows the relationship between mass flowrate passing through the axial plane and the impeller rotational speed. This relationship follows a linear expression in the form:

Below impellers (regression = 0.9983):

$$\dot{m} = 4.492N \qquad \text{- 7.69}$$

Between impellers (regression=0.9989):

$$\dot{m} = 5.723N \qquad \text{- 7.70}$$

Above impellers (regression=0.9997):

$$\dot{m} = 3.176N \qquad \text{- 7.71}$$

Figure 7.97 shows that the mass flowrate calculated from all three planes increased linearly as a function of impellers rotational speed. For example, if the impeller speed was increased to 120 rpm although the minimum speed required to draw-down the aluminium particles is 80 rpm, then from Table 7.8 above, the draw-down rate will be doubled, that is, it will take only half the time to draw-down the same amount of aluminium particles. Moreover, the rate of RDX particles suspension will also be 1.5 times faster than if the system was operated at a minimum impeller rotational speed of 80 rpm. Therefore, the recommended speed of 120 rpm will result in a faster incorporation of aluminium particles and suspension of RDX particles, thereby increasing the bomb making production rate. Results computed from the plane located between the impellers indicated strong axial flow since the mass flowrate increased substantially.

## 7.7.4 Proposed incorporator air draw-down

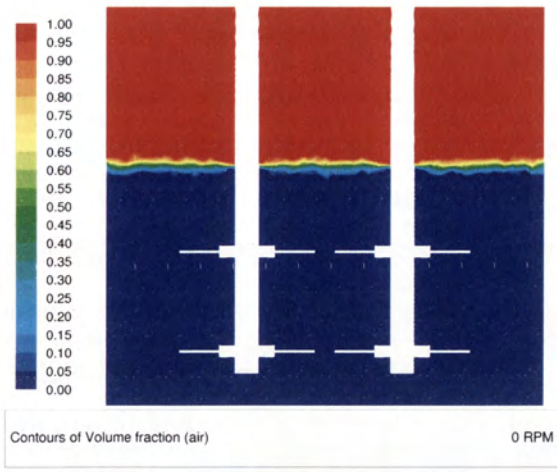


Figure 7.98: Volume fraction of air draw-down at 0 rpm

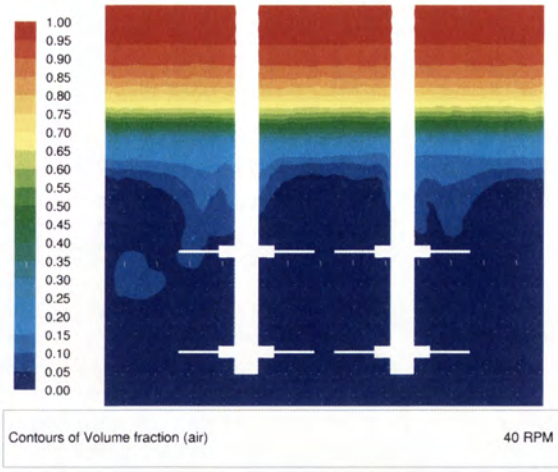


Figure 7.99: Volume fraction of air draw-down at 40 rpm

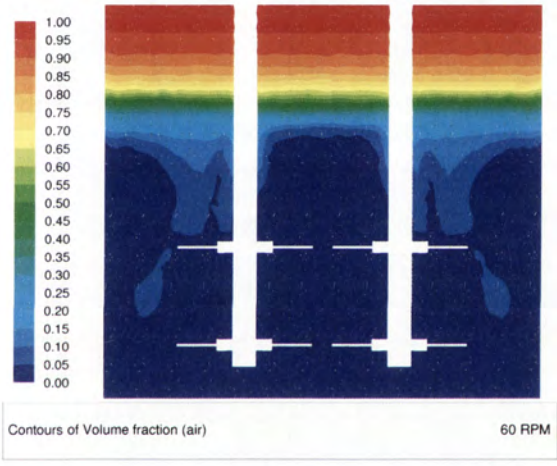


Figure 7.100: Volume fraction of air draw-down at 60 rpm

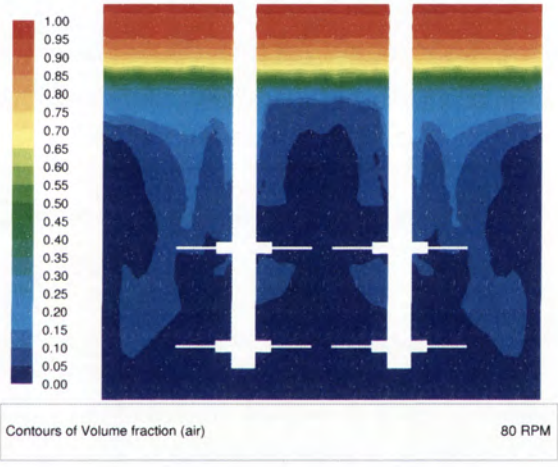


Figure 7.101: Volume fraction of air draw-down at 80 rpm

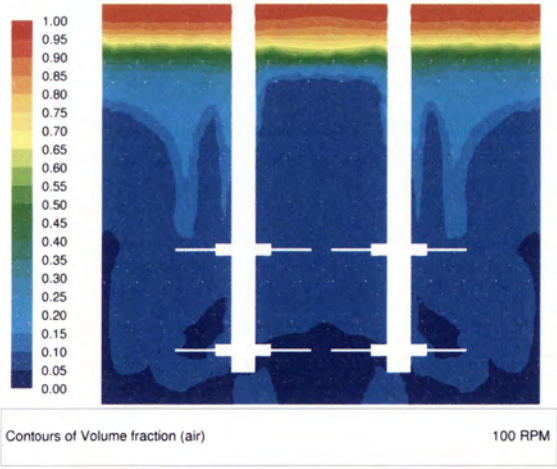


Figure 7.102: Volume fraction of air draw-down at 100 rpm

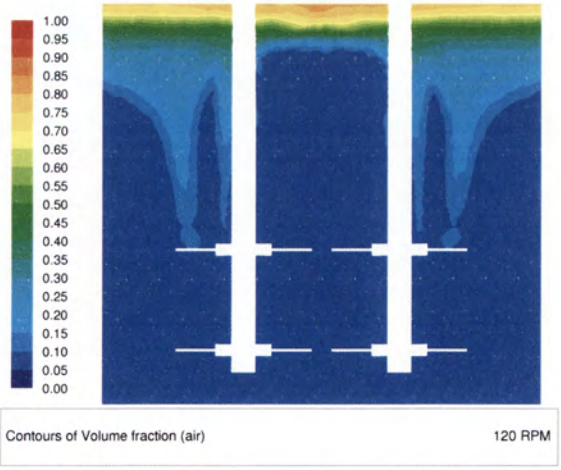


Figure 7.103: Volume fraction of air draw-down at 120 rpm

Figures 7.98-7.103 show the contour of air volume fraction at different impellers rotational speed ranging from 0 rpm to 120 rpm. Figure 7.98 shows the location of liquid free surface when the impellers were stationary. The red shade represents air, blue shade represents H6 and the green shades represent 50% air – 50% H6 mixture. At 40 rpm, some air was drawn down and reached the top impeller. However, the percentage of air drawn down in this case was only 5% and in physical significance can be translated as tiny bubbles. At 60 rpm, a small amount of these bubbles penetrated deeper and past beyond the top impellers. Moreover, a second wave of air has started to be drawn down. Although it was only a shallow draw-down, nevertheless its concentration was higher and registered as 10% air. At 80 rpm, this 10% air reached down to a level just slightly above the top impellers. In contrast, the first wave which consisted of 5% air has reached down to a level where the two bottom impellers were located. At 100 rpm, a third wave consisting of 20% air has started to be drawn down, while the second wave consisting of 10% has reached a level just slightly above the top impellers. The first wave consisting 5% air, has reached down to the bottom of the tank. Finally at 120 rpm, the third wave was halfway through between the top impellers and the free surface, while the second wave has reached the top impellers and the first wave has been dispersed throughout the tank.

Figure 7.104: Free surface 50%-50% air/H6 at 0 rpm

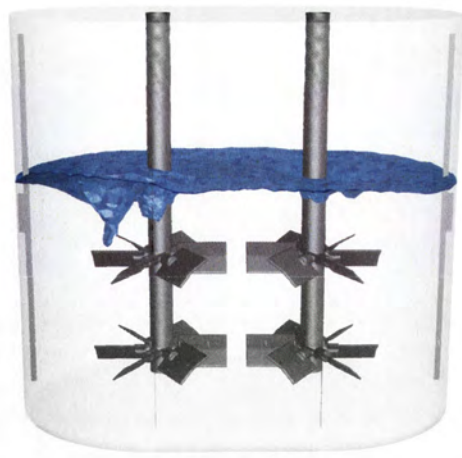

Figure 7.105: 10% volume of air drawn down at 40 rpm

Figure 7.106: 10% volume of air drawn down at 60 rpm

Figure 7.107: 10% volume of air drawn down at 80 rpm

Figure 7.108: 10% volume of air drawn down at 100 rpm

Figure 7.109: 10% volume of air drawn down at 120 rpm

Figure 7.110: 10% volume of air drawn down at 120 rpm

Figures 7.104-7.110 aimed to provide a clearer illustration on the draw-down of air at 120 rpm. Figure 7.104 shows the free surface level, separating air from the H6 mixture. Figures 7.105-7.110 show the contour plot of the air volume fraction at iso-surface 10% air. At 40 rpm, draw-down of bubbles started to occur on the left shaft, at 60 rpm, this draw-down was extended to the other shaft as well. At 80 rpm, deepened to a level just slightly above the top impellers and at 100 rpm, the bubbles reached down to the top impellers. Finally, bubbles drawn down passed through the top impeller at 120 rpm.

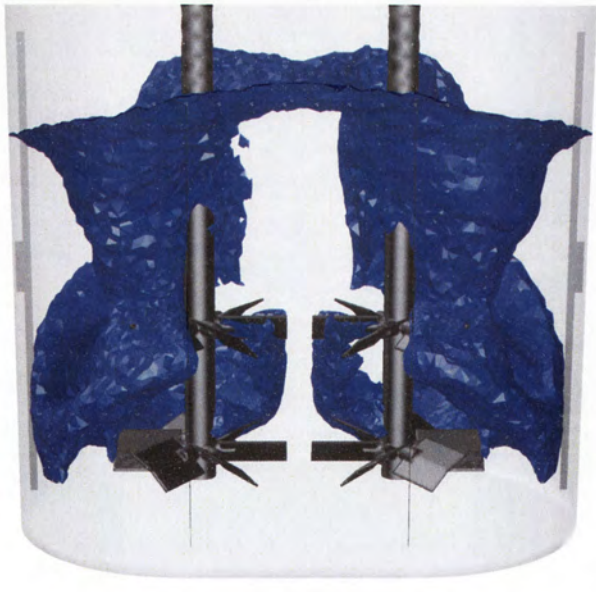

Figure 7.111: 6.8% volume of air drawn down at 120 rpm

Figure 7.111 shows the contour plot of the iso-surface created at 6.8% of air. It can be assumed that due to the utilisation of narrow baffles and axial flow impellers, the draw-down of floating particles will be rapid. However, in doing so, some bubble entrainments occurred and were drawn down as well. This might not necessarily means that the bubbles will be carried to the outlet located at the middle of the tank bottom, between the two shafts. Even if some were, these bubbles will rise to the H6 liquid free surface before being filled into the bomb.

Figures 7.112-7.117 show 3D representations of the phenomena that took place when the tank content was being transferred to another unit operation. At 80 rpm, 50% of air will be drawn-down to the region located just slightly above the bottom impellers. At 120 rpm, 50% of air will be drawn-down to the space located below the bottom impellers. Since the bottom outlet is located between the two shafts, this air drawn-down may not be entrained into the bombs because in the region between the two shafts draw-down speed is not high, thus the air drawn-down may rise up to the top of the bomb incorporator.

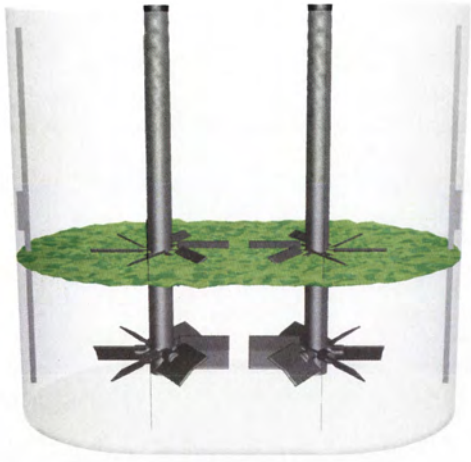

Figure 7.112: Free surface 0.4 m from tank bottom

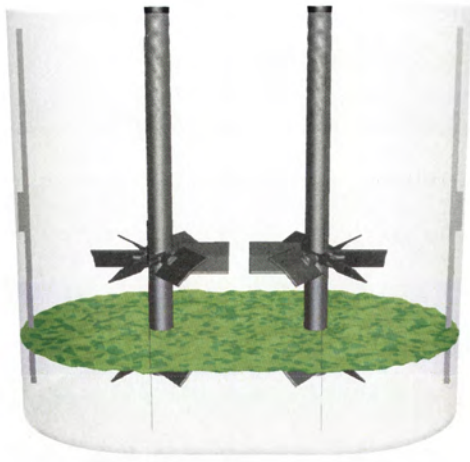

Figure 7.113: Free surface at 0.2 m from tank bottom

Figure 7.114: 50% volume of air drawn down at 80 rpm

Figure 7.115: 50% volume of air drawn down at 80 rpm

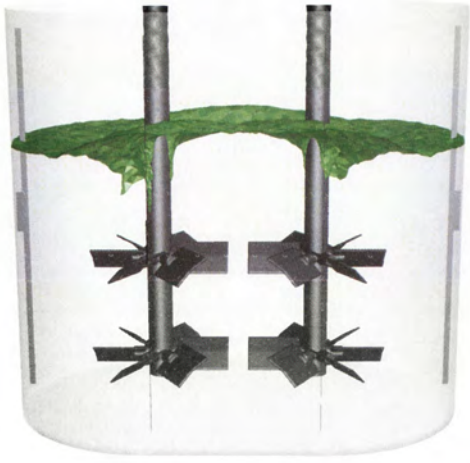

Figure 7.116: 50% volume of air drawn down at 120 rpm

Figure 7.117: 50% volume of air drawn down at 120 rpm

## 7.8 Modelling using Eulerian multiphase model

The H6 geometry was remeshed with a lower number of cells. This was required because the memory requirement using the Eulerian model to simulate three phases exceeded the memory available. The meshed geometry consisted of 793,034 cells. The maximum cells size for tank volume meshing used was 25. And for the impellers, the size function included a start size of 7, growth factor of 1.2 and size limit of 20. Equisize skew obtained was 0.8211.

Other numerical setup included using phase coupled SIMPLE for pressure-velocity coupling calculation and specifying Schaeffer equation which is not available in the mixture model, for frictional viscosity calculation. Lun et al. [1984] option was selected for granular bulk viscosity for RDX particles and a constant 0 value specified for aluminium particles.

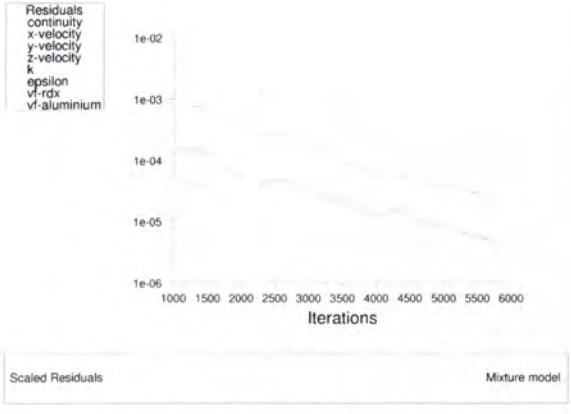


Figure 7.118: Mixture multiphase model

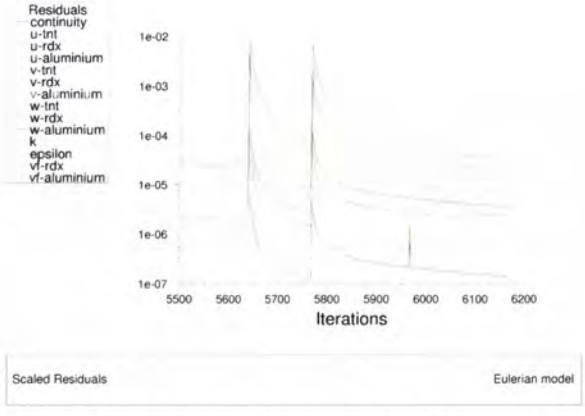


Figure 7.119: Eulerian multiphase mixture turbulence model

Figure 7.118 shows the residuals plot using the mixture model where most of the residuals have fallen below 1E-04 using the first-order upwind scheme. Moreover, the residuals representing the variables calculated included only the continuity, x-velocity, y-velocity, z-velocity (velocity magnitude of the mixed media), $k$ (turbulence kinetic energy), $\varepsilon$ (turbulence dissipation rate), vf-rdx (volume fraction of rdx) and vf-aluminium (volume fraction of aluminium). At around the 5,650$^{th}$ iteration, the calculation was switched to full Eulerian multiphase model using the first-order upwind scheme, as shown by the first spike (cf Figure 7.119). When the residuals dropped to below 1E-04, the accuracy of calculation was increased by utilising the second-order upwind scheme. This was represented by the

second spike which occurred at the 5,775$^{th}$ iteration. The residuals fall below 1E-04 at 5,950$^{th}$ iteration.

The main difference between the two models is that in the Eulerian model, the velocity magnitude in the three directions was calculated for each phase such as the u-tnt, v-tnt, w-tnt, u-rdx, v-rdx, w-rdx and u-aluminium, v-aluminium and w-aluminium. Although the $k$-$\varepsilon$ residuals were the same, that was because within the Eulerian model, the mixture turbulence model was employed. As previously mentioned the mixture turbulence model is the default multiphase turbulence model and represents the first extension of the single-phase $k$-$\varepsilon$ models. It is applicable when phases separate for stratified multiphase flows and when the density ratio between phases is close to 1. In these cases, using mixture properties and mixture velocities are sufficient to capture important features of the turbulent flow. The most general multiphase turbulence model solves a set of $k$-$\varepsilon$ transport equations for each phase. This turbulence model is the appropriate choice when the turbulence transfer among the phases plays a dominant role.

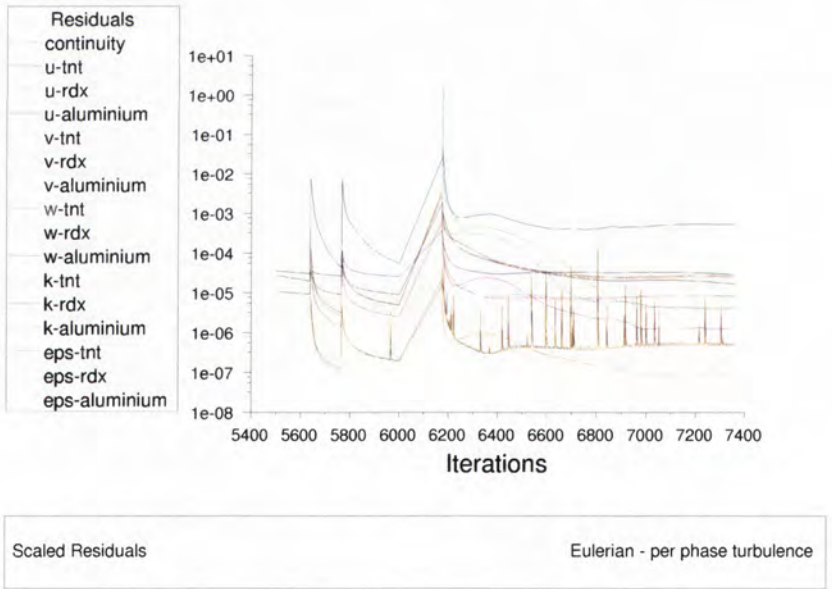


Figure 7.120: Eulerian multiphase per phase turbulence model

Figure 7.120 shows the residuals plot when the Eulerian multiphase per phase turbulence model was selected. The switch from Eulerian mixture turbulence model to Eulerian per phase turbulence model, represented by a spike is shown in 6,180$^{th}$ iteration. In this case, Fluent® solved two additional transport equations for each secondary phase rendering this model more computationally intensive than the other models. That is, the transport

equations for secondary phases RDX and aluminium were also computed as represented in the residuals plot by $k$-TNT (primary), $k$-RDX, $k$-aluminium and $\varepsilon$-TNT (primary), $\varepsilon$-RDX, and $\varepsilon$-aluminium.

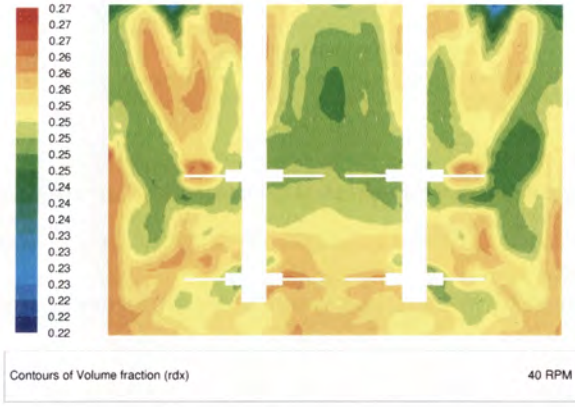


Figure 7.121: Vol fraction of RDX particles – mixture model

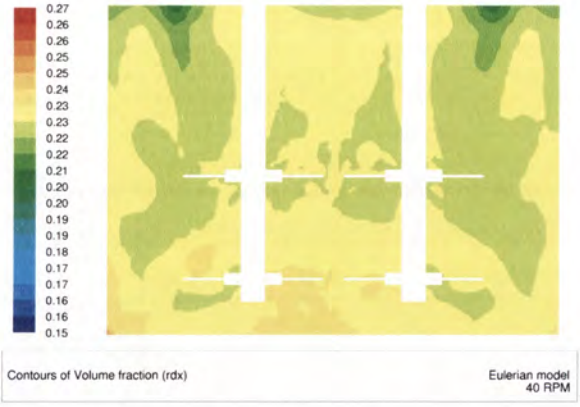


Figure 7.122: Vol fraction of RDX particles – Eulerian model

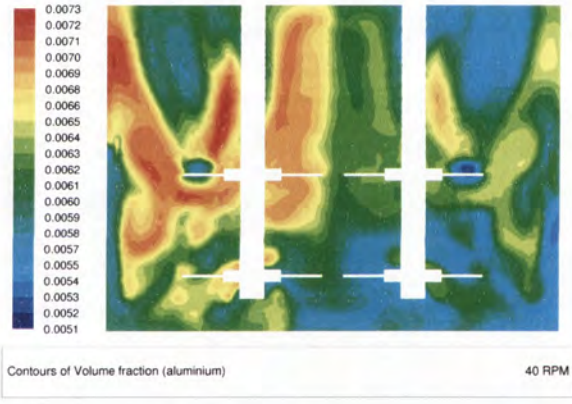


Figure 7.123: Vol fraction of aluminium particles – mixture model

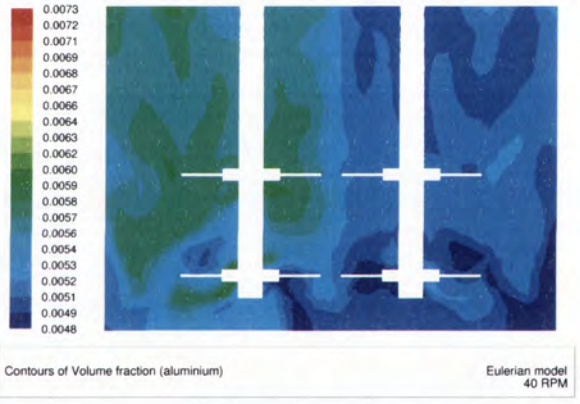


Figure 7.124: Vol fraction of aluminium particles – Eulerian model

Figure 7.121 and 7.123 are the contour plot of the volume fraction of RDX particles and aluminium particles respectively, computed via the Euler-Euler mixture model. Figures 7.122 and 7.124 represent the contour plot of RDX particles and aluminium particles respectively, computed via the full Eulerian multiphase model [Kerdouss et al. 2006]. When Figure 7.121 is compared to Figure 7.122, it can be seen that a certain degree of similarity in the pattern of the volume fraction exists. However, the mixture model overpredicted the amount of RDX particles by 8%, relative to that obtained via the Eulerian model. Similar phenomenon was experienced when Figure 7.123 was compared to Figure 7.124. In this case, the pattern is similar but the mixture model overpredicted the amount of aluminium particles by 10%, relative to the amount predicted by the Eulerian model.

Table 7.9: Comparison of the flowrates passing through an integrated plane between the mixture and Eulerian models

| Model, rpm | Mixture | Eulerian |
|---|---|---|
| Below impellers, kg $s^{-1}$ | 178 | 169 |
| Between impellers, kg $s^{-1}$ | 228 | 230 |
| Above impellers, kg $s^{-1}$ | 125 | 132 |

Table 7.9 shows the flowrates passing through horizontal planes, purposely built to determine the amount of flow passing through the impeller. The results obtained from the mixture and the Eulerian models were compared to each other. It shows that in all three planes, the difference between the two models is less than 6%. This is a good example where if the mixture model can be used, it should be used in place of the Eulerian model, which is computationally more demanding.

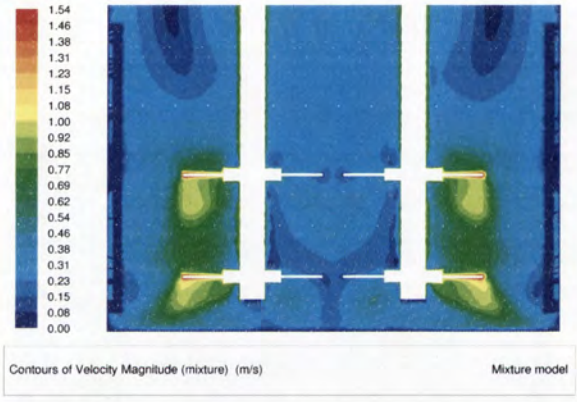


Figure 7.125: Velocity magnitude of mixture – mixture model

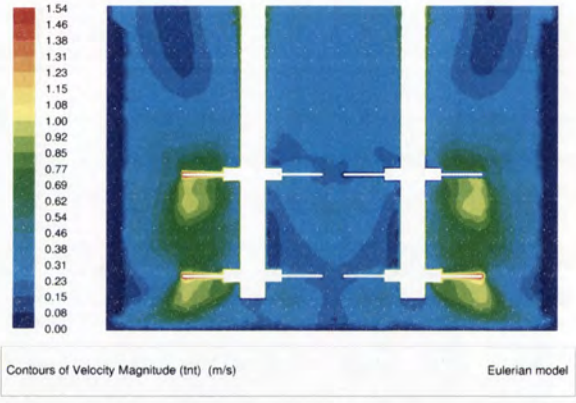


Figure 7.126: Velocity magnitude of TNT – Eulerian model

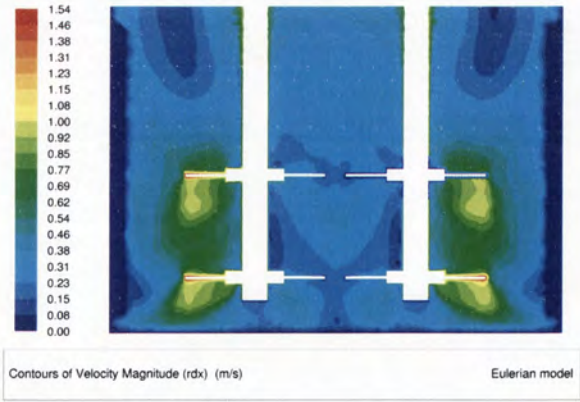


Figure 7.127: Velocity magnitude of RDX– Eulerian model

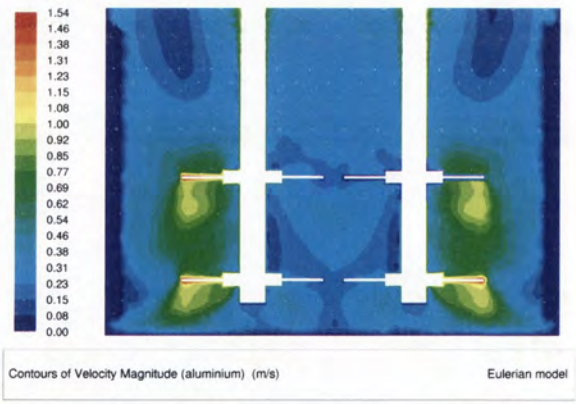


Figure 7.128: Velocity magnitude of aluminium– Eulerian model

Figure 7.125 shows that the mixture model can only produced a velocity magnitude of mixed components. In contrast, the Eulerian model can produce the contour of velocity magnitude of each component, as shown in Figures 7.126-7.128. They are similar because

from the Stokes number, the solid phase in this case followed a trajectory similar to the fluid flow pattern.

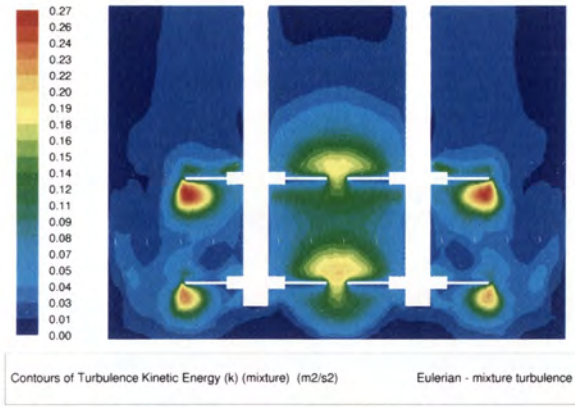


Figure 7.129: Eulerian mixture turbulence model - $k$

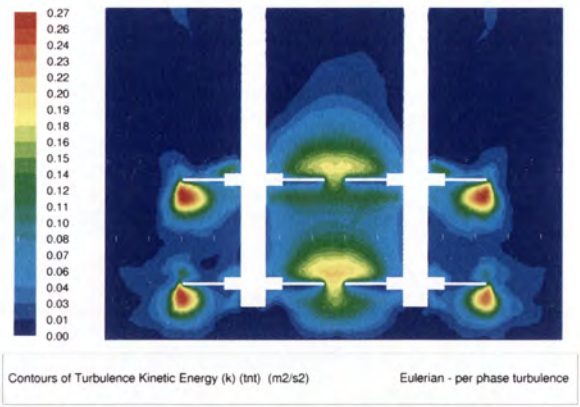


Figure 7.130: Eulerian per phase model - TNT - $k$

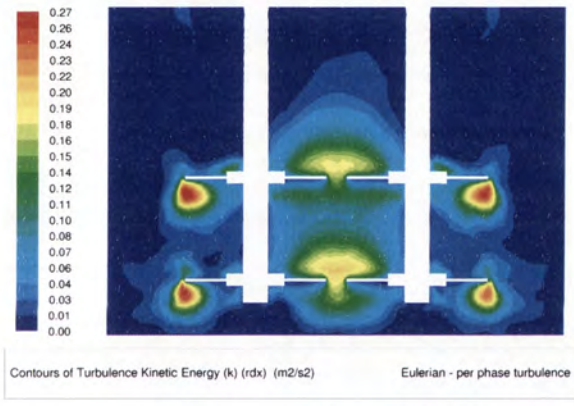


Figure 7.131: Eulerian per phase model - RDX - $k$

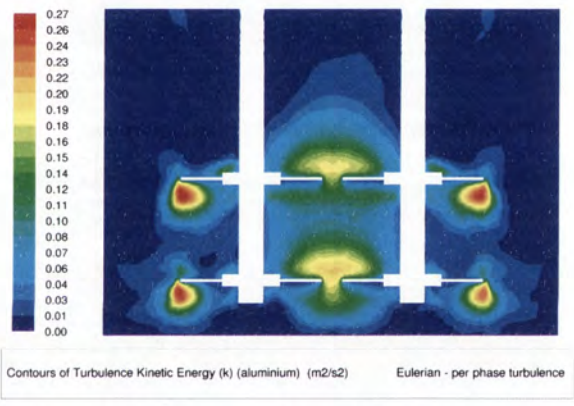


Figure 7.132: Eulerian per phase model - Aluminium - $k$

Similarly, Figure 7.129 shows that the mixture model can only produce contours of turbulence kinetic energy of all three mixed components. In contrast, the Eulerian model can produce the contour of turbulence kinetic energy of each component, as shown in Figures 7.130-7.132. They are similar because from the Stokes number where the solid phase in this case followed a trajectory similar to the fluid flow pattern. Had this study involved particles that move independently of the path taken by the fluid, the contours of turbulence kinetic energy would have been different from one another. This explanation covers the contours plot of the turbulence dissipation rate, as shown in Figure 7.133 (mixture model) and Figures 7.134-7.136 (Eulerian model).

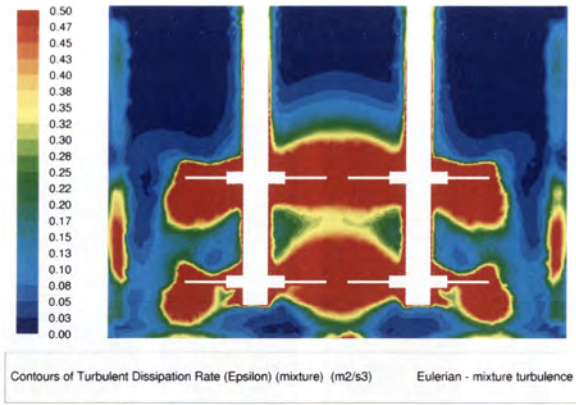


Figure 7.133: Eulerian mixture turbulence model - $\varepsilon$

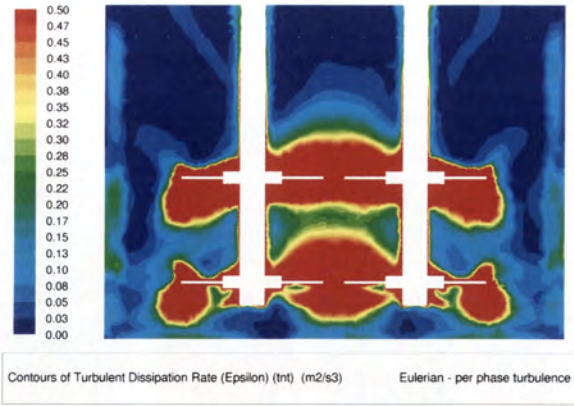


Figure 7.134: Eulerian per phase model - TNT - $\varepsilon$

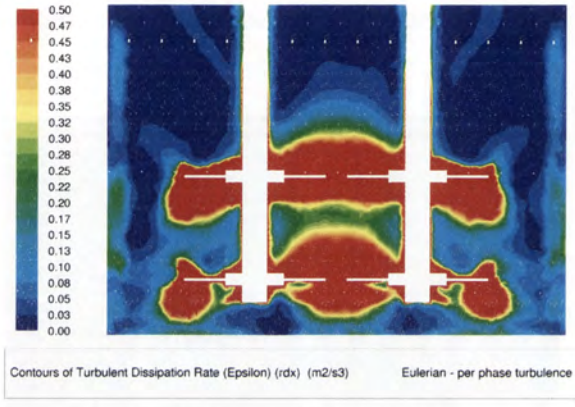


Figure 7.135: Eulerian per phase model - RDX - $\varepsilon$

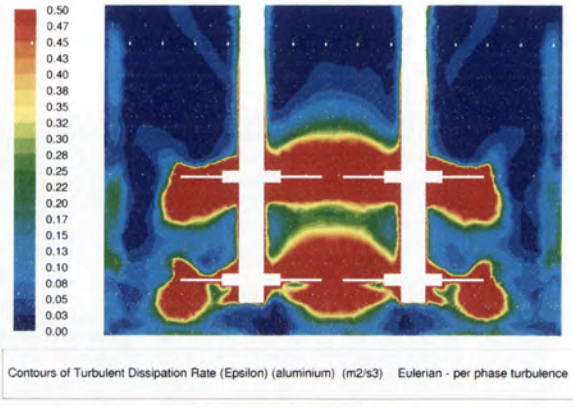


Figure 7.136: Eulerian per phase model - Aluminium - $\varepsilon$

## 7.9 Simulations using polyhedral cells

Several simulations were conducted using Fluent® 6.3 solver which incorporates a new type of cell called the polyhedral cells. The main feature present in Fluent® 6.3 but not available in Fluent® 6.2 is the availability of polyhedral cells that can be used to compute the solution. Besides this, there are several features elaborated below are not available in Fluent® 6.2.

### 7.9.1 Conversion to polyhedral cells

The main advantage that polyhedral cells have shown over some of the tetrahedra or hybrid cells is the lower overall cell count, almost 3-5 times lower for unstructured meshes than the original cell count. Currently, there are two options in Fluent® 6.3 that allows the conversion from nonpolyhedral to polyhedral cells, namely:

- Converting the entire domain into polyhedral cells
- Converting skewed tetrahedra cells to polyhedral cells

The conversion of a mesh to polyhedral only applies to 3D meshes that contain tetrahedral, wedge or prism cells. The conversion process begins by the decomposition of each non-polyhedral cell into multiple sub-volumes called 'duals'. Each dual is associated with one of the original nodes of the cell. These duals are then agglomerated into polyhedral cells around the original nodes. Thus, the collection of duals from all cells sharing a particular node makes up each polyhedral cell, as shown in Figure 7.137. The node that is now within the polyhedral cell is no longer needed and is removed.

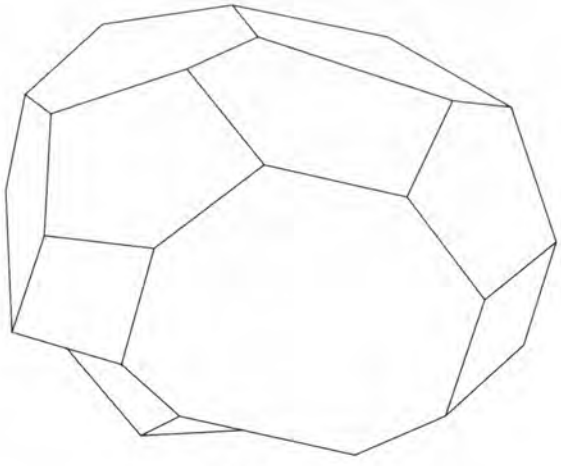

Figure 7.137: A polyhedral cell

A few limitations unique to polyhedral cells are:

- Meshes that already contain polyhedral cells cannot be converted
- Meshes with hanging nodes will not be converted
- Meshes in which the domain has been converted to polyhedral cells are not eligible for adaption
- The following grid manipulation tools are not available on polyhedral meshes:
    - ⇒ extrude-face-zone under the modify-zone option
    - ⇒ fuse
    - ⇒ skewness smoothing
    - ⇒ swapping will not affect polyhedral cells
- The dynamic mesh model cannot be used on polyhedral cells

Another method of cell agglomeration is the skewness-based cluster approach [Fluent 2007]. This type of conversion is designed to convert only part of the domain. The objective is to convert only skewed tetrahedral cells above a specified cell equivolume skewness threshold into polyhedral. By converting the highly skewed tetrahedral cells, the quality of the mesh can be improved significantly. A different algorithm is used for local conversion. This algorithm evaluates each highly skewed cell that best matches criteria for cell agglomeration. Then all of the cells which share this edge are combined into a polyhedral cell. During the process, the data is interpolated from the original cells to the resultant polyhedral.

A few limitations unique to this type of conversion are:

- Only tetrahedral cells are converted, as all other cells are skipped
- Meshes with hanging nodes will not be converted
- Meshes in which the domain has been converted to polyhedral cells are not eligible for adaption
- The following grid manipulation tools are not available on polyhedral meshes:
    - ⇒ extrude-face-zone under the modify-zone option
    - ⇒ fuse
    - ⇒ skewness smoothing
    - ⇒ swapping will not affect polyhedral cells

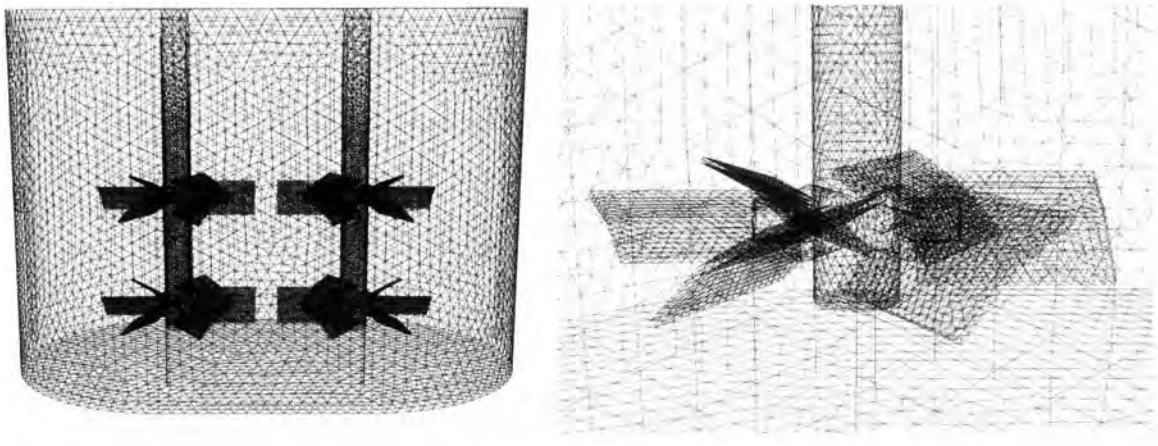

Figure 7.138: Grid display of 793,034 tetrahedra cells before conversion to polyhedral cells

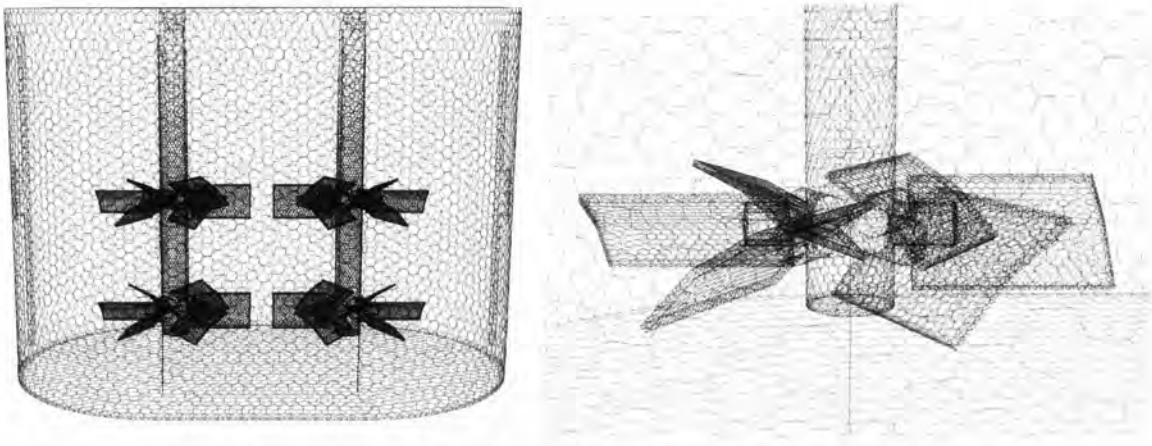

Figure 7.139: Grid display of 241,155 polyhedral cells after conversion from hexahedral cells

Figure 7.138 shows 793,034 tetrahedra cells which were converted to 241,155 polyhedral cells as shown in Figure 7.139. The conversion of process did not require a substantial amount of time but it did require more computer memory.

### 7.9.2 Numerical setup

In Fluent® 6.3, the two numerical methods offered are the pressure-based solver and the density-based solver. In general, the pressure-based approach (segregated equivalent in Fluent® 6.2) was developed for low-speed incompressible flows, while the density-based approach (coupled equivalent in Fluent® 6.2) was mainly used for high-speed compressible flows. However, recently both methods have been extended and reformulated to solve and operate for a wide range of flow conditions beyond their traditional or original intent. In

both methods the velocity field is obtained from the momentum equations. In the density-based approach, the continuity equation is used to obtain the density field while the pressure field is determined from the equation of state. In contrast, in the pressure-based approach, the pressure field is extracted by solving a pressure or pressure correction equation which is obtained by manipulating continuity and momentum equations. For this particular simulation, the pressure-based approach was adopted.

For the gradient selection, Fluent® 6.3 offers the Green-Gauss cell-based, Green-Gauss node-based and Least Squared cell-based. When the Green-Gauss theorem is used to compute the gradient of the scalar $\phi$ at the cell centre c0, the following discrete form is written as:

$$(\nabla\phi)_{c0} = \frac{1}{v}\sum_{f}\bar{\phi}_f \bar{A}_f \qquad \text{- 7.72}$$

where $\phi_f$ is the value of $\phi$ at the cell face centroid, computed depending on the method used. If the method used is Green-Gauss cell-based, then it is obtained by:

$$\phi_f = \frac{\phi_{c0} + \phi_{c1}}{2} \qquad \text{- 7.73}$$

Where the face value $\phi_f$ is taken from the arithmetic average of the values at the neighbouring cell centres. But if the method used is Green-Gauss node-based and $N_f$ is the number of nodes on the cell face, then $\phi_f$ is computed via:

$$\bar{\phi}_f = \frac{1}{N_f}\sum_{n}^{N_f}\bar{\phi}_n \qquad \text{- 7.74}$$

Finally, in the Least Squares cell-based method, the solution is assumed to vary linearly. The change in the cell values between cell *c0* and *ci* along the vector $\delta r_i$ from the centroid of cell *c0* to cell *ci*, can be expressed as:

$$(\nabla\phi)c0 \cdot \Delta r_i = (\phi ci - \phi c0) \qquad \text{- 7.75}$$

When a flow solution is solved on polyhedral meshes, the cell-based least squares gradients are recommended for use, especially if a more accurate flow solution is required, over the default cell-based gradients [Fluent 2007]. But for triangular or tetrahedral meshes, the accuracy obtained using the cell-based least squares gradients is similar to those obtained from node-based gradients. In this situation, the node-based gradients are recommended since they are more stable. In this simulation involving the polyhedral cells, the cell-based least squares gradients were employed.

For the pressure-velocity coupling selection, the coupled approach was adopted because it offers several advantages over the non-coupled or segregated approach. The coupled scheme obtains a robust and efficient single phase implementation for steady-state flows, with superior performance compared to the segregated solution schemes. This pressure-based coupled algorithm offers an alternative to the density-based and pressure-based segregated algorithm with SIMPLE-type pressure-velocity coupling. The pressure-based segregated algorithm solves the momentum equation and pressure correction equations separately, therefore, this semi-implicit solution method results in slow convergence. In contrast, the coupled algorithm solves the momentum and pressure-based continuity equations together, thus resulting in faster convergence [Fluent 2007]. This coupled approach is recommended for transient flows, when the quality of the mesh is poor or if large time steps are used.

### 7.9.3 Results using polyhedral cells

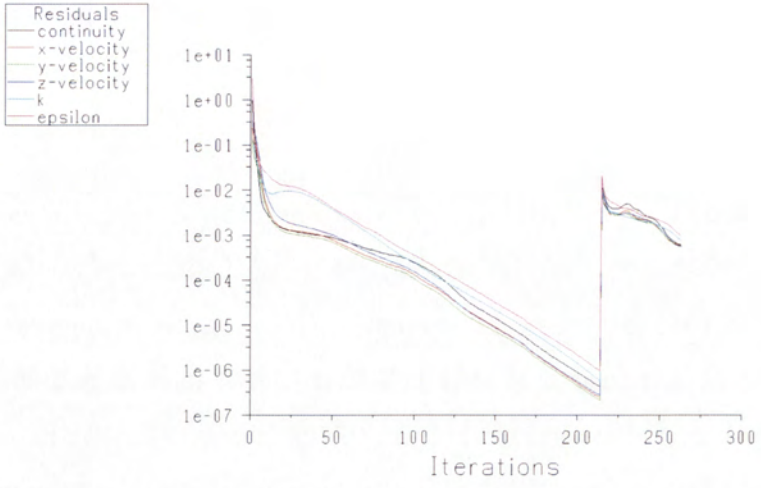


Figure 7.140: Residual plot of simulation using polyhedral cells

The residuals plot in Figure 7.140 shows that for the residuals to fall below 1E-03 required only 80 iterations, 1E-04 required only 127 iterations, 1E-5 required only 173 iterations and 1E-06 required only 214 iterations. Time taken for the residuals to fall below 1E-06 was 30 mins.

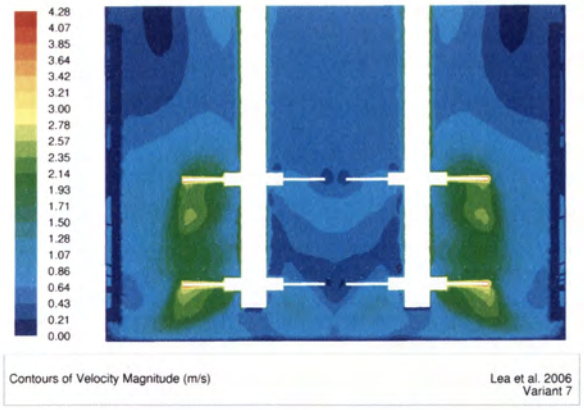


Figure 7.141: Simulation using tetrahedral cells

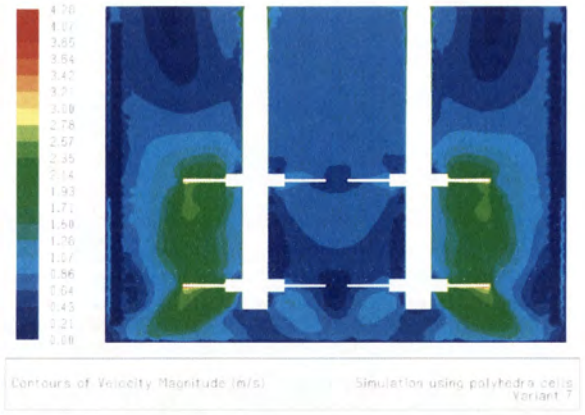


Figure 7.142: Simulation using polyhedral cells

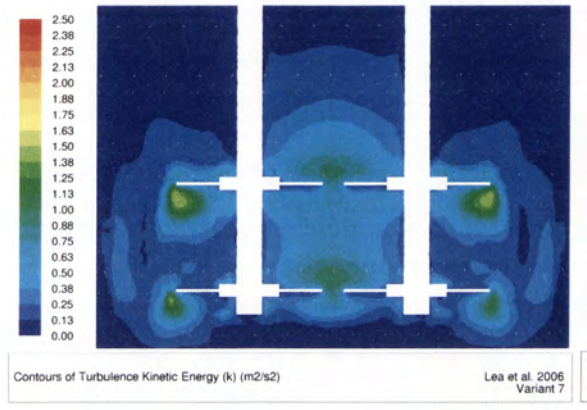


Figure 7.143: $k$-$\varepsilon$ simulation using tetrahedral cells

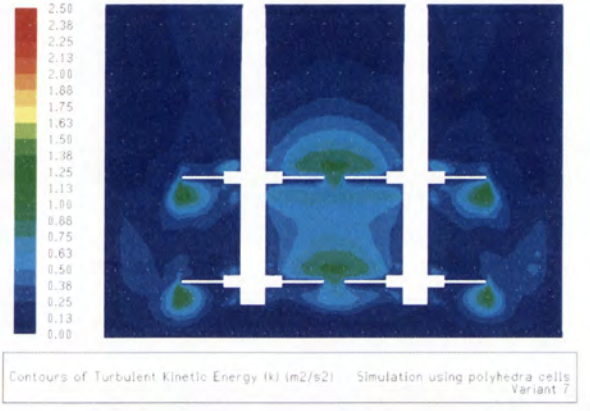


Figure 7.144: $k$-$\varepsilon$ simulation using tetrahedral cells

Figures 7.141 and 7.142 show the contours of velocity magnitude obtained using tetrahedra and polyhedral cells respectively. The variation between these two types of cells is minimal. Figures 7.143 and 7.144 show the contours of turbulence kinetic energy obtained using tetrahedra and polyhedral cells. Again the variation is smaller but the one produced from tetrahedra cells displayed a higher level of turbulence kinetic energy on the region surrounding the impellers.

## 7.10 Concluding remarks

In this chapter the multiphase modelling and simulation of H6 bomb incorporator were conducted. Cyclotol, discussed in Chapter 6 was melted and fed into this bomb incorporator, along with other ingredients such as aluminium powder and calcium chloride. A process description illustrating the manufacture of bombs, supported by a process flow diagram was provided to give the modelling of this bomb incorporator a sense of perspective. The objectives of this research work were to characterise the performance of an existing bomb incorporator and to provide a series of recommendations to optimise it with a view to increasing the rate of bomb production.

The proposed geometrical configuration for the bomb incorporator consisted of six narrow baffles, each attached to the incorporator wall. Fluid movement was realised by a set of shafts, each installed with a pair of 6-bladed modified pitch blade turbine, and rotating at 120 rpm in an opposite direction to each other. A 15 kW motor per shaft was required to fulfil this power requirement. Although the mixture model was employed in this chapter, nevertheless, a simulation was repeated using the full Eulerian multiphase model. By comparing the results obtained from these models, it was deduced that the results have strong resemblance to each other, thus justifying the use of the mixture model. Finally, a simulation was repeated using polyhedral cells and the results obtained were compared to those obtained via hexahedral cells. While the results obtained from both of these types of cells were similar, the computational time differed greatly. The hexahedral cells required much more computational time than the polyhedral cells.

The high explosive 2,4,6-trinitrotoluene (TNT) is prepared by nitration of toluene with a mixture of concentrated $HNO_3$ and $H_2SO_4$ in a continuous nitrator as shown in Figure 8.1.

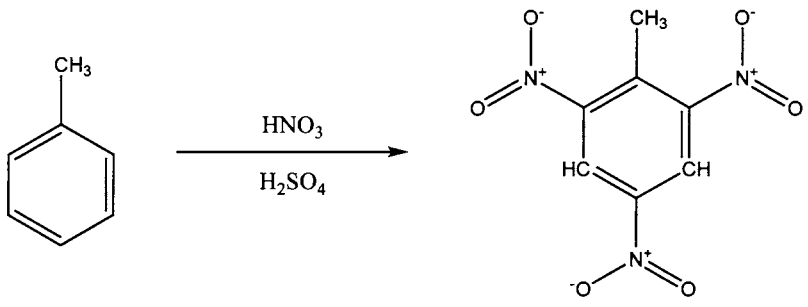


Toluene 2,4,6-trinitrotoluene

Figure 8.1: Nitration of toluene to 2,4,6-trinitrotoluene

In the course of nitration a variety of unwanted materials are produced which include unsymmetrical tri-nitrotoluenes and di-nitrotoluenes. These impurities are undesirable because they lower the melting point of TNT and this affects the ability of TNT to be used as cast-able support medium for other explosives. Fortunately, nitration impurities are easily removed from TNT by treatment with aqueous sodium sulphite, which is known industrially as 'sellite purification'. Whilst TNT will react with sulphite, it is very fortunate that reaction with unsymmetrical TNT isomers, as shown in Figure 8.2, is more facile and this provides a means of purifying TNT contaminated with a variety tri-nitro and di-nitrotoluenes.

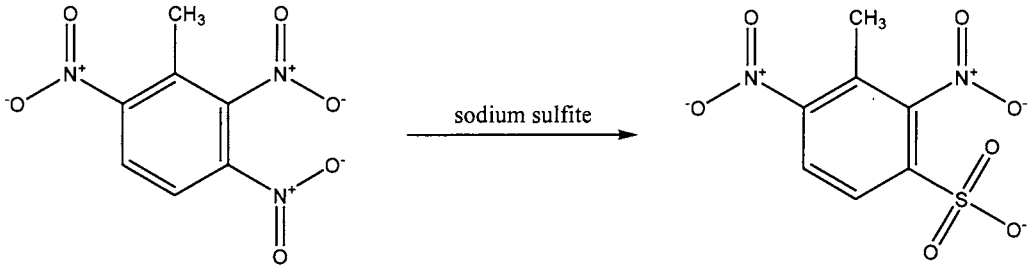


2,3,6-trinitrotoluene

2,6-dinitro-3-sulfonato-toluene

Figure 8.2: Unsymmetrical tri-nitrotoluenes and di-nitrotoluenes

Another advantage of the sellite purification method is that the products of this reaction (aromatic sulfonic acid salts) are water soluble and hence provide an easy method of separation from the organic phase containing TNT.

The waste phase from the sellite process is an aqueous based system containing a variety of sulphonated organic species and inorganic salts. The mixture is frequently referred to as 'red water' and represents a considerable problem from the perspectives of the environmental management and ethical disposal. Traditionally, red water is incinerated but this disposal methodology is highly undesirable due to the emission of combustion products ($NO_x$ and $SO_x$) and the high level of energy inefficiency of the process, the latter mainly being due to the energy input required to simply vaporise water.

The destruction methodology presented in this study, photocatalytic destruction of red-water, described in more detail in Chapter 2, offers the following advantages to incineration techniques currently employed [Oppenlander 2003]:

- No Air Emissions
- Energy is not lost evaporating water
- Reaction products (carbonates, nitrates and sulphates) can be easily disposed of or utilised as feedstock for other processes or products such as fertilisers
- Reaction progress can be easily monitored by a variety of instrumental means
- Red-water feed rate is readily adjusted to complement reaction progress
- If needed the system can be easily separated into a number of photoreactor stages

## 8.1 Objective of research

*The objective of this research was to conduct a preliminary study on the possibility of using photocatalysis technology to destroy organic wastes emanated from the manufacture of energetic products. Moreover, through CFD modelling and simulation of the reaction that occurred inside the photoreactor, the by-products from such photoreaction were made visible.*

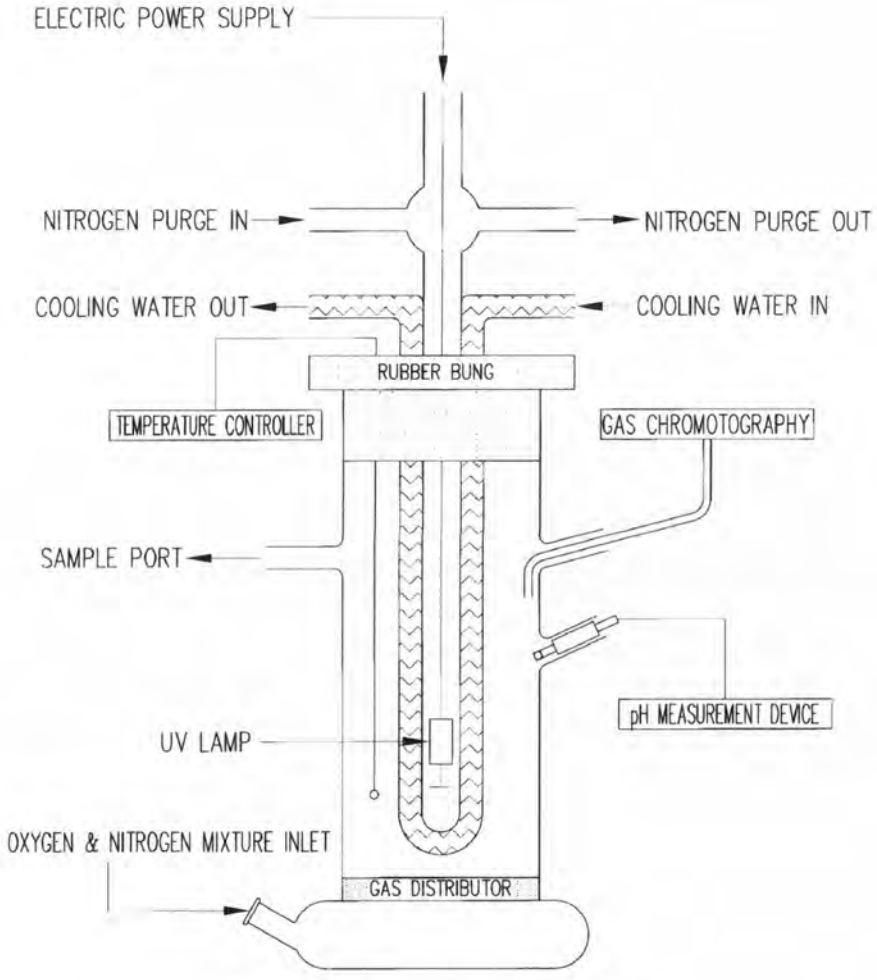


Figure 8.3: $k$-$\varepsilon$ simulation using tetrahedral cells

Figure 8.3 shows a schematic drawing of the photoreactor used in this study. Quartz was used to house the lamp because it allowed UV to pass through completely. The purpose of cooling water was to cool the compartment that housed the UV lamp. The purpose of nitrogen gas feed was to purge any ozone formed that had the potential to reduce the transparency of the quartz glass [Lea 1998]. The other features shown were self-explanatory.

## 8.2 Theoretical consideration

### 8.2.1 Photoreactor geometry construction

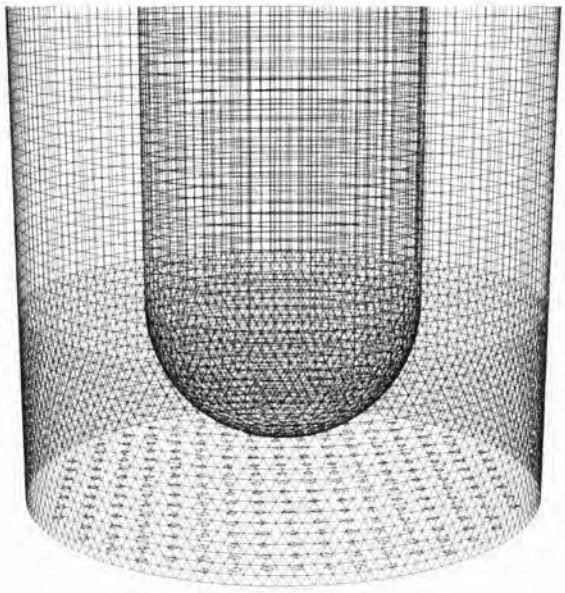

Figure 8.4: Meshed photoreactor geometry

The modelling of a photoreactor operation requires the bubbling of gas from the bottom of the tank to be taken into consideration. Several researchers have successfully performed CFD modelling involving gas-liquid interaction [Kerdous et al. 2006 and Laakkonen et al. 2007]. In this study, the photoreactor geometry was constructed using Gambit 2.3. Figure 8.4 shows the meshed geometry which consisted of hexahedral and tetrahedral cells. Total number of cells used was 419,223. The worst EquiAngle Skew quality had a value < 0.8 thus it was safely assumed that the cells quality was good.

### 8.2.2 Numerical setup

The inlet where air enters the photoreactor is defined as velocity inlet with air volume fraction equal to 1 [Kerdous et al. 2006]. The actual sparger design is beyond the scope of this study, instead, a simplified sparger design was constructed which consisted of 241 pores, each with 0.001 m in diameter, created to simulate the pores by which air enters the photoreactor, as shown in Figure 8.5. The volume fraction of $TiO_2$ for this boundary condition was set to 0, whereas the volume fraction of air was set to 1. Velocity magnitude of water and $TiO_2$ was set to 0 m $s^{-1}$ whereas it was set to 0.026 m $s^{-1}$ for air.

Figure 8.5: Photoreactor boundary conditions

Figure 8.6: Photoreactor boundary conditions

In contrast, the outlet where air exited was defined as the pressure outlet (red shading, Figure 8.6). The quartz and photoreactor wall were defined as wall. The static pressure at the pressure outlet was set to 0 because this variable was relative to the operating pressure set in the operating condition (101,325 Pa). The air backflow volume fraction was set to 1.

Although the flow regime in this system was calculated to be laminar, nevertheless a discussion on the impact of turbulence on these boundary conditions were provided should the need arise. The turbulence intensity, $I$, is defined as the ratio of the root-mean-square of the velocity fluctuations, $\upsilon'$, to the mean flow velocity, $\upsilon_{avg}$. A turbulent intensity of 1% or less is generally considered low and turbulence intensities greater than 10% are considered high. For internal flows, the turbulence intensity at the inlets is totally dependent on the upstream history of the flow. If the flow upstream is under-developed and undisturbed, low turbulence intensity can be used [Fluent 2006]. In contrast, if the flow is fully developed, the turbulence intensity may be as high as a few percent.

The turbulence intensity at the core of a fully-developed duct flow can be estimated from the following formula derived from an empirical correlation for pipe flows [Fluent 2006]:

$$I \equiv \frac{\upsilon'}{\upsilon_{avg}} = 0.16(\mathrm{Re}_{D_H})^{-\frac{1}{8}} \quad \text{- 8.1}$$

In this research work the Reynolds number was about 38 (laminar), thus $I = 0.1015\%$

The turbulence length scale, $\ell$, is a physical quantity related to the size of the large eddies that contain the energy in turbulent flows. In fully-developed duct flows, $\ell$ is restricted by the size of the duct because the turbulent eddies must be smaller than the duct. An approximate relationship between $\ell$ and the physical size of the duct is:

$$\ell = 0.07L \quad \text{- 8.2}$$

where $L$ is the relevant dimension of the duct. The factor 0.07 is based on the maximum value of the mixing length in fully-developed turbulent pipe flow, where $L$ is the diameter of the pipe. In a channel of non-circular cross-section, you can base $L$ on the hydraulic diameter.

### 8.2.3 Discretisation

In this research work, the solution domain was restricted to the region bounded by the photoreactor wall and the quartz wall. Region inside the quartz was not modelled or simulated because it was deemed unnecessary. The SIMPLE (semi-implicit method for pressure linked equations) scheme was used for the pressure-velocity coupling where a relationship between the pressure and velocity corrections was used to enforce conservation of continuity in order to obtain the pressure field. This scheme was employed on all steady-state calculations.

### 8.2.4 Convergence

Simulations were generally considered converged when the residuals for mass, momentum and turbulence kinetic energy and its dissipation rate fell below $1\times10^{-4}$ [Kerdouss et al. 2006]. Further checks for convergence were made by creating a monitoring point inside the tank and ensuring that the value monitored remained constant with repeated iterations.

Table 8.1 provides a summary of relevant information on the photoreactor and its operation.

Table 8.1: Summary of geometrical configuration and operating condition

| Parameter | Values |
|---|---|
| Diameter of pore | 0.001 m |
| Area of pore | 0.000000786 $m^2$ |
| Total area of 241 pores | 0.0001894 $m^2$ |
| Total gas flowrate of 300 mL $min^{-1}$ | 5E-06 $m^3$ $s^{-1}$ |
| Gas velocity per pore (5E-06 $m^3$ $s^{-1}$ ÷ 0.0001894 $m^2$) | 0.0264 m $s^{-1}$ |
| Photoreactor height and liquid height | 0.5 m and 0.31 m |
| Diameter of photoreactor and diameter of quartz | 0.094 m and 0.0496 m |
| Radius of quartz bottom | 0.0248 m |
| Volume of photoreactor | 0.002152 $m^3$ |
| Volume displaced by quartz | 0.0005345 $m^3$ |
| Volume occupied by water | 0.001617 $m^3$ |
| Average size of $TiO_2$ particles | 30 μm |
| Mass of catalyst used (0.5 kg $m^{-3}$ × 0.001617 $m^3$) | 0.0008085 kg of $TiO_2$ |
| Density of $TiO_2$ | 3,900 kg $m^{-3}$ |
| Volume occupied by $TiO_2$ | 0.0002073 $m^3$ |
| Height of $TiO_2$ to be patched | 0.03 m |

## 8.3 Modelling of reactive species

When the conservation of equations for chemical species are solved, Fluent® predicts the local mass fraction of each species, $Y_i$, through the solution of a convection-diffusion equation for the $i^{th}$ species. The conservation equation is given as:

$$\frac{\partial}{\partial t}(\rho Y_i)+\nabla\cdot(\rho\vec{v}Y_i)=-\nabla\cdot\vec{J}_i+R_i+S_i \qquad \text{- 8.3}$$

where

$R_i$ : net rate of production species $i$ by chemical reaction

$S_i$ : rate of creation by addition from the dispersed phase or any user-defined sources

An equation of this form will be solved for $N$-1 species where $N$ is the total number of fluid phase chemical species present in the system. Since the mass fraction of the species must sum to unity, the $N^{th}$ mass fraction is determined as one minus the sum of the $N$-1 solved mass fractions. To minimise numerical error, the $N^{th}$ species is selected as the species with the overall largest mass fraction.

From Equation (8.3), $\vec{J}_i$ is the diffusion flux of species $i$, which arises due to concentration gradients. By default, Fluent® uses the dilute approximation, under which the diffusion flux can be written as:

$$\vec{J}_i=-\rho D_{i,m}\nabla Y_i \qquad \text{- 8.4}$$

Where $D_{i,m}$ is the diffusion coefficient for species $i$ in the mixture. However, for certain laminar flows, the dilute approximation may not be acceptable but a full multicomponent diffusion is required. On the other hand, in turbulent flows, Fluent® computes the mass diffusion in the following form:

$$\vec{J}_i=-\left(\rho D_{i,m}+\frac{\mu_t}{Sc_t}\right)\nabla Y_i \qquad \text{- 8.5}$$

Where $Sc_t$ is the turbulent Schmidt number (default value = 0.7), $\mu_t$ is the turbulent viscosity and $D_t$ is the turbulent diffusivity. Since turbulent diffusion generally

overwhelms laminar diffusion, the specification of detailed laminar diffusion properties in turbulent flows is generally not needed.

For many multicomponent mixing flows, the transport of enthalpy due to species diffusion, $\nabla \cdot \left[ \sum_{i=1}^{N} h_i \vec{J}_i \right]$ can have a significant effect on the enthalpy field and must not be neglected. This is significant especially when the Lewis number given as:

$$Le_i = \frac{k}{\rho c_p D_{i,m}} \qquad -8.6$$

for any species is far from unity. In this situation, neglecting this term can lead to significant errors. By default, Fluent® includes this term.

In Fluent®, the net transport of species at inlets consists of both convection and diffusion components when the segregated solve is used. However, on the convection component is included when the coupled solver is used. While the convection component can be specified, the diffusion component depended on the gradient of the computed species field at the inlet.

In Fluent®, for cases which involved mixing, transport, reaction of chemical species or reactions on the surface of a wall or particle, the generalised finite-rate model can be used. Reaction rates can be computed by one of the three models below [Fluent 2007]:

*Laminar finite-rate model* – where the effect of turbulent fluctuations are ignored, and reaction rates are determined by Arrhenius expressions.

*Eddy-dissipation model* – reaction rates are assumed to be controlled by the turbulence, so expensive Arrhenius chemical kinetic calculations can be avoided. The model is computationally cheap but for realistic results one or two step heat-release mechanisms can be used.

*Eddy-dissipation-concept (EDC) model* – where detailed Arrhenius chemical kinetics can be incorporated in turbulent flames. But this model is computationally expensive.

### 8.3.1 Laminar finite-rate model

The laminar finite-rate model computes the chemical source terms using Arrhenius expressions but ignores the effects of turbulent fluctuations. The net source of chemical species $i$ due to reaction $R_i$ is computed as the sum of the Arrhenius reaction sources over the $N_R$ reactions that the species participate in [Fluent 2006]:

$$R_i = M_{w,i} \sum_{r=1}^{N_R} \hat{R}_{i,r} \qquad - 8.7$$

where

$M_{w,i}$ : molecular weight of species $i$ and $\hat{R}_{i,r}$

$\hat{R}_{i,r}$ : Arrhenius molar rate of creation/destruction of species $i$ in reaction $r$

Reaction may occur in the continuous phase between continuous-phase species only or at wall surfaces resulting in the surface deposition or evolution of a continuous-phase species.

For an $r^{th}$ reaction written as:

$$\sum_{i=1}^{N} \nu'_{i,r} M_i \underset{k_{b,r}}{\overset{k_{f,r}}{\longleftrightarrow}} \sum_{i=1}^{N} \nu''_{i,r} M_i \qquad - 8.8$$

where

$N$ : number of chemical species in the system

$\nu'_{i,r}$ : stoichiometric coefficient for reactant $i$ in reaction $r$

$\nu''_{i,r}$ : stoichiometric coefficient for product $i$ in reaction $r$

$M_i$ : symbol denoting species $i$

$k_{f,r}$ : forward rate constant for reaction $r$

$k_{b,r}$ : backward rate constant for reaction $r$

This equation is valid for both reversible and non-reversible reactions. For non-reversible reactions, the backward reaction rate constant, $k_{b,r}$ is simply omitted. In addition, the summations are for all chemical species in the system, but only species that appear as

reactants or products will have non-zero stoichiometric coefficients. Thus, species that are not involved will drop out of the equation.

The molar rate of creation or destruction of species *i* in reaction *r* is given as:

$$\hat{R}_{i,r} = \Gamma\left(v''_{ir} - v'_{ir}\right)\left( k_{f,r}\prod_{j=1}^{N_r}\left[C_{j,r}\right]^{n'_{j,r}} - k_{b,r}\prod_{j=1}^{N_r}\left[C_{j,r}\right]^{n''_{j,r}} \right) \quad \text{- 8.9}$$

$N_r$ : number of chemical species in reaction *r*

$C_{j,r}$ : molarity of each reactant and product species *j* in reaction *r*, kg mol $m^{-3}$

$n'_{j,r}$ : forward rate exponent for each reactant and product species *j* in reaction *r*

$n''_{j,r}$ : backward rate exponent for each reactant and product species *j* in reaction *r*

$\Gamma$ : represents the net effect of third bodies on the reaction rate

$\Gamma$ is mathematically defined as:

$$\Gamma = \sum_{j}^{N_r}\gamma_{j,r}C_j \quad \text{- 8.10}$$

$\gamma_{j,r}$ is the third-body efficiency of the $j^{th}$ species in the $r^{th}$ reaction.

The forward rate constant for reaction *r*, $k_{f,r}$ is computed using Arrhenius expression:

$$k_{f,r} = A_r T^{\beta r} e^{-\frac{E_r}{RT}} \quad \text{- 8.11}$$

where

$A_r$ : pre-exponential factor

$\beta_r$ : temperature exponent

$E_r$ : activation energy for the reaction J $kg^{-1}$ $mol^{-1}$

$R$ : universal gas constant, J $kg^{-1}$ $mol^{-1}$ $K^{-1}$

For the simulation to commence, the values of $\nu'_{i,r}$, $\nu''_{i,r}$, $n'_{j,r}$, $n''_{j,r}$, $\beta_r$, $A_r$ and $E_r$ must be specified. The specification of the value for $\gamma_{j,r}$ is optional.

If the reaction under investigation is reversible, the backward reaction rate constant for reaction $r$, $k_{b,r}$, is computed from the forward reaction rate constant using the following relation:

$$k_{b,r} = \frac{k_{f,r}}{K_r} \qquad \text{- 8.12}$$

where $K_r$ is the equilibrium constant for the $r^{th}$ reaction, computed from:

$$K_r = \exp\left(\frac{\Delta S_r^0}{R} - \frac{\Delta H_r^0}{RT}\right)\left(\frac{p_{\text{atm}}}{RT}\right)^{\sum_{r=1}^{N_R}\left(\nu''_{j,r}-\nu'_{j,r}\right)} \qquad \text{- 8.13}$$

$p_{\text{atm}}$ : denotes atmospheric pressure (101,325 Pa)

The term within the exponential function represents the change in Gibbs free energy, and its components are computed as follows:

$$\frac{\Delta S_r^0}{R} = \sum_{i=1}^{N}\left(\nu''_{i,r} - \nu'_{i,r}\right)\frac{S_i^0}{R} \qquad \text{- 8.14}$$

$$\frac{\Delta H_r^0}{RT} = \sum_{i=1}^{N}\left(\nu''_{i,r} - \nu'_{i,r}\right)\frac{h_i^0}{RT} \qquad \text{- 8.15}$$

Where $S_r^0$ and $h_i^0$ are the standard-rate entropy and standard-state enthalpy.

### 8.3.2 Eddy-dissipation model

For mass transfer limited reaction, the rate of reaction is dependent on the level of turbulence in the system. Magnussen and Hjertager [1976] provide the eddy-dissipation model to address this modelling requirement. The net rate of production of species *i* due to reaction *r* is given by the smaller limiting value of the two expressions below:

$$\hat{R}_{i,r} = \nu'_{i,r} M_{w,i} A \rho \frac{\varepsilon}{k} \left( \frac{Y_R}{\nu'_{R,r} M_{w,R}} \right) \qquad \text{- 8.16}$$

$$\hat{R}_{i,r} = \nu'_{i,r} M_{w,i} AB \rho \frac{\varepsilon}{k} \left( \frac{\Sigma P Y_P}{k \sum_{j}^{N} \nu''_{j,r} M_{w,j}} \right) \qquad \text{- 8.17}$$

where

$Y_P$ : mass fraction of any product species, $P$

$Y_R$ : mass fraction of a particular reactant, $R$

$A$ : empirical constant equal to 4.0

$B$ : empirical constant equal to 0.5

In Fluent®, for any multi-step reaction mechanism where the number of reaction > 2, employing the finite-rate/eddy-dissipation or eddy-dissipation model is allowed but will likely produce incorrect solutions. This is because multistep chemical reaction mechanisms are based on Arrhenius rates, which is different for each reaction. In the eddy-dissipation model, every reaction has the same turbulent rate, and therefore the model should be used only for one-step (reactant → product) or two-step (reactant → intermediate, intermediate → product) global reactions. This model cannot predict kinetically controlled species such as radicals. To incorporate multi-step chemical kinetic mechanisms in turbulent flows, the eddy-dissipation concept (EDC) model must be used.

### 8.3.3 Eddy-dissipation-concept (EDC) model

This model is an extension of the eddy-dissipation model to include detailed chemical reaction mechanisms in turbulent flows. It assumes that reaction occurs in small turbulent structures, called the fine scales. The length fraction of the fine scales is modelled according to [Gran and Magnussen 1996]:

$$\xi^* = C_\xi \left( \frac{\nu \varepsilon}{k^2} \right)^{\frac{1}{4}} \qquad \text{- 8.18}$$

where * denotes fine-scale quantities and

$C_\xi$ : volume fraction constant = 2.1377

$\nu$ : kinematic viscosity

The volume fraction of the fine scales is calculated as $\xi^{*3}$. Species are assumed to react in the fine structures over a time scale:

$$\tau^* = C_\tau \left( \frac{\nu}{\varepsilon} \right)^{\frac{1}{2}} \qquad \text{- 8.19}$$

where $C_\tau$ is a time scale constant value equal to 0.4082

Finally, the source term in the conservation equation for the mean species, *i*, is modelled as:

$$\hat{R}_i = \frac{\rho (\xi^*)^2}{\tau^* [1 - (\xi^*)^3]} \left( Y_i^* - Y_i \right) \qquad \text{- 8.20}$$

where $Y_i^*$ is the fine-scale species mass fraction after reacting over the time $\tau^*$. This model can incorporate detailed chemical mechanisms into turbulent reacting flows. However, typical mechanisms are invariable stiff and their numerical integration is computationally demanding. Thus, this model is used only when the assumption of fast reaction is invalid.

## 8.4 Multiphase modelling $TiO_2$ particles

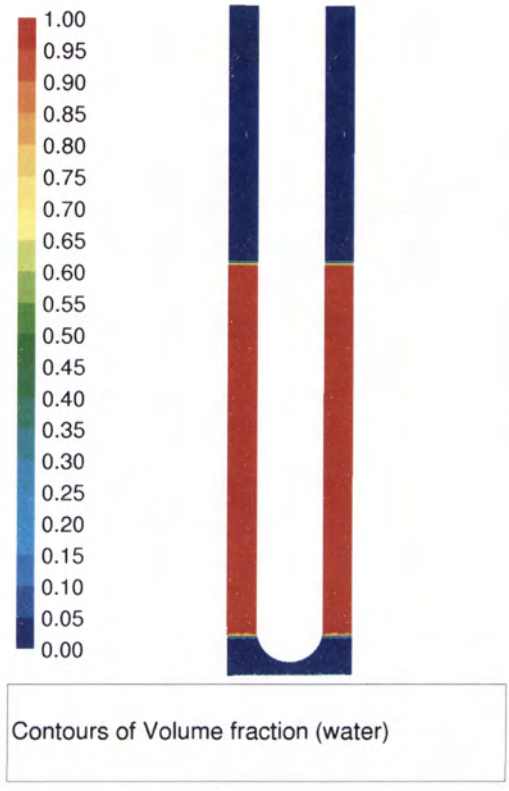


Figure 8.7: Zero gas flowrate

The simulation was initiated by patching $TiO_2$ particles at the bottom of the tank and air above the layer filled by water. Figure 8.7 shows a distinct three layers of fluid when the gas flowrate was set to the initial condition of zero. The bottom layer consisted of $TiO_2$ particles, the medium layer was occupied by water and the top layer was occupied by air.

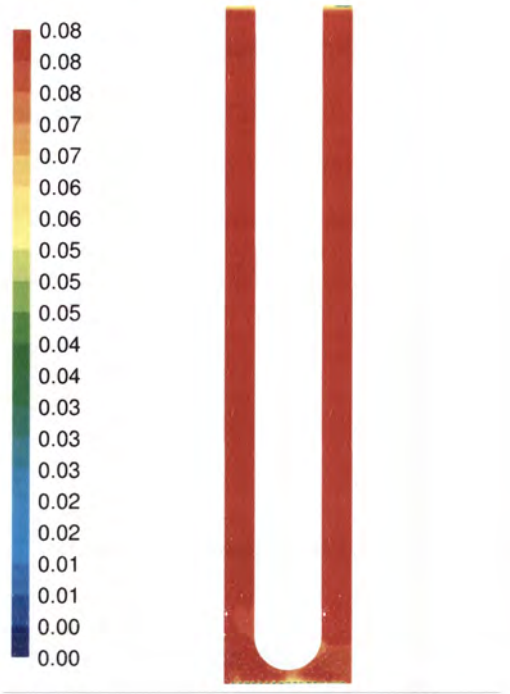


Figure 8.8: $TiO_2$ contours of volume fraction

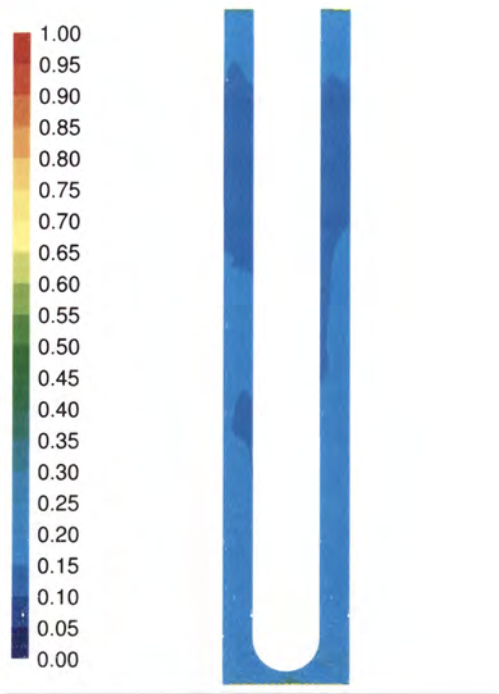


Figure 8.9: Air contours of volume fraction

Figure 8.8 shows that when the simulation results reached steady-state, the dispersion of $TiO_2$ was highly homogeneous. Around the sparger region, less $TiO_2$ was found which was due to a higher bubble concentration in this vicinity. Figure 8.9 shows that some regions contained slightly more air volume fraction than the other. Around the sparger region, a higher air volume fraction was found. This finding agreed with common engineering judgment.

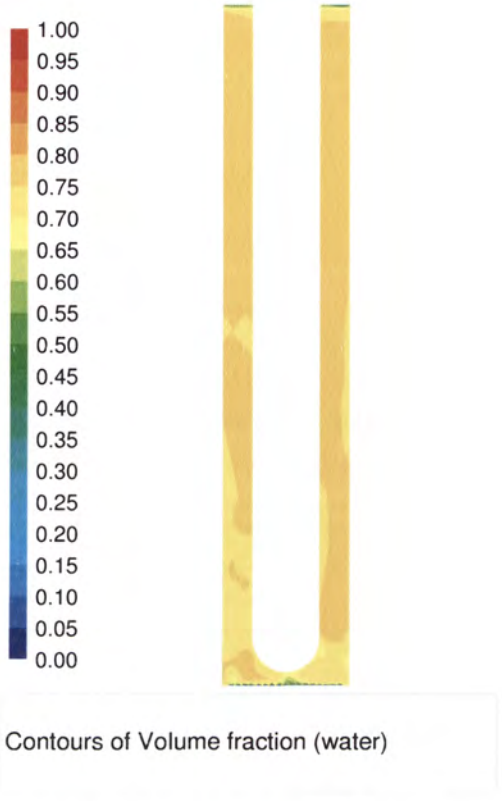


Figure 8.10: Water contours of volume fraction

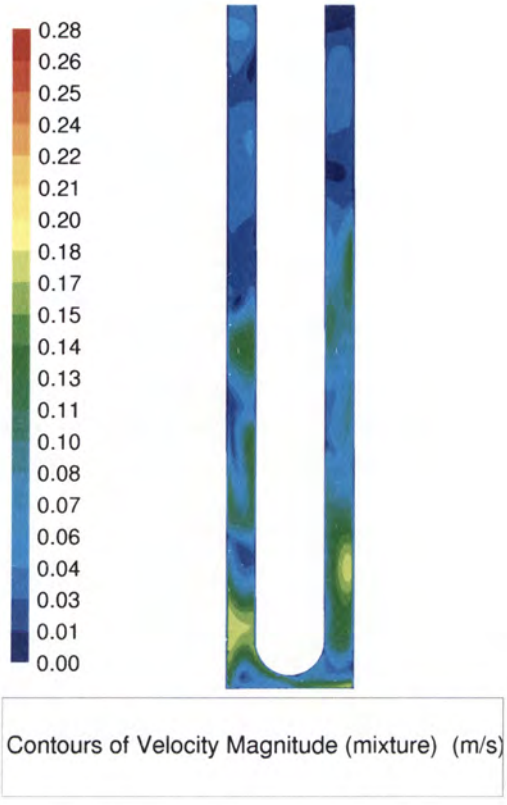


Figure 8.11: Contours of velocity magnitude for the mixture

Figure 8.10 shows that the volume fraction of water was also homogeneous from one region of the photoreactor to another. On the other hand, Figure 8.11 shows that the mixture velocity was highest starting from the bottom of the reactor and decreased with the height of the photoreactor. Again, this conclusion agreed with common engineering judgement.

## 8.5 Reaction mechanism for the destruction of red-water

$$C_6H_5CH_3 + HNO_3 \rightarrow C_6H_2CH_3(NO_2)_3$$

$$C_6H_2CH_3(NO_2)_3 \xrightarrow{NaSO_3} \underbrace{C_6H_2CH_3(NO_2)_2SO_3}_{red\ water}$$

Proposed reaction: $C_7H_5N_2O_7S + O_2 \rightarrow CO_2 + H_2O + H_2SO_4 + HNO_3$

$$C_aH_bN_cO_dS_e + xO_2 \rightarrow aCO_2 + yH_2O + eH_2SO_4 + cHNO_3$$

where $a = 7, \quad b = 5, \quad c = 2, \quad d = 7, \quad e = 1$

Hydrogen balance
$b = 2y + 2e + c$
$y = ½$

Oxygen balance
$d + 2x = 2a + y + 4e + 3c$
$x = 35/4$

Thus, balanced reaction:

$$C_7H_5N_2O_7S + \frac{35}{4}O_2 \xrightarrow{TiO_2 \text{ and } UV} 7CO_2 + \frac{1}{2}H_2O + H_2SO_4 + 2HNO_3$$

The reaction was assumed as a first-order reaction.

## 8.6 Reactive modelling results

The results presented in this section were obtained from steady-state simulation carried out on the reaction presented in the previous section.

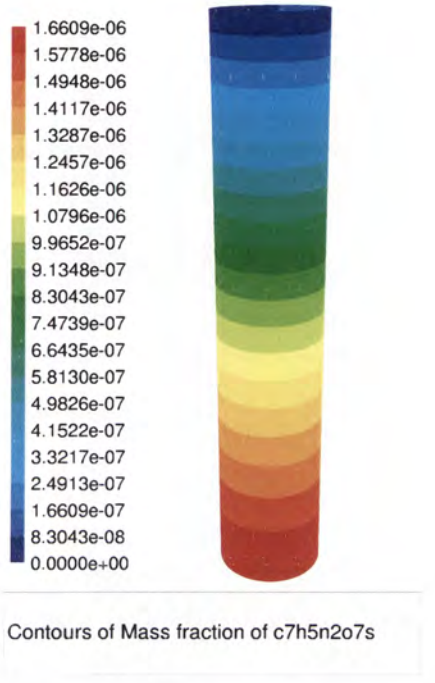


Figure 8.12: Mass fraction of red-water

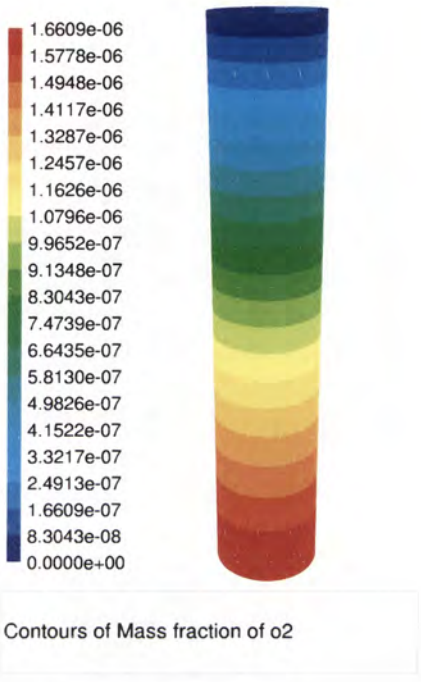


Figure 8.13: Mass fraction of oxygen

Figure 8.12 and 8.13 show the contours of mass fractions of red-water and oxygen respectively. The results were reasonable because after the reaction had taken place the amount consumed by both species should be equal. This was consistent with the reaction equation presented in the previous section where for every mole of red-water consumed, 35/4 oxygen would be fed to match it. In addition, it was observed that the value of mass fractions for both species were low which was attributed to the almost complete consumption of these species.

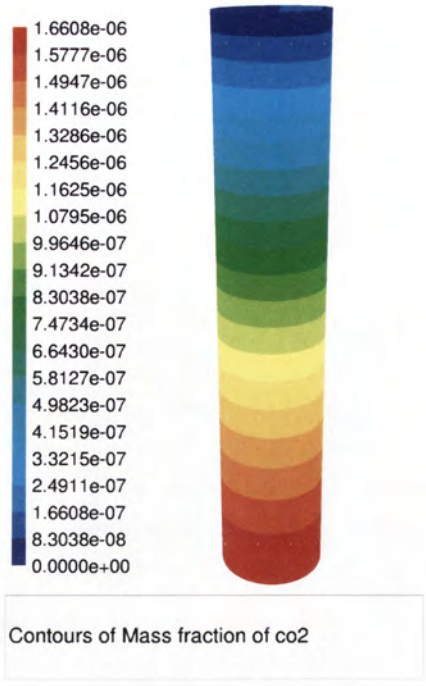


Figure 8.14: Mass fraction of carbon dioxide

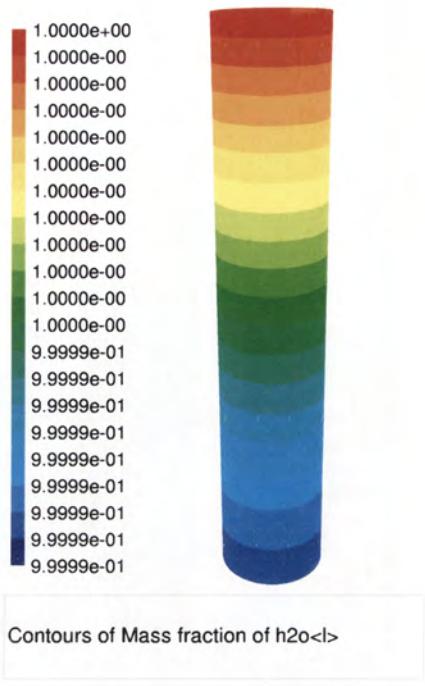


Figure 8.15: Mass fraction of water

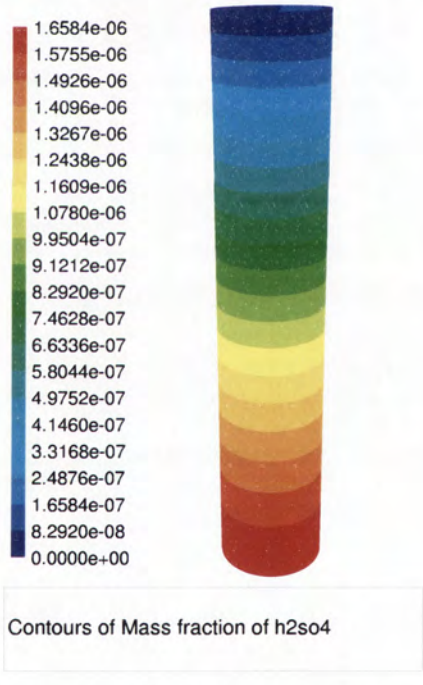


Figure 8.16: Mass fraction of sulphuric acid

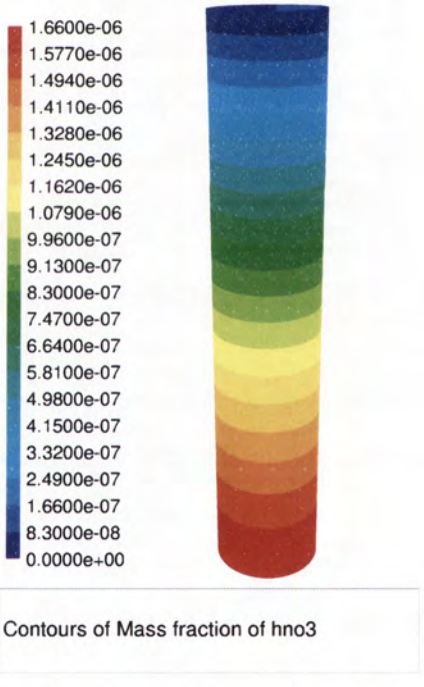


Figure 8.17: Mass fraction of nitric acid

Figure 8.14-8.17 show the by-products of this technology. And within this by-product, water was the major component. In other words, very negligible greenhouse gases would be released to the atmosphere.

## 8.7 Photoreactor quantum efficiency

The quantum efficiency of using this photoreactor to destruct red-water is defined as:

$$\eta = \frac{\text{amount of reactant consumed or product formed}}{\text{amount of photons absorbed}} \qquad \text{- 8.21}$$

The amount of reactant consumed or product formed during or after the reaction can be measured using total organic content (TOC) analyser (% TOC reduction). On the other hand, the amount of photons absorbed can be measured by a photometer, calibrated to appropriate wavelength. The efficiency of a given photoreactor can also be quantified by measuring other water quality indices such as the biological oxygen demand (BOD), chemical oxygen demand (COD), pH, total dissolve solids (TDS) and salinity. This efficiency can be taken as the key performance indicator (KPI) in the quest for optimisation.

The important variables affecting the quantum efficiency $\eta$ are:

1. Air or oxygen flowrate
2. % of oxygen
3. Catalyst loading
4. Homogeneity of catalyst
5. Reaction temperature
6. Intensity of light
7. Initial pH of pollutant
8. Initial TOC of red-water feed

## 8.8 Maintaining photoreactor temperature

To maintain the temperature inside the photoreactor, heat must be imparted into it from an external source. There are several ways of transferring heat into the photoreactor:

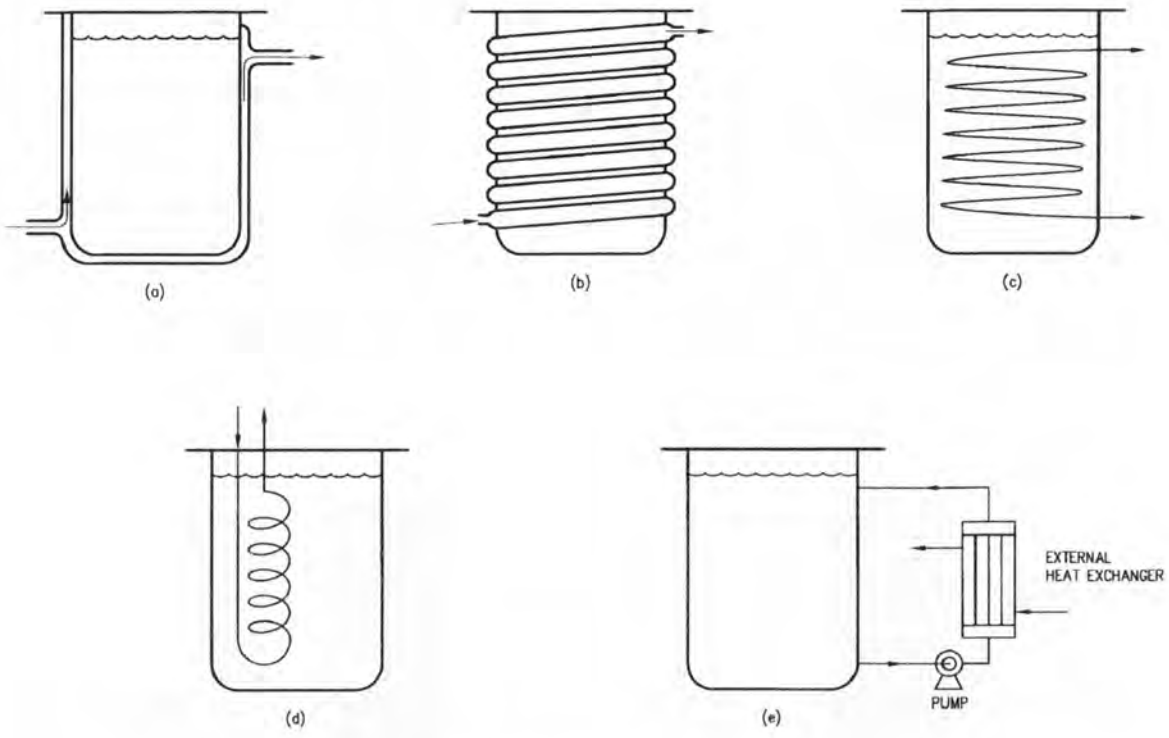


Figure 8.18: Various heat transfer geometrical configurations

The photoreactor may have an external jacket (Figure 8.18a), or coil (Figure 8.18b) through which warm or cooling water is circulated. Alternatively, helical (Figure 8.18c) or baffle coils (Figure 8.18d) may be located internally. Finally, the liquid to be treated can be pumped from the reactor through a separate heat-exchange unit (Figure 8.18e). There are advantages and disadvantages associated with each design configuration.

The surface area available for heat transfer is lower in the external jacket and coil designs than when internal coils are completely submerged in the reactor contents. Although the external jacket design on a photoreactor provide sufficient heat-transfer area for small-scale systems, they are likely to be inadequate for large-scale photoreactor.

Internal coils are frequently used in production vessels where the coil can be operated with high liquid velocity and the entire tube surface is exposed to the photoreactor contents providing a relatively large heat-transfer area. Despite such an advantage, such design configuration interferes with the hydrodynamic pattern inside the photoreactor and renders cleaning the photoreactor difficult. In addition, fouling of the internal coils can occur which reduces the effectiveness of the internal coils to transfer heat.

In contrast, the final design which incorporates an external heat exchanger, is independent of the reactor, easy to scale-up, and can provide better heat-transfer capabilities than any of the other configurations. However, this design performs well on the condition that the photocatalyst does not clog the pump or foul the heat exchanger tubes.

## 8.9 Economic consideration

The cost break-down per day to incinerate 9 $m^3$ of red-water is given in Table 8.2:

Table 8.2: Cost break-down of incinerating red-water

| Activities | Cost / day |
|---|---|
| Natural gas | $315 |
| Labour | $480 |
| 200 L drums | $40 |
| Disposal of ashes | $200 |
| Maintenance | $32 |
| Total | $1,067 |

The cost break-down by year to incinerate red-water is given in Table 8.3:

Table 8.3: Cost by year to incinerate red-water

| Year | Unit cost / day | No. of days | Cost / year |
|---|---|---|---|
| 2005 | $1,067 | 141 | $150,447 |
| 2006 | $1,067 | 175 | $186,725 |
| 2007 | $1,067 | 200 | $213,400 |

**Since the cost of operating red-water is approximately $180,000 per year**

| | |
|---|---|
| Total cost of research project | ~ $ 420,000 ($140,000 per year) |
| Total cost of actual photoreactor | ~ $ 300,000 |
| Running cost of photoreactor/year | ~ $ 30,000 |
| Total cost of investment | ~ $ 750,000 |
| | |
| Period of recovery | ~ 4 years |

After this period, Mulwala explosive facility will save ~ $150,000 per year

## 8.10 Other applications of photocatalysis technology

Another application of photocatalysis technology in explosive manufacturing facilities is in the treatment of mononitrotoluene, dinitrotoluene and trinitrotoluene dissolved in water. Currently these compounds were removed from the effluent stream using activated carbon. Activated carbon does not treat the wastes, rather only serves to transfer the contaminants from one phase to another. The spent activated carbons were sent into storage because the explosive manufacturing facilities did have a feasible method of disposing it. Currently, the explosive manufacturing facilities have produced about 230 drums, each about 200 kg, totalling to about 46 tonnes. In the next 20 years about 2.6 tonne/ year will continually be produced. Unless, a feasible method is employed, these wastes will occupy more spaces. Photocatalysis technology provides a technically and economically feasible solution to this problem.

## 8.11 Concluding remarks

Incinerating red-water was not efficient from either environmental or economic perspectives. This method of treating red-water was considered obsolete and should be replaced by a more effective environmentally friendly method. It was recommended that research into photocatalysis technology at pilot-plant scale be conducted with a view to replacing this method of treating red-water via incineration. Moreover, the photocatalysis technology was applicable to other organic wastes produced during the manufacture of explosives and their derivatives.

The benefits given for adopting photocatalysis technology were:

- It was a modern and efficient approach
- It provided a greener solution (100% reduction NOx and SOx)
- It was economical to operate (85% reduction in red-$H_2O$ incineration cost)
- It was energy efficient (95% reduction)

# OVERALL CONCLUSIONS

The main objectives of this research were to gain a thorough understanding of the hydrodynamic phenomena inside reactors and mixing tanks involved in the manufacture of military propellants, high explosives and bombs; to provide recommendations to improve their performance and to fill the research gap.

A single-phase CFD modelling and simulation was conducted on the unbaffled-reactor currently used to manufacture military propellant. Through CFD modelling and simulations, a detailed characterisation was developed, as shown in chapter 3, which provided a clear visualisation of the hydrodynamic phenomena that occurred inside this reactor. It was discovered that the absence of baffles led to ineffective mass transfer, thus the process required additional processing stages to complete the reaction. A recommendation to optimise the reactor performance was proposed, which included installing narrow baffles and a set of new high efficiency impellers.

A design template for a mixing tank tasked with suspending particles was created via numerical approach. This was achieved by investigating several crucial variables that determined the success of a given mixing tank to suspend particles. The trials conducted were created using factorial design of experiments which enabled multivariable analysis to be conducted. This design template created is applicable across the process industries and will provide guidance for the design of similar mixing tanks or for optimising existing mixing tanks. Two-phase CFD modelling and simulations were conducted on the suspension of RDX particles inside the slurry holding tank. It was discovered that the impellers used were not suitable thus effective suspension using the existing geometrical configuration could not be achieved. Using the design template formulated in Chapter 4, a recommendation to overcome the issues and optimise performance was made in Chapter 5. Based on this recommendation, a pilot-scale trial was conducted which shows that the geometrical configuration recommended was successful in suspending RDX particles.

A multi-phase CFD modelling and simulation was also conducted on the RDX/TNT mixing tank, in Chapter 6, to characterise the hydrodynamic occurring inside the tank. It was discovered that in this mixing tank, conflicting process requirements occurred every time it was operated thus the products manufactured frequently failed quality

specifications. These results show that process diagnosis via numerical simulation has provided production personnel with information not previously possible. This has enhanced their understanding of the process and hence shed some light on an on-going problem of excessive variation in final product composition.

In the munition plant, products emanating from the RDX/TNT mixing tank process are melted and fed into other mixing tanks, known as bomb incorporators and then combined with other ingredients such as aluminium powder and calcium chloride. A modelling and simulation exercise was conducted on this incorporator with the objectives of characterising the existing performance and providing a series of recommendations to optimise this unit operation with a view to increasing the rate of bombs production. This multi-phase simulation focused on both the suspension and the draw down of particles that occurred in the bomb incorporator. The results, in Chapter 7, show that the mixing tank used to manufacture aerial bombs was based on an obsolete design, thus rendering a sub-optimum manufacturing process. A new set of impellers, which promises better performance, were proposed to upgrade these bomb incorporators.

To destroy some of the wastes produced from explosives manufacturing, photocatalysis technology is recommended, as explained in Chapter 8. This technology when adopted will reduce greenhouse gases emissions and energy consumption.

Finally, it is believed that the proper implementation of these recommendations will provide an optimum operation that achieves high product throughput and concurrently by producing more defective-free products, reduce reject rate. This will translate into transforming an existing facility into an enhanced weapons manufacturing facility.

# MODEL SETUP

| | |
|---|---|
| Start-up | |
| File | Read case mesh file |
| Grid | Info size |
| | Scale |
| | Smooth/Swap |
| Display | Grid |
| Models | Multiphase |
| | Viscous |
| | |
| Models | |
| Solver type | Segregated |
| Formulation | Implicit |
| Time | Steady |
| Space | 3D |
| Velocity formulation | Absolute |
| Gradient option | Cell based |
| Porous formulation | Superficial velocity |
| Multiphase | VOF/Mix/Eulerian |
| Viscous | $k\varepsilon$-realisable/RSM |
| | |
| Fluid Materials | |
| Name 1 | Water |
| Name 2 | RDX |
| Phases setup | Primary for major |
| | Secondary for minor |
| | |
| Operating conditions | |
| Gravity | On |
| Direction | -9.81m $s^{-2}$ |
| Operating pressure | 101325Pa |
| | |
| Boundary conditions | |
| Tank wall motion | Stationary wall |
| Shear-condition | No slip |
| Wall roughness | r.hght=0 r.cst=0.5m |
| | |
| Tank volume | Stationary wall |
| Tank top | Stationary wall-close |
| Wall roughness | r.hght=0 r.cst=0.5m |
| | |
| Fluid top | MRF |
| Speed | 80 rpm |
| Rotation-axis origin | x=0 y=1 z=0 |
| Rotation-axis direct | x=0 y=-1 z=0 |

| | |
|---|---|
| Fluid bottom | MRF |
| Speed | 80 rpm |
| Rotation-axis origin | x=0 y=1 z=0 |
| Rotation-axis direct | x=0 y=-1 z=0 |
| | |
| Top shaft | Moving wall |
| Speed | 80 rpm |
| Motion | Absolute |
| | Rotational |
| Shear condition | No slip |
| Wall roughness | r.hght=0 r.cst=0.5m |
| Rotation-axis origin | x=0 y=1 z=0 |
| Rotation-axis direct | x=0 y=-1 z=0 |
| | |
| Top impeller | Moving wall |
| Speed | 0 rpm |
| Motion | Relative to adj cells |
| | Rotational |
| Shear condition | No slip |
| Wall roughness | r.hght=0 r.cst=0.5m |
| Rotation-axis origin | x=0 y=1 z=0 |
| Rotation-axis direct | x=0 y=-1 z=0 |
| | |
| Bottom impeller | Moving wall |
| Speed | 0 rpm |
| Motion | Relative to adj cells |
| | Rotational |
| Shear condition | No slip |
| Wall roughness | r.hght=0 r.cst=0.5m |
| Rotation-axis origin | x=0 y=1 z=0 |
| Rotation-axis direct | x=0 y=-1 z=0 |
| | |
| Patching | |
| Adapt | Region |
| Hex | Ref scale & mark |
| Manage | Display adaption |
| Solve | Initialise patch |
| | |
| Solution controls | |
| Equations | Flow & turbulence |
| Pressure-velocity | SIMPLE |
| Pressure discretise | PRESTO |
| Momentum | $1^{st}/2^{nd}$ order upwind |
| Turbulence KE | $1^{st}/2^{nd}$ order upwind |
| Turbulence Dis Rate | $1^{st}/2^{nd}$ order upwind |

***BLEND TIME SIMULATION***

- Switch to unsteady-state and 2nd order implicit
- Turn on species model
- Create tracer material that has the same property as bulk fluid
- Under material, select the working fluid and set a different name such as tracer
- Click change/create but do not overwrite
- Define mixture to include only the bulk liquid and tracer material (first on the list)
- Change density to volume-weighted-mixing-law
- Tick off the energy equation which was enabled when the species transport was turn on
- Adapt region, but mark only
- Shape of tracer material: spherical
- Internal region adaption coordinate inputs: X=0, Y=0.6, Z=0.2
- Radius of tracer material: 0.05m (it must not be too small)
- Create virtual probes via surface point (probe coordinates in the tables below)
- Create monitoring points by surface monitor per time-step (transient simulation)
- Report type: vertex average
- X-axis: flow time
- Report of: species - mass fraction
- Deselect flow, turbulence and energy equations
- Set PISO and 2nd order for tracer discretisation
- Reduce convergence criteria to 1E-5
- Patch tracer material as 1
- Iterate time step size 1s, number of time steps 500 and max iteration per time step 20
- Transparency of tank: 61%

| Nitrator | X | Y | Z |
|---|---|---|---|
| Existing | 0 | 0.6 | 0.2 |
| Proposed | 0.2 | 0.1 | 0.6 |

| EXISTING UNIT | | | |
|---|---|---|---|
| Probes | X | Y | Z |
| P1 | 0.3 | 0.2 | 0.2 |
| P2 | 0.3 | 0.8 | 0.2 |
| P3 | 0.3 | 0.4 | 0.2 |
| P4 | 0.1 | 0.4 | 0.2 |
| P5 | 0 | 0 | 0 |
| P6 | 0 | 0.2 | -0.35 |
| P7 | 0 | 0.4 | -0.1 |
| P8 | 0 | 0.8 | -0.1 |
| P9 | 0.25 | 0.6 | -0.25 |
| P10 | -0.25 | 0.35 | -0.2 |

| PROPOSED UNIT | | | |
|---|---|---|---|
| Probes | X | Y | Z |
| P1 | 0.3 | 0.2 | 0.2 |
| P2 | 0.3 | 0.2 | 0.8 |
| P3 | 0.3 | 0.2 | 0.4 |
| P4 | 0.1 | 0.2 | 0.4 |
| P5 | 0 | 0 | 0 |
| P6 | 0 | -0.35 | 0.2 |
| P7 | 0 | -0.1 | 0.4 |
| P8 | 0 | -0.1 | 0.8 |
| P9 | 0.25 | -0.25 | 0.6 |
| P10 | -0.25 | -0.2 | 0.35 |

## *TO PLOT MONITOR.OUT*

- Got to XY plot
- Load and select the file
- File will appear in the file data
- Plot
- Depends on how many line there are
- To see monitor.out data, just open using a note pad and import using excel spreadsheet
- For excel importation, the data must be imported via data column

## *ANIMATIONS USING PARTICLE TRACKS*

- Read steady-state file .cas and .dat
- Start injection from steady-state solution but do not initialise the solution
- Make sure interface is defined
- Switch species on
- Create tracer material (tracer and media)
- Switch from MRF to sliding mesh
- Define discrete particle model, click on injection and create
- Injection is surface type
- Select water first then go to material to change it under inert-particle
- X, Y, Z is 0 $ms^{-1}$, diameter is 1E-6m, temperature is 300K, start: 0.50s end: 0.57s
- Total flowrate: 0.01 $kgs^{-1}$ and select scale flowrate by face area
- Go to solve execute command and define macro-1
- Display particle tracks
- Release from injection 0, skip 30, colour by velocity magnitude, deselect auto range
- Draw grid adjust then click on display, close, then display particle tracks
- End macro and type macro-1
- Define macro-2
- File hardcopy, select jpeg, colour and resolution 1600 by 1600
- Save as NC-%t.jpg
- End macro and type /dis/hc NC-%t.jpg and click ok
- Deselect all equations and select tracer only
- Iterate time step size: 0.02, number of time step: 1000, max iteration per time step: 2

## *CONSTRUCTING MIXING TANK (STEADY-STATE) IN GAMBIT*

- Create tank wall, shaft and impellers
- Unite shaft and impellers to become one entity
- Create rotational zone around impellers
- Minus impellers-shaft volume from rotation zone volume (check retain option)
- Minus shaft volume from tank volume (uncheck retain option)
- Split rotational zone volume from the tank volume (check bidirectional and connected)
- Assign top, bottom and side faces of the rotational zone as interior
- Assign the face at the tank top as symmetry for open tank and wall for close tank
- Assign everything else as wall
- Assign size function: source-impeller faces and attachment-rotational zone volume
- Initialise size function, mesh the geometry, check mesh quality and then export mesh

# BIBLIOGRAPHY


Akhavan J. [1998] The chemistry of explosives, The Royal Society of Chemistry

Akiti O. and Armenante P.M. [2004], Experimentally-validated micromixing-based CFD model for fed-batch stirred-tank reactors, Vol 50, No 3, 566-577, AIChE Journal

Alder B.J. and Wainwright T.E. [1990], Studies in molecular dynamics II: behaviour of small number of spheres, Vol 33, 1439, Journal of Chemical Physics

Alexopoulos A.H., Maggioris D. and Kiparissides C. [2002], CFD analysis of turbulence non-homogeneity in mixing vessels – a two compartment model, Vol 57, 1735-1752, Chemical Engineering Science

Allen J.Y. and Matthews L.M. [2002], Radiation as a weapon of mass destruction, Vol 3, 248-255, Clinical Paediatrics Emergency Medicine

Alliet-Gaubert M., Sardeing R., Xuereb C., Hobbes P., Bertrand L. and Swaels P. [2006], CFD analysis of industrial multi-staged stirred vessels, Vol 45, 415-427, Chemical Engineering and Processing

Anderson J.D. Jr [1995], Computational fluid dynamics, Mc-Graw Hill

Anderson T.B. and Jackson R. [1967], A fluid mechanical description of fluidised beds, Vol 6, 527-534, I & EC Fundamentals

Aubin J., Fletcher D.F. and Xuereb C. [2004], Modelling turbulent flow in stirred tanks with CFD: the influence of the modelling approach, turbulence model and numerical scheme, Vol 28, 431-445, Experimental Thermal and Fluid Science

Aubin J., Le Sauze N., Bertrand J., Fletcher, D.F. and Xuereb C. [2004], PIV measurements of flow in an aerated tank stirred by a down- and an up-pumping axial flow impeller, Vol 28, 447-456, Experimental Thermal and Fluid Science

Aubin J. and Xuereb C. [2006], Design of multiple impeller stirred tanks for the mixing of highly viscous fluids using CFD, Vol 61, 2913-2920, Chemical Engineering Science

Bakker A. & Fasano J.B. [2000], Turbulent mixing and chemical reaction in stirred tanks, The Online CFM Book, www.bakker.org/cfm

Bakker A., Fasano J.B. & Myers K.J. [2000], Effects of flow pattern on the solids distribution in a stirred tank, The Online CFM Book, www.bakker.org/cfm

Bakker A., Haidari A.H. & Oshinowo L.M. [2001], Realise greater benefits from CFD, Chemical Engineering Progress

Baldyga J. and Makowski L. [2004], CFD modelling of mixing effects on the course of parallel chemical reactions carried out in a stirred tank, Vol 27, No 3, 225-231, Chemical Engineering Technology

Bao Y., Hao Z., Gao Z. & Smith J.M. [2005], Suspension of buoyant particles in a three phase stirred tank, Vol 60, 2283-2292, Chemical Engineering Science

Barkhudarov M.R. [1997], Is fluid flow important for predicting solidification ?, 7-10 July 1997, Presented at the Solidification Processing '97 Conference, Sheffield, U.K.

Basara B., Alajbegovic A. and Beader D. [2004], Simulation of single- and two-phase flows on sliding unstructured meshes using finite volume method, Vol 45, 1137-1159, International Journal For Numerical Methods In Fluids

Becker S. and Laurien E. [2003], Three-dimensional numerical simulation of flow and heat transport in high-temperature nuclear reactors, Vol 222, 189-201, Nuclear Engineering and Design

Beckermann C. [2002], Modelling of macrosegregation: applications and future needs, Vol 47, 243-261, International Materials Reviews

Bezzo F., Macchietto S. and Pantelides C.C. [2000], A general framework for the integration of computational fluid dynamics and process simulation, Vol 24, 653-658, Computers and Chemical Engineering

Bird R.B., Stewart W.E. and Lightfoot E.N [2002], Transport phenomena, John Wiley and Sons, second edition

Blazek J. [2001], Computational fluid dynamics: principles and applications, Elsevier Science

Bouyer D., Line A. and Do-Quang [2004], Experimental analysis of floc size distribution under different hydrodynamics in a mixing tank, Vol 50, Issue 9, 2064, AIChE Journal

Bowen R.M. [1976], Theory of mixtures, in Eringen A.C., editor, 1-127, Continuum Physics, Academic Press, New York

Brucato A., Ciofalo M., Grisafi F. and Tocco R. [2000], Non-Newtonian flow in the process industries, Vol 55, 291-302, Chemical Engineering Science

Cerny R., Kalbac A. and Prikryl P. [2000], Computational modelling of CdZnTe crystal growth from the melt, Vol 17, 34-60, Computational Materials Science

Chapman S. and Cowling T.G. [1990], The mathematical theory of non-uniform gases, Cambridge University Press, third edition

Chhabra R.P. and Richardson J.F. [1999], Non-Newtonian flow in the process industries, Butterworth-Heinemann

Chopey N.P. [2004], Handbook of chemical engineering calculations, McGraw-Hill, third edition

Chung T.J. [2003], Computational fluid dynamics, Cambridge University Press

Considine D.M. [1974], Chemical and process technology encyclopaedia, McGraw-Hill

Cooper P.W. [1996], Explosives engineering, Wiley-VCH

Coussot P. [2005], Rheometry of pastes, suspensions, and granular materials, Wiley Interscience,

Crowe C., SommerfieldM. And Tsuji Y. [1998], Multiphase flows with droplets and particles, CRC press

Cruse A., Marquardt W., Allgor R.J. and Kussi J. [2000], Integrated conceptual design of stirred tank reactors by periodic dynamic optimisation, Computers and Chemical Engineering

Dakshinamoorthy D., Khopkar A.R., Louvar J.F. and Ranade V.V. [2004], CFD simulations to study shortstopping runaway reactions in a stirred vessel, Vol 17, 355-364, Journal of Loss Prevention in the Process Industries

Date A.W. [2005], Introduction to computational fluid dynamics, Cambridge University Press

Dhotre M.T., Ekambara K. and Joshi J.B. [2004], CFD simulation of sparger design and height to diameter ratio on gas hold-up profiles in bubble column reactors, Vol 28, 407-421, Experimental Thermal and Fluid Science

Dijkstra M.F.J., Buwalda H., Jong A.W.F., Michorius A., Winkelman, J.G.M. and Beenackers A.A.C.M. [2001], Experimental comparison of three reactor designs for photocatalytic water purification, Vol 56, 547-555, Chemical Engineering Science

Ding J. and Gidaspow D. [1990], A bubbling fluidisation model using kinetic theory of granular flow, Vol 36, No 4, 523-538, AIChE Journal

Dinh T.N., Bui, V.A., Nourgaliev R.R., Okkonen T. and Sehgal B.R. [1996], Modelling of heat and mass transfer processes during core melt discharge from a reactor pressure vessel, Vol 163, 191-206, Nuclear Engineering and Design

Downey D., Giles D.K. and Delwiche M.J. [1998], Finite element analysis of particle and liquid flow through an ultraviolet reactor, Vol 21, 81-105, Computers and Electronics in Agriculture

Eadie, J. [1971], The viscosity of RDX/TNT suspensions, Report 431, Copy 29, Department of Supply, Australian Defence Scientific Service, Defence Standards Laboratories

Eadie, J. and Milne D.J. [1968], The rheology of composition B, Part I, The particle size distribution of Albion grade 1A RDX, Technical note 116, Department of Supply, Australian Defence Scientific Service, Defence Standards Laboratories

Eadie, J. and Milne D.J. [1968], The rheology of composition B, Part II, viscosity variations and mechanisms, Technical note 115, Department of Supply, Australian Defence Scientific Service, Defence Standards Laboratories

Eadie, J. and Milne D.J. [1969], The rheology of composition B, Part III, Influence of RDX particle size and shape changes, Technical note 125, Department of Supply, Australian Defence Scientific Service, Defence Standards Laboratories

Eder G. [1997], Mathematical modelling of crystallisation processes as occurring in polymer processing, Vol 30, No 6, 3807-3815, Nonlinear Analysis, Theory, Methods & Applications

Endo H., Kuwana K., Saito K., Qian D., Andrews R. and Grulke E.A. [2004], CFD prediction of carbon nanotube production rate in a CFD reactor, Vol 387, 307-311, Chemical Physics Letters

Ergun S. [1952], Fluid flow through packed columns, Vol 48, No 2, 89-94, Chemical Engineering Progress

Fedoroff B.T., Aaronson H.A., Reese E.F., Sheffield O.E. and Clift G.D. [1960], Encyclopaedia of explosives and related items Vol 1 & 2 Army Research and Development Command Tacom, Ardec, Warheads, Energetics and Combat Support Centre, Picatinny Arsenal, New Jersey, USA

Feinberg M. [2000], Non-Newtonian flow in the process industries, Vol 55, 3553-3565, Chemical Engineering Science

Fitzgerald, D.J., Sztajnkrycer M.D. and Grocco T.J. [2003], Chemical weapon functional exercise – Cincinnati: Observations and lessons learned from a 'typical medium-sized' city's response to simulated terrorism utilising weapons of mass destruction, Vol 118, 205-214, Public Health Reports

Fluent [2006], User's Manual, Release 6.2

Fluent [2007], User's Manual, Release 6.3

Fogler H.S. [1992], Elements of chemical reaction engineering, Prentice Hall PTR, second edition

Fordham S. [1980], High explosives and propellants, Pergamon Press

Fu, S., Launder B.E. and Leschziner M.A. [1987] Modelling strongly swirling recirculating jet flow with Reynolds-stress transport closures, in sixth symposium on Turbulent shear flows, Toulouse, France

Gao P.Z., Liu S.L., Chow W.K. and Fong N.K. [2004], Large eddy simulations for studying tunnel smoke ventilation, Vol 19, 577-586, Tunnelling and Underground Space Technology

Garner R.P., Wong K.L., Ericson S.C., Baker A.J. and Orzechowski J.A. [2004], CFD validation for contaminant transport in aircraft cabin ventilation flow fields, Report No A999324, 1-6, Federal Aviation Administration Oklahoma City

Gibson M.M. and Launder B.E. [1978], Ground effects on pressure fluctuations in the atmospheric boundary layer, Vol 86, 491-511, Journal of Fluid Mechanics

Gidaspow D., Bezburuah R. and Ding J. [1992], Hydrodynamics of circulating fluidised beds, kinetic theory approach, In Fluidisation VII, 75-82, Proceedings of the 7th Engineering Foundation Conference on Fluidisation

Graham A.L., Mammoli A.A. and Busch M.B. [1998], Effects of demixing on suspension rheometry, Vol 37, 139-150, Rheology Acta

Gran I.R. and Magnussen B.F. [1996], A numerical study of a bluff-body stabilised diffusion flame – part 2: influence of combustion modelling and finite-rate chemistry, 119-191, Combustion Science and Technology

Gumy D., Rincon A.G., Hajdu R. and Pulgarin C. [2006], Solar photocatalysis for detoxification and disinfection of water: different types of suspended and fixed $TiO_2$ catalysts study, Vol 80, 1376-1381, Solar Energy

Harvey III A.D., Wood S.P. and Leng D.E. [1997], Experimental and computational study of multiple impeller flows, Vol 52, 1479-1491, Chemical Engineering Science

Harzallah O.A. and Dupuis D. [2003], Rheological properties of suspensions of $TiO_2$ particles in polymer solutions, Vol 42, 10-19, Rheology Acta

Heinrich J.C. and Poirier D.R. [2004], Convection modelling in directional solidification, Vol 332, 429-445, Comptes Rendus Mecanique

Hirakawa T., Daimon T., Kitazawa M., Ohguri N., Koga C., Negishi N., Matsuzawa S. and Nosaka Y. [2007] An approach to estimating photocatalytic activity of $TiO_2$ suspension by monitoring dissolved oxygen and superoxide ion on decomposing organic compounds, Vol 190, 58-68, Journal of Photochemistry and Photobiology, A: Chemistry

Hirt C.W. and Nichols B.D. [1981], Volume of fluid (VOF) method for the dynamics of free boundaries, Vol 39, 201-225, Journal of Computational Physics

Hoffman J.D. [2001], Numerical methods for engineers and scientists, Marcel Dekker, second edition

Hoyle W. [1997], Pilot plants and scale-up of chemical processes, The Royal Society of Chemistry

Hoyle W. [1999], Pilot plants and scale-up of chemical processes II, The Royal Society of Chemistry

Ibdir H. and Arastoopour H. [2005], Modelling of multi-type particle flow using kinetic approach, Vol 51, No 6, 1620-1632, AIChE Journal

Im I-T., Kim W-S and Lee K-S [2001], A unified analysis of filling and solidification in casting with natural convection, Vol 44, 1507-1515, International Journal of Heat and Mass Transfer, in press, Chemical Engineering Science

Kee N.C.S. and Tan R.B.H. [2002], CFD simulation of solid suspensions in mixing vessels, Vol 80, 721-726, The Canadian Journal of Chemical Engineering

Kerdouss F., Bannari A. and Proulx P. [2006], CFD modelling of gas dispersion and bubble size in a double turbine stirred tank, Vol 61, 3313-3322, Chemical Engineering Science

Kelly W. and Gigas B. [2003], Using CFD to predict the behaviour of power law fluids near axial-flow impellers operating in the transitional flow regime, Vol 58, 2141-2152, Chemical Engineering Science

Khopkar A.R., Aubin J., Xuereb C., Le Sauze N., Bertrand J. and Ranade V.V. [2001], Measurement and simulation of fluid flow in agitated solid/liquid suspensions, Vol 24, No 6, 639-643, Chemical Engineering Technology

Kilander J., Blomstrom S., Rasmuson, A. [2007], Scale-up behaviour in stirred square flocculation tanks, Vol 62, 1606-1618, Chemical Engineering Science

Kohler J. and Meyer R. [1993], Explosives, VCH Publication, fourth edition

Kohnen C. and Bohnet M. [2001], Measurement and simulation of fluid flow in agitated solid/liquid suspensions, Vol 24, No 6, 639-643, Chemical Engineering Technology

Kolesar P.J. [1993], The relevance of research on statistical process control to the total quality movement, Vol 10, 317-338, Journal of Engineering and Technology Management

Kresta S.M., Mao D. and Roussinova V. [2006], Batch blend time in square stirred tanks, Vol 61, 2823-2825, Chemical Engineering Science

Krishna R., Van Baten J.M. and Urseanu M.I. [2000], Three-phase Eulerian simulations of bubble column reactors operating in the churn-turbulent regime: a scale up strategy, Vol 55, 3275-3286, Chemical Engineering Science

Kumaresan T. and Joshi J.B. [2006], Effect of impeller design on the flow pattern and mixing in stirred tanks, Vol 115, 173-193, Chemical Engineering Journal

Kuzmanic N. & Ljubicic B. [2001], Suspension of floating solids with up-pumping pitched blade impellers; mixing time and power characteristics, Vol 84, 325-333, Chemical Engineering Journal

Laakkonen M., Moilanen P., Alopaeus V., Aittamaa J. [2007] Modelling local bubble size distributions in agitated vessels, Vol 62, 721-740, Chemical Engineering Science

Lam R.C.W., Leung M.K.H., Leung D.Y.C. and Vrijmoed L.L.P. [2007], Visible-light-assisted photocatalytic degradation of gaseous formaldehyde by parallel-plate reactor coated with Cr ion-implanted $TiO_2$ thin film, Vol 91, 54-61, Solar Energy Materials and Solar Cells

Lamberto D.J., Alvarez M.M. and Muzzio F.J. [1999], Experimental and computational investigation of the laminar flow structure in a stirred tank, Vol 54, 919-942, Chemical Engineering Science

Lamberto D.J., Alvarez M.M. and Muzzio F.J. [2001], Experimental and computational investigation of the laminar flow structure in a stirred tank, Vol 56, 4887-4899, Chemical Engineering Science

Larson R.G. [1999], The structure and rheology of complex fluids, Oxford University Press

Launder B.E. [1989], Second-moment closure and its use in modelling turbulent industrial flows, Vol 9, 963-985, International journal for numerical methods in fluids

Launder B.E. [1989], Second-moment closure: present... and future?, Vol 10, No. 4, 282-300, International Journal of Heat and Fluid flow

Lea J. [1998], The photocatalytic degradation of organic contaminants in water, Masters Thesis, The University of New South Wales

Lea J. and Adesina A.A. [2007], CFD-assisted optimisation of the nitrator design for military propellant production, ICAEM July 2-4 2007, London, England

Lea J. and Adesina A.A. [2007], Development of the design guidelines using CFD technology for a particles suspension mixing tank, ICAEM July 2-4 2007, London, England

Lea J. and Adesina A.A. [2007], CFD diagnosis of the cyclotol manufacturing plant: product quality and process operation, Vol 2, Issue 1, Article 2, Page 1-43, Journal of Chemical Product and Process Modelling

Lea J. and Adesina A.A. [2006], Avoiding explosive outcomes, Fluent News, fall issue, 26-27, Fluent USA

Lea J. and Adesina A.A. [2006], Improving explosives production with fluid modelling, Engineers Australia, November, 56-57, IEAust

Lea J. and Adesina A.A [2006], Simulation of the mixing tank for the production of military high explosive RDX/TNT – A computational fluid dynamics approach, CHEMECA September 17-20 2006, Auckland, New Zealand

Lea J. and Adesina A.A [2006], Analysis of the mixing tank for cyclotol production, APCCHE August 27-30 2006, Kuala Lumpur, Malaysia

Lea J. and Adesina A.A. [2001], Oxidative degradation of 4-nitrophenol in UV-illuminated titania suspension, Vol 76, 803-810, Journal of Chemical Technology and Biotechnology

Lea J. and Adesina A.A. [1999], Continuous bubble column reactor for the photocatalytic causticisation of sodium oxalate, Vol 54, 2209-2216, Chemical Engineering Science

Lea J. and Adesina A.A. [1998], The photo-oxidative degradation of sodium dodecyl sulphate in aerated aqueous $TiO_2$ suspension, Vol 118, 111-122, Journal of Photochemistry and Photobiology A: Chemistry

Lea J., Gehrig A., Flavel P. and Adesina A.A [2005], Optimisation of the nitrator for the production of nitrocellulose using computational fluid dynamics modelling, PARARI Nov 8-10, Melbourne, Australia

Lea J., Gehrig A., Flavel P. and Adesina A.A [2005], Application of numerical method for the characterisation of the nitrator employed for the manufacture of rocket propellant, SciCADE May 23-27 2005, Nagoya, Japan

Lea J., Gehrig A., Flavel P. and Adesina A.A [2005], The computational fluid dynamics modelling and simulation of nitrator employed for the manufacture of military propellant, ICCHMT May 17-20 2005, Paris, France

Lea J., Reid J. and Adesina A.A. [2007], CFD simulations of a suspension mixing tank for the pharmaceutical industries, FLUIDS January 17-19 2007, Gold Coast, Australia

Lebowitz J.L. [1964], Exact solution of generalised Percus-Yevick equation for a mixture of hard spheres, Vol 133, No 4A, A895-A899, The Physics Review

Lee R.L., Albritton J.R. and Ermak D.L. Kim J. [1997], Computational fluid dynamics modelling for emergency preparedness and response, Vol 12, No 1, 43-50, Environmental Modelling and Software

Lee Y-H, Min K.G, Han C., Chang K.S. and Choi T.H. [2004], Process improvement methodology based on multivariate statistical analysis methods, Vol 12, 945-961, Control Engineering Practice

Lee Y.S. and Wagner N.J. [2003], Dynamic properties of shear thickening colloidal suspensions, Vol 42, 199-208, Rheology Acta

Letellier B., Xuereb C., Swaels P, Hobbes P. and Bertrand J. [2002], Scale-up in laminar and transient regimes of a multi-stage stirrer, a CFD approach, Vol 57, 4617-4632, Chemical Engineering Science

Lewis A.E. and Ochieng A. [2006], CFD simulation of solids off-bottom suspension and cloud height, Vol 82, 1-12, Hydrometallurgy

Li Y., Yang G.Q., Zhang J.P. and Fan L.-S [2001], Numerical studies of bubble formation dynamics in gas-liquid-solid fluidisation at high pressures, Vol 116, 246-260, Powder Technology

Lun C.K.K., Savage S.B., Jeffrey D.J. and Chepurniy N. [1984], Kinetic theories for granular flow: inelastic particles in couette flow and slightly inelastic particles in a general flow field, Vol 140, 223-256, Journal of Fluid Mechanics

Ma D. and Ahmadi G. [1990], A thermodynamical formulation for dispersed multiphase turbulent flows, Vol 16, 323-351, International Journal of Multiphase Flow

Magnussen B.F. and Hjertager B.H. [1976], On mathematical models of turbulent combustion with special emphasis on soot formation and combustion, 16th International Symposium on Combustion, The Combustion Institute.

Marti I., Hofler O., Fischer P. and Windhab E.J. [2005], Rheology of concentrated suspensions containing mixtures of spheres and fibres, Vol 44, 502-512, Rheology Acta

Mathiesen V., Solberg T. and Hjertager B.H. [2000], Predictions of gas/particle flow with an Eulerian model including a realistic particle size distribution, Vol 112, 34-45, Powder Technology

Matonis D., Gidaspow D. and Bahary M. [2002], CFD simulation of flow and turbulence in a slurry bubble column, Vol 48, No 7, 1413-1429, AIChE Journal

Meier A., Ganz J. and Steinfeld A. [1996], Modelling of a novel high-temperature solar chemical reactor, Vol 51, No 11, 3181-3186, Chemical Engineering Science

Micale G., Montante G., Grisafi F., Brucato A. And Godfrey J. [2000], CFD simulation of particle distribution in stirred vessels, Vol 78, Part A, 435-444, Trans IchemE

Mills A. and Hunte L. [1997], An overview of semiconductor photocatalysis, Vol 108, 1-35, Journal of Photochemistry and Photobiology, A: Chemistry

Missirlis K.A., Assimacopoulous D. and Mitsoulis E. [1998], A finite Vol approach in the simulation of viscoelastic expansion flows, Vol 78, 91-118, Journal of Non-Newtonian Fluid Mechanics

Montante G., Mostek M., Jahoda M. and Magelli F. [2005], CFD simulations and experimental validation of homogenisation curves and mixing time in stirred Newtonian and pseudoplastic liquids, Vol 60, 2427-2437, Chemical Engineering Science

Montante G., Lee K.C., Brucato A. and Yianneskis M. [2001], Experiments and predictions of the transition of the flow pattern with impeller clearance in stirred tanks, Vol 25, 729-735, Computers and Chemical Engineering

Montante G., Lee K.C., Brucato A. and Yianneskis M. [2001], Numerical simulations of the dependency of flow pattern on impeller clearance in stirred vessels, Vol 56, 3751-3770, Chemical Engineering Science

Montgomery D.C [2005], Introduction to statistical quality control, John Wiley and Sons, fifth edition

Morsi S.A. and Alexander A.J. [1972], An investigation of particle trajectories in two-phase flow systems, Vol 55, No 2, 193-208, Journal of Fluid Mechanics

Morud K.E. and Hjertager B.H. [1996], LDA measurements and CFD modelling of gas-liquid flow in a stirred vessel, Vol 51, 233-249, Chemical Engineering Science

Mousavi S.M., Zamankhan P. and Jafari A. [2006], Computer simulations of sodium formate solution in a mixing tank, In press, Communications in Nonlinear Science and Numerical Simulation

Myers K.J., Reeder M.F. and Fasano J.B. [2002], Optimise mixing by using the proper baffles, February 2002, Chemical Engineering Progress

Nowak A.J., Bialecki R.A., Fic A. and Wecel G. [2003], Analysis of fluid flow and energy transport in Czochralski's process, Vol 32, 85-95, Computers & Fluids

Nowak A.J., Bialecki R.A., Fic A., Wecel G., Wrobel L.C. and Sarler B. [2002], Coupling of conductive, convective and radiative heat transfer in Czochralski crystal growth process, Vol 25, 570-576, Computational Materials Science

Oakland J.S. [2003], Statistical Process Control, Butterworth-Heinemann, fifth edition

Oberkampf W.L. and Trucano G.T. [2002], Verification and validation in computational fluid dynamics, Vol 38, 209-272, Progress in Aerospace Sciences

Ogawa S., Umemura A. and Oshima N. [1980], On the equation of fully fluidised granular materials, Vol 31, 483, Journal of Applied Mathematical Physics

Oller I., Gernjak W., Maldonado M.I., Perez-Estrada L.A., Sanchez-Perex J.A. and Malato S. [2006], Solar photocatalytic degradation of some hazardous water-soluble pesticides at pilot-plant scale, Vol B138, 507-517, Journal of Hazardous Materials

Ollis, D.F., Pelizzetti, E. and Serpone, N. [1991], Photocatalysed destruction of water contaminants, Vol 25, No 9, 1522-1529

Oppenlander, T. [2003], Photochemical purification of water and air, Wiley VCH

Ozcan-Taskin G. & Wei H. [2003], The effect of impeller-to-tank diameter ratio on draw-down of solids, Vol 58, 2011-2022, Chemical Engineering Science

Pareek V.K., Cox S.J., Brungs M.P., Young B. and Adesina A.A. [2003], Computational fluid dynamic (CFD) simulation of a pilot-scale annular bubble column photocatalytic reactor, Vol 58, 859-865, Chemical Engineering Science

Parry M.A. and Billon H.H. [1987], The viscosity of (molten) RDX/TNT suspensions, Report 57-1 to 57-17, Materials Research Laboratories

Parry M.A. and Billon H.H. [1988], A note on the coefficient of viscosity of pure molten 2,4,6-trinitrotoluene (TNT), Vol 27, 661-663, Rheologica Acta

Paul E.L., Atiemo-Obeng V.A. and Kresta S.M. [2004], Handbook of industrial mixing – science and practice, Wiley Interscience

Perry R.H. and Green D.W. [1999], Perry's chemical engineers' handbook, McGraw-Hill, seventh edition

Popat N.R., Catlin C.A., Arntzen B.J., Lindstedt R.P., Hjertager B.H., Solberg T., Saeter O. and Van den Berg A.C. [1996], Investigations to improve and assess the accuracy of computational fluid dynamic based explosion models, Vol 45, 1-25, Journal of Hazardous Materials

Prieto O., Fermoso J., Nunez Y., Valle J.L. and Irusta R. [2005], Decolouration of textile dyes in wastewaters by photocatalysis with $TiO_2$, Vol 79, 376-383, Solar Energy

Radovic Z. and Lalovic M. [2004], Numerical simulation of steel ingot solidification process, Article in press, Journal of Materials Processing Technology

Rahimi A. and Mann R. [2001], Macro-mixing, partial segregation and 3-D selectivity fields inside a semi-batch stirred reactor, Vol 56, 763-769, Chemical Engineering Science

Rahimi M. and Parvareh A. [2005], Experimental and CFD investigation on mixing by a jet in a semi-industrial stirred tank, Vol 115, 85-92, Chemical Engineering Journal

Ranade V.V. [1997], An efficient computational model for simulating flow in stirred vessels: a case of Rushton turbine, Vol 52, No 24, 4473-4484, Chemical Engineering Science

Ranade V.V. [2002], Computational flow modelling for chemical reactor engineering, Process Systems Engineering, Academic Press

Ranade V.V. and Deshpande V.R. [1999], Macro-mixing, partial segregation and 3-D selectivity fields inside a semi-batch stirred reactor, Vol 54, 2305-2315, Chemical Engineering Science

Rehm W., Gerndt M., Jahn W., Semler F. and Jones I. [1998], CFD simulation of deflagration-detonation processes using vector- and parallel computing systems, Vol 22, 811-822, Applied Mathematical Modelling

Rerko R.S., de groh H.C. and Beckermann C. [2003], Effect of melt convection and solid transport on macrosegregation and grain structure in equiaxed Al-Cu alloys, Vol A347, 186-197, Applied Mathematical Modelling

Revstedt J., Fuchs L., Kovacs T. and Tragardh C. [1998], Large eddy simulations of the turbulent flow in a stirred reactor, Vol 53, No 24, 4041-4053, Chemical Engineering Science

Revstedt J., Fuchs L., Kovacs T. and Tragardh C. [2000], Influence of impeller type on the flow structure in a stirred reactor, Vol 46, No 12, 2373-2382, AIChE Journal

Richardson J.R. and Zaki W.N. [1954], Sedimentation and fluidisation: Part I Vol , 35-53, Trans IchemE

Rigopoulos S. and Jones A. [2003], A hybrid CFD – reaction engineering framework for multiphase reactor modelling: basic concept and application to bubble column reactors, Vol 58, 3077-3089, Chemical Engineering Science

Rudniak L., Machniewski P.M., Milewska A. and Molga E. [2004], CFD modelling of stirred tank chemical reactors: homogeneous and heterogeneous reaction systems, Vol 59, 5233-5239, Chemical Engineering Science

Sahu A.K., Kumar P., Patwardhan A. W. and Joshi J.B. [1999], CFD modelling and mixing in stirred tanks, Vol 54, 2285-2293, Chemical Engineering Science

Salas S., Hille E. and Etgen G. [2003], One and several variables calculus, John Wiley and Sons, ninth edition

Samanta D. and Zabaras N. [2004], Solidification and macrosegregation in aluminium alloys on uneven surfaces, CFD Modelling and Simulation in Materials Processes

Schaeffer D.G. [1987], Instability in the evolution equations describing incompressible granular flow, Vol 66, 19-50, Journal of Differential Equations

Schiller L. and Naumann Z. [1935], Vol 77, 318, Ver. Deutsch. Ing

Sha Z., Palosaari S., Oinas P. and Ogawa K. [2001], CFD simulation of solid suspension in a stirred tank, Vol 34, No 5, 621-626, Journal of Chemical Engineering of Japan

Sheng J., Meng H. and Fox R.O. [1998], Validation of CFD simulations of a stirred tank using particle image velocimetry data, Vol 76, 611-625, The Canadian Journal of Chemical Engineering

Shepel S.V. and Paolucci S. [2002], Numerical simulation of filling and solidification of permanent mould castings, Vol 22, 229-248, Applied Thermal Engineering

Srikaeo K, Furst J.E. and Ashton J. [2005], Characterisation of wheat-based biscuit cooking process by statistical process control techniques, Vol 16, 309-317, Food Control

Sinnott R.K. [1993], Coulson & Richardson's chemical engineering, Vol 6, Pergamon Press, second edition

Sommerfeld M. and Decker S. [2004] State of the art and future trends in CFD simulation of stirred vessel hydrodynamics, Vol 27, No. 3, Chemical Engineering Technology

Syamlal M. and O'Brien T.J. [1989], Computer simulation of bubbles in a fluidised bed, Vol 85, 22-31, AIChe Symposium Series

Syamlal M., Rogerss W. and O'Brien T.J. [1993], MFIX documentation: Vol 1, Theory guide, DOE/METC-9411004, NTIS/DE9400087, National Technical Information Service, Springfield, VA

Szalai E.S., Arratia P., Johnson, K. and Muzzio F.J. [2004], Mixing analysis in a tank stirred with Ekato Intermig impellers, Vol 59, 3793-3805, Chemical Engineering Science

Tatterson G.B. [1994], Scaleup and design of industrial mixing processes, McGraw-Hill Inc

Tewkesbury H., Stapley A.G.F. and Fryer P.J. [2000], Modelling temperature distributions in cooling chocolate moulds, Vol 55, 3123-3132, Chemical Engineering Science

Thomson J.R. and Koronacki J. [2002], Statistical process control – the Deming paradigm and beyond, Chapman and Hall, second edition

Tiburtius E.R.L., Peralta-Zamora P. and Emmel A. [2005], Treatment of gasoline-contaminated waters by advanced oxidation processes, Vol 26, 86-90, Journal of Hazardous Materials

Togawa T. [1999], Considering the long-term survival of the human race, Vol 21, 233-245, Technology in Society

Toorman E.A. [1997], Modelling the thixotropic behaviour of dense cohesive sediment suspensions, Vol 36, 56-65, Rheology Acta

Tweeddal E M. [2003], Managing risk and reliability of process plants, Gulf Professional Publishing

Uhl V.W. and Gray J.B. [1966], Mixing theory and practice, Academic Press

Uhl V.W. and Gray J.B. [1967], Mixing theory and practice II, Academic Press

Ullmann's [1998], Ullmann's encyclopaedia of industrial chemistry, Electronic Release, Wiley VCH, sixth edition

Urbanski T. [1964], Chemistry and technology of explosives I, Pergarmon Press

Urbanski T. [1965], Chemistry and technology of explosives II, Vol 2 Pergarmon Press

Urbanski T. [1967], Chemistry and technology of explosives III, Vol 3 Pergarmon Press

Urbanski T. [1984], Chemistry and technology of explosives IV, Vol 4, Pergarmon Press

Van Dam H A.J.H., Van der Hagen T.H.J.J. and Lathouwers D. [2002], Space-dependent kinetics simulation of a gas-cooled fluidised bed nuclear reactor, Vol 219, 225-245, Nuclear Engineering and Design

Wen C-Y. and Yu Y.H. [1966], Mechanics of fluidisation, Vol 62, 100-111, Chemical Engineering Progress Symposium Series

Wu J., Graham L.J., Nguyen B., Nabil Noui Mehidi M. [2006], Energy efficiency study on axial flow impellers, Vol 45, 625-632, Chemical Engineering and Processing

Wu M., Ludwig A., Buhrig-Polaczek A. and Fehlbier M. [2003], Influence of convection and grain movement on globular equiaxed solidification, Vol 46, 2819-2832, International Journal of Heat and Mass Transfer

Xu C., Killmeyer R., Gray M.L., Khan S.U.M. [2006], Enhanced carbon doping of n-TiO2 thin films for photoelectrochemical water splitting, Vol 8, 1650-1654, Electrochemistry Communications

Xu Y. and McGrath G. [1996], CFD predictions of stirred tank flows, Vol 74, Part A, 471-475, Trans IchemE

Xuereb C. and Bertrand J. [1996], 3-D hydrodynamics in a tank stirred by a double-propeller system and filled with a liquid having evolving rheological properties, Vol 51, 1725-1734, Chemical Engineering Science

Yildirim O.E. and Basaran O.A. [2001], Deformation and breakup of stretching bridges of Newtonian and shear-thinning liquids: comparison of one- and two-dimensional models, Vol 56, 211-233, Chemical Engineering Science

Youngs D.L. [1982], Time-dependent multi-material flow with large fluid distortion, in Morton K.W. and Baines M.J., editors, Academic Press, Numerical Methods for Fluid Dynamics.

Zakrzewska B. And Jaworski Z. [2004], CFD modelling of turbulent jacket heat transfer in a Rushton turbine stirred vessel, Vol 27, No 3, 237-242, Chemical Engineering Technology

Zalc J.M., Alvarez M.M., Muzzio F.J. and Arik B.E. [2001], Extensive validation of computed laminar flow in a stirred tank with three Rushton turbines, Vol 47, No 10, 2144-2154, AIChE Journal

Zou L., Luo Y., Hooper M. and Hu E. [2006], Removal of VOCs by photocatalysis process using adsorption enhanced $TiO_2$-$SiO_2$ catalyst, Vol 45, 959-964

Zukas J.A. and Walters W.P. [1998], Explosive effects and applications, Springer-Verlag New York

Zwietering T.N. [1958], Suspending of solid particles in liquid by agitators, Vol 8, 244-253, Chemical Engineering Science